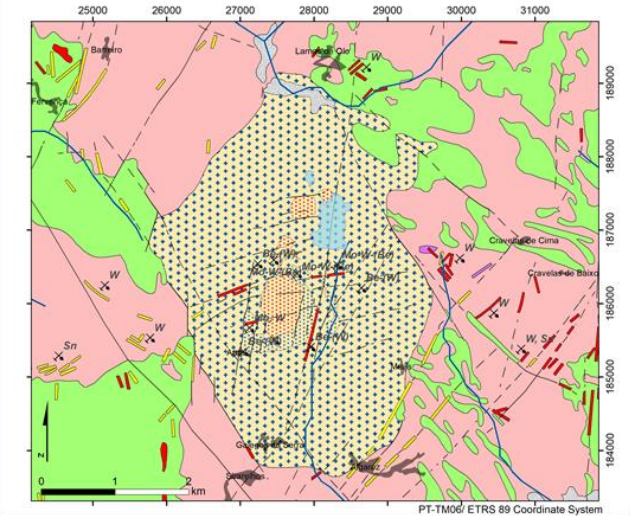


Post-tectonic Variscan magmatism from northwest Iberia. Implications for W-Mo metallogeny. Case study of Lamas de Olo Pluton

Cláudia da Conceição Ferreira da Cruz
Programa Doutoral em Geociências
Departamento de Geociências, Ambiente e Ordenamento do Território
2020

Orientador
Helena Maria Sant'Ovaia Mendes da Silva, Professor Associado, FCUP

Coorientador
Fernando Manuel Pereira de Noronha, Professor Catedrático, FCUP

This work was financially supported by SFRH/BD/109693/2015 (FCT Portugal).

This work was partially funded by the *Fundação para a Ciência e a Tecnologia* (FCT) under UID/GEO/04683/2013, UID/GEO/04683/2019, and UIDB/04683/2020 projects, NewOreS project (ERA-MIN/0002/2014), and ESMIMET project (0284_ESMIMET_3_E) funded by the European Regional Development Fund (FEDER) through the Spain-Portugal Interreg V-A Programme (POCTEP).

ACKNOWLEDGMENTS

"Aqueles que passam por nós não vão sós.
Deixam um pouco de si, levam um pouco de nós."
Antoine de Saint-Exupery

During this work, many people have contributed to its development and have helped me to complete this project. It is not an easy task, in a few words, to express my thanks to all those who supported and encouraged me throughout this work, therefore, I hope that over the years I have been able to express my appreciation and respect to all teachers and colleagues. Thus, I must express my gratitude to all who helped me complete this project.

A particular thank you to Professor Helena Sant'Ovaia and Professor Fernando Noronha as my Ph.D. supervisors, with whom I discussed firsthand the results and contributed to the improvement of the document. They supported me throughout this entire process, allowing me to grow, both in science and as a person. Thank you for the friendship!

To José Carlos, thank you very much for the helpful and crucial collaboration in the fieldwork. Collecting samples with a portable drill machine was a hard task, which was only possible with teamwork. Thank you for your help, positivity, and friendship.

This work has a multidisciplinary approach, thus it included the contribution of several researchers and professors from *Faculdade de Ciências da Universidade do Porto* (FCUP, Portugal) and other institutions. I express my thanks to:

Professor Irene Raposo from *Instituto de Geociências da Universidade de São Paulo* (Brasil), who helped us in remanence study on rock samples from studied granite. Her help was fundamental to the anisotropy of anhysteretic remanent magnetization acquisition data and a healthy partnership between FCUP and *Universidade de São Paulo* which was established.

Thank you Professor Philippe Olivier and Sonia Rousse for the thermomagnetic measurements carried out in Toulouse and for the helpful comments and explanations during the advanced training in the *Université de Toulouse III - Paul Sabatier* (France). To professor Philippe thanks for the hospitality, during the entire time I was in Toulouse and for your friendship.

Professor Eric Font from *Instituto Dom Luis* (Portugal), thank you for the helpful guidance in paleomagnetism and explanations during the analysis carried out in the *Instituto Dom Luis* facilities.

Thank you Professor Joaquim Góis, from *Faculdade de Engenharia da Universidade do Porto* (Portugal), for the helpful explanation on geostatistical approaches which allowed interesting results. I appreciate all of the comments and suggestions.

Professor José Martinho Lourenço, from *Universidade de Trás-os-Montes e Alto Douro* (Portugal), who was part of the field team during the gravimetric survey and helped in the gravimetric data processing. I express my thanks for your friendship and hospitality during the gravimetric acquisition data.

Professor Rui Teixeira, from *Universidade de Trás-os-Montes e Alto Douro* (Portugal), my thanks for the help in the DGPS acquisition data and during the gravimetric campaigns.

Professor Fernando Almeida, from *Universidade de Aveiro* (Portugal), for all geophysics explanations, especially in the gravimetric data processing. I'm grateful for the informatics support and for always being available to help and answer my doubts.

Thank you Professor Helena Brites, from FCUP, for the useful tips, suggestions, and guidance in the geochemical data interpretation.

Thank you Engineer Cristina Carvalho and Professor Machado Leite for allowing the density measurements in the *Laboratório Nacional de Energia e Geologia* (Porto, Portugal) facilities and for all of your support during the measurements.

Thank you to my colleague Ana Machadinho, from *Universidade de Coimbra* (Portugal), who taught me the basic topics to work with modeling software, the *Oasis Montaj*.

To all additional important people, who I had the opportunity to have excellent discussions and brainstorming: Professors Maria dos Anjos Ribeiro, Armanda Dória, Rui Dias, Rui Moura and Pedro Nogueira, as well Noel Moreira, Natália Ferreira, and Ivete Azevedo. To all, my sincere thanks. Thank you Professors Alexandre Lima, Ângela Almeida, António Guerner, and Deolinda Flores for kindness and for always being available when it was necessary.

I would like to thank the staff and my colleagues at the *Departamento de Geociências, Ambiente e Ordenamento do Território*. Thank you Mónica Alves, Isabel Sá, Cristina Vilas Boas, Joana Damásio, Paulo Ferreira, Irene Costa, and Cândida Neto for the availability

during all the years. I would like to thanks to António and Ricardo, who I spent some time discussing my work, to colleagues who I shared the office room with, namely Sara, Ana Marta, Luís, and Ana Cláudia, as well as to Joana, Paula, Violeta, and Lia, which were always present in my Ph.D. path. Thanks to all for their patience and support during all these years.

At last, to the most important people in my life, I would like to thank my family and friends:

To my parents, Maria da Conceição and Manuel Cruz, for all their support and patience, especially on the less quiet days. Thanks for the tranquility and peace which you transmit to me! Thanks to my godmother Cândida, and to my grand-uncles Joaquim Cruz and Luisinha, for all the support and for being present at all stages of my life.

To my course friends, Márcia S., Mariana, Sara, Márcia P., and Pedro, who have always been present since 2005. To my “caver” friends who were my escape from the daily routine. To “A Malta”, the family I chose, thank you for all! Alexandra, Lígia, Zaida, João, Carlos, Sara, Diogo, Silvia, Telma, Ivo, Nuno, Jorge, Fabiana, Cláudia, and Rodolfo, you are my support, and with you, happiness is guaranteed. Thanks for all of the adventures, board games, and laughs!

COLLABORATIONS AND PARTNERSHIPS

The obtained results are a fruit of scientific research collaborations involving academic universities, institutes, and organizations from Portugal and other countries, namely: Portugal, France, and Brasil.

Universities and faculties

- Portugal:
    - *Faculdade de Ciências da Universidade do Porto (FCUP)*
    - *Faculdade de Engenharia da Universidade do Porto (FEUP)*
    - *Universidade de Aveiro (UA)*
    - *Universidade de Trás-os-Montes e Alto Douro (UTAD)*
    - *Universidade de Coimbra (UC)*

- Other countries:
    - *Université de Toulouse III - Paul Sabatier, Toulouse, France*
    - *Universidade de São Paulo (USP), São Paulo, Brasil.*

Engaged laboratories, departments and institutes

- Portugal:
    - *Departamento de Geociências, Ambiente e Ordenamento do Território (DGAOT) – FCUP*
    - *Instituto de Ciências da Terra – Pólo Porto (ICT-Porto)*
    - *Laboratório Nacional de Energia e Geologia – Porto (LNEG – Porto)*
    - *Instituto Dom Luís (IDL)*
    - *Departamento de Engenharia de Minas – FEUP*
    - *Centro de Recursos Naturais e Ambiente (CERENA)*
    - *Departamento de Geociências – UA*
    - *Departamento de Geologia – UTAD*
    - *Departamento de Ciências da Terra – UC*

- Other countries:
    - *Instituto de Geociências – USP*

ABSTRACT

The Lamas de Olo Pluton (LOP) is a small outcrop located in the Northern part of Central Iberian Zone, in the Iberian Variscan belt. The LOP is a post-tectonic (*ca*. 297.19 ± 0.73 Ma) pluton composed of different biotite granites: Lamas de Olo (medium to coarse-grained porphyritic granite), Alto dos Cabeços (medium to fine-grained porphyritic granite), and Barragem (leucocratic fine- to medium-grained, slightly porphyritic granite). All the LOP granites are similar in the mineralogical composition and are mostly composed of quartz, plagioclase, K-feldspars, and biotite. As magnetic mineralogy, they have hematite, magnetite, and ilmenite, but in different proportions. However, in the Alto dos Cabeços granite, most of the magnetite was altered into hematite (martite), and in the Barragem granite, although the magnetite was not observed under the microscope, it was identified in minor amounts through other techniques (*e.g*. thermomagnetic curves and isothermal remanent magnetization). The geochemical data suggest the existence of two magma sources, one for the Lamas de Olo and Alto dos Cabeços granites and another one for the Barragem granite. The Barragem granite is a leucocratic granite and its chemical character shows that it is the most recent and evolved granite. The magnetic susceptibility strength varies between 21 µSI and 44382 µSI, suggesting that LOP is constituted by magnetite-type granites with both high (magnetic susceptibility ≥ 1000 µSI) and low (magnetic susceptibility < 1000 µSI) values. The Lamas de Olo granite shows a huge variability in the magnetic susceptibility values, and the Barragem is the one that has the lowest magnetic susceptibility mean values. The characterization of the magnetic fabric points out the presence of subvertical magnetic foliations and subhorizontal magnetic lineations, both with an azimuth *ca*. N 168º. The comparison between magnetic fabric identified by anisotropy of magnetic susceptibility (AMS) and anisotropy of anhysteretic remanent magnetization (AARM) studies was performed, pointing out that global magnetic fabric (magnetic foliations and magnetic lineations), for all samples from the granite set are coaxial in both tensors. On the other hand, the analysis of each sampling site showed some differences in the sites where the magnetic susceptibility is lower than 1000 µSI. In these areas, the AMS and AARM magnetic foliations are parallel but magnetic lineations are not coaxial. The detailed magnetic mineralogy studies pointed out the presence of magnetite/ Ti-poor magnetite in all LOP granites, even in the granites with low magnetic susceptibility. In granites with low magnetic susceptibility values, the magnetite is often oxidized to hematite (martite), which justifies the

non-coaxility on linear fabrics. The presence of magnetite in LOP points out the melt-oxidized conditions not commonly found in Iberian Variscan granites. The LOP occurs in the "Iberian Sn-W metallogenic province", which is characterized by the presence of W, W-(Sn), W-(Mo), and Sn deposits mainly related to granites emplaced during the post-collisional stage. Cutting LOP granites, several mineralized veins (mostly ENE-WSW) contain wolframite (ferberite), scheelite, molybdenite, cassiterite, and bismuth. Thus, related to LOP granites, W-(Mo, Bi) occurrences were described. The gravimetric data, and its correlation with all the information available for the studied area, allows concluding that LOP emplacement was controlled by NNW-SSE offsets conjugated with the ENE-WSW, as well as ENE-WSW and NNE-SSW conjugated fault systems. The ascending and emplacement of Lamas de Olo and Alto dos Cabeços magmas occurred in the intersection of NNW-SSW and ENE-WSW structures, once the magnetic fabric shows a magmatic flow with NNW-SSE trend and lineations dipping to north, in the north, and dipping to south, in the south of pluton. On the other hand, the Barragem magma ascending and emplacement took place in the intersection of NNE-SSW and ENE-WSW fault systems, once this granite outcrops in a thin band, located in the center of LOP, with NNE-SSW direction. The modeling of the gravimetric data indicated the presence of a feeder zone with ENE-WSW direction with two roots, that allowed the ascending of Lamas de Olo and Alto dos Cabeços magmas, and several conduits, related to the feeding of Barragem magma. The LOP is a wedge-shaped asymmetric pluton with a maximum thickness of slightly higher than 2.5 km. A comparison between LOP and other post-tectonic composite plutons, namely, Peneda-Gerês, and Lavadores-Madalena, with high magnetic susceptibility values (mean values of 6656 µSI) and low $\delta^{18}O$ values, ranging from 8.85 ‰ to 11.90 ‰, pointing out that these plutons have magnetite/ Ti-poor magnetite in their composition. Lamas de Olo and Peneda-Gerês plutons are composed of several granites and the emplacement of leucocratic evolved granites culminated the processes of W-(Mo, Bi) concentration related to the successive granite intrusions, during the composite plutons formation.

Keywords

Central Iberian Zone, Variscan granites, post-tectonic granites, Lamas de Olo Pluton, anisotropy of magnetic susceptibility, magnetite-type granites, magnetic mineralogy, W-(Mo, Bi) mineral occurrences, gravimetric survey, emplacement model.

RESUMO

O Plutão de Lamas de Olo (LOP) consiste num pequeno afloramento localizado a norte da Zona Centro Ibérica da Cadeia Ibérica Varisca. O LOP é um plutão pós-tectónico (*ca*. 297.19 ± 0.73 Ma), constituído por vários granitos biotíticos: Lamas de Olo (granito porfiróide de grão médio a grosseiro), Alto dos Cabeços (granito porfiróide de grão fino a médio) e Barragem (granito leucocrata de tendência porfiróide de grão fino a médio). Os granitos do LOP possuem uma composição mineralógica semelhante, sendo constituídos essencialmente por quartzo, plagioclase, feldspato potássico e biotite. Relativamente à mineralogia magnética, os granitos possuem hematite, magnetite e ilmenite, contudo em diferentes proporções. No granito de Alto dos Cabeços a magnetite encontra-se maioritariamente alterada em hematite (martite), e no granito da Barragem, embora a magnetite não tenha sido observada ao microscópio, foi identificada em pequenas quantidades através de outras técnicas (*e.g*. curvas termomagnéticas e magnetização remanescente isotérmica). As análises geoquímicas evidenciam a existência de duas fontes magmáticas, uma para os granitos de Lamas de Olo e Alto dos Cabeços e outra para o granito da Barragem. O granito da Barragem é caracterizado por ser leucocrata e a sua assinatura geoquímica evidencia que é o granito mais evoluído dos três. Os dados da suscetibilidade magnética possuem uma grande variabilidade de valores, variando entre 21 µSI e 44382 µSI, sugerindo que o LOP é um plutão constituído por granitos do tipo magnetite, havendo contudo, áreas com valores altos (suscetibilidade magnética ≥ 1000 µSI) e áreas com valores baixos (suscetibilidade magnética < 1000 µSI). O granito de Lamas de Olo é o que apresenta uma maior variabilidade nos valores de suscetibilidade magnética e o da Barragem é o que apresenta valores médios mais baixos. A caracterização do *fabric* magnético do LOP põe em evidência a presença de foliações magnéticas subverticais e lineações magnéticas sub-horizontais, ambas com azimute *ca*. N 168º. A correlação entre os *fabric* magnéticos obtidos através da anisotropia da suscetibilidade magnética (AMS) e da anisotropia da magnetização remanescente anisterética (AARM) permitiu concluir que analisando os valores médios obtidos, tanto as foliações como as lineações magnéticas são coaxiais. Contudo, quando se analisa separadamente cada um dos locais de amostragem, verificam-se algumas diferenças no *fabric* magnético dos locais com suscetibilidade magnética inferior a 1000 µSI. Nestes locais, as foliações magnéticas obtidas quer por AMS, quer por AARM são coaxiais, mas

as lineações magnéticas possuem orientações diferentes. O estudo detalhado da mineralogia magnética indica a presença de magnetite/ titanomagnetite em todos os granitos do LOP, mesmo naqueles que apresentam atualmente uma suscetibilidade magnética baixa. Isto deve-se ao facto de nos granitos com valores de suscetibilidade magnética baixa, a magnetite se encontrar maioritariamente oxidada para hematite (martite), justificando a não coaxialidade dos *fabrics*. A presença da magnetite nos granitos implica a existência de condições oxidantes, raramente encontradas na génese dos granitos Variscos da Ibéria. O LOP ocorre na "província metalogénica de Sn-W da Ibéria", caracterizada pela presença de vários jazigos de W, W-(Sn), W-(Mo) e Sn, maioritariamente relacionados com os granitos cuja instalação se deu durante o estádio pós-colisional. A cortar os granitos do LOP, verifica-se a presença de vários filões mineralizados (maioritariamente ENE-WSW) em volframite (ferberite), scheelite, molibdenite, cassiterite e bismuto. Associadas aos granitos do LOP estão descritas ocorrências de mineralizações de W-(Mo, Bi). Quanto à forma e modelo de instalação do plutão, a correlação de dados gravimétricos com toda a informação existente sobre a área em estudo permitiu concluir que a instalação do LOP foi controlada por vários sistemas de falha, nomeadamente NNW-SSE conjugados com ENE-WSW, assim como sistemas de falha ENE-WSW conjugados com NNE-SSW. A ascensão e instalação dos magmas graníticos de Lamas de Olo e Alto dos Cabeços estão relacionadas com a interseção de estruturas NNW-SSW e ENE-WSW, uma vez que o *fabric* magnético evidencia um fluxo magmático NNW-SSE e as lineações magnéticas possuem um comportamento característico onde as lineações na zona norte do plutão mergulham para norte e as localizadas na zona sul mergulham para sul. Por outro lado, a ascensão e instalação, do magma granítico da Barragem está relacionada com a interseção de falhas NNE-SSW e ENE-WSW, dado que os afloramentos deste granito se orientam segundo uma banda estreita, localizada na zona mais central do plutão e de tendência NNE-SSW. A modelação dos dados gravimétricos evidencia a presença de uma zona de alimentação com uma direção aproximada ENE-WSW, onde é possível identificar duas raízes que permitiram a ascensão dos magmas de Lamas de Olo e Alto dos Cabeços, assim como vários canais de alimentação relacionados com o granito da Barragem. Os dados obtidos permitem classificar o LOP como um plutão assimétrico, pertencente à família dos plutões em forma de cunha, com uma espessura máxima de cerca de 2,5 km. A comparação realizada entre o LOP e outros plutões pós-tectónicos, nomeadamente os plutões Peneda-Gerês e Lavadores-Madalena, com valores altos de suscetibilidade

magnética (valor médio de 6656 µSI) e valores baixos de $\delta^{18}O$, compreendidos entre 8,85 ‰ e 11,90 ‰, evidencia a presença de magnetite/ titanomagnetite na sua composição. Os plutões de Lamas de Olo e Peneda-Gerês são plutões constituídos por vários granitos, onde a instalação do granito leucocrata mais evoluído terá tido um papel fundamental para o culminar do processo de concentração das mineralizações de W-(Mo, Bi), relacionadas com as sucessivas intrusões graníticas durante a formação dos plutões compósitos.

Palavras-Chave

Zona Centro-Ibérica, Granitos Variscos, granitos pós-tectónicos, Plutão de Lamas de Olo, anisotropia da suscetibilidade magnética, granitos tipo-magnetite, mineralogia magnética, mineralizações de W-(Mo, Bi), prospeção gravimétrica, modelo de instalação.

CONTENTS

Acknowledgments i

Collaborations and partnerships iv

Abstract v

Resumo vii

List of figures xiv

List of tables xxvii

List of abbreviations and acronyms xxx

1 INTRODUCTION 1

1.1 Subject and the state of art 2

1.2 Main goals and objectives 4

1.3 Thesis structure 5

2 GENERAL FRAMEWORK 7

2.1 Geographic setting 7

2.2 Geological setting 10

2.2.1 The Iberian Variscan Belt 10

2.2.2 Variscan granites classification 12

2.2.3 Emplacement mechanisms of granitic plutons 16

2.2.4 Regional geological setting 18

2.3 Mineral occurrences 24

2.4 Cartographic information 27

2.4.1 Map specifications 27

2.4.2 Coordinate system 27

3 SAMPLING AND METHODOLOGIES 29
3.1 Fieldwork 29
3.1.1 Introduction 29
3.1.2 Sampling and sample preparation 29
3.2 Microscopic techniques 36
3.2.1 Introduction and generalities 36
3.2.2 Methodologies 36
3.3 Analytical techniques for the magnetic mineralogy 38
3.3.1 Introduction and generalities 38
3.3.2 Methodologies 51
3.4 Geochemical studies 61
3.4.1 Introduction and generalities 61
3.4.2 Methodologies 61
3.5 Gravimetric survey 64
3.5.1 Introduction and generalities 64
3.5.2 Acquisition data 68
3.5.3 Gravity reductions 72
3.5.4 Free-air and Bouguer anomalies 78
3.5.5 Rock densities 79
3.5.6 Interpretation of gravity anomalies 82
3.5.7 Modeling 84

4 RESULTS AND DISCUSSION 87
4.1 Cartographic and petrographic studies 87
4.1.1 Cartographic description 87
4.1.2 Petrographic studies 92

4.1.3 Mineralized veins 99
4.1.4 Highlights 108
4.2 Magnetic mineralogy 109
4.2.1 Magnetic susceptibility 109
4.2.2 Isothermal remanent magnetization data 116
4.2.3 Frequency-dependent susceptibility 117
4.2.4 Thermomagnetic experiments 120
4.2.5 Highlights 123
4.3 Magnetic fabric 125
4.3.1 Anisotropy of magnetic susceptibility 125
4.3.2 Anisotropy of anhysteretic remanent magnetization 134
4.3.3 Highlights 138
4.4 Geochemical studies 140
4.4.1 Classification diagrams 140
4.4.2 Major and trace elements 147
4.4.3 Rare Earth Elements 150
4.4.4 Iron content *versus* magnetic susceptibility 152
4.4.5 Whole-rock geochemical data as a pathfinder to specialization on mineral occurrences 153
4.4.6 Highlights 154
4.5 Metallogenic implications 156
4.5.1 Pathfinder to mineral occurrences: K_m *versus* W.R. $\delta^{18}O$ diagram 156
4.5.2 Highlights 159
4.6 Gravimetric survey 160
4.6.1 Fieldwork procedures 160
4.6.2 Gravity reductions 162
4.6.3 Rock densities 163

4.6.4 Gravity anomalies 167
4.6.5 Modeling 171
4.6.6 Highlights 177

5 FINAL REMARKS 179
5.1 Conclusions 179
5.2 Further works 182

References 185

LIST OF FIGURES

Figure 2-1. Geographic location of Lamas de Olo Pluton (LOP) with district and municipality information (based: Direção-Geral do Território, 2013a). 7

Figure 2-2. Rivers and streams in the studied area (based: Direção-Geral do Território, 2013a). 8

Figure 2-3. DEM of the studied area (20 m x 20m). 9

Figure 2-4. Sheet nº 101 – Lordelo (Vila Real) from military maps at scale 1:25 000 with the Lamas de Olo Pluton outline (modified). 9

Figure 2-5. Iberian Variscan belt with the location of the studied pluton: LOP - Lamas de Olo Pluton (modified: Ferreira *et al.*, 1987). CZ - Cantabric Zone, WALZ - West Asturian Leonese Zone, GTMZ - Galicia Trás-os-Montes Zone, CIZ - Central Iberian Zone, OMZ - Ossa Morena Zone, SPZ - Sul Portuguesa Zone (based: Julivert *et al.*, 1974; Farias *et al.*, 1987). 11

Figure 2-6. Geometry and kinematic of the main fault systems. σ_1 is the maximum compressive stress deduced from brittle late-Variscan fault sets during syn-D_3 to late-D_3 (N 25º and N 80º as conjugated fault systems (Marques *et al.*, 2002)..... 12

Figure 2-7. Cross-sections through granitic massifs from France and Spain, showing their morphology with depth, as inferred from 3D inversion of gravity data. All sections are shown at the same scale with no vertical exaggeration. On the left, cross sections are parallel to the major axis of the massifs, and on the right, they are perpendicular to it. Roots zones are evidenced by abrupt changes in dips of the walls (modified: Améglio *et al.*, 1997 in Vigneresse *et al.*, 1999). 17

Figure 2-8. Geological maps of the studied and surrounding areas: 06-C-Cabeceiras de Basto (1992); 06-D - Vila Pouca de Aguiar (1998); 10-A - Celorico de Basto (1987); 10-B – Vila Real (2015); 10-C - Peso da Régua (1967); 10-D - Alijó (1987) (GeoPortal–LNEG., 2010a). 18

Figure 2-9. Excerpt of the geological map 10-A (Celorico de Basto), showing the LOP granites and host rocks (adapted: Pereira *et al.*, 1987). 20

Figure 2-10. Geological map from the Celorico de Basto batholite made by Helal (1992). 21

Figure 3-1. Material for collecting drill-oriented cores: (1) Water jerrycan; (2) Pressure water hand pump; (3) Mixing gas tank; (4) STIHL petrol-powered portable drill; (5) Toolbox; (6) Orienting device. 30

Figure 3-2. Fieldwork photographs: (A) Sampling using STIHL petrol-powered portable drill; (B) Orientation *in situ* of the drill core; (C) Identification and notation of the azimuth and plunge in the core samples; (D) Oriented cores *in situ*. 30

Figure 3-3. Procedures in the laboratory: (A) Electric saw; (B) Sampler holder of the saw machine; (C) Examples of rock cores with the 25 x 22 mm dimensions; (D) Measurements of volume with a caliper from each rock core. 31

Figure 3-4. AMS sampling sites: (A) in the Lamas de Olo granite; (B) in the Alto dos Cabeços and Barragem granites (the basement is the geological map “10-A – Celorico de Basto” (Pereira *et al*., 1987). 32

Figure 3-5. Location of the magnetic susceptibility measurement points acquired by Terraplus KT-10 magnetic susceptibility meter (manual equipment) in the Lamas de Olo Pluton (the basement is the geological map “10-A – Celorico de Basto” (Pereira *et al*., 1987). 33

Figure 3-6. (A) Elaboration of oriented thin sections: (A.1) rock cylinder cut, (A.2) Glass slide glued to the slab with azimuth, (A.3) oriented thin section. (B to E) Examples of thin (with 30 µm of thickness) and polished sections: (B) Oriented rock cylinder and corresponded oriented thin section from LO granite; (C) Oriented rock cylinder and corresponded oriented thin section from AC granite; (D) Hand specimen and corresponded thin section from BA granite; (E) Hand specimen and polished section from quartz mineralized veins. 35

Figure 3-7. Equipment used in the petrographic studies: (A) binocular magnifying glass from LEICA-DFC295; (B) LEICA-ICC50HD petrographic polarizing microscope. 36

Figure 3-8. Schematic representation of: (A) Orbital motion and orbital magnetic moment of an electron around the atomic nucleus; (B) Spin motion and spin magnetic moment of an electron; (C) Magnetic moments inside a material with a volume, *V* (adapted: Lowrie, 2007). 39

Figure 3-9. Types of magnetic behavior in a material (modified: Lowrie, 2007 and Nédélec & Bouchez, 2015): (A) Schematic representation of the magnetic moment carried by atoms in the absence of an inducing field; (B) Magnetization as a function of the applied field (*M* – magnetization; *H* – applied field; M_s – saturation magnetization; M_r – remanent magnetization). 40

Figure 3-10. Magnetic moments of paramagnetic materials: (A) in the absence of an inducing field; (B) with a magnetic field applied. 41

Figure 3-11. Ferromagnetic behavior: (A) Susceptibility *versus* temperature plot for pure magnetite; (B) Hysteresis loop; (C) Day plot (Day *et al.*, 1977) showing the sorting of magnetite into monodomain or single-domain (SD), pseudo-monodomain (PSD) and multidomain (MD) grains. The SD grains have one magnetic domain per grain, are very small in size and show $M_{rs} \approx M_s$ and $H_{cr} \approx H_c$ in these grains; MD grains are made of several magnetic domains and are much larger than the SD grains (adapted: Nédélec & Bouchez, 2015). 43

Figure 3-12. Mean values and ranges of the magnetic susceptibility of some rock types (Lowrie, 2007). 45

Figure 3-13. Schematic representation of the crystallographic axis of: (A) biotite; (B) magnetite (AGICO, 2019). 46

Figure 3-14. TiO_2-FeO-Fe_2O_3 ternary diagram. Compositions of important Fe-Ti-oxide minerals are labeled along with mineral names; titanomagnetite and titanohematite solid solution series are indicated (modified: Butler, 2004). 48

Figure 3-15. Saturation magnetization and Curie temperature (T_C) for: (A) titanomagnetite series and (B) titanohematite series. The composition is indicated by parameter *x*; the left axis indicates saturation magnetization (j_S); the right axis indicates T_C. In (B), the compositions $x < 0.45$ have canted antiferromagnetic coupling; compositions $0.45 < x < 1.0$

have ferrimagnetic coupling. Redrawn after Nagata (1961) and Stacey & Banerjee (1974) *in* Butler, 2004. 49

Figure 3-16. (A) A portable device used for magnetic susceptibility measurements in the field; (B) Equipment used for AMS measurements; KLY-4S Kappabridge susceptometer Agico model (Czech Republic). 52

Figure 3-17. Representation of the triaxial AMS ellipsoid ($K_1 = K_{max}$; $K_2 = K_{int}$; $K_3 = K_{min}$) and definition of the virtual fabric elements: magnetic foliation and magnetic lineation (adapted: Siegesmund *et al.*, 1995). 53

Figure 3-18. Principles of AMS method for determining rock fabrics (adapted: Borradaile, 1988; Tarling & Hrouda, 1993). AMS ellipsoid, principal axis (K_1 - maximum, K_2 - intermediate and K_3 - minimum) and corresponding rock fabric. 55

Figure 3-19. Laboratoy equipment: (A) jaw crusher; (B) hammer crusher; (C) agata mill crusher..... 61

Figure 3-20. Reference surfaces: ellipsoid and geoid; N – geoid undulation; H – orthometric altitude; h – ellipsoidal altitude (modified: Lowrie, 2007). 66

Figure 3-21. The Earth's irregular shape - geoid (ESA, 2019). 66

Figure 3-22. Principle of: (A) A stable gravimeter operation; (B) A unstable gravimeter (*e.g. LaCoste & Romberg* gravimeter) (adapted: Kearey *et al.*, 2002; Lowrie, 2007)..... 67

Figure 3-23. Components of a DGPS system. 69

Figure 3-24. Gravimeter *LaCoste & Romberg G1054*. 70

Figure 3-25. Location of gravimetric stations in the Alvão area (the basement is the geological map “10-A – Celorico de Basto; 10-B – Vila Real (2015); 10-C - Peso da Régua (1967); 10-D - Alijó (1987) (GeoPortal-LNEG, 2010b). 71

Figure 3-26. A gravimetric drift curve constructed from repeated readings at a fixed location (base station). The drift correction to be subtracted for a reading taken at time *t* is *d*. (modified: Kearey *et al.*, 2002). 72

Figure 3-27 Example of tidal correction for one of the Alvão gravimetric stations. 73

Figure 3-28. After (A) terrain corrections; (B) the Bouguer correction, and (C) the free-air correction, the gravity measurements at stations P and Q can be compared to (D) the theoretical gravity at R on the reference ellipsoid (modified: Lowrie, 2007). 75

Figure 3-29. Hammer chart used in the calculation of terrain corrections (modified: Kearey *et al.*, 2002)..... 77

Figure 3-30. Representation of the regional anomaly on a gravity profile by visually fitting the large-scale trend with a smooth curve (modified: Lowrie, 2007). 84

Figure 4-1. Some aspects of LOP outcrops: (A) LO granite (B) porphyritic texture of LO granite; (C) fractures *ca*. N 50º (subvertical) with visible episienitization in LO granite; (D) Contact between LO and AC granites; (E) Outcrop (not *in situ*) of AC and BA granites. (E) Contact between LO and BA granites; (G) BA vein crosscut the LO granite; (H) BA vein detail. 88

Figure 4-2. Veins crosscut LO granite: (A) Quartz vein with fault gouge (*ca*. N10º); (B) Quartz vein *ca*. N 140º; (C) Subvertical quartz vein; (D) Aplite veins crosscut the LO granite; (E) Quartz with beryl mineralization; (F) Quartz with scheelite (ultraviolet light). 89

Figure 4-3. Some aspects of veins and host rocks outcrops: (A) and (B) Contacts between the DGM and two-mica granites from VRM; (C) Contact between two different facies from VRM; (D) and (E) Contacts between VRM and microgranite (γ'f - two mica fine-grained granite; γ'm - two mica medium- to coarse-grained granite with sparse megacrystals; $\mu\gamma$ - microgranite; θ - lamprophyre; Do – Desejosa Formation from Douro Group Metasediments). 90

Figure 4-4. Geological map of LOP granites and host rocks made on *ArcGIS* v.10 and using the PT-TM06/ ETRS89 projected coordinate system (modified: Pereira *et al.*, 1987; Pereira, 1989; Helal, 1992). 91

Figure 4-5. Macroscopic characteristics and binocular magnifying glass observations of LOP granites: (A) Lamas de Olo granite; (B) Alto dos Cabeços granite; (C) Barragem granite. 92

Figure 4-6. Photomicrographs of samples from Lamas de Olo Pluton: (A) Biotite and muscovite II aspects (transmitted light; parallel polars) - LO granite; (B) to (D) Some aspects of plagioclase (transmitted light; crossed polars) - BA granite; (E) Some aspects of plagioclase (transmitted light; parallel polars) - LO granite; (F) and (G) Microdeformation on quartz with undulatory extension and fluid inclusion planes (transmitted light; crossed polars) - AC granite; (H) Curved micas (transmitted light; parallel polars) - LO granite; (I) Biotite with brown and green colors and fluorite (transmitted light; parallel polars) - LO granite; (J) Alteration of biotite to chlorite and/or to muscovite II (transmitted light; parallel polars) - BA granite; (K) and (L) Some aspects of muscovite I (transmitted light; parallel and crossed polars, respectively) - BA granite; (M) Chlorite and rutile needles (transmitted light; parallel polars) - BA granite; (N) Alanite crystal on plagioclase (transmitted light; parallel polars) - LO granite; (O) to (Q) Fe-Ox and Fe-Ox-Ti minerals present in the LOP granites (reflected light; parallel polars) - LO, LO, and AC granites, respectively; (R) Fe-Ox-Ti mineral (transmitted light; parallel polars) - BA granite. Bt – biotite, Zr – zircon, Ms II – muscovite (secondary in origin), Qz – quartz, Pl – plagioclase, Ap – apatite, Fl – fluorite, Chl – chlorite, Ms I – muscovite (primary in origin), Rt – rutile, Aln – allanite, Ilm – ilmenite, Hem – hematite, Mag – magnetite, Ant – anatase, FIP – fluid inclusion planes, ThS – Thin section, PS – polished section (the figure continue below). 94

Figure 4-7. Photomicrographs and EDS spectrums of Lamas de Olo Pluton: (A) Association of magnetite and hematite (reflected light; parallel polars) - LO granite; (B) Fe-Ox and other minerals in minor amounts in SEM - LO granite - with the location of two EDS spectrums *z1* and *z2*; (C) Photomicrograph of magnetite and other minor amounts in SEM - LO granite; (D) Aspect of a mixture of Fe-Ox and (Fe-)Ox-Ti minerals (transmitted light; parallel polars) - BA granite; (E) Same aspect shown in (D) in SEM; (F) An example of Ox-Ti minerals with the location of EDS spectrum *z3*; (G) EDS spectrum of Fe-Ox mineral (hematite; *z1*) with semi-quantitative analyse; (H) EDS spectrum of Fe-Ox-Ti mineral (ilmenite; *z2*) with semi-quantitative analyze; (I) EDS spectrum of Ox-Ti mineral (anatase; *z3*) with semi-quantitative analyze; Mag – magnetite, Hem – hematite, Qz – quartz, Bt – biotite, Mnz – monazite, Ilm – ilmenite, Xtm – xenotime, Pl – plagioclase, Fl – fluorite, Ght – goethite, U salts – uranium salts, Chl – Chlorite, Ant – anatase; Fe-Ox - iron oxide, Fe-Ox-Ti – iron oxide with titanium, Ox-Ti – titanium oxide; ThS – thin section, PS – polished section. 96

Figure 4-8. *Raman* spectra of Fe-Ox minerals from Lamas de Olo Pluton of: (A) Magnetite; (B) Hematite; (C) Ilmenite. 97

Figure 4-9. Photomicrographs of oxides in quartz mineralized veins: (A) to (D) Some aspects of wolframite and scheelite under parallel polars; W – wolframite, Sch – scheelite, Ccp – chalcopyrite; PS – polished section..... 102

Figure 4-10. Examples of some EDS spectrum, and respectively semi-quantitative analysis, performed in polished sections from mineralized veins, showing the presence of wolframite, scheelite and areas in wolframite richer in niobium; the location of EDS spectrums z1, z2, and z3 are present in the photomicrographs; Sch – scheelite, W – wolframite, PS – polished section. 103

Figure 4-11. X-ray microanalysis map showing the presence of scheelite (areas richer in Ca) located near fractures on the wolframite crystal. 104

Figure 4-12. Photomicrographs of sulfides in quartz mineralized veins: (A) to (D) Some aspects of sulfides and native bismuth under parallel polars; Py – pyrite, Ccp – chalcopyrite, Apy – arsenopyrite, Sp - sphalerite, Cv – covellite, Bi – bismuth (native), Bis – bismuthinite; PS – polished section. 106

Figure 4-13. Examples of some EDS spectrum, and respectively semi-quantitative analysis, performed in polished sections from mineralized veins, showing the presence of a complex sulfide with intergrown textures; the location of EDS spectrums z1, and z2 are present in the photomicrograph; PS – polished section. 107

Figure 4-14. Map of the magnetic susceptibility (K_m) values in LOP (interpolation made by Inverse Distance Weighted in the *ArcGIS* 10.7 software). Km values were acquired using both KT-10 magnetic susceptibility meter (portable device) and KLY-4S Kappabridge susceptometer AGICO model. 109

Figure 4-15. Relative frequency magnetic susceptibility histograms for LOP granites (LO, AC, and BA granites) and host rocks (VRM, and DGM). K_m expressed in µSI..... 110

Figure 4-16. (A) Experimental variogram and its adjustment to the theoretical variogram of the regionalized variable (magnetic susceptibility); (B) Map of the magnetic susceptibility

(K_m) values in the Lamas de Olo Pluton (interpolation made by kriging in the *Surfer* 10 software) with the location of sampling sites and LOP outline. 114

Figure 4-17. IRM acquisition curves for the representative samples from LOP: LM 5 and LM 16 from LO granite; LM 26 from AC granite (with zoom showing the absence of saturation); LM 7 from BA granite (with zoom showing the absence of saturation). The CLG treatment was made using the software developed by Kruiver *et al.* (2001)..... 118

Figure 4-18. (A) SIRM *versus* $B_{1/2}$ plot illustrating the distributions of magnetic phases in LOP; (B) DP *versus* $B_{1/2}$ plot distinguishing the 3 heterogeneous components (the heterogeneity of the components can be related to the varying degrees of oxidation of magnetite, different Ti-content in the Ti-poor magnetite, and different magnetic grain sizes for hematite. The field limit between magnetite/hematite is arbitrarily stated at around 100 mT. 120

Figure 4-19. Normalized K_t *versus* T during heating (arrow toward right) and cooling (arrow toward left) from representative samples from LOP granites: (A) to (F) LO granite; (G) to (J) AC granite; (K) to (N) BA granite. 122

Figure 4-20. Histogram of the anisotropy of magnetic susceptibility degree (%) and the correlation between K_m and P% in the LOP granites (LO, AC, BA) and host rocks (VRM and DGM). 125

Figure 4-21. Map of the anisotropy of magnetic susceptibility degree (%) in the LOP (LO, AC and BA granites). 128

Figure 4-22. Map of the shape parameter (T) of LOP (LO, AC, and BA granites)..... 129

Figure 4-23. Correlation plots from LOP (LO, AC, and BA granites) and host rocks (VRM and DGM). (A) T *versus* K_m; (B) T *versus* P%. 130

Figure 4-24. Map of the magnetic foliations with orientation stereonets for the magnetic foliations poles (K_3) for LOP (LO, AC, and BA granites) (Schmidt, lower hemisphere projection, 1–5% area contours). 132

Figure 4-25. Map of the magnetic lineations with orientation stereonets for the magnetic lineations (K_1) for LOP (LO, AC, and BA granites) (Schmidt, lower hemisphere projection, 1–5% area contours)..... 133

Figure 4-26. Correlation plots of *T versus P%* from selected representative samples from LOP (LO, AC, and BA granites); (A) *T versus P%* obtain by AARM experiments*; (B) T versus P%* obtain by AMS experiments for the same sampling sites. 134

Figure 4-27. Magnetic fabric determined by AARM and AMS for the selected sampling sites from LOP. Squares represent the maximum remanence ($AARM_{max}$ *or* $AARM_1$) and maximum susceptibility (K_{max} *or* K_1); triangles are intermediate remanence ($AARM_{int}$ or $AARM_2$) and intermediate susceptibility (K_{int} or K_2); circles are minimum remanence ($AARM_{min}$ or $AARM_3$) and minimum susceptibility (K_{min} or K_3). The full line ellipses correspond to the 95% confidence ellipse. Data plotted in the lower hemisphere stereonets. 137

Figure 4-28. Magnetic fabric determined by AARM and AMS for the selected sampling sites from LOP with orientation stereonets for the magnetic foliations poles ($\perp$ $AARM_3$ *and* K_3) and magnetic lineations (// $AARM_1$ *and* K_1) (Schmidt, lower hemisphere projection, 1–5% area contours)..... 138

Figure 4-29. Variation diagrams of K_2O/ Na_2O and Na_2O + K_2O in the function of the B parameter. 142

Figure 4-30. Granite classification diagram using R_2 and R_1 parameters (De La Roche *et al.*, 1980). 142

Figure 4-31. Classification diagrams according to Frost *et al.* (2001): (A) Fe number *versus* SiO_2 (in wt %); (B) Modified alkali-lime index (MALI) *versus* SiO_2 (in wt %); (C) A/NK *versus* ASI diagram; Fe-number is calculated as weight proportion of FeO=FeO+MgO; MALI is defined as Na_2O+K_2O-CaO (in wt %); ASI is defined as molecular Al_2O_3=(Na_2O+K_2O+CaO-3:33P_2O_5) (molar). 143

Figure 4-32. Classification granite diagrams: (A) SiO_2 *versus* K_2O diagram from Peccerillo & Taylor (1976); (B) A *versus* B from Villaseca *et al.* (1998); h-P – highly peraluminous; f-P – Felsic peraluminous; m-P – Moderately peraluminous; l-P – Low peraluminous. 144

Figure 4-33. Rb-Ba-Sr diagram (El Bouseily & El Sokkary, 1975). 145

Figure 4-34. A suite of diagrams for discrimination of the geotectonic environment of LOP granite; ORG - Ocean Ridge granites; VAG - Volcanic Arc granites; WPG - Within Plate granites; syn-COLG – syn-collision granites; the dashed line represents the upper compositional boundary for ORG from anomalous ridge segments (Pearce *et al.*, 1984). 146

Figure 4-35. Triangular diagram proposed by Harris *et al.* (1986) for classification of collisional granites; G1 (Group 1) - Pre-collision calc-alkaline intrusions (Volcanic-Arc granites); G2 (Group 2) - Syn-collision peraluminous intrusions; G3 (Group 3) - Late or post-collision calc-alkaline intrusions; G4 (Group 4) - Post-collision alkaline intrusions (Within-Plate granites)..... 147

Figure 4-36. Variation diagrams for LOP granites (major element concentrations in percentage). 148

Figure 4-37. Variation diagrams for LOP granites (trace element concentrations in ppm). 149

Figure 4-38. Ba *versus* Rb and Ba *versus* Sr diagrams from LOP granites. 150

Figure 4-39. Rare Earth elements (REE) spectra normalize to chondrite (Boynton, 1984). 151

Figure 4-40. Spider plot normalized to the bulk continental crust (Taylor & McLennan, 1995). 152

Figure 4-41. Geochemical plots of representative samples for Lamas de Olo Pluton: (A) K_m *versus* Fe_2O_3t, showing the variation of magnetic susceptibility with Fe (total) content; (B) Evolution of Nb/Ta as a function of K/Rb, where Nb/Ta < 5 points out the interaction with hydrothermal fluids (Ballouard *et al.*, 2016). 153

Figure 4-42. LOP and possible mineral occurrences related to their granites: (A) Plot of total alkalis *versus* SiO_2 (Le Maitre, 1989); (B) Plot of Fe_2O_3/FeO *versus* Rb/Sr (Blevin & Chappell, 1992); (C) Nb/Ta *versus* Zr/Hf diagram differentiating barren peraluminous crustal granites and granites hosting ore deposits (Ballouard *et al.*, 2016). 154

Figure 4-43. (A) Location of the studied Variscan plutons in northern Portugal (modified from: Ferreira *et al.*, 1987; Corrêa-Ribeiro, 2018; Antunes, 2019; Gonçalves *et al*., 2019): 1 – Lavadores-Madalena; 2 – Vila Pouca de Aguiar; 3 – Águas-Frias-Chaves; 4 – Peneda-Gerês; 5 – Porto; 6 – Lamas de Olo; 7 – Mangualde; 8 – Castelo Branco; 9 – Serra da Estrela; 10 – Vieira do Minho; 11 – Castelo do Queijo; 12 – Vila Real; (B) Semi-log plot of K_m (in SI units) *versus* $\delta^{18}O$ for the studied granites, considering the data in Antunes *et al.* (2008), Martins *et al.* (2009), Neiva *et al.* (2009), and Sant'Ovaia *et al.* (2013a): LV g. - Lavadores-Madalena granites; VPA g. - Vila Pouca de Aguiar granite; PSG g. - Pedras Salgadas granite; CH g. - Chaves granite; GR g. - Gerês granite; PO g. - Porto granite; LO g. - Lamas de Olo granite; BA g. - Barragem granite; AC g. - Alto dos Cabeços granite; MA g. - Mangualde granite; MZ g. - Monzogranito de Castelo Branco; CB g. - Castelo Branco granite; MT g. - Manteigas granite; CA g. - Cabeço granite; SE g. - Serra da Estrela granite (Torre); VM g. - Vieira do Minho granite; CQ g. - Castelo do Queijo granite; VR g. - Vila Real granite. 158

Figure 4-44. Fieldwork for gravimetric surveying: (A) DGPS and gravimeter equipment; (B) Aquisition data using the gravimeter *LaCoste & Romberg G1054*; (C) Examples of fieldwork annotations. 160

Figure 4-45. Calibration Table for the *LaCoste & Romberg* gravimeter model G-1054 (LaCoste & Romberg, 2004). 161

Figure 4-46. Print screen of *Rede Gravimétrica Nacional* in the *Direção-Geral do Território* site (Direção-Geral do Território, 2013c), where the absolute gravity value was obtained. 162

Figure 4-47. Correlation between the two methods used for terrain corrections (TC): Hammer chart *versus* script for *MatLab*. 163

Figure 4-48. Density determination by Nettleton's method and mean value (d = 2.55 g/cm^3) for all the rocks in the Alvão studied area. 164

Figure 4-49. (A) Density determination by Nettleton's method for each path; (B) Mean and median values of density for the Alvão area; (C) Location of each path over the geological contour of LOP and host-rocks. 165

Figure 4-50. Rock density determination in the LNEG facilities: (A) Specimens in the ventilated oven; (B) Specimens placed on top of non-oxidizing and non-absorbent supports to minimize the contact between specimens and the surface of the container (this is important because during saturation all the specimen should be in contact with water; (C) Sample markings detail on the specimens at $^1/_2$ of its height and ¾ of its height; (D) Specimens immersed in water (the water surface is about 25 mm above the specimens' top); (E) Immersed weighing of a specimen. 166

Figure 4-51. Bouger anomaly map (interpolation by kriging using the *Oasis Montaj* software). 167

Figure 4-52. Regional anomaly maps according to: (A) 1st, (B) 2nd, and (C) 3rd order polynomial surfaces. 169

Figure 4-53. Residual anomaly maps according to: (A) 1st, (B) 2nd, and (C) 3rd order polynomial surfaces. 170

Figure 4-54. The selected residual anomaly map (3rd order) with geological contours and faults. 171

Figure 4-55. The location of the 3 gravimetric profiles (P1 –WSW-ENE, P2 – NNE-SSW, and P3 – NNW-SSE) used to infer the shape and the LOP emplacement model. 172

Figure 4-56. Observed and calculated anomaly and interpretative 2D model along the WSW-ENE direction (error *ca*. 0.385; the yellow and pink stars indicate the zone of intersection of P1 and P2, and P1 and P3, respectively); LO – Lamas de Olo granite; AC – Alto dos Cabeços granite; BA – Barragem granite; VRM – Vila Real Massif; DGM – Douro Group Metassediments..... 173

Figure 4-57. Observed and calculated anomaly and interpretative 2D model along the NNE-SSW direction (error *ca*. 0.369; the yellow and green stars indicate the zone of intersection of P2 and P1, and P2 and P3, respectively); LO – Lamas de Olo granite; AC – Alto dos Cabeços granite; BA – Barragem granite; VRM – Vila Real Massif; DGM – Douro Group Metassediments..... 174

Figure 4-58. Observed and calculated anomaly and interpretative 2D model along the NNW-SSE direction (error *ca*. 0.952; the green and pink stars indicate the zone of intersection of P3 and P2, and P3 and P1, respectively); LO – Lamas de Olo granite; AC – Alto dos Cabeços granite; BA – Barragem granite; VRM – Vila Real Massif; DGM – Douro Group Metassediments..... 175

Figure 4-59. Block diagram of LOP: (A) LOP cutting section along WSW-ENE direction; (B) LOP cutting section along NNE-SSW direction; (C) LOP model interpretation according to the intersection of 2 profiles; (D) 3D model of LOP. 176

LIST OF TABLES

Table 2-1. Summary of some granite classifications by: [(1)]Schermerhorn (1956); [(2)]Oen (1970); [(3)]Ferreira *et al.* (1987); [(4)]Dias *et al.* (1998); [(5)]Martins (1998); [(6)]Dias *et al.* (2010); [(7)]Albuquerque (1971); [(8)]Capdevila *et al.* (1973); [(9)]Corretgé *et al.* (1974); [(10)]Capdevila & Floor (1970) ; [(11)]Chappell & White (1974); [(12)]Chappell & White (2001); [(13)]Ishihara (1977); [(14)]Sheppard (1977); [(15)]Ellwood & Wenner (1981)..... 15

Table 3-1. Simplified table with sampling sites and magnetic methodologies applied to each site in the Lamas de Olo Pluton (LO - Lamas de Olo granite; BA - Barragem granite; AC - Alto dos Cabeços granite; K_m (μSI) – magnetic susceptibility in μSI; AARM - Anisotropy of anhysteretic remanent magnetization; K_t *versus T* - Thermomagnetic experiments; IRM - Isothermal remanent magnetization; χ_{fD}% - Frequency-dependent susceptibility (%)..... 34

Table 3-2. Mean values of magnetic susceptibility, at room temperature, of some important minerals in rocks (*in* Borradaile, 1988)..... 45

Table 3-3. Laboratory data of heating-induced thermochemical reactions (Gubbins & Herrero-Bervera, 2007)..... 51

Table 3-4. Terrain corrections for Hammer zones B to M (adapted: Kearey *et al.*, 2002): n - number of compartments in the zone; r_1 - inner radius of zone (m); r_2 - outer radius of zone (m)..... 78

Table 3-5. Density ranges (g/cm^3) of some common rock types (Kearey *et al.*, 2002)..... 79

Table 4-1. Macroscopic characteristics and field observations of the LOP granites. 87

Table 4-2. Petrographic description of Lamas de Olo Pluton..... 98

Table 4-3. Old mining concessions associated with granites from the Lamas de Olo Pluton (SIORMINP, 2019)..... 100

Table 4-4. Magnetic susceptibility values per site in Lamas de Olo Pluton and host rocks. The K_m was measured using both analytical techniques: MS – magnetic susceptibility measurements using a portable device, and AMS - anisotropy of magnetic susceptibility. M,

P – GPS coordinates from each measurement site in TM06/ ETRS89 coordinate system; K_m – magnetic susceptibility values (in µSI); n: number of samples per site; n.a. – not attributed. 111

Table 4-5. Mean and range values for magnetic susceptibility for Lamas de Olo and host rocks. The K_m was measured using both analytical techniques: MS – magnetic susceptibility measurements using a portable device, and AMS - anisotropy of magnetic susceptibility; K_m – magnetic susceptibility values (in µSI); n.a. – not attributed. 112

Table 4-6. Statistics data from magnetic susceptibility values (K_m in µSI). 114

Table 4-7. Isothermal remanent magnetization data from LOP. IRM_{1T} - Isothermal remanent magnetization at 1T; $IRM_{0.3T}$ - Isothermal remanent magnetization at 300mT. The Cumulative log-Gaussian (CLG) analysis were performed in the LOP samples, allowing to define for each magnetic component: % - percent contribution; SIRM - values of saturation of isothermal remanent magnetization; $S_{0.3T}$ - the ratio of IRM at 0.3 T to SIRM; $B_{1/2}$ - the field at which half of the SIRM is reached; DP - dispersion parameter; $S_{0.3T} = IRM_{0.3T}/IRM_{1T}$ (Robertson & France, 1994). The CLG treatment was made using the software developed by Kruiver *et al.* (2001). n.a. – not attributed. 119

Table 4-8. Frequency-dependent susceptibility measurements in samples from LOP. Magnetic Susceptibility F1 (LF) – Magnetic susceptibility at field 1 (low frequency = 0.46 kHz); Magnetic Susceptibility F2 (HF) – Magnetic susceptibility at field 2 (high frequency = 4.6 kHz); M 1 – measurement 1; M 2 – measurement 2; χfD% - Frequency-dependent susceptibility in percent. 119

Table 4-9. AMS data for the sampling sites. M, P – GPS coordinates from the sampling sites in TM06/ ETRS89 coordinate system. K_m – mean magnetic susceptibility in µSI; *P*% – anisotropy degree (%); *T* – shape parameter; K_1 – long axis of the mean ellipsoid orientation; K_3 - short axis of the mean ellipsoid orientation; Dec, Inc – declination, inclination; E_{12}, E_{23}, and E_{31} – 95% confidence angles corresponding to the three axes; n – number of specimens per site; $*$ – not enough data; n.a. – not attributed. 126

Table 4-10. AARM data for the selected representative sampling sites in the LOP (LO, AC, and BA granites). *P%* - magnetic anisotropy degree (%); *T* – shape parameter; $AARM_1$ –

maximum axes of anhysteretic remanence; $AARM_3$ – minimum axes of anhysteretic remanence; Dec, Inc – declination, inclination; E_{12}, E_{23}, and E_{31} – 95% confidence angles corresponding to the three axes; n – number of specimens per site; n.a. – not attributed. 135

Table 4-11. Geochemical data from LOP granites; LO - Lamas de Olo granite; AC - Alto dos Cabeços granite; BA - Barragem granite; L.d. – Limit detection; K_m – magnetic susceptibility. 141

Table 4-12. Some geochemical parameters calculated for the LOP granites. 142

Table 4-13. Characterizing parameters of the REE profiles calculated for the LOP granite; LO - Lamas de Olo granite; AC - Alto dos Cabeços granite; BA - Barragem granite; N - values normalized to chondrite according to Boynton (1984); $Eu/Eu^* = Eu_{Nc}/(Sm_{Nc}*Gd_{Nc})^{1/2}$. 151

Table 4-14. W.R. $\delta^{18}O$ normalize to SMOW (Standard Mean Ocean Water) and K_m of Variscan granites according to our study data on Lamas de Olo Pluton and Vila Real Massif, as well as previous studies compiled from the bibliography (Antunes *et al.*, 2008; Martins *et al.*, 2009; Neiva *et al.*, 2009 and Sant'Ovaia *et al.*, 2013a); (*) K_m value for the analyzed sample. 157

Table 4-15. Density mean values obtained for each lithology..... 166

LIST OF ABBREVIATIONS AND ACRONYMS

All the abbreviations and acronyms are defined the first time they are used. Furthermore, all of them are listed below.

AARM – Anisotropy of Anhysteretic Remanent Magnetization
AC – Alto Dos Cabeços granite
Aln – Allanite
AMS – Anisotropy of Magnetic Susceptibility
Ant – Anatase
Ap – Apatite
Apy – Arsenopyrite
BA – Barragem granite
Bi – Bismuth
Bis – Bismuthinite
Bt – Biotite
ca. – circa
Ccp – Chalcopyrite
CEMUP – *Centro de Materiais da Universidade do Porto*
Chl – Chlorite
CIZ – Central Iberian Zone
CLG – Cumulative log-Gaussian function
Cv – Covellite
DEM – Digital Elevation Model
DGAOT – *Departamento de Geociências Ambiente e Ordenamento do Território*
DGM – Douro Group Metasediments
DGPS – Differential Global Positional Satellite
e.g. – exempli gratia
EDS – Dispersive Energy Spectra
ETRS89 – European Terrestrial Reference System 1989
FCUP – *Faculdade de Ciências da Universidade do Porto*
Fe-Ox – Iron oxide
Fe-Ox-Ti – Iron oxide with titanium
FEUP – *Faculdade de Engenharia da Universidade do Porto*

Fl – Fluorite

Ght – Goethite

GIS – Geographic Information Systems

GPS - Global Positional Satellite

GTMZ – Galicia Trás-os-Montes Zone

Hem – Hematite

HREE – Heavy Rare Earth Elements

ICP-MS – Inductively coupled plasma mass spectrometry

ICT – *Instituto de Ciências da Terra*

IDL – *Instituto Dom Luís*

IDW – Inverse Distance Weighted

Ilm – Ilmenite

IRM – Isothermal Remanent Magnetization

Late- to post-D_3 – Late- to post-tectonic granites relatively to D_3 Variscan phase

Late-D_3 – Late-tectonic granites relatively to D_3 Variscan phase

LNEG – *Laboratório Nacional de Energia e Geologia*

LO – Lamas de Olo granite

LOP – Lamas de Olo Pluton

LREE – Light Rare Earth Elements

Ma – Million Years

Mag – Magnetite

MD – Multidomain

Mnz – Monazite

Ms – Muscovite

Ox-Ti – Titanium oxide

Pl – Plagioclase

Post-D_3 – Post-tectonic granites relatively to D_3 Variscan phase

PS – Polished section

PSD – Pseudo-monodomain

Py – Pyrite

Qz – Quartz

R.V. – Regionalized Variables

REE – Rare Earth Elements

Rt – Rutile

S.D. – Single Domain

s.l. – sensu lato

s.s. – sensu stricto

Sch – Scheelite

SEM – Scanning Electron Microscope

SIRM - Saturation of Isothermal Remanent Magnetization

Sp – Sphalerite

Syn-D_3 – Syn-tectonic granites relatively to D_3 Variscan phase

ThS – Thin Section

TIN – Triangulated Irregular Network

UA – *Universidade de Aveiro*

UC – *Universidade de Coimbra*

UTAD – *Universidade de Trás-os-Montes e Alto Douro*

VRM – Vila Real Massif

VRPF – Verín-Régua-Penacova Fault

VSMOW - Vienna Standard Mean Ocean Water

W – Wolframite

W.R. – Whole-rock

WGS84 – World Geodetic System 1984

Xtm – Xenotime

Zr – Zircon

CHAPTER 1:

INTRODUCTION

“It is the time you have wasted for your rose that makes your rose so important.”
Antoine de Saint-Exupéry

1 INTRODUCTION

At the same time that I was writing this thesis, I published several papers and short abstracts. During the Ph.D. academic path, 4 papers in national/ international journals were published, and several abstracts and short papers were submitted to national/ international conferences and its exhibition was performed as posters or oral presentations. The published papers and the principal conference abstracts/ short articles are mentioned below and are attached in the topic Appendix.

Papers in national/ international journals:

- Cruz, C., Góis, J., Sant'Ovaia, H. & Noronha, F. (2020). Geostatistical approach in the study of the magnetic susceptibility variation: Lamas de Olo Pluton case study. Journal of Iberian Geology: 1-11.
- Cruz, C., Sant'Ovaia, H. & Noronha, F. (2020). Magnetic mineralogy of Variscan granites from northern Portugal: an approach to their petrogenesis and metallogenic potential. Geologica Acta 18(5): 1-20.
- Cruz, C., Sant'Ovaia, H. & Noronha, F. (2016). Magnetic susceptibility and $\delta^{18}O$ characterization of Variscan granites related to W-(Mo) and Sn-(W) mineralizations: Lamas de Olo Pluton case study. Comunicações Geológicas 103 (1): 143-147.
- Cruz, C, Sant'Ovaia, H. & Noronha, F. (2016). Magnetite and ilmenite granites in the Lamas de Olo Pluton (North Portugal): Petrophysic and metallogenic implications. 16th InternationalMultidisciplinary Scientific GeoConference SGEM2016, Science and Technologies in Geology, Exploration and Mining: SGEM 2016, Bulgária, 345-352.

Conference abstracts/ short articles:

- Cruz, C., Sant'Ovaia, H., Raposo, M.I.B. & Noronha, F. (2020). Magnetic fabric of Lamas de Olo Pluton: AMS and AARM fabrics comparison. EGU2020 online conference (poster presentation).
- Cruz, C., Sant'Ovaia, H., Lourenço, J.M., Almeida, F. & Noronha, F. (2019). Integração de dados de anisotropia da suscetibilidade magnética e de gravimetria para determinação da geometria e modelo de instalação do Plutão de Lamas de Olo. MAGIBER, Condeixa-a-Nova, Portugal (oral presentation).

- Cruz, C., Sant'Ovaia, H. & Noronha, F. (2018). Emplacement of Lamas de Olo Pluton: relation between magnetic fabric and regional structures. X Congresso Nacional de Geologia, S. Miguel-Açores, Portugal, 19-20 (oral presentation).
- Cruz, C., Góis, J., Sant'Ovaia, H. & Noronha, F. (2018). Geostatistical approach in the study of the magnetic susceptibility variation: Lamas de Olo Pluton case study. X Congresso Nacional de Geologia, S. Miguel-Açores, Portugal, 215-216 (poster presentation).
- Cruz, C., Sant'Ovaia, Olivier, P. & Noronha, F. (2017). Magnetic mineralogy of Variscan granites: relation to its metallogenic potential on rare metals. Goldschmidt2017 (poster presentation).

Some of the results obtained during the academic works are not present in this document, namely, the laboratory results obtained from other post-tectonic granites (Vila Pouca de Aguiar, Lavadores-Madela, and Peneda-Gerês plutons; Cruz *et al.*, 2020). However, the principal discussions and conclusions are mentioned along with the document with associated references.

1.1 SUBJECT AND THE STATE OF ART

The studied area belongs to northern Portugal, where granite rocks dominate. Our studies focused on a small pluton in the Alvão Natural Parque (Vila Real), the Lamas de Olo Pluton (LOP). The studied pluton, perhaps due to its small size, has not been the target of many publications.

LOP is classified as post-tectonic pluton (Pereira, 1989), circumscribed and is constituted of 3 biotite granites: (i) Lamas de Olo, a medium to coarse-grained porphyritic granite; (ii) Alto dos Cabeços, a fine- to medium-porphyritic granite; and (iii) Barragem, which is a slightly porphyritic and fine-grained leucocratic granite. This pluton outcrops in a small area and is intrusive in both Douro Group Metasediments (DGM) and in the two-mica granites from Vila Real Massif (VRM; Pereira, 1989; Fernandes, 2013). The LOP emplacement was controlled by a NE-SW and NW-SE fault system, related to the Verín-Régua-Penacova Fault (VRPF; Pereira, 1989).

Studies carried out by Helal (1992), and recently by Fernandes *et al.* (2013) and Teixeira *et al.* (2014), classified the LOP granites according to their geochemical characteristics.

Studies of major and trace elements, as well as Rare Earth Elements (REE), have been made on Lamas de Olo Pluton by Helal (1992). Recently, Fernandes *et al.* (2013) and Teixeira *et al.* (2014), published some data about the isotopic signatures and dating, and natural radiation from this pluton. Fernandes *et al.* (2013) and Teixeira *et al.* (2014), presented signatures of $(^{87}Sr/^{86}Sr)_i$ = 0.7038 to 0.7045 and εNd = -1.7 to -0.6 to LOP, suggesting the involvement of mid-crustal sources, probably mixed with asthenospheric material.

Scarce information was also obtained in the description of granites in northern Portugal in the *Notícia Explicativa da Folha 2 - Carta Geológica de Portugal* at scale 1:200 000 (Noronha *et al.*, 2006). According to the same authors, the LOP consists of high-K calc-alkaline and is a metaluminous to slightly peraluminous granite, having a composition compatible with magmas resulting from the fusion of materials from the middle crust with contamination of asthenospheric material.

Some studies regarding natural radiation from Lamas de Olo Pluton was carried out by Teixeira *et al.* (2014). The U and Th average contents of the Lamas de Olo granite (9.6 ppm and 17.0 ppm, respectively) are higher than the crustal average, showing a significant radon potential. These studies show that the main concentration of these elements is spatial related to E-W fractures that cut the LOP granites, commonly affected by episienitization processes. The U and Th contents of the Lamas de Olo granite are correlated with indoor radon concentrations, however, the average radon levels did not exceed the indoor radon recommended value, suggesting that the LOP presents a moderate radon risk in dwellings.

Fernandes *et al.* (2013), established that LOP emplacement occurred at the upper crust, so their granites were emplaced in higher structural crustal levels, testifying the occurrence of a crustal growth episode after the major recycling processes that occurred during the deformation phase D_3.

The LOP has mineral occurrences relatively rare in northern Portugal, having mineralization of W-Mo-Be in quartz veins that cut the pluton granites (Helal, 1992). The W-Mo-Be mineralized veins (quartz veins with wall rocks altered by greisenization, greisens,

and muscovites) are related to the central outcrop of Barragem granite. The later granite is slightly greisenized (pervasive alteration) but alteration processes are strongly controlled by the NNE-SSW subvertical fault (parallel to the main Variscan fault, the Verín-Régua-Penacova Fault), often filled by aplites which represents the late stage of the magmatic history of the intrusion. The W-Mo-Be mineralized veins are related to convective circulation generated by the heat of Barragem granite. One of the particularities of the hydrothermal activity in the Lamas de Olo intrusion is the occurrence of "beryllites" (rocks equivalent to greisens but where the aluminous mineral that replaces the feldspar is not muscovite but beryl, due to the high Be content of the fluids). In the Lamas de Olo Pluton, as the Peneda-Gerês Pluton, the ore deposits are mostly related to the late leucocratic granites. The mineralized veins and the paragenetic associations are similar in both intrusions, and this similarity, despite strong differences in the host rocks, suggests an essentially magmatic origin for W, Mo, and Be (Helal, 1992).

1.2 MAIN GOALS AND OBJECTIVES

Given the scarce information about Lamas de Olo Pluton, a multidisciplinary study was carried out. This study contributes to the knowledge of post-tectonic granites, in special about its petrophysical characterization (*e.g*. magnetic susceptibility and fabric characterization), the emplacement model, and its metallogenic potential, having LOP as a case study.

The integration of all data obtained allows to:

- Characterize LOP granites regarding their magnetic susceptibility and magnetic fabric;
- Describe the magnetic mineralogy, and discuss the importance of its presence in LOP;
- Clarify the geometry and emplacement mechanism, assessing the structural level of the intrusion, and relate the LOP intrusion with host-rock, verifying if LOP is concordant or not with host-rocks;
- Characterize genetic mechanisms related to the evolution of LOP granites, contributing to the knowledge of the evolutionary processes of the lithosphere in the final stages of the Variscan orogeny in this sector of the orogen;
- Understand the genesis of mineralizations in this specific context.

To achieve the main goals for this thesis, several tasks were performed:

- Detailed geological mapping of LOP granites and host-rocks, using Geographic Information Systems (*e.g. ArcGIS* software);
- Petrographic and geochemical characterization of LOP granites, clarifying aspects related to their genesis;
- Detailed study of the magnetic properties, and magnetic mineralogy of LOP granites, identifying similarities and differences between them;
- Determination of the magnetic fabric (magnetic foliations and magnetic lineations);
- Investigation about redox conditions in the magma chamber, based on the magnetic susceptibility values and isotopic geochemistry, namely whole-rock $\delta^{18}O$, establishing a relation between LOP granites and associated mineralizations;
- Establishment of LOP geometry using gravimetric studies, and understanding about the kinematic emplacement model based on magnetic fabric and residual anomaly;
- Tectonic setting of magmatic processes evaluating possible relationships between LOP emplacement and other plutons spatially associated with the Verín-Régua-Penacova Fault (*e.g.* Vila Pouca de Aguiar pluton);
- Comparison with post-tectonic granites from the Variscan belt (*e.g.* Vila Pouca de Aguiar, Lavadores-Madalena, and Peneda-Gerês plutons);
- Dissemination of results through papers in national/ international journals, and through presentations (posters/ oral presentations) in national/ international scientific meetings.

1.3 THESIS STRUCTURE

The thesis is organized into 5 chapters, and its content is shortly explained below:

- Chapter 1 – Introduction, with a small description of the subject and the main goals attained with this study.
- Chapter 2 – General framework, which aims to describe the geological framework and give some information about the used maps.
- Chapter 3 – Sampling and methodologies, including the description of all the methodologies used, and information about fieldwork campaigns and sampling.

- Chapter 4 – Results and discussion, displaying most of the results obtained during field and laboratory works, as well as some highlights for each topic.
- Chapter 5 – Final remarks, which aims to gather all the information and establish a general conclusion about the Lamas de Olo Pluton, in special about its magnetic properties, emplacement model, and associated mineral occurrences. Moreover, further works are proposed.

In References, all the cited bibliography is listed, and in the Attachments, some additional information is included. Published and submitted papers and abstracts, are including in the Appendix.

CHAPTER 2:

GENERAL FRAMEWORK

“[Geology] the subject that brings a student down to earth.”
Evan Esar

2 GENERAL FRAMEWORK

2.1 GEOGRAPHIC SETTING

The Lamas de Olo Pluton (LOP) belongs to the municipality of Vila Real, and Vila Real District in the north of Portugal (fig. 2-1). Vila Real district has an area of *ca.* 4 328 km², being the 11th largest Portuguese district, and the Vila Real municipality, has an area of *ca*. 379 km². The Vila Real municipality is surrounded by the municipalities of Ribeira de Pena and Vila Pouca de Aguiar to the north. It is also west of Sabrosa, north of Peso da Régua, northwest of Santa Marta de Penaguião, east of Amarante (Porto district) and southwest of Mondim de Basto (Direção-Geral do Território, 2013a; fig. 2-1).

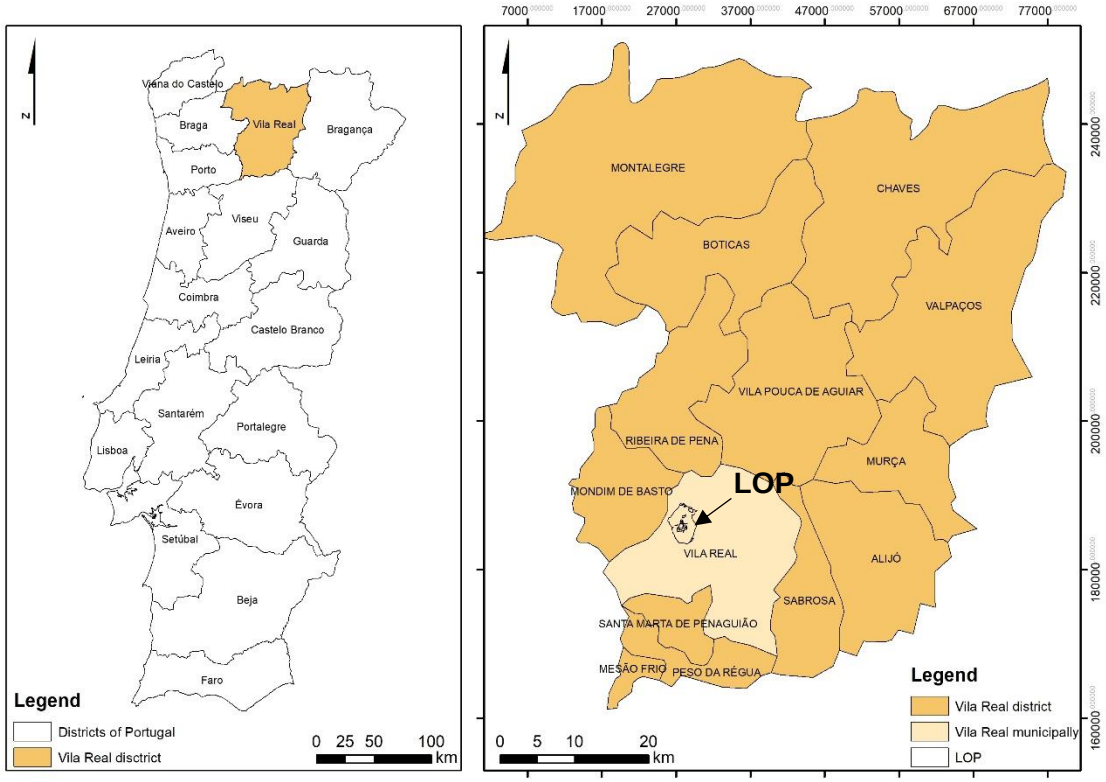


Figure 2-1. Geographic location of Lamas de Olo Pluton (LOP) with district and municipality information (based: Direção-Geral do Território, 2013a).

Hydrologically, the LOP is located in the Douro basin and the studied area is bathed by the Olo, Cabril, Sião, Corgo, Cabrão, Felgueiras and Pequeno rivers, and by numerous streams like Marinheira, Vale do Longo, Fervença, Maila, Ribeira, Beja, Arca, Mezio, Tourinhas, Paul and Olgas (Direção-Geral do Território, 2013a; fig. 2-2).

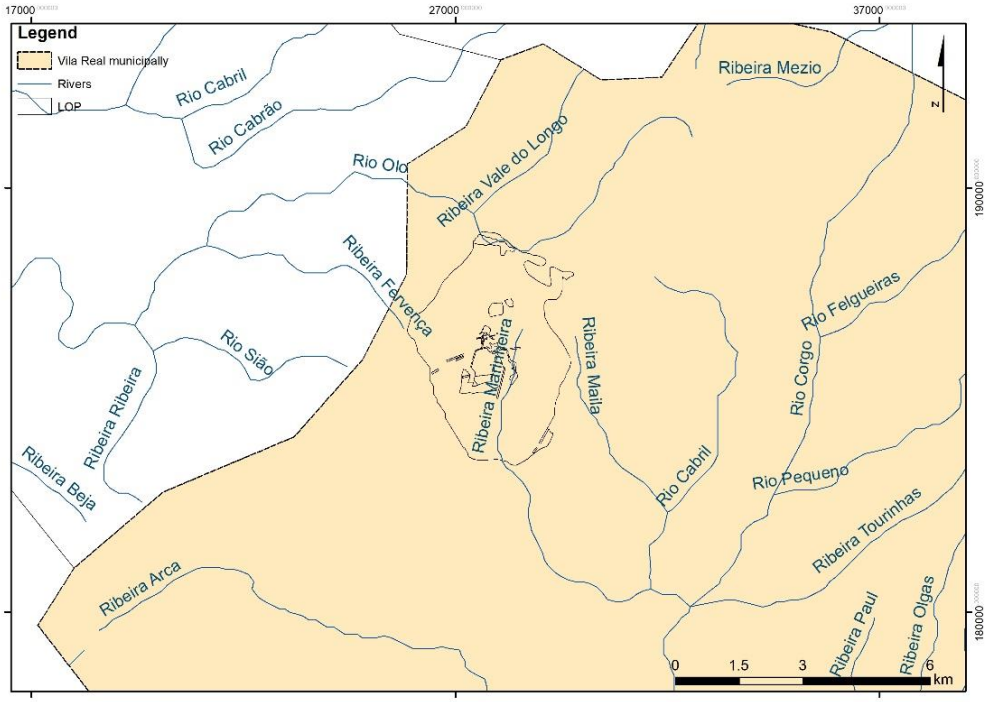


Figure 2-2. Rivers and streams in the studied area (based: Direção-Geral do Território, 2013a).

The studied area is hilly and standing between roughly 190 m and 1320 m above sea level (fig. 2-3). Figure 2-3 was interpolated using a Digital Elevation Model[1] (DEM) with a cell size of 20 m x 20 m.

The studied area is represented in the sheet number 101 – Lordelo (Vila Real) from military maps at scale 1:25 000 (fig. 2-4) and, is part of Alvão Natural Park.

[1] DEM kindly provided by Professor José Alberto Gonçalves from DGAOT-FCUP.

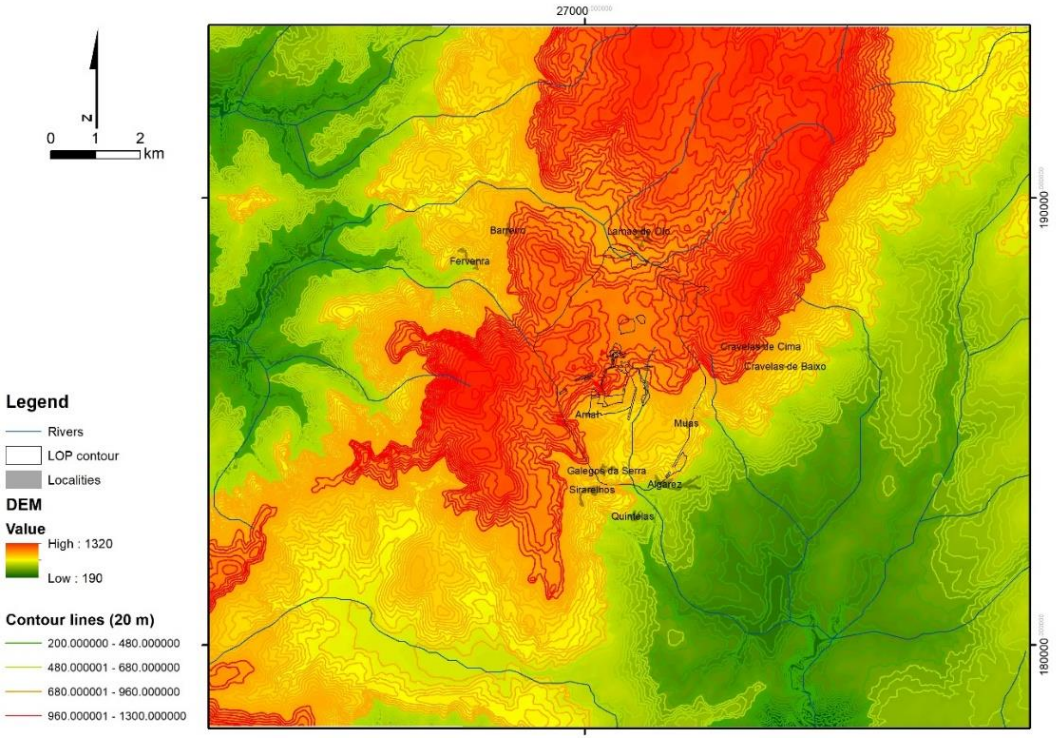


Figure 2-3. DEM of the studied area (20 m x 20m).

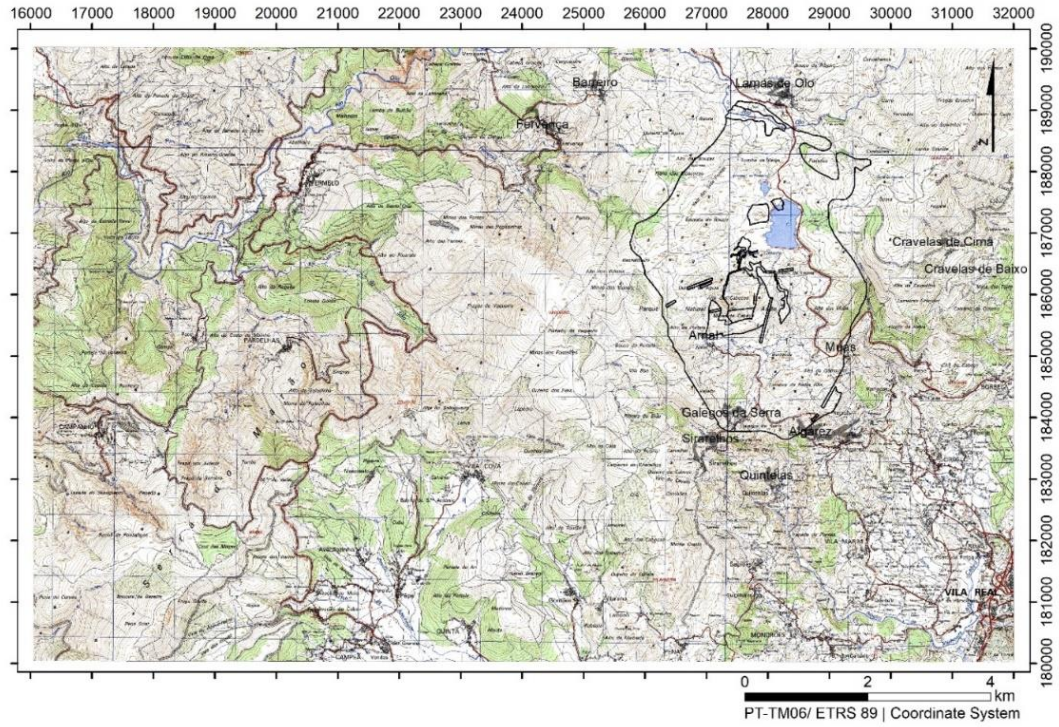


Figure 2-4. Sheet nº 101 – Lordelo (Vila Real) from military maps at scale 1:25 000 with the Lamas de Olo Pluton outline (modified).

2.2 GEOLOGICAL SETTING

2.2.1 The Iberian Variscan Belt

The Iberian Variscan belt, also known as Iberian Massif, is a large curved segment of the European Variscan belt resulting from the Laurussia-Gondwana collision during Devonian to Carboniferous times (Franke, 1989; Ribeiro *et al.*, 1990, Kroner & Romer, 2013). After the collision, during the late Paleozoic, the Pangea amalgamation leads to continuous rock deformation and the C-shaped Cantabrian orocline was formed (*e.g*. Gutiérrez-Alonso *et al.*, 2012; Weil *et al.*, 2013). Other authors suggest a more complex scenario, with the existence of two oroclines, in S-shaped, the Cantabrian, and Central-Iberian (*e.g.* Shaw *et al.*, 2012; Pastor-Galán *et al.*, 2012).

The Iberian Belt is subdivided into several geotectonic zones (fig. 2-5): the Cantabrian Zone, the West Asturian Leonese Zone, the Central Iberian Zone (CIZ), the Ossa Morena Zone and the South Portuguese Zone (Lotze, 1945; Julivert *et al.*, 1974). Farias *et al.* (1987) identified allochthonous and parautochthonous units in the CIZ, which led them to consider another zone, the Galicia Trás-os-Montes Zone (GTMZ).

Three main ductile deformation phases have been documented in northern Portugal, namely D_1, D_2, and D_3 (Noronha *et al.*, 1981). In the CIZ, the autochthonous terrane from the Iberian Belt, two main phases of deformation can be recognized: D_1 (*ca*. 360–337 Ma, *e.g.* Dallmeyer *et al.,* 1997; Castiñeiras *et al.,* 2008; Martínez Catalán *et al.,* 2014; Díez Fernández *et al.*, 2016; Pereira *et al.*, 2018) and D_3 (*ca*. 321–300 Ma, *e.g*. Ferreira *et al.*,1987; Pereira *et al.*, 2018) phases. D_1 produced isoclinal folds with a subvertical axial plane with an NW-SE strike and a well-marked axial plane schistosity (S_1), and D_3 is characterized by wide folding of small amplitude with the subvertical axial plane and NW-SE sub-horizontal axis. Simultaneously, during D_3, vertical ductile shear zones were developed in lower structural levels. In the upper structural levels, a brittle deformation occurred, leading to fracture-conjugate systems with NNE-SSW and NNW-SSE directions (Marques *et al.*, 2002). D_2 (*ca*. 337–316 Ma; *e.g.* Dallmeyer *et al.* 1997; Díez Fernández *et al.*, 2016; Martínez Catalán *et al.* 2014; Pereira *et al.*, 2018) is well represented in allochthonous terranes in the GTMZ and is characterized by recumbent folds with axial plane crenulation cleavage or schistosity associated with large thrust units or sub-horizontal extensional shear zones.

The late-Variscan time is considered as the period of a widespread episode of fracturing in the Variscan belt of SW Europe (Ribeiro, 1974; Arthaud & Matte, 1975; Marques *et al.*, 2002). References terrain in SW Europe show that all post-kinematic granitoids (dated between 295-270 Ma by Dallmeyer *et al.*, 1997; $^{40}Ar/^{39}Ar$ isotope dating) are affected by the widespread late-Variscan wrench faulting, thus the strike-slip event has a lower limit age *ca*. 312 Ma, and should be younger than 270 Ma (K/Ar isotope dating of fault rocks; Marques *et al.*, 2002).

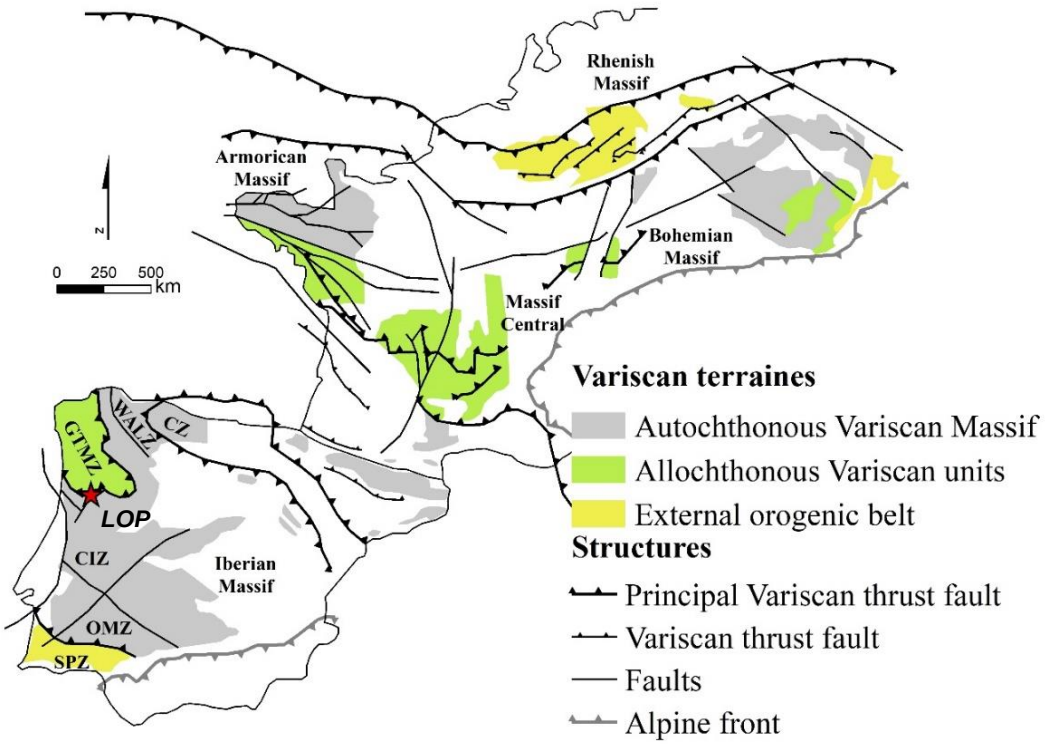


Figure 2-5. Iberian Variscan belt with the location of the studied pluton: LOP - Lamas de Olo Pluton (modified: Ferreira *et al.*, 1987). CZ - Cantabric Zone, WALZ - West Asturian Leonese Zone, GTMZ - Galicia Trás-os-Montes Zone, CIZ - Central Iberian Zone, OMZ - Ossa Morena Zone, SPZ - Sul Portuguesa Zone (based: Julivert *et al.*, 1974; Farias *et al.*, 1987).

In NW Iberia, four sub-vertical fracture systems are recognized: N 80º ± 20º, N 25º ± 25º, N 155º ± 15º, and N 110º ± 10º systems (fig. 2-6). The maximum compressive stress, σ_1, during the late-Variscan times is NE-SW, resulting in two conjugate systems, with N 80º (sinistral) and N 25º (dextral) directions. N 25º fault system minimum age yield by K/Ar dating in muscovites was *ca.* 312 Ma, considered as late-Variscan wrench-faulting period (Marques *et al*., 2002).

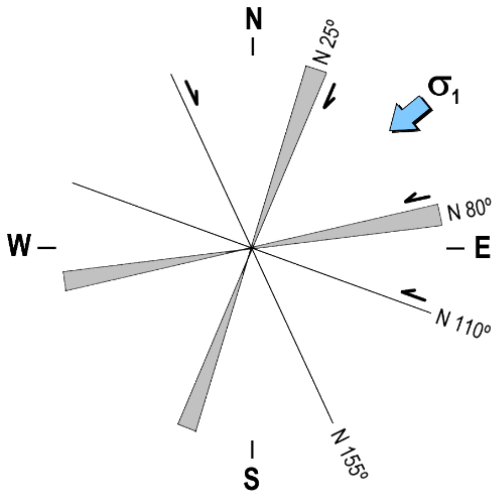


Figure 2-6. Geometry and kinematic of the main fault systems. σ_1 is the maximum compressive stress deduced from brittle late-Variscan fault sets during syn-D_3 to late-D_3 (N 25º and N 80º as conjugated fault systems (Marques *et al.*, 2002).

2.2.2 Variscan granites classification

The CIZ is characterized by the presence of huge volumes of granitic rocks that represent about 60% to 70% of the outcropping rocks. These granites *s.l.*[2] show a high variability regarding their characteristics due to the magmatic differentiation, assimilation, and the possibility of the mixing of magmas during the ascending in the crust. To better distinguish the different groups of granitoids, several classifications have been proposed by different authors. These classifications have different criteria in consideration like tectonic-metamorphic and geotectonic data, chronological information, textural, mineralogic, petrographic, and geochemical data. In table 2-1, some of the Variscan granite classifications are indicated.

In the northwestern part of Portugal, most of the granite intrusions were emplaced during the post-collisional stage of the Variscan orogeny (321-300 Ma; *e.g*. Ferreira *et al.*, 1987; Dias *et al.*, 2010; Pereira *et al.*, 2018).

The magmatic intrusions and the surrounding metasedimentary rocks show a relation with regional structures, which is expressed by: (i) the presence of large antiformal alignments such as the magmatic-metamorphic belts of Porto-Viseu, Cabeceiras de Basto-Vila Real-Torre de Moncorvo, and Meda-Penedono-Lumbrales, where the two-mica granites prevail; (ii) the development of first-order crustal ductile shear zones (Vigo-Régua and

[2]The term “granite(s)” is used in the *s.l. (sensu lato),* including all the rocks with granitic composition like *granites s.s. (sensu stricto)*, leucogranites, granodiorites and adamellites.

Juzbado-Penalva do Castelo) where the biotitic granites (generally integrating complexes with acid-base associations) are predominantly associated; (iii) the last intrusion of less voluminous magmatism (Peneda-Gerês, Vila Pouca de Aguiar, Águas Frias-Chaves, Lamas de Olo and Lavadores-Madalena plutons) associated with late-Variscan fragile deformation phase (Gerês-Loivos, Verín-Régua-Penacova, and Porto-Tomar faults; Ribeiro *et al.*, 2019).

Schermerhorn (1956) and Oen (1970) classified the Variscan granites in oldest, older, and younger granites. Recently, some authors (*e.g*. Ferreira *et al.*, 1987; Noronha *et al.*, 2006; Dias *et al.*, 2010) subdivided the granites into four groups relative to the last Variscan ductile deformation phase (D_3): syn-D_3 (~321-312 Ma), late-D_3 (~312-305 Ma), late- to post-D_3 (~300 Ma) and post-D_3 (~299-290 Ma).

Among these granites, some result from the melting of metasedimentary materials and others from igneous rocks, corresponding to S-type and I-type granites, respectively (Chappell & White, 1974). The first group (S-type granite) is formed by anatectic leucogranites, with color index M < 10 (< 10 vol.% of dark, mafic minerals) and characterized by peraluminous chemistry with alumina saturation index, ASI > 1. A second group (I-type granite) is formed by granodiorites and monzogranites, showing characteristic affinities to calc-alkaline batholith associations of active continental margins. They may be metaluminous (ASI < 1) or slightly peraluminous (ASI > 1). Biotite is the dominant mafic mineral. Contamination with the local host metasedimentary rocks may produce locally a subtype of granites that, though retaining typical features of calc-alkaline granites of the second group, have peraluminous chemistry and contain metamorphic minerals (I-S type granite). This subgroup is referred to here as calc-alkaline contaminated (Chappell & White, 1974; Ribeiro *et al.*, 2019).

The Chappell & White (1974) classification is supported namely by the fact that these two types of granites have distinctive oxygen isotope ratios of whole-rock ($\delta^{18}O$) values. The highest $\delta^{18}O$ values (between 12.3‰ and 13.5‰) indicate a crustal origin, through anatexis of metasedimentary protoliths, and the lowest values (between 8.9‰ and 12.2‰) suggest a mantle contribution and/or source dominated by mafic and meta-igneous rocks (Ishihara, 1977; Ellwood & Wenner, 1981). Considering the petrographic characteristics, the granites are divided into two groups: two-mica and biotite granites (Capdevilla & Floor, 1970; Capdevilla *et al.*, 1973). Two-mica granites are peraluminous and must have primary biotite and muscovite in their mineralogical composition and are related to regional metamorphism.

Otherwise, the biotite granites have a deeper origin in the crust and with relatively dry magmas.

The different redox conditions in the magma chamber are responsible for different characteristics of the granites and for the presence of certain Fe minerals like magnetite and ilmenite. Then, the presence of magnetite or ilmenite in the protolith rocks allows the genesis of the oxidized- or magnetite-type and reduced- or ilmenite-type granites, respectively (Ishihara, 1977). The magnetite-series granites are considered to have been generated at high depth (upper mantle and lowest crust) where no carbonaceous material exists, whereas the ilmenite-series were originated at a shallower level (middle to lower continental crust) where small amounts of crustal carbon are present (Ishihara, 1977; Sheppard, 1977; Ellwood & Wenner, 1981).

Table 2-1. Summary of some granite classifications by: [(1)]Schermerhorn (1956); [(2)]Oen (1970); [(3)]Ferreira *et al.* (1987); [(4)]Dias *et al.* (1998); [(5)]Martins (1998); [(6)]Dias *et al.* (2010); [(7)]Albuquerque (1971); [(8)]Capdevila *et al.* (1973); [(9)]Corretgé *et al.* (1974); [(10)]Capdevila & Floor (1970) ; [(11)]Chappell & White (1974); [(12)]Chappell & White (2001); [(13)]Ishihara (1977); [(14)]Sheppard (1977); [(15)]Ellwood & Wenner (1981).

Classification									
Tectono-metamorphic (1, 2)	**Geotectonic** (3)	**Geochronologic (Ma)** (3, 4, 5, 6)		**Genetic** (7, 8, 9, 10, 11, 12)		**Protolith** (8, 9)	**Petrographic and geochemical** (7, 10)		**Oxidizing conditions** (13, 14, 15)	**Common facies**
Oldest	Pre-orogenic	Ante-D_3	> 321	Supracrustal	S-type	Mostly metasedimentary rocks with organic matter; and in minor amounts igneous rocks	Two-mica granites	Alkaline	Ilmenite-type	Leucogranites, granites, granodiorites
Older	Syn-orogenic	Syn-D_3	321-312							
		Late-D_3	312-305	Infra- to mid-crustal	I-type or S-type	Mostly igneous rocks	Two-mica and biotite granites	Chalco-alkaline (sometimes peraluminous)	Ilmenite or magnetite-type	Granodiorites, adamellites
		Late- to post-D_3	*ca*. 300							
Younger	Late-orogenic	Post-D_3	299-290				Biotite granites			

2.2.3 Emplacement mechanisms of granitic plutons

The structure of a granite pluton results not only of its nature but also of the ascending process, emplacement, and cooling conditions. Regarding the ascending of magmas into the crust, space must be created for their accommodation in the crust (Cobbing, 2000). This space can be created according to different tectonic regimes: transpressive, transient, distensive, and compressive regime (Vigneresse, 1995a, 1995b, 2004).

Granitic emplacement models can be divided into forced (diapirism and ballooning) and passive (stoping and cauldron subsidence) mechanisms. The former deforms the host rock (concordant plutons), while the latter take advantage of the space created by regional deformation (discordant plutons; Castro, 1987; Hutton, 1988). Castro (1987) also refers that the concordant plutons are mostly syntectonic, while the discordant plutons are late- or post-tectonic.

The (vertical) ascent of magmas in the crust, is done essentially through channels (Petford *et al.*, 2000), along dikes (*e.g*. Clemens & Mawer, 1992), along pre-existing faults (*e.g.* Petford *et al.*, 1993) or through a network of shear zones (*e.g.* D'Lemos *et al.*, 1992).

The integrated study of the magnetic fabric (obtain by anisotropy of magnetic susceptibility data) and the regional anomaly (obtain by gravimetric surveys) allows characterizing the granitic plutons according to their shape, roots location, and emplacement model.

The shape of the plutons has been described by several authors like Vigneresse (1990), Vigneresse *et al*. (1999), Bouchez (1997), and Améglio *et al.* (1997).

The plutons can be classified as flat-floor plutons or flat-shaped plutons and wedge-shaped plutons (Améglio *et al.*, 1997; fig. 2-7). Améglio *et al.* (1997) characterized several plutons concerning their shape, both in Spain and France. As examples of flat-floor plutons, the authors described the Saint-Sylvestre and Sidore pluton (both in France), and as the wedge-shaped plutons, the Cabeza de Araya pluton (Spain) and Mortagne pluton (France) can be considered.

In Portugal, studies carried out by Martins *et al.* (2009), Sant'Ovaia (2014), and Machadinho (2015) described the emplacement model of Vila Pouca de Aguiar and Águas Frias plutons, Santa Eulália Plutonic Complex, and Beiras batholith, respectively. The Vila Pouca de Aguiar and Águas Frias plutons are located in the Galicia Trás-os-Montes Zone and their emplacements are related to the Verín-Régua-Penacova Fault. These plutons,

although both related to the same regional structure, have different shapes: the Vila Pouca de Aguiar pluton is classified as a thin laccolith type (~ 1 km) with several roots, and the Águas Frias pluton is wedge-shaped with higher crustal expression (~ 5 km; Martins *et al.*, 2009). Sant'Ovaia *et al.* (2014) carried out studies in a massif in the Ossa Morena Zone, namely in the Santa Eulália Plutonic Complex, verifying that it is a composite pluton classified as a flat-floor pluton. The Beiras batholite has *ca*. 5 km in-depth and is classified as a flat-shaped pluton (Machadinho, 2015).

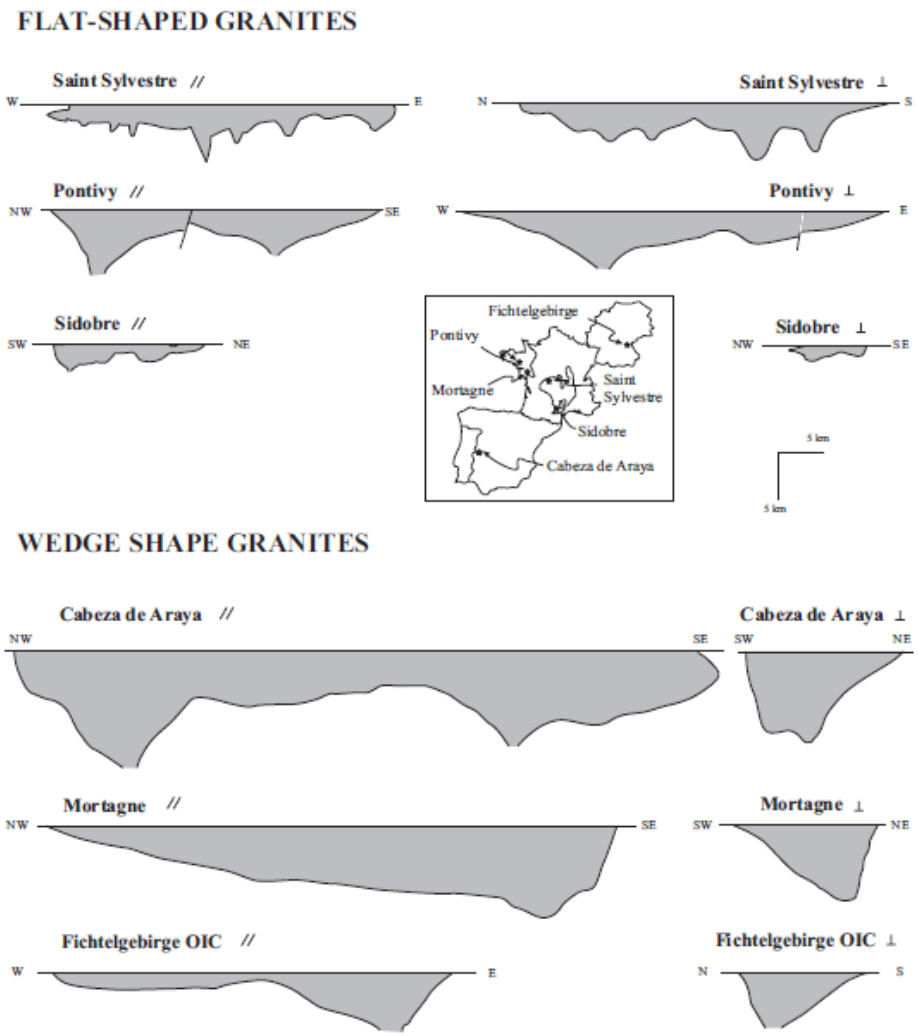


Figure 2-7. Cross-sections through granitic massifs from France and Spain, showing their morphology with depth, as inferred from 3D inversion of gravity data. All sections are shown at the same scale with no vertical exaggeration. On the left, cross sections are parallel to the major axis of the massifs, and on the right, they are perpendicular to it. Roots zones are evidenced by abrupt changes in dips of the walls (modified: Améglio *et al.*, 1997 in Vigneresse *et al.*, 1999).

2.2.4 Regional geological setting

The description of the regional geological setting from the studied area is based on previous studies carried out by several authors.

The studied granites belong to the LOP, which is a small outcrop with a rhombus shape that occupies an area of *ca*. 13.7 km^2. The LOP is a post-tectonic (post-D_3) pluton and is located on the northern border of CIZ (fig. 2-5). It was mapped in the *Folha 10-A – Celorico de Basto* (Pereira *et al.*, 1987) from the Geological map on 1:50 000 (fig. 2-8). The LOP is cut by several fractures, namely, by NNW-SSE offsets (*ca*. N 150º) conjugated with the NNE-SSW (*ca*. N 10º) subparallel to the Verín-Régua-Penacova Fault (VRPF). Another WSW-ENE fault system (*ca*. N 80º), conjugated with N 25º ± 25º fault system, is visible, mostly in the middle and in the SE part of the pluton. The VRPF belongs to the N 25º ± 25º fault system and is a regional fault still active and marked by several hot CO_2 rich mineral water springs.

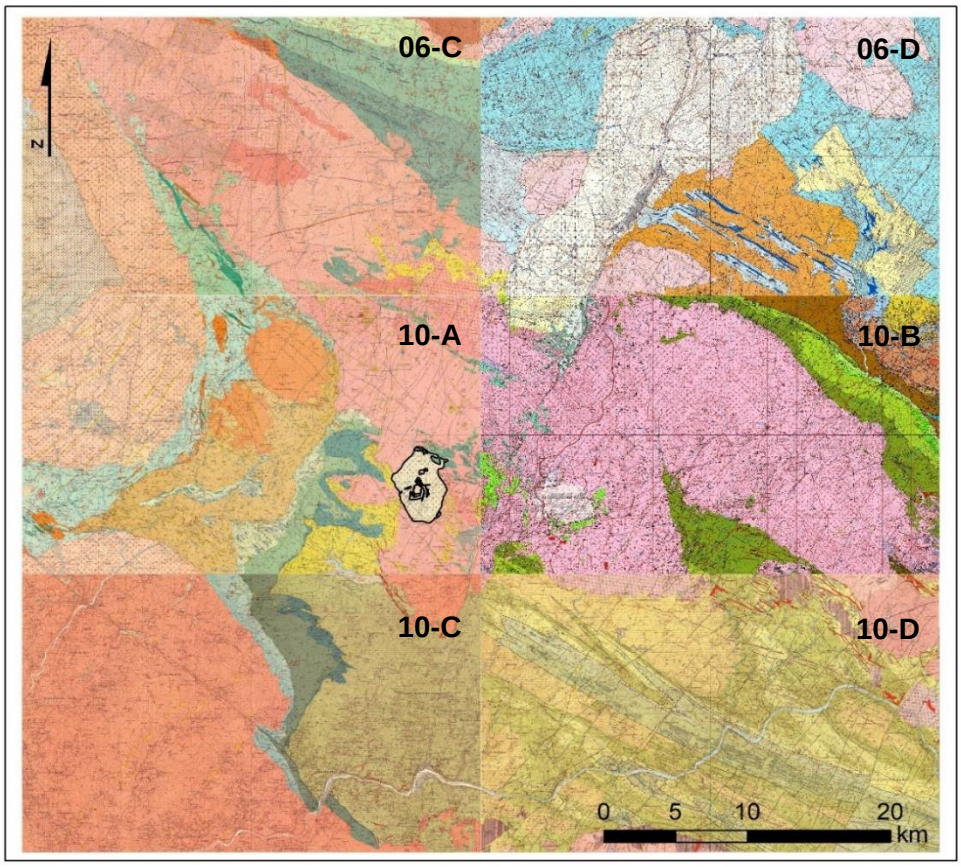


Figure 2-8. Geological maps of the studied and surrounding areas: 06-C-Cabeceiras de Basto (1992); 06-D - Vila Pouca de Aguiar (1998); 10-A - Celorico de Basto (1987); 10-B – Vila Real (2015); 10-C - Peso da Régua (1967); 10-D - Alijó (1987) (GeoPortal–LNEG., 2010a).

The LOP (fig. 2-9) is composed of distinct outcropping biotite granites similar in mineralogical composition but with different grain size (Pereira, 1989; Fernandes *et al.*, 2013):

- Lamas de Olo – LO (γGgπ) is the main granite, and corresponds to a medium- to coarse-grained porphyritic granite;
- Alto dos Cabeços – AC (γGmπ), outcrops near Arnal village and is a fine- to medium-grained porphyritic granite;
- Barragem – BA (γG), outcrops near the *Cimeira* Dam (in Portuguese *Barragem da Cimeira*) and is classified as leucocratic fine- to medium-grained and slightly porphyritic granite.

Studies on Lamas de Olo Pluton carried out by Helal (1992), conducted to a more detailed cartographic information (fig. 2-10). In his work, B. Helal named the studied pluton as Celorico de Basto batholite, and classified the intrusions as adamellites (or quartz monzonite):

- LO is named as LOGgn, is a porphyritic biotite adamellite of Lamas de Olo (coarse-grained);
- AC is named as LOGmp, is a porphyritic biotite adamellite (fine-grained);
- BA is distinguished in 4 leucocratic outcrops types, the LOLa (the central and principal outcrop with evidence of hydrothermal fluids circulation), LOG1 and LOG2 (two small outcrops located near the *Cimeira* Dam) and LOGfilon, that outcrops in veins.

Aplite veins crosscut the LOP granites, filling fractures mostly N 80º, but also N 10º. Quartz veins (some of them mineralized), N 80º trending, are also present.

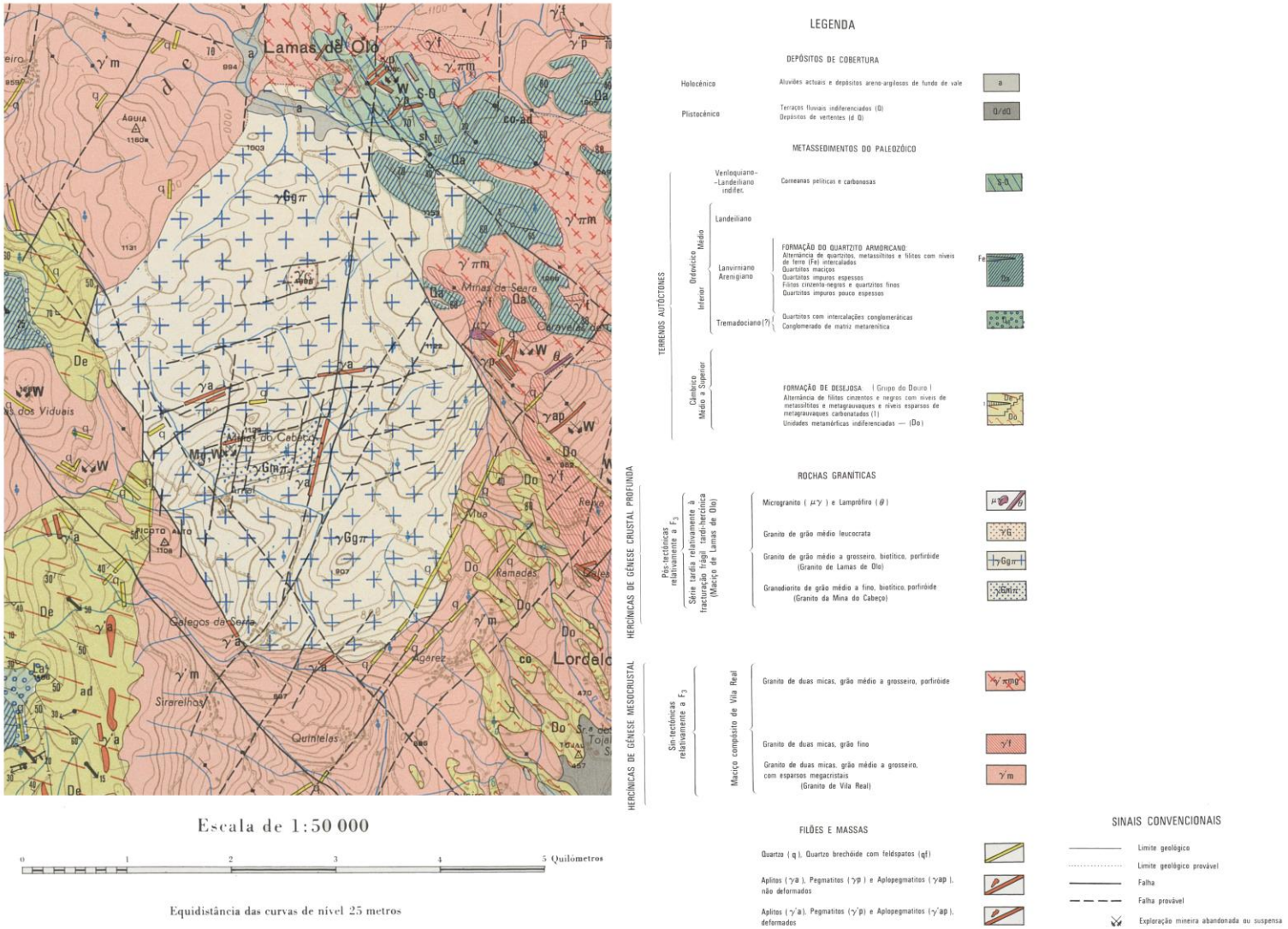


Figure 2-9. Excerpt of the geological map 10-A (Celorico de Basto), showing the LOP granites and host rocks (adapted: Pereira *et al.*, 1987).

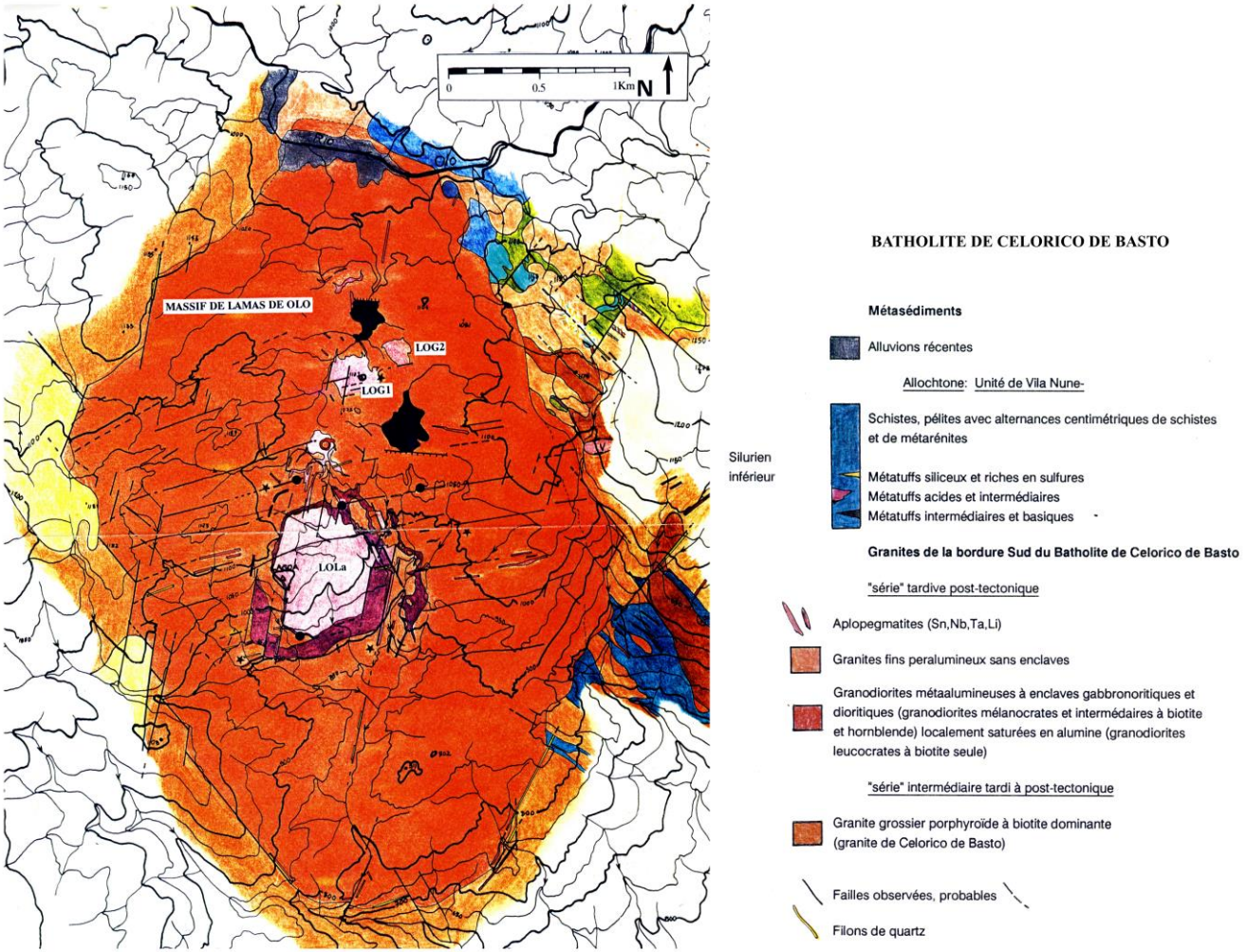


Figure 2-10. Geological map from the Celorico de Basto batholite[3] made by Helal (1992).

[3] Helal (1992) named the studied pluton as Celorico de Basto batholite, but in this study, the Lamas de Olo Pluton is the name used. Beyond that, instead of B. Helal symbology of LOGgn, LOGmp, LOLa, LOG1, LOG2 and LOGfilon, the abbreviations LO, AC and BA are used to enumerate LOP granites.

$^{207}Pb/^{235}U$ in monazite yields an age of 297.19 ± 0.73 Ma to LO granite (Fernandes *et al.*, 2013).

The LOP intrudes Armorican Quartzite Formation and schists from Upper Silurian to Medium Ordovician (Lower Paleozoic Formations), the Desejosa Formation (belongs to the Douro Group Metasediments – DGM – from Upper to Medium Cambrian in age), and two-mica syntectonic granites from Vila Real Massif (VRM; figs. 2-8).

Cover deposits:

- Terrace and sands (Pleistocenic to Holocenic age):
    - Current alluviums (a);
    - Undifferentiated fluvial terraces (Q).

Metasedimentary rocks comprise:

- Autochthonous terrains from Ordovician age:
    - Pelitic and carbonous hornfels (S-O; Medium Ordovician to Upper Silurian);
    - Armorican Quartzite Formation (Qa; Lower to Medium Ordovician): quartzites and metasiltites.

- Autochthonous terrains from Cambrian age:
    - Desejosa Formation from Douro Group Metasediments (De; Upper Cambrian): grey to black phyllite with metasiltites and metagraywacke levels and sparse levels of carbonated metagraywackes;
    - Desejosa Formation from Douro Group Metasediments (Do; Upper Cambrian): undifferentiated metamorphic unites.

The VRM, it is a composite massif constituted by five syntectonic (syn-D_3) two-mica granites with small texture differences. This massif is emplacement in the hinge zone of the Monção-Vila Real-Torre de Moncorvo antiform (Vilela de Matos, 1991). Available monazite and zircon analysis yield $^{207}Pb/^{235}U$ ages of *ca*. 311 ± 1 Ma (Cabeceiras de Basto granite; Almeida *et al.*, 1998) and of *ca*. 316 ± 7 Ma (Carrazeda de Ansiões granite; Teixeira, 2008; Teixeira *et al*., 2012) for two granites located in this massif.

In the studied area three facies of the VRM are present (Pereira, 1989; fig. 2-8):

- Medium to coarse-grained porphyritic granite (γ'πm);
- Fine-grained granite (γ'f);
- Medium to coarse-grained granite with sparse megacrystals (also known as Vila Real granite; γ'm).

All VRM granites are essentially composed of quartz, plagioclase (mostly albite), K-feldspar (microcline-pertite and Na-microcline), muscovite, and biotite. As subordinated mineralogy, the VRM has Fe-Ti-oxide minerals, sphene-leucoxene, rutile, zircon, apatite, tourmaline, monazite, hydrate Fe-oxide, muscovite II, myrmekite, chlorite, and sillimanite. Some granites from VRM have associated Sn mineralizations, in pegmatites, and W-Sn in hydrothermal quartz veins (Pereira, 1989).

Aplite, pegmatite, aplite-pegmatite, and quartz veins crosscut both VRM and DGM, filling fractures with different directions.

Other lithologies outcrop in the studied area, although without spatial relation with LOP outcrops, like (Pereira, 1989):

- Autochthonous terrains from Ordovician age:
  - Quartzites with conglomeratic intercalations (O_1).
- Autochthonous terrains from Cambrian age:
  - Lapedro and Alto da Cota conglomerates (Discordance; La).
- Intrusions post-D_3:
  - Microgranites (μγ);
  - Lamprophyres (θ).

2.3 MINERAL OCCURRENCES

Several studies have been done in granites searching their association with ore deposits but many doubts about the formation of these deposits and the relationship with the magmatism still exist.

Neiva (1944) emphasizes the importance of tungsten and tin mineralizations in northern and central Portugal and proposed the existence of a “W-Sn metallogenic province”. Thadeu (1965) described several “Mineralogenic provinces” in Portugal: Meridional, Setentrional, and Central provinces (with ante-Variscan and Variscan mineralizations), and also a Hesperic province (including the post-Variscan mineralizations). In the “Setentrional Province”, there are two types of mineralizations: syngenetic deposits (*e.g*. Fe, Mn, coal), and granite related deposits (*e.g*. Be, Mo, Sn, W, Au).

Most of the granite intrusions in the Variscan belt are coeval with D_3 and others are late- and post-D_3 (*e.g.* Ferreira *et al.*, 1987; Dias, 2001). The development of different tectonic structures namely shear zones during D_3 and successive reactivation events controlled the granite emplacement and concurrently, they caused an extensive hydrothermal activity throughout the entire crust, involving distinct fluid sources, some of them comprising significant amounts of ore mineral phases (Mateus & Noronha, 2010). The granites can reflect several metallogenic events: (i) Sn-Li pegmatites are essentially associated with two-mica granites; (ii) W (Sn) and W (Mo) quartz-vein deposits are related to biotite granites; (iii) W (Mo) deposits are related to post-D_3 biotite sub-alkaline granites (*e.g.* Neiva, 1944; Thadeu, 1965; Schermerhorn, 1981; Noronha *et al.*, 2006; Mateus & Noronha, 2010; Noronha, 2017).

In recent bibliography concerning metallogenic studies associated with post-tectonic magmatism, Romer & Kroner (2015, 2016) present a model that combines the different tectonic environments and/or different heat sources with the occurrence of metallogenic Sn-W deposits. They argue that Sn and/or W mineralizations result from a sequence of processes: the source enrichment, the source accumulation, and the metal extraction from the source rocks, followed by additional metal concentration through fractionated crystallization and late-stage fluid-controlled processes. Beyond this, the distribution of Sn, W, and Mo mineral occurrences are not restricted to a single tectonic setting and may be

also related to crustal extension and rifting. Romer & Kroner (2015, 2016) consider that in Europe, these mineralizations are associated with synorogenic granites, except for Cornwall, which they consider to be related to post-orogenic granites, associated with episodes of regional extension. Noronha *et al.* (2013) described for Portugal the occurrence of metallogenic deposits of W-(Sn)-Mo-Be with post-tectonic granites, which may represent an independent metallogenic period equivalent to that described as associated with episodes of regional extension.

Studies carried out by Ellwood & Wenner (1981), show that the magnetic susceptibility of granites, indicative of magnetite content, is inversely related to the whole-rock (W.R.) $\delta^{18}O$ variability. The magnetic susceptibility (K_m) and W.R. $\delta^{18}O$ data allow us to establish a relationship between granite type (ilmenite- or magnetite-type granite, and I-, I (peraluminous)- or S-type granites) and associated mineralizations (Kwak & White, 1982; Belvin & Chappell, 1992; Takagi & Tsukimura, 1997; Kumar, 2010), once redox conditions are responsible for the specific mineral occurrences.

The occurrence of ore deposits associated with plutons of ilmenite-type and/or magnetite-type granites are largely described in southern Korea and southwestern Japan (Ishihara *et al.*, 1981), and in Indonesia (Maulana *et al.*, 2013). In southern Korea and southwestern Japan (Ishihara *et al.*, 1981), W-Mo occurrences were described in areas with both ilmenite- and magnetite-type granites with no clear separation in the distribution of the two types of granites. Otherwise, the composite bodies in Sulawesi, Indonesia, have ilmenite-type granites grouped in the southern zone of the island while the magnetite-type granites occur in the northern area. Both granites are associated with ore mineralization, where Cu-Au-Mo mineralizations are associated with magnetite-series granitic rocks, but potential Sn-W mineralization related to ilmenite-type granites has not yet been reported (Maulana *et al.*, 2013).

Recently, studies using the magnetic susceptibility as a pathfinder to the principal metal associations were made in granites from the northern Portugal (*e.g.* Mateus & Noronha, 2010; Sant'Ovaia *et al.*, 2013a, 2013b). The magnetic susceptibility *versus* whole-rock $\delta_{18}O$ (K_m *versus* W.R. $\delta_{18}O$) diagram proposed by Sant'Ovaia *et al.* (2012), points out that the Sn-ore deposits are associated with S- and ilmenite-type granites and the W-(Sn) mineralizations occur in veins that cut the I (peraluminous)- and ilmenite-type granites, both

with high $\delta^{18}O$ values. The W-(Mo, Bi) occurrences are spatially related to I (peraluminous)- and magnetite-type granites (*e.g.* Sant'Ovaia *et al.*, 2012, 2013b).

For the studied pluton, Pereira (1989) and Helal (1992) described the presence of mineral occurrences association relatively rare in northern Portugal of W-Mo-Be. These mineralizations occur in association with the LOP granites, mostly in N 80º E sub-vertical quartz veins.

2.4 CARTOGRAPHIC INFORMATION

Published geological information was used and modified according to new data. The cartographic information, namely the geological maps, were consulted and paper and digital databases were used.

2.4.1 Map specifications

Several cartographic information was obtained in *geoPortal* (GeoPortal-LNEG, 2010a, 2010b) from the *Laboratório Nacional de Energia e Geologia* (LNEG). These data were downloaded and processed in *ArcGIS*, providing information used to create thematic raster and vector maps. The location of mineral occurrences was also obtained in LNEG site.

Information downloaded:

- Geological maps at 1:50 000 (GeoPortal–LNEG, 2010a):
    - *Folha 10-A - Celorico de Basto* (1987)
    - *Folha 10-B - Vila Real* (2015)
    - *Folha 10-C - Peso da Régua* (1967)
    - *Folha 10-D - Alijó* (1987)

- *ArcGIS* supplements (on *MapServer*; GeoPortal–LNEG, 2010b)*:*
    - Cartogram from geology at 1:50 000 (CGP50k)
    - Cartogram from geology at 1:200 000 (CGP200k)
    - Cartogram from geology at 1:500 000 (CGP500k)
    - Mineral occurrences at 1:500 000

2.4.2 Coordinate system

The data processing was made using several Geographic Information System (GIS) software namely: *ArcGIS* 10.7, *Surfer* 10, *MatLab,* and *Oasis Montaj* 8.3.3.

In all the used software the data, namely sampling sites and gravimetric stations have a spatial location associated, in order to create georeferenced thematic maps, with the geological information obtained. The spatial location of sampling sites was obtained by Global Positional Satellite (GPS) and the gravimetric stations by Differential Global Positional Satellite (DGPS; see topic 3.5.2).

There are several Datum, however the commonly used are:

- *WGS84 – World Geodetic System 1984*: is a global Datum, which is incorporated in all GPS devices. It is materialized by a set of IGS (International GPS Service for Geodynamics) stations distributed throughout the planet (Direção-Geral do Território, 2013b).

- *ETRS89 – European Terrestrial Reference System 1989*: is the global reference systems recommended by the European Reference Frame, which is a subcommittee of the International Geodesy Association. The ETRS89 is a European Datum, currently recommended for Continental Portugal. This Datum matches with the WGS84 in 1989 (Altamimi & Boucher, 2001; Vasconcelos *et al.*, 2007). Based on the ETRS89, a PT-TM06 coordinate system was created for a Continental Portugal. The establishment of PT-TM06/ ETRS89 was based on international campaigns (carried out in 1989, 1995 and 1997), which aimed to connect the Portuguese network to the European network (Direção-Geral do Território, 2013b; Gonçalves, 2009).

In LOP studies, the GPS data was obtained in the WGS84 and then was converted to PT-TM06/ ETRS89. However, for gravimetric stations, a DGPS device was used, and the information was given directly in PT-TM06/ ETRS89.

CHAPTER 3:

SAMPLING AND METHODOLOGIES

“I am among those who think that science has great beauty."
Marie Curie

3 SAMPLING AND METHODOLOGIES

To achieve the thesis main goals, several sampling campaigns and methodologies were carried out.

3.1 FIELDWORK

3.1.1 Introduction

The fieldwork was made in order to increase the geological knowledge about Lamas de Olo Pluton (LOP). During the fieldwork, several tasks were performed:

- Field observations and structural measurements of geological features like faults, fractures, veins, and geological contacts. Previous studies have been made by several authors, but our field observations, revealed new information about LOP and host rocks; the new geological data is detailed in the topic 4.1.
- Representative sampling in LOP granites and quartz veins; hand samples and oriented rock cylinders were collected (see topic 3.1.2).
- Gravimetric campaigns (see topic 3.5.2).

3.1.2 Sampling and sample preparation

Hand samples were collected, and oriented rock cylinders were also sampled for the magnetic mineralogy studies. GPS coordinates and field observations were annotated in the field book. Sampling was performed according to the road accesses and the presence of fresh and *in situ* outcrops.

- **Magnetic and petrophysics studies**

The drill-oriented cores were collected with a STIHL petrol-powered portable drill from the *Instituto de Ciências da Terra – Polo Porto* (ICT-Porto). This machine has a drill bit constituted of a non-magnetic tube that ends in a diamond crown. The drill bit is cooled by pressurized water using an external hand pump (fig. 3-1).



Figure 3-1. Material for collecting drill-oriented cores: (1) Water jerrycan; (2) Pressure water hand pump; (3) Mixing gas tank; (4) STIHL petrol-powered portable drill; (5) Toolbox; (6) Orienting device.

The samples were oriented and identified *in situ* concerning the geographical framework using a specific instrument equipped with a compass (figs. 3-1 and 3-2).



Figure 3-2. Fieldwork photographs: (A) Sampling using STIHL petrol-powered portable drill; (B) Orientation *in situ* of the drill core; (C) Identification and notation of the azimuth and plunge in the core samples; (D) Oriented cores *in situ*.

At each sampling site, oriented cores (25 mm in diameter and 60 to 70 mm in length) were collected, and then, they were sawed in the laboratory (fig. 3-3), in order to obtain cylinders with 22 mm long. For the drill cores sawing, a saw machine that belongs to the ICT-Porto was used.

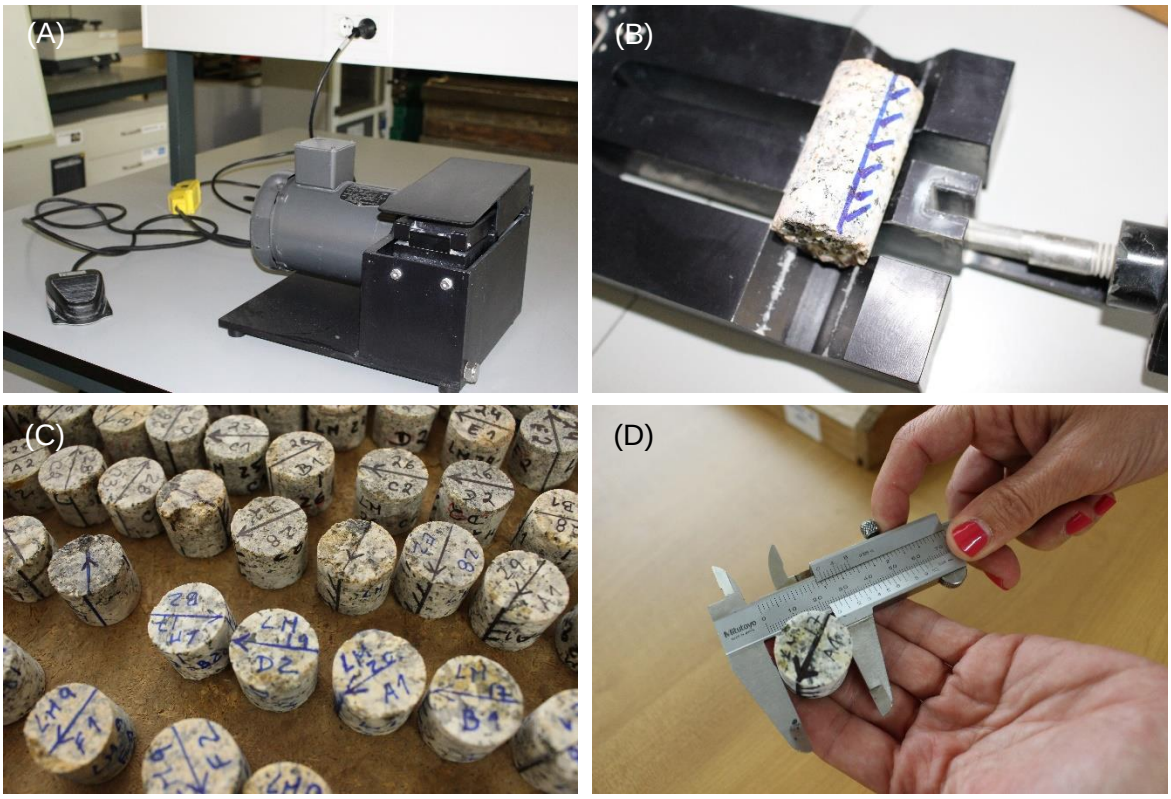


Figure 3-3. Procedures in the laboratory: (A) Electric saw; (B) Sampler holder of the saw machine; (C) Examples of rock cores with the 25 x 22 mm dimensions; (D) Measurements of volume with a caliper from each rock core.

In the studied area 350 oriented cores, from the 48 sampling sites, were collected, roughly distributed in the LOP granites (fig. 3-4 and attachment 1):

- 39 sites in LO granite → corresponding to 293 oriented cores;
- 5 sites in BA granite → corresponding to 28 oriented cores;
- 4 sites in AC granite → corresponding to 29 oriented cores.

Furthermore, some magnetic susceptibility measurements were acquired by Terraplus KT-10 magnetic susceptibility meter from ICT-Porto (manual equipment; see topic 3.3.2.1) in the Lamas de Olo Pluton (fig. 3-5 and attachment 1).

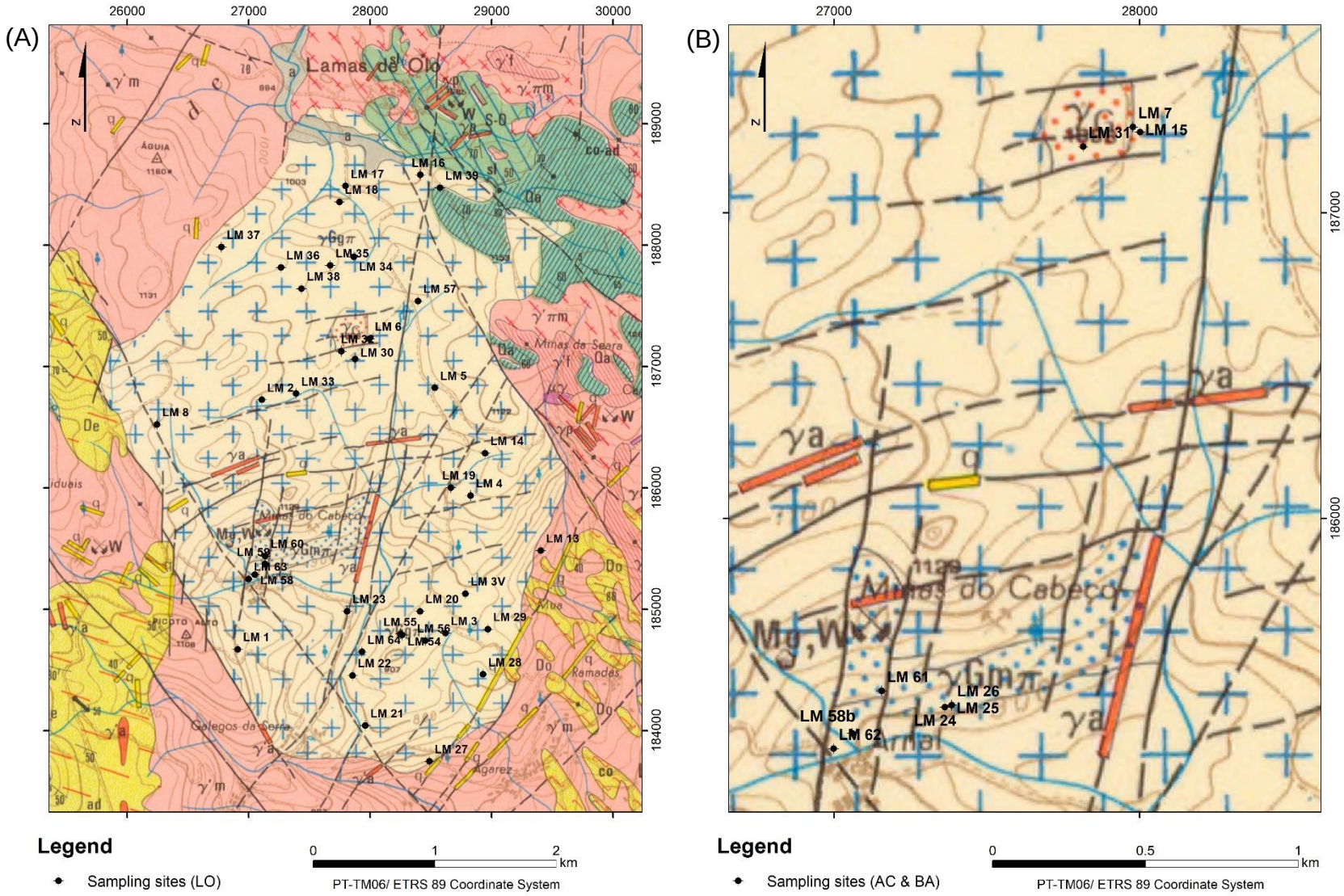


Figure 3-4. AMS sampling sites: (A) in the Lamas de Olo granite; (B) in the Alto dos Cabeços and Barragem granites (the basement is the geological map “10-A – Celorico de Basto” (Pereira *et al*., 1987).

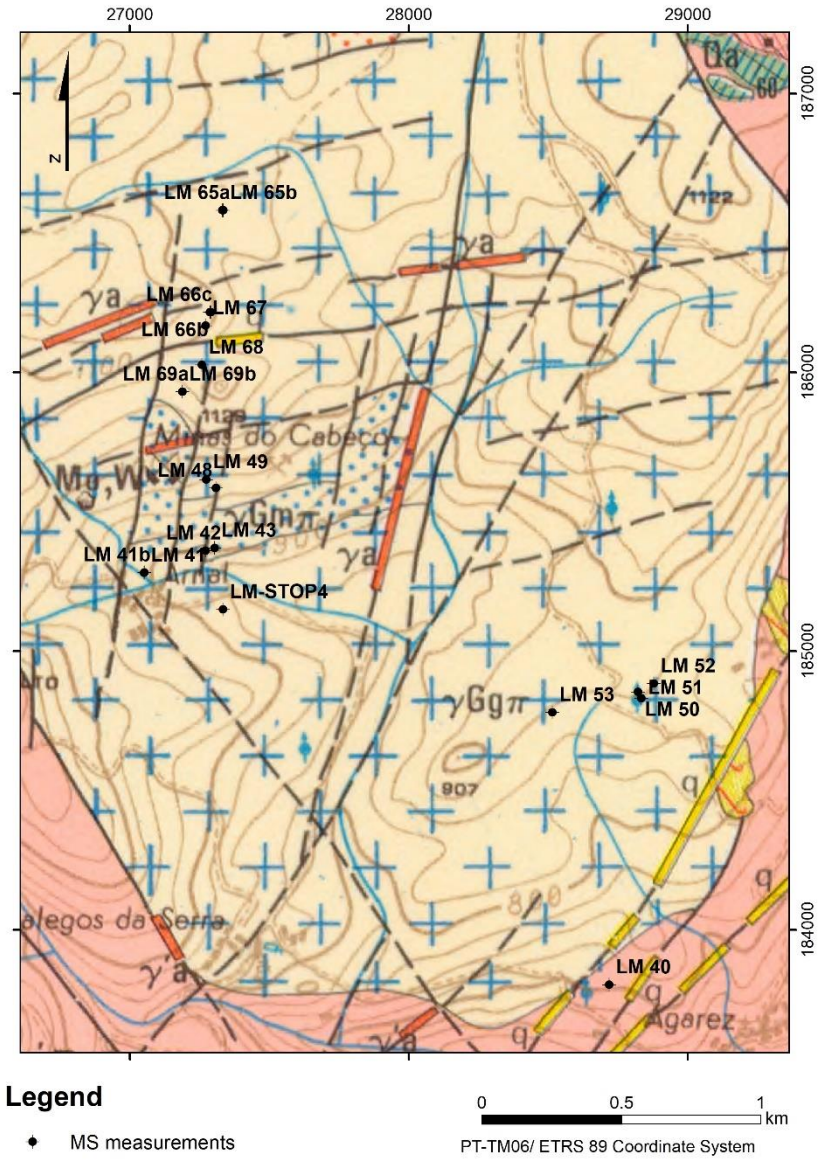


Figure 3-5. Location of the magnetic susceptibility measurement points acquired by Terraplus KT-10 magnetic susceptibility meter (manual equipment) in the Lamas de Olo Pluton (the basement is the geological map "10-A – Celorico de Basto" (Pereira *et al*., 1987).

For the anisotropy of magnetic susceptibility (AMS) measurements, all the 350 oriented cores from LOP were analyzed. However, for other analytical techniques, only representative LOP samples were selected. For the anisotropy of anhysteretic remanence magnetization (AARM) studies, 60 oriented cores (10 sampling sites), were selected; the thermomagnetic experiments were made in 14 oriented cores; the isothermal remanent magnetization (IRM) curves was realized in 4 oriented cores; and the frequency-dependence susceptibility (χ_{fD}%) was performed in 10 samples (table 3-1, attachment 1).

Table 3-1. Simplified table with sampling sites and magnetic methodologies applied[4] to each site in the Lamas de Olo Pluton (LO - Lamas de Olo granite; BA - Barragem granite; AC - Alto dos Cabeços granite; K_m (μSI) – magnetic susceptibility in μSI; AARM - Anisotropy of anhysteretic remanent magnetization; K_t *versus T* - Thermomagnetic experiments; IRM - Isothermal remanent magnetization; χ_{fD}% - Frequency-dependent susceptibility (%).

Sampling sites	Lithology	K_m (μSI)	AARM	K_t *versus T*	IRM	χ_{fD}%
LM 2	LO	1848	×			
LM 3	LO	2489	×			
LM 5	LO	2769		×	×	×
LM 8	LO	1564	×	×		×
LM 13	LO	44382	×	×		
LM 14	LO	2179	×			
LM 28	LO	2065	×			
LM 30	LO	2385	×			
LM 38	LO	1559		×		×
LM 16	LO	67		×	×	
LM 18	LO	79	×			
LM 22	LO	513		×		×
LM 7	BA	38		×	×	×
LM 15	BA	24	×	×		
LM 49	BA	54		×		
LM 62	BA	22		×		×
LM 58	BA	21				×
LM 24	AC	239		×		×
LM 25	AC	254	×			
LM 26	AC	962		×	×	×
LM 43	AC	271		×		
LM 61	AC	125		×		×
TOTAL of sampling sites			***10***	***14***	***4***	***10***

- **Petrographic studies**

For petrographic studies, hand specimens, and drill-oriented cores of granites and/or quartz veins were used for making thin/ polished sections.

At the laboratory, the rock samples were cleaned and examined. Then, representative samples were selected for the preparation of thin and polished sections. Oriented sections were made using oriented cores. In these cases, sections are cut perpendicular to the core axis, and the corresponding azimuth was drawn in the section (fig. 3-6).

[4] In this table the AMS methodology was not considered; for AMS information see the Attachment 1.

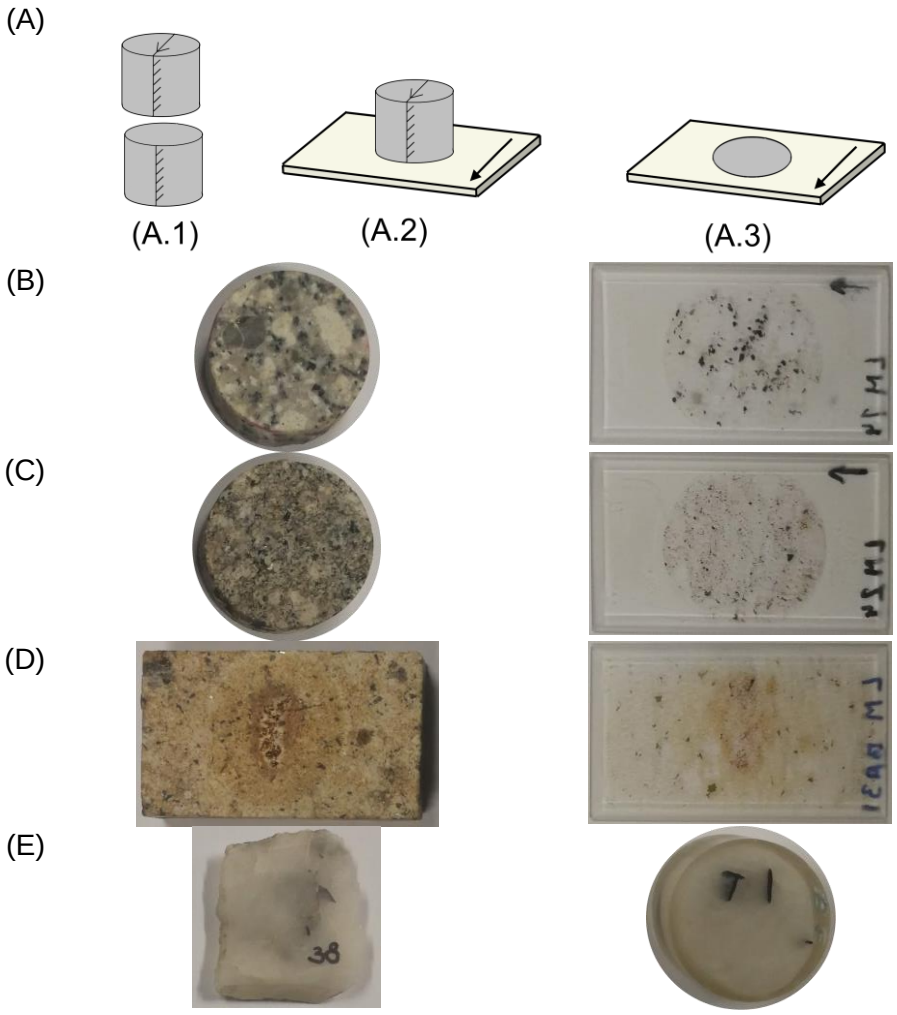


Figure 3-6. (A) Elaboration of oriented thin sections: (A.1) rock cylinder cut, (A.2) Glass slide glued to the slab with azimuth, (A.3) oriented thin section. (B to E) Examples of thin (with 30 µm of thickness) and polished sections: (B) Oriented rock cylinder and corresponded oriented thin section from LO granite; (C) Oriented rock cylinder and corresponded oriented thin section from AC granite; (D) Hand specimen and corresponded thin section from BA granite; (E) Hand specimen and polished section from quartz mineralized veins.

A total of 25 thin sections and 10 polished sections of LOP granites and mineralized veins were used for petrographic studies (attachment 1). Nine of them were selected for SEM-EDS and 8 for micro-*Raman* analyses.

3.2 MICROSCOPIC TECHNIQUES

3.2.1 Introduction and generalities

Petrographic studies in LOP granites complemented the previous studies made by *e.g.* Pereira *et al.* (1987), Pereira (1989), Helal (1992), and Fernandes *et al.* (2013).

3.2.2 Methodologies

3.2.2.1 Petrographic studies

All the thin and polished sections were firstly studied using a binocular magnifying glass from LEICA-DFC295 (fig. 3-7A). Then, the LEICA-ICC50HD petrographic polarizing microscope (fig. 3-7-B) was used for the petrographic studies in reflected and transmitted light. Both devices have an image editing software associated, the LAS v4.6, allowing the capture of photomicrographs with scale. The petrographic studies were undertaken at the *Departamento de Geociências, Ambiente e Ordenamento do Território (DGAOT)* of the *Faculdade de Ciências da Universidade do Porto (FCUP)* and in the ICT-Porto.

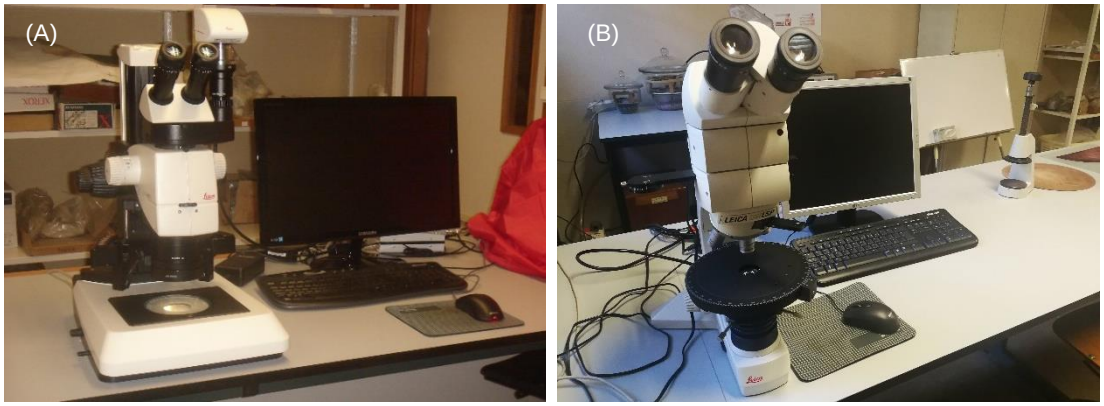


Figure 3-7. Equipment used in the petrographic studies: (A) binocular magnifying glass from LEICA-DFC295; (B) LEICA-ICC50HD petrographic polarizing microscope.

3.2.2.2 Scanning electron microscope and EDS microanalysis

Complementary studies for identifying minor mineral amounts and for the characterization of magnetic mineralogy were carried out using a scanning electron microscope (SEM) and dispersive energy spectra (EDS) at the *Centro de Materiais da Universidade do Porto* (CEMUP). The SEM-EDS studies were performed using a high-resolution JEOL JSM 6301F SEM coupled with an Oxford INCA Energy 350 system. Samples were carbon-coated using a JEOL JEE-4X Vacuum Evaporator. These analyzes

had as main objective the application of a direct method to obtain qualitative and semi-quantitative data related to the composition of certain minerals.

3.2.2.3 Micro-Raman spectroscopy analyses

The micro-*Raman* spectra of different opaque minerals were obtained using a *Raman* LabRAM HORIBA Jobin Yvon Spex spectrometer interfaced with an Olympus microscope with 50x objective lens, diffraction gratings with 1800 lines mm^{-1} and equipped with a 632.8 nm emission line of a HeNe laser at a power of 20 mW. The incident beam perpendicular to the plane of the sample is focused through the microscope lens, which also collects the *Raman* scattered radiation in back-scattering geometry. A highly sensitive CCD camera was used to collect the *Raman* spectra. Extended scans were performed on the spectral range 50 to 1200 cm^{-1}. The time of acquisition and the number of accumulations varied in order to obtain an optimized spectrum for each analyzed mineral. This technique was performed in DGAOT-ICT-Porto.

3.3 ANALYTICAL TECHNIQUES FOR THE MAGNETIC MINERALOGY

3.3.1 Introduction and generalities

3.3.1.1 Basic concepts about rock magnetism

Before the description of the methodologies used to characterize the magnetic mineralogy of studied rocks, some concepts about the magnetic properties are discussed.

3.3.1.1.1 The magnetic properties of materials

All the materials are constituted by charged subatomic particles – electrons and protons – which behave like magnets and have a magnetic moment, *m* inherent of the particle. The orbital magnetic moment is related to the spin magnetic moment (fig. 3-8) and is intrinsic related to the magnetic behavior of the solid materials (Lowrie, 2007).

The subatomic particles are in constant motion, where the electrons have an orbital motion around the atomic nucleus (fig. 3-8A). The orbiting charge forms an electrical current with which an orbital magnetic moment is associated. Moreover, each electron rotates about its axis-spin motion (fig. 3-8B). The spinning electrical charge produces a spin magnetic moment, directly related to the corresponding angular momentum. The spin magnetic moment is usually more important than the orbital moment in the rock-forming minerals.

The magnetic moment, *m* per unit volume, *V* of the material is called its magnetization, *M* (eq. 1). M (A m^{-1}) is the vector sum of all the atomic magnetic moments (A m^2) in the material divided by the volume (m^3) (fig. 3-8C; Lowrie, 2007).

$$\mathrm{M} = \sum \frac{m_i}{V} \qquad \text{(equation 1)}$$

In a solid, the atoms and ions are not completely randomly distributed but occupy fixed positions in a regular lattice, which reflects the symmetry of the crystalline structure. Concerning the type of magnetic behavior, in addition to the always present diamagnetic minerals, a rock can also have paramagnetic, antiferromagnetic and ferromagnetic *s.l.* minerals (figs. 3-9A and B; Lowrie, 2007; Nédélec & Bouchez, 2015).

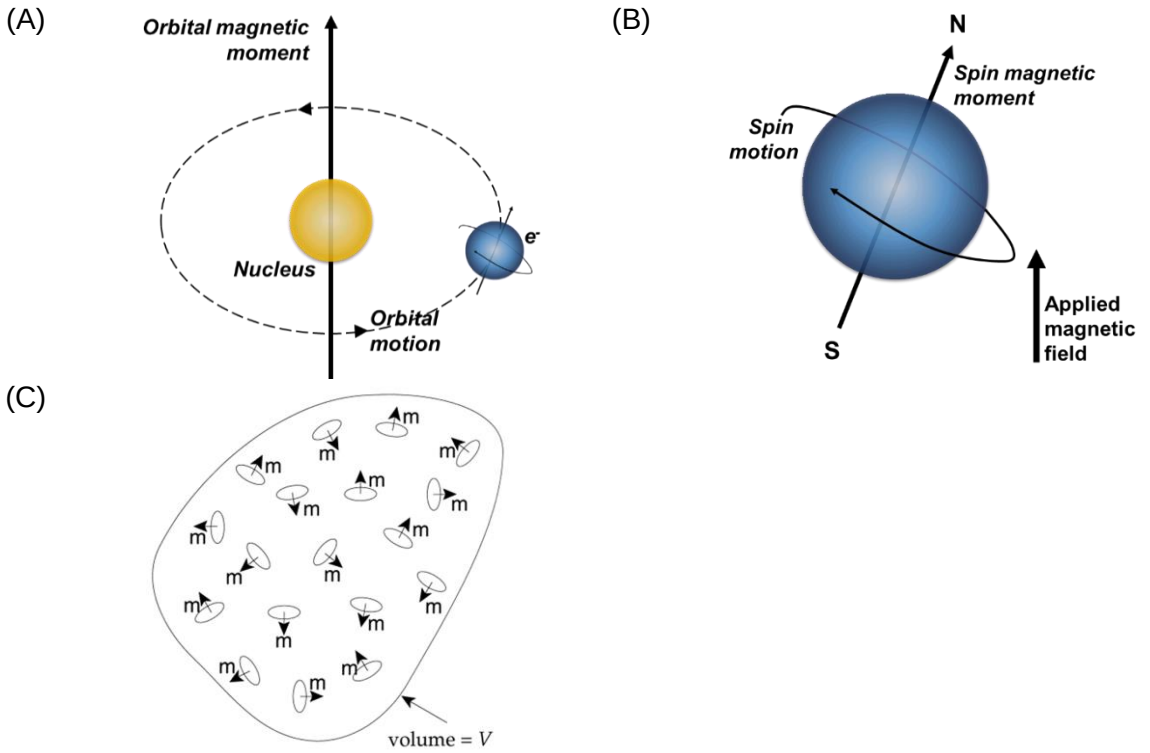


Figure 3-8. Schematic representation of: (A) Orbital motion and orbital magnetic moment of an electron around the atomic nucleus; (B) Spin motion and spin magnetic moment of an electron; (C) Magnetic moments inside a material with a volume, *V* (adapted: Lowrie, 2007).

- **Diamagnetic minerals**

The diamagnetic minerals have, in general, a weaker magnetic moment, *m* which is often masked by stronger paramagnetic or ferromagnetic *s.l.* properties. The diamagnetic susceptibility is reversible, negative and very weak (fig. 3-9B), on the order of -10^{-6} SI, independent of the temperature and the magnitude of the inducing field, *H*. A magnetization develops in the opposite direction to the applied field and disappears when it is absent (Lowrie, 2007; Nédélec & Bouchez, 2015). Quartz, calcite, and feldspar are examples of diamagnetic minerals.

(A)

	Paramagnetism	Antiferromagnetism	Ferromagnetism *s.l.*		
			Ferromagnetism *s.s.*	Parasitic ferromagnetism	Ferrimagnetism
Types of magnetic behavior					
Resulting moment (without inducing field)	Null	Null	Strong 	Very weak	Weak
			Spontaneous magnetization		

(B)

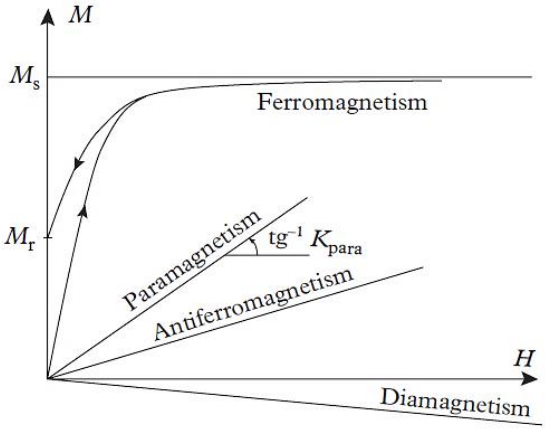


Figure 3-9. Types of magnetic behavior in a material (modified: Lowrie, 2007 and Nédélec & Bouchez, 2015): (A) Schematic representation of the magnetic moment carried by atoms in the absence of an inducing field; (B) Magnetization as a function of the applied field (M – magnetization; H – applied field; M_s – saturation magnetization; M_r – remanent magnetization).

- **Paramagnetic minerals**

In paramagnetic behavior, the magnetic moments are randomly arranged in the absence of a magnetic field (figs. 3-9A and 3-10A). However, if a magnetic field is applied, the magnetic moments statistically tend to become parallel to the induced field (fig. 3-10B), yielding a weak, reversible, and positive magnetic susceptibility (fig. 3-9B).

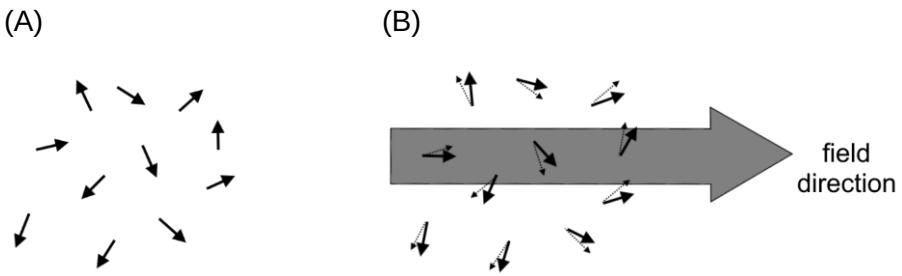


Figure 3-10. Magnetic moments of paramagnetic materials: (A) in the absence of an inducing field; (B) with a magnetic field applied.

This behavior is independent of the magnitude of the inducing field, hence it is represented by a straight line on the *M* = f (*H*) plot. In contrast to the diamagnetism, the paramagnetic behavior is sensitive to the temperature, resulting in a paramagnetic susceptibility, *k* inversely proportional to temperature, *T* (Nédélec & Bouchez, 2015), once the thermal energy favors chaotic orientation of the spin magnetic moments. This property as given by the *Curie law* (eq. 2), where the constant *C* is characteristic of the material (Lowrie, 2007):

$$k = \frac{C}{T} \qquad \text{(equation 2)}$$

The temperature above which a solid is paramagnetic, is called the *paramagnetic Curie temperature* or *Weiss constant* of the material, denoted by θ, and it is close to zero kelvin (*ca*. -273ºC) in paramagnetic solids. At temperatures T > θ the paramagnetic susceptibility *k* is given by the *Curie-Weiss law* (eq. 3; Lowrie, 2007):

$$k = \frac{C}{T - \theta} \qquad \text{(equation 3)}$$

The mainly paramagnetic minerals are the silicates with Fe^{2+}, Fe^{3+} and Mn^{2+} ions in their structure as biotite, iron-bearing muscovite, chlorite, and amphiboles. At room temperature, their susceptibilities are around 10^{-5} and 10^{-4} SI.

- **Antiferromagnetic minerals**

The antiferromagnetism is characterized by the antiparallel directions of adjacent atomic magnetic moments, giving two sublattices with equal and opposite intrinsic magnetic

moments (fig. 3-9A). Consequently, the susceptibility of these crystals is weak and positive, and remanent magnetization is not possible (fig. 3-9B). The antiferromagnetic alignment breaks down at the *Néel* temperature (T_N), above which the material becomes paramagnetic (low and positive susceptibility). In granites, the common antiferromagnetic minerals are ilmenite ($FeTiO_3$; T_N ~ -223ºC) and goethite (FeOOH; T_N ~ 122ºC), all having very low susceptibilities at room temperature and low field strength (Lowrie, 2007; Nédélec & Bouchez, 2015). It should be noted that ilmenite has a paramagnetic behavior at room temperature.

- **Ferromagnetic *s.l.* minerals**

The ferromagnetic *s.l.* minerals have a spontaneous magnetization, in the absence of an inducing field. The ferromagnetism is characterized by a high susceptibility at room temperature, and at a low magnetic field (< 1 T) the magnetic moments being parallel to the applied field (fig. 3-9; Nédélec & Bouchez, 2015). Rock-forming magnetic minerals often have natural remanences with very high coercive properties. The bulk susceptibility changes with temperature, whereby around the *Curie* temperature (T_C ~ 580º for pure magnetite), thermal motion is responsible for a drastic decrease in susceptibility (fig. 3-11A). The magnetization loop of a rock sample, which can have many tiny ferromagnetic mineral grains, shows the effects of magnetic hysteresis (fig. 3-11B; Lowrie, 2007; Nédélec & Bouchez, 2015).

The hysteresis loop is an *M versus H* plot, where several information can be obtained. The magnetization saturation value, M_s can reach in strong fields, at which the individual magnetic moments are aligned with the applied field. If the magnetizing field is reduced to zero, a ferromagnetic material retains part of the induced magnetization and, this residual magnetization is called the isothermal remanent magnetization (IRM), or remanence. If the sample is magnetized to saturation, the remanence is a saturation IRM (M_{rs}). If a magnetic field is applied in the opposite direction to the IRM, part of the material remagnetizes in the antiparallel direction. For a coercive force value (H_c) of the reverse field, the induced reverse magnetization cancels the original remanence and the net magnetization is zero. If at this phase the reverse field is removed, the residual remanence is smaller than the original IRM. When repeating the process in increasingly strong reverse fields, a back-field H_{cr} (coercivity of remanence) is found, giving a reverse remanence that cancels the IRM, so that the

residual remanence is zero. The shape of the hysteresis loop changes relatively the M_{rs}/M_s and H_{cr}/H_c ratios and depends on the grain size of ferromagnetic mineral (Lowrie, 2007; Nédélec & Bouchez, 2015).

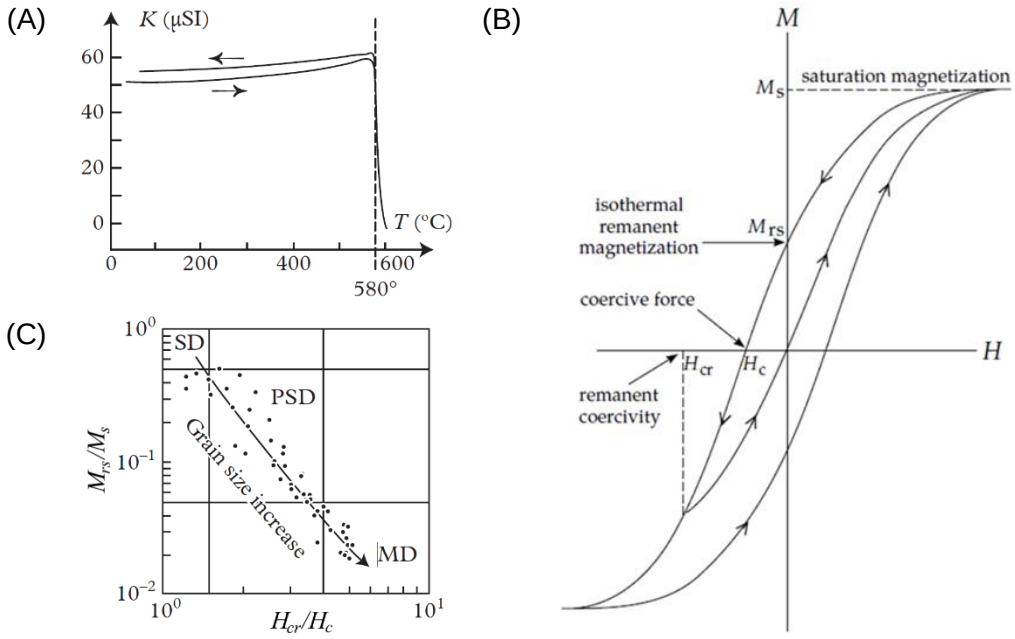


Figure 3-11. Ferromagnetic behavior: (A) Susceptibility *versus* temperature plot for pure magnetite; (B) Hysteresis loop; (C) Day plot (Day *et al.*, 1977) showing the sorting of magnetite into monodomain or single-domain (SD), pseudo-monodomain (PSD) and multidomain (MD) grains. The SD grains have one magnetic domain per grain, are very small in size and show $M_{rs} \approx M_s$ and $H_{cr} \approx H_c$ in these grains; MD grains are made of several magnetic domains and are much larger than the SD grains (adapted: Nédélec & Bouchez, 2015).

In granites, the most common ferromagnetic *s.l.* mineral is the magnetite, mostly primary origin and coarse-grained. When a magnetite grain is bigger than a few micrometers in diameter, the magnetic energy associated with its magnetization becomes too large for the magnetization to remain uniform. This phenomenon occurs because self-demagnetizing energy was generated due to the interaction between the demagnetizing field of uniformly magnetized grains with spontaneous magnetization. In order to reduce this energy, the magnetization subdivides into smaller uniformly magnetized units (named as *Weiss* domains). Therefore, the primary magnetite is made of several magnetic domains (multidomain magnetite, MD). In contrast, fine-grained magnetite (a few microns in size, between 0.03 and 0.1 μm in equant grains and up to about 1 μm in elongate grains), have a single-domain (SD) effect (fig. 3-11C). In the SD magnetite, the entire grain is uniformly magnetized as a single magnetic domain. Sometimes, the SD effect can generate an inverse fabric (obtain for example by the anisotropy magnetic susceptibility). If the magnetite grains

are finer than 0.03 μm in diameter, they exhibit an unstable type of magnetic behavior and are classified as superparamagnetic at room temperature (Hunt *et al.*, 1995; Lowrie, 2007). The superparamagnetic behavior can be deduced by frequency-dependence susceptibility experiments (see topic 3.3.2.5).

The ferromagnetism *s.l.* includes (fig. 3-9A; Lowrie, 2007; Nédélec & Bouchez, 2015):

a) *Ferromagnetism s.s.* – The materials have a high susceptibility at room temperature and a low magnetic field (< 1 T). They show the magnetic moments parallel to the applied field. The iron is the most common material with this type of behavior.

b) *Parasitic ferromagnetism* (or *canted antiferromagnetism*) – A weak "defect moment" can result due to the presence of lattice imperfections as some defects, vacancies, or impurities of the magnetic crystal. This kind of ferromagnetism *s.l.* also occurs if the spins are not exactly antiparallel but are inclined at a small angle, and they do not cancel out completely and again a ferromagnetic type of magnetization can result. The parasitic ferromagnetic materials have the typical characteristics of a true ferromagnetic metal (*e.g.* hysteresis, a spontaneous magnetization, and a *Curie* temperature). One important geological example is the hematite, in which both the spin-canted and defect moments contribute to the ferromagnetic properties.

c) *Ferrimagnetic* – Appears when the two sublattices of a mineral acquire unequal magnetization, and leads to behavior slightly different from ferromagnetism *s.s.*, particularly for the variation of magnetization with temperature. The magnetic moments are antiparallel and show a different intensity (*e.g.* magnetite, monocyclic pyrrhotite).

The magnetic susceptibility of rocks results from the contribution of all constituted minerals (table 3-2) but, the remanent magnetic properties only depend on a small quantity of ferrimagnetic minerals. The variable concentrations of ferrimagnetic and matrix minerals (mostly diamagnetic and also paramagnetic) result in a wide range of susceptibilities in rocks (fig. 3-12).

Table 3-2. Mean values of magnetic susceptibility, at room temperature, of some important minerals in rocks (*in* Borradaile, 1988).

Magnetic behavior	Mineral	Magnetic susceptibility (SI)
Diamagnetic	Calcite	-13.8×10^{-6}
	Galena	-0.3×10^{-4}
	Quartz	-13.4×10^{-6}
Paramagnetic	Arsenopyrite	0.003
	Biotite	$10 - 12.9 \times 10^{-4}$
	Chalcopyrite	4×10^{-4}
	Cassiterite	0.001
	Chlorite	$0.7 - 15.5 \times 10^{-4}$
	Ilmenite	1.8
	Muscovite	1.7×10^{-4}
	Pyrite	0.001
	Sphalerite	$0.1 - 7 \times 10^{-4}$
	Tourmaline	9×10^{-4}
Antiferromagnetic	Goethite	0.003
Parasitic ferromagnetism	Hematite	0.007
Ferrimagnetic	Maghemite	3.0
	Magnetite	6.2
	Monoclinic pyrrhotite	1.5
	Titanomagnetite	0.01

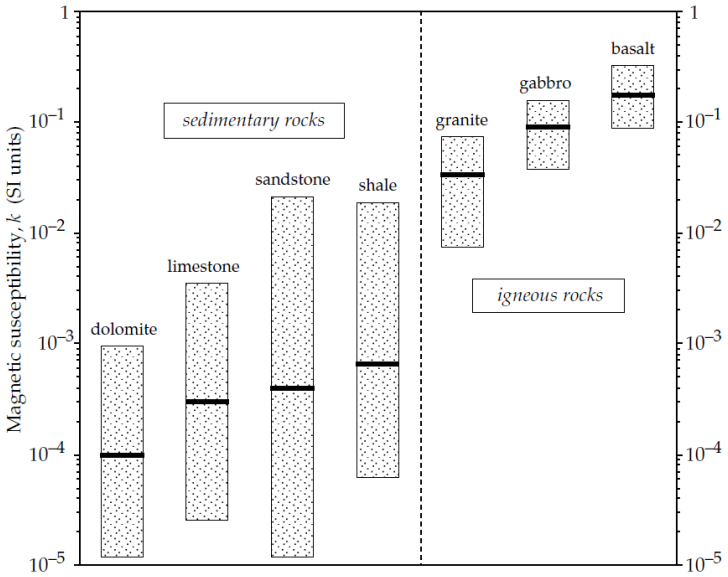


Figure 3-12. Mean values and ranges of the magnetic susceptibility of some rock types (Lowrie, 2007).

3.3.1.1.2 The magnetic anisotropy

The magnetic anisotropy is the directional dependence of magnetic properties and three types were distinguished: magnetocrystalline, shape (or magnetostatic), and magnetostrictive anisotropies (Lowrie, 2007).

- **Magnetocrystalline anisotropy**

The saturation magnetization of ferromagnetic minerals is easier along one specific direction, which is related to the crystallographic arrangement. Thus, the direction of the saturation magnetization is not isotropic, gives rise to magnetocrystalline anisotropy energy. The minimum values are parallel to a favored direction referred to as the easy axis of magnetization (Lowrie, 2007). As examples: the phyllosilicates (including the biotite) have the minimum magnetic susceptibility axis (k_3) perpendicular to the cleavage plane [001] (fig. 3-13A; Nédélec & Bouchez, 2015).

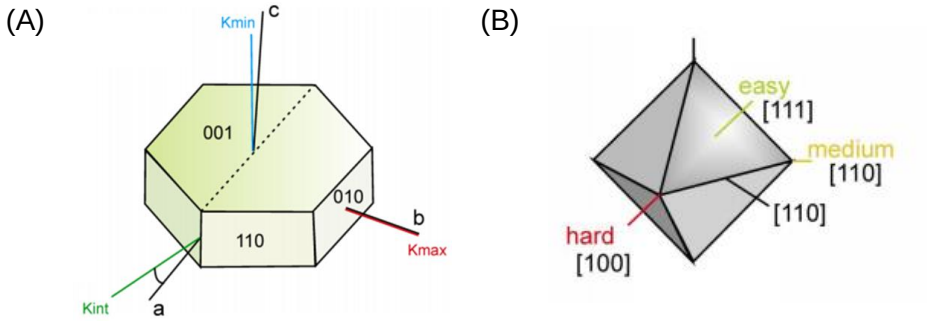


Figure 3-13. Schematic representation of the crystallographic axis of: (A) biotite; (B) magnetite (AGICO, 2019).

- **Shape anisotropy**

This kind of anisotropy is characteristic of stronger magnetic materials. In rocks, the shape anisotropy is associated with the shapes of the ferrimagnetic grains (manly non-spherical shape), and to a lesser extent with the shape of the rock sample. The magnetite has an inverse spinel structure and consequently has cubic anisotropy, with minimum magnetic susceptibility axis parallel to the [100] axis and maximum magnetic susceptibility axis parallel to the [111] axis (fig. 3-13B; Nédélec & Bouchez, 2015). In spherical grains, the shape anisotropy is smaller than in the elongate grains. As an example, in very fine grains of magnetite (and maghemite), which the longest axis exceeds the shortest axis by only about 20%, the shape anisotropy is the predominant form of anisotropy. The maximum magnetic susceptibility axis is usually parallel to the elongate magnetite grain (Lowrie, 2007).

- **Magnetostrictive anisotropy**

Some materials change their shape when submitted to a magnetization process. The interaction energy between atomic magnetic moments depends on the bond length of the crystal lattice and on the direction of the magnetic field. If the atomic magnetic moments

change their orientation due to the magnetic applied field, the interaction energy is increased, and the bond lengths are adjusted in order to reduce the total energy. This process leads to an alteration of the shape of the ferromagnetic material and is called magnetostriction. Magnetostriction is positive when the material elongates parallel to the direction of magnetization and, is negative if the material shortens in magnetization direction (Lowrie, 2007).

3.3.1.1.3 Rock magnetism

The type of ferrimagnetic mineral, its grain size, and the way it acquires a remanent magnetization are the principal factors that influencing the rock magnetism.

- **Type of ferrimagnetic minerals**

The most important ferromagnetic *s.l.* minerals are the iron-titanium (FeTi) oxides. The composition of the FeTi oxides is usually displayed on the TiO_2 – FeO – Fe_2O_3 ternary diagram (fig. 3-14). Concerning the diagram, the positions from left to right indicate increasing ratios of ferric (Fe^{3+}) to ferrous (Fe^{2+}) iron and, positions from bottom to top indicate increasing Ti content (Ti^{4+}). The ternary diagram edges represent the minerals rutile (TiO_2), wustite (FeO), and hematite (Fe_2O_3). The maghemite, present in the same edge of hematite, can be produced by low-temperature oxidation of magnetite and has the same chemical composition of hematite. It is a strongly magnetic mineral but, is easier revert to hematite when heated above 300-350ºC, once is a metastable mineral (Butler, 2004; Lowrie, 2007).

The most magnetic minerals present in rocks belong to a two solid-solution series (Butler, 2004; Lowrie, 2007):

a) *Titanomagnetite* – The end members of the solid-solution series are magnetite (Fe_3O_4), which is strongly ferrimagnetic, and ulvospinel (Fe_2TiO_4), which is antiferromagnetic at very low temperature and paramagnetic at the room temperature (fig. 3-15A).

b) *Titanohematite* – The end members of the solid-solution series are hematite (Fe_2O_3), which is parasitic ferromagnetic, and ilmenite ($FeTiO_3$), which is antiferromagnetic at low temperature and paramagnetic at the room temperature. For titanium contents between 0.5 and 0.95, the titanohematite is ferrimagnetic and for values bellow 0.5 it exhibits parasitic ferromagnetism (or canted antiferromagnetism; fig. 3-15B). The hematite can occur in rocks as a primary mineral but also with a secondary origin, due to the oxidation of a precursor mineral, such as magnetite or by precipitation from late fluids.

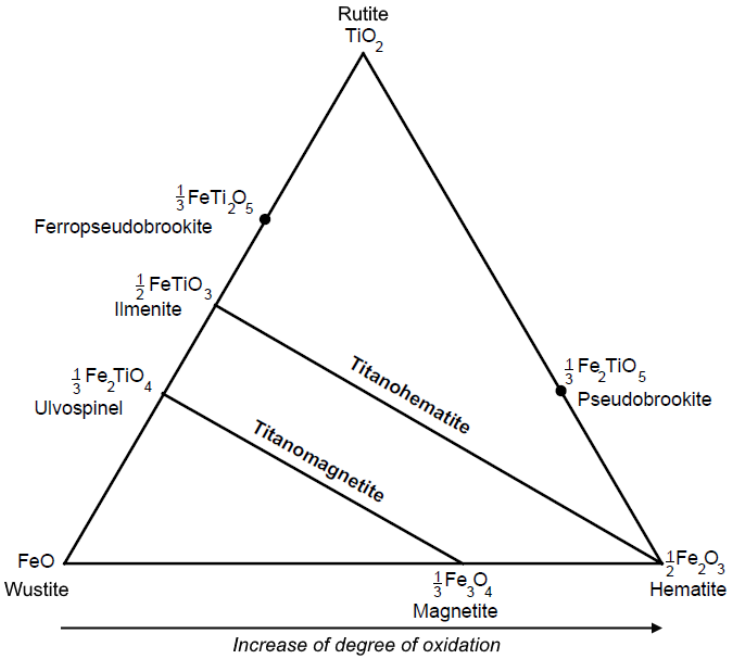


Figure 3-14. TiO_2-FeO-Fe_2O_3 ternary diagram. Compositions of important Fe-Ti-oxide minerals are labeled along with mineral names; titanomagnetite and titanohematite solid solution series are indicated (modified: Butler, 2004).

In both solid-solution series, the spontaneous magnetization decreases with the increase of the amount of titanium.

Beyond the iron-titanium oxides, the rocks contain other minerals with ferromagnetic *s.l.* properties like pyrrhotite (FeS_2) and goethite (FeOOH).

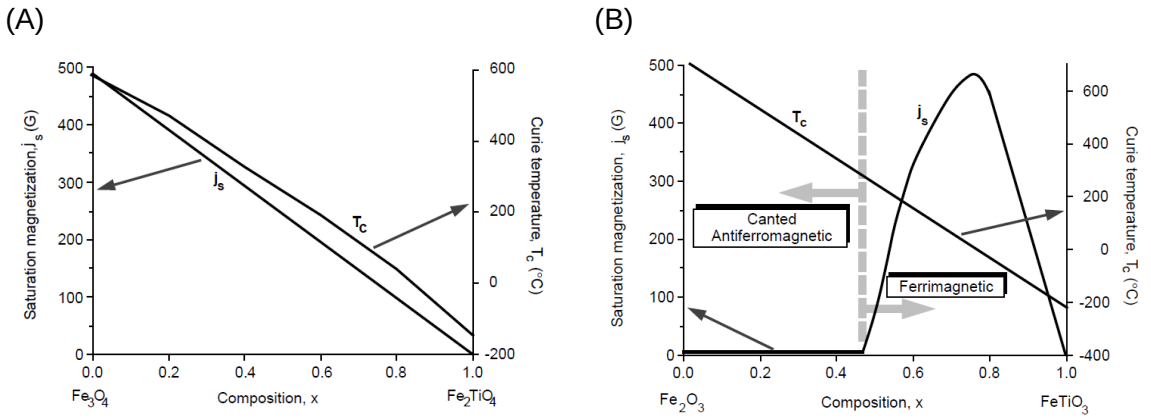


Figure 3-15. Saturation magnetization and Curie temperature (T_C) for: (A) titanomagnetite series and (B) titanohematite series. The composition is indicated by parameter *x*; the left axis indicates saturation magnetization (j_S); the right axis indicates T_C. In (B), the compositions $x < 0.45$ have canted antiferromagnetic coupling; compositions $0.45 < x < 1.0$ have ferrimagnetic coupling. Redrawn after Nagata (1961) and Stacey & Banerjee (1974) *in* Butler, 2004.

- **Identification of ferrimagnetic minerals**

The ferrimagnetic minerals are often difficult to identify in rocks, once they occur in general in low concentration. If the rock sample is coarse-grained, these minerals can be identified by studies under the reflected light microscope. However, if the ferrimagnetic minerals are present in very fine grains, other techniques should be addressed. These minerals can be identified by its properties of *Curie* temperature (*e.g.* thermomagnetic experiments – see topic 3.3.2.3) and coercivity (*e.g.* isothermal remanent magnetization – see topic 3.3.2.4).

Each kind of ferromagnetic *s.l.* minerals have a characteristic *Currie/ Néel* temperatures. The *Curie* temperature (T_C) is the temperature above which a ferromagnetic *s.s.* material becomes paramagnetic, while the *Néel* temperature (T_N), is analogous to the T_C, but for antiferromagnetic materials. The *Curie/ Néel* temperature is typical for a particular mineral and therefore is commonly used to identify its composition. For example, the *Curie/ Néel* temperature is 580ºC for pure magnetite, 680ºC for hematite, 320ºC for pyrrhotite, and 120ºC for goethite. However, in the titanomagnetite and titanohematite series (fig. 3-15), the *Curie* point decreases as the Ti content increases. Thus, for example, in the titanomagnetite series, the T_C can range between 580ºC (T_C of pure magnetite) and -150ºC (T_C of pure ulvospinel; Butler, 2004).

Regarding that, the *Currie/ Néel* temperature is not always enough to identify the magnetic mineralogy. For example, the T_C = 580ºC can indicate either titanomagnetite/ Ti-poor magnetite or titanohematite. In the same way, a drop at 200ºC can be due to the

presence of titanomagnetite or titanohematite (fig. 3-15). In these cases, other experiments and analyzes (*e.g.* micro-*Raman* spectroscopy or electron microprobe analyzes) should be made (Butler, 2004).

- **Mineralogical transformation**

In rock magnetism studies, is important to know about the possible mineralogical transformations both during the fluid-rock interaction in the outcrop, and/or in-deep, as well as during some laboratory analyses, like thermomagnetic experiments.

The fluid-rock interaction related to the circulation of hydrothermal fluids can strongly modify the physicochemical properties of the rocks. The hydrothermal processes can be responsible for changes in the magnetic properties like an increase or decrease of magnetic susceptibility of the rocks. Magnetic susceptibility data, as well as thermomagnetic experiments, confirm both the increase of the bulk susceptibility (K_t) in altered rocks, due to the formation of secondary magnetite and, in contrast, the drop of K_t due to the destruction and/or reduction in the size of magnetic minerals under acid conditions (*e.g*. Riveros *et al.*, 2014). The primary mineralogy can be either dissolved and/or chemically modified, allowing the precipitation of new minerals directly from the hydrothermal fluids. On the other hand, the Fe-Ti oxides can also experience major compositional and textural changes caused by intense and long-lived hydrothermal fluid-rock interaction. This process, in porphyry-type ore deposits, can create significant quantities of magnetite during the early potassic alteration stages (*e.g.* Arancibia & Clark, 1996), whereas circulation of late-stage acidic fluids associated with phyllic alteration tends to destroy this mineral (*e.g*. Beane & Bodnar, 1995).

Beyond the natural causes, some laboratory analyses may induce some mineralogical changes in the rock samples (table 3-3). For example, in the thermomagnetic experiments, the susceptibility of rock samples (Gubbins & Herrero-Bervera, 2007):

a) Increases during the heating cycle – resulted mainly from the formation of FeTi oxides (*e.g.* titanomagnetite and Ti-poor magnetite).

b) Decreases during heating – due to the transformation of oxides (*e.g.* martitization).

Table 3-3. Laboratory data of heating-induced thermochemical reactions (Gubbins & Herrero-Bervera, 2007).

From	To	ºC
Magnetite	Maghemite	150-250
Goethite	Hematite	250-400
Impure titanomagnetites	Magnetite	> 300
Maghemite	Hematite	350-450
Pyrite	Magnetite	350-500
Magnetite	Hematite	> 500
Pyrrhotite	Magnetite	> 500

3.3.2 Methodologies

3.3.2.1 Magnetic susceptibility and anisotropy of magnetic susceptibility

The magnetic susceptibility studies are an important tool to identify the magnetic behavior in granites due to the presence of certain iron minerals, like magnetite, which is easily detected because it increases the magnetic susceptibility values to higher than 10^{-3} SI (Kropácek & Krs, 1968; Tarling & Hrouda, 1993; Bouchez, 1997, 2000). Several studies have been made in order to classify granites regarding their magnetic behavior, in Japan (*e.g.* Ishihara *et al.* 1981), in Korea (*e.g*. Maulana *et al.* 2013), in Spain (*e.g*. Román-Berdiel *et al.,* 1995; Aranguren *et al.,* 1996; Olivia-Urcia *et al.,* 2012; Villaseca *et al.,* 2017; Porquet *et al.,* 2017) and in Portugal (*e.g.* Sant'Ovaia *et al.* 2012; Corrêa-Ribeiro, 2018; Gonçalves *et al*., 2019).

In this study, the magnetic susceptibility values were obtained using two analytical techniques: measurements using a portable device named T*erraplus KT-10 magnetic susceptibility meter* (fig. 3-16A) and using the *KLY-4S Kappabridge susceptometer Agico model* (fig. 3-16B).

The anisotropy of magnetic susceptibility (AMS) measurements were undertaken in a 0.3 mT field (low field; reversible magnetization) and performed using the KLY-4S Kappabridge susceptometer Agico model (Czech Republic) from the ICT-Porto at room temperature (fig. 3-16). This methodology enables us to obtain two types of data: scalar and directional parameters. After AMS measurements and, for each sampling site (table 3-1, attachment 1), the ANISOFT 5 program package (Chadima & Jelinek, 2019) enabled us to calculate the scalar parameters: magnetic susceptibility (*K)*, magnetic anisotropy (*P, P%* P_{para} and/or P_{para}*%*), and shape parameter (*T*).

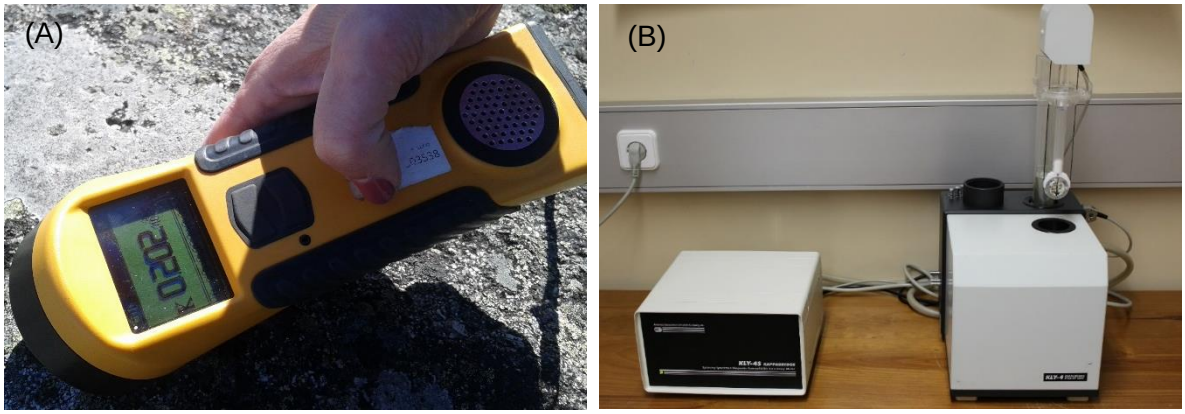


Figure 3-16. (A) A portable device used for magnetic susceptibility measurements in the field; (B) Equipment used for AMS measurements; KLY-4S Kappabridge susceptometer Agico model (Czech Republic).

The AMS also gives us directional parameters regarding the maximum (K_1) and minimum (K_3) axis from the AMS ellipsoid. Traditionally, magnetic fabrics have been interpreted based on empirical relationships. For example, AMS fabric reflects the macroscopic foliation and lineation in many rocks, where the maximum susceptibility (K_1) indicates lineation, and the minimum susceptibility (K_3) is normal to foliation. However, magnetic and mineral fabrics are not always parallel (*e.g*. single-domain magnetite). Hence, observed anisotropy is controlled by both the degree of mineral alignment, as well as intrinsic mineral anisotropy, and mineralogy plays an important role in defining magnetic fabrics (Biedermann, 2018).

- **Scalar parameters**

Magnetic susceptibility is based on the relationship between the magnetization induced in a material *M* and the external field *H* defined as:

$$M = KH \qquad \text{(equation 4)}$$

K can be a scalar or a second rank tensor if the rock is isotropic or anisotropic, respectively. On the other words, if the magnetic susceptibility of a rock does not depend on its orientation with respect to the inducing field, *K* is a scalar but, if the material is anisotropic, magnetic susceptibility is at a first approximation a second rank tensor, K_{ij}, relating *H* to *M* (*i, j* = 1, 2, 3). M_i represents the magnetization on the direction *i*, and H_j represents the inducing field on the direction *j* (Hrouda, 1982; Nédélec & Bouchez, 2015):

$$M_i = K_{ij} H_j \qquad \text{(equation 5)}$$

K is the magnetic susceptibility and the *K* values are dimensionless because *M* (per unit volume) and *H* have the same units (*e.g.* Hrouda, 1982; Bouchez, 1997). The *K* reflects the mineral composition of the whole-rock, comprising the diamagnetic (*e.g.* quartz, feldspar), paramagnetic (*e.g*. biotite and ilmenite at room temperature), ferromagnetic (*e.g.* magnetite, pyrrhotite) and antiferromagnetic (*e.g.* goethite) minerals.

The AMS describes the variation of magnetic susceptibility with the direction within rock samples and represents the contribution of all the rock-forming minerals (Tarling & Hrouda, 1993). AMS data allow establishing the magnetic susceptibility tensor, which is represented by a triaxial ellipsoid, where $K_1 \geq K_2 \geq K_3$ (or $K_{max} \geq K_{int} \geq K_{min}$). The intensities and orientations of the three axes, which are the tensorial means of the $k_1 \geq k_2 \geq k_3$ axes of measured specimens, and the 95% confidence angles E_{12}, E_{23}, and E_{31} corresponding to these three axes were calculated. The geometrical representation of such a tensor is an ellipsoid, called "the AMS ellipsoid" (fig. 3-17).

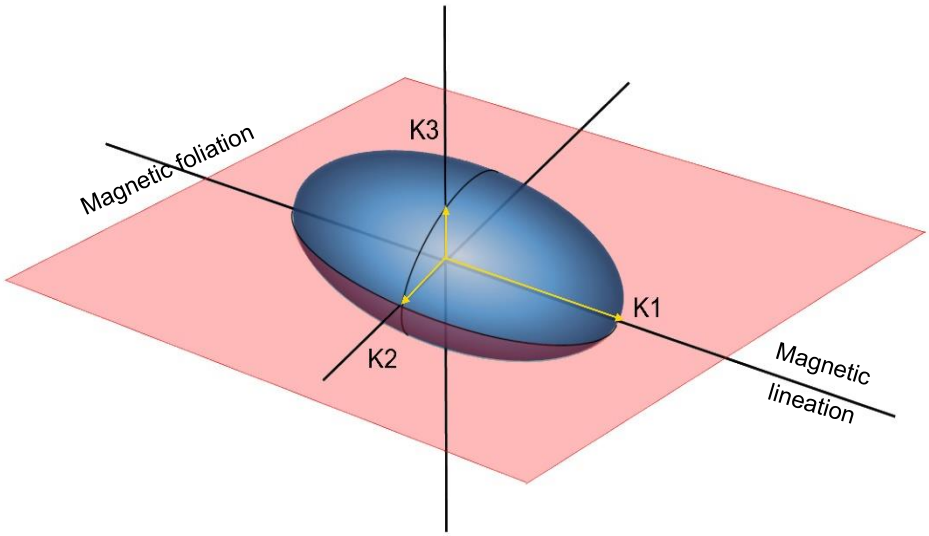


Figure 3-17. Representation of the triaxial AMS ellipsoid ($K_1 = K_{max}$; $K_2 = K_{int}$; $K_3 = K_{min}$) and definition of the virtual fabric elements: magnetic foliation and magnetic lineation (adapted: Siegesmund *et al.*, 1995).

Ratios between moduli provide several magnetic parameters (Tarling & Hrouda, 1993):

a) The mean susceptibility K_m, which is the mean of the individual arithmetic means:

$$K_m = \frac{K_1 + K_2 + K_3}{3} \quad \text{(equation 6)}$$

b) The magnetic anisotropy *P* degree:

$$P = \frac{K_1}{K_3} \quad \text{(equation 7)}$$

c) The magnetic anisotropy percentage *P*% corresponds to:

$$P\% = \left(\frac{K_1}{K_3} - 1\right) \times 100 \quad \text{(equation 8)}$$

d) However, in the case of very low anisotropies, the P_{para} or P_{para}% equation is used:

$$P_{para} = \frac{K_1 - K_{dia}}{K_3 - K_{dia}} \quad \text{(equation 9)}$$

$$P_{para}\,\% = 100 \times \left[\left(\frac{K_1 - K_{dia}}{K_3 - K_{dia}}\right)\right] - 1 \quad \text{(equation 10)}$$

The P_{para} (or P_{para}%) equation should be used once the K_{dia} (≈ −14 μSI) is the ubiquitous diamagnetic contribution (susceptibility of quartz) and is considered as isotropic and, this is the way to avoid artificially high anisotropy degrees.

e) To describe the shape of the anisotropy of magnetic susceptibility ellipsoid (fig. 3-17 and fig. 3-18), the shape parameter *T* is defined (Jelinek, 1981) as:

$$T = 2\left[\left(\frac{ln\,(K_2/K_3)}{ln\,(K_1/K_2)}\right) - 1\right] \quad \text{(equation 11)}$$

The *T* value varies from *T* = +1 (pure planar, or oblate ellipsoids) to *T* = -1 (pure linear, or prolate ellipsoids), through *T* = 0 (triaxial ellipsoid; fig. 3-18).

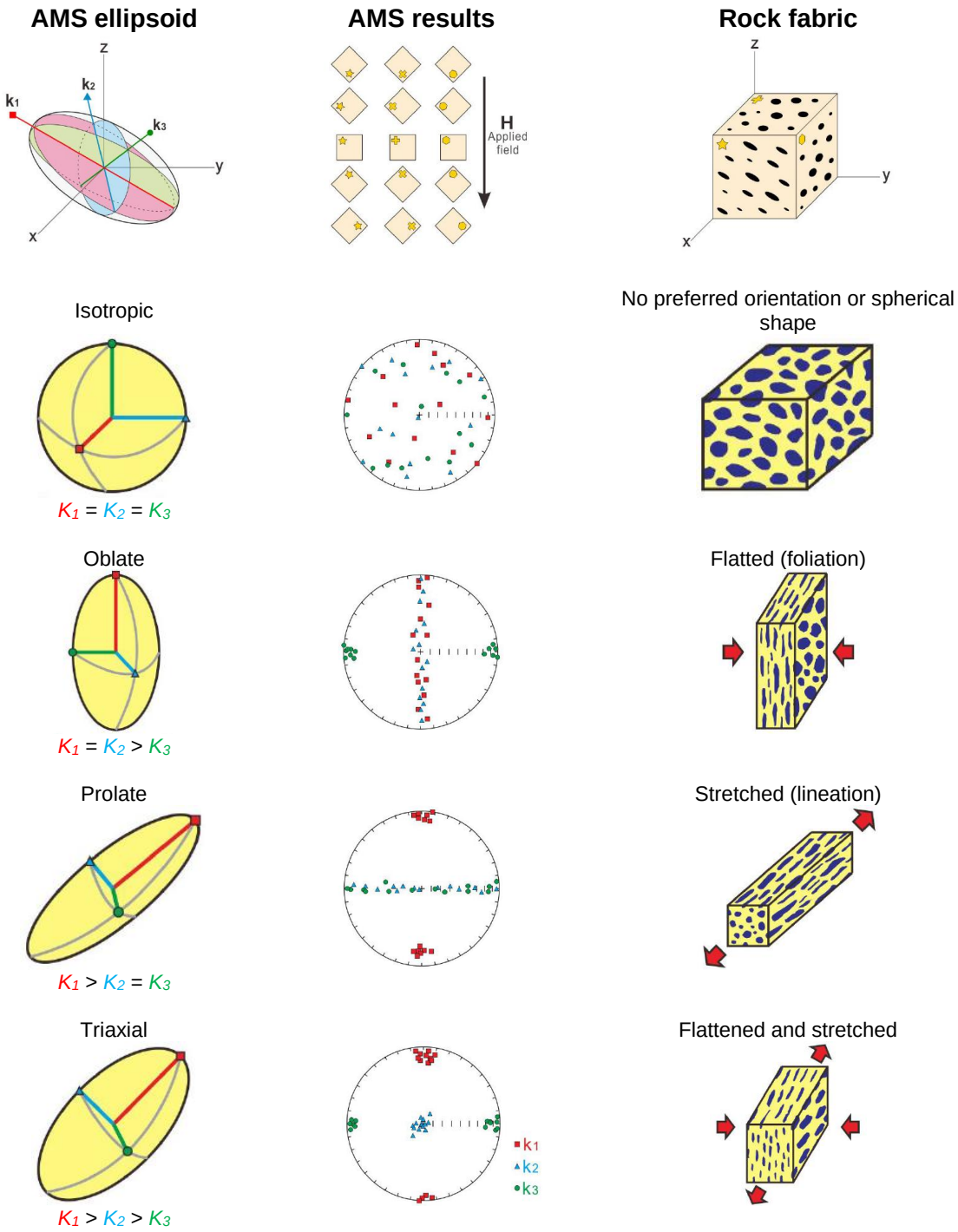


Figure 3-18. Principles of AMS method for determining rock fabrics (adapted: Borradaile, 1988; Tarling & Hrouda, 1993). AMS ellipsoid, principal axis (K_1 - maximum, K_2 - intermediate and K_3 - minimum) and corresponding rock fabric.

- **Directional parameters**

Mathematically, the AMS ellipsoid (fig. 3-17) is similar to the stress or strain ellipsoid, allowing to characterize the magnetic fabric, which is defined by the magnetic lineation and the magnetic foliation (fig. 3-18). The magnetic foliation is the plane perpendicular to the orientation of the short axis, K_3 (or K_{min}) and the magnetic lineation is parallel to the long axis of the mean ellipsoid orientation average, K_1 (or K_{max}). In granites, the biotite is an excellent marker of the foliation, and the amphiboles (*e.g.* hornblende) are a good marker for the magnetic lineation (Gleizes *et al*., 1993; Bouchez, 1997; Nédélec & Bouchez, 2015).

The magnetic fabric can be (fig. 3-18):

a) *Flatted*: characterized by a well-marked magnetic foliation and an ill-defined magnetic lineation;

b) *Stretched*: characterized by a well-marked magnetic lineation and an ill-defined magnetic foliation;

c) *Flattened and stretched*: characterized by a well-marked magnetic lineation and magnetic foliation.

The magnetic fabric can be linked to the petrofabric, giving information about the magmatic flow and regional tectonic.

3.3.2.2 Anisotropy of anhysteretic remanent magnetization

The magnetization *M* of a material is a vector sum of two components: the induced magnetization (M_i), and the remanent magnetization (M_r):

$$M = M_i + M_r \qquad \text{(equation 12)}$$

The remanent magnetization is the magnetization that remains after the material is removed from an applied magnetic field. The mathematical description is analogous to AMS and is defined by Stacey & Banerjee (1974) as:

$$M_r = K_r H \qquad \text{(equation 13)}$$

M_r is the remanent magnetization, and K_r is the remanent susceptibility.

The anisotropy of anhysteretic remanent magnetization (AARM) isolates the magnetic fabric of remanence-bearing minerals (*e.g.* magnetite) from the paramagnetic and/or diamagnetic matrix (Jackson, 1991; Raposo & Gastal, 2009). This technique has distinct advantages because it precludes the effect of inverse AMS fabric due to SD Ti-poor magnetites/ titanomagnetites or SD magnetites (Stephenson *et al*., 1986) since the magnetization occurs always parallel to the long axis of the magnetic grains (Jackson, 1991). For it determination, an artificial anhysteretic remanent magnetization was imposed along different directions on the specimens using a MOLSPIN (Molspin, Newcastle-upon-Tyne, UK) alternating–field (AF) demagnetizer as the source of the alternating magnetic field, with superimposition of a steady field (DC field) attained by a (home-made) small coil inside and coaxial to the demagnetizer, which was controlled by a MOLSPIN apparatus.

The AARM tensor was determined by magnetizing the specimen in an AF peak of 60 mT (irreversible magnetization) with a DC field of 0.16 mT in the desired orientation, measuring the resulting remanence, and AF tumble-demagnetizing in 100 mT before proceeding to the next step. Before AARM determinations, the samples were demagnetized by AF tumbling at 200 mT to establish the base level. A seven positions measurement scheme was used, and the best-fit AARM tensors were calculated by the least-squares method which showed root-mean-squares of less than 5%, indicating that the ellipsoids are well-resolved (Jackson, 1991).

The AARM tensor is similar to the AMS and is expressed by its principal eigenvectors $AARM_1 \geq AARM_2 \geq AARM_3$ (or $AARM_{max} \geq AARM_{int} \geq AARM_{min}$) representing the maximum, intermediate, and minimum axes of remanence, respectively. Similar to AMS scalar parameters, the AARM allows defining the *P*% and *T* consequent from the ferromagnetic *s.l.* minerals. The $AARM_1$ (or $AARM_{max}$) corresponds to the magnetic lineation and the $AARM_3$ (or $AARM_{min}$) is the magnetic foliation pole.

For the AARM measurements, representative samples from LOP (table 3-3, attachment 1) were selected taking into account their magnetic behavior. All measurements were performed at the *Laboratório de Anisotropias Magnéticas e de Magnetismo de Rocha*, from *Universidade de São Paulo (Brazil)*.

3.3.2.3 Thermomagnetic experiments

The thermomagnetic experiments (K_t *versus* T) allow the identification of the ferromagnetic *s.l.* minerals based on their *Curie /Néel* temperature. The *Curie/ Néel* temperature of ferromagnetic *s.l*. minerals can be determined in low-field thermomagnetic experiments where the magnetic susceptibility of a sample is monitored, while the temperature is increased or decreased, and it is defined as the point of a major decrease in magnetic susceptibility of the sample during the heating cycle (Butler, 2004).

The temperature of this drop in magnetic susceptibility corresponds to the temperature at which a magnetic mineral loses its spontaneous magnetization. In contrast, if magnetic susceptibility, with values much lower than ferromagnetic values, decreases regularly with increasing temperature, the sample has the typical behavior of paramagnetic minerals (Dunlop & Özdemir, 1997).

The temperature dependence of low field magnetic susceptibility was monitored with a CS-2 furnace apparatus attached to the KLY-3 susceptometer from the *Laboratoire Géosciences Environnement Toulouse, Université de Toulouse III – Paul Sabatier* (France), using fragment samples obtained from 14 rock specimens from LOP (table 3-3, attachment 1). The samples were exposed to increasing temperatures up to 700°C in heating/ cooling cycles. The measurements were made in an argon flux in order to minimize oxygen fugacity, which reduces the oxidation of the samples and the consequent formation of new minerals with the increase and/or decrease of temperature. However, a small amount of oxygen is always present in the sample holder, thus although the probability is lower, some mineralogical changes may still occur.

3.3.2.4 Isothermal remanent magnetization

For the detailed magnetic mineralogy study, the acquisition of isothermal remanent magnetization (IRM) curves was performed. The IRM acquisition curves are important for estimating the characteristic coercivity of the ferromagnetic minerals (Butler, 2004). The IRM refers to the remanence acquired by a sample exposed to a direct magnetic field *H,* at room temperature.

These measurements were performed in the *Laboratório de Paleomagnetismo* at the *Instituto Dom Luís*, *Lisboa*. Beforehand, standard samples were demagnetized through an

alternating field cleaning at *ca*. 100 mT, with an LDA-3A (Agico) demagnetizer. Then, the magnetic field (*H*) was imparted using an Impulse Magnetizer IM-10-30 (ASC Scientific) and the resulting remanence was measured using a spinner magnetometer JR-6A (Agico). Samples were magnetized in the same direction with increasing magnetic fields from *ca*. 3.51 mT up to 1.15 T in different steps (*ca*. 40 steps) and the induced magnetization acquired by the specimens was measured after each step of induction.

For the IRM studies, 4 samples from LOP were selected according to their magnetic behavior: 2 from LO granite (1 from areas with high magnetic susceptibility, and 1 from areas with low magnetic susceptibility), 1 from BA granite, and 1 from AC granite (table 3-3, attachment 1).

Data were analyzed using a cumulative log-Gaussian (CLG) function (Robertson & France, 1994) with the software developed by Kruiver *et al.* (2001). The treatment by the CLG function (Robertson & France, 1994; Kruiver *et al.*, 2001), consists in obtain the best fits of the raw IRM curves. This treatment allows determining the quantity of the magnetic mineral components within the sample, and obtaining information for each one of them, like: (i) the relative contribution (%) of each component to the total measured magnetization; (ii) the values of saturation of isothermal remanent magnetization (SIRM); (iii) the field at which half of the SIRM is reached (B½), and (iv) the dispersion parameter (DP). The B½ gives us information about the coercive force for each component allowing us to identify what components are present in the measurement samples, once the ranging B½ values for the coercive magnetic minerals are published (*e.g.* Robertson & France, 1994; Kruiver *et al.*, 2001; Lowrie, 2007; Abrajevitch & Kodama, 2011; Font *et al.*, 2014; Maxbauer *et al.*, 2016). DP values can be clustered or scattered, depends on the alteration degree of components, as well as grain sizes or different content in some elements (*e.g*. Ti content in the magnetite/ titanomagnetite) in mineral composition (*e.g*. Kruiver *et al.*, 2001; Font *et al.*, 2009, 2014).

3.3.2.5 Frequency-dependent susceptibility

Additionally, measurements of frequency-dependent susceptibility were done with an MFK1-FA (Multi-function Kappabribge) from AGICO in the *Laboratório de Paleomagnetismo* at the *Instituto Dom Luís*, *Lisboa.* The low-field magnetic susceptibility was measured at two applied field frequencies (0.46 kHz and 46 kHz). The percentage of frequency-dependent susceptibility (χ_{fD}%) was obtained (Dearing *et al.*, 1996) in selected samples from LOP (table 3-1, attachment 1).

This method identifies the presence of very fine magnetic particles, lower than 0.03 μm, named as superparamagnetic. These particles are identified due to their unstable magnetic behavior, shown by the absence of a magnetization stable direction. Samples, where ultrafine minerals are present, will show slightly lower *K* values when measured at high frequency, and the samples without these superparamagnetic minerals will show identical *K* values at the two frequencies.

3.4 GEOCHEMICAL STUDIES

3.4.1 Introduction and generalities

Helal (1992) made several geochemical analyses in the LOP granites, including the analysis of major, trace, and rare earth elements (REE). More recently, whole-rock geochemistry, $^{87}Sr/^{86}Sr$ and $^{207}Pb/^{235}U$ dating, and natural radiation (U and Th) studies were performed by Fernandes *et al.* (2013) and Teixeira *et al.* (2014). Despite the existence of available geochemical data, geochemical analyses have been carried out to clarify some aspects not contemplated in previous studies.

3.4.2 Methodologies

3.4.2.1 Sample preparation

For geochemical studies, samples were previously selected and then crushed using sequentially the jaw crusher, the hammer crusher, and the agata mill crusher, to obtain the required grain size *ca*. 75 µm (fig. 3-19). This equipment belongs to the DGAOT and ICT-Porto.

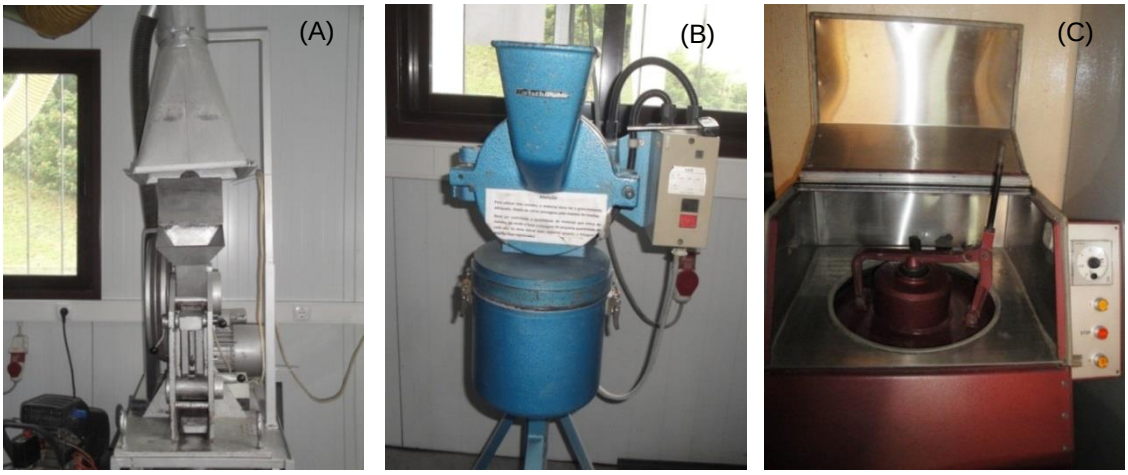


Figure 3-19. Laboratoy equipment: (A) jaw crusher; (B) hammer crusher; (C) agata mill crusher.

3.4.2.2 Whole-rock geochemistry

The geochemical studies were made in representative selected samples from LOP granites at *Activation Laboratories* (Actalabs), Canada. Whole-rock (W.R.) geochemical compositions were analyzed for major-, trace- and rare-earth elements by a lithium metaborate/ tetraborate fusion ICP/ ICP-MS (Inductively Coupled Plasma Mass Spectrometry). To know the different content of both iron-oxides, the FeO and the Fe_2O_3,

the titration analysis was required too. The FeO content was determined through titration, using a cold acid digestion of ammonium metavanadate, and hydrofluoric acid in an open system. The analysis methods, as well as the detection limits, can be found on the Actlabs website (Actlabs, 2020).

The geochemical analyses were made on:

- 6 samples from LO granite: 3 from areas with high magnetic susceptibility (LM 5, LM 13, and LM 30) and 3 from areas with low magnetic susceptibility (LM 1, LM 16, and LM 22);
- 2 samples from AC granite: LM 24 and LM 61;
- 3 samples from BA granite: 2 from the outcrop near the *Cimeira* dam (LM 7 and LM 15) and 1 from the central outcrop (LM 49)

The geochemical diagrams were performed using the GCDkit 6.0 software.

3.4.2.3 Oxygen isotope data

In nature, the oxygen occurs mainly in the form of the ^{16}O isotope, but it can also occur in very small quantities in the stable ^{18}O isotope form. The abundance of the ^{18}O isotope is expressed as a percentage of the ^{18}O isotope relative to ^{16}O, indicated by *R* in the equation:

$$R = \frac{^{18}O}{^{16}O} \times 100\ \% \qquad \text{(equation 14)}$$

However, when the differences in both isotopes abundance, on the rocks, are very small, the quantity of the isotope is expressed as its ratio in the sample relative to an internationally accepted standard, normally the Vienna Standard Mean Ocean Water (VSMOW standard). This relative portion in rock samples, represented as $\delta^{18}O$, is multiplied by 1000 and is expressed by the equation (Morrill & Koch, 2002):

$$\delta^{18}O = \left[\frac{R_{sample}}{R_{standard}} - 1\right] \times 1000\ ‰ \qquad \text{(equation 15)}$$

Where the $R_{standard}$ (VSMOW) is 0.00200522 ± 0.45 (Baertschi, 1976). The higher W.R. $\delta^{18}O$ values indicate a crustal origin, through anatexis of metasedimentary protoliths and the low

values suggest a mantle origin and/or source regions dominated by mafic and meta-igneous rocks (Ishihara, 1977; Ellwood & Wenner, 1981).

The granite rocks reflect redox states of their corresponding magmas, and the presence of magnetite or ilmenite as accessory minerals represents oxidized- and reduced-type respectively. These two types of granites also result from exposure to different oxygen fugacity during the magma genesis. The magnetite-type is generated at a great depth where no carbonaceous material exists, whereas the ilmenite-type is originated at a shallow level where small amounts of crustal carbon are present (Ishihara, 1977; Sheppard, 1977; Ellwood & Wenner, 1981).

Oxygen isotope data measurements were performed at the *Stable Isotopic Laboratory of Salamanca*. Oxygen was extracted from rocks (in W.R.) by laser fluorination techniques, quantitatively converted to CO_2 by the reaction with a heated carbon rod, and analyzed for $^{18}O/^{16}O$ ratio with a dual inlet VG SIRA-II Mass Spectrometer.

From LOP granites, 6 representative samples were selected:

- 3 samples from LO granite: 2 from areas with high magnetic susceptibility (LM 5 and LM 13) and 1 from areas with low magnetic susceptibility (LM 16);
- 1 sample from AC granite: LM 26;
- 2 samples from BA granite: 1 from the outcrop near the *Cimeira* dam (LM 7) and 1 from the central outcrop (LM 62).

This data was used in the K_m *versus* W.R. $\delta^{18}O$ diagram (Ellwood & Wenner, 1981), allowing to establish a relationship between each type of granite (ilmenite- and magnetite-type granites and I-, I-peraluminous, and S-type granites) and a particular metal association (Takagi & Tsukimura, 1977; Kumar, 2010).

3.5 GRAVIMETRIC SURVEY

3.5.1 Introduction and generalities

Gravity surveying measures variations in the Earth's gravitational field caused by differences in the density of subsurface rocks. The variation of the acceleration due to gravity is measured in the field. Although this method is usually known as the "gravity method", it is, in fact, the variation of the acceleration due to the gravity that is measured (Reynolds, 1997).

Gravimetry is based on the concept that a causative body, in our case a rock unit, has a different density from the surroundings (host rocks). A causative body represents a subsurface zone of anomalous mass and causes a gravity anomaly, which is a localized perturbation in the gravitational field. Many geological situations give rise to zones of anomalous mass that produce significant gravity anomalies (*e.g.* bedrock surface, salt domes, granite plutons, or sedimentary basins). Interpretation of gravity anomalies allows an assessment of the probable depth and shape of the causative body (Reynolds, 1997; Kearey *et al.*, 2002; Lowrie, 2007).

Gravity methods have been used both in regional and global scale, such as in the hydrocarbon exploration, exploration and mass estimation of mineral deposits, military concerns, and detection of subsurface cavities (*e.g*. Parasnis, 1972; Nettleton, 1976; Reynolds, 1997). Although that, the gravity is a useful and precise technique to know the shape and infer about the emplacement model of granitic intrusions (*e.g.* Vigneresse, 1990, 1995a, Aranguren *et al.*, 1996, Améglio *et al.*, 1997; Sant'Ovaia *et al.*, 2000, Sant'Ovaia & Noronha, 2005; Joly *et al.*, 2009; Sant'Ovaia *et al.*, 2014; Machadinho, 2015).

3.5.1.1 Basic concepts about gravity

The gravity survey depends on two laws derived by Isaac Newton: Newton's Universal Law of Gravitation and Newton's Second Law of Motion.

The first of these two laws states that the force of attraction, F between two masses m_1 and m_2, whose dimensions are small concerning the distance r between them, is given by equation 16, where G is the Gravitational Constant ($G = 6.67 \times 10^{-11}$ m^3 kg^{-1} s^{-2}; Kearey *et al.*, 2002).

$$F = \frac{G\, m_1 m_2}{r^2} \qquad \text{(equation 16)}$$

Considering that the Earth is spherical, non-rotating and homogeneous, with mass *M* and radius *R*, the gravitational attraction on a small mass *m* on its surface is given by the equation, which corresponds to Newton's Second Law of Motion:

$$F = \frac{G\,M}{R^2}\,m \qquad \Leftrightarrow \qquad F = m\,g \qquad \text{(equation 17)}$$

Thus, the force is related to mass by an acceleration, where *g* is the gravitational acceleration (or gravity):

$$g = \frac{GM}{R^2} \qquad \text{(equation 18)}$$

On Earth, gravity would be constant with $g = 9.81\ m\ s^{-1}$ (~981 Gal). However, the Earth's characteristics (Earth's ellipsoidal shape, rotation, irregular surface relief, and internal mass distribution) cause some oscillation of gravity over its surface, where *g* has a maximum value in the poles (~979 Gal) and a minimum value in the equator (~982 Gal; Kearey *et al.*, 2002; Lowrie, 2007).

The variations in gravity caused by density variations in the Earth's subsurface have small values, of the order of 100 μm s^{-2}. This unit of the *micrometer* per second is referred to as the *gravity unit* (gu). Currently, due to the high sensibility of the gravimeters, gravity is expressed in *miligal* (mGal) and/or *microgal* (μGal; Lowrie, 2007).

$$1\ mGal = 1000\ \mu Gal = 10^{-3}\ Gal = 10^{-5}\ m\ s^{-2} = 10\ gu$$

3.5.1.2 Reference surfaces in geodesy

The Earth is considered as a spheroid flattened at the poles. The Earth's shape and gravimetry are intimately associated. Consequently, it is necessary to know the exact Earth's shape, to define the acceleration of gravity at any point on Earth's surface. Two reference surfaces are recognized: the ellipsoid and the geoid (fig. 3-20). The international reference ellipsoid is a close approximation to the equipotential surface of gravity, but it is a mathematical convenience. The physical equipotential surface of gravity is called the geoid (Lowrie, 2007).

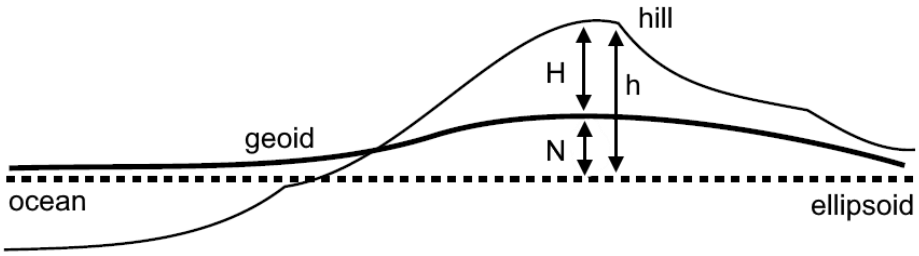


Figure 3-20. Reference surfaces: ellipsoid and geoid; N – geoid undulation; H – orthometric altitude; h – ellipsoidal altitude (modified: Lowrie, 2007).

Precise observations of the orbits of artificial Earth satellites are used to define a best-fitting oblate ellipsoid, called the International Reference Ellipsoid. The geoid reflects the true distribution of mass inside the Earth and differs from the theoretical ellipsoid by small amounts (fig. 3-21). The mass within the ellipsoid causes a downward gravitational attraction toward the center of the Earth, and a hill or mountain whose center of gravity is outside the ellipsoid causes an upward attraction, causing a local elevation of the geoid above the ellipsoid. The displacement between the geoid and the ellipsoid is called a geoid undulation (N; fig. 3-20) and can range from -100 to +100 m. The elevation caused by the mass above the ellipsoid is a positive undulation (Kearey *et al.*, 2002; Lowrie, 2007).

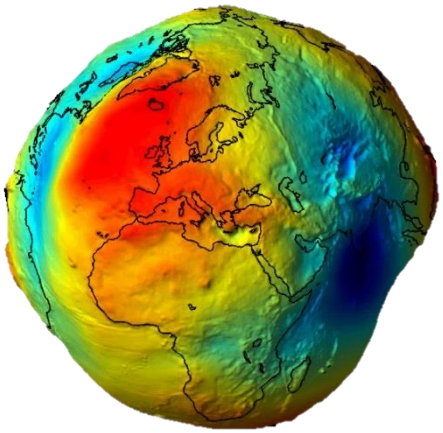


Figure 3-21. The Earth's irregular shape - geoid (ESA, 2019).

3.5.1.3 The gravimeters

The first gravimeters were based on the straightforward application of *Hooke's law*, where the gravimeters are spring balances carrying a constant mass. Variations in the weight of the mass caused by variations in gravity allow the variation of the length of the

spring, giving a measure of the change in gravity. In figure 3-22A a spring of initial length *s* has been stretched by an amount δs as a result of an increase in gravity δg increasing the weight of the suspended mass *m*. The extension of the spring is proportional to the extending force (*Hooke's Law*), where *k* is the elastic spring constant (Kearey *et al.*, 2002; Lowrie, 2007):

$$m\delta g = k\delta s \quad \Leftrightarrow \quad \delta s = \frac{m}{k}\,\delta g \qquad \text{(equation 19)}$$

This type of gravimeter, based directly on *Hooke's law*, is called a stable type. The stable gravimeter has been replaced by more sensitive unstable (or astatized) types, which are constructed so that an additional force acts in the same direction as gravity and opposes the restoring force of the spring. The instrument is then in a state of unstable equilibrium due to the design of the spring.

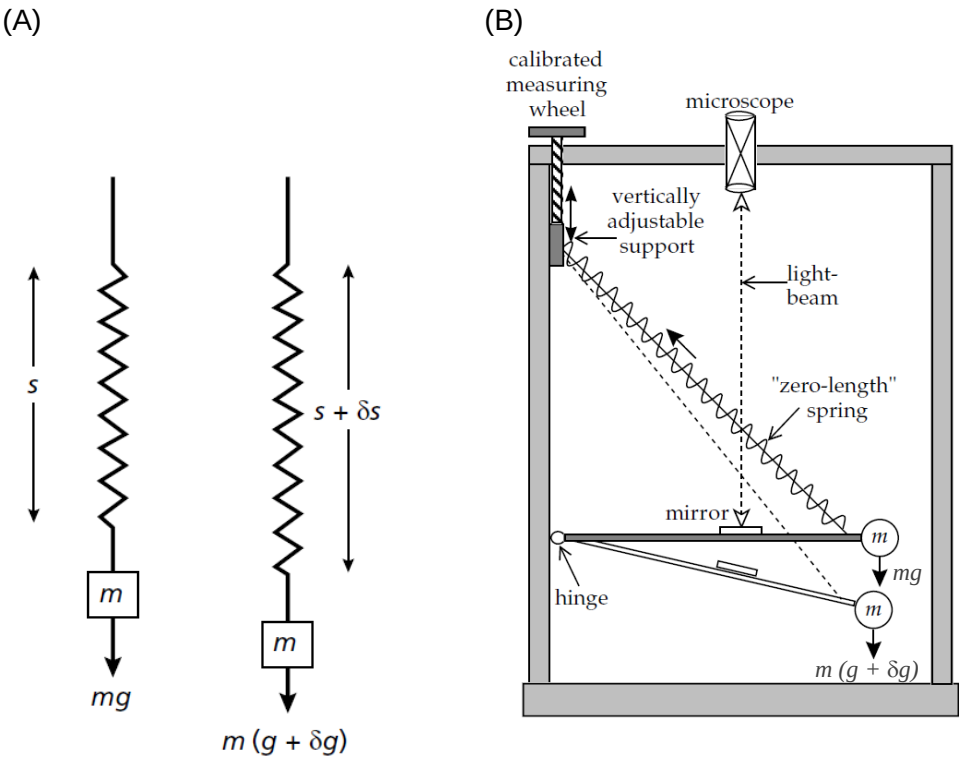


Figure 3-22. Principle of: (A) A stable gravimeter operation; (B) A unstable gravimeter (*e.g. LaCoste & Romberg* gravimeter) (adapted: Kearey *et al.*, 2002; Lowrie, 2007).

Figure 3-22B shows the operation of an unstable gravimeter. A mass is supported by a horizontal rod to which a mirror is attached. The position of the rod is observed with a light-

beam reflected into a microscope. If gravity changes, the zero-length spring is extended or shortened and the position of the rod is altered, which deflects the light beam. The null-deflection principle is utilized. An adjusting screw changes the position of the upper attachment of the spring, which alters its tension and restores the rod to its original horizontal position as detected by the light-beam and microscope. The turns of the adjusting screw are calibrated in units of the change in gravity, usually in mGal (Lowrie, 2007).

An example of an unstable instrument is the *LaCoste & Romberg* gravimeter. This equipment is made of rugged metal parts. However, its components can suffer thermal expansion or contraction with temperature variations, which induces instrumental drift errors. Since metals creep when thermally expanded or contracted, it is best to maintain gravimeters at constant thermostat temperature whenever practical (LaCoste & Romberg, 2004). The modern gravimeter has a sensitivity of about 0.01 mGal (or 10 µGal; Kearey *et al.*, 2002; Lowrie, 2007).

The gravimeter is calibrated at a known location. If gravity is different at another location, the extension of the spring changes, and from this, the change in gravity can be computed.

3.5.2 Acquisition data

3.5.2.1 Topographic information

For the gravimetric campaigns, a differential GPS (DGPS) was used to obtain precise coordinates and elevation for each gravimetric station (fig. 3-23). DGPS is essentially a system to provide positional corrections to GPS signals. DGPS uses a fixed, known position to adjust real-time GPS signals to eliminate pseudo-range errors (Racelogic Support Center, 2018; ESRI, 2019).

The pseudo-range errors consist of the delays (random and specific to each satellite) caused by the trajectory from satellites to the GPS device, due to the signal has to travel through layers of the Earth's atmosphere (ionosphere, troposphere). The delay affects the time taken for the signal to travel from any given satellite to a GPS receiver, introducing a slight error into the GPS engine, causing an error in the measured position. To correct this delay, a static base station can be used to provide correction messages to signal delays. This is done by setting the base station up in a set point on the ground and then calculating its exact position on the Earth's surface. This is done by leaving it recording GPS data, as long as possible. Over the time that the base station is capturing data, the ionosphere and troposphere change, causing the delays in the signals to change, randomly. Because the

delays are subject to random changes, they can be averaged out. Knowing the exact position of the base station on the Earth, as well as the exact position of the satellite (their exact position is transmitted live, at all times), the distance between those two points should be calculated.

Differential GPS is the difference between the “real” distance – which has passed through the ionosphere and troposphere – measurement and the “theoretical” distance – which should be shorter. For each satellite, a correction signal can be sent to the GPS receiver, which will apply that correction to each measurement that it makes, which will cancel out a large percentage of the different pseudo-range errors from each satellite signal. This only works because the receiver is close to the base station, thus, the signals to both units will have traveled through the same bits of the atmosphere (ESRI, 2019).

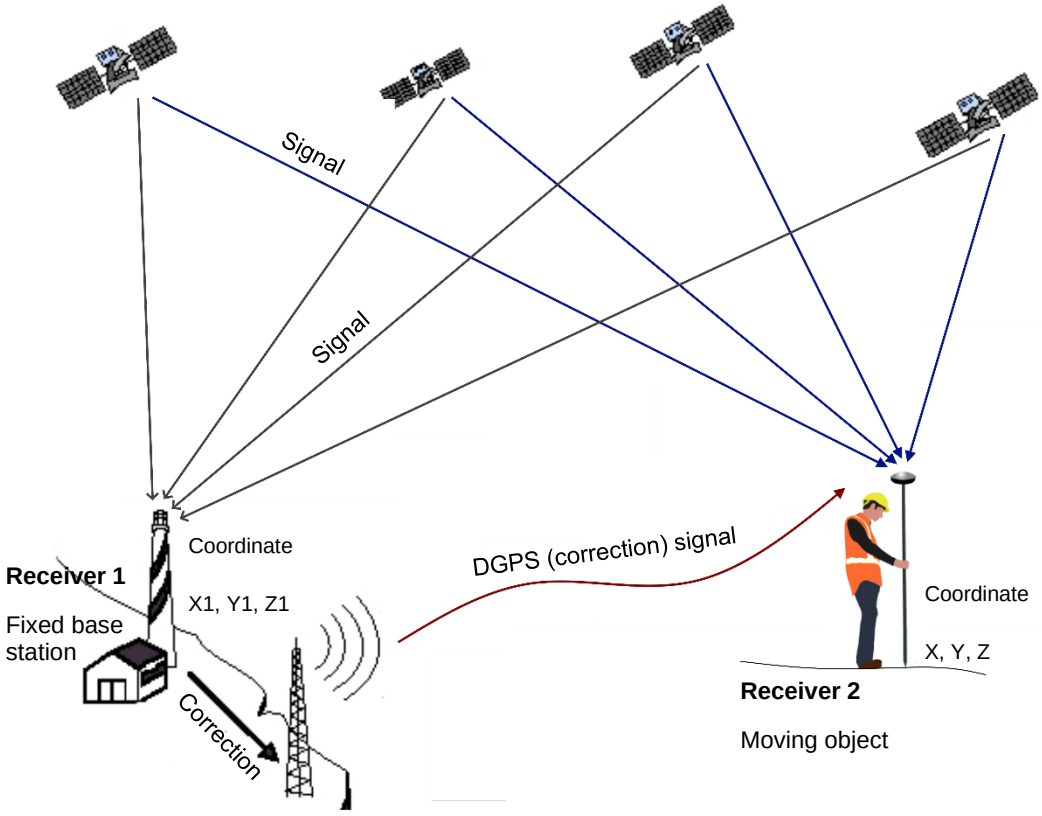


Figure 3-23. Components of a DGPS system.

3.5.2.2 Gravimetric data

For two months, in 10 fieldwork campaigns, the acquisition data was performed in LOP granites and host rocks, within an area which we called Alvão area. The gravity measurements were performed by a team of 2 or 3 persons[5], using a gravimeter *LaCoste & Romberg G1054* from *Observatório Astronómico de Gaia* (fig. 3-24). This type of gravimeter has a particularity of having a stable temperature system (T ~ 57.5ºC), which helps in the stability of the spring (LaCoste & Romberg, 2004), producing small instrumental drift values.



Figure 3-24. Gravimeter *LaCoste & Romberg G1054*.

The gravity survey was performed on 271 gravimetric stations, along with 3 gravimetric profiles (fig. 3-25):

- NNE-SSW, subparallel to the late-Variscan N 25º ± 25º fault system;
- WSW-ENE; subparallel to the late-Variscan N 80º ± 20º fault system;
- NNW-SSE; subparallel to the sin-D_3 regional alignment *ca*. N 120º.

The gravimetric stations are spaced about 100 m inside the LOP, increasing the spacing in the host rocks. Outside the LOP, a spacing of 200 m or 400 m between gravimetric stations was applied. The measurements extended about 5 km in the host rocks.

[5] The gravity measurements were performed in collaboration with Professor José Martinho Lourenço and Professor Rui Teixeira from UTAD.

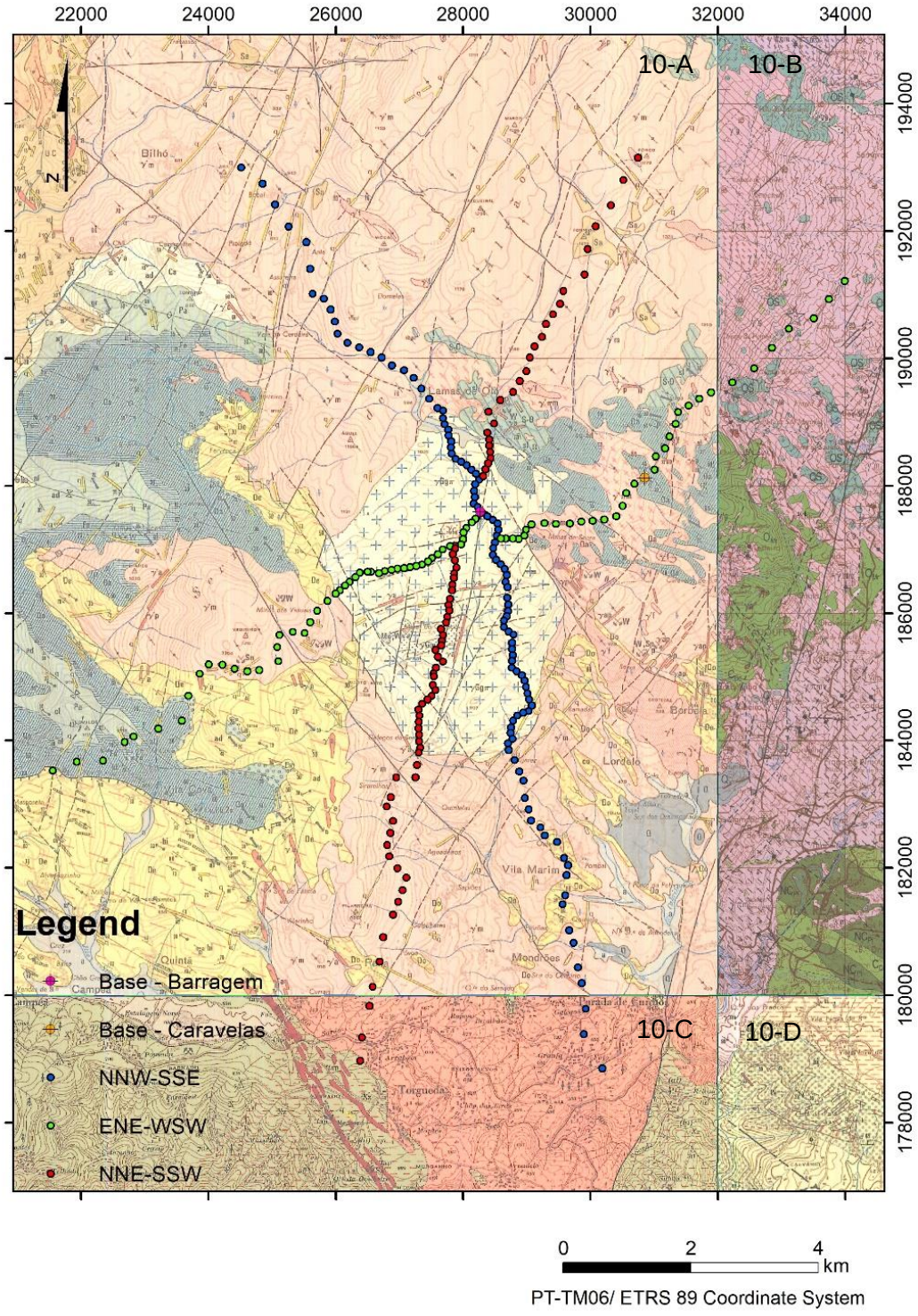


Figure 3-25. Location of gravimetric stations in the Alvão area (the basement is the geological map "10-A – Celorico de Basto; 10-B – Vila Real (2015); 10-C - Peso da Régua (1967); 10-D - Alijó (1987) (GeoPortal-LNEG, 2010b).

3.5.3 Gravity reductions

Gravimeters do not give direct measurements of gravity. A gravimeter reading is taken in divisions and then multiplied by an instrumental calibration factor to produce a value of observed gravity (g_{obs}). Before the interpretation of the results of a gravity survey, it is necessary to correct for all variations in the Earth's gravitational field which do not result from the differences of density in the underlying rocks. This process is known as gravity reduction (LaFehr, 1991) or reduction to the geoid, as sea-level is usually the most convenient datum level. The difference between the value of observed gravity (g_{obs}) and that determined either from International Gravity Formula/ Geodetic Reference System 67 for the same location or relative to a local base station, is known as the gravity anomaly.

The corrections that can be applied are (Reynolds, 1997; Kearey *et al.*, 2002; Lowrie, 2007):

- **Drift correction**

The gravimeter reading change (drift) with time as a result of elastic creep on the springs, which produce an apparent change in gravity at a given station. Correction for the instrumental drift is based on repeated readings at the same station (base station) at different times of the day, typically every 1-2 hours. The difference between successive measurements at the same station are plotted to produce a drift curve (fig. 3-26). Observed gravity values from intervening stations can be corrected by subtracting the amount to drift from the observed gravity value. The range of drift of gravimeters is from a small fraction of 0.1 mGal to about 1 mGal per hour.

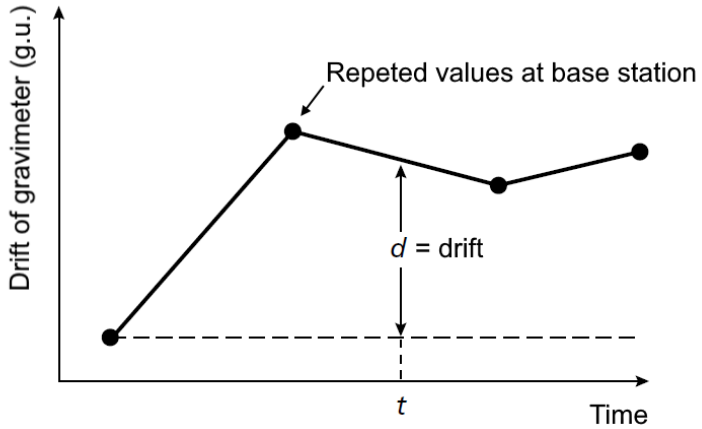


Figure 3-26. A gravimetric drift curve constructed from repeated readings at a fixed location (base station). The drift correction to be subtracted for a reading taken at time *t* is *d*. (modified: Kearey *et al.*, 2002).

- **Tidal correction**

Like as the water in the oceans responds to the gravitational pull of the Moon, and to a lesser extent of the Sun, the solid Earth can differ too. Earth tides give rise to a change in gravity of up to 0.3 mGal with a minimum period of about 12 hours. The tidal correction can be made using periodically published tide tables (*e.g*. Tidal Gravity Corrections for 1991, European Association of Exploration Geophysicists, the Hague), or by software like *Tides.jar.*

In this study the script *Tides.jar* (fig. 3-27), which gives us the value of the tidal correction in µGal was used. After that, the tidal corrections are added to the gravimetric reading (in mGal).

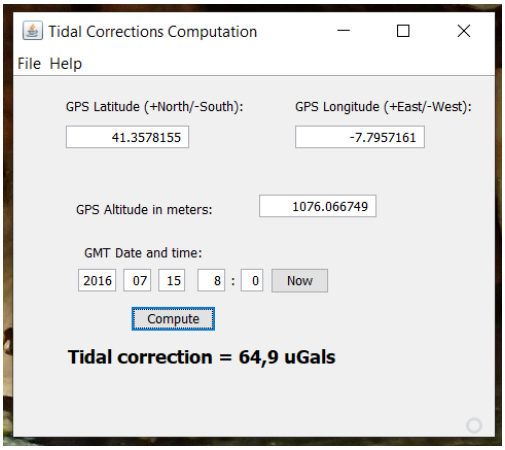


Figure 3-27 Example of tidal correction for one of the Alvão gravimetric stations.

- **Latitude correction**

Gravity varies with latitude because of the non-spherical shape of the Earth and because of the angular velocity of a point on the Earth's surface. Therefore, the gravity increases from the equator to the poles. Clairaut's formula relates gravity to latitude on the reference spheroid according to an equation of the form:

$$g_\phi = g_0\,(1 + \alpha\, sin^2\,\phi - \beta\, sin^2\, 2\phi) \qquad \text{(equation 20)}$$

where g_ϕ is the predicted value of gravity at latitude ϕ, g_0 is the value of gravity at the equator and α and β are constants dependent on the shape and speed of rotation of the Earth. The values of g_0, α and β in current use define the *International Gravity Formula 1967* (IGF), where: g_0 = 978031.846 mGal, α = 0.0053024 and β = 0.0000058.

The value g_ϕ gives the predicted value of gravity at sea-level at any point on the Earth's surface and is subtracted from the observed gravity (g_{obs}) to correct for latitude variation.

The latitude correction can be made in two ways: one station is considered as reference latitude for which the latitude correction is calculated, and then, the other stations will be referred to the reference latitude; or, if the latitude of each station is known precisely, the calculation of the *g* value for each station can be performed. In this study, we calculated the latitude correction for all gravimetric stations using the g_ϕ formula.

- **Elevation correction**

Correction for the differing elevations of gravity stations is made in three parts: free-air correction; Bouguer correction, and terrain correction.

  - **Free-air correction**

The δg_{FA}, corrects for the decrease in gravity with height in free air resulting from increased distance from the center of the Earth, irrespective of the nature of the rock bellow. The δg_{FA} is the difference between gravity measured at sea level and at an elevation *h* meters with no rock in between (fig. 3-28). A value of 0.308766 mGal/m is accepted for most practical applications and is positive at elevations above sea level, and negative below. To reduce to datum an observation taken at height *h*:

$$\delta g_{FA} = \pm 0.308766\, h\, mGal \qquad \text{(equation 21)}$$

The δg_{FA} term varies slightly with latitude from 0.3083 mGal/m at the equator to 0.3088 mGal/m at the poles. This correction is positive for an observation point above datum to correct for the decrease in gravity elevation.

The quantity calculated by applying both the latitude and free-air corrections is called the **free-air anomaly**.

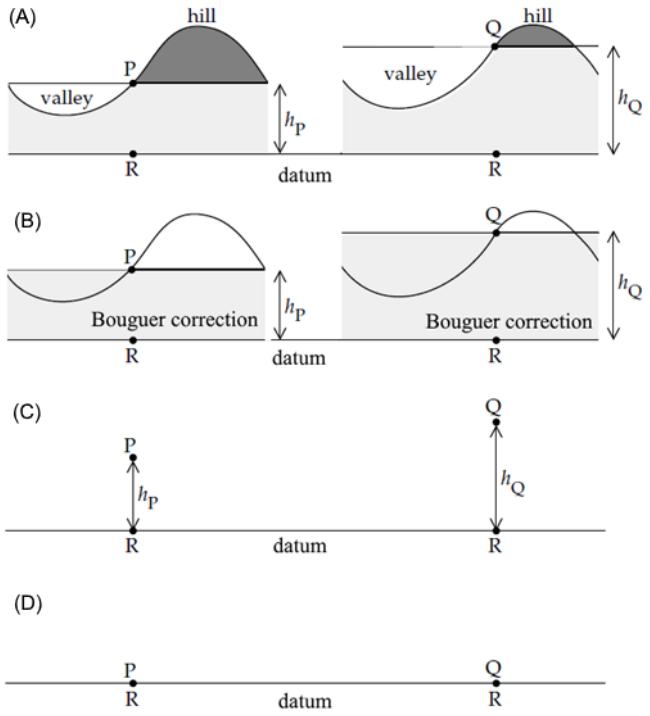


Figure 3-28. After (A) terrain corrections; (B) the Bouguer correction, and (C) the free-air correction, the gravity measurements at stations P and Q can be compared to (D) the theoretical gravity at R on the reference ellipsoid (modified: Lowrie, 2007).

- **Bouguer correction**

The Bouguer correction (δg_B) is used to account for the rock mass between the measuring station and sea level (fig. 3-28). The δg_B calculates the extra gravitational pull exerted by a rock slab of thickness *h* meters and mean density ρ, which results in measurements of gravity (g_{obs}) being overestimated by an amount equal:

$$\delta g_B = 0.04191\, h\rho\, mGal \qquad \text{(equation 22)}$$

where height *h* is in meters and density ρ is in g/cm^3.

On the land, the δg_B should be subtracted from the observed gravity value for station above sea level. Thus, this correction has the opposite signal than the free-air correction.

The free-air (δg_{FA}) and Bouguer (δg_B) corrections are commonly combined into the **elevation correction** (δg_E):

$$\delta g_E = \delta g_{FA} - \delta g_B \quad \text{(equation 23)}$$

Substituting in the terms $\delta g_{FA} = 0.308766\ h$ and $\delta g_B = 0.04191\ h\rho$:

$$\delta g_E = (0.308766 - 0.04191) h\rho\, mGal \quad \text{(equation 24)}$$

However, one of the problems with the Bouguer correction is to know the density to use. The rock density methodologies are explained in the topic below (see topic 3.5.5).

- **Terrain corrections**

The Bouguer correction assumes that the topography around the gravity station is flat. However, this is rare and a further correction, the terrain correction (T_C), must be made to account for topographic relief in the vicinity of the gravity station. This correction is always positive (fig 3-28).

Classically, terrain corrections are applied using a circular graticule known as a Hammer chart (fig. 3-29; Hammer, 1939), divided by radial and concentric lines into a large number of compartments. The outermost zone extends to 21.9 km, beyond which the effect of topography on *g* is negligible.

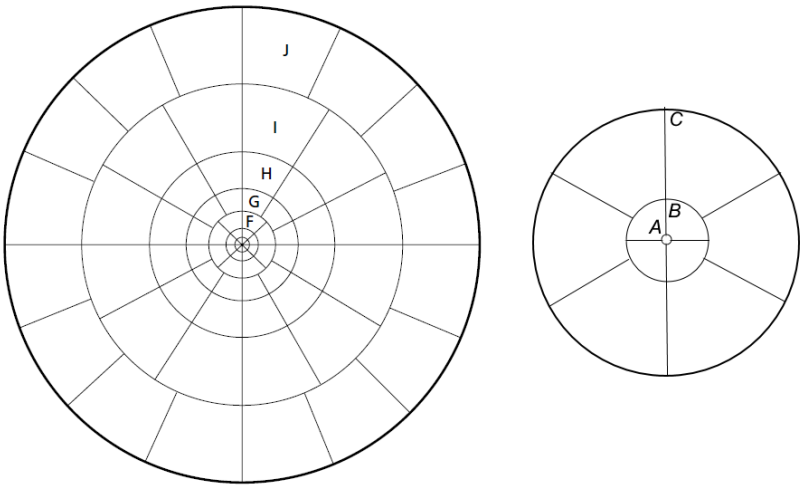


Figure 3-29. Hammer chart used in the calculation of terrain corrections (modified: Kearey *et al.*, 2002).

The Hammer chart can be laid on a topographic map with its center on the gravity station and the average topographic elevation of each compartment is determined. The elevation of the gravity station is subtracted from these values, and the gravitational effect of each compartment is determined by reference to tables constructed using the formula for the gravitational effect of a sector of a vertical cylinder at its axis. Then, the terrain correction is calculated by summing the gravitational contribution of all compartments.

Table 3-4 shows the calculation method. To reduce the labor, the averaging topography within a rectangular grid can be made. Only single digitization is required as the topographic effects may be calculated at any point within the grid by summing the effects of the right rectangular prisms defined by the grid squares and their elevation difference with the gravity station.

The terrain correction method works on the principle of determining the value of *g* at the center of a ring of inner (r_1) and outer (r_2) radii and using the equation:

$$T_C = 0.4191 \frac{\rho}{n}\left(r_2 - r_1 + \sqrt{r_1^2 + z^2} - \sqrt{r_2^2 + z^2}\right) \qquad \text{(equation 25)}$$

The T_C means terrain correction, ρ is the Bouguer correction density, *n* corresponding to the number of the compartment in the zone, and *z* is the modulus of elevation difference between the observation point and mean elevation of the compartment (m).

Table 3-4. Terrain corrections for Hammer zones B to M (adapted: Kearey *et al.*, 2002): n - number of compartments in the zone; r_1 - inner radius of zone (m); r_2 - outer radius of zone (m).

Zones	n	Radius			Opening	
		r_1	r_2	$r_2 - r_1$	º	RAD
B	4	2.0	16.6	14.6	90.0	1.570796
C	6	16.6	53.3	36.7	60.0	1.047198
D	6	53.3	170.1	116.8	60.0	1.047198
E	8	170.1	390.1	220	45.0	0.785398
F	8	390.1	894.8	504.7	45.0	0.785398
G	12	894.8	1529.4	634.6	30.0	0.523599
H	12	1529.4	2614.4	1085	30.0	0.523599
I	12	2614.4	4468.8	1854.4	30.0	0.523599
J	16	4468.8	6652.2	2183.4	22.5	0.392699
K	16	6652.2	9902.5	3250.3	22.5	0.392699
L	16	9902.5	14740.9	4838.4	22.5	0.392699
M	16	14740.9	21943.3	7202.4	22.5	0.392699

The classical methods of graphical correction (*e.g*. Hammer method) evolved into methods and algorithms proceeded by computers. The increased efficiency of terrain correction methods is mainly due to the use of digital elevation models (DEM; Ketelaar, 1987).

For the Alvão case study, two methods of terrain corrections were used (see topic 4.6.2): Hammer chart and a script for *MatLab* software developed by Almeida *et al.* (2018).

3.5.4 Free-air and Bouguer anomalies

The free-air anomaly (Δg_{FA}) and Bouger anomaly (Δg_B) can be defined (Reynolds, 1997; Kearey *et al.*, 2002; Lowrie, 2007):

$$\Delta g_{FA} = g_{obs} - g_{\Phi} + \delta g_{FA} \qquad \text{(equation 26)}$$

$$\Delta g_B = g_{obs} + \sum(corrections) - g_{base} \qquad \text{(equation 27)}$$

With:

$$\sum(corrections) = g_{\Phi} + (\delta g_{FA} - \delta g_B) + T_C - d \qquad \text{(equation 28)}$$

where *d* corresponds to the instrumental drift, including the Earth tides correction.

The main end-product of gravity data reduction is the Bouguer anomaly, which should correlate only with lateral variations in the density of the upper crust. The Bouguer anomaly

is the difference between the observed gravity value (g_{obs}), adjusted by the algebraic sum of all the necessary corrections, and that at some base station (g_{base}).

In this study, in addition to a base station, an absolute gravimetric base station was also used to correct the readings (see topic 4.6.2).

The computation of the Bouguer anomaly allows direct comparison of gravity anomalies and allows the combination of data into gravity contour maps.

3.5.5 Rock densities

Most common rock types have densities in the range between 1.60 and 3.20 g/cm^3. The density of rock is dependent on both its mineral composition and porosity. The density ranges for common rock types are present in table 3-5.

Gravity anomalies result from the difference in density, or density contrast, between a body of rock and its surroundings. The sign of the density contrast determines the sign of the gravity anomaly.

Table 3-5. Density ranges (g/cm^3) of some common rock types (Kearey *et al.*, 2002).

Rock type	Range values
Alluvium (wet)	1.96–2.00
Clay	1.63–2.60
Shale	2.06–2.66
Sandstone:	
- Cretaceous	2.05–2.35
- Triassic	2.25–2.30
- Carboniferous	2.35–2.55
Limestone	2.60–2.80
Dolomite	2.28–2.90
Granite	2.52–2.75
Granodiorite	2.67–2.79
Anorthosite	2.61–2.75
Basalt	2.70–3.20
Gabbro	2.85–3.12
Gneiss	2.61–2.99
Quartzite	2.60–2.70
Amphibolite	2.79–3.14

In the case of granitic bodies, since the densities are generally lower than the host rocks (mostly metasediments), the gravimetric anomaly is usually negative.

The geological observations allow defining the granite intrusions as heterogeneous bodies, since they can have different facies, which can have different mineralogical

composition, and then with different densities. A well representative sampling of the granitic body and its density measurements can control the effects of facies variations. Density usually increases with depth in the crust. However, this variation in depth is similar for both granite or metamorphic rocks and does not influence the relative density contrast (Vigneresse, 1990).

Knowledge of rock density is necessary both for the application of the Bouguer and terrain corrections and for the interpretation of gravity anomalies (Reynolds, 1997; Kearey *et al.*, 2002; Lowrie, 2007).

Density can be determined by indirect methods or by direct measurements on rock samples.

- **Indirect methods**

  The indirect methods for density determination, the Nettleton method (Nettleton, 1939) is the most used. Nettleton's method consists of searching for the minimum correlation existing between the topography and the variations of the gravity anomaly using different densities.

  Nettleton's method of density determination involves taking gravity observations over a small isolated topographic area. Field data are reduced using a series of different densities for the Bouguer and terrain corrections. The density value that yields a Bouguer anomaly with the least correlation (positive or negative) with the topography is taken to represent the density of the studied area. The method is useful, once no borehole or mineshaft is required, and a mean density of the rocks is provided. However, the disadvantage of the method is that isolated relief features may be formed of anomalous materials which are not representative of the area in general (Kearey *et al.*, 2002; Lowrie, 2007).

  In this study, the Nettleton indirect method was used to obtain the mean/ median value of density rocks to determine the Bouguer anomaly (see section 4.6.3).

- **Direct methods**

Density direct measurements can be made in rock samples from the surface, or borehole samples, if available. The apparent density of LOP rocks and their hosts (Vila Real Massif and Douro Group Metassediments) was determined, once its values were necessary to run software *Oasis Montaj*, used to interpret gravity anomalies and modeling.

Density was determined in LNEG (Porto) facilities and obtained by atmospheric pressure saturation method. Since the rock samples available for testing consisted of cylinders, with about 22 mm in diameter and 22 mm in height, a much larger number of samples than usual was tested, in order to compensate for the reduced volume of the test specimens and to obtain a consistent apparent density mean value and variance. Thus, the number of specimens tested was: LOP granites – 24 from LO, 14 from AC and 11 from BA granites; host rocks – 21 from Vila Real Massif and 10 from Douro Group Metassediments.

Test procedure consisted of different steps:

- Specimens of each rock sample were washed with tap water to wipe out dust and small loose debris;
- Specimens were dried in a ventilated oven at a temperature of [70 ± 5] °C for 72 h;
- Specimens were taken from the oven and cooled to room temperature;
- Dried specimens were weighed, and dry mass of each specimen was recorded (W_{dry}, g);
- Specimens were placed in an immersion tank on top of non-oxidizing and non-absorbent supports;
- Tap water was added to the tank, up to half the height of the specimens (time t_0);
- At time t_0 + [60 ± 5] min tap water was added until the level of the water reached three-quarter of the height of the specimens;
- At time t_0 + [120 ± 5] min tap water was added until the specimens are completely immersed to a depth of [25 ± 5] mm of water;

- At time t_0 + [48 ± 2] h the specimens were taken out of the water, quickly wiped with a damp cloth and then weighed within 1 min (W_{Sat1} = m_1, g);
- At time t_0 + [72 ± 2] h the specimens were taken out of the water, quickly wiped with a damp cloth and then weighed within 1 min (W_{Sat2} = m_2, g);
- The test continued, with saturated weighing performed every 24 h, up to a constant mass of the specimens; constant mass is assumed to be reached when the difference between two successive weighings was not greater than 0.1 % of the first of the two masses;
- When constant mass was reached, specimens were weighed under water and the mass in water was recorded ($W_{immersed}$, g)
- The apparent density of each rock specimen was calculated using the following equation:

$$\rho = \frac{W_{dry}}{W_{satn} - W_{immersed}} \times \rho_{water} \qquad \text{(equation 29)}$$

- The tap water density (ρ_{water}) was determined by calculating the weight of the water in a container (m_{water}) of known volume (a volumetric flask was used for this calculation):

$$\rho_{water} = \frac{m_{water}}{volume\ of\ container} = 996.2\ \text{kg/m}^3 \qquad \text{(equation 30)}$$

- The apparent density of each rock sample corresponds to the mean value obtained for the respective set of specimens.

3.5.6 Interpretation of gravity anomalies

- **Regional and residual anomalies**

A gravity anomaly results from the heterogeneous distribution of density in the Earth. Assume that the density of rocks in a subsurface body is ρ and the density of the rocks surrounding the body is ρ_0. The difference $\Delta\rho = \rho - \rho_0$ is called the density contrast of the body concerning the surrounding rocks. The contrast density can be: (i) positive density contrast if the body has a higher density than the host rock; or (ii) negative density contrast

if a body has a lower density than the host rock. Over a high-density body, the measured gravity is amplified, and after reduction to the reference ellipsoid and subtraction of the normal gravity, a positive gravity anomaly is obtained. Likewise, a negative anomaly results in a region of low density. The presence of a gravity anomaly indicates a body or structure with anomalous density, where the sign of the anomaly is the same as that of the density contrast and shows whether the density of the body is higher or lower than normal (Reynolds, 1997; Kearey *et al.*, 2002; Lowrie, 2007).

The appearance of a gravity anomaly is affected by the characteristics of the anomalous body (*e.g*. dimensions, density contrast, and depth). The horizontal extent of an anomaly is often called its apparent wavelength. The wavelength of an anomaly is a measure of the depth of the anomalous mass, where large, and deep bodies give rise to broad, and low amplitude anomalies (long-wavelength), while small, and shallow bodies cause narrow and sharp anomalies (short-wavelength). Usually, a map of Bouguer gravity anomalies contains superposed anomalies from several sources (fig. 3-30; Kearey *et al.*, 2002; Lowrie, 2007).

$$Bouguer_{anomaly} = Regional_{anomaly} + Residual_{anomaly} \qquad \text{(equation 31)}$$

The long-wavelength anomalies due to deep density contrasts are called **regional anomalies**. They are important for understanding the large-scale structure of the Earth's crust under major geographic features, such as mountain ranges, oceanic ridges, and subduction zones. Short-wavelength are the **residual anomalies** and are due to shallow anomalous masses that may be of interest for geological studies. Geological knowledge is essential for interpreting the residual anomalies.

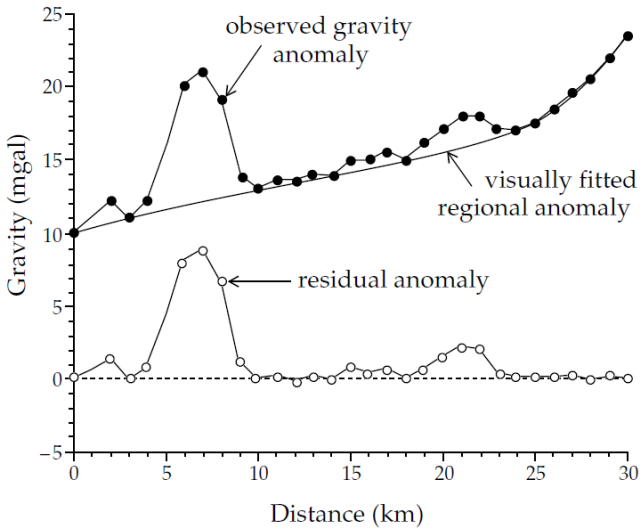


Figure 3-30. Representation of the regional anomaly on a gravity profile by visually fitting the large-scale trend with a smooth curve (modified: Lowrie, 2007).

- **Separation of regional and residual anomalies**

The separation of anomalies of regional and local origin is an important step in the interpretation of a gravity map. The separation of the regional anomaly can be performed by geological methods, graphical methods (fig. 3-30; visual analysis made by simple observation), by analytical grid methods using polynomial representation (using mathematical models, with 1st, 2nd, or 3rd polynomial order), representations by Fourier series or, by spectral filtering methods, that is incorporated in a specific software (Reynolds, 1997; Kearey *et al.*, 2002; Lowrie, 2007; Hinze *et al.*, 2013). Regardless of the used method for the separation of the regional component, it is convenient that the isoline from zero-value of the residual anomaly, roughly coincides with the line corresponding to the studied outcrop (*e.g.* granite body; Vigneresse, 1990).

In this study, separation of regional and residual anomalies was made through the *Oasis Montaj* 8.3.3. (see topic 4.6.4).

3.5.7 Modeling

After the removal of regional effects, the residual gravity anomaly must be interpreted in terms of anomalous density distribution.

Nowadays, the analyses are made using iterative modeling incorporated on software. Earlier methods of interpretation utilized a comparison of the observed gravity anomalies with the computed anomalies of geometric shapes.

There are forward or direct, and reverse or inverse methods of interpreting gravimetric data (Vigneresse, 1990; Lowrie, 2007). The forward method is the oldest and most used method. In the forward method, an initial model for the source body is constructed based on geologic and geophysical intuition. The model's anomaly is calculated and compared with the observed anomaly, and model parameters are adjusted in order to improve the fit between the two anomalies. The process is repeated until calculated and observed anomalies are deemed sufficiently alike. On the other hand, in the reverse method, starting with the observed geophysical response, an earth model that will provide the best fit for that data is calculated. In the reverse method, simplifying assumptions are inevitable (NGA, 2004; Blakely, 1995).

It should be noted that the interpretation of gravity anomalies is mathematically non-unique because multiple theoretical solutions are always possible. To acquire a precise model, the combination of results from multiple disciplines should be performed (Saltus *et al.*, 2011).

In the Alvão study, the modeling was made using specific software. The Gravity Profiles (2-D model) were produced using the *Gravity and Magnetic Modelling Software* (GM-SYS) that is incorporated in the *Oasis Montaj* software. GM-SYS is a forward modeling program allowing interactive manipulation of the geologic model and real-time calculation of the gravity response (NGA, 2004).

CHAPTER 4:

RESULTS AND DISCUSSION

“The unexamined life is not worth living.”

Sócrates

4 RESULTS AND DISCUSSION

4.1 CARTOGRAPHIC AND PETROGRAPHIC STUDIES

4.1.1 Cartographic description

The cartographic studies were made in LOP granites, quartz/ aplite veins, and host rocks. The LOP is composed of 3 outcrop granites (figs. 4-1A to H). The granites are heterogranular with porphyritic or slightly porphyritic texture, with scarce euhedral feldspar, with no visible preferential orientation.

Table 4-1. Macroscopic characteristics and field observations of the LOP granites.

Granites	Macroscopic characteristics	Observations
Lamas de Olo (LO)	• Medium to coarse-grained porphyritic biotite granite; • Heterogranular texture • Mostly xenomorphic to hypidiomorphic texture with scarce euhedral feldspar and quartz crystals; • No visible preferential orientation.	The more representative outcrop granite.
Alto dos Cabeços (AC)	• Fine to medium-grained porphyritic biotite granite; • Heterogranular texture; • Mostly xenomorphic to hypidiomorphic texture with scarce euhedral feldspar and quartz crystals; • No visible preferential orientation.	In the field, the contacts between AC-LO granites are generally diffuse.
Barragem (BA)	• Leucocratic fine to medium-grained and slightly porphyritic biotite granite; • Mostly heterogranular texture; • Mostly xenomorphic to hypidiomorphic texture; • No visible preferential orientation.	In the field, the contacts between BA-LO granites are generally diffuse but abrupt contacts also occur; some BA veins crosscut the LO granite.

The LOP is a small post-tectonic pluton of *ca*. 13.7 km^2, with a rhomboid shape. In the field, the contacts between LO-AC and LO-BA granites are generally diffuse (figs. 4-1D to F), however, field observations show that BA granite crosscuts the granite that mostly outcrops, the LO granite (figs. 4-1G and H).

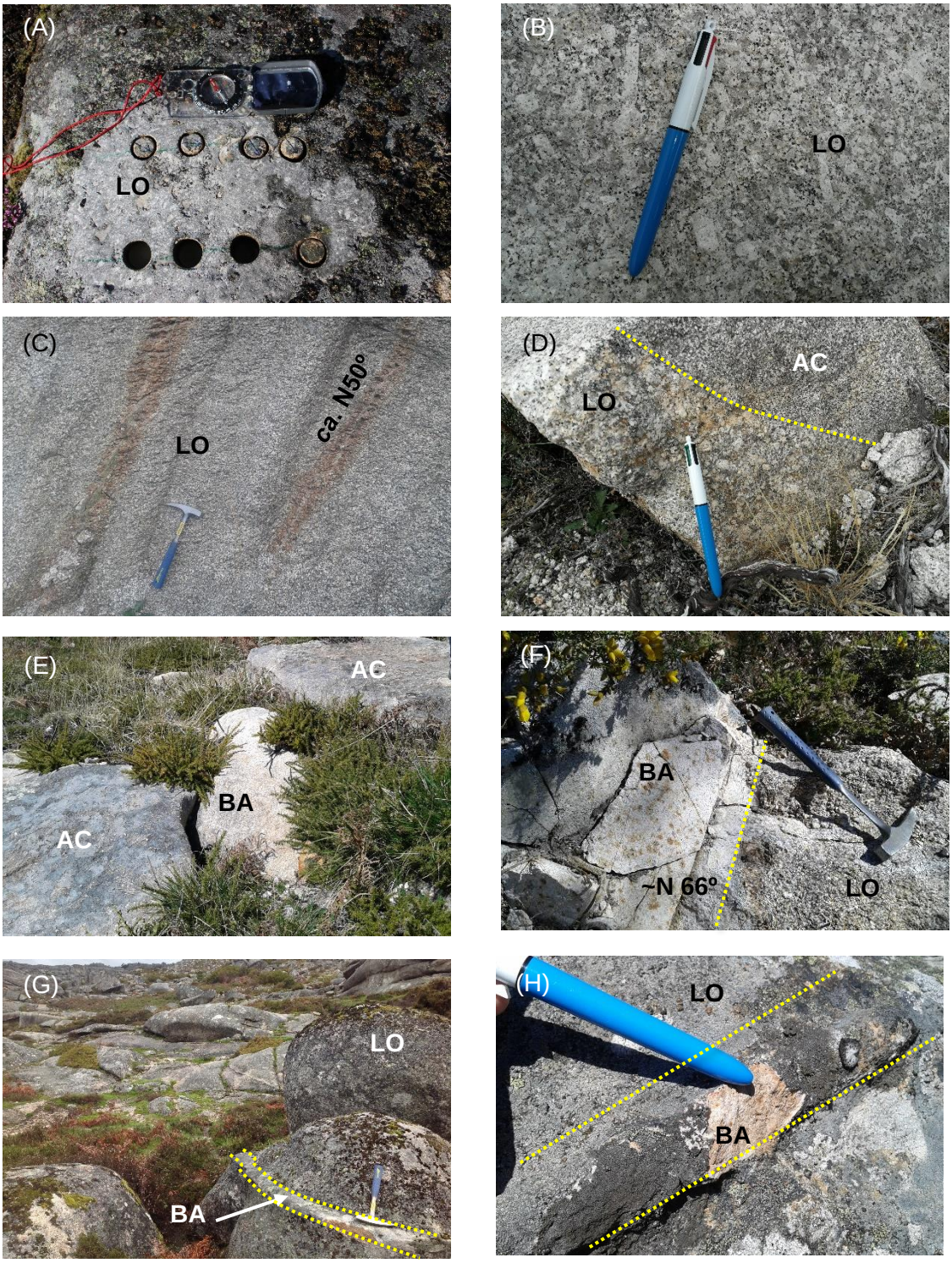


Figure 4-1. Some aspects of LOP outcrops: (A) LO granite (B) porphyritic texture of LO granite; (C) fractures *ca.* N 50º (subvertical) with visible episienitization in LO granite; (D) Contact between LO and AC granites; (E) Outcrop (not *in situ*) of AC and BA granites. (E) Contact between LO and BA granites; (G) BA vein crosscut the LO granite; (H) BA vein detail.

Associated with the LOP granites, aplite and quartz veins were also visible. The veins cut the granites filling fractures mostly N 80º, but also N 10º. Related to the N 80º fractures, some quartz veins with wolframite/ scheelite and beryl were observed (fig. 4-2).

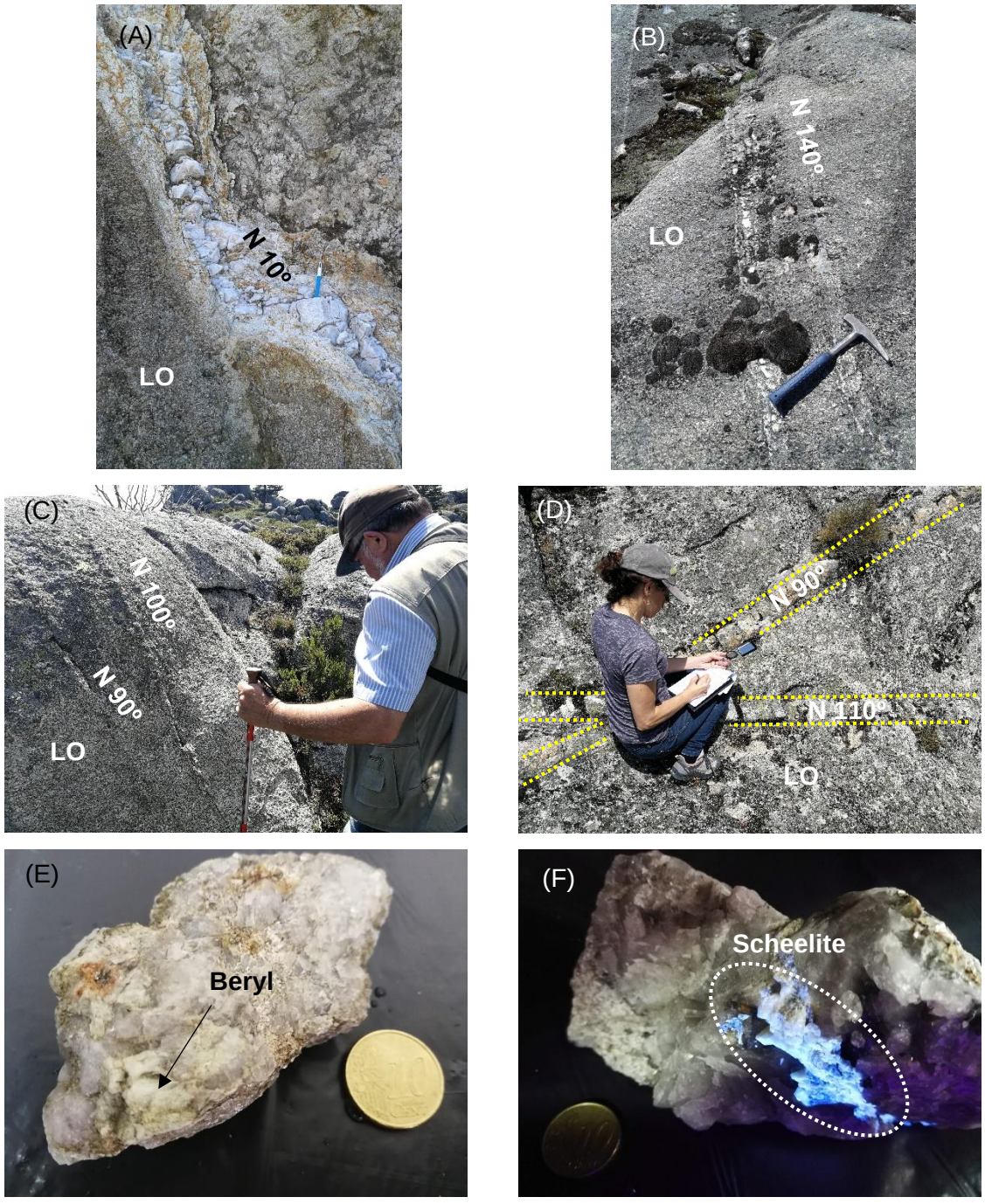


Figure 4-2. Veins crosscut LO granite: (A) Quartz vein with fault gouge (*ca*. N10º); (B) Quartz vein *ca*. N 140º; (C) Subvertical quartz vein; (D) Aplite veins crosscut the LO granite; (E) Quartz with beryl mineralization; (F) Quartz with scheelite (ultraviolet light).

Regarding the host rocks, LOP intrudes mostly on the Douro Group Metasediments (DGM) and on syn-D_3 two-mica granites from Vila Real Massif (VRM). Aplite, pegmatite, aplite-pegmatite, and quartz veins crosscut both DGM and VRM, filling fractures with different directions. Shists, quartzites, and hornfels are also present in the area. Located at NE of LOP granites, microgranites and lamprophyres are present, crosscutting the VRM (fig. 4-3).



Figure 4-3. Some aspects of veins and host rocks outcrops: (A) and (B) Contacts between the DGM and two-mica granites from VRM; (C) Contact between two different facies from VRM; (D) and (E) Contacts between VRM and microgranite (γ'f - two mica fine-grained granite; γ'm - two mica medium- to coarse-grained granite with sparse megacrystals; μγ - microgranite; θ - lamprophyre; Do – Desejosa Formation from Douro Group Metasediments).

A geological map, based on previous studies and including the new observation data, was made using the *ArcGIS* 10.7 software (fig. 4-4).

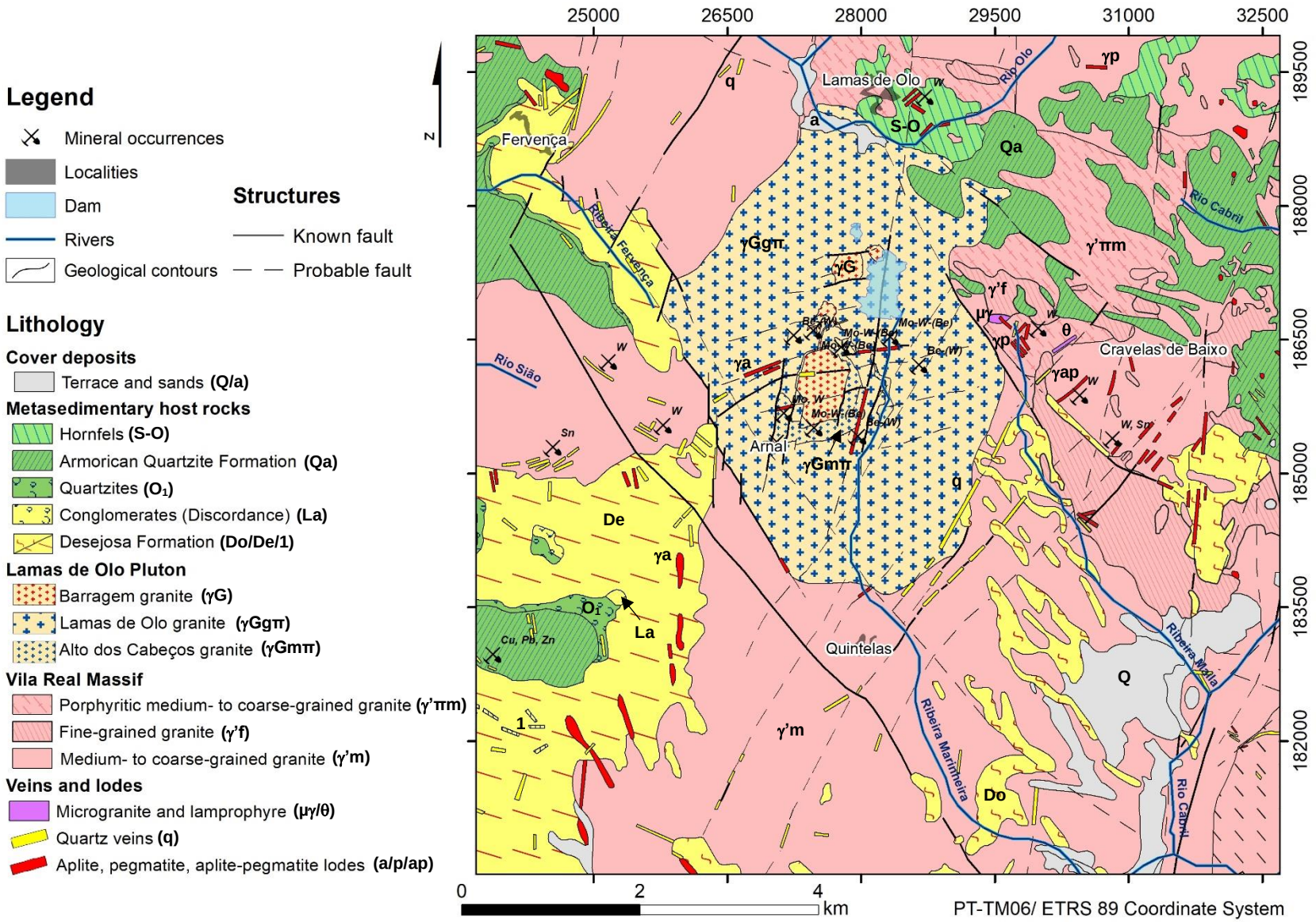


Figure 4-4. Geological map of LOP granites and host rocks made on *ArcGIS* v.10 and using the PT-TM06/ ETRS89 projected coordinate system (modified: Pereira *et al.*, 1987; Pereira, 1989; Helal, 1992).

4.1.2 Petrographic studies

Petrographic studies were made in LOP granites, and associated mineralized veins. The LOP granites (fig. 4-5) are mostly composed of quartz, plagioclase (oligoclase, albite, and oligoclase-andesine), K-feldspars (orthoclase and microcline), and biotite (fig. 4-6A). Muscovite I and II, zircon, sphene, fluorite, allanite, magnetite, hematite, ilmenite, anatase, chlorite, rutile, apatite, goethite, epidote, and tourmaline are also present (fig. 4-6). In the BA granite, the muscovite is more abundant than in the LO and AC granites but is mostly of secondary origin resulting from deuteric processes (table 4-2; fig. 4-6).

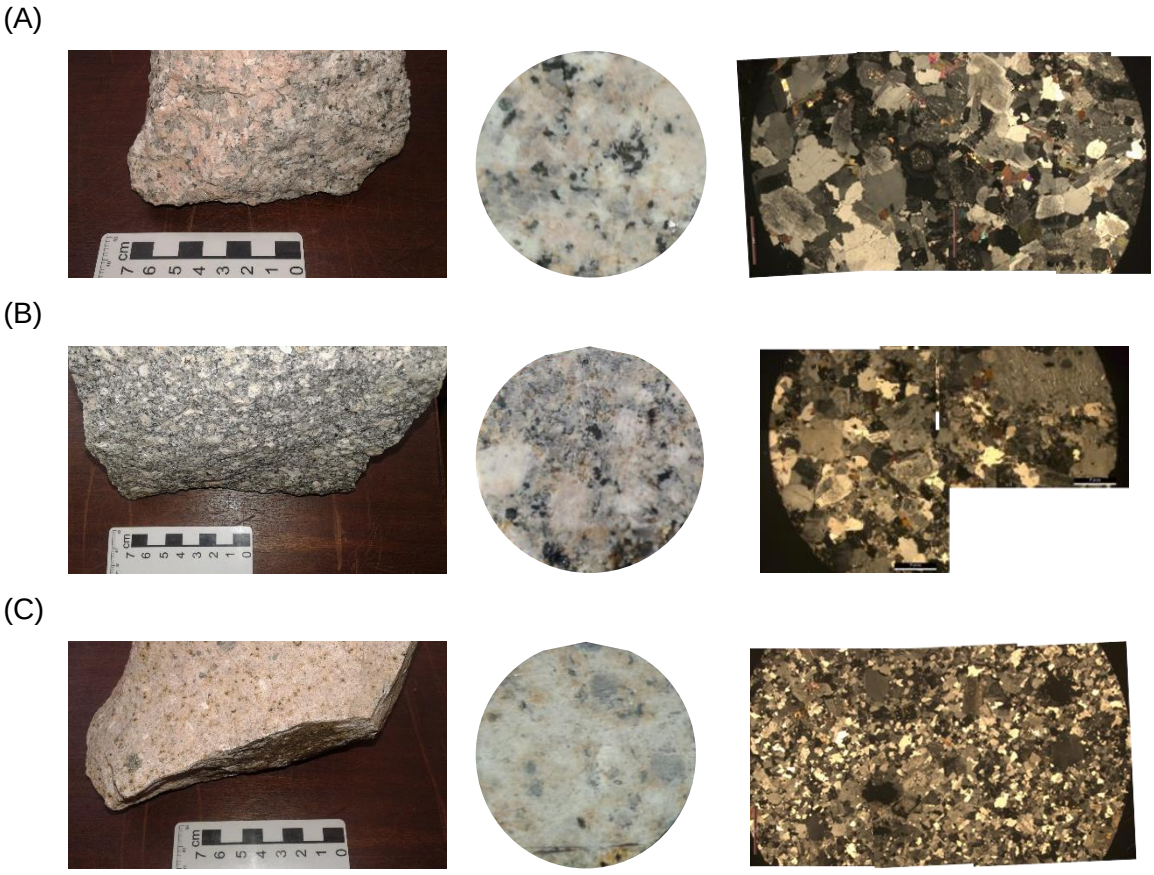


Figure 4-5. Macroscopic characteristics and binocular magnifying glass observations of LOP granites: (A) Lamas de Olo granite; (B) Alto dos Cabeços granite; (C) Barragem granite.

The plagioclases occur frequently zoned in all granites (fig. 4-6B) and are mostly oligoclase in LO, oligoclase-andesine in the AC, and albite (fig. 4-6C) in the BA granite. Occasionally, the plagioclases exhibit myrmekitic intergrowths with quartz, common mostly in the LO granite (fig. 4-6E), and are altered by sericitization (*e.g.* figs. 4-6C and F). The K-feldspar, perthitic orthoclase and microcline occur as heterogranular crystals. Sometimes

some K-feldspar megacrystals with small plagioclase inclusions and some K-feldspar with an albitic border are observed. The quartz has sometimes undulatory extinction (fig. 4-6F), subgrain boundaries, and fluid inclusion planes (FIP; fig. 4-6G). The biotite – brownish to greenish (*e.g*. fig. 4-6I) are present in all granites – sometimes appears partially to completely chloritized (figs. 4-6J and M). Occasionally, biotite is altered to muscovite (fig. 4-6A, H, and J), mainly in the BA leucocratic granite, where biotite is observed in minor amounts. Frequently, biotite has pleochroic halos associated with zircon inclusions (fig. 4-2A) and curved biotites, and sometimes with kinks, are present in all granites (fig. 4-6H). The primary muscovite is very scarce in the LO and AC granites and is observed as large crystals in the BA granite (figs. 4-6K and L). The allanite is scarce but present in all granites (fig. 4-6N). In all LOP granites were also observed magnetite, hematite, and scarce ilmenite (figs. 4-6O to Q). In the AC granite, most of the magnetite is altered to hematite (martite), and in BA granite the anatase (fig. 4-6R) and ilmenite are the dominant opaque minerals.

For a detailed magnetic mineralogy characterization, complementary studies of some minerals were conducted to identify the presence of magnetite, hematite, and ilmenite. Anatase and rutile were also identified. The SEM-EDS analyses (fig. 4-7) showed the presence of different Fe-Ox, Fe-Ox-Ti, and Ox-Ti minerals (figs. 4-7A to F) and small amounts of other minerals like fluorite, xenotime, monazite (fig. 4-7B), and columbo-tantalite. Figures 4-7G to I are examples of some EDS spectrum performed in LOP thin sections, showing the presence of Fe-Ox, Fe-Ox-Ti, and Ox-Ti minerals.

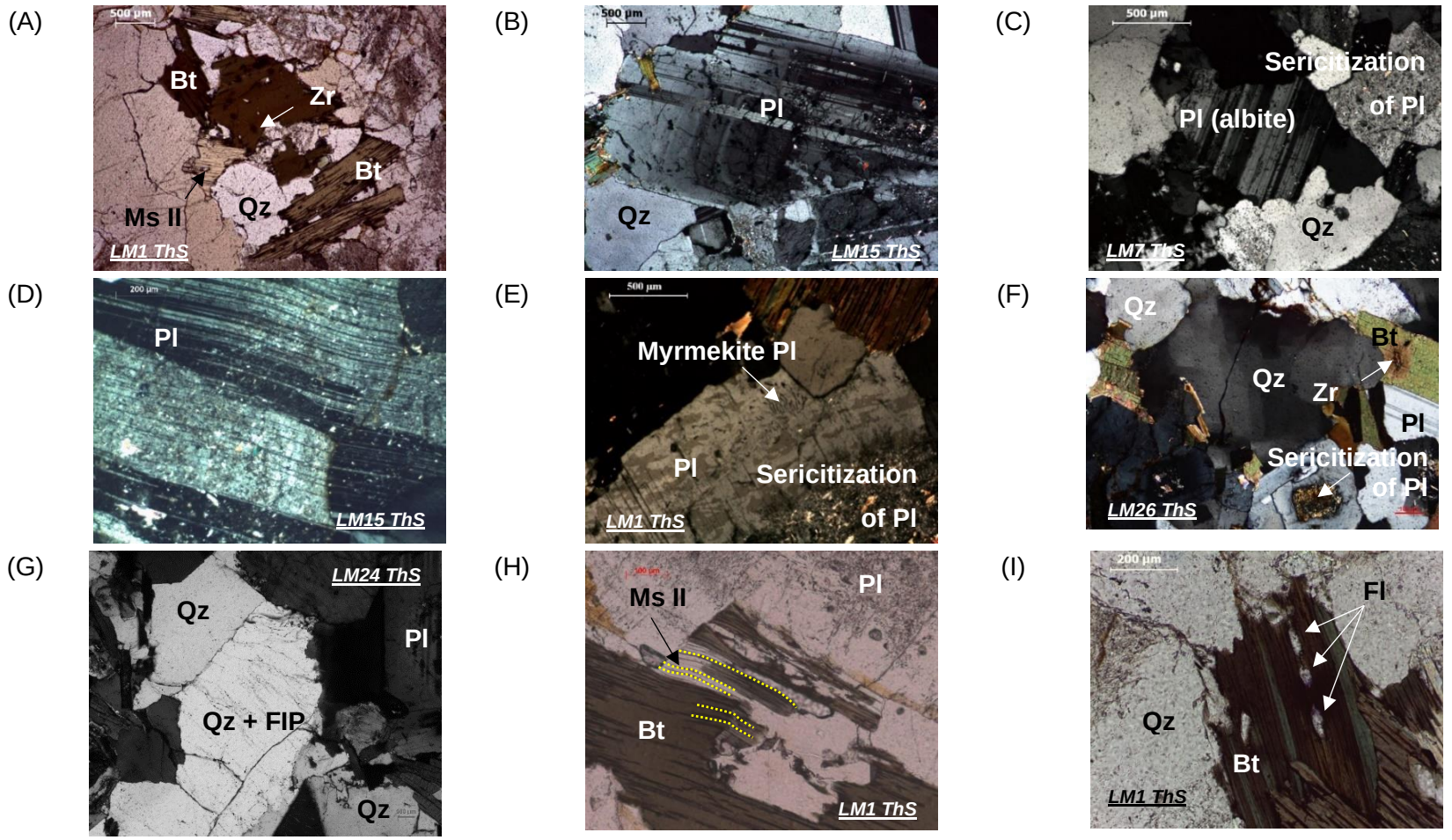


Figure 4-6. Photomicrographs of samples from Lamas de Olo Pluton: (A) Biotite and muscovite II aspects (transmitted light; parallel polars) - LO granite; (B) to (D) Some aspects of plagioclase (transmitted light; crossed polars) - BA granite; (E) Some aspects of plagioclase (transmitted light; parallel polars) - LO granite; (F) and (G) Microdeformation on quartz with undulatory extension and fluid inclusion planes (transmitted light; crossed polars) - AC granite; (H) Curved micas (transmitted light; parallel polars) - LO granite; (I) Biotite with brown and green colors and fluorite (transmitted light; parallel polars) - LO granite; (J) Alteration of biotite to chlorite and/or to muscovite II (transmitted light; parallel polars) - BA granite; (K) and (L) Some aspects of muscovite I (transmitted light; parallel and crossed polars, respectively) - BA granite; (M) Chlorite and rutile needles (transmitted light; parallel polars) - BA granite; (N) Alanite crystal on plagioclase (transmitted light; parallel polars) - LO granite; (O) to (Q) Fe-Ox and Fe-Ox-Ti minerals present in the LOP granites (reflected light; parallel polars) - LO, LO, and AC granites, respectively; (R) Fe-Ox-Ti mineral (transmitted light; parallel polars) - BA granite. Bt – biotite, Zr – zircon, Ms II – muscovite (secondary in origin), Qz – quartz, Pl – plagioclase, Ap – apatite, Fl – fluorite, Chl – chlorite, Ms I – muscovite (primary in origin), Rt – rutile, Aln – allanite, Ilm – ilmenite, Hem – hematite, Mag – magnetite, Ant – anatase, FIP – fluid inclusion planes, ThS – Thin section, PS – polished section (the figure continue below).

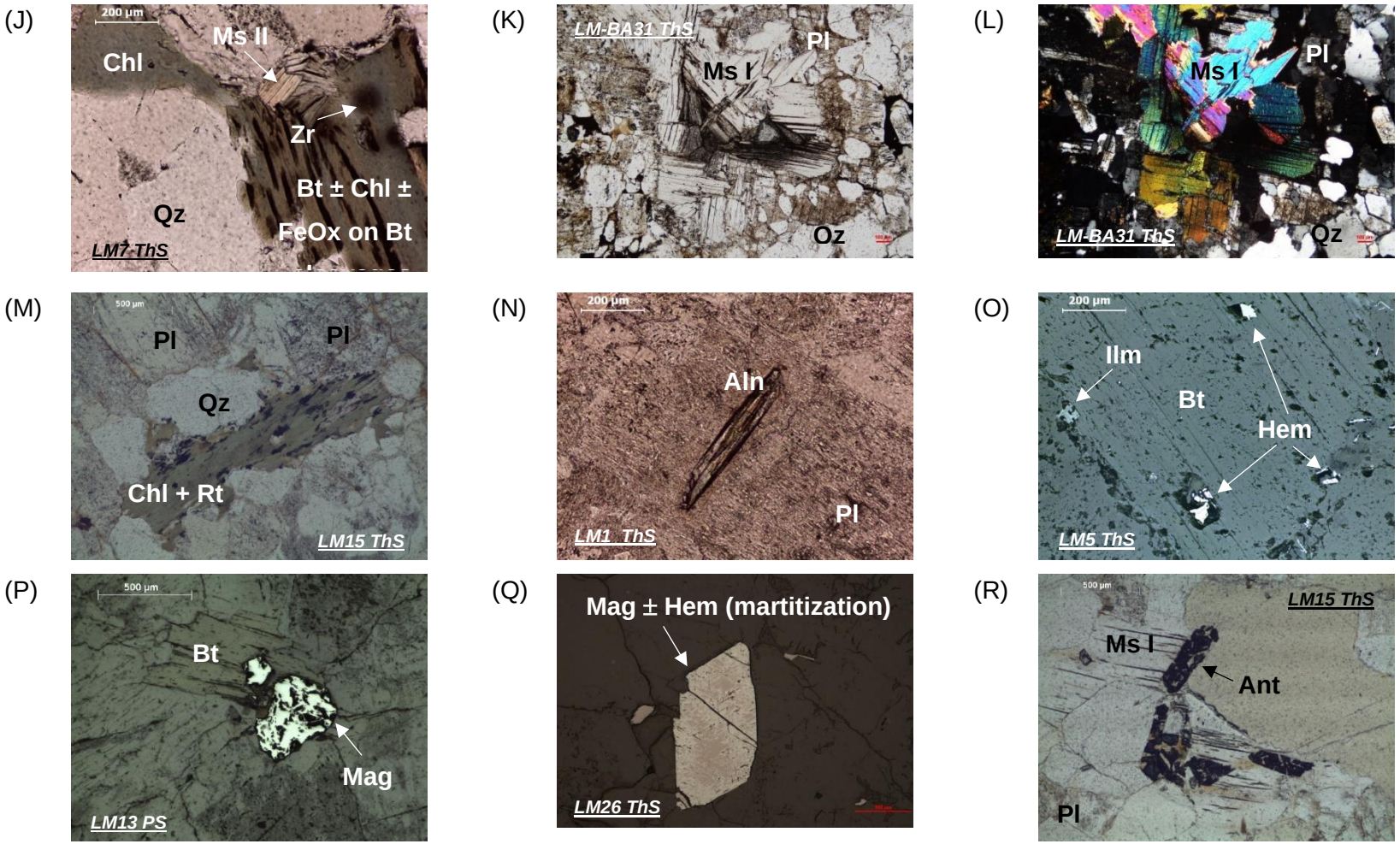
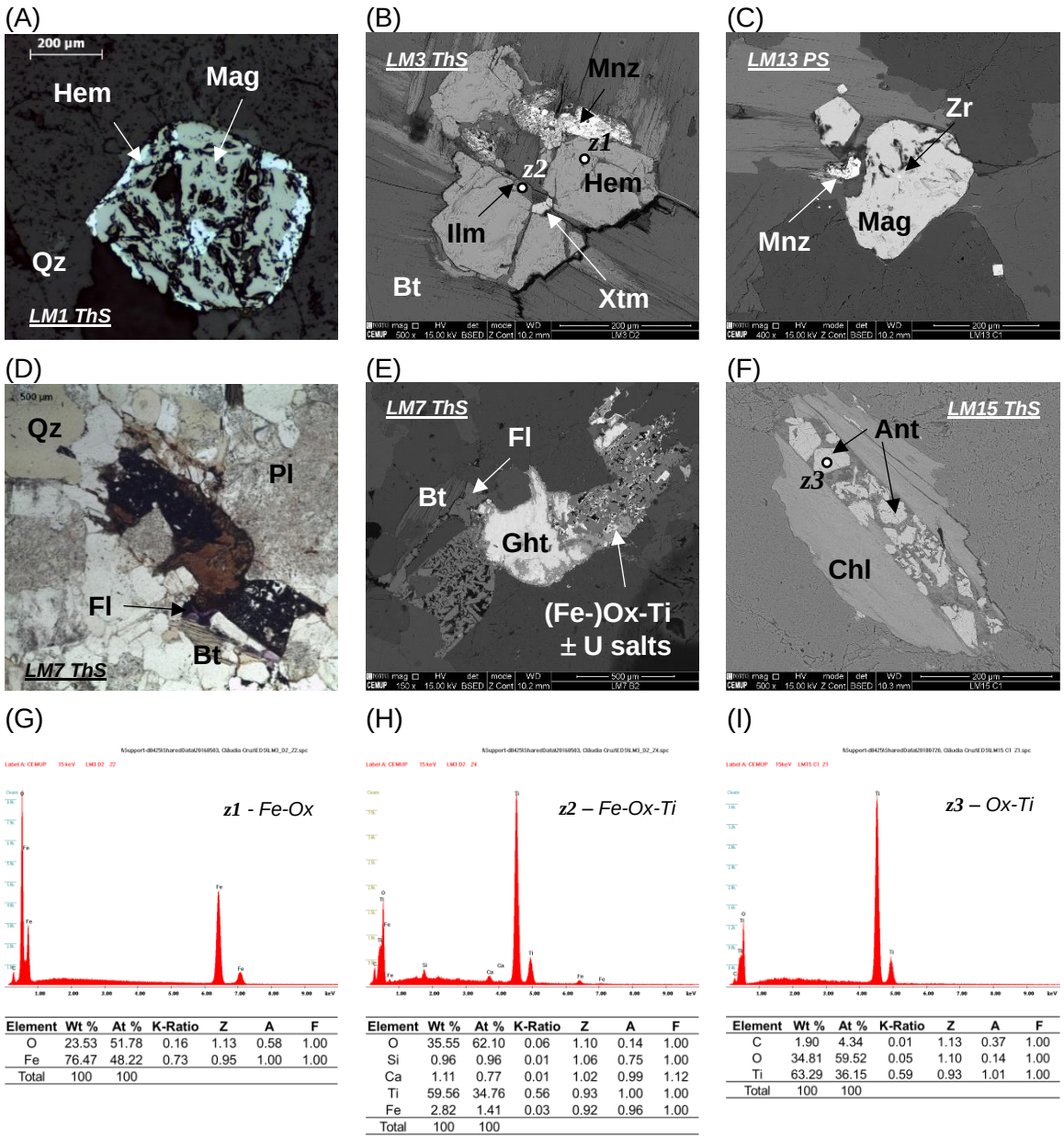


Figure 4-6 (cont.)



Element	Wt %	At %	K-Ratio	Z	A	F
O	23.53	51.78	0.16	1.13	0.58	1.00
Fe	76.47	48.22	0.73	0.95	1.00	1.00
Total	100	100				

Element	Wt %	At %	K-Ratio	Z	A	F
O	35.55	62.10	0.06	1.10	0.14	1.00
Si	0.96	0.96	0.01	1.06	0.75	1.00
Ca	1.11	0.77	0.01	1.02	0.99	1.12
Ti	59.56	34.76	0.56	0.93	1.00	1.00
Fe	2.82	1.41	0.03	0.92	0.96	1.00
Total	100	100				

Element	Wt %	At %	K-Ratio	Z	A	F
C	1.90	4.34	0.01	1.13	0.37	1.00
O	34.81	59.52	0.05	1.10	0.14	1.00
Ti	63.29	36.15	0.59	0.93	1.01	1.00
Total	100	100				

Figure 4-7. Photomicrographs and EDS spectrums of Lamas de Olo Pluton: (A) Association of magnetite and hematite (reflected light; parallel polars) - LO granite; (B) Fe-Ox and other minerals in minor amounts in SEM - LO granite - with the location of two EDS spectrums *z1* and *z2*; (C) Photomicrograph of magnetite and other minor amounts in SEM - LO granite; (D) Aspect of a mixture of Fe-Ox and (Fe-)Ox-Ti minerals (transmitted light; parallel polars) - BA granite; (E) Same aspect shown in (D) in SEM; (F) An example of Ox-Ti minerals with the location of EDS spectrum *z3*; (G) EDS spectrum of Fe-Ox mineral (hematite; *z1*) with semi-quantitative analyse; (H) EDS spectrum of Fe-Ox-Ti mineral (ilmenite; *z2*) with semi-quantitative analyze; (I) EDS spectrum of Ox-Ti mineral (anatase; *z3*) with semi-quantitative analyze; Mag – magnetite, Hem – hematite, Qz – quartz, Bt – biotite, Mnz – monazite, Ilm – ilmenite, Xtm – xenotime, Pl – plagioclase, Fl – fluorite, Ght – goethite, U salts – uranium salts, Chl – Chlorite, Ant – anatase; Fe-Ox - iron oxide, Fe-Ox-Ti – iron oxide with titanium, Ox-Ti – titanium oxide; ThS – thin section, PS – polished section.

Micro-*Raman* complementary studies were made in some selected samples to better identify the LOP main magnetic minerals. Figure 4-8 shows the micro-*Raman* spectrum of magnetite (fig. 4-8A), hematite (fig. 4-8B), and ilmenite (fig. 4-8C).

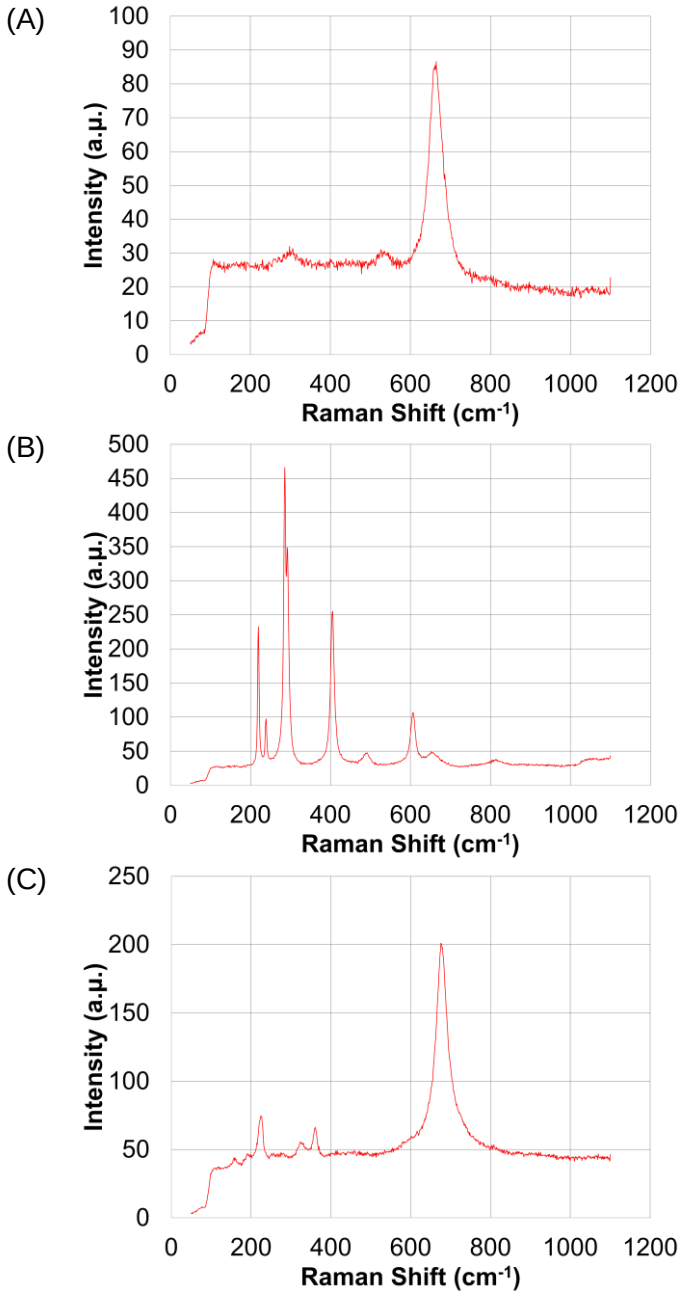


Figure 4-8. *Raman* spectra of Fe-Ox minerals from Lamas de Olo Pluton of: (A) Magnetite; (B) Hematite; (C) Ilmenite.

Table 4-2. Petrographic description of Lamas de Olo Pluton.

		LOP granites		
		Lamas de Olo granite (LO)	**Alto dos Cabeços granite (AC)**	**Barragem granite (BA)**
Texture		Medium to coarse-grained porphyritic granite (biotite > muscovite)	Fine- to medium-grained porphyritic granite (biotite > muscovite)	Leucocratic fine- to medium-grained and slightly porphyritic granite (biotite ≅ muscovite)
Main mineralogy	Quartz (Qz)	Fluid inclusion planes (FIP) are present; sometimes occur with undulatory extinction and subgrain boundaries.		FIP are very scarce; sometimes occur with undulatory extinction and subgrain boundaries.
	Plagioclase (Pl)	Oligoclase	Oligoclase-andesine	Albite
		• Megacrystals and frequently with a well-marked zonation; • Sometimes exhibiting myrmekitic intergrowths with quartz, common mostly in LO granite; • Frequently altered by sericitization.		
	K-Feldspar (Fsp)	Perthitic orthoclase + Microcline	Perthitic orthoclase + Microcline	Perthitic orthoclase + Microcline
		• Heterogranular crystals; • Some megacrystals have small plagioclase inclusions.		
	Biotite (Bt)	• Green to brown colors; • Appears sometimes partially to completely chloritized; • Frequently, has pleochroic halos of associated zircon and/or monazites; Curved biotites and kinks are scarce but present.		
	Muscovite (Ms I and/or Ms II)	Ms I is very scarce; Ms II is scarce and replaces Bt and/ or Pl.		Ms I is common; Ms II is common and replaces Bt and/ or Pl.
Accessory minerals		Zircon, sphene, allanite, fluorite, hematite, magnetite, ilmenite, chlorite, rutile, apatite, monazite, xenotime, goethite, epidote, and tourmaline		Zircon, sphene, allanite, fluorite, hematite, anatase and/or ilmenite, chlorite, rutile, apatite, goethite, monazite, xenotime, epidote and tourmaline
Other observations		• Magnetite is present as pure magnetite, Ti-poor magnetite and sometimes partially altered to hematite (martite).	• Magnetite is present as pure magnetite, Ti-poor magnetite and frequently partially altered to hematite (martite).	• Magnetite is not observed under a microscope; • Ilmenite is present in higher contents in BA than in LO and AC granites; • Anatase is observed only in BA granite.

4.1.3 Mineralized veins

4.1.3.1 Description of mineralized veins in the area

In the Lamas de Olo area, several occurrences of mineralized veins have been recognized. These mineralizations occur in quartz veins hosted in the post-D_3 LOP granites, in Douro Group Metasediments (DGM), or in syn-D_3 two-mica granites from the Vila Real Massif (VRM). Special attention was given to mineralized veins hosted in LOP.

As most of the veins were exploited during the Second World War, scarce records about the production are available. However, in the *Direção Regional de Economia do Norte* (Porto) archives and in the *Sistema de Informação de Ocorrências e Recursos Minerais Portugueses* – SIORMINP – database (SIORMINP, 2019), references to mining concessions in the Lamas de Olo region were found (table 4-3).

- **Mineralized veins in LOP granites**

In LOP area, two mining concessions for wolfram exploitation in veins were recorded: *Arnal* (concession 775) and *Alto dos Cabeços* (concession 3250), both located in Vila Marim village, in the Vila Real municipality (table 4-3; SIORMINP, 2019).

- *Arnal*: Mineralized veins occur hosted in BA granite and are composed of milky quartz with wolframite (cassiterite, arsenopyrite, pyrite). The vein has *ca.* 20 cm thickness and is subvertical with E-W trend. Beyond that, in an old report (dated from 1944) the existence of two quartz veins is also mentioned, one with N-S direction and other N 30º E, dipping *ca*. 80º to NW. These orientations were identified by trenches (*ca*. 2 m in depth) still visible in the field.

- *Alto dos Cabeços*: Quartz veins with scheelite and wolframite and aplites with molybdenite and beryl occur cutting the AC granite with N-S direction, with a variable thickness from 5 cm to 30 cm. The main vein outcrops *ca.* 200 m in length and has been completely worked, with places where the works penetrated from 20 m to 30 m. These works were recognized in-depth with 4 galleries in direction. The records show that the scheelite content was 7 kg/ t and the wolframite content was 1 kg/ t.

Table 4-3. Old mining concessions associated with granites from the Lamas de Olo Pluton (SIORMINP, 2019).

Name	Locality/ municipally	Mineralization type	Local	Mineral occurrences	Secondary mineralizations
Arnal	Vila Marim/ Vila Real	Mostly wolframite occurrences in quartz veins (related to granites)	Located within BA granite	Wolframite and cassiterite	Arsenopyrite and pyrite
Alto dos Cabeços	Vila Marim/ Vila Real	Mostly wolframite/ scheelite occurrences in quartz veins (related to granites)	Located within AC granite	Wolframite and molybdenite	Arsenopyrite, beryl, and pyrite

- **Mineralized veins in LOP exocontact – in the west**

Quartz veins hosted, both in shists from de DGM and in two-mica granites from the VRM were identified, defining an E-W set of concessions. *Bouça da Portela* (concessions 3251 and 3252), with wolframite, and wolframite and tin; *Barroco Velho* or *Fonte do Furado* (concession 2457) with wolframite and tin; *Viduais* (concession 2883), with wolframite; and *Linhares* (concession 3253), with wolframite and tin. *Bouça da Portela*, and *Viduais* are located in Vila Marim village, in the Vila Real municipality, *Barroco Velho*/ *Fonte do Furado* belongs to the Vila Cova village (Vila Real), and *Linhares* is located in Ermelo (Mondim de Basto; SIORMINP, 2019).

- **Mineralized veins in LOP exocontact – in the east**

Two old concessions, *Cevadilha* (concession 601) and *Cales* (concession 776) were identified in Borbela (Vila Real) and Lordelo (Vila Real), respectively. The mineralized veins, with wolframite and tin, occur hosted in the two-mica granites from VRM.

4.1.3.2 Mineralogic studies

A total of 9 polished sections were made from hand samples collected in mining wastes. All polished sections were studied under the reflected light microscope, and some representative samples were studied in SEM-EDS, to obtain the qualitative and semi-quantitative analysis.

Our studies showed that quartz veins exploited in the *Arnal* and *Alto dos Cabeços* mines are composed of an association of quartz with wolframite, scheelite, and sulfides. The wolframite and scheelite are the main oxides, and the sulfides are mostly chalcopyrite, with small amounts of pyrite, sphalerite, bismuthinite, arsenopyrite, and molybdenite.

The mineral association can be divided into two episodes: (i) 1st episode: the earliest, characterized by the precipitation of oxides, or tungstates, and (ii) 2nd episode: latest, and characterized by the deposition of sulfides.

- **Oxides description**

Wolframite:

The distribution of the wolframite in the veins is irregular. It occurs in anhedral masses (figs. 4-9A to C) and/or in subhedral crystals (fig. 4-9D) isolated within the minerals that constitute the veins. Wolframite may also occur, and this is the most frequent case, in prismatic crystal aggregates which are concentrated preferably in the vicinity of the vein wall. The crystals are often fractured.

The study under the microscope reveals that the crystals are generally heterogeneous and showing differences in their optical characteristics due to variations in composition (different proportions of MnO and FeO). The periphery of the crystals is usually lighter than in the central areas because wolframite crystals begin to grow by a phase with low reflecting power (rich on MnO), then are corroded or fractured, and finally, a phase with a higher reflecting power (lighter grey; rich on FeO) is deposited. This last phase appears systematically along with the fractures or in the proximity of quartz, scheelite, or sulfides.

Scheelite:

Scheelite is well represented and precipitates in anhedral crystals. Frequently occurs replacing wolframite (fig. 4-9A).

In figures 4-9 and 4-10 several aspects can be observed regarding the mineralogy of wolframite and scheelite.

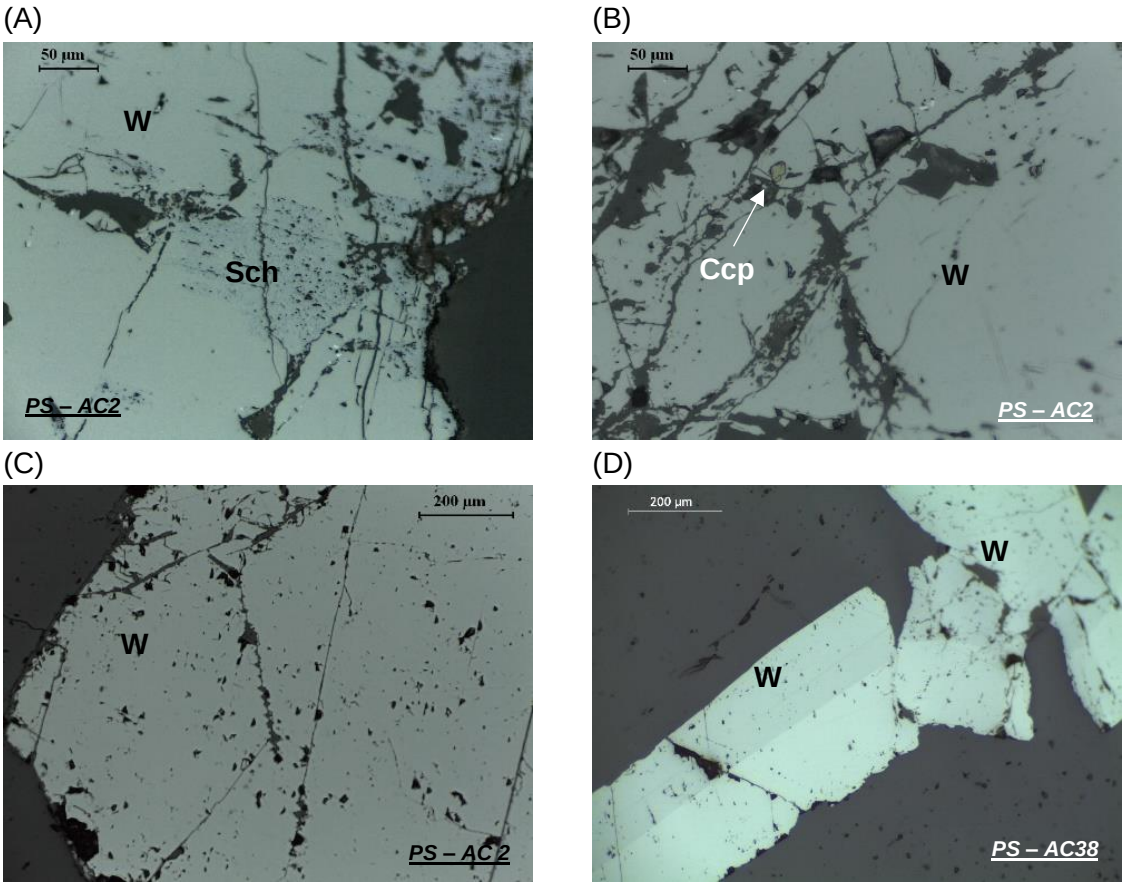
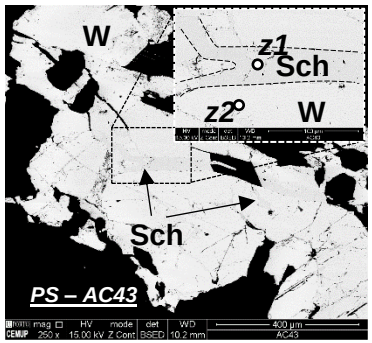
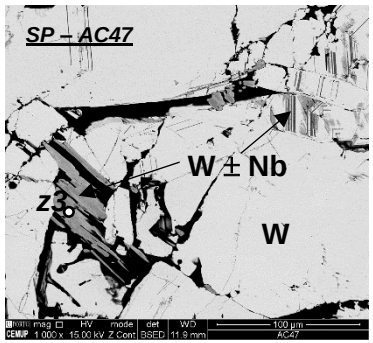
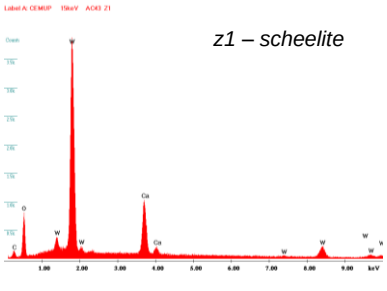


Figure 4-9. Photomicrographs of oxides in quartz mineralized veins: (A) to (D) Some aspects of wolframite and scheelite under parallel polars; W – wolframite, Sch – scheelite, Ccp – chalcopyrite; PS – polished section.

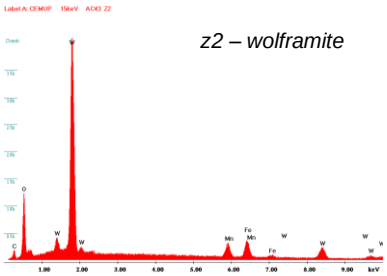
To obtain a qualitative and semi-quantitative analysis of selected tungstate minerals, SEM-EDS data were obtained, showing the presence of wolframite, scheelite, and areas in wolframite richer in niobium (fig. 4-10).



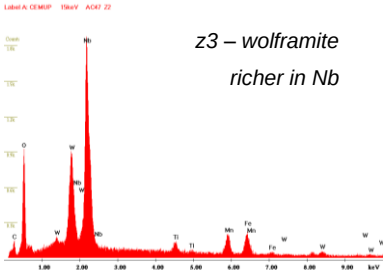




z1 – scheelite



z2 – wolframite



z3 – wolframite richer in Nb

Semi-quantitative analysis - z1

Element	Wt %	At %	K-Ratio	Z	A	F
C	2.64	11.76	0.0076	1.2754	0.2259	1.0003
O	15.28	51.04	0.0409	1.2495	0.2142	1
Ca	12.8	17.07	0.1226	1.1718	0.8155	1.0016
W	69.27	20.13	0.573	0.8216	1.0067	1
Total	100	100				

Semi-quantitative analysis - z2

Element	Wt %	At %	K-Ratio	Z	A	F
C	3.42	14.89	0.0094	1.281	0.214	1.0002
O	15.54	50.75	0.0557	1.255	0.2854	1.0004
Mn	7.03	6.69	0.0733	1.0739	0.955	1.0168
Fe	10.18	9.53	0.1111	1.0993	0.9664	1.0265
W	63.83	18.14	0.5257	0.8207	1.0037	1
Total	100	100				

Semi-quantitative analysis - z3

Element	Wt %	At %	K-Ratio	Z	A	F
C	4.77	15.9	0.0096	1.2135	0.1657	1.0002
O	20.4	51.1	0.055	1.1894	0.2267	1.0004
W	21.5	4.68	0.1694	0.7827	1.0068	1.0002
Nb	35.91	15.48	0.2841	0.9166	0.8631	1.0002
Ti	2.09	1.75	0.0196	1.0143	0.9166	1.0101
Mn	6.88	5.02	0.0667	0.9983	0.9647	1.0064
Fe	8.46	6.07	0.0848	1.019	0.9742	1.0102
Total	100	100				

Figure 4-10. Examples of some EDS spectrum, and respectively semi-quantitative analysis, performed in polished sections from mineralized veins, showing the presence of wolframite, scheelite and areas in wolframite richer in niobium; the location of EDS spectrums z1, z2, and z3 are present in the photomicrographs; Sch – scheelite, W – wolframite, PS – polished section.

The X-ray microanalysis map in one representative sample (polished section AC 43) from a mineralized quartz vein, was made, showing the distribution of elements: Ca, Fe, Mn, O, and W. The figure 4-11 shows the presence of both wolframite and scheelite, and preferential deposition of scheelite in fractures.

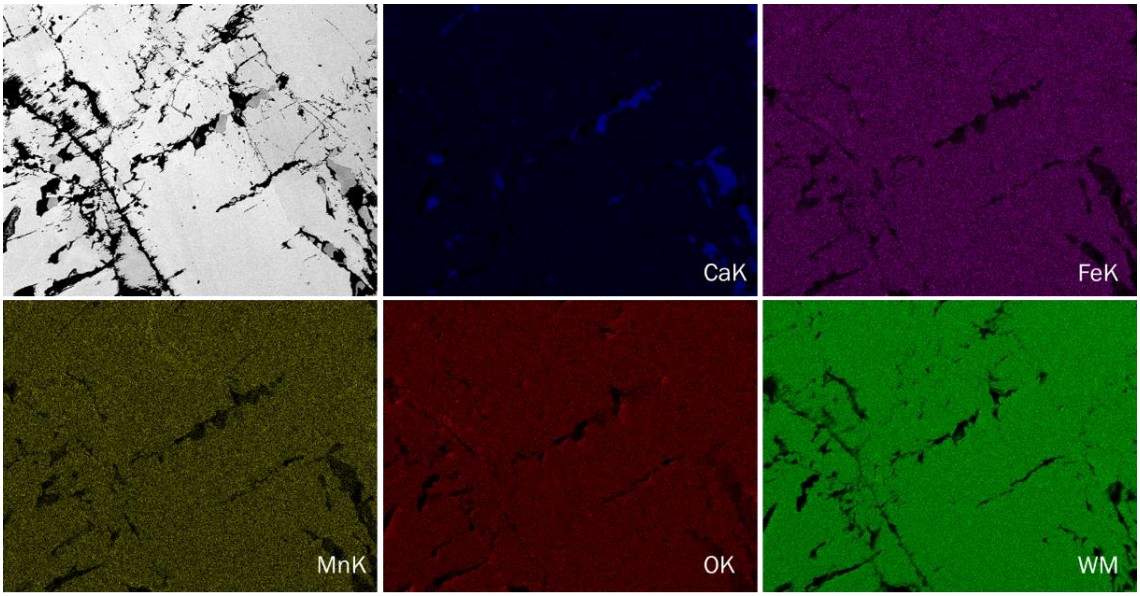


Figure 4-11. X-ray microanalysis map showing the presence of scheelite (areas richer in Ca) located near fractures on the wolframite crystal.

- **Sulfides description**

The sulfides, namely the chalcopyrite, sphalerite, bismuthinite, galena, arsenopyrite, pyrite (figs. 4-12A to C), and the native bismuth (fig. 4-12D) were identified. The minor amounts of molybdenite, cassiterite, and beryl were also present.

Chalcopyrite and sphalerite:

Chalcopyrite is the most common sulfide, generally present in masses, and very rarely in euhedral crystals (fig 4-12A). Chalcopyrite usually occurs in twinning crystals. Sphalerite is less abundant than chalcopyrite and hardly visible to the unarmed eye. The two sulfides are frequently associated (fig. 4-12B).

The chalcopyrite-sphalerite association involves two types of occurrence: (i) chalcopyrite, in twinning crystals, with sphalerite inclusions; and (ii) chalcopyrite included in subhedral sphalerite crystals. Sometimes, the chalcopyrite appears with covellite in its borders, due to alteration reactions (fig. 4-12C). Chalcopyrite filling fractures and in empty spaces of wolframite and scheelite were also observed.

Bismuth minerals:

Bismuthinite and native bismuth are the two most common bismuth minerals. They are always in association with sulfides, like chalcopyrite, sphalerite, and pyrite. Bismuthinite appears within the chalcopyrite, associated with other sulfides or with native bismuth, or filling fractures in wolframite. It is always present in small and very subordinate crystals.

The native bismuth (fig. 4-12D) presents in small drops within the chalcopyrite and in close association to bismuthinite, lead, and/or galena. This association is more frequent in the vicinity of chalcopyrite-quartz contact. More rarely, the bismuth-galena association occurs inside the pyrite.

Complex sulfides:

Associated with chalcopyrite and, usually located in chalcopyrite-quartz contacts, other mineral phases occur. They are complex sulfides with lead and silver in their composition.

Galena:

Galena is considered a minor sulfide that occurs in anhedral crystals spatially associated with chalcopyrite and sphalerite or in intergrown association with the native bismuth.

The intergrows with bismuth and lead/ galena were subject to detailed SEM-EDS analyzes. Therefore, in a spatial association with chalcopyrite and bismuthinite, a complex sulfide was described. Our studies point out that this mineral belongs to the aikinite-bismuthinite series (fig. 4-13; aikinite – (Pb, Cu, Bi) S_3; bismuthinite – Bi_2S_3). This association occurs as an intergrow texture, which is developed in chalcopyrite, rarely within pyrite, in the vicinity of chalcopyrite-quartz contact.

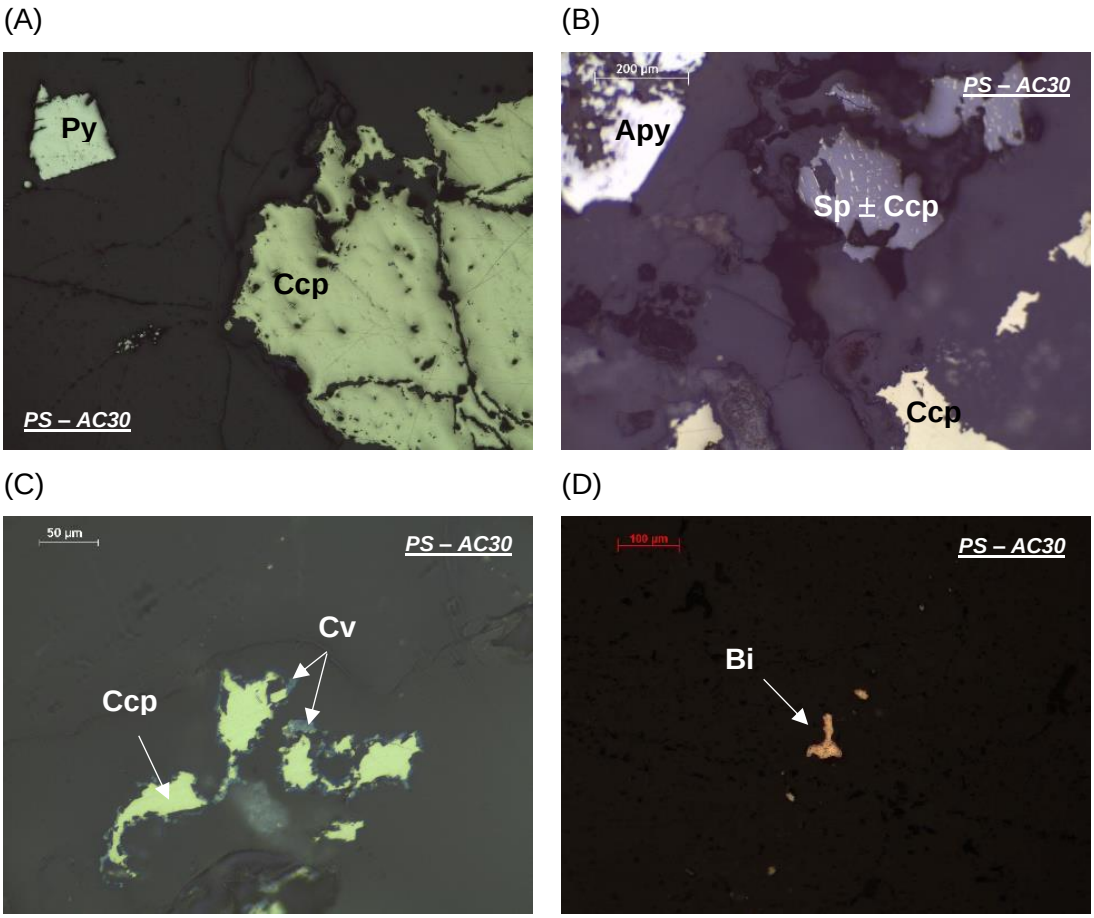
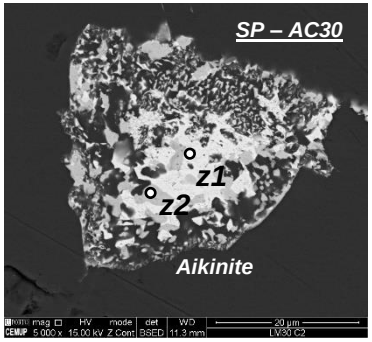
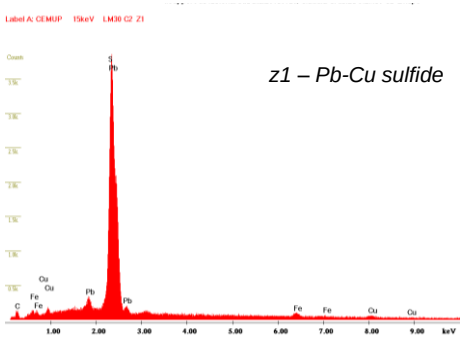


Figure 4-12. Photomicrographs of sulfides in quartz mineralized veins: (A) to (D) Some aspects of sulfides and native bismuth under parallel polars; Py – pyrite, Ccp – chalcopyrite, Apy – arsenopyrite, Sp - sphalerite, Cv – covellite, Bi – bismuth (native), Bis – bismuthinite; PS – polished section.

Other aspects were observed namely the presence of a subhedral and fractured chalcopyrite crystal, with exsolutions of sulfide with intergrowths of lead and bismuth. The EDS spectra show that this sulfide has 49.3% of Pb and 36.1% of Bi. These aspects are present mostly in the contact between chalcopyrite and quartz (fig. 4-13).

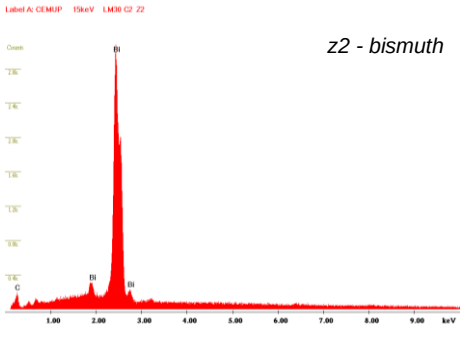




z1 – Pb-Cu sulfide

Semi-quantitative analysis - z1

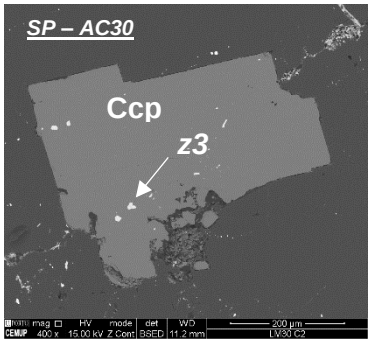
Element	Wt %	At %	K-Ratio	Z	A	F
C	4.6	29.68	0.0092	1.3418	0.1498	1.0000
S	14.09	34.08	0.1497	1.274	0.8337	1.0001
Pb	74.95	28.05	0.6942	0.8819	1.0504	1.0000
Fe	2.6	3.6	0.0286	1.1714	0.9376	1.0048
Cu	3.76	4.59	0.0427	1.1589	0.971	1.0092
Total	100	100				

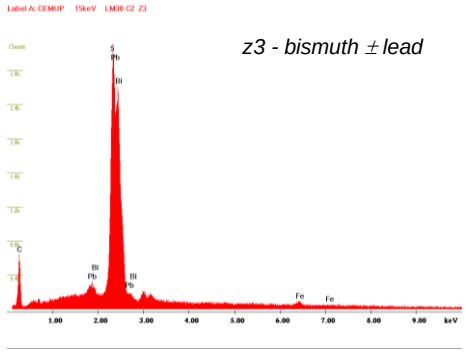


z2 - bismuth

Semi-quantitative analysis - z2

Element	Wt %	At %	K-Ratio	Z	A	F
C	5.41	49.88	0.0162	1.4416	0.2075	1.0000
Bi	94.59	50.12	0.9241	0.958	1.0198	1.0000
Total	100	100				





z3 - bismuth ± lead

Semi-quantitative analysis - z3

Element	Wt%	At%	K-Ratio	Z	A	F
C	13.81	59.98	0.0252	1.2092	0.1512	1.0000
S	11.75	19.12	0.0852	1.1381	0.6368	1.0002
Fe	3.28	3.06	0.0285	1.0524	0.8087	1.0227
Pb	32.4	8.16	0.2863	0.8666	1.0198	1.0000
Bi	38.77	9.68	0.3437	0.8679	1.0215	1.0000
Total	100	100				

Figure 4-13. Examples of some EDS spectrum, and respectively semi-quantitative analysis, performed in polished sections from mineralized veins, showing the presence of a complex sulfide with intergrown textures; the location of EDS spectrums z1, and z2 are present in the photomicrograph; PS – polished section.

4.1.4 Highlights

The LOP is constituted by biotite granites: Lamas de Olo, Alto dos Cabeços and Barragem. LOP granites are heterogranular with a porphyritic or slightly porphyritic texture, varying in their grain size where LO is medium- to coarse-grained, AC is fine- to medium-grained and BA is leucocratic fine- to medium-grained granite.

All the LOP granites are similar in the mineralogical composition and are mostly composed of quartz, plagioclase, K-feldspars, and biotite.

Regarding opaque minerals, they have essentially magnetite, hematite, and scarce ilmenite. However, in the AC granite, most of the magnetite is altered to hematite (martite), and in the BA granite, the magnetite is not observed under the microscope and the anatase and ilmenite are the dominant opaque minerals. Some microstructures are shown in LOP granites, namely some fluid inclusion planes, subgrain boundaries and undulatory extension in quartz, as well as, some kinks and curved biotites.

Hosted in LOP granites, two old concessions, *Arnal* and *Alto dos Cabeços* were recognized. In both concessions, quartz veins with an association of wolframite, scheelite, and sulfides have been exploited. The sulfides are mostly chalcopyrite, with small amounts of pyrite, sphalerite, bismuthinite, galena, arsenopyrite, and molybdenite. Complex sulfides, in intergrow associations with bismuth-lead and aikinite-bismuthinite, were also described.

4.2 MAGNETIC MINERALOGY

To characterize the magnetic properties and mineralogy from LOP granites, several methodologies were performed. Some magnetic analyses in the host rocks, namely in granites from the Vila Real Massif and in schists from Douro Group Metasediments were also made.

4.2.1 Magnetic susceptibility

The magnetic susceptibility (K_m) from LOP was determined by both: magnetic susceptibility (MS), using a portable device, and anisotropy of magnetic susceptibility (AMS) studies, showing the presence of two types of granites: granites with low magnetic susceptibility (K_m < 1000 μSI) and granites with high magnetic susceptibility values ($K_m \geq$ 1000 μSI) (figs. 4-14, 4-15, and 4-16B; table 4-4; attachment 2).

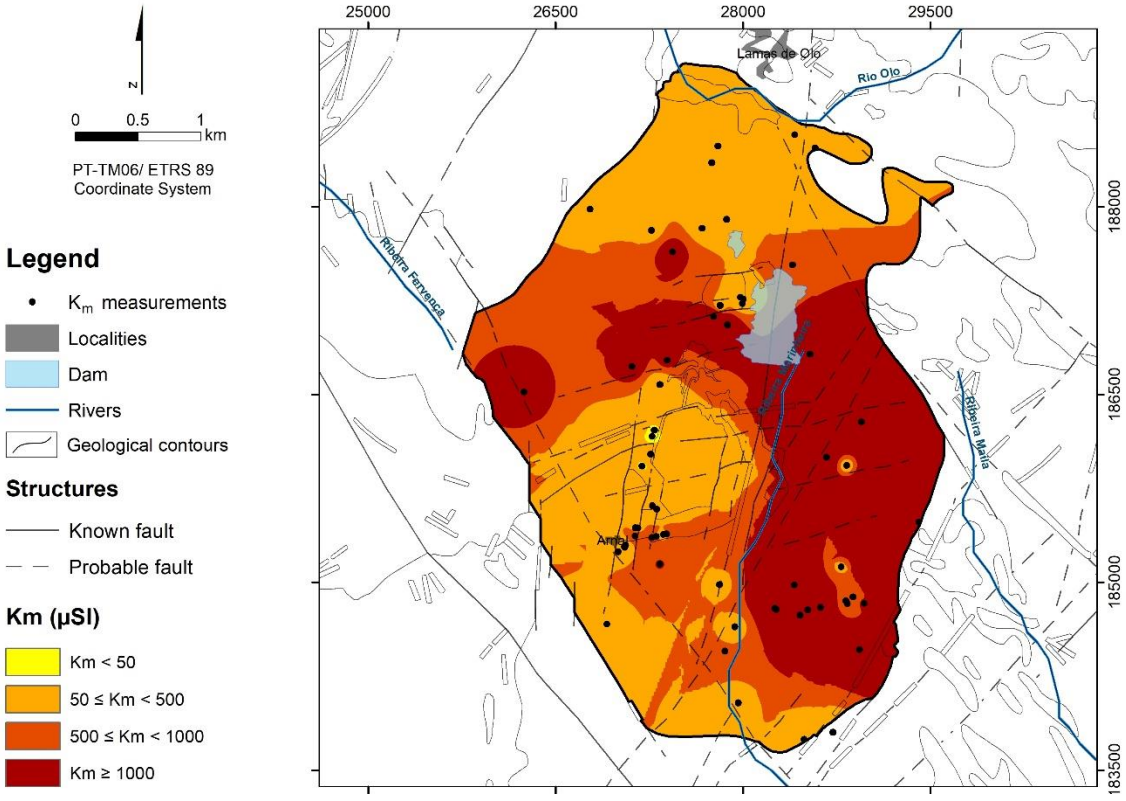


Figure 4-14. Map of the magnetic susceptibility (K_m) values in LOP (interpolation made by Inverse Distance Weighted in the *ArcGIS* 10.7 software). Km values were acquired using both KT-10 magnetic susceptibility meter (portable device) and KLY-4S Kappabridge susceptometer AGICO model.

Studies on LOP indicate that the K_m values in the LO granite has a huge variability (ranging from low to high values; K_m range between 30 µSI and 44382 µSI), the AC granite has intermediate K_m values (K_m range between 70 µSI and 962 µSI) and the BA granite has lower K_m values (K_m range between 12 µSI and 79 µSI) than the others (tables 4-4 and 4-5). The LO is the most heterogeneous granite of the pluton, suggesting that both high and low magnetic susceptibility areas are present in the same granite. On the other hand, the BA granite has very low K_m values (figs. 4-14 and 4-15).

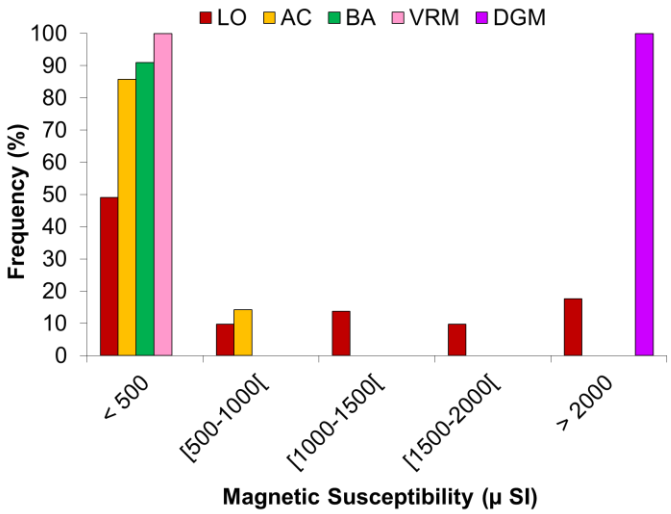


Figure 4-15. Relative frequency magnetic susceptibility histograms for LOP granites (LO, AC, and BA granites) and host rocks (VRM, and DGM). K_m expressed in µSI.

In the host rocks, VRM has K_m around 51 µSI, and DGM has K_m around 48474 µSI (fig. 4-15; tables 4-4 and 4-5; attachment 2).

Table 4-4. Magnetic susceptibility values per site in Lamas de Olo Pluton and host rocks. The K_m was measured using both analytical techniques: MS – magnetic susceptibility measurements using a portable device, and AMS - anisotropy of magnetic susceptibility. M, P – GPS coordinates from each measurement site in TM06/ ETRS89 coordinate system; K_m – magnetic susceptibility values (in µSI); n: number of samples per site; n.a. – not attributed.

Site	TM06/ ETRS89		Lithology	Method	K_m (µSI)	n
	M	P				
LM 1	26910	184668	LO	AMS	174	15
LM 2	27108	186726	LO	AMS	1848	11
LM 3	28620	184802	LO	AMS	2489	8
LM 3V	28785	185127	LO (red granite)	AMS	316	3
LM 4	28828	185935	LO	AMS	112	8
LM 5	28533	186823	LO	AMS	2769	6
LM 6	27994	187228	LO	AMS	252	8
LM 8	26244	186521	LO	AMS	1564	10
LM 13	29406	185482	LO	AMS	44382	9
LM 14	28946	186285	LO	AMS	2179	8
LM 16	28413	188578	LO	AMS	67	8
LM 17	27797	188487	LO	AMS	77	5
LM 18	27747	188355	LO	AMS	79	6
LM 19	28665	186002	LO	AMS	1869	8
LM 20	28411	184982	LO	AMS	2760	6
LM 21	27960	184040	LO	AMS	233	9
LM 22	27854	184453	LO	AMS	513	8
LM-STOP4	27334	185150	LO	MS	1078	n.a.
LM 23	27810	184982	LO	AMS	254	7
LM 27	28488	183746	LO	AMS	69	6
LM 28	28930	184463	LO	AMS	2065	10
LM 29	28969	184834	LO	AMS	1147	8
LM 30	27875	187061	LO	AMS	2385	11
LM 32	27762	187125	LO	AMS	2031	9
LM 33	27391	186776	LO	AMS	1261	15
LM 34	27866	187902	LO	AMS	100	8
LM 35	27671	187832	LO	AMS	205	5
LM 36	27266	187815	LO	AMS	242	9
LM 37	26776	187983	LO	AMS	101	6
LM 38	27435	187641	LO	AMS	1559	7
LM 39	28575	188473	LO	AMS	81	11
LM 40	28718	183804	LO	MS	49	n.a.
LM 41	27051	185281	LO	MS	1110	n.a.
LM 42	27271	185360	LO	MS	1390	n.a.
LM 48	27309	185585	LO	MS	117	n.a.
LM 50	28821	184853	LO	MS	1027	n.a.
LM 51	28834	184831	LO	MS	580	n.a.
LM 52	28878	184884	LO	MS	335	n.a.
LM 53	28515	184781	LO	MS	1584	n.a.
LM 54	28265	184787	LO	AMS	787	7
LM 55	28252	184795	LO	AMS	2260	4
LM 56	28454	184741	LO	AMS	876	8
LM 57	28395	187539	LO	AMS	845	5
LM 58a	27050	185285	LO	AMS	103	5
LM 59	27134	185371	LO	AMS	1348	4
LM 60	27136	185438	LO	AMS	392	3
LM 63	27000	185248	LO	AMS	1025	4
LM 64	27934	184648	LO	AMS	76	5
LM 65b	27336	186581	LO	MS	156	n.a.
LM 66a	27287	186216	LO	MS	36	n.a.
LM 67	27272	186167	LO	MS	30	n.a.
LM 69b	27188	185931	LO	MS	64	n.a.

Table 4-4. (cont.)

Site	TM06/ ETRS89		Lithology	Method	K_m (μSI)	n
	M	P				
LM 24	27363	185384	AC	AMS	239	7
LM 25	27385	185389	AC	AMS	254	9
LM 26	27386	185390	AC	AMS	962	8
LM 43	27304	185369	AC	MS	271	n.a.
LM 61	27157	185437	AC	AMS	125	5
LM 66c	27291	186216	AC	MS	79	n.a.
LM 68	27259	186026	AC	MS	70	n.a.
LM 7	27978	187281	BA	AMS	38	4
LM 15	28002	187263	BA	AMS	24	8
LM 31	27816	187216	BA	AMS	32	9
LM 41b	27052	185282	BA	MS	26	n.a.
LM 49	27274	185615	BA	MS	54	n.a.
LM 58b	27060	185298	BA	AMS	21	3
LM 62	26999	185248	BA	AMS	22	4
LM 65a	27331	186581	BA	MS	79	n.a.
LM 66b	27288	186216	BA	MS	12	n.a.
LM 69a	27188	185931	BA	MS	26	n.a.
LM 9	25725	186083	VRM	AMS	49	11
LM 10	30778	184395	VRM	AMS	52	6
LM 11	30270	184876	VRM	AMS	51	8
LM 70	27721	180953	VRM	AMS	40	8
LM 72	29593	187246	VRM	AMS	35	7
LM 12	29676	185373	DGM	AMS	48474	8

Table 4-5. Mean and range values for magnetic susceptibility for Lamas de Olo and host rocks. The K_m was measured using both analytical techniques: MS – magnetic susceptibility measurements using a portable device, and AMS - anisotropy of magnetic susceptibility; K_m – magnetic susceptibility values (in μSI); n.a. – not attributed.

Lithologies		K_m (μSI)		
		mean	range	sites
LOP	Lamas de Olo	1701	30 - 44382	52
	Alto dos Cabeços	286	70 - 962	7
	Barragem	84	12 - 79	11
VRM	Vila Real granites	45	35 - 52	5
DGM	Desejosa formation	48474	n.a.	1

In this study, although the traditional qualitative study, a quantitative approach of the magnetic susceptibility values using geostatistical methods was carried out. The geostatistical approach improves the knowledge about the magnetic susceptibility spatial distribution on the LOP and validates the previous information obtained with simpler interpolations methods, namely inverse distance weighted (IDW), carried out through the *ArcGIS* software (fig. 4-14). For this, and assuming that the variation of the magnetic susceptibility on rocks may be variable with the direction (Zawadzki *et al*., 2012, 2015), the kriging interpolation is the only method that considers the influence of spatial structure (the trend) on the regionalized variables (the magnetic susceptibility values). Other interpolation

methods, such as IDW or the polynomial fitting location (*e.g*. Coleman *et al.*, 2012), do not consider the existence of a possible main direction for the distribution of magnetic susceptibility values.

A geostatistical approach was made in order to make a more detailed mapping of the magnetic susceptibility data, quantifying its spatial dispersion. Geostatistics is the application of the formalism of random functions to the characterization and estimation of a natural phenomenon (Journel & Huijbrechts, 1978), applied to a geological context. The natural phenomena have a spatial organization or structure and can be characterized by the distribution of one or more variables called Regionalized Variables (*R.V*). A *R.V.* is defined as a variable distributed in space, which is purely descriptive, and from a mathematical point of view, it is simply a function that considers an output value for every point within a spatial field or temporal domain.

For the geostatistical approach, only measurements acquired in rock cylinders were takin into account, and one site from the LO granite was not considered. This site (LM 13) has an unusually much higher K_m value (44382 µSI) than that recorded in the remaining sampling sites, and in the geostatistical analysis, outlier values are usually removed to smooth data. Therefore, in the geostatistical study, the extreme value was removed, as it differs significantly from the others (it is 16 times greater than the second higher value). The geostatistical analysis and corresponding interpolation map were performed through the *Surfer* 10 software.

The calculation of the basic statistics values (table 4-6) and the observation of the kriging map (fig. 4-16) pointed out: (i) the heterogeneity of the pluton, where both high and low magnetic susceptibility areas were present, as previously proved in the IDW interpolation map; (ii) the K_m mean value *ca.* 809 µSI shows that areas with low magnetic susceptibility are predominant over the areas with high values; and the median of 254 µSI indicates that more than half K_m values are lower than the typical magnetite-type according to the Ishihara (1977); (iii) the higher standard deviation value (879 µSI) and the range of 2748 µSI, confirm the heterogeneity and the high scattering of K_m values.

Table 4-6. Statistics data from magnetic susceptibility values (K_m in µSI).

Statistical Parameters	Value
Mean value	809
Median	254
Standard deviation	879
Range	2748
Minimum	21
Maximum	2769
Count	47

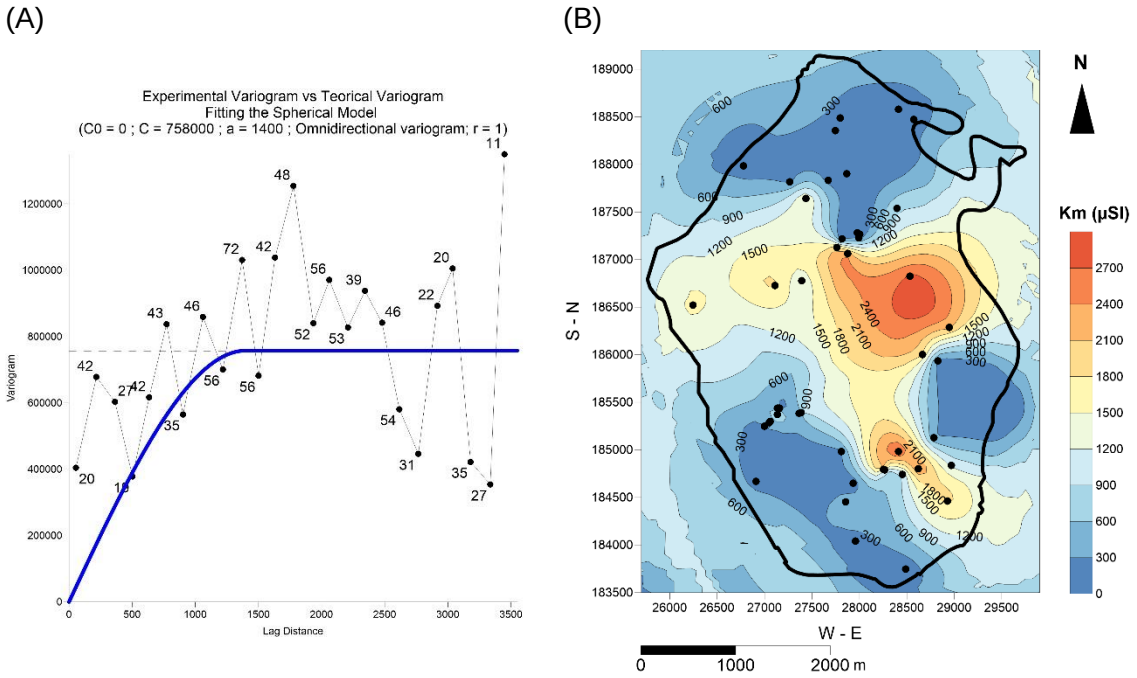


Figure 4-16. (A) Experimental variogram and its adjustment to the theoretical variogram of the regionalized variable (magnetic susceptibility); (B) Map of the magnetic susceptibility (K_m) values in the Lamas de Olo Pluton (interpolation made by kriging in the *Surfer* 10 software) with the location of sampling sites and LOP outline.

The variographic analysis was carried out to find the spatial feature of the magnetic susceptibility (our *R.V*). In order to detect the preferential directions of continuity (anisotropy of the *R.V.*), experimental variograms, with different interval directions of 15º and a tolerance angle of 30º, were tested. Then, the theoretical models and their parameters were adjusted accordingly.

Figure 4-16A represents omnidirectional the experimental variogram adjusted to the theoretical variogram of the magnetic susceptibility *R.V*. The spherical model (eq. 32) is the theoretical variogram that better adjusts to the magnetic susceptibility data.

$$\gamma(h) = \begin{cases} (C_0 + C_1)\left[1.5\,\frac{h}{a} - 0.5\,\frac{h^3}{a^3}\right] & h \leq a \\ C_0 + C_1 & h > a \end{cases} \qquad \text{(equation 32)}$$

Where, γ(h) represents the function of the spherical model, C_0 is the nugget effect, the sum of geological microstructure or measurement error and corresponds to the value in the plot origin, $C=C_1+C_0$ is the total sill, *h* is the lag vector representing the separation distance between two spatial locations and *a* is the range variation (Journel & Huijbregts, 1978). Other theoretical variograms were tested, such as the exponential or gaussian model, but they did not produce such good results. The spherical semivariogram was the model selected, once is the experimental variogram that clearly shows the existence of a sill and, is the only model that fits the first values of the experimental variogram. The spherical model adjusts to the majority of the experimental variograms without significant variation of *a* parameter, therefore, in this study, an omnidirectional variogram was adopted.

The study of the experimental variograms, and the subsequently adjusted model, allow us to verify several aspects, namely:

(i) In the variographic study, the ranges recorded in all the adjusted experimental variograms were approximately *a* = 1400 m; this means that, although the K_m values strongly vary within a few meters (fig. 4-16B), a spatial correlation between two points that are up to 1400 m apart was verified; beyond this limit, the data are no longer spatially correlated;

(ii) The absence of the nugget effect, C_0 = 0, means that sampling errors do not exist and for one sampling site, only one value is attributed;

(iii) Sill value (a priori variance), approximately *C* = 758 000, represents the variance of the variable (K_m);

(iv) The anisotropy ratio is *r* = 1, meaning that the used variogram is isotropic since it exhibits the same parameters regardless of the direction.

After the analysis of the relational structure of the georeferenced data and once the model that supported the theoretical variogram was identified, the kriging interpolation was done. This interpolation represents the spatial behavior of the magnetic susceptibility (fig. 4-16B), allowing recognize two kinds of behavior in the same pluton (fig. 4-16B): (i) areas with high magnetic susceptibility ($K_m \geq$ 1200 µSI), which are present mainly in the eastern part of

the pluton and along an ENE-WSW direction (*ca*. N 80º) fault system; these areas showed the presence of pure magnetite or Ti-poor magnetite in granites; (ii) areas with low magnetic susceptibility values (21 μSI ≥ K_m < 1200 μSI), which are dominant in LOP. The magnetic susceptibility varies between sites spaced a few meters apart, as it is visible in areas with close isolines.

Comparing the magnetic susceptibility maps obtained by both interpolations made by IDW in the *ArcGIS* software (fig. 4-14) and by kriging in the *Surfer* 10 (fig. 4-16B), the discussion is similar. The areas with high K_m values are present mainly in the eastern part of the pluton and along an ENE-WSW direction (*ca*. N 80º), and the areas with low K_m values occupy the most LOP area.

4.2.2 Isothermal remanent magnetization data

The isothermal remanent magnetization (IRM) data from LOP are present in figure 4-17 and table 4-7. The LM 5 (LO granite) shows saturation at fields *ca*. 338 mT, suggesting the dominance of low coercive minerals, while LM 16 (LO granite) does not reach saturation at the maximum imparted field. The ratio of IRM at 0.3 T to saturation isothermal remanent magnetization (SIRM), $S_{0.3T,}$ for these samples is 0.999 and 0.839, respectively, showing the magnetic heterogeneity of the LO granite, where areas with a predominance of low coercive minerals are present, as well as areas where ferrimagnetic minerals are scarce. The curve for sample LM 26 (AC granite), indicates high amounts of ferrimagnetic minerals ($S_{0.3T}$ = 0.961), however, does not show saturation at the applied field. The acquisition curve at *ca*. 950 mT is apparently stable, however, a zoom shows a small increase in intensity with increasing fields indicating a small amount of a high coercive mineral such as hematite. The LM 7 (BA granite) sample, shows some oscillations in the intensity with increasing fields due to a weak magnetic signal. Nevertheless, the $S_{0.3T}$ from this sample is 0.995, suggesting the presence of low coercive minerals.

After treatment by the Cumulative log-Gaussian function (CLG; Robertson & France, 1994; Kruiver *et al.*, 2001), the best fit of the raw IRM curves was obtained by considering two or three components (fig. 4-17 and table 4-7). All specimens have, at least two components: component 1 with a low coercive phase and $B_{1/2}$ (the field at which half of the values of saturation of isothermal remanent magnetization - SIRM - is reached) *ca*. 17 mT

and component 2, showing an intermediated coercive phase and $B_{1/2}$ *ca*. 59 mT. Two samples show a third component, with high coercivity with $B_{1/2}$ *ca*. 466 mT.

The dispersion parameter (DP) ranges between 0.25 and 0.42 for all components, with mean values of 0.36, 0.31, and 0.34 for components 1, 2, and 3, respectively. According to Dunlop & Özdemir (1997), the coercivity increases with the replacement of Fe^{3+} by Ti in titanomagnetite/ Ti-poor magnetites. Take this into account the component 1, 2 and 3 are interpreted as magnetite, Ti-poor magnetite, and hematite, respectively (Robertson & France, 1994; Kruiver *et al.*, 2001; Abrajevitch & Kodama, 2011; Font *et al.*, 2014; Maxbauer *et al.*, 2016). Ti-poor magnetite (component 2) is dominant in all samples (contributes to more than 50% of the total remanence), with exception of LM 7 with 13% of Ti-poor magnetite and 87% of magnetite (component 1; table 4-7).

The differences in $B_{1/2}$ and DP values are interpreted according to some authors (*e.g.* Kruiver *et al.*, 2001; Font *et al.*, 2009, 2014), as varying degrees of oxidation of magnetite for component 1, as different Ti-content in the Ti-poor magnetite for component 2, and different magnetic grain sizes for component 3 (fig. 4-18).

4.2.3 Frequency-dependent susceptibility

Frequency-dependent susceptibility (χ_{fD}%) studies were made on 10 samples from LOP. In the BA granite, χ_{fD}% is higher than 10% (table 4-8), which is interpreted by some authors (*e.g.* Dearing *et al.*, 1996) due to the presence of superparamagnetic fine grains, a weak magnetic signal or a high alteration degree. On the other hand, the values acquired for LO granite (χ_{fD}% < 2%) indicated the absence of superparamagnetic grains, and for AC samples (4% < χ_{fD}% < 7%) shown an admixture of superparamagnetic and coarser non-superparamagnetic grains (Dearing *et al.*, 1996). The presence of superparamagnetic minerals in samples from BA granite can explain the lower magnetic susceptibility values (mean K_m *ca.* 27 μSI) and the presence of low coercive minerals.

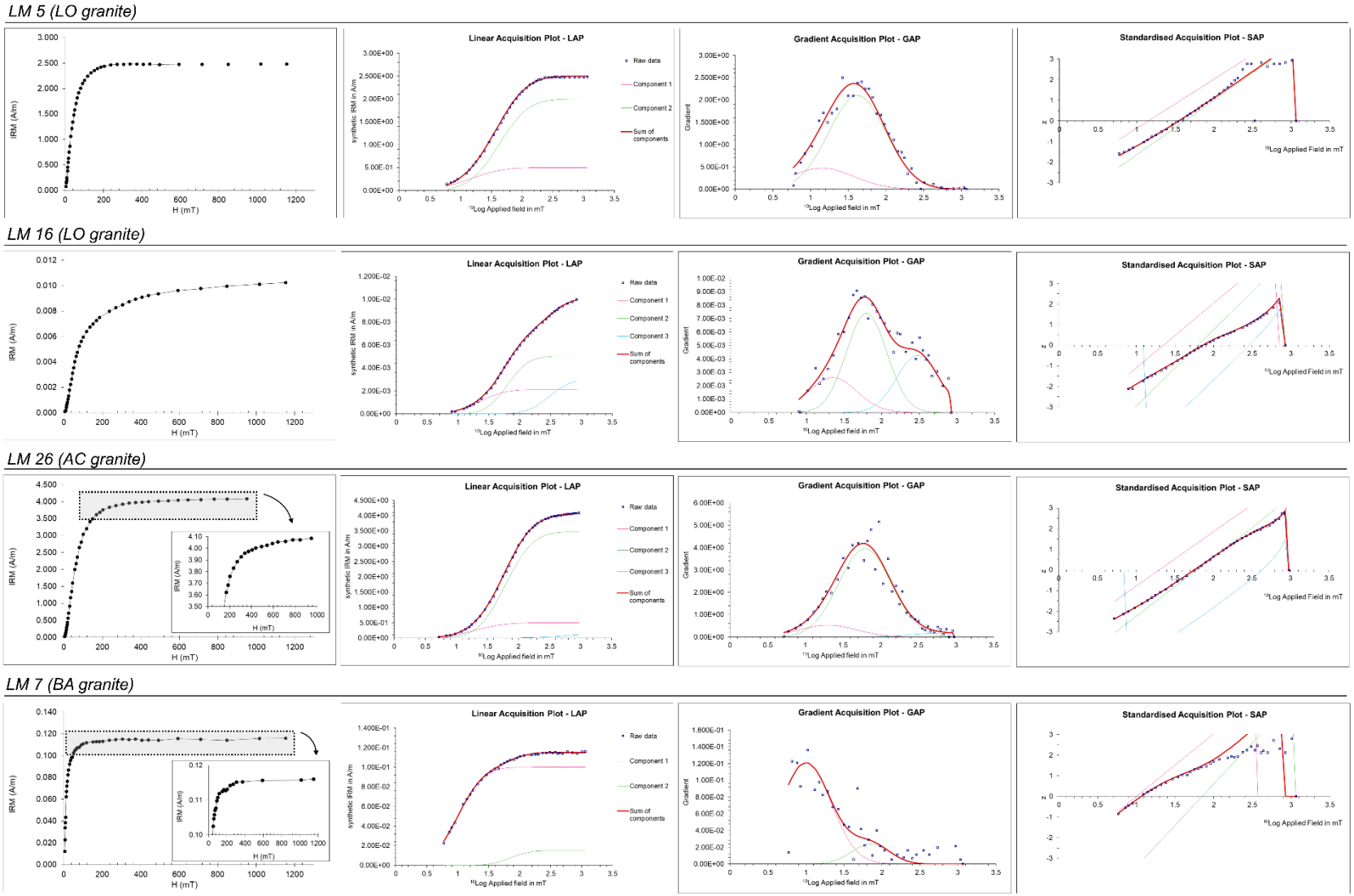


Figure 4-17. IRM acquisition curves for the representative samples from LOP: LM 5 and LM 16 from LO granite; LM 26 from AC granite (with zoom showing the absence of saturation); LM 7 from BA granite (with zoom showing the absence of saturation). The CLG treatment was made using the software developed by Kruiver *et al.* (2001).

Table 4-7. Isothermal remanent magnetization data from LOP. IRM_{1T} - Isothermal remanent magnetization at 1T; $IRM_{0.3T}$ - Isothermal remanent magnetization at 300mT. The Cumulative log-Gaussian (CLG) analysis were performed in the LOP samples, allowing to define for each magnetic component: % - percent contribution; SIRM - values of saturation of isothermal remanent magnetization; $S_{0.3T}$ - the ratio of IRM at 0.3 T to SIRM; $B_{1/2}$ - the field at which half of the SIRM is reached; DP - dispersion parameter; $S_{0.3T} = IRM_{0.3T}/IRM_{1T}$ (Robertson & France, 1994). The CLG treatment was made using the software developed by Kruiver *et al.* (2001). n.a. – not attributed.

LOP granite	Sample	IRM_{1T} (A/m)	$IRM_{0.3T}$ (A/m)	$S_{0.3T}$	CLG analysis											
					Component 1 (20-40 mT)				Component 2 (50-80 mT)				Component 3 (100-250 mT)			
					%	SIRM (A/m)	$B_{1/2}$ (mT)	DP	%	SIRM (A/m)	$B_{1/2}$ (mT)	DP	%	SIRM (A/m)	$B_{1/2}$ (mT)	DP
LO	LM 5-E1	2.480	2.477	0.999	20	0.50	14.13	0.42	80	2.00	41.69	0.38	n.a.			
	LM 16-D2	0.010	0.008	0.839	21	0.00	22.39	0.32	50	0.01	63.10	0.27	30	0.00	302.00	0.28
AC	LM 26-A1	4.086	3.925	0.961	12	0.50	19.95	0.38	84	3.47	61.66	0.35	4	0.17	630.96	0.4
BA	LM 7-A1	0.116	0.115	0.995	87	0.10	10.00	0.33	13	0.02	70.79	0.25	n.a.			

Table 4-8. Frequency-dependent susceptibility measurements in samples from LOP. Magnetic Susceptibility F1 (LF) – Magnetic susceptibility at field 1 (low frequency = 0.46 kHz); Magnetic Susceptibility F2 (HF) – Magnetic susceptibility at field 2 (high frequency = 4.6 kHz); M 1 – measurement 1; M 2 – measurement 2; χfD% - Frequency-dependent susceptibility in percent.

LOP granite	Sample	Magnetic Susceptibility F1 (LF)			Magnetic Susceptibility F3 (HF)				χ_{fD}%
		M 1	M 2	Mean	M 1	M 2	M 3	Mean	
LO	LM 5-E1	9.11E-03	9.04E-03	9.08E-03	9.33E-03	9.20E-03	9.11E-03	9.21E-03	-1
	LM 8-D2	7.30E-03	7.33E-03	7.32E-03	7.26E-03	7.27E-03	6.91E-03	7.15E-03	2
	LM 22-B1	2.11E-03	2.10E-03	2.10E-03	2.09E-03	2.05E-03	2.12E-03	2.08E-03	1
	LM 38-E1	6.27E-03	6.27E-03	6.27E-03	6.30E-03	6.09E-03	6.28E-03	6.22E-03	1
AC	LM 24-A1	7.14E-04	7.14E-04	7.14E-04	6.81E-04	6.86E-04	6.79E-04	6.82E-04	4
	LM 26-A1	3.36E-03	3.37E-03	3.37E-03	3.29E-03	3.14E-03	3.42E-03	3.28E-03	3
	LM 61-C1	5.44E-04	5.48E-04	5.46E-04	5.16E-04	5.05E-04	4.93E-04	5.05E-04	8
BA	LM 7-A1	1.61E-04	1.64E-04	1.63E-04	1.05E-04	1.06E-04	1.06E-04	1.06E-04	35
	LM 58-B	1.04E-04	1.04E-04	1.04E-04	7.59E-05	7.16E-05	7.16E-05	7.31E-05	30
	LM 62-B	1.15E-04	1.16E-04	1.15E-04	9.63E-05	6.63E-05	1.00E-04	8.76E-05	24

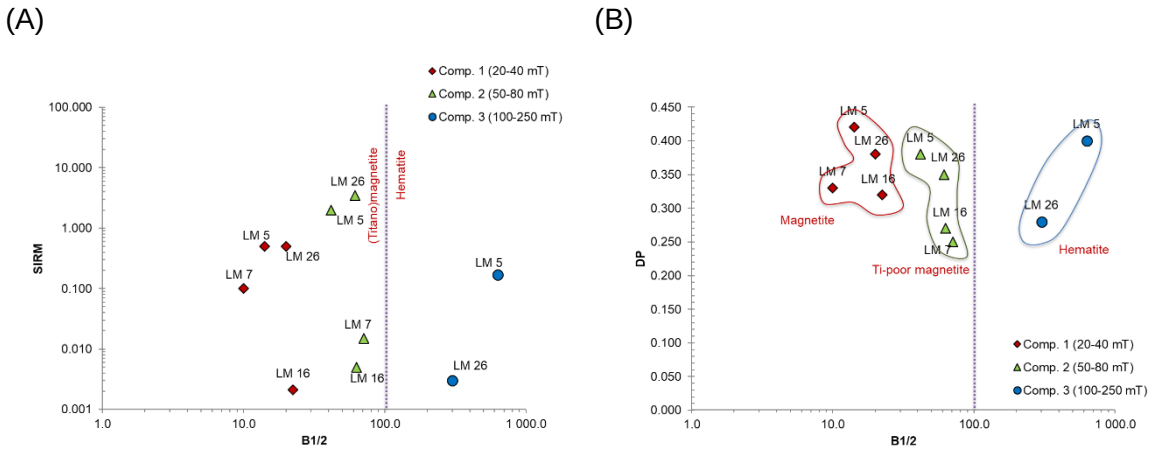


Figure 4-18. (A) SIRM *versus* $B_{1/2}$ plot illustrating the distributions of magnetic phases in LOP; (B) DP *versus* $B_{1/2}$ plot distinguishing the 3 heterogeneous components (the heterogeneity of the components can be related to the varying degrees of oxidation of magnetite, different Ti-content in the Ti-poor magnetite, and different magnetic grain sizes for hematite. The field limit between magnetite/hematite is arbitrarily stated at around 100 mT.

4.2.4 Thermomagnetic experiments

Figure 4-19 shows different kinds of magnetic susceptibility-temperature curves (K_t *versus T* plots) obtained from the studied granites. It should be noted that in the K_t *versus T* plots the susceptibility data, marked on the y-axes, is referred to as total susceptibility (K_t), and is not corrected by volume or mass. These values are, therefore, quite different from the K_m values measured in the AMS experiments, where the K_m values are corrected for the specimen volume or mass. The heating curves are drawn with a small (red) arrow to the right, while the cooling curves have a small (blue) arrow to the left. In figure 4-19, the y-axes are not on the same scale in all plots, so it is necessary to consider the K_t values themselves.

The K_t *versus T* curves from selected LO granite samples show a significant fall of K_t at *ca.* 580°C, indicating magnetite T_C (fig. 4-19A). Other curves have a K_t drop just before the 580ºC (*ca*. 560ºC – 565ºC) corresponding to Ti-poor magnetite (figs. 4-19B to F). Some samples have a slighter drop than the others because they have a smaller Ti-poor magnetite content, or the composition of the magnetite is increased in Ti rather than in Fe (fig. 4-19D). In AC granite, the K_t values are, in general, lower than in LO granite, but K_t *versus T* curves show a slight drop just before 580ºC (*ca*. 563ºC – 572ºC), pointing to the presence of some traces of Ti-poor magnetite (figs. 4-19G to J). The K_t *versus T* curves from BA samples show the presence of hematite, essentially (figs. 4-19K to N). A slighter drop in K_t before 580°C evidenced some traces of the Ti-poor magnetite. This could be due to the circulation of post-magmatic fluids able of changing the characteristics of the primary magnetic minerals with the formation of new, less magnetic minerals like hematite (martite), maghemite, or goethite

(Lagoeiro, 1998; Nédélec & Bouchez, 2015). In some K_t *versus* T plots, an inflection around 300ºC was observed on the heating curves (figs. 4-19A, B, C, E, and H). This inflection may correspond to pyrrhotite or maghemite: (i) the pyrrhotite is a ferromagnetic mineral, with T_C at *ca*. 320ºC (Butler, 2004), and is very common in granites (*e.g*. Jover *et al.*, 1989); the presence of this mineral can explain the inflection on the heating curves, however, the monoclinic pyrrhotite is chemically stable up to its Curie point (Dekkers, 1989), which cannot explain the disappearance of the inflection in the cooling cycling; (ii) the presence of maghemite in the analyzed samples is possible due to the oxidation of magnetite with increased furnace temperatures and may be due to the presence of oxygen in the system (Evans & Heller, 2003); this mineral is normally destroyed before 350ºC, which can explain the inflection around 300ºC in the heating curves and the absence in the cooling cycle. For that reason, the magnetic mineral responsible for the inflection on 320ºC should be maghemite.

All the LOP curves show the presence of hematite and, in some cases (figs. 4-19J and L), during the cooling cycle, K_t progressively increases below 580°C up to values higher than those observed on the heating curve, suggesting the formation of a magnetic mineral, probably Ti-poor magnetite.

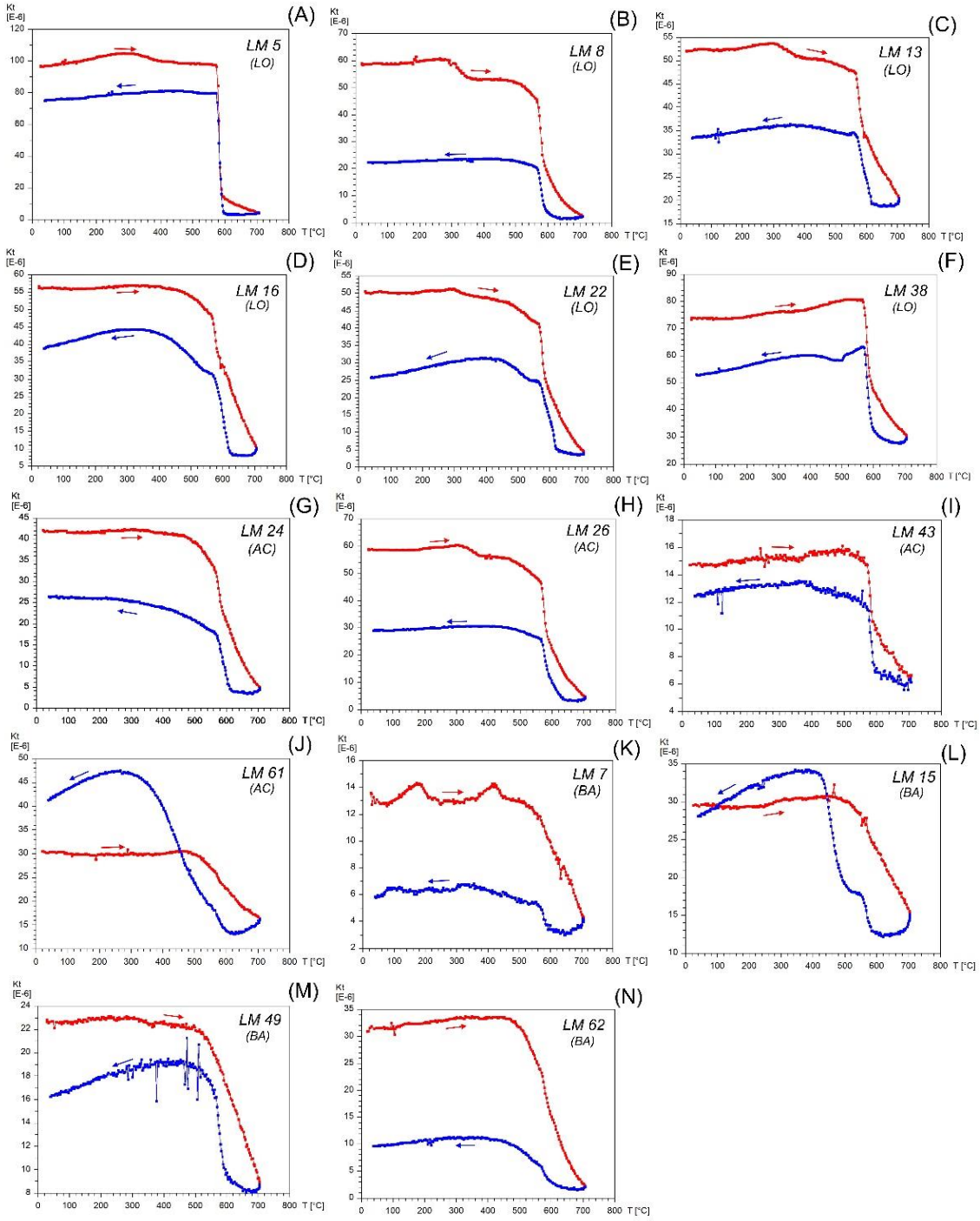


Figure 4-19. Normalized K_t *versus* T during heating (arrow toward right) and cooling (arrow toward left) from representative samples from LOP granites: (A) to (F) LO granite; (G) to (J) AC granite; (K) to (N) BA granite.

4.2.5 Highlights

The integrated study of magnetic susceptibility, IRM, χ_{fD}%, and K_t *versus T* curves allows classified the LOP granites regarding their magnetic behavior.

The magnetic mineralogy studies in the LOP allow concluding that:

- LOP is a complex pluton with areas with high ($K_m \geq 1000$ µSI) and low ($K_m < 1000$ µSI) magnetic susceptibility.
- The magnetic susceptibility maps obtained by interpolation techniques (by IDW in the *ArcGIS* software and by kriging in the *Surfer* 10) show that the areas with high K_m values are present mainly in the eastern part of the pluton and along an ENE-WSW (*ca*. N 80º) fault system direction.
- The concentration of pure magnetite has an inhomogeneous distribution in the LO granite, which is not observed in the field. The presence of hematite (mostly as martite pseudomorph), causes the magnetic susceptibility decreasing.
- In the LO granite, both pure magnetite/ Ti-poor magnetite and hematite/ martite are present, and in the AC granite, mostly magnetite was total or partially altered into hematite. The BA granite has minor amounts of magnetite and higher amounts of ilmenite and anatase.

A relation between LOP and other post-tectonic biotite plutons (Lavadores-Madalena, Peneda-Gerês, and Vila Pouca de Aguiar plutons) was performed and was published by Cruz *et al.* (2020). In this paper, a compilation of all the information published for these plutons (namely petrographic, AMS, thermomagnetic, and IRM studies) was performed, and some additional data were acquired to described in detail the magnetic mineralogy of these Portuguese Variscan granites. The thermomagnetic curves of these granites are quite similar and show the presence of magnetite/ Ti-poor magnetite and hematite in all the plutons, though in different proportions. When the magnetite content is compared, a sequence can be established: Lavadores-Madalena > Lamas de Olo > Peneda-Gerês >> Vila Pouca de Aguiar. The magnetic mineralogy studies, allowed us to conclude that Lamas de Olo (K_m = 2078 µSI, 334 µSI, and 27 µSI for LO, AC, and BA granites, respectively), as well as Lavadores-Madalena (K_m = 15971 µSI and 7037 µSI for Lavadores and Madalena granites, respectively), and Peneda-Gerês (K_m = 463 µSI, 81 µSI, and 33 µSI for Gerês, Illa, and Carris granites, respectively) plutons are magnetite type-granites, and the Vila Pouca

de Aguiar (K_m = 68 µSI and 135 µSI for Pedras Salgadas and Vila Pouca de Aguiar granites, respectively), is ilmenite-type granite, even with scarce Ti-poor magnetite in their granites. The presence of magnetite in the Lavadores-Madalena, Lamas de Olo, and Peneda-Gerês plutons, pointed out the depth generation of the magma, on oxidized conditions. During or after the emplacement of Lamas de Olo and Peneda-Gerês plutons, occurred the oxidation reactions, able to modify the magnetite into other oxidized minerals, like hematite, which causes the decreasing of magnetic susceptibility values.

It should be noted that LOP, as well as Peneda-Gerês pluton, have K_m values lower than those proposed by Ishihara (1977) to the magnetite-type granites from Japan. However, the detailed magnetic mineralogy studies proved the existence of magnetite and/or Ti-poor magnetite in LOP and Peneda-Gerês Pluton (Cruz *et al.*, 2020).

4.3 MAGNETIC FABRIC

4.3.1 Anisotropy of magnetic susceptibility

The AMS allows characterizing the magnetic fabric using two types of parameters: scalar (K_m, *P%* and *T*), and directional (magnetic foliation and lineation).

4.3.1.1 Scalar parameters

The magnetic anisotropy (*P*%) ranges between 1.2% and 10.8% for LO granite, between 3.0% and 5.3% for AC granite, and 2.3% and 11.8% for BA granite (table 4-9). The LO granite has the highest variability of *P*% values (fig. 4-20A) but the BA granite has the highest *P*% mean value: 5.0% from LO granite, 4.0% from AC granite, and 6.1% from BA granite (table 4-9).

In general, the *P*% increases with K_m (fig. 4-20B), once the magnetite grains are usually stubby and frequently form anisometric sections. However, in the BA granite for the same K_m value, *P%* presents variable values. The *P%* values around 11.8% can be explained by the presence of an iron-bearing mineral (*e.g.* martite). The high *P%* range of granites can also be explained due to the presence of hematite, which is a mineral with a wide range of anisotropy degree (range between 2.5 and 100), as described by Hrouda (1982).

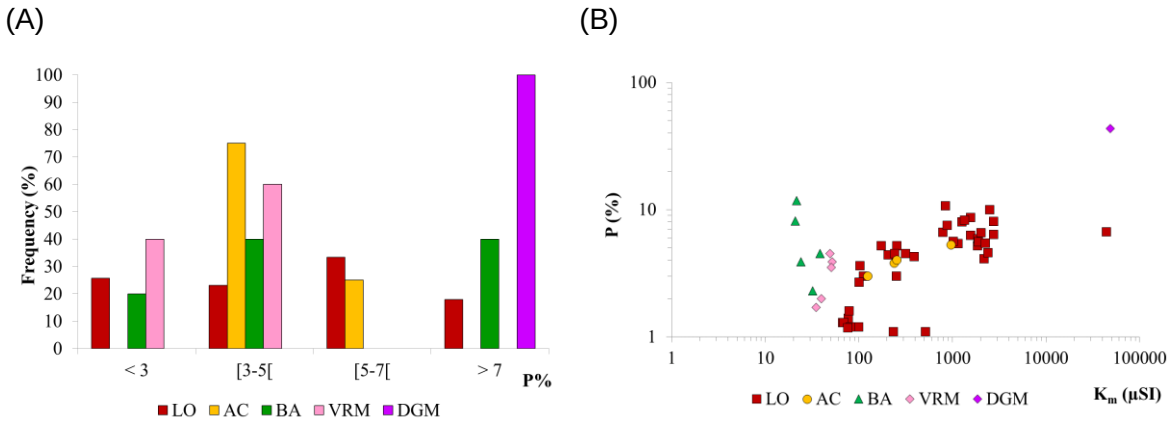


Figure 4-20. Histogram of the anisotropy of magnetic susceptibility degree (%) and the correlation between K_m and *P*% in the LOP granites (LO, AC, BA) and host rocks (VRM and DGM).

Table 4-9. AMS data for the sampling sites. M, P – GPS coordinates from the sampling sites in TM06/ ETRS89 coordinate system. K_m – mean magnetic susceptibility in μSI; *P*% – anisotropy degree (%); *T* – shape parameter; K_1 – long axis of the mean ellipsoid orientation; K_3 - short axis of the mean ellipsoid orientation; Dec, Inc – declination, inclination; E_{12}, E_{23}, and E_{31} – 95% confidence angles corresponding to the three axes; n – number of specimens per site; ∗ – not enough data; n.a. – not attributed.

Site	TM06/ ETRS89		Lithology	Mean AMS parameters			Mean AMS eigenvectors				Foliation	Lineation	E_{12}	E_{23}	E_{31}	n
	M	P		K_m (μSI)	*P*%	*T*	K_1		K_3							
							dec	inc	dec	inc						
LM 1	26910.0100	184668.1500	LO	174	5.2	0.059	234	47	58	43	N 148º; 47º SW	47º → N 234º	45	55	17	15
LM 2	27108.2951	186725.6164	LO	1848	5.2	-0.003	348	46	85	7	N 175º; 83º W	46º → N 348º	12	29	7	11
LM 3	28619.9686	184802.0425	LO	2475	10.0	0.286	122	31	279	57	N 9º; 33º E	31º → N 122º	40	25	11	8
LM 3V	28784.6014	185126.6620	LO (red granite)	316	4.5	0.154	128	52	332	38	N 62º; 52º SE	52º → N 128º	*	*	*	3
LM 4	28827.5984	185935.2563	LO	112	3.0	0.017	326	71	72	6	N 162º; 84º SW	71º → N 326º	63	40	18	8
LM 5	28532.9979	186823.4816	LO	2873	8.1	0.347	40	64	253	22	N 163º; 68º NE	64º → N 40º	30	11	9	6
LM 6	27993.8986	187227.8714	LO	229	3.0	-0.098	338	35	70	3	N 160º; 87º SW	35º → N 338º	23	20	30	8
LM 8	26244.1753	186521.0845	LO	1677	6.3	0.349	168	65	258	0	N 167º; 90º	65º → N 168º	23	13	8	10
LM 13	29405.6268	185481.7737	LO	44382	6.7	0.239	169	3	260	23	N 170º; 77º NE	3º → N 169º	64	20	8	9
LM 14	28945.9786	186285.0192	LO	2179	4.1	0.426	151	13	245	16	N 155º; 75º NE	13º → N 151º	36	5	9	8
LM 16	28413.3121	188578.1373	LO	67	1.3	-0.031	2	13	100	30	N 190º; 60º NW	13º → N 2º	10	73	16	8
LM 17	27796.7672	188486.6761	LO	77	1.4	0.090	357	42	253	14	N 163º; 76º NE	42º → N 357º	11	22	7	5
LM 18	27747.0678	188355.2095	LO	79	1.6	-0.215	358	24	252	33	N 162º; 58º NE	24º → N 358º	16	74	9	6
LM 19	28665.0416	186001.6944	LO	1869	5.9	0.142	162	38	265	16	N 175º; 74º NE	38º → N 162º	58	12	9	8
LM 20	28410.8193	184981.9196	LO	2760	6.4	0.160	160	31	278	38	N 8º; 52º SE	31º → N 160º	13	20	7	6
LM 21	27959.9728	184040.3811	LO	233	5.1	-0.090	57	66	306	9	N 36º; 81º SE	66º → N 57º	51	39	20	9
LM 22	27854.4095	184452.6823	LO	513	5.9	0.106	179	51	63	20	N 153º; 71º SW	51º → N 179º	42	21	16	8
LM 23	27809.5193	184982.1655	LO	254	5.2	-0.259	188	71	65	11	N 155º; 80º SW	71º → N 188º	30	31	24	7
LM 27	28488.4887	183746.4537	LO	69	1.3	0.135	165	43	55	20	N 145º; 70º SW	43º → N 165º	4	18	11	6
LM 28	28929.7156	184462.6600	LO	2065	5.6	0.274	223	74	25	15	N 115º; 75º SW	74º → N 223º	24	7	8	10
LM 29	28969.0079	184834.2153	LO	1147	5.4	-0.004	124	75	259	10	N 169º; 80º E	75º → N 124º	21	31	10	8
LM 30	27875.3732	187060.7101	LO	2385	4.6	0.233	168	35	260	2	N 170º; 88º E	35º → N 168º	65	12	7	11
LM 32	27762.2250	187124.7914	LO	2031	6.6	-0.023	343	14	74	6	N 164º; 84º SW	14º → N 343º	25	14	31	9
LM 33	27390.6728	186776.0007	LO	1261	8.0	-0.092	355	11	264	4	N 174º; 86º E	11º → N 355º	24	27	37	15
LM 34	27865.5311	187901.9721	LO	100	1.2	-0.036	350	3	85	56	N 175º; 34º W	3º → N 350º	19	39	9	8
LM 35	27671.0821	187831.7026	LO	205	4.4	0.123	352	16	260	5	N 170º; 85º E	16º → N 352º	50	5	15	5
LM 36	27266.4777	187815.0663	LO	242	4.5	-0.006	337	41	79	13	N 196º; 77º SW	41º → N 337º	15	25	11	9

Table 4-9. (cont.)

Site	TM06/ ETRS89		Lithology	Mean AMS parameters			Mean AMS eigenvectors				Foliation	Lineation	E_{12}	E_{23}	E_{31}	n
	M	P		K_m (μSI)	P%	T	K_1		K_3							
							dec	inc	dec	inc						
LM 37	26776.4234	187983.2781	LO	101	2.7	0.247	356	33	100	20	N 190º; 90º	33º → N 356º	22	26	11	6
LM 38	27435.4115	187641.3347	LO	1559	8.7	-0.431	6	42	228	40	N 138º; 51º NE	42º → N 6º	23	36	4	7
LM 39	28574.7904	188472.9286	LO	81	1.2	-0.046	354	28	248	28	N 158º; 62º NE	28º → N 354º	39	29	17	11
LM 54	28265.0004	184786.8807	LO	752	6.7	-0.167	166	50	300	30	N 30º; 60º SE	50º → N 166º	34	19	8	7
LM 55	28252.0750	184795.4932	LO	2260	5.5	0.056	183	32	291	23	N 21º; 67º SE	32º → N 183º	*	*	*	4
LM 56	28454.2872	184741.3068	LO	876	7.5	0.130	187	51	76	16	N 166º; 74º SW	51º → N 187º	27	54	20	8
LM 57	28394.7886	187538.8498	LO	845	10.8	-0.333	332	4	239	30	N 149º; 60º NE	4º → N 332º	21	65	30	5
LM 58a	27049.8908	185284.8094	LO	103	3.6	-0.241	177	52	79	7	N 169º; 83º SW	52º → N 177º	27	43	12	5
LM 59	27134.4464	185371.4202	LO	1348	8.3	0.336	158	20	56	30	N 146º; 60º SW	20º → N 158º	*	*	*	4
LM 60	27136.4582	185437.8429	LO	392	4.3	-0.031	212	71	66	20	N 156º; 70º SW	71º → N 212º	*	*	*	3
LM 63	26999.8033	185247.9725	LO	1025	5.7	0.491	277	60	24	17	N 114º; 73º SW	60º → N 277º	*	*	*	4
LM 64	27933.5267	184648.3253	LO	76	1.2	0.020	165	30	273	27	N 183º; 63º E	30º → N 165º	18	52	8	5
LM 24	27362.7488	185383.6243	AC	239	3.8	0.002	146	68	248	5	N 158º; 85º NE	68º → N 146º	51	23	9	7
LM 25	27384.8259	185389.2605	AC	167	4.0	0.037	195	46	84	19	N 174º; 71º SW	46º → N 195º	55	22	21	9
LM 26	27386.2464	185389.9324	AC	804	5.3	0.213	263	80	87	10	N 177º; 80º W	80º → N 263º	17	23	8	8
LM 61	27156.7188	185436.8080	AC	125	3.0	0.039	161	45	60	11	N 150º; 79º SW	45º → N 161º	9	21	8	5
LM 7	27978.2965	187280.7881	BA	34	4.5	0.618	328	29	168	55	N 78º; 35º NW	29º → N 328º	*	*	*	4
LM 15	28001.6277	187263.4412	BA	24	3.9	0.371	349	2	259	2	N 169º; 88º SW	2º → N 349º	22	4	12	8
LM 31	27815.7779	187216.1912	BA	32	2.3	-0.132	347	32	84	10	N 174º; 80º W	32º → N 347º	30	24	8	9
LM 58b	27059.8340	185298.1830	BA	21	8.2	0.360	194	85	279	4	N 9º; 86º SE	85º → N 194º	*	*	*	3
LM 62	26999.3028	185247.5263	BA	22	11.8	0.564	6	32	269	17	N 179º; 73º E	32º → N 6º	*	*	*	4
LM 9	25724.7386	186083.1948	VRM	49	4.5	0.085	132	13	226	18	N 136º; 72º NE	13º → N 132º	5	14	2	11
LM 10	30777.7300	184394.8259	VRM	52	3.9	-0.355	311	27	43	5	N 133º; 85º SW	27º → N 271º	7	12	1	6
LM 11	30269.6466	184876.4791	VRM	51	3.5	0.479	132	13	228	23	N 138º; 67º NE	13º → N 139º	17	5	9	8
LM 70	27720.5853	180952.8151	VRM	40	2.0	-0.057	145	9	38	63	N 128º; 27º SW	9º → N 145º	12	29	6	8
LM 72	29593.2997	187245.9901	VRM	35	1.7	-0.258	229	31	100	47	N 10º; 43º W	31º → N 229º	21	25	24	7
LM 12	29675.9375	185373.0326	DGM	48474	43.5	0.050	323	26	83	45	N 173º; 45º W	26º → N 323º	12	3	2	8
Mean values			LO	2078	5.0	0.059	168	25	257	3	N 167º; 87º NE	25º → N 168º	n.a.	n.a.	n.a.	293
			AC	334	4.0	0.073	176	63	75	9	N 165; 81 SW	63º → N 176º	n.a.	n.a.	n.a.	29
			BA	27	6.1	0.356	347	32	268	2	N 178; 88 NE	32º → N 347º	n.a.	n.a.	n.a.	28
			LOP	1719	5.1	0.091	168	28	258	2	N 168º; 88º NE	28º → N 168º	n.a.	n.a.	n.a.	350
			VRM	45	3.1	-0.021	135	3	50	6	N 140; 84ºSW	3º → N 135º	n.a.	n.a.	n.a.	40

The *P%* reflects the anisotropy degree of rocks, and it is directly proportional to the deformation degree that the magma suffered during and after its emplacement/ solidification. This parameter shows a decreasing trend as granites tend to be more recent due to the cessation of the Variscan deformation. However, it is necessary to take into account other factors that may influence the magnetic anisotropy of granites such as the shape anisotropy of each rock mineral (Lowrie, 2007). In the magnetite-type granites, the presence of magnetite, which has shape anisotropy, can mask the magmatic fabric of the rocks. All the Variscan magnetite-type granites are post-tectonic, and then, the *P%* is mostly due to the presence of magnetite and is not correlated with deformation events.

Observing the *P%* map in figure 4-21, it is possible to conclude that LOP granites have high values of anisotropy and the areas with high *P%* values (*P%* > 5) corresponding to areas with high K_m values (fig. 4-14). Regarding the sin-D_3 VRM, the *P%* values range between 1.7% and 4.8%, showing the evidence of some deformation in some sites. The DGM, as expected, has *P%* high values due to the metamorphic deformation and also the presence of magnetite (fig. 4-20; table 4-9).

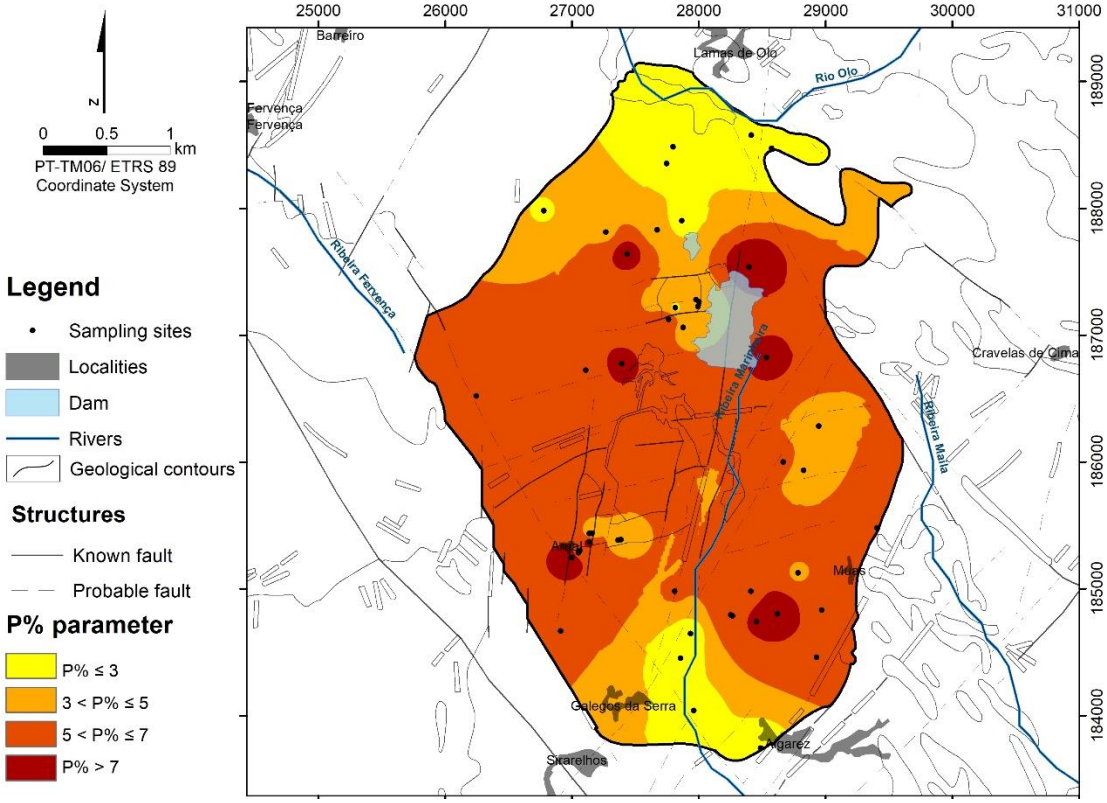


Figure 4-21. Map of the anisotropy of magnetic susceptibility degree (%) in the LOP (LO, AC and BA granites).

The ellipsoid shape parameter (*T*) ranges between -0.431 and 0.618 in the LOP. The ellipsoids are strong oblate in the BA granite (mean 0.356) and slightly oblate in LO and AC granites (mean 0.059 and 0.073, respectively; table 4-9; figs. 4-22 and 4-23).

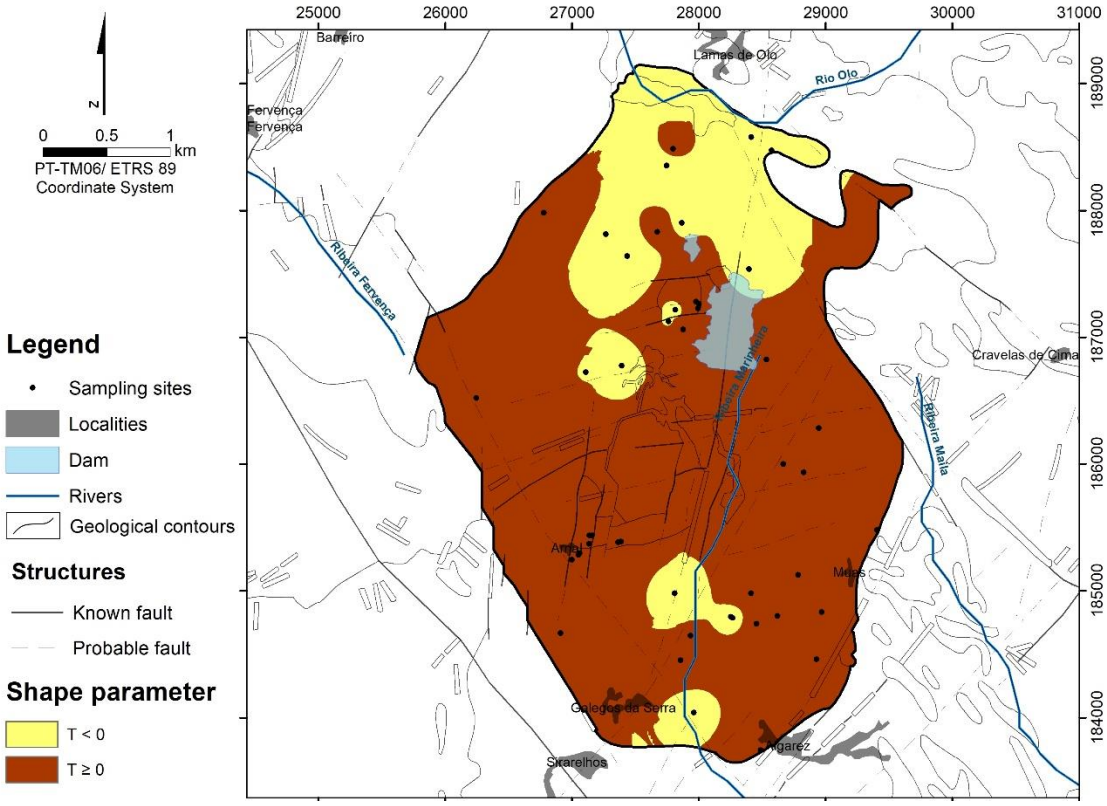


Figure 4-22. Map of the shape parameter (*T*) of LOP (LO, AC, and BA granites).

The oblate ellipsoids are mainly due to the magnetocrystalline anisotropy of biotite and are more evident in the BA granite. Although this granite has minor amounts of biotite than the others (LO and AC granites), the ellipsoid form is defined mostly by this iron-bearing phyllosilicate. On the other hand, in LO and AC granites, the shape parameter is defined mostly by the biotite flakes but also by the (Ti-poor) magnetite. The correlation between *T versus* K_m is evident in figure 4-23A, which prove the affinity of BA granite with strong oblate ellipsoids and the high heterogeneity in the shape parameter in the heterogeneous LO granite. This heterogeneity is due to the different distribution of pure magnetite (areas with high K_m values) and its alteration into hematite (martitization).

Figure 4-23B points out the heterogeneous behavior of LOP granites, where the oblate ellipsoids are dominant and the *P%* values have high dispersion.

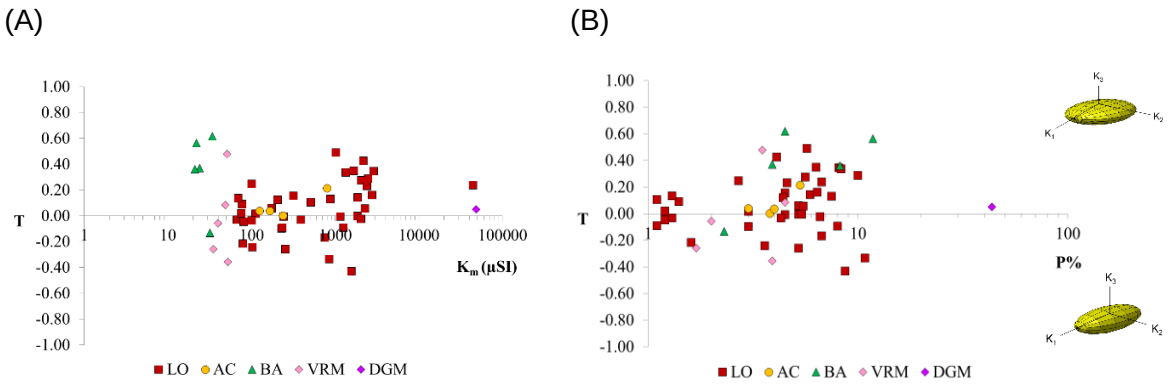


Figure 4-23. Correlation plots from LOP (LO, AC, and BA granites) and host rocks (VRM and DGM). (A) *T versus* K_m; (B) *T versus P%*.

In the host rocks, the shape parameter corresponds to the prolate ellipsoids with mean values around -0.021 for VRM and the oblate ellipsoid for DGM with mean *T* value around 0.050 (table 4-8; fig. 4-23).

4.3.1.2 Directional parameters: magnetic foliations and magnetic lineations

In the LOP granites, since the microstructures are mainly magmatic to sub-magmatic, the magnetic foliations and lineations are markers of flattening and stretching, respectively, of the granite magmas in the latest stages of its emplacement.

The magnetic foliations in LOP granites are mainly subvertical and with NNW-SSE (N 168º) main trend (table 4-9; fig. 4-24). The magnetic foliations point out the significance of NNW-SSE (*ca.* N 155º ± 15º) offsets in the LOP emplacement. It is marked by the trend of foliation which points to SW (N 168º; 88º SW) in the west of LOP, and to NE (N 168º; 88º NE) in the east of the LOP.

The magnetic lineations, have a distinct behavior over the pluton mostly subhorizontal, to gently dipping to NNW or SSE (table 4-9; fig. 4-25). The magnetite lineations show plunges dipping to the north (*ca.* NNW), in the north of LOP, and dipping to the south (*ca*. SSE) in the southern pluton. This pattern is related to another important main structure in this area, the ENE-WSW fault system (*ca*. 80º ± 20º). In the center of the LOP, the intersection of NNW-SSE with ENE-WSW opening structures provided the space for magma

ascending, with an NNW-SSE magmatic flow, as shown by the magnetic foliations and lineations trends.

The presence of both subvertical magnetic foliations and subhorizontal magnetic lineations also suggests that LOP granites ascended through strike-slip faults and this movement was recorded in magnetic fabric.

The fabric in the host rocks has the general trend of Variscan orogeny (NW-SE). The magnetic foliations are N 140º; 84º SW, and N 173º; 45ºW in the synorogenic granites of VRM and the DGM host rocks, respectively (table 4-9; attachment 3). The magnetic lineations are subhorizontal in both lithologies (table 4-9; attachment 3).

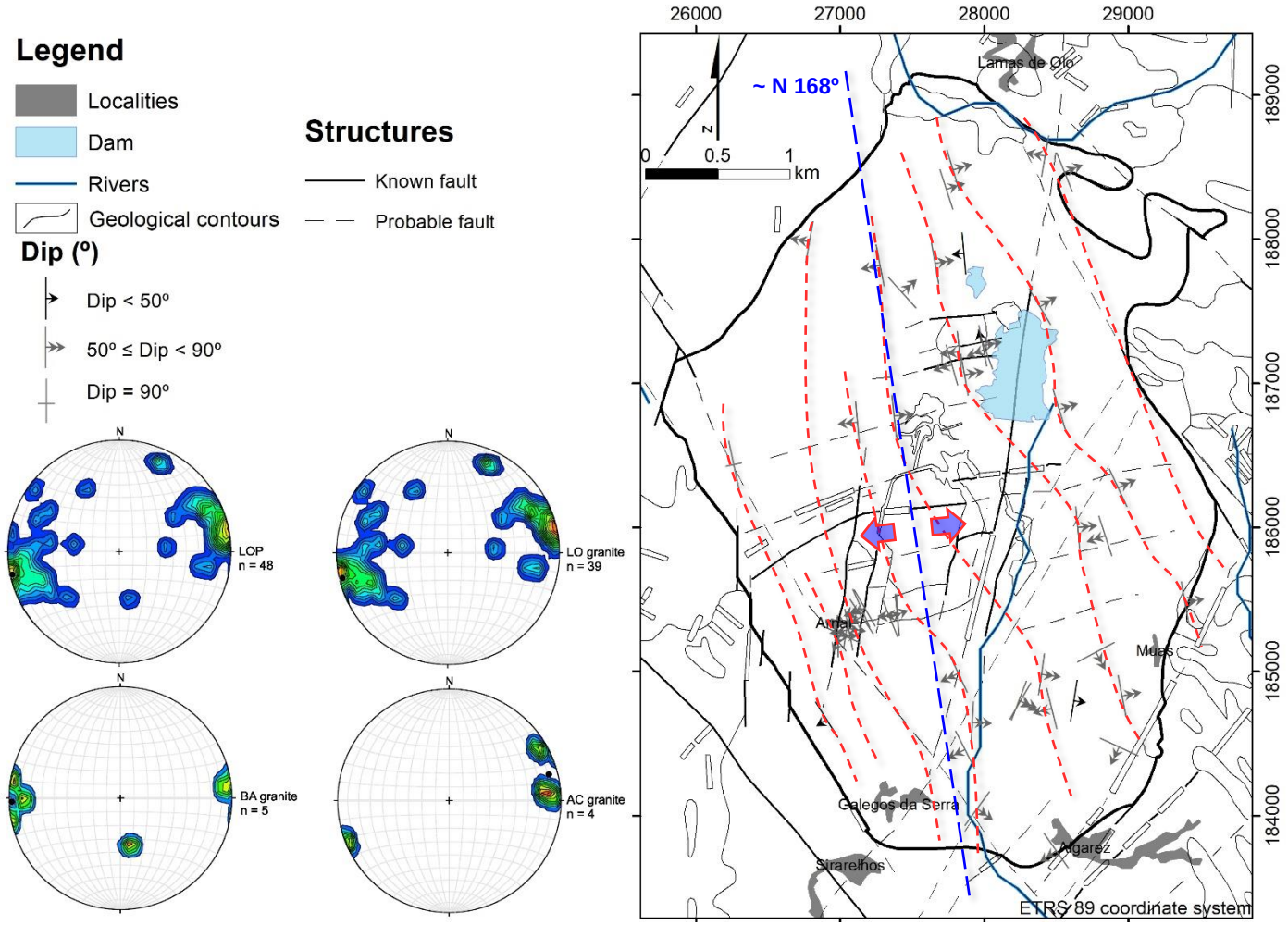


Figure 4-24. Map of the magnetic foliations with orientation stereonets for the magnetic foliations poles (K_3) for LOP (LO, AC, and BA granites) (Schmidt, lower hemisphere projection, 1–5% area contours).

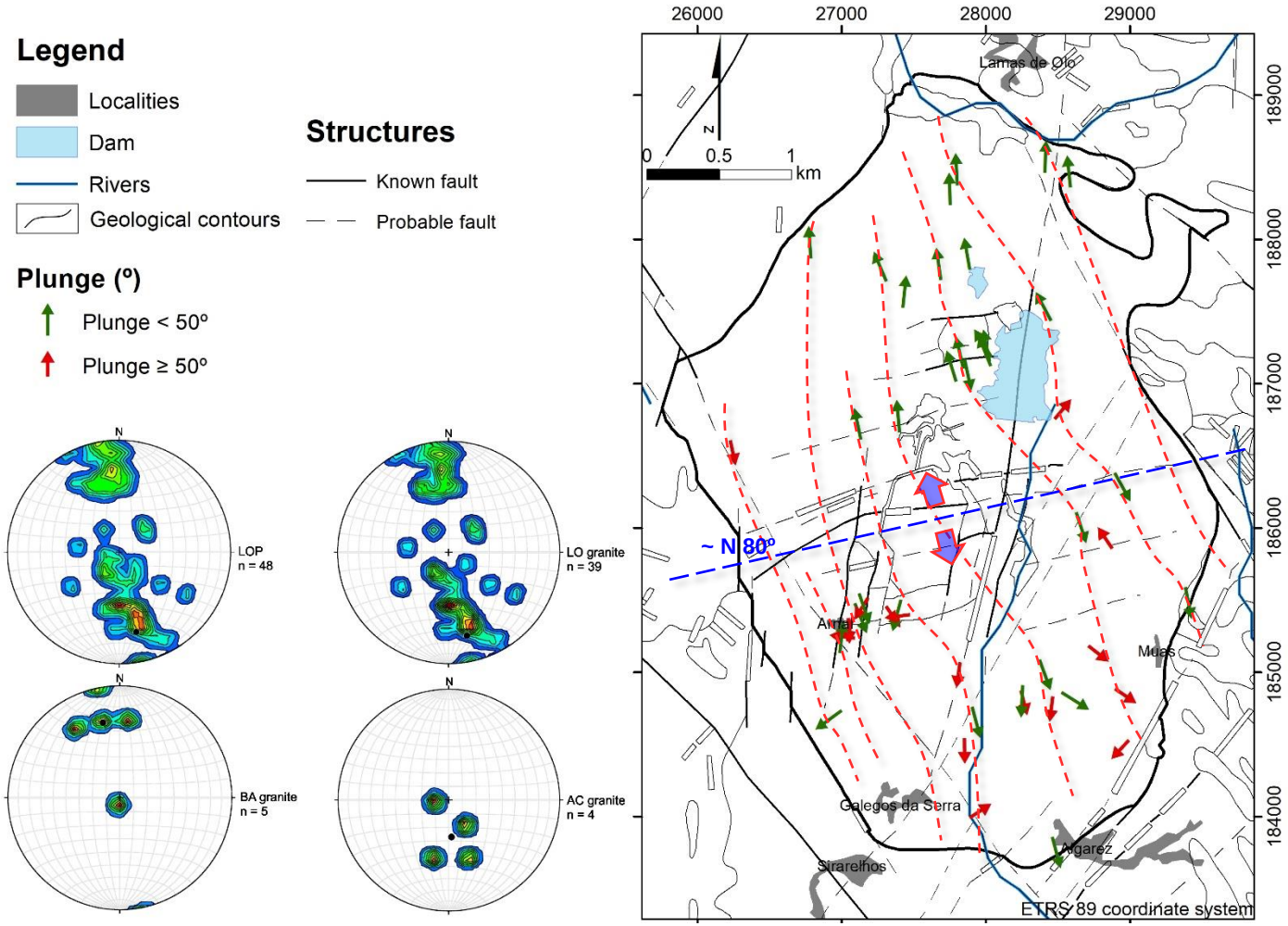


Figure 4-25. Map of the magnetic lineations with orientation stereonets for the magnetic lineations (K_1) for LOP (LO, AC, and BA granites) (Schmidt, lower hemisphere projection, 1–5% area contours).

4.3.2 Anisotropy of anhysteretic remanent magnetization

4.3.2.1 Scalar parameters

The AARM scalar and directional data are present in table 4-10. To compare the *P*% and *T* parameters obtained by AARM and AMS methodologies, the *T versus P*% plot (fig. 4-26), as well as the stereogram plots (figs. 4-27 and 4-28) are performed with the same selected sampling sites (10 sampling sites).

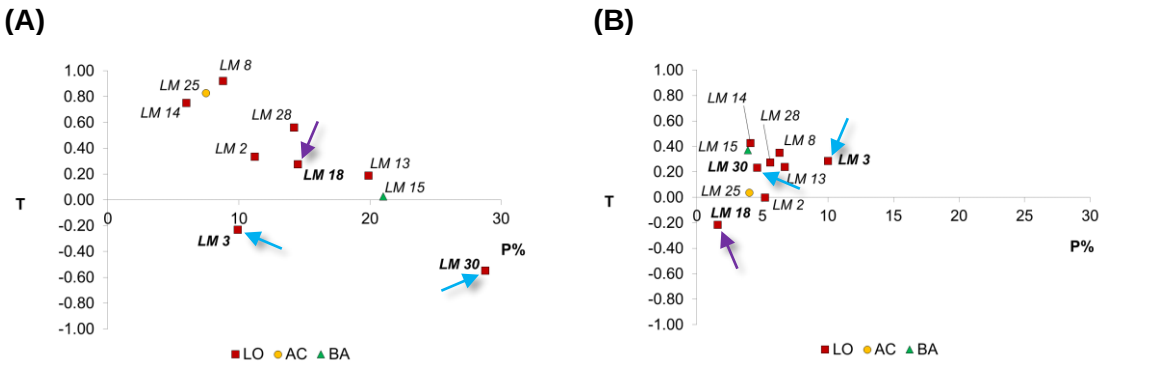


Figure 4-26. Correlation plots of *T versus P%* from selected representative samples from LOP (LO, AC, and BA granites); (A) *T versus P%* obtain by AARM experiments*; (B) T versus P%* obtain by AMS experiments for the same sampling sites.

The mean *P*% given by AARM (*P%* = 14.2%) is higher than the *P*% calculate based on AMS measurements, for the same sites (*P*% = 5.2%). These results were expected, once the influence of matrix minerals is eliminated (Jackson, 1991). Regarding the Jelinek shape parameter, *T*, are mostly oblate for both methodologies and have mean values around, 0.310 and 0.200 in AARM and AMS experiments, respectively. Figure 4-26 points out the increase of *P*% in AARM experiments (fig. 4-26A). Regarding the *T* parameter, some differences are observed: (i) 2 sites (LM 3 and LM 30) have oblate shapes for AMS (fig. 4-26B and table 4-9) but, eliminating the matrix effect, the ferromagnetic fabric is characterized by elongate ellipsoids in AARM (fig. 4-26A and table 4-10); both sites corresponding to the magnetite-type granites with high K_m values (meaning that pure magnetite is present) which can explain the high influence of magnetite shape in the AARM experiments; (ii) 1 site (LM 18) changes from prolate, in AMS, to oblate ellipsoid in AARM experiments (fig. 4-26; tables 4-9 and 4-10); the LM 18 have low magnetic susceptibility (K_m = 79 µSI) and the ferromagnetic *s.l.* minerals are scarce. The oxidation of magnetite to hematite (martite) justifies the change in the ellipsoid shape.

Table 4-10. AARM data for the selected representative sampling sites in the LOP (LO, AC, and BA granites). *P%* - magnetic anisotropy degree (%); *T* – shape parameter; $AARM_1$ – maximum axes of anhysteretic remanence; $AARM_3$ – minimum axes of anhysteretic remanence; Dec, Inc – declination, inclination; E_{12}, E_{23}, and E_{31} – 95% confidence angles corresponding to the three axes; n – number of specimens per site; n.a. – not attributed.

Sampling sites	LOP granite	Mean AARM parameters		Mean AARM eigenvectors				Foliation	Lineation	E_{12}	E_{23}	E_{31}	n
		P%	*T*	$AARM_1$		$AARM_3$							
				Dec	Inc	Dec	Inc						
LM 2	LO	11.2	0.334	355	36	263	1	N 173º; 89º NE	36º → N 355º	28	13	7	6
LM 3	LO	9.9	-0.232	133	24	251	47	N 161º; 43º NE	24º → N 133º	16	27	54	6
LM 8	LO	8.8	0.921	176	62	80	3	N 170º; 87º SE	62º → N 176º	84	15	7	6
LM 13	LO	19.9	0.187	142	51	253	16	N 163º; 74º NE	51º → N 142º	29	22	11	6
LM 14	LO	6.0	0.751	171	60	270	6	N 180º; 85º E	60º → N 171º	67	26	18	6
LM 28	LO	14.2	0.561	272	58	15	8	N 105º; 82º SW	58º → N 272º	29	8	10	6
LM 30	LO	28.8	-0.549	167	34	266	12	N 176º; 78º E	34º → N 167º	7	26	7	6
LM 18	LO	14.5	0.277	69	85	227	5	N 137º; 85º NE	85º → N 69º	29	30	5	6
LM 25	AC	7.5	0.827	344	69	96	8	N 6º; 82º W	69º → N 344º	82	32	2	6
LM 15	BA	21.0	0.027	169	60	78	1	N 168º; 89º SW	60º → N 169º	30	13	21	6
Mean values LOP		14.2	0.310	163	68	156	83	N 166º; 83º NE	68º → N 163º	n.a.	n.a.	n.a.	60

4.3.2.2 AARM versus AMS tensors

In granites with both iron-bearing silicates and magnetite, a mixed para- and ferro-fabric are present. The AARM and the AMS stereograms, as well as the confidence ellipse, are represented in figure 4-27.

Analyzing each sampling site it was verified that in all the LO granite, samples with K_m higher than 1000 µSI (LM 2, LM 3, LM 8, LM 13, LM 14, LM 28 and LM 30), the magnetic lineations marked by the $AARM_1$ (or $AARM_{max}$) and K_1 (or K_{max}) have the same direction. This inference can also be made for the magnetic foliation, where $AARM_3$ (or $AARM_{min}$) and K_3 (or K_{min}) are coaxial in both tensors. Thus, both fabrics, respectively related to the magnetite fabric in the AARM tensor, and the paramagnetic fabric (mainly biotite) in AMS tensor are parallel. The parallelism between both tensors in the set of granites with high K_m values excludes the presence of a single domain (SD) effect on the AMS fabric of those granites. This fact also means that the magnetite grains and paramagnetic (or diamagnetic) matrix minerals have the same orientation. The coaxial AARM and AMS magnetic foliations are due to magnetite grains imitating the fabrics of paramagnetic phases, through preferred collage, or crystallization of magnetite along grain boundaries, or exsolutions of magnetite along biotite cleavage planes.

However, in a set of samples with low magnetic susceptibility (LM 18 for LO, LM 25 for AC, and LM 15 for BA granites) the magnetic foliation orientations are parallel in both AARM and AMS fabrics but the magnetic lineations have different orientations. Previous magnetic mineralogy studies (*e.g.* thermomagnetic experiments and isothermal remanent magnetization; see topic 4.2) pointed out the presence of magnetite/ Ti-poor magnetite in LOP granites, even in the areas with low magnetic susceptibility, but in different proportions. The petrographic observations (see topic 4.1.2) also showed that in the areas with low magnetic susceptibility, the magnetite is often oxidized to hematite (martite), able to decrease the magnetic signal. The presence of this pseudomorph (martite) may justify the non-coaxility linear fabrics.

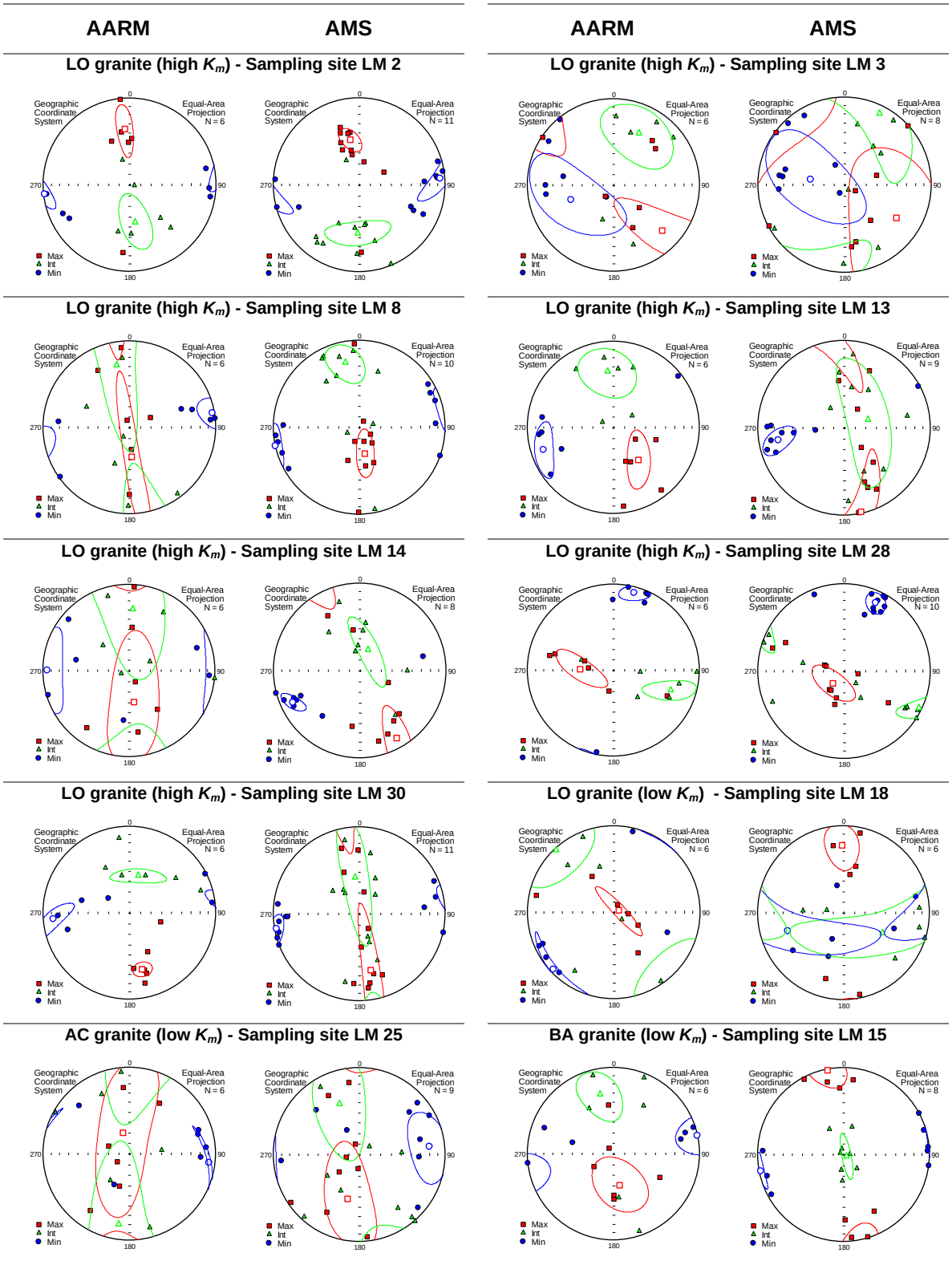


Figure 4-27. Magnetic fabric determined by AARM and AMS for the selected sampling sites from LOP. Squares represent the maximum remanence ($AARM_{max}$ *or* $AARM_1$) and maximum susceptibility (K_{max} *or* K_1); triangles are intermediate remanence ($AARM_{int}$ or $AARM_2$) and intermediate susceptibility (K_{int} or K_2); circles are minimum remanence ($AARM_{min}$ or $AARM_3$) and minimum susceptibility (K_{min} or K_3). The full line ellipses correspond to the 95% confidence ellipse. Data plotted in the lower hemisphere stereonets.

Considering the global magnetic fabric for all samples of all the granite set (fig. 4-28), the magnetic foliations (AARM: N 166°; 83° NE; AMS: N 166°; 82° NE) and the magnetic lineations (AARM: 68° → N 163°; AMS: 23° → N 166°) are coaxial in both tensors. These results show that in plutons like LOP, which is classified as magnetite-type granite, where both high, and low magnetic susceptibility values are present, the AMS fabric can be safely used to characterize the magmatic fabric flow during the emplacement.

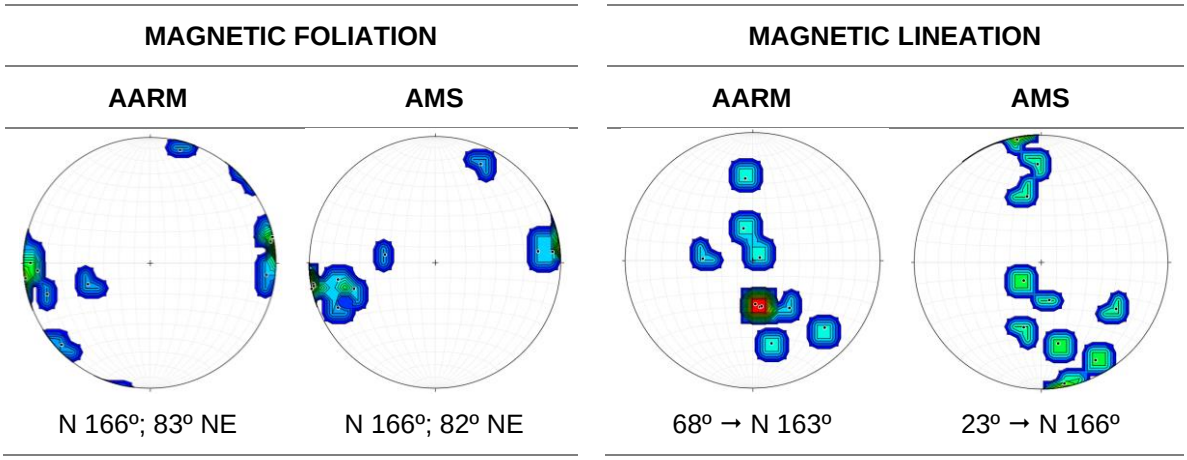


Figure 4-28. Magnetic fabric determined by AARM and AMS for the selected sampling sites from LOP with orientation stereonets for the magnetic foliations poles (⊥ *AARM₃ and K₃*) and magnetic lineations (// *AARM₁ and K₁*) (Schmidt, lower hemisphere projection, 1–5% area contours).

4.3.3 Highlights

The magnetic fabric is correlated with magmatic magma flow, which was controlled by NNW-SSE (N 160º - N 170º) structures, showed by the magnetic foliations and lineation trends in LOP granites. The magnetic fabric data allow concluding that the emplacement was mainly controlled by NNW-SSE structures, conjugated with the ENE-WSW fault system, which corresponds to a known fault system network in central-northern Portugal, N 155º ± 15º and N 80º ± 20º, respectively (Marques *et al.*, 2002). These fault systems are recognized in early Variscan ductile deformation stages (*e.g.* Ribeiro, 1974; Arthaud & Matte, 1975). Posteriorly post-Miocene Alpine maximum compression (σ_1) in W Iberia reactivated the N 155º ± 15º fault systems still as dextral (Marques *et al.*, 2002).

The ENE-WSW fault system (*ca.* 80º ± 20º) is well marked by the pattern of the magnetic lineations, that mainly dip to the north, in the north of LOP, and to the south in the southern pluton. Thus, the magnetic fabric suggests that LOP emplacement was mainly conditioned

by NNW-SSE and ENE-WSW Variscan systems rather than related to the NNE-SSW system which is parallel to the VRPF.

The absence of outcrop deformation and the lack of solid-state microstructures precludes the substantial deformation after full crystallization of LOP. Correlate the LOP magnetic fabric with the main fabric trend of the host rocks, allowed verifying that both are not coaxial: the LOP has the main fabric trend NNW-SSE and the host rocks (VRM and DGM) have an NW-SE Variscan trend.

The comparison between both AMS and AARM tensors allowed concluded that the global magnetic fabric, obtain for all samples from all the granite set, are coaxial. Their coaxiality, means that the AMS can be safely used in heterogeneous and complex magnetite-type plutons with both high and low magnetic susceptibility values. However, if the magnetic fabric of each site was compared, some differences are observed: (i) in the granite set with high K_m, both AMS and AARM tensors are coaxial, meaning that magnetite grains imitated the fabrics of paramagnetic phases, through preferred collage, or that crystallization of magnetite occurs along grain boundaries or as exsolutions of magnetite along biotite cleavage planes; thus, the magnetite and paramagnetic (or diamagnetic) minerals have the same orientation; (ii) in the granite set with low K_m, a partial coaxiality was observed, which AMS and AARM foliations are parallel but the AMS and AARM lineations are not coaxial; the non-coaxiality of the linear fabrics is due to the martitization.

4.4 GEOCHEMICAL STUDIES

The main motivation to perform geochemical analysis was the need to identify differences/ similarities between granites with low and high K_m values (see topic 4.2). The differences can result from the existence of two magma types, magnetite- and ilmenite-type (oxidized- and reduced-magmas, respectively) or, the granites can correspond to a magnetite-type with later alteration processes, able to change their magnetic behavior. Nevertheless, the presence of magnetite in all LOP granites was proved by the detailed magnetic mineralogy studies.

The W.R. geochemical analyses were made on 11 samples from LOP (fig. 3-4; table 4-11): 3 from LO granite with high K_m values (LM 5, LM 13, and LM 30), 3 from LO granite with low K_m values (LM 1, LM 16, and LM 22), 2 samples from AC granite (LM 24, and LM 61), and 3 from BA granite (LM 7, LM 15, and LM 49).

4.4.1 Classification diagrams

The potassic character (K_2O/ Na_2O ratio) points out the high potassic character in BA, and then LO > AC. On the other hand, the alkalis content (K_2O + Na_2O), varies between 7.40 to 8.54, for LOP granites, with a LO > BA > AC relation (table 4-12; fig. 4-29).

The LOP granites were classified according to several diagrams. As expected, the LOP samples are projected into the "granite" field, near or on the line between “granite” and “alkali granite” fields (fig. 4-30).

Table 4-11. Geochemical data from LOP granites; LO - Lamas de Olo granite; AC - Alto dos Cabeços granite; BA - Barragem granite; L.d. – Limit detection; K_m – magnetic susceptibility.

			LO granite (with low K_m values)			LO granite (with high K_m values)			AC granite (with low K_m values)		BA granite (with low K_m values)		
Analyte Symbol	**Units**	**L.d.**	**LM 1**	**LM 16**	**LM 22**	**LM 5**	**LM 13**	**LM 30**	**LM 24**	**LM 61**	**LM 7**	**LM 15**	**LM 49**
SiO_2	%	0.01	75.04	74.90	72.79	72.71	71.69	74.65	73.60	72.80	76.64	77.65	76.23
TiO_2	%	0.001	0.168	0.175	0.198	0.206	0.190	0.170	0.229	0.215	0.092	0.084	0.098
Al_2O_3	%	0.01	13.60	13.59	13.76	14.04	14.04	13.30	13.21	13.42	12.31	12.35	12.37
Fe_2O_3	%	0.01	1.96	1.91	2.09	2.23	1.95	1.93	1.91	1.87	0.99	0.83	1.41
FeO	%	0.1	0.6	1.13	0.98	1.01	0.95	1.04	0.69	0.64	0.21	0.28	0.41
Fe_2O_3t	%	0.01	1.20	0.70	1.00	1.10	0.90	0.80	1.10	1.10	0.70	0.50	0.90
MnO	%	0.001	0.067	0.039	0.061	0.064	0.061	0.063	0.075	0.061	0.022	0.020	0.052
MgO	%	0.01	0.29	0.29	0.34	0.41	0.34	0.29	0.46	0.46	0.16	0.17	0.16
CaO	%	0.01	0.73	0.96	0.98	1.16	1.01	1.02	1.42	1.40	0.32	0.29	0.55
Na_2O	%	0.01	3.48	3.41	3.39	3.74	3.46	3.48	3.23	3.22	3.15	2.99	3.15
K_2O	%	0.01	4.54	4.73	4.68	4.80	4.98	4.39	4.25	4.18	4.41	4.67	4.47
P_2O_5	%	0.01	0.05	0.06	0.06	0.07	0.07	0.06	0.07	0.08	0.03	0.04	0.04
LOI	%		0.73	0.42	0.62	0.42	0.66	0.39	0.66	0.99	0.99	0.92	0.51
Total	%	0.01	100.50	100.4	98.86	99.74	98.34	99.66	99	98.57	99.04	99.97	98.94
Sc	ppm	1	5	5	5	5	5	5	5	5	5	5	4
Be	ppm	1	5	4	4	5	10	4	6	11	132	6	6
V	ppm	5	14	14	15	17	14	14	22	20	8	7	10
Cr	ppm	20	150	100	110	110	80	150	130	100	40	80	260
Co	ppm	1	3	3	3	3	3	3	3	3	1	1	2
Ni	ppm	20	30	< 20	< 20	< 20	< 20	< 20	40	30	< 20	20	80
Cu	ppm	10	< 10	< 10	< 10	< 10	< 10	< 10	30	10	20	20	140
Zn	ppm	30	40	40	< 30	40	40	30	50	40	< 30	40	110
Ga	ppm	1	18	17	17	18	18	18	17	18	17	17	18
Ge	ppm	1	3	2	2	2	2	2	2	2	3	3	2
As	ppm	5	< 5	< 5	< 5	< 5	< 5	< 5	< 5	< 5	7	6	< 5
Rb	ppm	2	265	231	223	246	250	237	261	277	291	301	321
Sr	ppm	2	81	93	101	111	114	88	152	142	21	23	37
Y	ppm	1	33	32	37	35	29	33	23	33	32	52	28
Zr	ppm	2	101	100	111	118	107	106	117	113	48	45	58
Nb	ppm	1	18	16	18	20	18	18	19	20	37	48	27
Mo	ppm	2	4	2	2	3	2	3	2	2	3	2	6
Ag	ppm	0.5	< 0.5	< 0.5	< 0.5	< 0.5	< 0.5	0.5	< 0.5	< 0.5	< 0.5	< 0.5	0.6
In	ppm	0.2	< 0.2	< 0.2	< 0.2	< 0.2	< 0.2	< 0.2	< 0.2	< 0.2	< 0.2	< 0.2	< 0.2
Sn	ppm	1	10	3	7	8	8	8	7	13	7	7	14
Sb	ppm	0.5	< 0.5	< 0.5	< 0.5	< 0.5	< 0.5	< 0.5	< 0.5	< 0.5	< 0.5	< 0.5	< 0.5
Cs	ppm	0.5	18.5	7.6	9.9	11.2	10.2	9.0	13.1	18.4	12.0	9.4	13.9
Ba	ppm	2	282	369	438	436	483	320	525	481	50	61	132
Hf	ppm	0.2	3.5	3.0	3.1	3.8	3.1	3.2	3.5	3.8	2.5	2.5	2.7
Ta	ppm	0.1	5.2	3.9	4.0	4.2	3.7	4.6	3.3	5.0	11.4	13.6	7.8
W	ppm	1	8	3	3	4	2	4	3	3	4	9	9
Tl	ppm	0.1	1.2	1.3	1.2	1.3	1.4	1.3	1.4	1.5	1.3	1.5	1.6
Pb	ppm	5	32	29	31	30	32	31	30	29	35	47	41
Bi	ppm	0.4	0.5	0.8	< 0.4	< 0.4	< 0.4	< 0.4	< 0.4	< 0.4	0.7	1.4	16.0
Th	ppm	0.1	14.3	14.9	16.1	18.3	13.2	14.2	15.6	16.0	9.4	9.5	9.4
U	ppm	0.1	20.9	6.1	9.4	7.9	5.6	10.0	5.4	7.9	33.1	38.9	12.1
La	ppm	0.1	18.6	19.2	21.6	26.0	18.5	19.4	27.9	27.2	12.0	12.1	12.3
Ce	ppm	0.1	36.4	43.8	43.7	50.6	37.4	41.7	55.6	50.2	22.4	17.4	28.9
Pr	ppm	0.05	4.40	4.61	5.05	5.86	4.28	4.74	6.19	6.24	3.53	2.82	3.00
Nd	ppm	0.1	16.8	18.0	19.0	22.8	16.6	17.6	22.6	23.0	12.9	10.6	11.0
Sm	ppm	0.1	4.3	4.2	4.5	5.6	3.9	4.3	4.6	5.1	3.9	3.9	3.0
Eu	ppm	0.05	0.55	0.58	0.56	0.64	0.61	0.54	0.68	0.75	0.18	0.23	0.25
Gd	ppm	0.1	4.6	4.8	4.5	5.5	4.3	4.6	4.1	5.3	4.1	5.2	3.3
Tb	ppm	0.1	0.8	0.9	0.9	1.0	0.7	0.9	0.7	0.9	0.8	1.3	0.6
Dy	ppm	0.1	5.2	5.0	5.6	5.8	4.5	5.3	4.2	5.8	5.4	8.9	4.3
Ho	ppm	0.1	1.1	1.0	1.2	1.2	0.9	1.1	0.8	1.2	1.1	1.8	0.9
Er	ppm	0.1	3.4	3.1	3.8	3.6	2.7	3.2	2.5	3.5	3.6	5.8	2.8
Tm	ppm	0.05	0.54	0.51	0.61	0.55	0.45	0.49	0.38	0.56	0.62	0.99	0.51
Yb	ppm	0.1	3.8	3.4	4.1	3.6	3.1	3.5	2.7	4.0	4.9	7.7	3.8
Lu	ppm	0.01	0.59	0.53	0.64	0.57	0.47	0.55	0.43	0.55	0.81	1.24	0.62

Table 4-12. Some geochemical parameters calculated for the LOP granites.

	LO granite (with low K_m values)			LO granite (with high K_m values)			AC granite (with low K_m values)		BA granite (with low K_m values)		
	LM 1	**LM 16**	**LM 22**	**LM 5**	**LM 13**	**LM 30**	**LM 24**	**LM 61**	**LM 7**	**LM 15**	**LM 49**
B=Fe+Mg+Ti	33.54	33.35	37.14	40.77	35.24	33.49	38.25	48.39	17.47	15.69	22.89
K_2O/Na_2O (%)	1.30	1.39	1.38	1.28	1.44	1.26	1.32	1.30	1.40	1.56	1.42
Na_2O+K_2O (%)	8.02	8.14	8.07	8.54	8.44	7.87	7.48	7.40	7.56	7.66	7.62
ASI (molar)	1.14	1.09	1.11	1.05	1.09	1.08	1.06	1.09	1.31	1.17	1.18

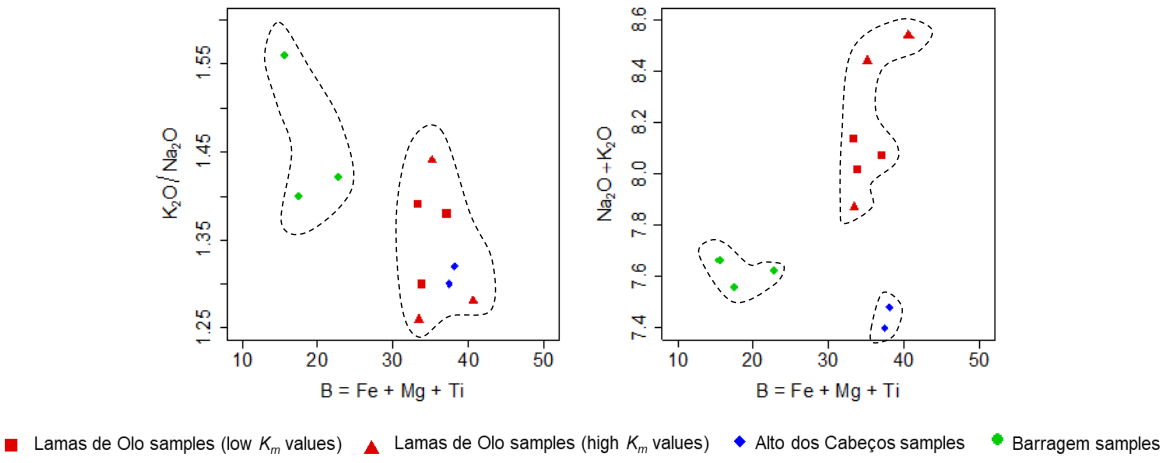


Figure 4-29. Variation diagrams of K_2O/ Na_2O and $Na_2O + K_2O$ in the function of the B parameter.

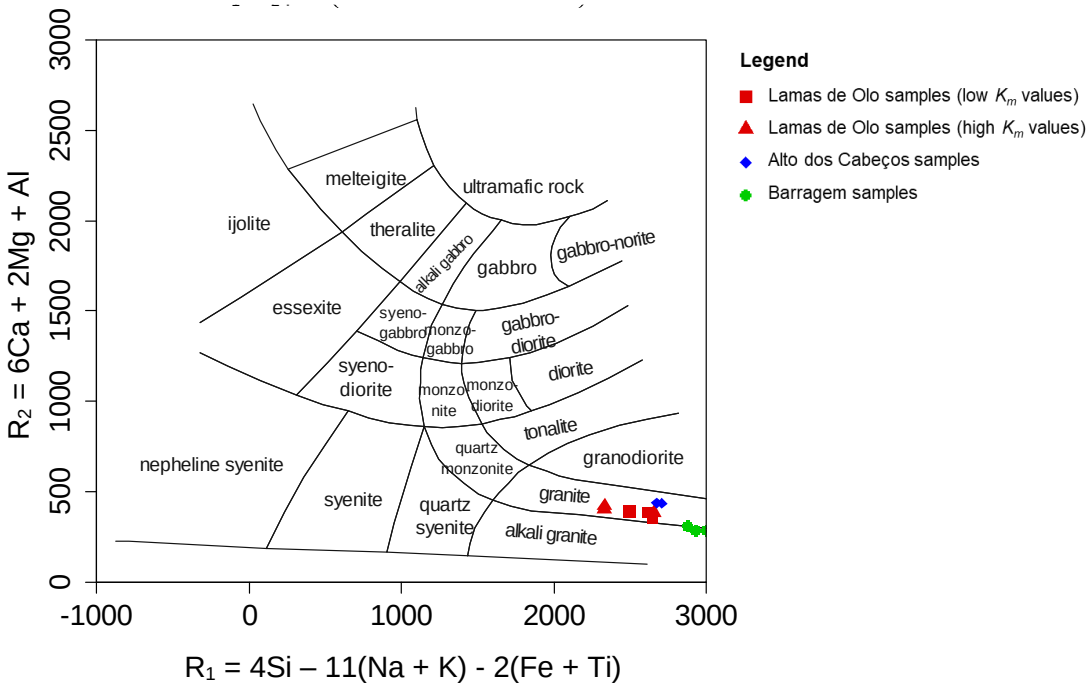


Figure 4-30. Granite classification diagram using R_2 and R_1 parameters (De La Roche *et al.*, 1980).

Frost *et al.* (2001) diagrams point out that LOP granites: (i) have an intermediate composition between magnesian and ferric (fig. 4-31A); (ii) have calc-alkaline to alkali-calcic character (fig. 4-31B); and (iii) are peraluminous granites (fig. 4-31C). The Alumina Saturation Index is higher than 1 (ASI > 1; table 4-12) in all granites, having mean values of 1.10 for LO, 1.08 for AC, and 1.16 for BA granites.

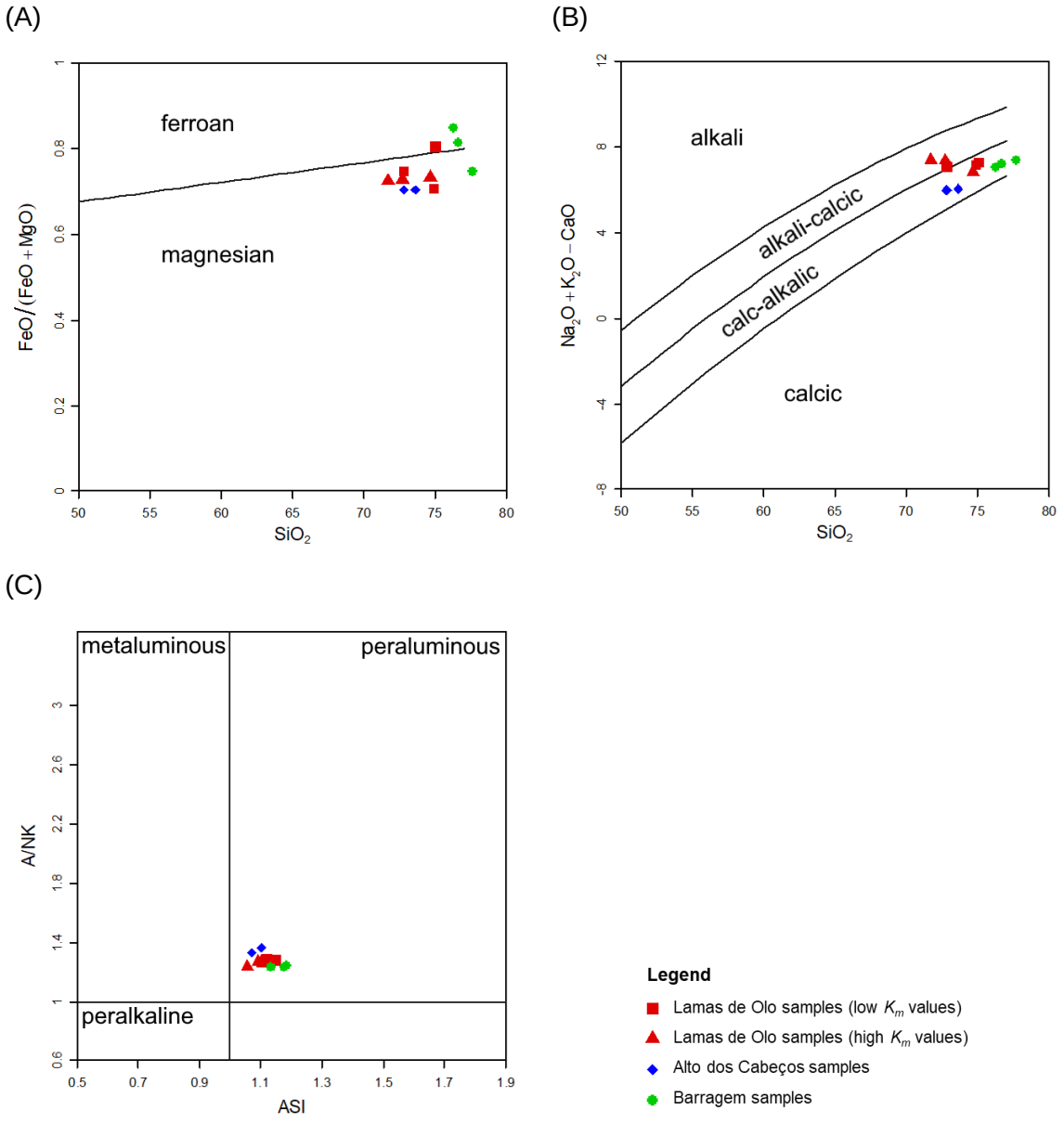


Figure 4-31. Classification diagrams according to Frost *et al.* (2001): (A) Fe number *versus* SiO_2 (in wt %); (B) Modified alkali-lime index (MALI) *versus* SiO_2 (in wt %); (C) A/NK *versus* ASI diagram; Fe-number is calculated as weight proportion of FeO=FeO+MgO; MALI is defined as Na_2O+K_2O-CaO (in wt %); ASI is defined as molecular Al_2O_3=(Na_2O+K_2O+CaO-3:33P_2O_5) (molar).

Although these diagrams are recent, authors like Peccerillo & Taylor (1976) and Villaseca *et al.* (1998) have proposed other more discriminative diagrams. The K_2O *versus* SiO_2 diagram allows characterizing the LOP granites as highly-K calc-alkaline (figs. 4-32A), and the A *versus* B diagram modified by Villaseca *et al.* (1998), allows discriminating the LOP granites in two groups: the LO+AC granites are low-peraluminous and BA is a felsic peraluminous granite (fig. 4-32B).

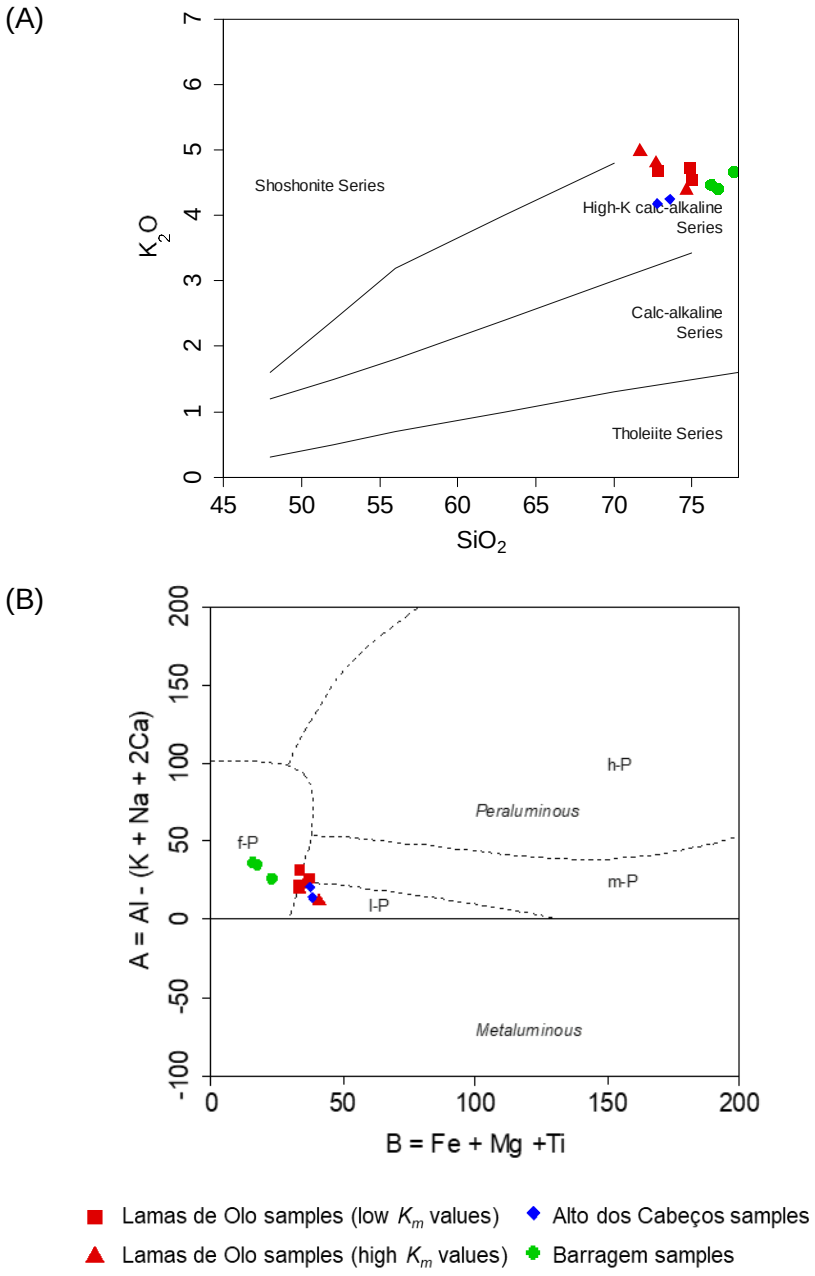


Figure 4-32. Classification granite diagrams: (A) SiO_2 *versus* K_2O diagram from Peccerillo & Taylor (1976); (B) A *versus* B from Villaseca *et al.* (1998); h-P – highly peraluminous; f-P – Felsic peraluminous; m-P – Moderately peraluminous; l-P – Low peraluminous.

These results show that BA granite should have a different magma source from the other two granites. The Rb-Ba-Sr diagram shows that BA is the most evolved granite and the LO+AC granites are projected close to the normal granites (fig. 4-33).

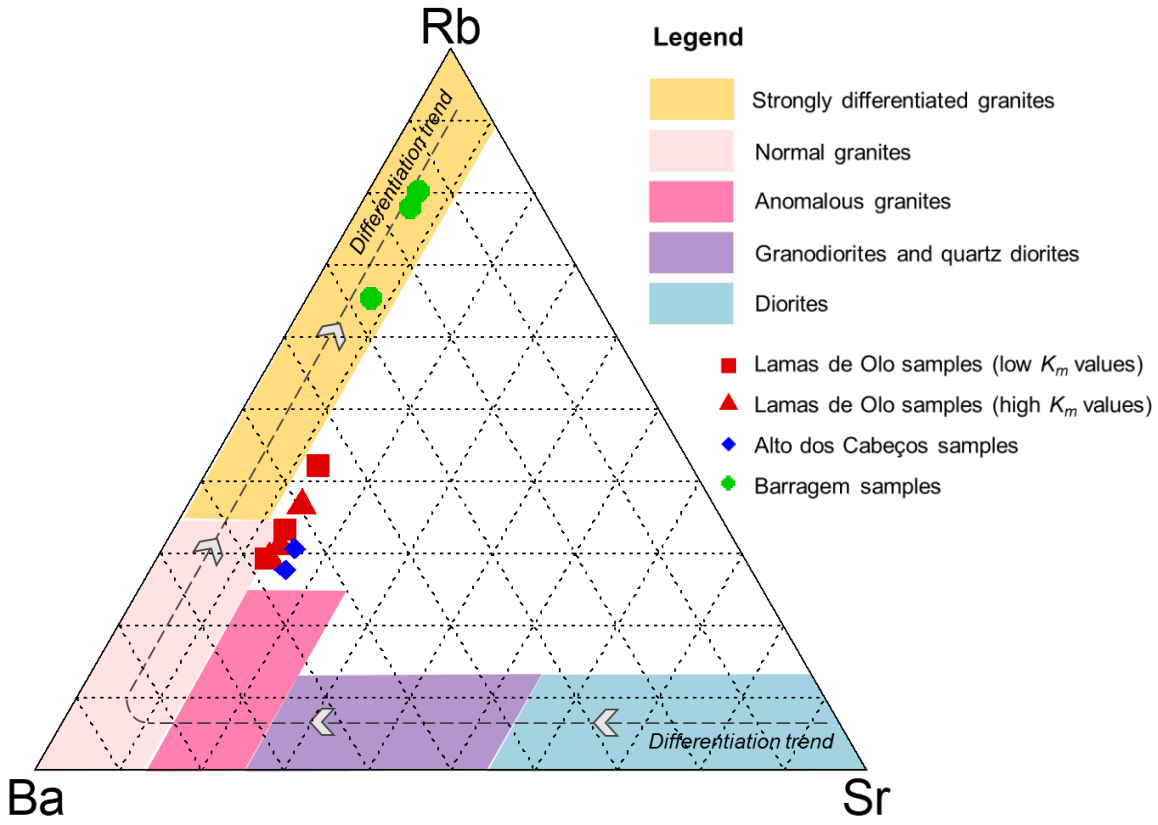


Figure 4-33. Rb-Ba-Sr diagram (El Bouseily & El Sokkary, 1975).

When plotting the data on the geotectonic discriminative plots proposed by Pearce *et al.* (1984), the LOP granites are projected at the “triple point” (VAG, syn-COLG, and WPG; fig. 4-34) precluding a direct interpretation. Although that, in Ta *versus* Yb diagram the samples were projected in Within Plate Granites (WPG) field, points out the contribution of mantle source for all granites.

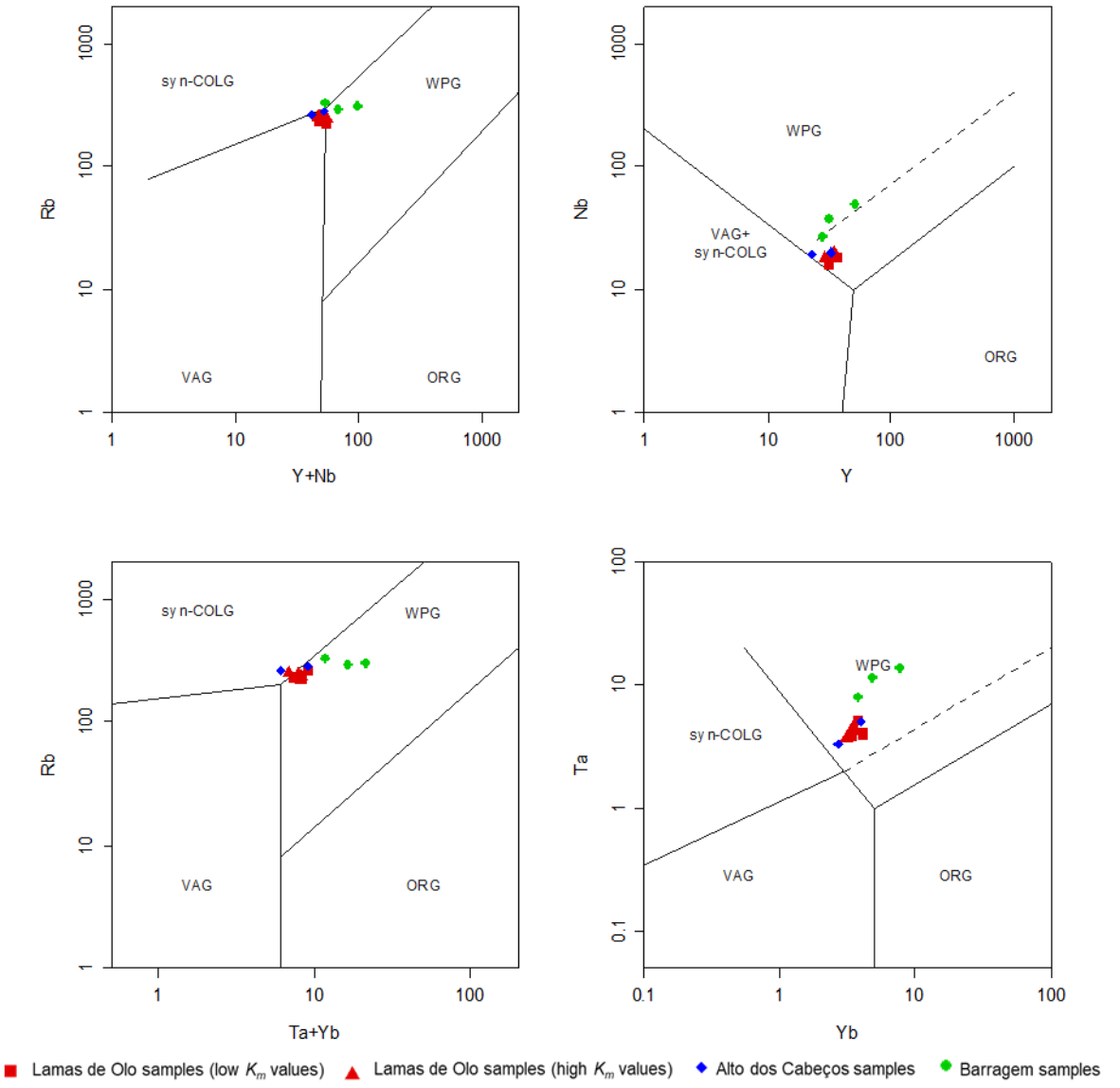


Figure 4-34. A suite of diagrams for discrimination of the geotectonic environment of LOP granite; ORG - Ocean Ridge granites; VAG - Volcanic Arc granites; WPG - Within Plate granites; syn-COLG – syn-collision granites; the dashed line represents the upper compositional boundary for ORG from anomalous ridge segments (Pearce *et al.*, 1984).

In order to obtain more detailed information about the geodynamic context of LOP granites, the Hf-Rb/ 30-Hf-3Ta plot (Harris *et al.*, 1986) was made (fig. 4-35). The diagram is more discriminative, showing that LOP granites are late- or post-collisional granites. Figures 4-34 and 4-35 show that BA granite is the youngest and more alkaline granite from the set.

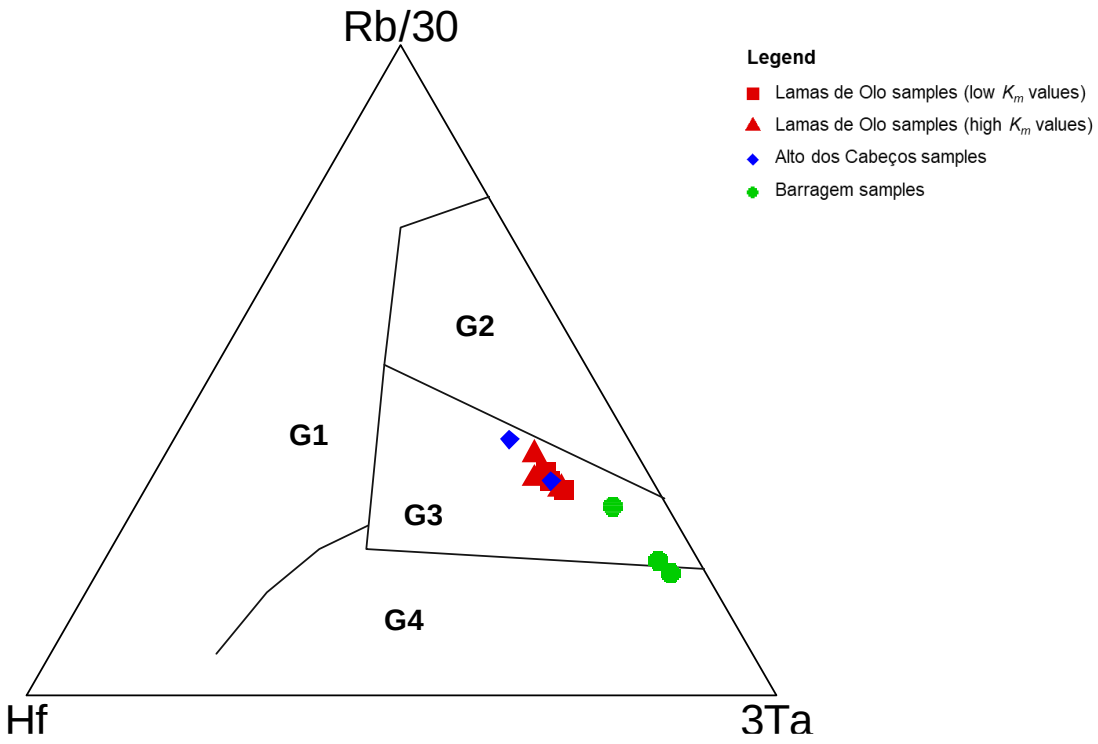


Figure 4-35. Triangular diagram proposed by Harris *et al.* (1986) for classification of collisional granites; G1 (Group 1) - Pre-collision calc-alkaline intrusions (Volcanic-Arc granites); G2 (Group 2) - Syn-collision peraluminous intrusions; G3 (Group 3) - Late or post-collision calc-alkaline intrusions; G4 (Group 4) - Post-collision alkaline intrusions (Within-Plate granites).

4.4.2 Major and trace elements

As LOP is constituted by biotite granites, the B parameter (Fe + Mg + Ti) was chosen as an indicator for differentiation mechanisms (fig. 4-36, table 4-11), once this parameter reflects the content of ferromagnesian minerals in the rock, especially biotite. B parameter is expressed in millications (1000 gram-atoms per 100 grams) (*e.g*. Debon & Le Fort, 1983, 1988).

The variation of major elements regarding the B parameter, shows an inverse or negative correlation with SiO_2, as expected, and a positive correlation with Al_2O_3, MgO, CaO, TiO_2, P_2O_5, and Fe_2O_3t.

The MgO, CaO, TiO_2, and Fe_2O_3t *versus* B diagrams indicate that LO and AC granites have more calcium plagioclase and ferromagnesian (*e.g*. biotite) and/or ferromagnetic minerals (*e.g.* magnetite, hematite, and titanomagnetite/ Ti-poor magnetite) than BA granite.

The higher P values (P_2O_5 *versus* B) on the former granites, is indicative of having more apatite and biotite than the BA granite.

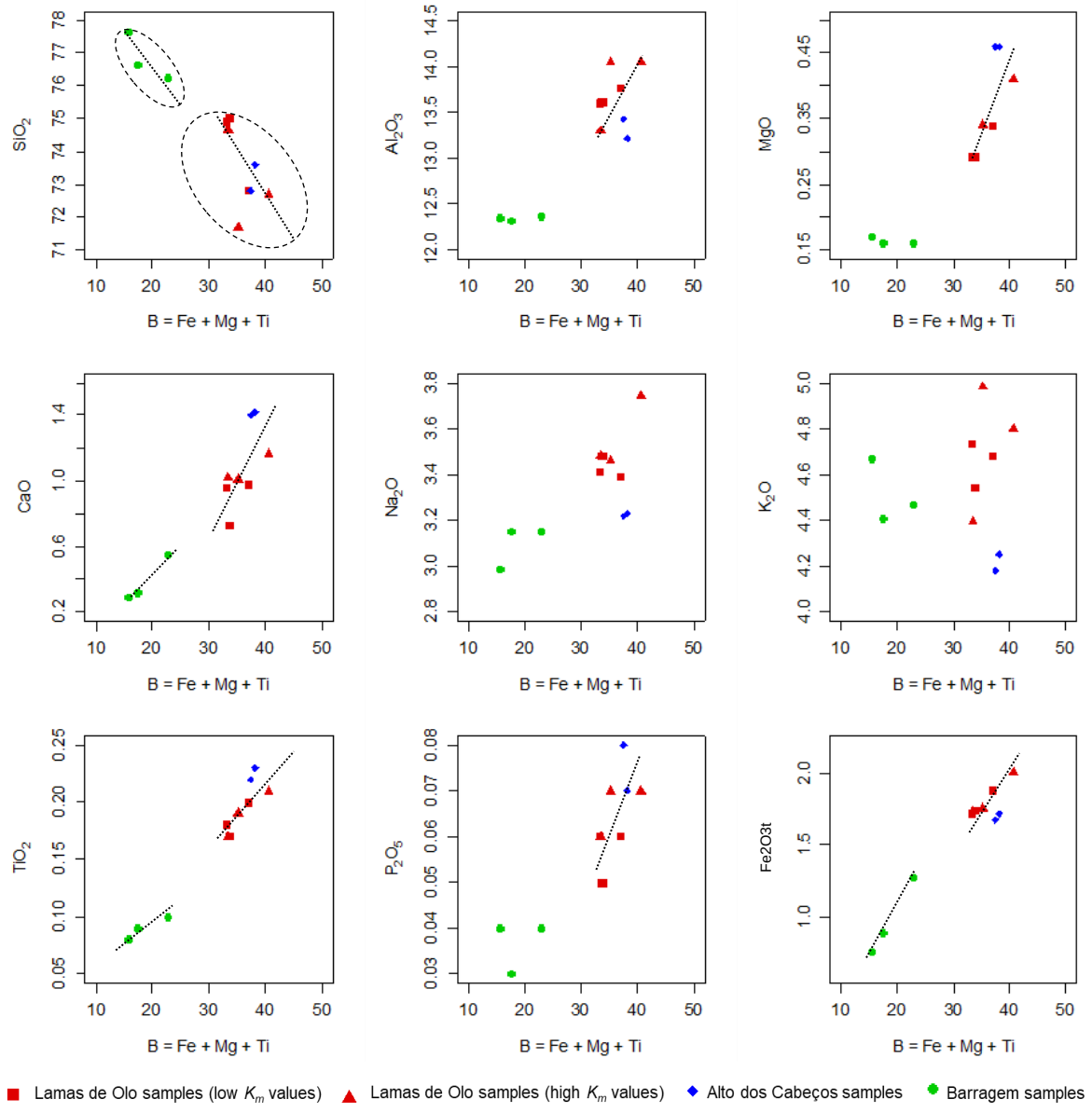


Figure 4-36. Variation diagrams for LOP granites (major element concentrations in percentage).

Similar to shown in the major elements diagrams, the trace elements diagrams show that the LO and AC granites have a slightly higher dispersion of B parameter, due to the presence of biotite. The BA granite has minor amounts of biotite, and then, shows a minor dispersion of B parameter (table 4-11; fig. 4-37).

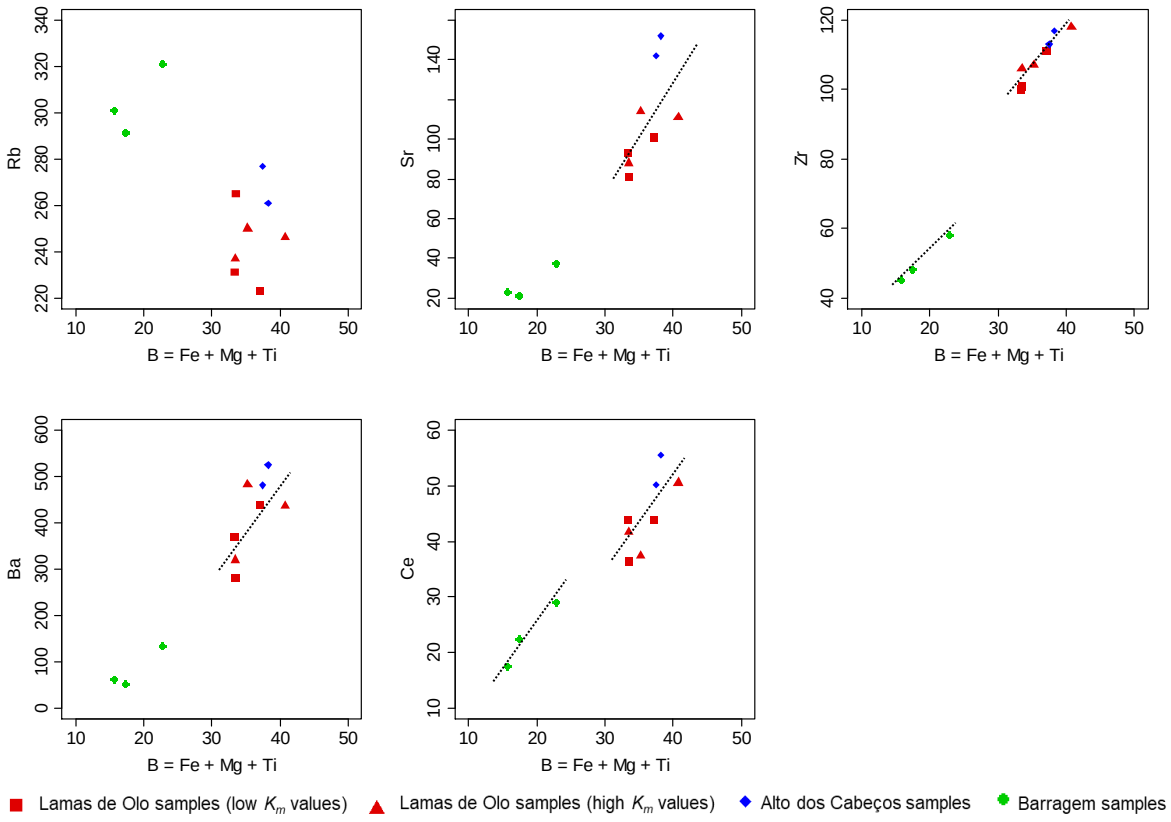


Figure 4-37. Variation diagrams for LOP granites (trace element concentrations in ppm).

Most of the trace elements (Sr, Zr, Ba, and Ce) are compatible with the B parameter. The positive correlations for Sr, Zr, and Ba indicates that BA granite is the most evolved (lowest B content) and the poorest in these elements.

Figures 4-36 and 4-37 show that the B parameter is low in BA granite and that decreases with differentiation. The occurrence of two distinct groups in all diagrams, LO+AC and BA, suggests the existence of two magma sources: (i) the LO+AC granites are geochemically similar, suggesting that both are generated from the same magma, and (ii) the BA granite has a different magma source, once there are no transition terms between them.

The Rb, Ba, and Sr behavior, point out that BA granite has the highest values of Rb and the lowest of Ba (fig. 4-38A). The Ba-Sr diagram (fig. 4-38B) shows that each granite has Sr and Ba contents distinct from each other, with AC > LO > BA.

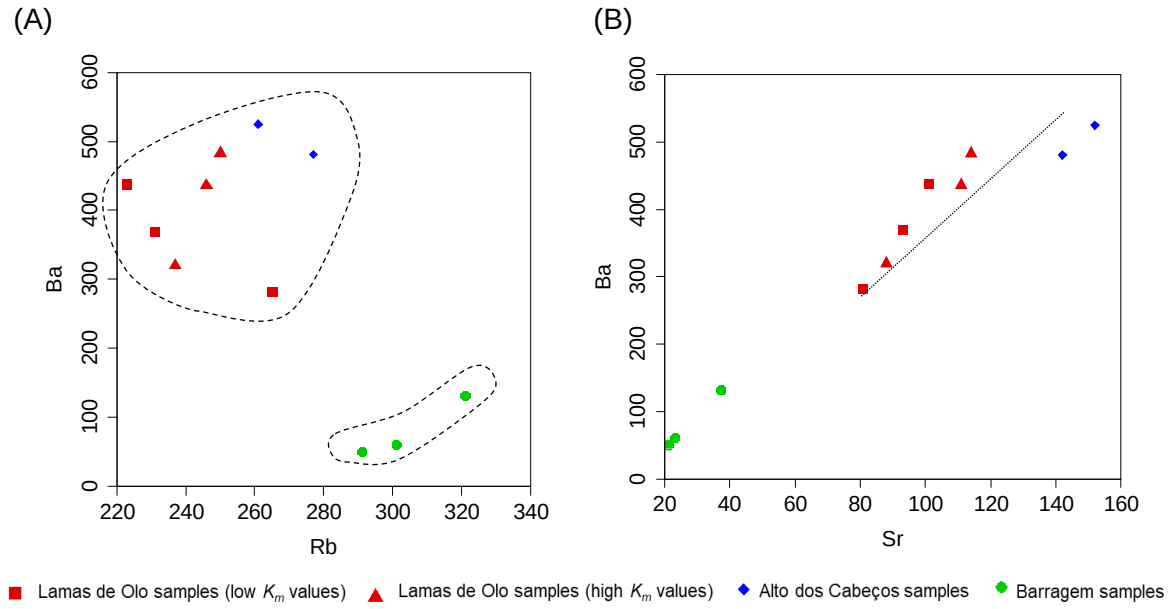


Figure 4-38. Ba *versus* Rb and Ba *versus* Sr diagrams from LOP granites.

4.4.3 Rare Earth Elements

The fractionation of the REE is a very common process in granites and is attributed to the crystallization of accessory minerals, like monazite and allanite (Light Rare Earth Elements, LREE), or zircon and xenotime (Heavy Rare Earth Elements, HREE).

The REE spectra are flat for all granites (LO granite – LaN/YbN 3.30 to 4.87 and GdN/YbN 0.89 to 1.23; AC granite – LaN/YbN 4.58 to 6.97 and Gd/YbN 1.07 to 1.23; BA granite – LaN/YbN 1.06 to 2.18 and Gd/YbN 0.55 to 0.70), with a slight pronounced Eu anomaly in LO (Eu/Eu* 0.35 to 0.46) and AC (Eu/Eu* 0.44 to 0.48) granites and a more pronounced in BA (Eu/Eu* 0.14 to 0.24). The REE spectra of the LO and AC granites are subparallel, but different from the REE spectra of BA granite (table 4-13; fig. 4-39). Figure 4-39 shows a perfect flat-spectrum to one sample of BA granite (LM 7).

Table 4-13. Characterizing parameters of the REE profiles calculated for the LOP granite; LO - Lamas de Olo granite; AC - Alto dos Cabeços granite; BA - Barragem granite; N - values normalized to chondrite according to Boynton (1984); Eu/Eu*= $Eu_{Nc}/(Sm_{Nc}*Gd_{Nc})^{1/2}$.

	LO granite (with low K_m values)			LO granite (with high K_m values)			AC granite (with low K_m values)		BA granite (with low K_m values)		
Analyte Symbol	**LM 1**	**LM 16**	**LM 22**	**LM 5**	**LM 13**	**LM 30**	**LM 24**	**LM 61**	**LM 7**	**LM 15**	**LM 49**
Eu/Eu*	0.38	0.39	0.38	0.35	0.46	0.37	0.48	0.44	0.14	0.16	0.24
LaN/YbN	3.30	3.81	3.55	4.87	4.02	3.74	6.97	4.58	1.65	1.06	2.18
LaN/SmN	2.72	2.88	3.02	2.92	2.98	2.84	3.82	3.35	1.94	1.95	2.58
CeN/YbN	2.48	3.33	2.76	3.64	3.12	3.08	5.33	3.25	1.18	0.58	1.97
GdN/YbN	0.98	1.14	0.89	1.23	1.12	1.06	1.23	1.07	0.68	0.55	0.70
Sum_REE ppm	101	110	116	133	98	108	133	134	76	80	75
Sum_LREE ppm	81	90	94	111	81	88	117	112	55	47	58
Sum_HREE ppm	21	20	22	22	18	20	16	23	22	33	17

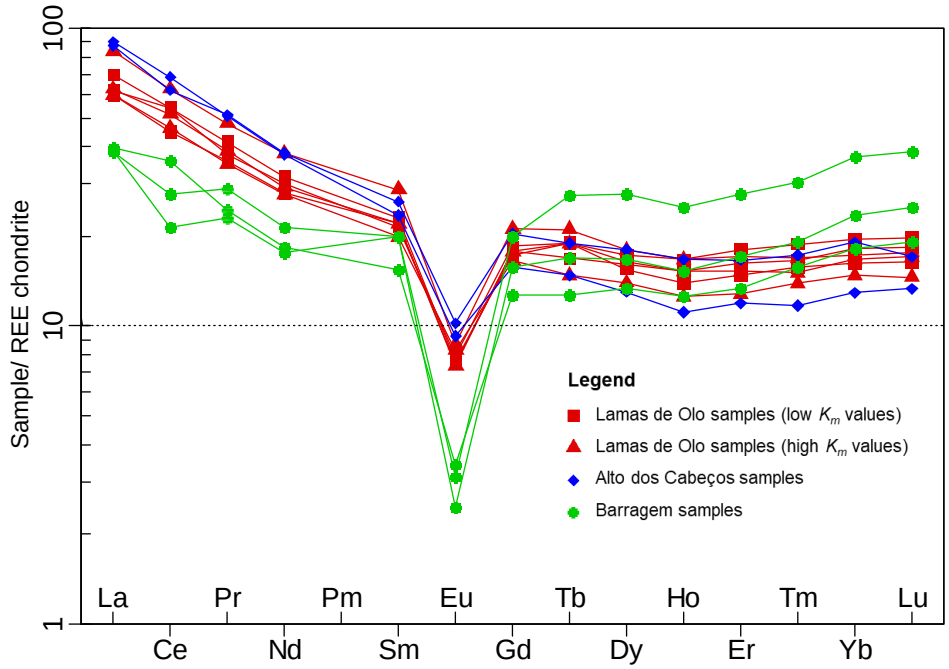


Figure 4-39. Rare Earth elements (REE) spectra normalize to chondrite (Boynton, 1984).

In the same way, the multielement spider plot for LOP granites (fig. 4-40; normalized to the bulk continental crust) shows that BA granite is the most evolved granite, once it has Ba, Sr, and Ti in minor amounts, and is richer in U and Nb.

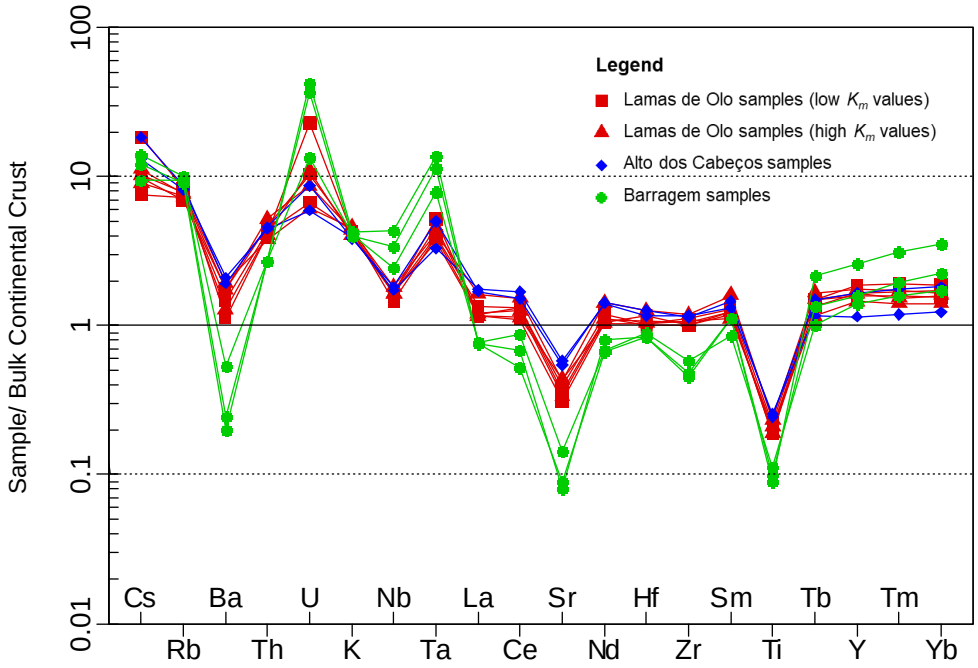


Figure 4-40. Spider plot normalized to the bulk continental crust (Taylor & McLennan, 1995).

Both REE spider plots (figs. 4-39 and 4-40) corroborate the fact that the LO+AC granites have a different origin from BA granite.

4.4.4 Iron content *versus* magnetic susceptibility

When comparing LO granitic samples from the areas with high and low susceptibility, both sets of samples have similar mineralogy and similar geochemical content. Both granite types show the same proportion of FeO and Fe_2O_3, contrary to the expected since magnetite incorporates more FeO than Fe_2O_3 (table 4-11).

In the figure 4-41A, two groups are individualized: (i) one with lower K_m values, corresponding to the BA granite, and another one, (ii) constituted by LO+AC granites with higher content in Fe_2O_3t and with a higher K_m values range. Figure 4-41A also shows that in the BA granite a positive correlation exists between the K_m and the Fe_2O_3t. However, in the group composed by the LO+AC granites, no correlation is observed since, for the same Fe_2O_3t content, the K_m values have a high variation.

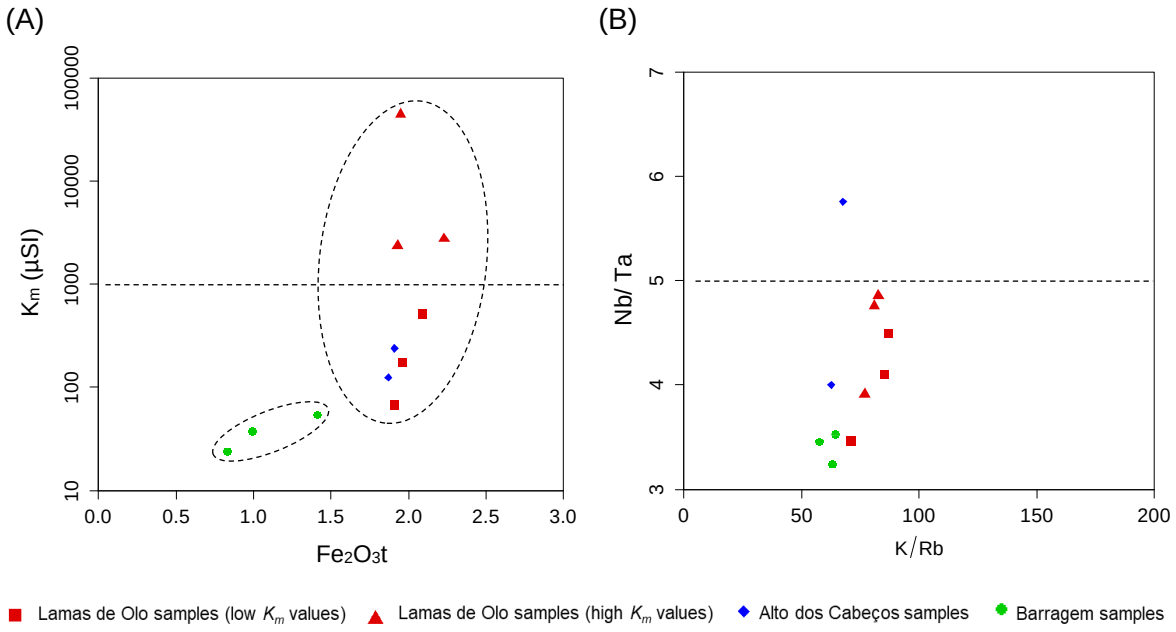


Figure 4-41. Geochemical plots of representative samples for Lamas de Olo Pluton: (A) K_m *versus* Fe_2O_3t, showing the variation of magnetic susceptibility with Fe (total) content; (B) Evolution of Nb/Ta as a function of K/Rb, where Nb/Ta < 5 points out the interaction with hydrothermal fluids (Ballouard *et al.*, 2016).

Studies carried out by Ballouard *et al.* (2016) show the influence of magmatic differentiation and hydrothermal alteration as a function of Nb-Ta fractionation. Is expected that the Nb/Ta ratio decreases during the magmatic differentiation of granite melts, and the Nb/Ta < 5 points out interaction with fluids. Figure 4-41B shows that most samples have Nb/Ta < 5, which proves the existence of hydrothermal fluid percolation, able to change the magnetic mineralogy (*e.g*. martitization), decreasing the K_m values.

4.4.5 Whole-rock geochemical data as a pathfinder to specialization on mineral occurrences

The W.R. geochemical data points out that LOP granites are specialized in some metals, like W, Mo, Sn, and Be concerning to the average on the continental crust (*Clarke;* 1.9 ppm to W, 2.1 ppm to Sn, 1.1 ppm to Mo and 2.1 ppm to Be), defined by Rudnick & Gao (2014). The contents for the W, Mo, Sn, and Be can be consulted in the table 4-11, and the mean values for these elements are:

(i) LO granite: 4.0 ppm to W, 2.7 ppm to Mo, 7.3 ppm to Sn and 5.3 ppm to Be;

(ii) AC granite: 3.0 ppm to W, 2.0 ppm to Mo, 8.7 ppm to Sn and 7.3 ppm to Be;

(iii) BA granite: 7.3 ppm to W, 3.7 ppm to Mo, 9.3 ppm to Sn and 4.8 ppm to Be.

Figure 4-42 shows the affinity of LOP granites for Sn and W mineralizations (figs. 4-42A and B), but not for the Mo occurrences (fig. 4-42C). However, the existence of W, Mo, Sn, and Be mineralizations along quartz/ aplite veins are described (see topic 4.1.3).

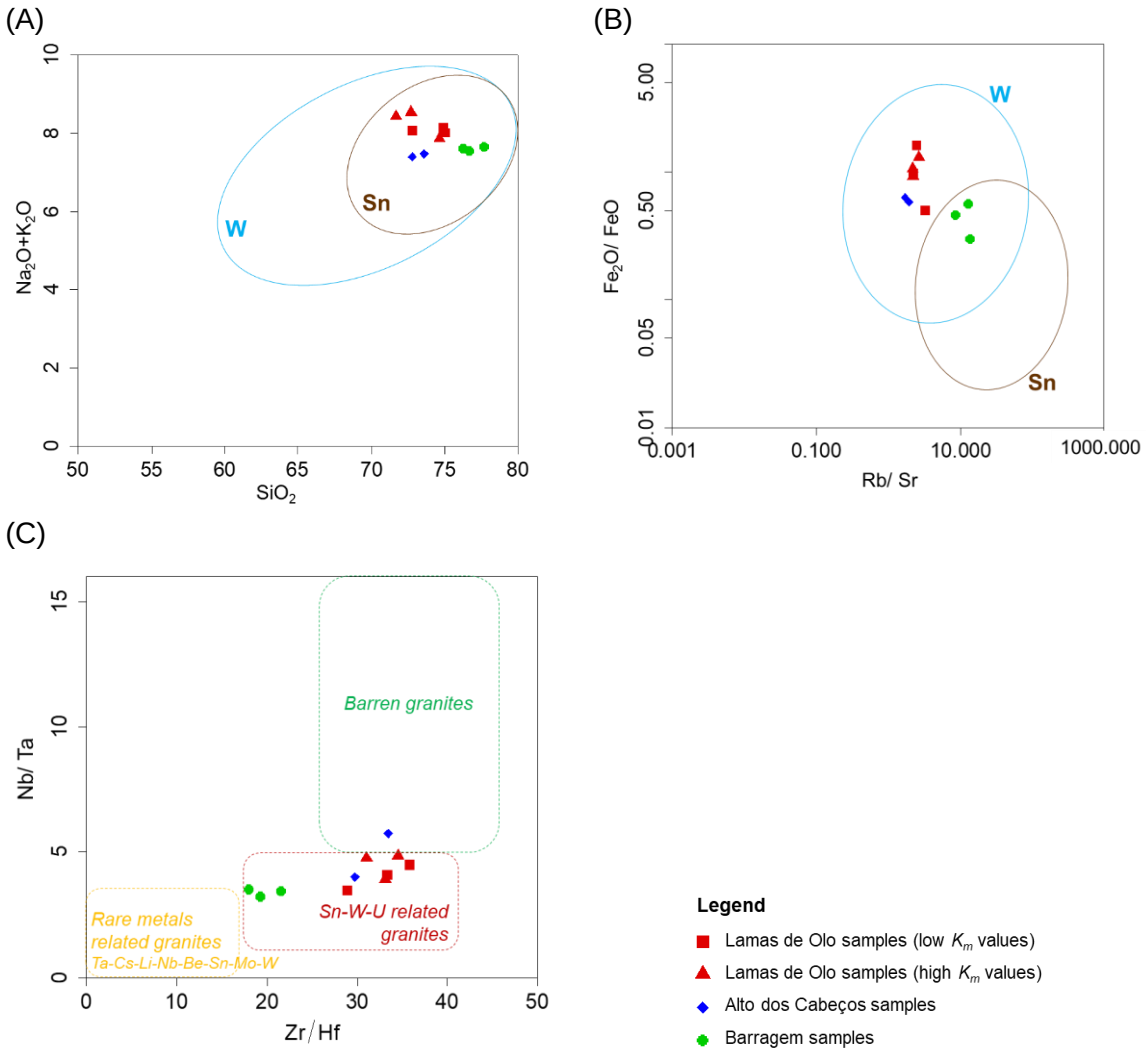


Figure 4-42. LOP and possible mineral occurrences related to their granites: (A) Plot of total alkalis *versus* SiO_2 (Le Maitre, 1989); (B) Plot of Fe_2O_3/FeO *versus* Rb/Sr (Blevin & Chappell, 1992); (C) Nb/Ta *versus* Zr/Hf diagram differentiating barren peraluminous crustal granites and granites hosting ore deposits (Ballouard *et al.*, 2016).

4.4.6 Highlights

The geochemical data indicate that LOP granites are calc-alkaline to alkali-calcic and peraluminous granites. The REE spectra are flat for all granites, having a slight pronounced Eu anomaly in LO+AC granites and a pronounced Eu anomaly in BA granite.

The results suggest the existence of two magma sources: (i) the LO+AC granites are geochemically similar, suggesting that both are generated from the same magma, and (ii) the BA has a different magma source and is the most evolved granite.

LO granitic samples with high and low susceptibility have similar geochemical character and show the same proportion of FeO and Fe_2O_3, which corroborate the presence of magnetite-type granites with different degrees of oxidation of magnetite into hematite.

BA is an alkaline granite and is the youngest and evolved granite showing a REE spectra with a similar pattern to anarogenic granites. These facts point out that BA granite was the last to ascent and emplaced in the crust.

LOP granites are specialized in several metals, like W, Mo, Sn, and Be when comparing to the average on the continental crust.

4.5 METALLOGENIC IMPLICATIONS

4.5.1 Pathfinder to mineral occurrences: K_m *versus* W.R. $\delta^{18}O$ diagram

The multidisciplinary study of granites made it possible to establish a relation between LOP and the mineral occurrences related to their granites.

K_m *versus* W.R. $\delta_{18}O$ diagram (Ellwood & Wenner, 1981) is useful pathfinders to infer about the mineral occurrences, namely W-(Mo, Bi), W-(Sn) and Sn, related to each type of granite. To establish a relationship between LOP granites and mineralizations, some W.R. $\delta^{18}O$ data were performed (table 4-14).

Furthermore, previous studies for magnetic susceptibility and W.R. $\delta_{18}O$ data were considered (Antunes *et al.*, 2008; Martins *et al.*, 2009; Neiva *et al.*, 2009 and Sant'Ovaia *et al.*, 2013a) in order to project all the existing data for the Variscan granites. The data from the Variscan granites (original data and data compiled from the literature) are present in table 4-14 and figure 4-43.

The majority of the Portuguese Variscan granites correspond to reduced- or ilmenite-type granites (K_m mean value of 88 μSI) and the W.R. $\delta^{18}O$ values are heterogeneous, ranging between 9.70 ‰ and 13.54 ‰. The magnetite-type granites are scarce in Portugal and are represented by some post-tectonic plutons (Lavadores-Madalena, Peneda-Gerês, and Lamas de Olo). They have high K_m values (mean values of 6656 μSI) and low $\delta^{18}O$ values, ranging from 8.85 ‰ to 11.90 ‰.

Figure 4-43B points out that the Sn and W-(Sn) mineralizations are associated with ilmenite-type granites. However, the Sn are associated with S-type peraluminous granites and W-(Sn) are related to I-type peraluminous granites, both with high W.R. $\delta^{18}O$ values. The W-(Mo, Bi) occurrences are associated with I-type peraluminous and magnetite-type granites.

Table 4-14. W.R. $\delta^{18}O$ normalize to SMOW (Standard Mean Ocean Water) and K_m of Variscan granites according to our study data on Lamas de Olo Pluton and Vila Real Massif, as well as previous studies compiled from the bibliography (Antunes *et al.*, 2008; Martins *et al.*, 2009; Neiva *et al.*, 2009 and Sant'Ovaia *et al.*, 2013a); (*) K_m value for the analyzed sample.

Pluton/ Massif	Granites	W.R. $\delta^{18}O_{SMOW}$	K_m µSI (*)
1 – Lavadores-Madalena	Lavadores biotite granite	10.20	16480
	Madalena biotite granite	10.40	1040
2 – Vila Pouca de Aguiar	Vila Pouca de Aguiar granite (external facies)	10.30	97
	Vila Pouca de Aguiar granite (external facies)	10.30	92
	Pedras Salgadas granite (internal facies)	10.50	66
	Pedras Salgadas granite (internal facies)	11.00	77
	Pedras Salgadas granite (internal facies)	10.30	61
3 – Águas-Frias-Chaves	Chaves granite	9.70	70
	Chaves granite	9.80	98
4 – Peneda-Gerês	Gerês biotite granite	10.90	122
	Gerês biotite granite	11.20	122
5 – Porto	Porto two-mica granite	12.90	63
6 – Lamas de Olo	Lamas de Olo granite	9.60	92100
	Lamas de Olo granite	10.40	46
	Lamas de Olo granite	10.00	3160
	Barragem granite	11.10	28
	Barragem granite (central facies)	10.90	20
	Alto dos Cabeços granite	9.70	722
7 – Mangualde	Mangualde granite	10.65	85
8 – Castelo Branco	Monzogranite	12.35	86
	Porphyritic monzogranite	12.75	85
	Two-mica granite	12.91	49
	Two-mica granite - Alcains	13.54	51
9 – Serra da Estrela	Manteigas granite	8.85	15783
	Cabeço granite	13.40	43
	Seia granite	12.10	77
	Seia granite	11.45	66
10 – Vieira do Minho	Vieira do Minho granite	11.00	111
	Vieira do Minho granite	10.60	181
	Vieira do Minho granite	10.50	151
	Vieira do Minho granite	9.90	153
11 – Castelo do Queijo	Castelo do Queijo biotite granite	10.60	105
	Castelo do Queijo biotite granite	10.70	105
12 – Vila Real	Vila Real granite	12.00	54

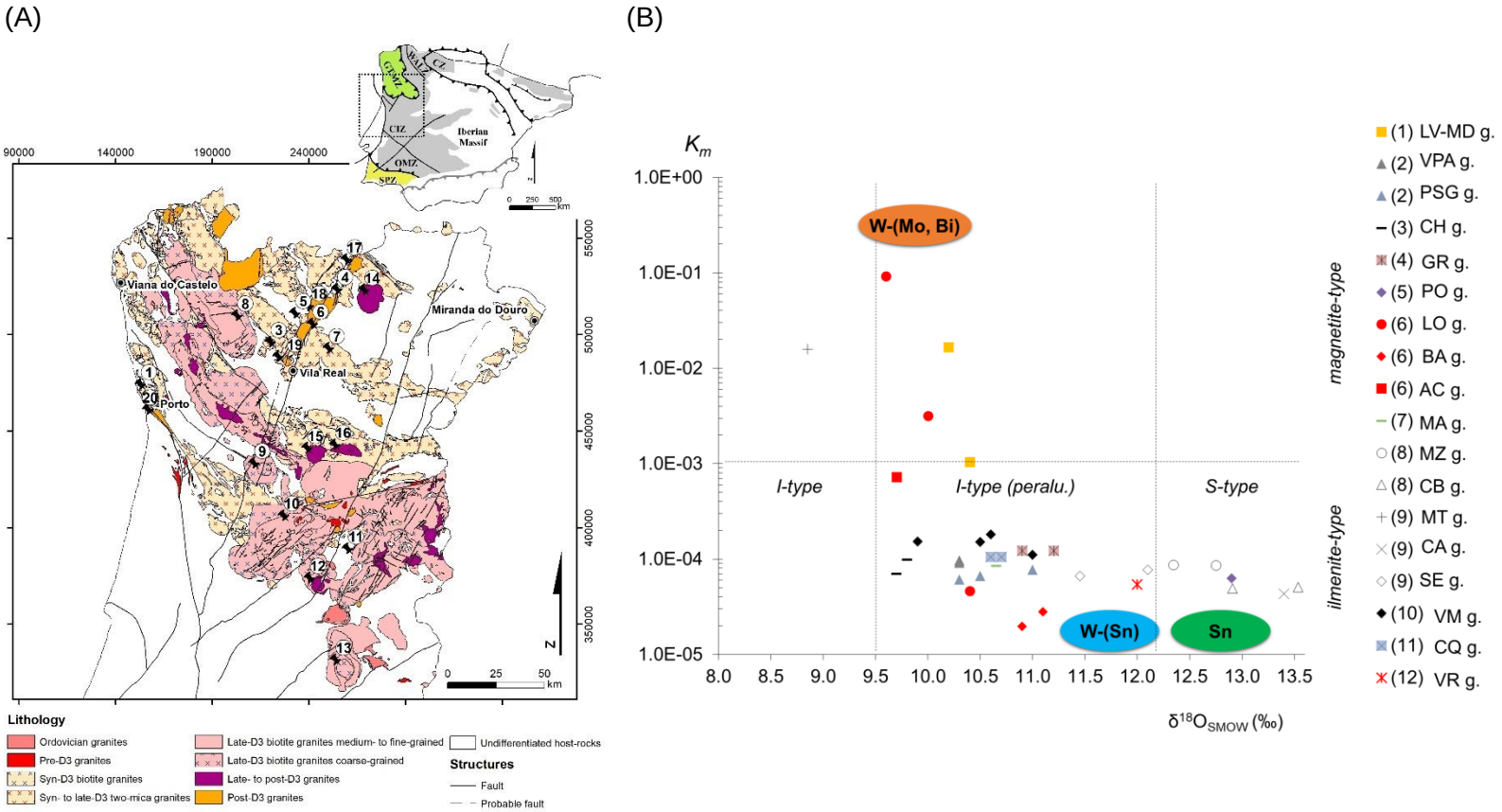


Figure 4-43. (A) Location of the studied Variscan plutons in northern Portugal (modified from: Ferreira *et al.*, 1987; Corrêa-Ribeiro, 2018; Antunes, 2019; Gonçalves *et al*., 2019): 1 – Lavadores-Madalena; 2 – Vila Pouca de Aguiar; 3 – Águas-Frias-Chaves; 4 – Peneda-Gerês; 5 – Porto; 6 – Lamas de Olo; 7 – Mangualde; 8 – Castelo Branco; 9 – Serra da Estrela; 10 – Vieira do Minho; 11 – Castelo do Queijo; 12 – Vila Real; (B) Semi-log plot of K_m (in SI units) *versus* $\delta^{18}O$ for the studied granites, considering the data in Antunes *et al.* (2008), Martins *et al.* (2009), Neiva *et al.* (2009), and Sant'Ovaia *et al.* (2013a): LV g. - Lavadores-Madalena granites; VPA g. - Vila Pouca de Aguiar granite; PSG g. - Pedras Salgadas granite; CH g. - Chaves granite; GR g. - Gerês granite; PO g. - Porto granite; LO g. - Lamas de Olo granite; BA g. - Barragem granite; AC g. - Alto dos Cabeços granite; MA g. - Mangualde granite; MZ g. - Monzogranito de Castelo Branco; CB g. - Castelo Branco granite; MT g. - Manteigas granite; CA g. - Cabeço granite; SE g. - Serra da Estrela granite (Torre); VM g. - Vieira do Minho granite; CQ g. - Castelo do Queijo granite; VR g. - Vila Real granite.

4.5.2 Highlights

The relationship between magnetite-type granites and W-(Mo, Bi) mineralizations were found in the Lamas de Olo Pluton, as well as in other post-tectonic plutons, namely Peneda-Gerês (280 Ma), and Lavadores-Madalena (299 Ma) plutons. All plutons have magnetite/ Ti-poor magnetite in their granites, reflecting melt oxidized conditions, on deep crustal levels, which played an important role in the origin of the granites related to this kind of mineralizations. The LOP has W-(Mo, Bi) mineralizations associated with their granites, the Peneda-Gerês Pluton has W-(Sn, Mo, Bi) (Cottard, 1979; Cheilletz & Giuliani, 1982; Noronha, 1984), and in the Lavadores-Madalena Pluton, W-(Mo) local occurrences have been described associated with the Madalena granite (Teixeira & Perdigão, 1962).

In the studied case, the emplacement of the leucocratic BA granite culminated the processes of ore concentration, which are also related to the successive intrusions during the LOP formation. It should be noted that Lamas de Olo and Peneda-Gerês plutons have several similarities: both are composed of different post-tectonic and magnetite-type granites, most of their granites are biotitic but leucocratic granites are also present (Barragem granite in LOP and Illa granite in Peneda-Gerês Pluton), and W-(Mo, Bi) mineral occurrences are associated to their granites.

The K_m *versus* W.R. $\delta^{18}O$ diagram points out the presence of magnetite-type granites in the LOP and the relation between them and W-(Mo, Bi) mineralizations. The mineralizations of W-Mo, as well as minor amounts of Bi-Be-Sn, occur in association with LOP granites, mostly in N 80º E sub-vertical quartz veins, showing a spatial relation with the presence of pure magnetite (areas with high K_m values).

4.6 GRAVIMETRIC SURVEY

To improve the magnetic fabric interpretation, the gravimetric study was performed. The interpretation of AMS and gravimetric data together make it possible to infer the location of the feeder zone, the shape of the pluton, and its emplacement model.

The gravimetric data interpretation was carried out in collaboration with Professors José Martinho Lourenço (UTAD) and Fernando Almeira (UA).

4.6.1 Fieldwork procedures

4.6.1.1 Acquisition of topographic and gravimetric data

In the fieldwork campaigns, the DGPS and gravimetric data were obtained along 3 gravimetric profiles (fig. 4-44). As gravimeter gives the readings in divisions, a “Calibration Table for G-1054” to convert gravity values in mGal, was used (fig. 4-45).

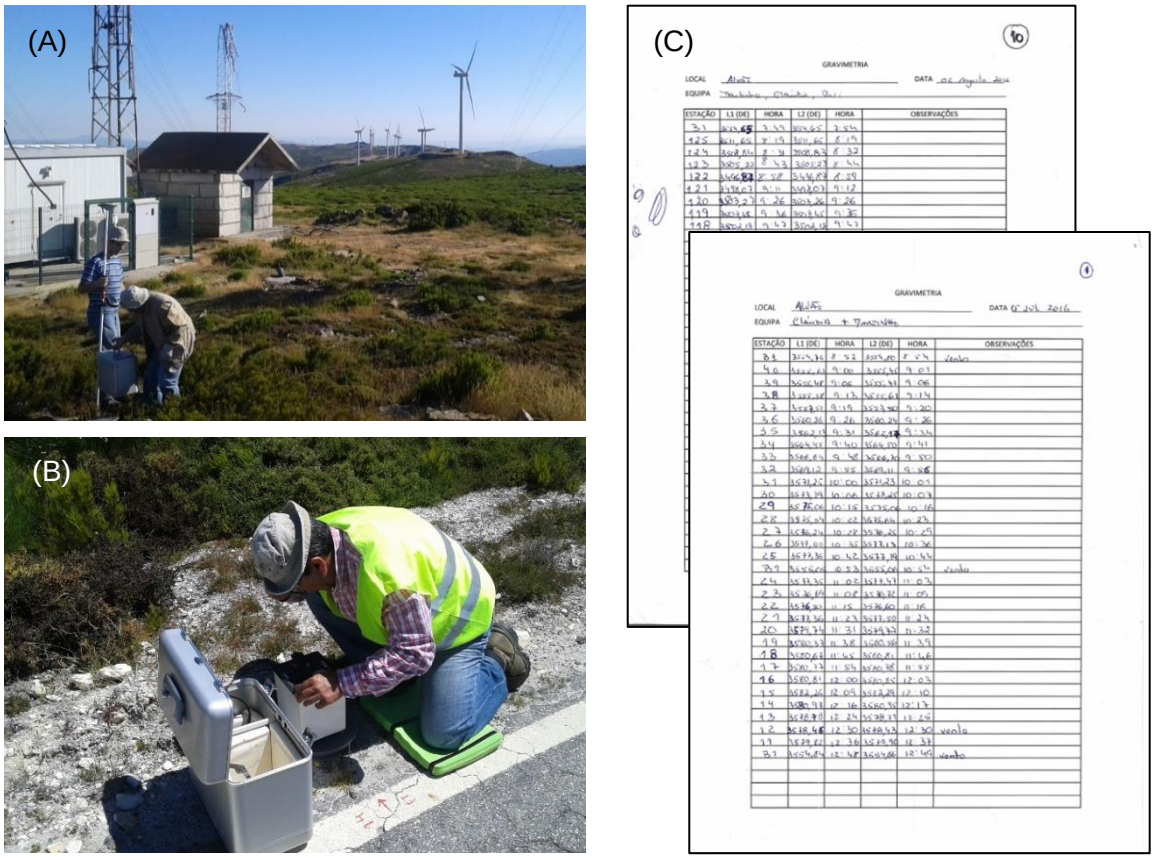


Figure 4-44. Fieldwork for gravimetric surveying: (A) DGPS and gravimeter equipment; (B) Aquisition data using the gravimeter *LaCoste & Romberg G1054*; (C) Examples of fieldwork annotations.

CALIBRATION TABLE FOR G-1054

MILLIGAL VALUES FOR LACOSTE & ROMBERG, INC. MODEL G GRAVITY METER

COUNTER READING*	VALUE IN MILLIGALS	FACTOR FOR INTERVAL	COUNTER READING*	VALUE IN MILLIGALS	FACTOR FOR INTERVAL
000	000.00	1.01017			
100	101.02	1.00995	3600	3634.32	1.01064
200	202.01	1.00977	3700	3735.38	1.01073
300	302.99	1.00963	3800	3836.46	1.01082
400	403.95	1.00951	3900	3937.54	1.01090
500	504.90	1.00942	4000	4038.63	1.01099
600	605.85	1.00934	4100	4139.73	1.01106
700	706.78	1.00927	4200	4240.83	1.01114
800	807.71	1.00921	4300	4341.95	1.01121
900	908.63	1.00916	4400	4443.07	1.01128
1000	1009.54	1.00912	4500	4544.20	1.01133
1100	1110.46	1.00908	4600	4645.33	1.01139
1200	1211.36	1.00905	4700	4746.47	1.01144
1300	1312.27	1.00901	4800	4847.61	1.01150
1400	1413.17	1.00899	4900	4948.76	1.01153
1500	1514.07	1.00899	5000	5049.92	1.01158
1600	1614.97	1.00901	5100	5151.07	1.01162
1700	1715.87	1.00905	5200	5252.24	1.01164
1800	1816.78	1.00908	5300	5353.40	1.01166
1900	1917.68	1.00914	5400	5454.56	1.01168
2000	2018.60	1.00920	5500	5555.73	1.01169
2100	2119.52	1.00927	5600	5656.90	1.01168
2200	2220.44	1.00934	5700	5758.07	1.01164
2300	2321.38	1.00942	5800	5859.23	1.01160
2400	2422.32	1.00949	5900	5960.39	1.01155
2500	2523.27	1.00956	6000	6061.55	1.01148
2600	2624.23	1.00966	6100	6162.69	1.01141
2700	2725.19	1.00975	6200	6263.84	1.01133
2800	2826.17	1.00984	6300	6364.97	1.01123
2900	2927.15	1.00994	6400	6466.09	1.01114
3000	3028.14	1.01004	6500	6567.21	1.01104
3100	3129.15	1.01013	6600	6668.31	1.01094
3200	3230.16	1.01024	6700	6769.40	1.01084
3300	3331.19	1.01034	6800	6870.49	1.01074
3400	3432.22	1.01045	6900	6971.56	1.01062
3500	3533.26	1.01055	7000	7072.62	

*Note: Right-hand wheel on counter indicates approximately 0.1 milligal

11-14-1994

DLP

Reading Line: 2.60 Temperature: 57.5 C

Figure 4-45. Calibration Table for the *LaCoste & Romberg* gravimeter model G-1054 (LaCoste & Romberg, 2004).

The readings in the Alvão area range between 3496.47 and 3687.83 divisions and were converted to mGal according to the following equations:

$$R_{mGal} = (R_d - 3400) \times 1.01045 + 3432.22 \quad \text{(equation 33)}$$

$$R_{mGal} = (R_d - 3500) \times 1.01055 + 3533.26 \quad \text{(equation 34)}$$

$$R_{mGal} = (R_d - 3600) \times 1.01064 + 3634.32 \quad \text{(equation 35)}$$

where R_{mGal} is the gravimetric reader of the gravimeter expressed in mGal and R_d is the reader of the gravimeter in divisions.

4.6.2 Gravity reductions

The gravity reductions were made manually, using an Excel sheet. For each gravimetric station, the drift and tidal correction have been applied. The drift is very low, usually having values lower than 0.1 mGal/s. After that, the absolute g_{obs} was calculated. In Alvão gravimetric survey, in addition to a base station – *Barragem* (gravimetric base used in all gravimetric paths, and located near the *Cimeira* dam) – an absolute gravimetric base station – *Caravelas* – was also used. The absolute gravity value in *Caravelas* is 979981.05 mGal (fig. 4-46).

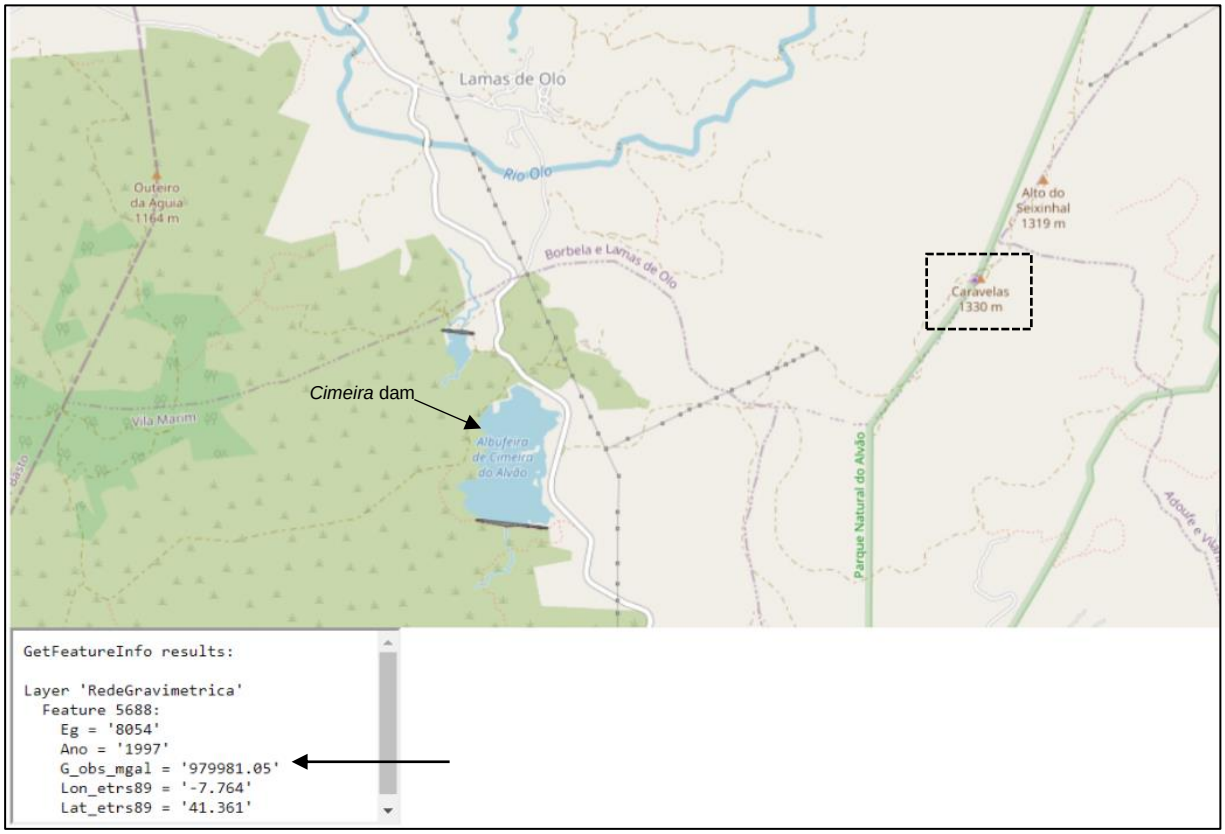


Figure 4-46. Print screen of *Rede Gravimétrica Nacional* in the *Direção-Geral do Território* site (Direção-Geral do Território, 2013c), where the absolute gravity value was obtained.

Then, the latitude and elevation (including free-air, Bouguer, and terrain) corrections were applied, and the Bouguer anomaly for each gravity station was found.

Regarding terrain corrections, two methods were used: (i) Hammer chart using an Excel sheet; and (ii) Script for *MatLab* software developed by Almeida *et al.* (2018).

For the corrections performed by Hammer chart, a digital terrain model obtained through the Triangulated Irregular Network (TIN) was used. TIN was interpolated in *ArcGIS* and created from the altimetric information published at a scale of 1: 25 000 (contour lines with an altimetric range of 10 m and quoted points). All interpolations were done directly on the TIN model, to avoid the generalizations that occur when digital elevation models (DEM) are changed to the raster models. On the other hand, in terrain corrections using *MatLab* script, a DEM 30 m x 30 m was used (EU-DEM, 2017).

The comparison between the two methods was made pointing out that both have high accuracy, with correlation R^2 equal to 0.979 (fig. 4-47).

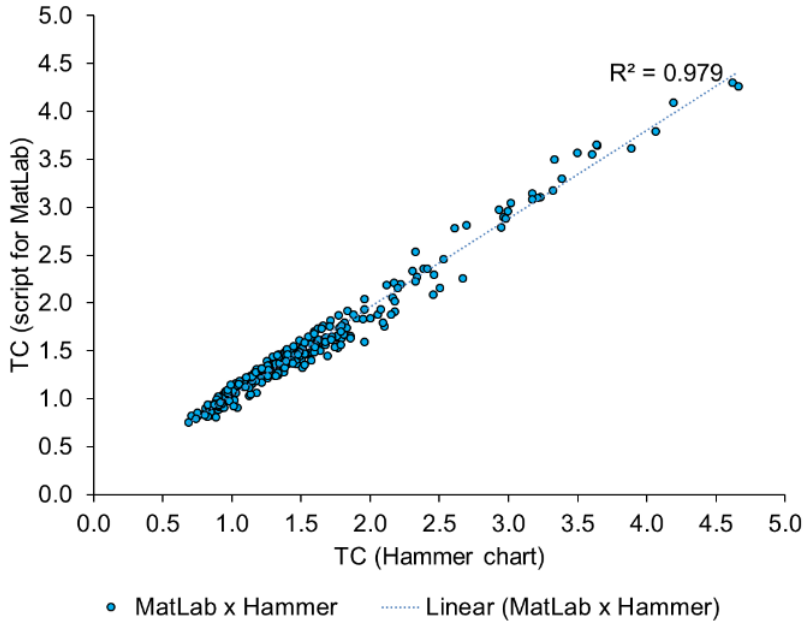


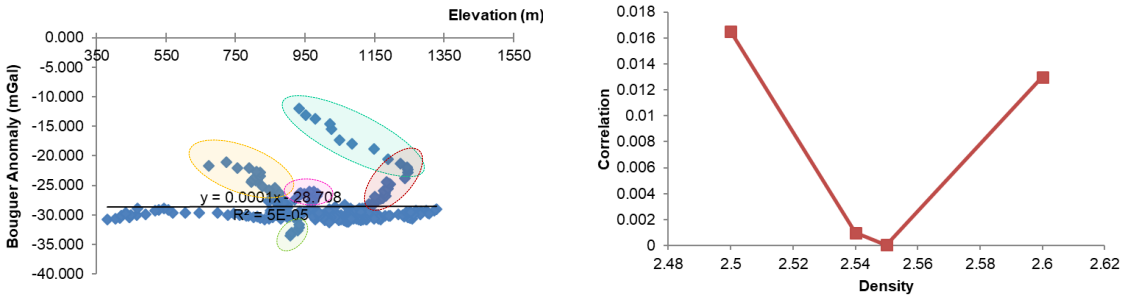
Figure 4-47. Correlation between the two methods used for terrain corrections (TC): Hammer chart *versus* script for *MatLab*.

For the acquisition of a complete Bouguer anomaly, the terrain corrections obtain by the traditional method (Hammer chart) were chosen.

4.6.3 Rock densities

The rock densities in the Alvão area were determined by both Nettleton and atmospheric pressure saturation method.

The rock density obtained by the Nettleton indirect method (Nettleton, 1939), was used to determine the Bouguer anomaly. In the Alvão area, the density calculated by Nettleton's method was 2.55 g/cm^3. However, some paths have a different pattern from the main trend (the colored circles in the plot of fig. 4-48).

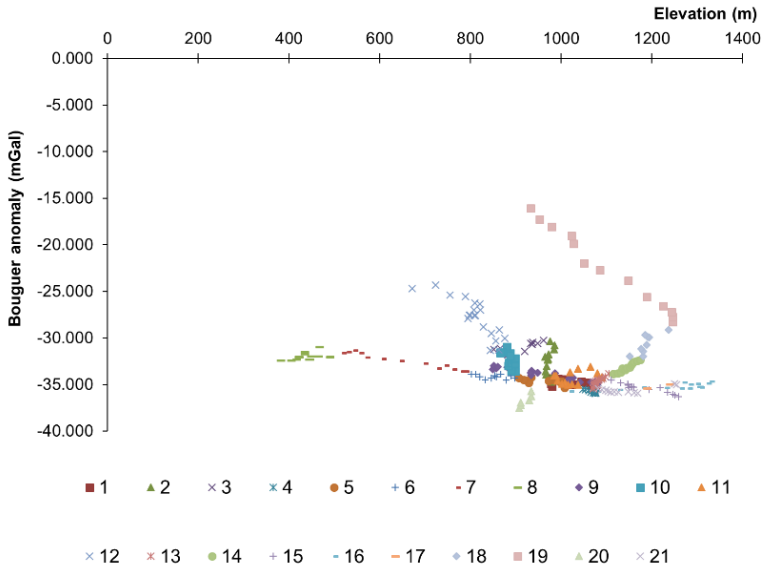


Density	R2
2.6	0.013
2.55	0.00005
2.54	0.001
2.5	0.0165

Figure 4-48. Density determination by Nettleton's method and mean value (d = 2.55 g/cm^3) for all the rocks in the Alvão studied area.

The studied area is very accidentally (the topography widely varies in a few meters) and many fault systems are recognized. The detected density anomalies may be due to the presence of lithologic contacts and faults. In order to minimize this noise, Nettleton's method was applied separately for each path and then, mean and median values were determined (fig. 4-49). The median value of 2.66 g/cm^3 was used in the Bouguer anomaly calculation.

(A)



(B)

Paths	Density
1	2.56
2	3.30
3	3.20
4	2.54
5	2.56
6	2.59
7	2.47
8	2.83
9	2.48
10	1.90
11	2.83
12	1.66
13	3.95
14	3.49
15	2.41
16	2.73
17 to 21	2.80
18	3.87
19	1.58
20	6.30
mean	2.90
median	2.66

(C)

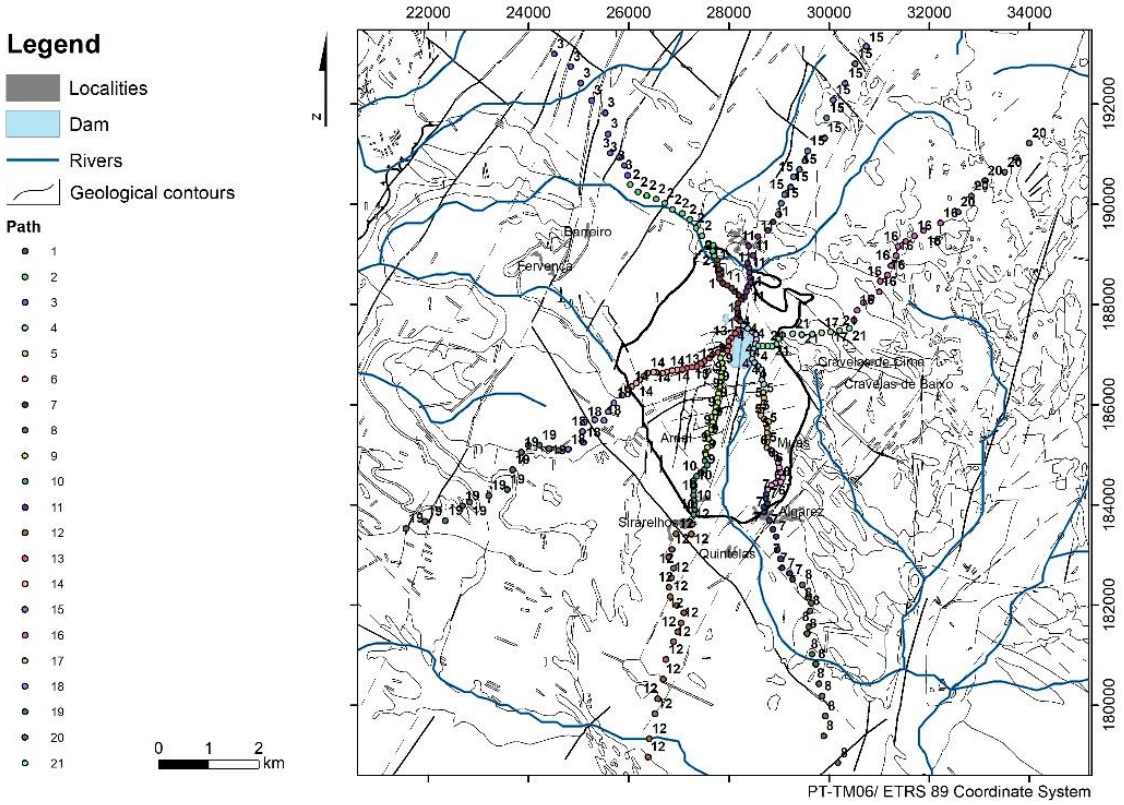


Figure 4-49. (A) Density determination by Nettleton's method for each path; (B) Mean and median values of density for the Alvão area; (C) Location of each path over the geological contour of LOP and host-rocks.

The apparent density of LOP and their host rocks was necessary to model the LOP granites through the *Oasis Montaj* software. The apparent density was determined in LNEG facilities (fig. 4-50) and the mean values are present in table 4-15 and attachment 4.

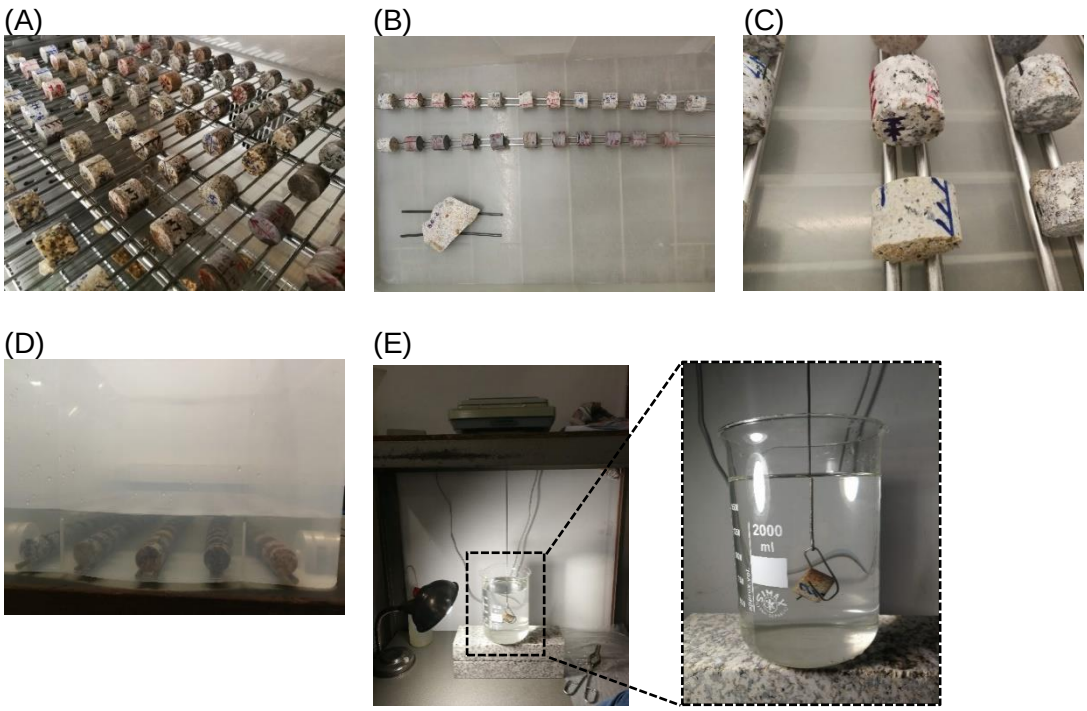


Figure 4-50. Rock density determination in the LNEG facilities: (A) Specimens in the ventilated oven; (B) Specimens placed on top of non-oxidizing and non-absorbent supports to minimize the contact between specimens and the surface of the container (this is important because during saturation all the specimen should be in contact with water; (C) Sample markings detail on the specimens at $^1/_2$ of its height and ¾ of its height; (D) Specimens immersed in water (the water surface is about 25 mm above the specimens' top); (E) Immersed weighing of a specimen.

Table 4-15. Density mean values obtained for each lithology.

Lithology	**Density (g/cm^3)**
Lamas de Olo granite	2.56
Alto dos Cabeços granite	2.58
Barragem granite	2.53
Granites from Vila Real Massif	2.50
Metasedimentary host rocks	2.74
Global mean values	2.58

4.6.4 Gravity anomalies

The gravimetric campaigns are an efficient way to identify discontinuities (faults and geological contacts), to establish the geometry and depth of intrusive rocks, and to infer about the granite feeder zone(s). The gravity anomalies maps were obtained through kriging interpolation using the *Oasis Montaj 8.3.3*.

Having all data georeferenced and the values of Bouguer anomaly for each gravimetric station calculated (using reduction density of 2.66 g/cm^3, obtained by Nettleton indirect method), the Bouguer anomaly map was obtained (fig. 4-51).

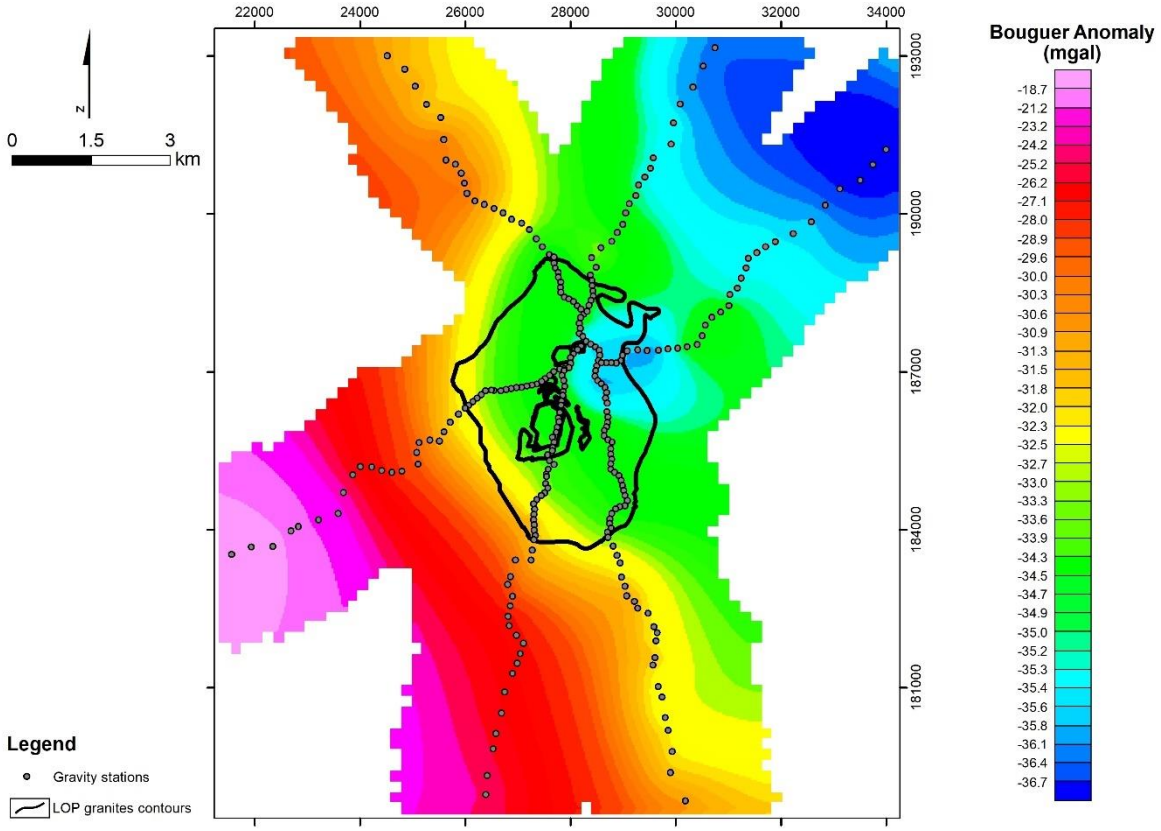


Figure 4-51. Bouger anomaly map (interpolation by kriging using the *Oasis Montaj* software).

The Bouguer anomaly in the studied area ranges between -37.53 mGal and -16.22 mGal, with a mean value of -31.27 mGal and a standard deviation equal to 4.663 mGal. The low negative anomalies are spatial correlated to the presence of granites (LOP granites and two-mica Vila Real granites), and the high values, mostly in the SW area, correspond to the presence of rocks that belongs to the DGM.

As mentioned above, the gravimetric anomalies include the overlap of regional and residual anomalies. Thus, it is necessary to remove the regional field in order to isolate the residual anomaly. The separation of the two anomalies was made using the spectral filtering methods, according to the polynomial adjustment, through the *Oasis Montaj* 8.3.3.

In the studied area, the regional anomaly was removed according to 1st, 2nd, and 3rd order polynomial surfaces (fig. 4-52), and the corresponding residual anomaly maps were obtained (fig. 4-53). In all regional anomaly maps, a regional NNE-SSW trend is observed, which increases from NNE to SSW.

Observing the 3 residual anomaly maps and analyzing them with geological knowledge (geological contacts, the shape of the LOP in outcrop, and faults), the residual anomaly map obtained through a 3rd order polynomial surface (fig. 4-54) is the model that best fits the surface of the Bouguer anomaly.

The selection of this map was due to:

- The line-zero of residual anomaly shows the best adjustment for the LOP outlines in the outcrop;
- The shape of the residual anomaly caused by LOP adjusts to the existing faults, namely the *ca*. N 150º to N 170º, and *ca.* N 10º to N 20º.

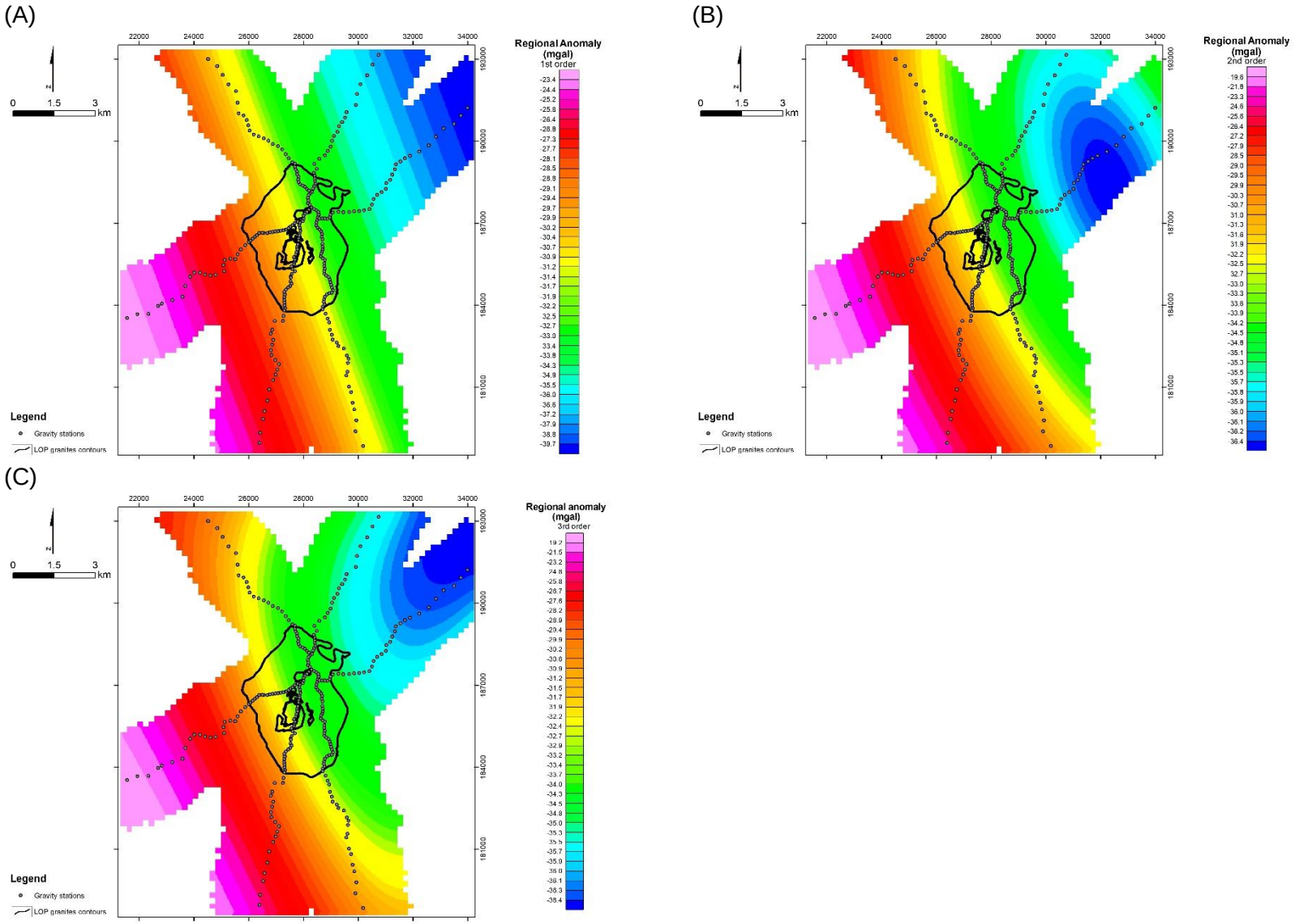


Figure 4-52. Regional anomaly maps according to: (A) 1st, (B) 2nd, and (C) 3rd order polynomial surfaces.

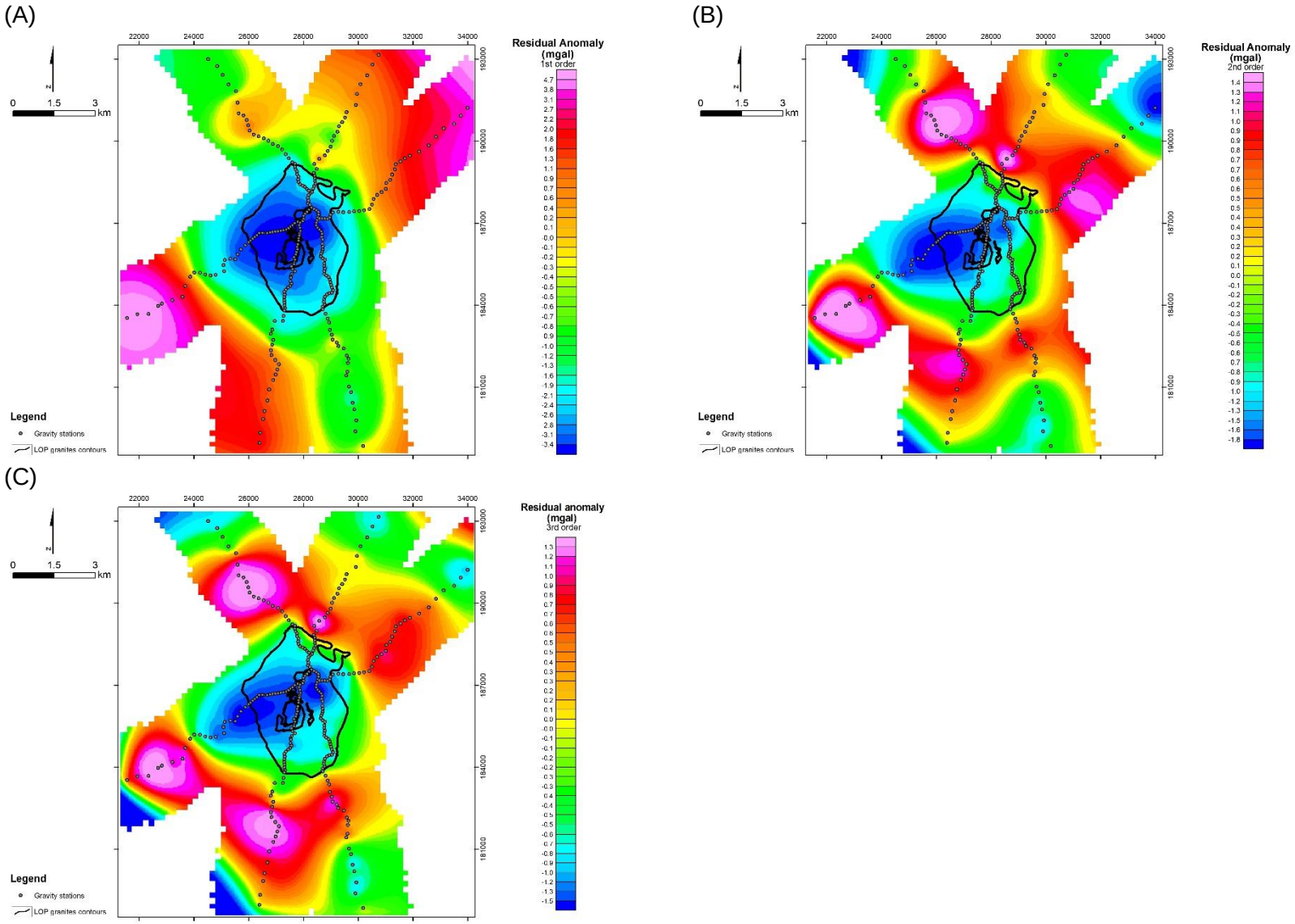


Figure 4-53. Residual anomaly maps according to: (A) 1st, (B) 2nd, and (C) 3rd order polynomial surfaces.

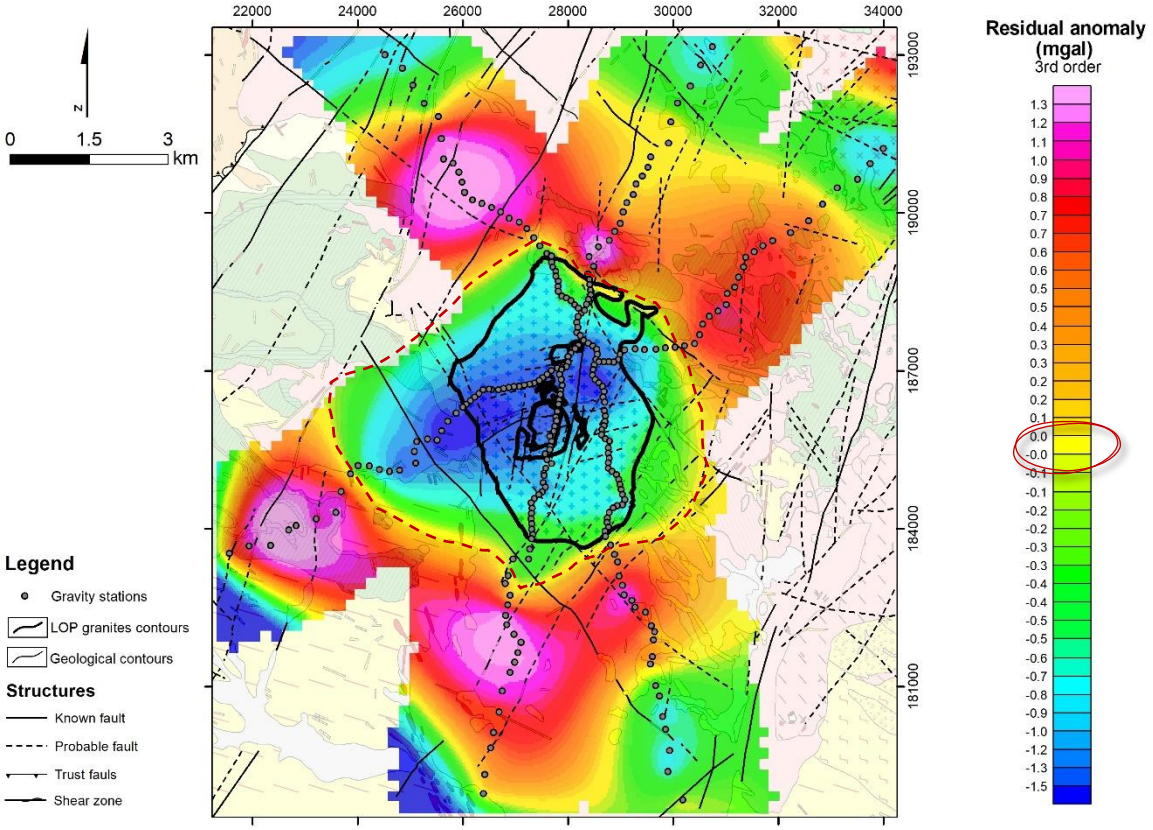


Figure 4-54. The selected residual anomaly map (3rd order) with geological contours and faults.

4.6.5 Modeling

The shape, depth, and emplacement model were inferred in different directions. Each model constitutes a possible solution for the geometry of the blocks that best represents the observed anomaly, considering the gravimetric data and all the additional information available. Thus, for the modeling, fieldwork observations, petrographic, geochemical, magnetic fabric, and cartographed lithologies and structures, were compiled with the information obtained through the residual anomaly map.

The lithologies and geological contacts both in outcrops and in-depth, as well as the visible and probable faults, are represented in the 2D models.

Figure 4-55 shows the profiles used to modeling the LOP granites, P1 was made along WSW-ENE direction, P2 was drawn along NNE-SSW direction, and P3 represents the section along NNW-SSE direction.

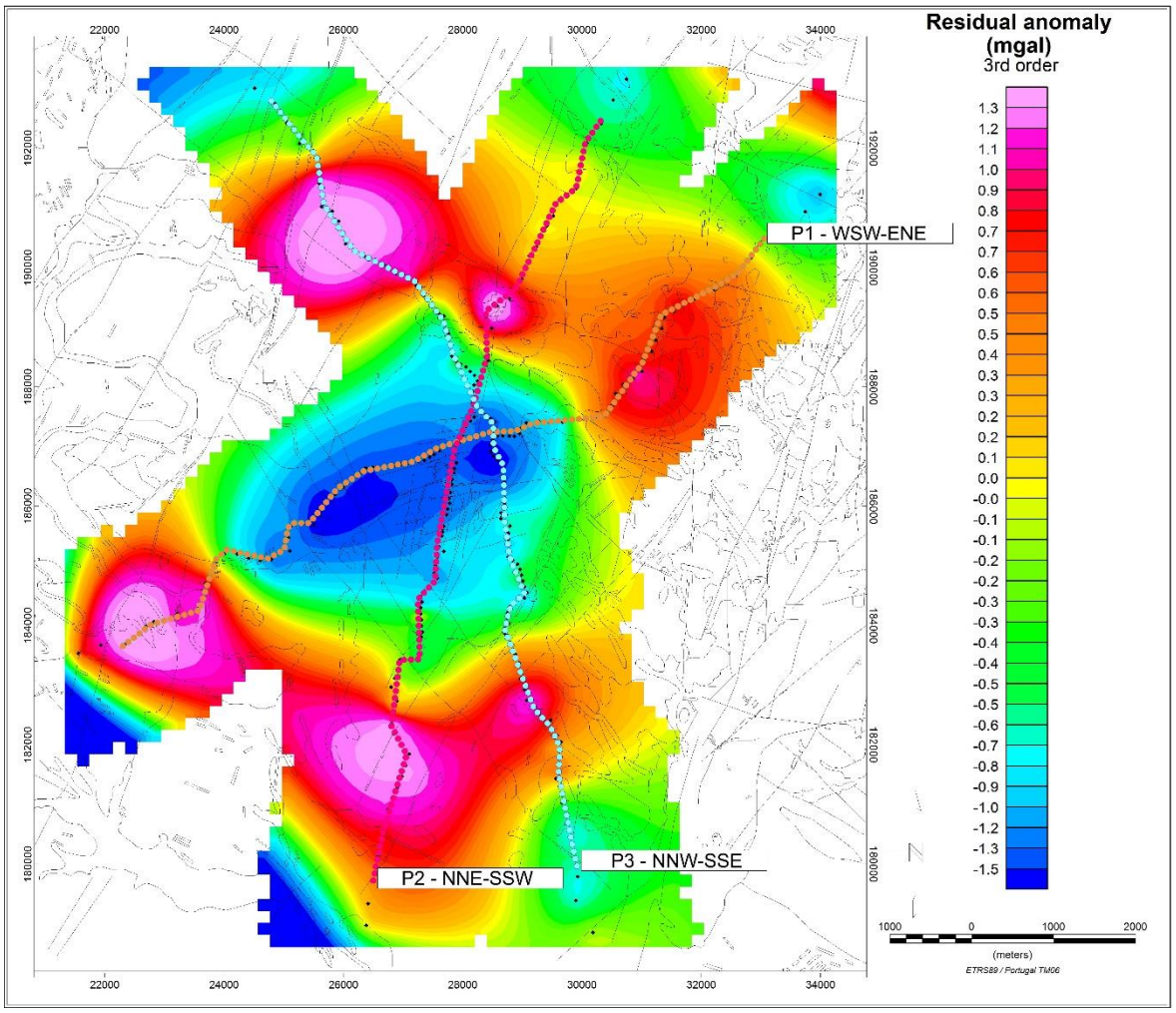


Figure 4-55. The location of the 3 gravimetric profiles (P1 –WSW-ENE, P2 – NNE-SSW, and P3 – NNW-SSE) used to infer the shape and the LOP emplacement model.

It should be noted that for the modeling, a precise density of each lithology was needed. However, due to the presence of 4 granites with similar density (LO, AC and BA granites from LOP, and hosted two-mica granites from VRM), the modeling was not straightforward.

- **Gravimetric survey through WSW-ENE direction**

Profile P1 – WSW-ENE (fig. 4-56) was drawn according to the ENE-WSW orientation to acquire information about the negative residual anomaly zone, which was interpreted as a feeder zone. This profile cuts the LO granite at the surface, and the other two granites were identified in depth. In this feeder zone, two individual feeder roots are identified. One of the feeder roots is located underneath the host rocks, in the western limit of the current LOP outcrop, suggesting that pluton has continuity, in deep, to the west. The other root is located

in the NE part of the pluton. The location of the feeder zone was inferred according to the lowest values of the residual anomaly as well as taken into account the local geological knowledge, namely the intersection of late-Variscan fault systems (WSW-ENE with both NNE-SSW and NNE-SSW). The interpretation of magnetic fabric, also helps in the feeder zone identification, once the magnetic lineations pattern suggests a WSW-ENE opening structure that allows a magma flow spreading to the NW at the north of the mentioned fault system, and spreading to the SE in the southern part of LOP.

This profile also shows the dominance of two-mica granites from Vila Real Massif in the area, outcropping mostly in the east of LOP. In the WSW, a higher positive residual anomaly was observed, indicating the presence of rocks with high density, belongs to the Douro Group Metasediments.

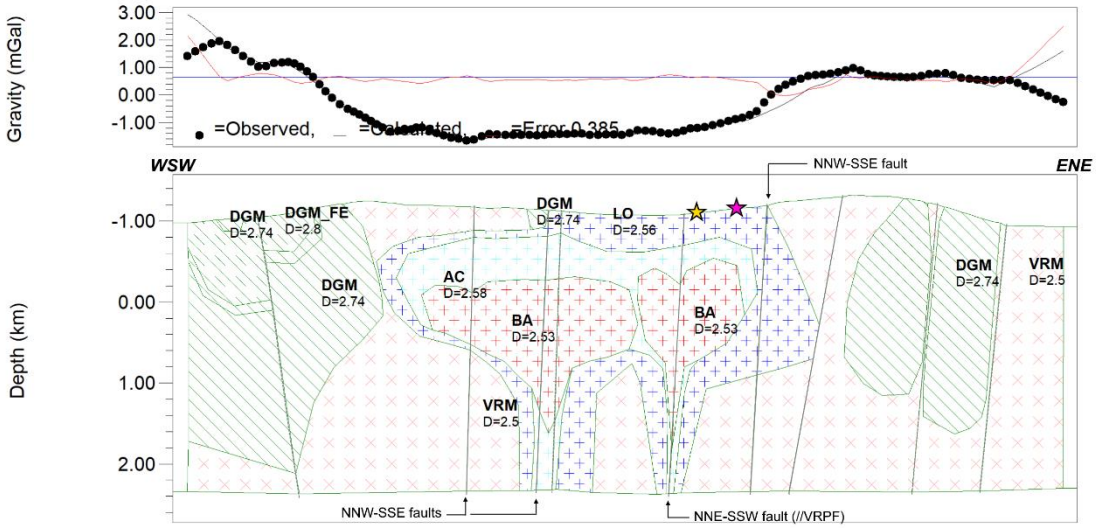


Figure 4-56. Observed and calculated anomaly and interpretative 2D model along the WSW-ENE direction (error *ca*. 0.385; the yellow and pink stars indicate the zone of intersection of P1 and P2, and P1 and P3, respectively); LO – Lamas de Olo granite; AC – Alto dos Cabeços granite; BA – Barragem granite; VRM – Vila Real Massif; DGM – Douro Group Metassediments.

- **Gravimetric survey through NNE-SSW direction**

Profile P2 – NNE-SSE (fig. 4-57) was drawn roughly parallel to the NNE-SSW fault, which is parallel to VRPF. This profile intersects P1 (yellow star in figs. 4-56 and 4-57) and cut all LOP granites at surface, allowing infer about their relations both in outcrop and in-depth. In profile P2, the second root identified in profile P1, is well defined, showing a main and two smaller conduits. These several conduits acted as channels to the ascent of the BA granite. This fact is also in agreement with field observations, which indicates that BA

outcrops as a thin band (*ca*. 1 km in width by 3 km in length) oriented *ca*. NNE-SSW (*ca*. N 10º) and parallel to VRPF. Field observations support the assumption that BA granite outcrops in 3 different areas (the larger outcrop is located in the center of LOP and the other two are located near to a Dam in the northern part of LOP). Furthermore, the geochemical analyses point out that BA is the most evolved and recent granite corroborating the gravimetric data which indicates that BA granite cut the other two LOP granites.

The host rocks cut by the P2 are dominantly two-mica granites and few outcrops of Douro Group Metasediments.

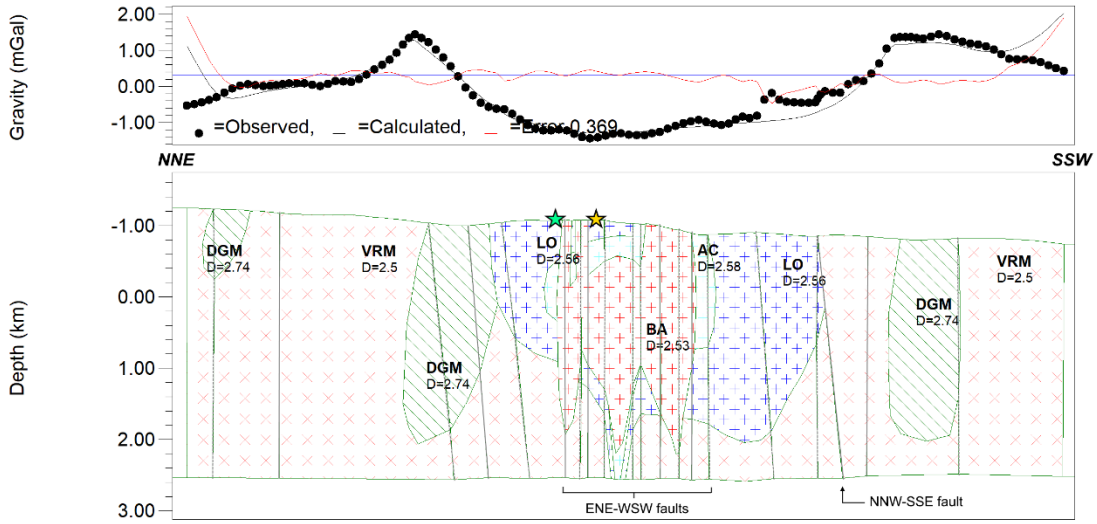


Figure 4-57. Observed and calculated anomaly and interpretative 2D model along the NNE-SSW direction (error *ca*. 0.369; the yellow and green stars indicate the zone of intersection of P2 and P1, and P2 and P3, respectively); LO – Lamas de Olo granite; AC – Alto dos Cabeços granite; BA – Barragem granite; VRM – Vila Real Massif; DGM – Douro Group Metassediments.

- **Gravimetric survey through NNW-SSE direction**

Profile P3 – NNW-SSE (fig. 4-58) was drawn along NNW-SSE direction, cutting the east part of LOP. This profile cuts the LO granite at the surface, and the other two granites are identified in depth. The LO and AC feeder roots are not visible in this section, once those roots are not crossed by the P3 (figs. 4-55 and 4-58). Only one of BA conduits, located along the NNE-SSW fault system (parallel to the VRPF) is visible in this section.

The host rocks cut by the P3 are dominantly the two-mica granites and one outcrop of Douro Group Metasediments. In the NNW zone of the studied area outcrops several quartz veins, however, these structures are not represented in the gravimetric profiles and this fact justifies the increased error on the left side of the gravimetric profile, in the gravity modeling.

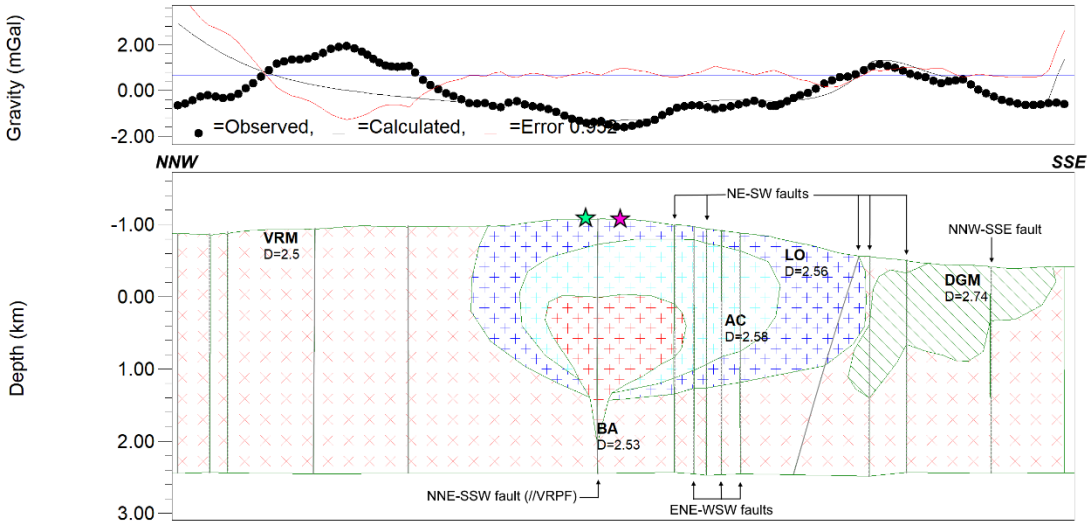


Figure 4-58. Observed and calculated anomaly and interpretative 2D model along the NNW-SSE direction (error *ca*. 0.952; the green and pink stars indicate the zone of intersection of P3 and P2, and P3 and P1, respectively); LO – Lamas de Olo granite; AC – Alto dos Cabeços granite; BA – Barragem granite; VRM – Vila Real Massif; DGM – Douro Group Metassediments.

- **Block diagram – 3D model**

Using the information obtained through inversion of gravimetric data, in other words, using the 2D models drawn along the profiles, a 3D model of LOP was inferred (fig. 4-59).

The 3D LOP model was drawn using two gravimetric profiles made through *Oasis Montaj* 8.3.3., namely P1 – WSW-ENE, and P2 – NNE-SSW.

Our model shows the presence of one feeder zone along ENE-WSW with two roots for the LO and AC granites and several conduits for the ascent of the BA granite. Our data also suggest that LOP belongs to the family of wedge-shaped plutons, having an asymmetric shape with a maximum thickness slightly higher than 2.5 km.

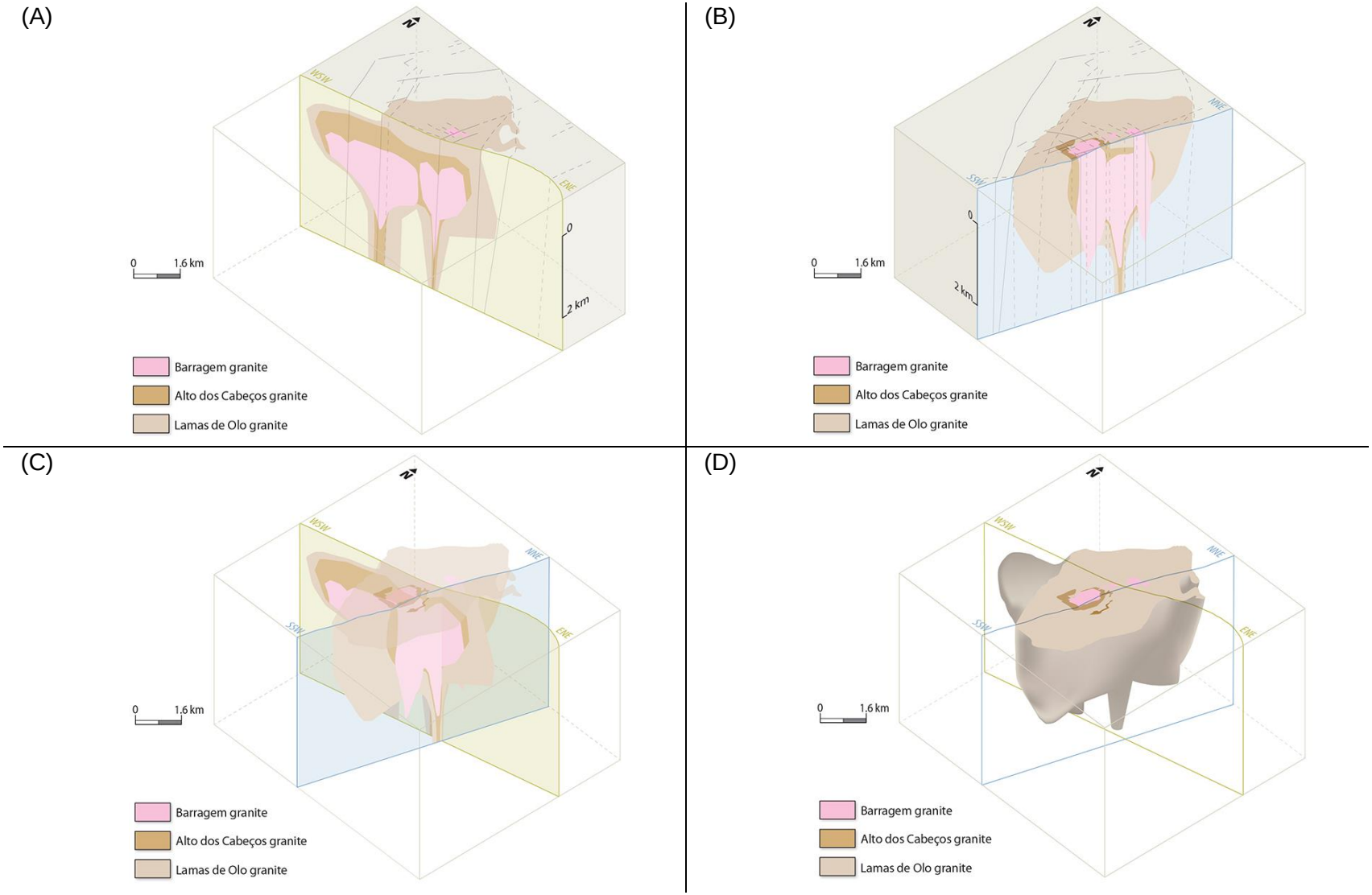


Figure 4-59. Block diagram of LOP: (A) LOP cutting section along WSW-ENE direction; (B) LOP cutting section along NNE-SSW direction; (C) LOP model interpretation according to the intersection of 2 profiles; (D) 3D model of LOP.

4.6.6 Highlights

The multidisciplinary study of LOP, particularly in view of the interpretation of magnetic fabric (structural data) and gravimetric residual anomaly (geophysical data), allows inferring the pluton geometry and its emplacement model, accordingly:

- The gravimetric study, namely the existence of a pronounced negative residual anomaly aligned approximately ENE-WSW (*ca.* N 80º), suggests that LOP feeding zone is located along a fracture zone in this same direction.
- The 3D model shows that the feeder zone, with ENE-WSW direction, extents to the western limit of the current LOP outcrop, suggesting that the pluton has continuity to the west underneath the host rocks. In this feeder zone, a root located in the intersection of NNW-SSE and ENE-SWS fault systems was identified.
- In the NE part of LOP another root was identified, with several conduits, in the intersection of the NNE-SSW (// VRPF) and ENE-WSW fault systems.
- The magnetic foliations are mostly subvertical with an NNW-SSE trend (*ca.* N 168º), pointing out the importance of this fracture system in the emplacement of the pluton. Magnetic foliations dipping to the east in the eastern of the pluton, and to the west in its western zone, materialize the importance of the NNW-SSE fractures during ascent and emplacement.
- The magmatic ascent of the two main granites (LO and AC granites) occurred along with the ENE-WSW fractures, with an NNW-SSE magmatic flow as showed by the magnetic lineations gently plunging to the north, in the north, and gently plunging to south, in the south of the pluton.
- The magnetic lineations are mostly subhorizontal or gently dipping, suggesting that the LOP feeder zone should be distant in-depth and its emplacement took place at high structural levels.
- LOP is an asymmetric body and belongs to the family of wedge-shaped plutons, having a maximum thickness slightly higher than 2.5 km.
- The proposed model for kinematics of ascending and emplacement of LOP enhances the main role of the intersection of late-Variscan faults (NNW-SSE with ENE-WSW, and NNE-SSW with ENE-WSW). Since no interference with the regional stress pattern was detected, magma ascending was passive through

opening fractures and controlled by magma pressure, and LOP is viewed as a true post-tectonic pluton.

- Studies carried out by *e.g.* Martins *et al*. (2009) described the emplacement model of Vila Pouca de Aguiar and Águas Frias plutons, both located in the Galicia Trás-os-Montes Zone, and related to the VRPF. Although the emplacement models of these two plutons are related to this main fault, they have different shapes: the Vila Pouca de Aguiar pluton was classified a thin laccolith type (~ 1 km) with several roots, and the Águas-Frias pluton belongs to the wedge-shaped family plutons with higher crustal expression (~ 5 km; Martins *et al*., 2009). In the Lamas de Olo region, the intersection of NNW-SSE with ENE-WSW, and of NNE-SSW with ENE-WSW fault systems, provided the opening and space to the ascending and building of an asymmetrical wedge-shape pluton, with several roots.

CHAPTER 5:

FINAL REMARKS

“The important thing is to never stop questioning.”
Albert Einstein

5 FINAL REMARKS

5.1 CONCLUSIONS

The general conclusions can be subdivided into 5 topics:

(i) Lamas de Olo Pluton is a composite body

LOP is constituted by 3 biotite granites: Lamas de Olo (LO), Alto dos Cabeços (AC), and Barragem (BA). The studied granites have a similar mineralogical composition (mostly composed of quartz, plagioclase, K-feldspars, and biotite) and are heterogranular with a porphyritic or slightly porphyritic texture, varying in their grain size (LO is medium- to coarse-grained granite, AC is fine- to medium-grained granite, and BA is a leucocratic fine- to medium-grained granite).

LOP granites are calc-alkaline to alkali-calcic, peraluminous granites. The REE spectra are flat for all granites, having a slight pronounced Eu anomaly in LO+AC granites and a pronounced Eu anomaly in BA granite.

The field observations, petrographic and geochemical data allows concluding that LO+AC granites are geochemically similar and were generated from the same magma source, and the BA is the most evolved granite with a different source.

(ii) Lamas de Olo Pluton is a heterogeneous pluton constituted by magnetite-type granites

Magnetic susceptibility data, as well as the detailed magnetic mineralogy studies (IRM, χ_{fD}%, and K_t *versus* T curves), allow classified the LOP facies as magnetite-type granites. However, the magnetic susceptibility has a heterogeneous distribution, having areas with high values ($K_m \geq 1000$ μSI), mostly along with ENE-WSW direction and in the SE area of LOP, and areas with low magnetic susceptibility ($K_m < 1000$ μSI) values.

The classification of LOP as magnetite-type granite is due to the existence of magnetite and/or Ti-poor magnetite in all granites, even in areas with low magnetic susceptibility values. The low values of the magnetic susceptibility are due to later oxidation, as a result of the circulation of post-magmatic fluids that occurs during the ascend and granite emplacement.

The oxidation process changes (total or partially) the primary magnetic mineralogy, namely magnetite, into hematite (martitization), which has a parasitic ferromagnetic behavior, causing the decrease of magnetic susceptibility.

(iii) Lamas de Olo Pluton has mineral occurrences of W-Mo, and minor amounts of Bi-Be-Sn, associated with their granites

The study of mineralized veins associated with LOP granites, as well as fieldwork observations, indicate the presence of wolframite (ferberite), scheelite, molybdenite, cassiterite, and bismuth. Small beryl crystals are also identified in the fieldwork. The mineral occurrences occur in association with the LOP granites, mostly in N 80º sub-vertical quartz veins, showing a spatial relation with the presence of pure magnetite. Our studies point out that LOP has W-Mo as well as some amounts of Bi, Be, and Sn mineralizations associated with their granites.

Establish a relationship with LOP and other post-tectonic plutons, namely Peneda-Gerês, and Lavadores-Madalena, it is possible to conclude that all plutons have an identical mineral association. Furthermore, all these plutons have magnetite as accessory minerals, which attest to the existence of oxidative conditions in the magma chamber. Thus, the presence of magnetite is an important metallogenic indicator of the W-(Mo, Bi) mineralizations. Our studies point out that magnetic mineralogy can be a useful pathfinder for the W-Mo mineralizations in the Iberian Peninsula.

Lamas de Olo and Peneda-Gerês plutons have another similarity, once both are composed of biotite and by evolved leucocratic granites. In both cases, the emplacement of the leucocratic granites culminated the processes of ore concentration related to the successive granite intrusions, during the composite plutons formation.

The LOP modeling shows that the pluton, despite its small-expression in outcrops (with an area *ca*. 13.7 km^2), has a high volume at subsurface. Beyond that, the presence of mineralizations should be related to convective circulation generated by the heat of several granite intrusions (LOP is constituted by 3 granites from two different sources), culminated by the BA emplacement. The 2D and 3D models also point out the importance of the intersection of several late-Variscan fault systems, where two of them, namely the structures *ca.* N 80º and *ca.* N 10º are both related to the LOP granites emplacement and the occurrence of mineralized veins (quartz and/ or aplite mineralized veins are mainly N 80º and N 10º).

(iv) The emplacement of the Lamas de Olo Pluton was controlled by the intersection of ENE-WSW fault system with NNW-SSE and NNE-SSW structures

The magnetic fabric points out that *ca*. NNW-SSE magma flow was controlled by structures with the same trend, NNW-SSE (N 155º ± 15º). The ENE-WSW (N 80º ± 20º) trend is indicated by the pattern of the lineations plunge, dipping to NNW in the north of LOP, and dipping to the SSE in the south part of LOP. This pattern suggests that in the center of the LOP, ENE-WSW opening structures provided the space for magma ascending, with NNW-SSE magmatic flow controlled by regional structures.

The magnetic fabric suggests that LOP emplacement was mainly conditioned by NNW-SSE and ENE-WSW Variscan systems rather than related to the NNE-SSW (N 25º ± 25º) structures which are subparallel to VRPF. The subvertical magnetic foliations and subhorizontal magnetic lineations also suggest that during magma ascent the faults acted as strike-slip faults and its movement was recorded in the magnetic fabric pattern.

AMS and AARM tensors are coaxial when all the granitic samples from LOP are considered. This coaxiality, means that the AMS can be safely used in heterogeneous and complex magnetite-type plutons with both high and low magnetic susceptibility values. On the other hand, the partial coaxiality observed in the granite set with low magnetic susceptibility is due to martitization, which altered the magnetite into hematite. The presence of this pseudomorph (martite) may justify the non-coaxility linear fabrics.

(v) Lamas de Olo Pluton is a wedge-shaped pluton with asymmetric shape, having maximum thickness ca. 2.5 km and a feeder zone along ENE-WSW direction with several roots

The interpretation of all data (cartographic, petrographic, magnetic fabric, geochemical, and gravimetric studies) suggests the existence of one feeder zone along the ENE-WSW direction. The magma ascending took place mostly at the intersection of NNW-SSW and ENE-WSW fault systems. Magmatic flow has spread to the west of the actual LOP outcrop, underneath the host rocks. The BA granite ascent is spatially related to the NNE-SSW fault systems and cuts the LO and AC granites. The gravimetric modeling points out the presence of two roots for LO and AC granites, and several conduits for the BA granite. LOP has an asymmetric shape with a maximum thickness slightly higher than 2.5 km and is a wedge-shaped pluton.

The essentially magmatic microstructures indicated that no interference with the regional stress pattern was detected, magma ascending was passive through opening fractures and controlled by magma pressure and LOP is viewed as a true post-tectonic pluton.

5.2 FURTHER WORKS

The interpretation of the data obtained in this study points out some issues that could be clarified through the realization of new fieldwork campaigns and the use of other techniques. The further works are listed below:

- ***Petrographic studies of fluid inclusion planes***

  Although the LOP granites are post-tectonic, some fluid inclusion planes are observed under the microscope. The study of the direction of these microstructures will contribute to the knowledge about the stress field evolution during the emplacement of granites.

- ***Acquisition of more data about the anisotropy of magnetic remanence***

  The complexity in the magnetic mineralogy of LOP granites deserved further studies, namely the anisotropy of partial anhysteretic remanence studies, in order to isolate the fabric contribution of the remanence bearing grains (magnetite) and the fabric due to the paramagnetic fraction. Furthermore, this technique allows inferring about magnetic grain sizes.

  Additionally, several samples from LOP granites, as well as from Lavadores-Madalena pluton (post-tectonic and magnetite-type granite; located in CIZ, in north Portugal; *ca*. 280 Ma; Martins *et al*., 2011) and Santa Eulália Plutonic Complex (late- to post-tectonic and magnetite-type granite; located in Ossa-Morena Zone, in SE Portugal; *ca*. 290 Ma; Sant'Ovaia *et al*., 2014), were already sent to Professor William McCarthy from the University of St. Andrews (United Kingdom), in order to obtain more AARM data.

- ***Acquisition of out-of-phase AMS measurements***

  The acquisition of out-of-phase AMS (opAMS) and in-phase AMS (ipAMS) data separately allows obtaining more information about the magnetic mineralogy present in

rock specimens. The opAMS reflects a fraction of the ferromagnetic *s.l.* minerals (*e.g*. SD magnetite, titanomagnetite, hematite), and several studies were been made to the determination of magnetic subfabrics of some minerals (Hrouda *et al*., 2017), and to infer about magnetic granulometry (Hrouda *et al*., 2013, 2018). In the study case, the main goals will be: verify if the normal AMS (ipAMS) differs from the opAMS results, and establish a comparison between the maximum (K_{max}), and the minimum (K_{min}) axis of opAMS and AARM, to obtain more information about the fabric (magnetic foliations and lineations) of ferromagnetic minerals.

Several subspecies of LOP, Lavadores-Madalena pluton, and Santa Eulália Plutonic Complex, were already sent to Professor William McCarthy from the University of St. Andrews (United Kingdom), in order to obtain opAMS data.

- ***Acquisition of low-temperature AMS measurements***

The room temperature AMS data results from the bulk contribution of all rock-forming minerals regardless of their magnetic behavior. On the other hand, the low-temperature AMS (LT-AMS), which samples are immersed in liquid nitrogen for 30 minutes, allows investigating the paramagnetic subfabric (*e.g*. Olivia-Urcia *et al.*, 2009).

- ***Stable isotopes studies***

Stable sulfur and oxygen isotopes studies in mineralizations can provide information about their sources. To perform these studies, more fieldwork will be made to collect more mining waste samples.

- ***Perform magnetic surveys***

The modeling of LOP granites was difficult due to the low difference in densities between the 3 LOP granites, as well as between them and the host rocks (granites from Vila Real Massif). A magnetic survey will precise and restrain the LOP modeling.

REFERENCES

REFERENCES

Abrajevitch, A. & Kodama, K. (2011). Diagenetic sensitivity of paleoenvironmental proxies: A rock magnetic study of Australian continental margin sediments. Geochemistry, Geophysics, Geosystems, 12: Q05Z24.

Actlabs. (2020). Geochemistry: Lithogeochemistry and whole rock analysis: https:// https://actlabs.com/. Accessed on 9th of January of 2020.

AGICO. (2019). Manuals and AGICO prints: https://www.agico.com/. Accessed on 20th of February of 2019.

Albuquerque, C.A.R. (1971). Petrochemistry of a series of granitic rocks from northern Portugal. Geological Society of America Bulletin, 82: 2783-2798.

Almeida, A., Leterrier, J., Noronha, F. & Bertrand, J.M. (1998). U-Pb zircon and monazite geochronology of the Hercynian two mica granite composite pluton of Cabeceiras de Basto (Northern Portugal). Comptes rendus de l'Académie des Sciences, Paris, 326: 779-785.

Almeida, F., Matias, M., Lourenço, M. & Martins, A. (2018). A MatLab Script to Perform Gravity Terrain Corrections using DEM-EU Digital Elevation Model in a Teaching Lab. Conference & Exhibition Near Surface Geoscience (EAGE), 5 pp.

Altamimi, Z. & Boucher, C. (2001). The ITRS and ETRS89 Relationship: New Results from ITRF2000. Report on the Symposium of the IAG Subcommission for Europe (EUREF), Dubrovnik: http://www.euref.eu/symposia/book2001/1_3.pdf. Accessed on 19th of September of 2019.

Améglio, L., Vigneresse, J.L. & Bouchez, J.L. (1997). Granite pluton geometry and emplacement mode inferred from combined fabric and gravity data. In: Granite: From Segregation of Melt to Emplacement Fabrics (eds. Bouchez, J.L., Hutton, D.H.W., Stephens, W.E.), Kluwer Academic Publishers, 199–214.

Antunes, I.M.H.R. (2019). Características geoquímicas e geocronológicas do plutão de Fundão – implicações geotectónicas. Livro de atas do XII Congresso Ibérico de Geoquímica, XX Semana da Geoquímica, 133-136.

Antunes, I.M.H.R., Neiva, A.M.R., Silva, M.M.V.G. & Corfu, F. (2008). Geochemistry of S-type granitic rocks from the reversely zoned Castelo Branco pluton (central Portugal). Lithos, 103: 445-465.

Arancibia, O.N. & Clark, A.H. (1996). Early magnetite-amphibole-plagioclase alteration-mineralization in the Island Copper porphyry copper-gold-molybdenum deposit. Economic Geology, 91: 402-438.

Aranguren, A., Tubia, J., Bouchez, J.L. & Vigneresse, J.L. (1996). The Guitiriz granite, Variscan belt of northern Spain: extension-controlled emplacement of magma during tectonic escape. Earth and Planetary Science Letters, 139(1-2): 165-176.

Arthaud, F. & Matte, Ph. (1975). Les décrochements Tardi-Hercyniens du Sud-ouest de l'Europe. Géometrie et essai de reconstitution des conditions de la déformation. Tectonophysics, 25: 139-171.

Baertschi, P. (1976). Absolute ^{18}O Content of Standard Mean Ocean Water. Earth and Planetary Science Letters, 31: 341-344.

Ballouard, C., Poujol, M., Boulvais, P., Branquet, Y., Tartèse, R. & Vigneresse, J.L. (2016). Nb-Ta fractionation in peraluminous granites: A marker of the magmatic-hydrothermal transition. Geological Society of America, 4 pp.

Beane, R.E. & Bodnar, R.J. (1995). Hydrothermal fluids and hydrothermal alterations in porphyry copper deposits. In: Porphyry copper deposits of the American Cordillera (eds. Pierce, F.W., Bohm, J.G.), Arizona Geol Soc Digest, 20: 83-93.

Biedermann, A.R. (2018). Magnetic Anisotropy in Single Crystals: A Review. Geosciences, 8, 302: 16 pp.

Blevin, P.L. & Chappell, B.W. (1992). The role of magma sources, oxidation states and fractionation in determining the granite metallogeny of eastern Australia. Trasactions of the Royal Society of Edinburgh-Earth Sciences, 83: 305-316.

Borradaile, G.J. (1988). Magnetic susceptibility, petrofabrics and strain (review). Tectonophysics, 156: 1-20.

Bouchez, J.L. (1997). Granite is never isotropic: an introduction to AMS studies of granitic rocks. In: Granite: from melt to emplacement fabrics (eds. Bouchez, J.L., Hutton, D.H.W. & Stephens, W.E.), Kluwer Academic Publishers, 95-112.

Bouchez, J.L. (2000). Magnetic susceptibility anisotropy and fabrics in granites. Comptes Rendus de l'Académie des Sciences de la Terre et des planètes - Earth and Planetary Science, 330(1): 1-14.

Boynton, W.V. (1984). Cosmochemistry of the rare earth elements: meteorite studies. In: Rare Earth Element Geochemistry (eds. Henderson, P.), Elsevier, 63-114.

Butler, R.F. (2004). Paleomagnetism: magnetic domains to geologic terranes. Electronic edition, 158 pp.

Capdevila, R. & Floor, P. (1970). Les différents types de granites hercyniens et leur distribution dans le nord ouest de l'Espagne. Boletin Geologico y Minero de España, 81(2/3): 215-225.

Capdevila, R., Corretgé, L.G. & Floor, P. (1973). Les granitoïdes Varisques de la Méséta Ibérique. Bil. Soc. Géol. de France, 80: 209-228.

Castiñeiras, P., Villaseca, C., Barbero, L. & Martín Romera, C. (2008). SHRIMP U-Pb zircon dating of anatexis in high-grade migmatite complexes of Central Spain: implications in the Hercynian evolution of Central Iberia. International Journal of Earth Sciences, 97: 35-50.

Castro, A. (1987). On granitoid emplacement and related structures. A review. Geologische Rundschau, 76(1): 101-124.

Chadima, M. & Jelinek, V. (2019). Anisoft 5.1.03: Advanced Treatment of Magnetic Anisotropy Data (for windows). AGICO. Inc, Brno.

Chappell, B.W. & White, A.J.R. (1974). Two contrasting granite types. Pacific Geology, 8: 173-174.

Chappell, B.W. & White, A.J.R. (2001). Two contrasting granite types: 25 years later. Australian Journal of Earth Sciences, 48: 489-499.

Cheilletz, A. & Giuliani, G. (1982). Role de la Deformation du Granite dans la Genese des Episyenites Feldspathiques des Massifs de Lovios-Geres (Galice) et des Zaer (Maroc Central). Mineralium Deposita, 17(3): 387-400.

Clemens, J.D. & Mawer, C.K. (1992). Granitic magma transport by fracture propagation. Tectonophysics, 204(3-4): 339-360.

Cobbing, J. (2000). The geology and mapping of granite batholiths. Lecture notes in earth sciences, vol. 96. Springer, Berlin, 141 pp.

Coleman, D.S., Bartley, J.M., Glazner, A.F. & Pardue, M.J. (2012). Is chemical zonation in plutonic rocks driven by changes in source magma composition or shallow-crustal differentiation? Geosphere, 8: 1568-1587.

Corrêa-Ribeiro, H. (2018). Génese e cinemática de instalação do plutão granítico de Valpaços. Ph.D. thesis (published thesis), Universidade do Porto, Portugal, 196 pp.

Corretgé, L.G., Ugidos & J.M., Martinez, F.J. (1974). Les series granítiques varrisques du secteur Centre-Occidental Espagnol. In: La Chain Varisque d'Europe Moyenne et Occidentale. Colloque Int. CNRS Rennes, 243: 453-461.

Cottard, F. (1979). Pétrologie structurale et métallogénie du Complexe Granitique de Lovios Geres. Le modèle de mise en place de la mine de Las Sombras (Sn-W-Mo-Bi) (Sud Galice – Espagne). PhD thesis (published thesis), Universite de Nancy I, France, 243 pp.

Cruz, C., Sant'Ovaia, H. & Noronha, F. (2020). Magnetic mineralogy of Variscan granites from northern Portugal: an approach to their petrogenesis and metallogenic potential. Geologica Acta 18(5): 1-20.

D'Lemos, R.S., Brown, M. & Strachan, R.A. (1992). Granite magma generation, ascent and emplacement within a transpressional orogen. Journal of the Geological Society Lodon, 149(4): 487-490.

Dallmeyer, R.D., Martínez Catalán, J.R., Arenas, R., Gil Ibarguchi, J.I., Gutiérrez-Alonso, G., Farias, P., Bastida, F. & Aller, J. (1997). Diachronous Variscan tectonothermal activity in the NW Iberian Massif: evidence from $^{40}Ar/^{39}Ar$ dating of regional fabrics. Tectonophysics, 277: 307-337.

Day R., Fuller M. & Schmidt V.A. (1977). Hysteresis properties of titanomagnetites: grain size and compositional dependence. Earth Planetary Sciences Letter, 13: 260-267

De La Roche, H., Leterrier, J., Grandclaude, P. & Marchal M. (1980). A classification of volcanic and plutonic rocks using R1R2 - diagram and major element analyses - its relationships with current nomenclature. Chemical Geology, 29: 183-210

Dearing, J.A., Dann, R.J.L., Hay, K., Lees, J.A., Loveland, P.J., Maher, B.A. & O'Grady, K. (1996). Frequency-dependent susceptibility measurements of environmental materials. Geophysical Journal International, 124: 228-240.

Debon, F. & Le Fort, P. (1983). A chemical-mineralogical classification of common plutonic rocks and associations. Transactions of the Royal Society of Edinburgh Earth Sciences, 73: 135-149.

Debon, F. & Le Fort, P. (1988). A cationic classification of common plutonic rocks and their magmatic associations: principles, method, applications. Bulletin de Minéralogie, 111: 493-511.

Dekkers, M.J. (1989). Magnetic properties of natural pyrrhotite. II. High- and low-temperature behaviour of Jrs and TRM as function of grain size. Physics of the Earth and Planetary Interiors, 57: 266-283.

Dias, G. (2001). Fontes de Granitóides Hercínicos da Zona Centro-Ibérica (Norte de Portugal): evidências isotópicas (Sr, Nd). Memórias Academia das Ciências-Lisboa, tomo XXXIX, 121-143.

Dias, G., Leterrier, J., Mendes, A., Simões, P., Bertrand, & J.M. (1998). U-Pb zircon and monazite geochronology of syn- to post-tectonic Hercynian granitoids from the Central Iberian Zone (Northern Portugal). Lithos, 45: 349-369.

Dias, G., Noronha, F., Almeida, A., Simões, P.P., Martins, H.C.B. & Ferreira, N. (2010). Geocronologia e petrogénese do plutonismo tardi-Varisco (NW de Portugal): síntese e inferências sobre o processo de acreção e reciclagem crustal na Zona Centro-Ibérica. In Geologia Clássica, Volume I - Ciências Geológicas: Ensino, Investigação e sua História. Geologia Clássica (eds. Cotelo Neiva, J.M., Ribeiro, A., Victor, M., Noronha, F. & Ramalho, M.), Escolar Editora, 143-160.

Díez Fernández, R., Arenas, R., Pereira, M.F., Sánchez Martínez, S., Albert, R., Martín Parra, L.M., Rubio Pascual, F.J. & Matas, J. (2016). Tectonic evolution of Variscan Iberia: gondwana–Laurussia collision revisited. Earth-Science Reviews, 162: 269-292.

Direção-Geral do Território. (2013a). Cartografia e Geodesia - Carta Administrativa Oficial de Portugal (versão 2018): http://www.dgterritorio.pt/cartografia_e_geodesia/cartografia/carta_administrativa_oficial_de_portugal_caop/. Accessed on 10th of October of 2019.

Direção-Geral do Território. (2013b). Cartografia e Geodesia - PT-TM06/ETRS89 - European Terrestrial Reference System 1989: http://www.dgterritorio.pt/cartografia_e_geodesia/geodesia/sistemas_de_referencia/portugal_continental/pt_tm06_etrs89___european_terrestrial_reference_system_1989_2/. Accessed on 9th of September of 2019.

Direção-Geral do Território. (2013c). Rede Nacional de Gravimetria: http://mapas.dgterritorio.pt/geodesia/geodesiaredegravimetricawms.html. Accessed on 26th of September of 2018.

Dunlop, D.J. & Özdemir, Ö. (1997). Rock magnetism: fundamentals and frontiers. Cambridge University Press, Cambridge, 573 pp.

El Bouseily, A.M & El Sokkary, A.A. (1975). The relation between Br, Ba and Sr in granitic rocks. Chemical Geology, 16: 207-219.

Ellwood, B.B. & Wenner, D.B. (1981). Correlation of magnetic susceptibility with $^{18}O/^{16}O$ data in late orogenic granites of the southern Appalachian Piedmont. Earth and Planetary Science Letters, 54: 200-202.

ESA. (2019). Applications: The Earth's gravity field (geoid): https://www.esa.int/ESA_Multimedia/Images/2005/04/The_Earth_s_gravity_field_geoid#.XgZIlMI0ERE.link. Accessed on 27th of December of 2019.

ESRI. (2019). Differential GPS Explained: https://www.esri.com/news/arcuser/0103/differential1of2.html. Accessed on 9th of September of 2019.

EU-DEM. (2017). Copernicus Land Monitoring Service - Data Prod-ID: DAT-193-en. https://www.eea.europa.eu/data-and-maps/data/copernicus-land-monitoring-service-eu-dem. Accessed on 11st of September of 2019.

Evans, M.E. & Heller, F. (2003). Environmental Magnetism: Principles and Applications of Enviromagnetics. Academic Press, San Diego, California, 304 pp.

Farias, P., Gallastegui, G., González Lodeiro, L., Marquínez, J., Martín Parra, L.M., Martínez Catalán, J.R., Pablo Maciá, J.G. & Rodríguez Fernández, L.R. (1987). Aportaciones al conocimiento de la litoestratigrafia y estructura de Galicia Central, Memórias nº1, IX Reunião sobre a geologia do oeste peninsular. Museu Laboratório Mineralogia e Geologia-Faculdade de Ciências da Universidade do Porto, 1: 411-431.

Fernandes, S., Gomes, M., Teixeira, R. & Corfu, F. (2013). Geochemistry of biotite granites from the Lamas de Olo Pluton, northern Portugal. Geophysical Research Abstracts, EGU General Assembly, Vol. 15: https://meetingorganizer.copernicus.org/EGU2013/EGU2013-11566.pdf. Accessed on 22th of April of 2016.

Ferreira, N., Iglésias, M., Noronha, F., Pereira, E., Ribeiro, A. & Ribeiro, M.L. (1987). Granitóides da Zona Centro Ibérica e seu enquadramento geodinâmico. In: Geología de los Granitoides y Rocas Asociadas del Macizo Hesperico. Libro de Homenaje a L.C. García de Figuerola (eds. Bea, F., Carnicero, A., Gonzalo, J., Lopez Plaza, M. & Rodriguez Alonso, M.). Editorial Rueda, 37-51.

Font, E., Ernesto, M., Silva, P.F., Correia, P.B. & Nascimento, M.A.L. (2009). Palaeomagnetism, rock magnetism and AMS of the Cabo Magmatic Province, NE Brazil, and the opening of South Atlantic. Geophysical Journal International, 179: 905-922.

Font, E., Veiga-Pires, C., Pozo, M., Carvalho, C., Neto, A.C.S., Camps, P., Fabre, S. & Mirão, J. (2014). Magnetic fingerprint of southern Portuguese speleothems and implications for paleomagnetism and environmental magnetism. Journal of Geophysical Research: Solid Earth, 119: 7993-8020.

Franke, W. (1989). Variscan plate tectonics in Central Europe – current ideas and open questions. Tectonophysics, 169: 221-228.

Frost, B.R., Barnes, C.G., Collins, W.J., Arculus, R.J., Ellis, D.J. & Frost, C.D. (2001). A geochemical classification for granitic rocks. Journal of Petrology, 42: 2033-2048.

GeoPortal–LNEG. (2010a). Download de Cartografia Geológica, à escala 1:50 000: http://geoportal.lneg.pt/index.php?option=com_wrapper&view=wrapper&Itemid=60. Accessed on 9th of September of 2019.

GeoPortal–LNEG. (2010b). ArcGIS REST Services Directory: http://geoportal.lneg.pt/arcgis/rest/services. Accessed on 9th of September of 2019.

Gleizes, G, Nédélec, A, Bouchez, J.L., Autran, A. & Rochette, P. (1993). Magnetic susceptibility of the Mont-Louis-Andorra ilmenite-type granite (Pyrenees): a new tool for the petrographic characterisation and the regional maping of zoned granite plutons. Journal of Geophysical Research, 98:4317–4331

Gonçalves, A., Sant'Ovaia, H. & Noronha, H. (2019). Emplacement mechanism of Caria-Vila da Ponte Pluton (Northern Portugal): building and internal magmatic record. Journal of Structural Geology, 124: 91-111.

Gonçalves, J.A. (2009). Conversões de sistemas de coordenadas nacionais para ETRS89 utilizando grelhas. In: Actas da Conferência Nacional de Cartografia e Geodesia. VI CNCG: https://www.fc.up.pt/pessoas/jagoncal/coordenadas/paper_cncg2009.pdf. Accessed on 19th of September of 2019.

Gubbins. D. & Herrero-Bervera, E. (2007). Encyclopedia of Geomagnetism and Paleomagnetism. Springer-Verlag, New York, 1054 pp.

Gutiérrez-Alonso, G., Johnston, S.T., Weil, A.B., Pastor-Galán, D. & Fernández-Suárez, J. (2012). Buckling an orogen: The Cantabrian Orocline. GSA Today, Vol. 22(7): 4-9.

Hammer, S. (1939). Terrain corrections for gravimeter stations. Geophysics, 4 (3): 184-194.

Harris, N.B.W, Pearce, J.A. & Tindle, A.G. (1986). Geochemical characteristics of collision-zone magmatism. In: Collision Tectonics. Geological Society London (eds. Coward, M.P & Ries, A.C.). Special Publication, 19: 67-81.

Helal, B. (1992). Granitoïdes, granites à métaux rares et hydrothermalisme associe: géologie, minéralogie et géochimie de plusieurs suites tardi-hercyniennes (Nord du

Portugal). PhD thesis (published thesis), Ecole Nacionale Superieure des Mines de Saint-Etienne, France, 508 pp.

Hinze, W.J., Von Frese, R.R.B. & Saad, A.H. (2013). Gravity and Magnetic Exploration – Principals, practices and applications. Cambridge University Press, Cambridge, 512 pp.

Hrouda, F. (1982). Magnetic anisotropy of rocks and its application in geology and geophysics. Geophysical Surveys, 5: 37-82.

Hrouda, F., Pokorný, J., Jezek, J. & Chadima, M. (2013). Out-of-phase magnetic susceptibility of rocks and soils: a rapid tool for magnetic granulometry. Geophysical Journal Internation, 194: 170-181.

Hrouda, F., Chadima, M., Jezek, J. & Pokorný, J. (2017). Anisotropy of out-of-phase magnetic susceptibility of rocks as a tool for direct determination of magnetic subfabrics of some minerals: an introductory study. Geophysical Journal Internation, 208: 385-402.

Hrouda, F., Chadima, M., Jezek, J. & Kadlec, J. (2018). Anisotropy of in-phase, out-of-phase, and frequency-dependent susceptibilities in three loess/ palaesol profiles in Czech Republic; methodological implications. Studia Geophysica et Geodaetica, 62: 272-290.

Hunt, C.P., Moskowitz, B.M. & Banerjee, S.K. (1995). Magnetic properties of rock and minerals. American Geophysical Union, 189-204.

Hutton, D.H.W. (1988). Granite emplacement mechanisms and tectonic controls: inferences from deformation studies. Trasactions of the Royal Society of Edinburgh: Earth Sciences, 79(2-3): 245-255.

Ishihara, S. (1977). The Magnetite-series and Ilmenite-series Granitic Rocks. Mining Geology, 27: 292-305.

Ishihara, S., Lee, D.S. & Kim, S.Y. (1981). Comparative study of Mesozoic granitoids and related W-Mo mineralization in Southern Korea and Southwestern Japan. Mining Geology, 31(4): 311-320.

Jackson, M. (1991). Anisotropy of magnetic remanence: a brief review of mineralogical sources, physical origins and geological applications, and comparison with susceptibility anisotropy. Pure and Applied Geophysics, 136: 1-28.

Jelinek, V. (1981). Characterization of the magnetic fabric of rocks. Tectonophysics 79, 63-67.

Joly, A., Faure, M., Martelet, G. & Chen, Y. (2009). Gravity inversion, AMS and geochronological investigations of syntectonic granitic plutons in the southern part of the Variscan French Massif Central. Journal of Structural Geology, 31(4): 421-443.

Journel, A.G. & Huijbregts, C.J. (1978). Mining Geostatistics. Academic Press, New York, 600 pp.

Jover, O., Rochette, P., Lorand, J.P., Maeder, M. & Bouchez, J.L. (1989). Magnetic mineralogy of some granites from the French Massif Central: origin of their low-field susceptibility. Physics of the Earth and Planetary Interiors, 55: 79-92.

Julivert, M., Fontboté, J.M., Ribeiro, A. & Conde, L. (1974). Mapa tectónico de la península Ibérica y Baleares a escala 1:1.000.000 y memoria explicativa. Instituto Geologico y Mineiro de España, 113 pp.

Kearey, P., Brooks, M. & Hill, I. (2002). An Introduction to Geophysical Exploration. Blackwell Science Ltd, Oxford, 281 pp.

Ketelaar, A.C.R. (1987). Terrain correction for gravity measurements, using a digital terrain model. Geoexploration, 24: 109-124.

Kroner, U. & Romer, R.L. (2013). Two plates – many subduction zones: The Variscan orogeny reconsidered. Gondwana Research, 24: 298-329.

Kropácek, V. & Krs, M. (1968). Magnetism and Ferromagnetism of Natural Minerals of the Spinel Group. Studia Geophysica et Geodaetica, 12: 385-397.

Kruiver, P., Dekkers, M. & Heslop, D. (2001). Quantification of magnetic coercivity components by the analysis of acquisition curves of isothermal remanent magnetization. Earth and Planetary Science Letters, 189(3-4): 269-276.

Kumar, S. (2010). Magnetite and ilmenite series granitoids of Ladakh batholith, Northwest Indian Himalaya: implications on redox conditions of subduction zone magmatism. Current Science, 99(9): 1260-1264.

Kwak, T.A.P. & White, A.J.R. (1982). Contrasting W-Mo-Cu and W-Sn-F Skarn Types and Related Granitoids. Mining Geology, 32: 339-351.

LaCoste, L.J.B. & Romberg, A. (2004). Instruction Manual. Model G and D gravity meters. LaCoste & Romberg, USA, 127 pp.

LaFehr, T.R. (1991). Standardization in gravity reductions. Geophysics, 56(8): 1170-1178.

Lagoeiro, L.E. (1998). Transformation of magnetite to hematite and its influence on the dissolution of iron oxide minerals. Journal of Metamorphic Geology, 16: 415-423.

Le Maitre. R.W., Bateman, P., Dudek, A., Keller, J., Lameyre, J., Le Bas, M.J., Sabine, P.A., Schmid, R., Sorensen, H., Streckeisen, A., Woolley, A.R. & Zanettin, B. (1989). A classification of igneous rocks and glossary of terms: Recommendations of the International Union of Geological Sciences Subcommission on the Systematics of Igneous Rocks. Blackwell Scientific Publications, Oxford, 193 pp.

Lotze, F. (1945). Zur gliederung der Varisziden der Iberischen Meseta. Geoteckt. Forsch, 6: 78-92.

Lowrie, W. (2007). Fundamentals of geophysics. Cambridge University Press, Cambridge, 381 pp.

Machadinho, A.T.G. (2015). Modelação da geometria de rochas granitóides recorrendo a métodos geofísicos gravimétricos e magnéticos: uma contribuição para a avaliação do potencial geotérmico na região centro de Portugal. PhD thesis (published thesis), Universidade de Coimbra, Portugal, 312 pp.

Marques, F.O., Mateus, A. & Tassinari, C. (2002). The Late-Variscan fault network in central–northern Portugal (NW Iberia): a re-evaluation. Tectonophysics, 359(3-4): 255-270.

Martínez Catalán, J.R., Rubio Pascual, F.J., Díez Montes, A., Díez Fernández, R., Gómez Barreiro, J., Dias da Silva, Í., González Clavijo, E., Ayarza, P. & Alcock, J.E. (2014). The late Variscan HT/LP metamorphic event in NW and Central Iberia: relationships to crustal thickening, extension, orocline development and crustal evolution. Geological Society of London, Special Publications, 405: 225-247.

Martins, H.C.B. (1998). Geoquímica e petrogénese de granitóides biotiticos tarditectónicos e pós-tectónicos. Implicações metalogénicas. PhD thesis (published thesis), University of Trás-os-Montes e Alto Douro, Portugal, 288 pp.

Martins, H.C.B., Sant'Ovaia, H. & Noronha, F. (2009). Genesis and emplacement of felsic Variscan plutons within a deep crustal lineation, the Penacova-Régua-Verín fault: an integrated geophysics and geochemical study (NW Iberian Peninsula). Lithos, 111: 142-155.

Martins, H.C.B., Sant'Ovaia, H., Abreu, J., Oliveira, M. & Noronha, F. (2011). Emplacement of Lavadores granite (NW Portugal): U/Pb and AMS results. Comptes Rendus Geocience, 343: 387-396.

Mateus, A. & Noronha, F. (2010). Sistemas mineralizantes epigenéticos na Zona Centro-Ibérica; expressão da estruturação orogénica Meso- a Tardi-Varisca. In: Geologia Aplicada, Volume II - Ciências Geológicas: Ensino, Investigação e sua História (eds. Cotelo Neiva, J. M., Ribeiro, A., Victor, M., Noronha, F. & Ramalho, M.), Escolar Editora, 47-61.

Maulana, A., Watanabe, K., Imai, A. & Yonezu, K. (2013). Origin of magnetite- and ilmentite-series granitic rocks in Sulawesi, Indonesia: magma genesis and regional metallogenic constrains. Earth and Plenatary Sciences, 6: 50-57.

Maxbauer, D.P., Feinberg, J.M. & Fox, D.L. (2016). MAX UnMix: A web application for unmixing magnetic coercivity distributions. Computers & Geosciences, 95: 140-145.

Morrill, C. & Koch, P.L. (2002). Elevation or alteration? Evaluation of isotopic constraints on paleoaltitudes surrounding the Eocene Green River Basin. Geological Society of America, Vol. 30(2): 151-154.

Nédélec, A. & Bouchez, J.L. (2015). Granites: Petrology, structure, geological setting, and metallogeny. Oxford University Press, New York, 335 pp.

Neiva, A.M.R., Williams, I.S., Ramos, J.M.F., Gomes, M.E.P., Silva, M.M.V.G. & Antunes, I.M.H.R. (2009). Geochemical and isotopic constraints on the petrogenesis of Early Ordovician granodiorite and Variscan two-mica granites from the Gouveia area, central Portugal. Lithos, 111: 186-202.

Neiva, J.M.C. (1944). Jazigos portugueses de volframite e cassiterite. Comunicações dos Serviços Geológicos de Portugal, 25: 1-251.

Nettleton, L.L. (1939). Determination of Density for Reduction of Gravimeter Observations. Geophysics, Vol. 4(3): 176-183.

Nettleton, L.L. (1976). Gravity and magnetics in oil prospecting. McGraw-Hill Inc., U.S., 480 pp.

Noronha, F. (1984). Mineralizações espacial e geneticamente associadas ao maciço granítico da Serra do Gerês, Cuadernos do Laboratorio Xeolóxico de Laxe, 7: 87–99.

Noronha, F. (2017). Fluids and Variscan metallogenesis in granite related systems in Portugal. Procedia Earth and Planetary Science, 17: 1-4.

Noronha, F., Ramos, J.M.F., Rebelo, J., Ribeiro, A. & Ribeiro, M.L. (1981). Essai de corrélation des phases de déformation hercyniennes dans le NW de la péninsule Ibérique. Leidse Geologische Mededelingen, 52(1): 87-91.

Noronha, F., Ferreira, N. & Marques de Sá, C. (2006). Rochas granitóides: caracterização petrológica e geoquímica. In: Notícia Explicativa da Folha 2 – Carta Geológica de Portugal à escala 1:200 000. (Coord. Pereira, E.). IGM/INETI, 49-68.

Noronha, F., Ribeiro, M. A., Almeida, A., Dória, A., Guedes, A., Lima, A., Martins, H.C.B., Sant'Ovaia, H., Nogueira, P., Martins, T., Ramos, R. & Vieira, R. (2013). Jazigos filonianos hidrotermais e aplitopegmatíticos espacialmente associados a granitos (norte de Portugal). In: Geologia de Portugal (eds. Dias, R., Araújo, A., Terrinha, P. & Kullberg, J.C.), Escolar Editora, Vol I: 403-438.

Oen, I.S. (1970). Granite intrusion, folding and metamorphism in central northern Portugal. Boletim Geológico Mineiro de Portugal, 81(2-3): 271-298.

Olivia-Urcia, B., Larrasoaña, J.C., Pueyo, E.L., Gil, Al., Mata, P., Parés, J.M., Schleicher, A.M. & Pueyo, O. (2009). Disentangling magnetic subfabrics and their link to deformation processes in cleaved sedimentary rocks from the Internal Sierras (west cenral Pyrenees, Spain). Journal of Structural Geology, 31: 163-176.

Olivia-Urcia, B., Casas, A.M., Ramón, M.J., Leiss, B., Mariani, E. & Román-Berdiel, T. (2012). On the reliability of MAS in ilmenite-type granites: an insight from the Marimanha pluton, central Pyrenees. Geophysical Journal International, 189: 187-203.

Parasnis, D.S. (1972). Mining geophysics (Vol. 3). eBook. Elsevier, 372 pp.

Pastor-Galán, D., Gutierrez-Alonso, G., Zulauf, G. & Zanella, F. (2012). Analogue modeling of lithospheric-scale orocline buckling: Constraints on the evolution of the Iberian-Armorican Arc. Geological Society of America Bulletin, 124: 1293-1309.

Pearce, J.A., Harris, N.W. & Tindle, A.G. (1984). Trace element discrimination diagrams for the tectonic interpretation of granitic rocks. Journal of Petrology, 25: 956-983.

Peccerillo, A. & Taylor, S.R. (1976). Geochemistry of Eocene calc-alkaline volcanic rocks from the Kastamonu area, Northern Turkey. Contributions to Mineralogy and Petrology, 58: 63-81

Pereira, E. (1989). Carta Geológica de Portugal à escala 1:50 000. Notícia Explicativa da Folha 10-A (Celorico de Basto). Serviços Geológicos de Portugal, Lisboa, 53 pp.

Pereira, E., Silva, N., Moreira, A. & Ribeiro, A. (1987). Folha 10-A Celorico de Basto da Carta Geológica de Portugal na escala 1/50 000. Serviços Geológicos de Portugal.

Pereira, M.F., Díez Fernández, R., Gama, C., Hofmann, M., Gärtner, A. & Linnemann, U. (2018). S-type granite generation and emplacement during a regional switch from extensional to contractional deformation (Central Iberian Zone, Iberian autochthonous domain, Variscan Orogeny). International Journal of Earth Sciences, 107: 251-267.

Petford, N., Cruden, A.R., McCaffrey, K.J.W. & Vigneresse, J.L. (2000). Granite magma formation, transport and emplacement in the Earth's crust. Nature, 408: 669-673.

Petford, N., Kerr, R.C. & Lister, J.R. (1993). Dike transport of granitoid magmas. Geology, 21(9): 845-848.

Porquet, M., Pueyo, E.L., Róman-Berdiel, T., Olivier, P., Longares, L.A., Cuevas, J., Ramajo, J. & Geokin3DPyr working group. (2017). Anisotropy of magnetic susceptibility of the Pyrenean granites. Journal of Maps, 13(2): 438-448.

Racelogic Support Center. (2018). How Does DGPS (Differential GPS) Work?: https://racelogic.support/01VBOX_Automotive/01General_Information/Knowledge_Base/How_Does_DGPS_(Differential_GPS)_Work%3F. Accessed on 9th of September of 2019.

Raposo, M.I.B. & Gastal, M.C.P. (2009). Emplacement mechanism of the main granite pluton of the Lavras do Sul intrusive complex, South Brazil, determined by magnetic anisotropies. Tectonophysics, 466: 18-31.

Reynolds, J.M. (1997). An Introduction to applied and environmental geophysics. John Wiley & Sons, Chichester, 796 pp.

Ribeiro, A. (1974). Contribution à l'étude de Trás-os-Montes Oriental. Serviços Geológicos de Portugal. PhD thesis (published thesis). Memórias Serviços Geológicos de Portugal. Lisboa-Portugal, 24: 168 pp.

Ribeiro, A., Pereira, E. & Dias, R. (1990). Structure of the Northwest of the Iberian Peninsula. In: Pre-Mesozoic Geology of Iberia (eds. Dallmeyer, D. & Martinez Garcia, E.). Springer, 220-236.

Ribeiro, M.L., Castro, A., Almeida, A., González Menéndez, L., Jesus, A., Lains, J.A., Lopes, J.C., Martins, H.C.B., Mata, J., Mateus, A., Moita, P., Neiva, A.M.R., Ribeiro, M.A., Santos, J.F. & Solá, A.R. (2019). Variscan Magmatism. In: The Geology of Iberian: A Geodynamic Approach (eds: Quesada, C. & Oliveira, J.T.) Vol. II, Springer, 497-526.

Riveros, K., Veloso, E., Campos, E., Menzies, A. & Véliz, W. (2014). Magnetic properties related to hydrothermal alteration processes at the Escondida porphyry copper deposit, northern Chile. Mineralium Deposita, 49: 693-707.

Robertson, D. & France, D. (1994). Discrimination of remanence-carrying minerals in mixtures, using isothermal remanent magnetization acquisition curves. Physics of the Earth and Planetary Interiors, 82(3-4): 223-234.

Román-Berdiel, T., Pueyo-Morer, E.L. & Casas-Sainz, A.M. (1995). Granite emplacement during contemporary shortening and normal faulting: structural and magnetic study of the Veiga Massif (NW Spain). Journal of Structural Geology, Vol. 17, 12: 1689-1706.

Romer, R.L. & Kroner, U. (2015). Sediment and weathering control on the distribution of Paleozoic magmatic tin-tungsten mineralization. Mineralium Deposita, 50: 327-338.

Romer, R.L. & Kroner, U. (2016). Phanerozoic tin and tungsten mineralization – Tectonic controls on the distribution of enriched protoliths and heat sources for crustal melting. Gondwana Reserch, 31: 60-95.

Rudnick, R.L. & Gao, S. (2014). Composition of the Continental Crust. In: Treatise on Geochemistry, 2nd edition (eds. Holland, H. & Turekian, K.), Elsevier, Oxford, 1–51.

Saltus, R.W. & Blakely, R.J. (2011). Unique geologic insights from “non-unique” gravity and magnetic interpretation. GSA Today, Vol. 21(12): 4-11.

Sant’Ovaia, H., Bouchez, J.L., Noronha, F., Leblanc, D. & Vigneresse, J.L. (2000). Composite-laccolith emplacement of the post-tectonic Vila Pouca de Aguiar granite pluton (northern Portugal): a combined AMS and gravity study. Transactions of the Royal Society of Edinburgh Earth Sciences, 91: 123-137.

Sant’Ovaia, H. & Noronha, F. (2005). Gravimetric anomaly modelling of the post-tectonic granite pluton of Águas Frias – Chaves (Northern Portugal). Cuadernos do Laboratorio Xeolóxico de Laxe, 30: 87-98.

Sant’Ovaia, H., Martins, H.C.B., Lopes, J.C., Machado, J. & Noronha, F. (2012). Correlation of magnetic susceptibility with $\delta^{18}O$ data in magnetite- and ilmenite-type granites from Iberian massif. Mineralogical Magazine, 76(6), 23-25.

Sant’Ovaia, H., Martins, H.C.B. & Noronha, F. (2013a). Oxidized and reduced Portuguese Variscan granites associated with W and Sn hydrothermal lode deposits: magnetic susceptibility results. Comunicações Geológicas, Vol. 100 (1): 33-39.

Sant’Ovaia, H., Martins, H.C.B. & Noronha, F. (2013b). Magnetic susceptibility and $\delta^{18}O$ characterization of granites related with W, Sn, Mo and Bi (Au) hydrothermal vein deposits. Mineralogical Magazine, 77 (5): 2130.

Sant’Ovaia, H., Nogueira, P., Carrilho Lopes, J., Gomes, C., Ribeiro, M.A., Martins, H.C.B., Dória, A., Cruz, C., Lopes, L., Sardinha, R., Rocha, A. & Noronha, F. (2014). Building up of a nested granite intrusion: magnetic fabric, gravity modelling and fluid inclusion planes studies in Santa Eulália Plutonic Complex (Ossa Morena Zone, Portugal). Geological Magazine, 1-20.

Schermerhorn, L.J.G. (1956). Igneous, metamorphic and ore geology of Castro de Aire – São Pedro do Sul – Sátão region (northern Portugal). Comunicações dos Serviços Geológicos de Portugal, 37 pp.

Schermerhorn, L.J.G. (1981). Framework and evolution of Hercynian mineralization in the Iberian Meseta. Leidse Geologische Mededelingen, 52 (1): 23-56.

Shaw, J., Johnston, S.T., Gutiérrez-Alonso, G. & Weil, A.B. (2012). Oroclines of the Variscan orogen of Iberia: Paleocurrent analysis and paleogeographic implications. Earth and Planetary Science Letters, 329-330: 60-70.

Sheppard, S.M.F. (1977). Identification of the origin of ore forming solutions by the use of stable isotopes. Volcanic Processes in Ore Genesis. Institution of Mining and Metallurgy and Geological Society, London, 254 pp.

Siegesmund, S., Ullemeyer, K. & Dahms, M. (1995). Control of magnetic rock fabrics by mica preferred orientation: a quantitative approach. Journal of Structural Geology, 17: 1601-1613.

SIORMINP. (2019). Sistema de Informação de Ocorrências e Recursos Minerais Portugueses. http://geoportal.lneg.pt/geoportal/egeo/bds/siorminp/. Accessed on 10th of December of 2019.

Stacey, F.D. & Banerjee, S.K. (1974). The Physical Principles of Rock Magnetism. Elsevier Scientific Publishing Company, Amsterdam, 195 pp.

Stephenson, A., Sadikum, S. & Potter, D.K. (1986). A theoretical and experimental comparison of the anisotropies of magnetic susceptibility and remanence in rocks and minerals. Geophysical Journal of the Royal Astronomical Society, 84: 185-200.

Takagi, T. & Tsukimura, M. (1997). Genesis of oxidized- and reduced-type granites. Economic Geology, 92: 81-86.

Tarling, D.H. & Hrouda, F. (1993). The magnetic anisotropy of rocks. Chapman & Hall, London, 217 pp.

Taylor S.R. & McLennan, S.M. (1995). The geochemical evolution of the continental crust. Reviews in Geophysics, 33: 241-265.

Teixeira, C. & Perdigão, J. (1962). Folha 13-A Espinho da Carta Geológica de Portugal na escala 1/50 000. Serviços Geológicos de Portugal.

Teixeira, R.J.S. (2008). Mineralogia, petrologia e geoquímica dos granitos e seus encraves da região de Carrazeda de Ansiães. PhD thesis (published thesis), Universidade de Trás-os-Montes e Alto Douro, Portugal, 463 pp.

Teixeira, R.J.S., Neiva, A.M.R., Gomes, M.E.P., Corfu, F., Cuesta, A. & Croudace, I.W. (2012). The role of fractional crystallization in the genesis of early syn-D3, tin-mineralized Variscan two-mica granites from the Carrazeda de Ansiães area, northern Portugal. Lithos, 153: 177-191.

Teixeira, R.J.S., Gomes, M.E.P., Martins, L.M.O., Pereira, A.J.C.S. & Neves, L.J.P.F. (2014). Natural radiation and geochemistry of the Lamas de Olo biotite granite, northern Portugal. Goldschmidt abstracts, 2458.

Thadeu, D. (1965). Carta Mineira de Portugal. Notícia explicativa. Serviços Geológicos de Portugal, Lisboa-Portugal, 46 pp.

Vasconcelos, M., Botelho, H., Kol, H. & Casaca, J. (2007). The Portuguese Geodetic Reference Frames (poster). XXIV IUGG General Assembl. Perugia, Italia: https://www.researchgate.net/profile/Manuela_Vasconcelos2/publication/338804171_The_Portuguese_Geodetic_Reference_Frames/links/5e2b2586a6fdcc70a148e5b7/The-Portuguese-Geodetic-Reference-Frames.pdf. Accessed on 9th of September of 2019.

Vigneresse, J.L. (1990). Use and misuse of geophysical data to determine the shape at depth of granitic intrusions. Geological Journal, 25: 249-260.

Vigneresse, J.L. (1995a). Control of granite emplacement by regional deformation. Tectonophysics, 249(3-4): 173-186.

Vigneresse, J.L. (1995b). Crustal regime of deformation and ascent of granitic magma. Tectonophysics, 249(3-4): 187-202.

Vigneresse, J.L. (2004). A new paradigma for granite generation. Geological Society of America Special Papers, 389: 11-22.

Vigneresse, J.L., Tikoff, B. & Améglio, L. (1999). Modification of the regional stress field by magma intrusion and formation of tabular granitic plutons. Tectonophysics 302: 230-224.

Vilela de Matos, A. (1991). A Geologia da Região de Vila Real. PhD thesis (publisehd thesis), Universidade de Trás-os-Montes e Alto Douro, Portugal, 312 pp.

Villaseca, C., Barbero, L. & Herreros, V. (1998). A re-examination of the typology of peraluminous granite types in intracontinental orogenic belts. Transactions of the Royal Society of Edinburgh Earth Sciences, 89: 113-119.

Villaseca, C., Ruiz-Martínez, V.C. & Pérez-Soba, C. (2017). Magnetic susceptibility of Variscan granite-types of the Spanish Central System and the redox state of magma. Geologica Acta, 15(4): 379-394.

Weil, A., Gutiérrez-Alonso, G., Johnston, S.T. & Pastor-Galán, D. (2013). Kinematic constraints on buckling a lithospheric-scale orocline along the northern margin of Gondwana: a geologic synthesis. Tectonophysics, 582: 25-49.

Zawadzki, J., Magiera, T., Fabijańczyk, P., & Kusza, G. (2012). Geostatistical 3-dimensional integration of measurements of soil magnetic susceptibility. Environmental Monitoring and Assessment, 184(5): 3267–3278.

Zawadzki, J., Fabijańczyk, P., Magiera, T. & Rachwał, M. (2015). Geostatistical Microscale Study of Magnetic Susceptibility in Soil Profile and Magnetic Indicators of Potential Soil Pollution. Water, Air, and Soil Pollution, 226(5): 142 pp.

ATTACHMENTS

Table A1-1. Sampling sites and methodologies applied to each site on Lamas de Olo Pluton (LO - Lamas de Olo granite; AC - Alto dos Cabeços granite; BA - Barragem granite; AMS - Anisotropic of magnetic susceptibility; MS - Magnetic susceptibility; AARM - Anisotropy of anhysteretic remanent magnetization; K_t *versus* T - Thermomagnetic experiments; IRM - Isothermal remanent magnetization; χfD% - frequency-dependent susceptibility (%); BMG - Binocular magnifying glass; TL - Transmitted light microscopy; RL - Reflected light microscopy; SEM-EDS - Scanning electron microscope and dispersive energy spectra microanalysis; Raman - Micro-Raman spectroscopy analyses; $\delta^{18}O$ – Oxygen isotope studies (W.R.); M-, T-, REE + Tit. – Major-, trace- and Rare Earth Elements and titration analyses (W.R.); ThS - Thin section; PS - Polished sections).

Sampling site/ sample	ETRS89-TM06 (projected system)		Lithology	Methodology applied														
				Magnetic mineralogy studies							Optical studies						Geochemical studies	
	M	P		AMS	MS	K_m (μSI)	AARM	K_t *versus* T	IRM	χfD%	Type of section	BMG	TL	RL	SEM-EDS	Raman	$\delta^{18}O$	M-, T-, REE, Tit.*
LM 1	26910.01	184668.15	LO	x	x	174					ThS	x	x	x		x		x
LM 2	27108.295	186725.616	LO	x	x	1848	x											
LM 3	28619.969	184802.042	LO	x	x	2489	x				ThS	x	x	x	x			
LM 3V	28784.601	185126.662	LO	x	x	316					ThS	x	x	x				
LM 4	28827.598	185935.256	LO	x	x	112												
LM 5	28532.998	186823.482	LO	x	x	2769		x	x	x	ThS	x	x	x	x		x	x
LM 6	27993.899	187227.871	LO	x	x	252												
LM 7	27978.297	187280.788	BA	x	x	38		x	x	x	ThS	x	x	x	x		x	x
LM 8	26244.175	186521.084	LO	x	x	1564	x	x		x	ThS	x	x	x		x		
LM 13	29405.627	185481.774	LO	x	x	44382	x	x			ThS	x	x	x	x	x	x	x
LM 14	28945.979	186285.019	LO	x	x	2179	x				ThS	x	x	x				
LM 15	28001.628	187263.441	BA	x	x	24	x	x			ThS	x	x	x	x	x		x
LM 16	28413.312	188578.137	LO	x	x	67		x	x								x	x
LM 17	27796.767	188486.676	LO	x	x	77												
LM 18	27747.068	188355.21	LO	x	x	79	x											
LM 19	28665.042	186001.694	LO	x	x	1869												
LM 20	28410.819	184981.92	LO	x	x	2760												
LM 21	27959.973	184040.381	LO	x	x	233												
LM 22	27854.41	184452.682	LO	x	x	513		x		x								x
LM-STOP4	27333.68	185149.84	LO		x	1078												
LM 23	27809.519	184982.165	LO	x	x	254												
LM 24	27362.749	185383.624	AC	x	x	239		x		x	ThS	x	x	x				x
LM 25	27384.826	185389.261	AC	x	x	254	x											

Table A1-1. (cont.)

Sampling site/ sample	ETRS89-TM06 (projected system)		Lithology	Methodology applied														
				Magnetic mineralogy studies								Optical studies					Geochemical studies	
	M	P		AMS	MS	K_m (μSI)	AARM	K_t *versus* T	IRM	χfD%	Type of section	BMG	TL	RL	SEM-EDS	Raman	$\delta^{18}O$	M-, T-, REE, Tit.*
LM 26	27386.246	185389.932	AC	x	x	962		x	x	x	ThS	x	x	x			x	
LM 27	28488.489	183746.454	LO	x	x	69												
LM 28	28929.716	184462.66	LO	x	x	2065	x											
LM 29	28969.008	184834.215	LO	x	x	1147												
LM 30	27875.373	187060.71	LO	x	x	2385	x											x
LM 31	27815.778	187216.191	BA	x	x	32												
LM 32	27762.225	187124.791	LO	x	x	2031												
LM 33	27390.673	186776.001	LO	x	x	1261												
LM 34	27865.531	187901.972	LO	x	x	100												
LM 35	27671.082	187831.703	LO	x	x	205												
LM 36	27266.478	187815.066	LO	x	x	242												
LM 37	26776.423	187983.278	LO	x	x	101												
LM 38	27435.411	187641.335	LO	x	x	1559		x		x								
LM 39	28574.79	188472.929	LO	x	x	81												
LM 40	28717.842	183803.535	LO		x	49												
LM 41	27051.328	185281.039	LO		x	1110												
LM 41b	27052.386	185281.515	BA		x	26												
LM 42	27271.264	185360.271	LO		x	1390												
LM 42b	27273.169	185365.986	BA		x	586												
LM 43	27303.876	185369.279	AC		x	271		x										
LM 48	27308.925	185584.869	LO		x	117												
LM 49	27273.738	185615.39	BA		x	54		x										x
LM 50	28821.347	184853.261	LO		x	1027												
LM 51	28833.743	184830.543	LO		x	580												
LM 52	28877.73	184884.138	LO		x	335												
LM 53	28515.161	184780.528	LO		x	1584												
LM 54	28265	184786.881	LO	x	x	787												

Table A1-1. (cont.)

Sampling site/ sample	ETRS89-TM06 (projected system)		Lithology	Methodology applied														
				Magnetic mineralogy studies							Optical studies						Geochemical studies	
	M	P		AMS	MS	K_m (μSI)	AARM	K_t *versus* T	IRM	χfD%	Type of section	BMG	TL	RL	SEM-EDS	Raman	$\delta^{18}O$	M-, T-, REE, Tit.*
LM 55	28252.075	184795.493	LO	x	x	2260												
LM 56	28454.287	184741.307	LO	x	x	876												
LM 57	28394.789	187538.85	LO	x	x	845												
LM 58	27049.891	185284.809	LO	x	x	103												
LM 58b	27059.834	185298.183	BA	x	x	21				x								
LM 59	27134.446	185371.42	LO	x	x	1348												
LM 60	27136.458	185437.843	LO	x	x	392												
LM 61	27156.719	185436.808	AC	x	x	125		x		x								x
LM 62	26999.303	185247.526	BA	x	x	22		x		x							x	
LM 63	26999.803	185247.973	LO	x	x	1025												
LM 64	27933.527	184648.325	LO	x	x	76												
LM 65a	27331.373	186581.183	BA		x	79												
LM 65b	27335.721	186581.079	LO		x	156												
LM 66a	27286.714	186216.175	LO		x	36												
LM 66b	27288.388	186216.071	BA		x	12												
LM 66c	27291.239	186215.936	AC		x	79												
LM 67	27271.748	186167.363	LO		x	30												
LM 68	27258.551	186026.486	AC		x	70												
LM 69a	27188.351	185930.82	BA		x	26												
LM 69b	27188.017	185930.708	LO		x	64												
LM-BA31	27815.778	187216.191	BA								ThS	x	x	x				
LM-G1	Arnal (close to the AC granite)		BA								ThS	x	x	x				
LM-Qz1	27403.118	186553.466	Qz vein								ThS	x	x	x				
LM-Qz2	27403.118	186553.466	Qz vein								ThS	x	x	x				
LM13-G1	29405.627	185481.774	LO								PS	x		x	x	x		
LM-AC1	Arnal - mining wastes		Qz vein								PS	x		x				
LM-AC2	Arnal - mining wastes		Qz vein								PS	x		x				
AC23	Arnal (close to the AC granite)		Qz vein								PS	x		x				

Table A1-1. (cont.)

Sampling site/ sample	ETRS89-TM06 (projected system)		Lithology	Methodology applied															
				Magnetic mineralogy studies							Optical studies						Geochemical studies	
	M	P		AMS	MS	K_m (μSI)	AARM	K_t *versus* T	IRM	χfD%	Type of section	BMG	TL	RL	SEM-EDS	Raman	$\delta^{18}O$	M-, T-, REE, Tit.*
AC30	Arnal (close to the AC granite)		Qz vein								PS	x		x	x	x		
AC38	Arnal (close to the AC granite)		Qz vein								PS	x		x				
AC43	Arnal (close to the AC granite)		Qz vein								PS	x		x	x	x		
AC44	Arnal (close to the AC granite)		Qz vein								PS	x		x				
AC47	Arnal (close to the AC granite)		Qz vein								PS	x		x	x	x		
AC48	Arnal (close to the AC granite)		Qz vein								PS	x		x				
TOTAL	**Alvão**			**48**	**70**	**70**	**10**	**14**	**4**	**10**	**25**	**25**	**15**	**25**	**9**	**8**	**6**	**11**

Table A1-2. Sampling sites and methodologies applied to each site host rocks (VRM - Vila Real Massif; DGM - Douro Group Metasediments; AMS - Anisotropic of magnetic susceptibility; MS - Magnetic susceptibility; AARM - Anisotropy of anhysteretic remanent magnetization; K_t *versus* T - Thermomagnetic experiments; IRM - Isothermal remanent magnetization; χfD% - frequency-dependent susceptibility (%); TL - Transmitted light microscopy; RL - Reflected light microscopy; BMG - Binocular magnifying glass; SEM-EDS - Scanning electron microscope and X-ray microanalysis; Raman - Micro-Raman spectroscopy analyses; $\delta^{18}O$ – Oxygen isotope studies (W.R.); M-, T-, REE + Tit. – Major-, trace- and Rare Earth Elements and titration analyses (W.R.); ThS - Thin section; PS - Polished sections).

Sampling site/ sample	ETRS89-TM06 (projected system)		Lithology	Methodology applied															
				Magnetic mineralogy studies							Optical studies						Geochemical studies	
	M	P		AMS	MS	K_m (μSI)	AARM	K_t *versus* T	IRM	χfD%	Type of section	BMG	TL	RL	SEM-EDS	Raman	$\delta^{18}O$	M-, T-, REE, Tit.*
LM 9	25724.739	186083.195	VRM	x	x	49	x		x									
LM 10	30777.73	184394.826	VRM	x	x	52	x	x	x								x	
LM 11	30269.647	184876.479	VRM	x	x	51												
LM 12	29675.937	185373.033	DGM	x	x	48474												
LM 70	27720.585	180952.815	VRM	x	x	40												
LM 71	29508.23	181951.66	DGM															
LM 72	29593.299	187245.99	VRM	x	x	35												
TOTAL	**Host rocks**			**6**	**6**	**6**	**2**	**1**	**2**	**0**	**0**	**0**	**0**	**0**	**0**	**0**	**1**	**0**

Table A2-1. AMS data from all measured samples from LOP granites and host rocks.

Sample	Granites	Km x 10-3 SI	Km x 10-6 SI	StErr (%)	Pkmax	Pkint	Pkmin	Kmax	Kint	Kmin	L	F	P	P%	Ppara%	T	Kmax Dec	Kmax Inc	Kint Dec	Kint Inc	Kmin Dec	K min Inc
LM1-A1	LO	0.199	199.00	0.082	1.0348	1.0062	0.9590	205.925	200.234	190.841	1.028	1.049	1.079	7.9	7.36	0.263	224.2	28.9	343.8	41.7	112	35
LM1-A2	LO	0.176	176.00	0.052	1.0160	1.0068	0.9772	178.816	177.197	171.987	1.009	1.030	1.040	4.0	3.67	0.534	206.0	6.1	106.1	58.0	300	31
LM1-A3	LO	0.153	153.00	0.090	1.0226	1.0110	0.9664	156.458	154.683	147.859	1.012	1.046	1.058	5.8	5.31	0.596	8.7	6.2	268.6	58.2	103	31
LM1-A4	LO	0.201	201.00	0.109	1.0264	0.9953	0.9783	206.306	200.055	196.638	1.031	1.017	1.049	4.9	4.59	-0.282	216.7	46.7	6.2	39.0	109	16
LM1-B1	LO	0.167	167.00	0.037	1.0145	1.0015	0.9840	169.422	167.251	164.328	1.013	1.018	1.031	3.1	2.86	0.151	119.7	22.4	243.8	53.6	18	27
LM1-B2	LO	0.169	169.00	0.028	1.0229	0.9987	0.9784	172.870	168.780	165.350	1.024	1.021	1.045	4.5	4.19	-0.078	271.5	18.0	4.2	8.3	118	70
LM1-B3	LO	0.180	180.00	0.066	1.0258	0.9993	0.9749	184.644	179.874	175.482	1.027	1.025	1.052	5.2	4.84	-0.029	192.7	35.8	17.9	54.1	285	3
LM1-C1	LO	0.172	172.00	0.063	1.0206	1.0016	0.9778	175.543	172.275	168.182	1.019	1.024	1.044	4.4	4.04	0.122	270.0	55.1	133.1	27.0	32	20
LM1-C2	LO	0.164	164.00	0.048	1.0290	0.9968	0.9741	168.756	163.475	159.752	1.032	1.023	1.056	5.6	5.18	-0.160	207.9	35.5	84.4	37.8	325	32
LM1-C3	LO	0.162	162.00	0.048	1.0123	1.0013	0.9863	163.993	162.211	159.781	1.011	1.015	1.026	2.6	2.42	0.158	133.1	38.4	312.7	51.6	43	0
LM1-C4	LO	0.191	191.00	0.098	1.0379	0.9999	0.9622	198.239	190.981	183.780	1.038	1.039	1.079	7.9	7.31	0.017	106.7	11.7	227.1	67.7	13	19
LM1-C5	LO	0.164	164.00	0.033	1.0189	0.9995	0.9816	167.100	163.918	160.982	1.019	1.018	1.038	3.8	3.50	-0.028	165.1	40.5	261.9	7.8	1	48
LM1-D1	LO	0.209	206.00	0.036	1.0348	0.9924	0.9728	213.169	204.434	200.397	1.043	1.020	1.064	6.4	5.96	-0.353	260.5	54.5	152.4	12.5	54	33
LM1-D2	LO	0.154	154.00	0.033	1.0213	1.0133	0.9654	157.280	156.048	148.672	1.008	1.050	1.058	5.8	5.29	0.722	294.0	33.6	185.4	25.6	66	45
LM1-D3	LO	0.155	155.00	0.058	1.0416	0.9831	0.9752	161.448	152.381	151.156	1.059	1.008	1.068	6.8	6.23	-0.755	291.0	39.6	196.8	5.1	101	50
Mean		**0.174**	**174.20**										**1.052**	**5.2**	**4.85**	**0.059**						
LM2-A1	LO	1.740	1740.00	0.013	1.0286	1.0045	0.9669	1789.764	1747.830	1682.406	1.024	1.039	1.064	6.4	6.33	0.232	341.1	30.8	209.0	48.4	87	25
LM2-A2	LO	2.070	2070.00	0.009	1.0145	1.0043	0.9812	2100.015	2078.901	2031.084	1.010	1.024	1.034	3.4	3.37	0.398	178.6	23.9	331.4	63.6	84	11
LM2-B1	LO	1.690	1690.00	0.024	1.0222	0.9943	0.9835	1727.518	1680.367	1662.115	1.028	1.011	1.039	3.9	3.90	-0.437	335.8	45.7	220.1	22.9	113	35
LM2-B2	LO	1.930	1930.00	0.007	1.0263	0.9917	0.982	1980.759	1913.981	1895.260	1.035	1.01	1.045	4.5	4.48	-0.555	339.6	36.2	171.3	53.2	74	6
LM2-B3	LO	1.730	1730.00	0.100	1.0292	0.998	0.9728	1780.516	1726.540	1682.944	1.031	1.026	1.058	5.8	5.75	-0.092	333.5	52.6	216.7	19.0	115	31
LM2-C1	LO	1.760	1760.00	0.005	1.0315	0.9902	0.9784	1815.440	1742.752	1721.984	1.042	1.012	1.054	5.4	5.38	-0.545	349.5	38.1	173.4	51.8	81	2
LM2-C2	LO	1.700	1700.00	0.009	1.0227	1.0039	0.9735	1738.590	1706.630	1654.950	1.019	1.031	1.051	5.1	5.01	0.247	346.4	55.9	164.6	34.1	255	1
LM2-C3	LO	2.070	2070.00	0.210	1.031	1.0087	0.9604	2134.170	2088.009	1988.028	1.022	1.05	1.074	7.4	7.30	0.384	62.0	63.8	158.3	3.1	250	26
LM2-C4	LO	1.870	1870.00	0.021	1.0222	1.0013	0.9765	1911.514	1872.431	1826.055	1.021	1.025	1.047	4.7	4.64	0.095	10.3	67.8	182.4	22.0	274	3
LM2-D1	LO	1.680	1680.00	0.030	1.0211	1.0031	0.9758	1715.448	1685.208	1639.344	1.018	1.028	1.046	4.6	4.60	0.216	346.4	60.4	212.2	21.6	114	19
LM2-D2	LO	2.090	2090.00	0.003	1.0275	1.0002	0.9723	2147.475	2090.418	2032.107	1.027	1.029	1.057	5.7	5.64	0.026	347.1	39.1	186.4	49.3	85	10
Mean		**1.85**	**1848.18**										**1.052**	**5.2**	**5.13**	**-0.003**						
LM 3-A1	LO	3.190	3190.00	0.014	1.022	1.017	0.961	3260.499	3244.549	3064.952	1.005	1.059	1.064	6.4	6.35	0.842	169.0	34.7	36.2	44.5	278	26
LM3-B1	LO	2.570	2570.00	0.024	1.038	1.003	0.959	2667.146	2578.224	2464.630	1.034	1.046	1.082	8.2	8.17	0.141	72.5	58.7	181.4	11.1	278	29
LM3-C1	LO	2.190	2190.00	0.029	1.169	0.970	0.862	2559.234	2123.643	1887.342	1.205	1.125	1.356	35.6	35.34	-0.225	306.9	0.7	37.1	8.8	212	81
LM3-D1	LO	2.300	2300.00	0.082	1.023	1.018	0.959	2353.590	2340.250	2206.160	1.006	1.061	1.067	6.7	6.64	0.826	118.4	79.0	238.5	5.6	329	10
LM3-E1	LO	2.790	2790.00	0.184	1.035	0.994	0.971	2887.092	2773.260	2709.648	1.041	1.023	1.065	6.5	6.51	-0.268	143.7	49.1	11.8	30.0	266	25
LM3-F1	LO	2.390	2390.00	0.009	1.027	1.019	0.954	2454.530	2435.410	2280.060	1.008	1.068	1.076	7.6	7.61	0.789	47.0	1.0	147.8	84.7	317	5
LM3-G1	LO	2.050	2050.00	0.011	1.021	0.998	0.981	2093.460	2045.900	2010.640	1.023	1.018	1.041	4.1	4.09	-0.135	242.2	0.9	151.9	20.2	335	70
LM3-K1	LO	2.320	2320.00	0.036	1.020	1.005	0.976	2365.704	2330.440	2264.088	1.015	1.029	1.045	4.5	4.46	0.315	174.1	30.4	49.1	44.4	284	30
Mean		**2.48**	**2475.00**										**1.100**	**10.0**	**9.90**	**0.286**						
LM3v-H1	LO – red g.	0.173	173.00	0.060	1.0142	1.0033	0.9825	175.457	173.571	169.973	1.011	1.021	1.032	3.2	2.98	0.320	123.8	68.6	256.4	14.9	350	15
LM3v-I1	LO – red g.	0.337	337.00	0.031	1.0242	1.0031	0.9727	345.155	338.045	327.800	1.021	1.031	1.053	5.3	5.08	0.195	138.4	40.4	246.8	20.4	357	43
LM3v-J1	LO – red g.	0.438	438.00	0.105	1.0243	0.999	0.9767	448.643	437.562	427.795	1.025	1.023	1.049	4.9	4.72	-0.053	120.1	46.5	17.5	11.7	277	41
Mean		**0.32**	**316.00**										**1.045**	**4.5**	**4.26**	**0.154**						
LM4-A1	LO	0.0960	96.00	0.061	1.0114	1.0062	0.9824	97.094	96.595	94.310	1.005	1.024	1.030	3.0	2.57	0.646	323.1	28.5	134.8	61.2	231	4
LM4-A2	LO	0.0764	76.40	0.047	1.009	0.9979	0.9932	77.088	76.240	75.880	1.011	1.005	1.016	1.6	1.34	-0.404	170.2	48.3	28.0	35.1	284	19
LM4-B1	LO	0.0825	82.50	0.021	1.0163	1.0007	0.983	83.845	82.558	81.098	1.016	1.018	1.034	3.4	2.89	0.072	9.6	0.8	278.0	62.7	100	27
LM4-B2	LO	0.0583	58.30	0.054	1.0187	0.9912	0.9901	59.390	57.787	57.723	1.028	1.001	1.029	2.9	2.32	-0.922	268.4	80.1	146.1	5.4	55	8
LM4-C1	LO	0.0111	11.10	0.017	1.0156	1.0094	0.975	11.273	11.204	10.823	1.006	1.035	1.042	4.2	1.82	0.702	308.8	75.0	91.9	12.1	184	9
LM4-C2	LO	0.0674	67.40	0.158	1.0119	1.0007	0.9873	68.202	67.447	66.544	1.011	1.014	1.025	2.5	2.06	0.098	351.2	9.0	91.7	48.9	254	40
LM4-D1	LO	0.0596	59.60	0.092	1.0177	0.9939	0.9884	60.655	59.236	58.909	1.024	1.006	1.030	3.0	2.40	-0.618	149.4	35.7	344.8	53.2	245	8
LM4-D2	LO	0.0647	64.70	0.169	1.0134	1.0061	0.9806	65.567	65.095	63.445	1.007	1.026	1.033	3.3	2.74	0.559	342.9	35.4	225.2	33.1	106	37
Mean		**0.06**	**64.50**										**1.030**	**3.0**	**2.27**	**0.017**						

Table A2-1. (cont.)

Sample	Granites	Km x 10-3 SI	Km x 10-6 SI	StErr (%)	Pkmax	Pkint	Pkmin	Kmax	Kint	Kmin	L	F	P	P%	Ppara%	T	Kmax Dec	Kmax Inc	Kint Dec	Kint Inc	Kmin Dec	K min Inc
LM5-A1	LO	2.48	2480.00	0.258	1.0283	1.0213	0.9504	2550.184	2532.824	2356.992	1.007	1.075	1.082	8.2	8.15	0.827	25.9	69.9	166.1	15.7	260	12
LM5-B1	LO	3.16	3160.00	0.178	1.0443	1.015	0.9406	3299.988	3207.400	2972.296	1.029	1.079	1.110	11.0	10.97	0.456	23.0	41.0	155.1	37.7	268	26
LM5-C1	LO	3.82	3820.00	0.024	1.035	0.9986	0.9664	3953.700	3814.652	3691.648	1.036	1.033	1.071	7.1	7.07	-0.044	113.7	71.3	314.9	17.5	223	6
LM5-D1	LO	2.50	2500.00	0.016	1.0112	0.9984	0.9904	2528.000	2496.000	2476.000	1.013	1.008	1.021	2.1	2.09	-0.229	2.8	25.7	110.3	32.0	242	47
LM5-D2	LO	2.90	2900.00	0.041	1.0276	1.0222	0.9503	2980.040	2964.380	2755.870	1.005	1.076	1.081	8.1	8.09	0.865	141.1	20.1	28.9	46.0	247	37
LM5-E1	LO	2.38	2380.00	0.109	1.0525	1.0068	0.9408	2504.950	2396.184	2239.104	1.045	1.07	1.119	11.9	11.80	0.208	26.9	67.2	150.1	13.0	245	19
Mean		**2.87**	**2873.33**										**1.081**	**8.1**	**8.03**	**0.347**						
LM6-A1	LO	0.208	208.00	0.026	1.0163	0.9952	0.9885	211.390	207.002	205.608	1.021	1.007	1.028	2.8	2.63	-0.513	341.3	44.1	92.4	20.4	200	39
LM6-A2	LO	0.204	204.00	0.048	1.0188	0.9924	0.9887	207.835	202.450	201.695	1.027	1.004	1.030	3.0	2.85	-0.754	319.0	3.1	227.4	27.9	55	62
LM6-B1	LO	0.304	304.00	0.083	1.0251	0.9954	0.9794	311.630	302.602	297.738	1.030	1.016	1.047	4.7	4.46	-0.291	318.3	32.1	124.9	57.2	225	6
LM6-B2	LO	0.274	274.00	0.027	1.0089	1.0042	0.9868	276.439	275.151	270.383	1.005	1.018	1.022	2.2	2.13	0.576	204.5	56.8	313.9	12.3	51	30
LM6-C1	LO	0.271	271.00	0.027	1.013	1.007	0.98	274.523	272.897	265.580	1.006	1.027	1.034	3.4	3.20	0.641	343.8	46.0	179.3	42.9	82	8
LM6-C2	LO	0.266	266.00	0.05	1.0167	1.005	0.9783	270.442	267.330	260.228	1.012	1.027	1.039	3.9	3.72	0.401	8.4	7.0	160.3	82.0	278	4
LM6-D1	LO	0.168	168.00	0.033	1.0069	1.0002	0.9928	169.159	168.034	166.790	1.007	1.007	1.014	1.4	1.31	0.055	78.1	46.3	188.5	18.4	294	38
LM6-D2	LO	0.133	133.00	0.023	1.0173	0.992	0.9907	135.301	131.936	131.763	1.026	1.001	1.027	2.7	2.43	-0.898	348.1	50.3	252.4	4.7	159	39
Mean		**0.23**	**228.50**										**1.030**	**3.0**	**2.84**	**-0.098**						
LM7-A1	BA	0.0507	50.70	0.972	1.2095	1.1349	0.6555	61.322	57.539	33.234	1.066	1.731	1.845	84.5	59.47	0.792	338.6	0.2	248.3	60.6	69	29
LM7-B1	BA	0.0302	30.20	0.169	1.0177	1.0055	0.9768	30.735	30.366	29.499	1.012	1.029	1.042	4.2	2.84	0.413	321.1	3.2	118.6	86.6	231	1
LM7-C1	BA	0.0280	28.00	0.115	1.0151	1.0096	0.9753	28.423	28.269	27.308	1.005	1.035	1.041	4.1	2.70	0.731	175.0	34.4	350.5	55.5	84	2
LM7-D1	BA	0.0281	28.10	0.12	1.0213	1.0091	0.9695	28.699	28.356	27.243	1.012	1.041	1.053	5.3	3.53	0.537	349.4	31.2	141.6	55.6	251	13
Mean		**0.03**	**34.25**										**1.045**	**4.5**	**3.02**	**0.618**						
LM8-A1	LO	1.89	1890.00	0.048	1.0251	1.0128	0.9621	1937.439	1914.192	1818.369	1.012	1.053	1.066	6.6	6.50	0.618	356.3	4.3	246.8	77.3	87	12
LM8-B1	LO	1.57	1570.00	0.039	1.0246	1.005	0.9704	1608.622	1577.850	1523.528	1.020	1.036	1.056	5.6	5.53	0.289	161.5	76.8	355.1	12.9	264	3
LM8-C1	LO	1.77	1770.00	0.018	1.0298	1.000	0.9703	1822.746	1770.000	1717.431	1.030	1.031	1.061	6.1	6.08	0.013	171.5	53.4	335.4	35.5	71	8
LM8-C2	LO	1.52	1520.00	0.033	1.0244	0.9995	0.9761	1557.088	1519.240	1483.672	1.025	1.024	1.050	5.0	4.90	-0.020	200.1	56.9	18.5	33.1	109	8
LM8-D1	LO	1.87	1870.00	0.01	1.0217	1.0116	0.9667	1910.579	1891.692	1807.729	1.010	1.046	1.057	5.7	5.65	0.642	200.1	76.6	332.9	9.2	65	10
LM8-D2	LO	1.67	1670.00	0.022	1.0318	1.008	0.9602	1723.106	1683.360	1603.534	1.024	1.050	1.075	7.5	7.39	0.352	180.9	3.3	76.7	76.9	272	13
LM8-E1	LO	1.66	1660.00	0.029	1.0265	1.0103	0.9632	1703.990	1677.098	1598.912	1.016	1.049	1.066	6.6	6.51	0.502	121.0	78.0	330.9	10.4	240	6
LM8-E2	LO	1.67	1670.00	0.013	1.0339	1.0044	0.9618	1726.613	1677.348	1606.206	1.029	1.044	1.075	7.5	7.43	0.199	140.6	71.6	343.8	17.0	252	7
LM8-F1	LO	1.36	1360.00	0.045	1.0257	1.0063	0.968	1394.952	1368.568	1316.480	1.019	1.040	1.060	6.0	5.90	0.342	158.2	54.3	323.6	34.8	58	7
LM8-F2	LO	1.79	1790.00	0.009	1.0232	1.0102	0.9666	1831.528	1808.258	1730.214	1.013	1.045	1.059	5.9	5.81	0.552	32.2	83.1	169.3	5.1	260	5
Mean		**1.68**	**1677.00**										**1.063**	**6.3**	**6.17**	**0.349**						
LM9-A1	VRM	0.0493	49.30	0.039	1.0261	1.0031	0.9708	50.587	49.453	47.860	1.023	1.033	1.057	5.7	4.41	0.181	135.2	12.7	329.8	76.9	226	3
LM9-A2	VRM	0.0509	50.90	0.09	1.0275	1.0017	0.9708	52.300	50.987	49.414	1.026	1.032	1.058	5.8	4.55	0.103	139.8	15.0	340.3	74.0	231	5
LM9-B1	VRM	0.0520	52.00	0.062	1.0263	0.9965	0.9772	53.368	51.818	50.814	1.030	1.02	1.050	5.0	3.94	-0.201	329.7	48.3	82.9	19.4	187	35
LM9-C1	VRM	0.0469	46.90	0.078	1.0166	0.9997	0.9837	47.679	46.886	46.136	1.017	1.016	1.034	3.4	2.57	-0.017	136.7	8.2	6.9	77.3	228	10
LM9-C2	VRM	0.0438	43.80	0.047	1.0198	0.9989	0.9813	44.667	43.752	42.981	1.021	1.018	1.039	3.9	2.96	-0.078	133.8	12.7	348.6	74.6	226	9
LM9-D1	VRM	0.0476	47.60	0.042	1.0254	0.9967	0.978	48.809	47.443	46.553	1.029	1.019	1.049	4.9	3.73	-0.200	128.3	24.2	1.5	53.1	231	26
LM9-D2	VRM	0.0492	49.20	0.078	1.026	1.0052	0.9688	50.479	49.456	47.665	1.021	1.038	1.059	5.9	4.56	0.287	120.9	21.0	5.9	47.8	226	35
LM9-E1	VRM	0.0465	46.50	0.102	1.0187	1.0027	0.9786	47.370	46.626	45.505	1.016	1.025	1.041	4.1	3.13	0.210	132.1	15.6	6.8	64.3	228	20
LM9-E2	VRM	0.0416	41.60	0.103	1.0116	1.0023	0.9861	42.083	41.696	41.022	1.009	1.016	1.026	2.6	1.93	0.281	115.8	26.8	350.7	48.7	222	29
LM9-F1	VRM	0.0448	44.80	0.102	1.016	1.0008	0.9832	45.517	44.836	44.047	1.015	1.018	1.033	3.3	2.53	0.080	135.3	21.3	333.3	67.7	228	6
LM9-F2	VRM	0.0469	46.90	0.126	1.0195	1.0039	0.9766	47.815	47.083	45.803	1.016	1.028	1.044	4.4	3.36	0.283	122.8	31.7	346.7	49.4	228	23
Mean		**0.0472**	**47.23**										**1.045**	**4.5**	**3.42**	**0.084**						
LM10-A1	VRM	0.0529	52.90	0.087	1.0232	0.9944	0.9824	54.127	52.604	51.969	1.029	1.012	1.042	4.2	3.27	-0.403	311.9	23.9	172.8	59.7	50	18
LM10-A2	VRM	0.0466	46.60	0.104	1.0266	0.9986	0.9748	47.840	46.535	45.426	1.028	1.024	1.053	5.3	4.06	-0.067	313.9	23.8	162.7	63.3	49	11
LM10-B1	VRM	0.0541	54.10	0.079	1.0215	0.996	0.9825	55.263	53.884	53.153	1.026	1.014	1.040	4.0	3.14	-0.295	308.3	33.8	126.9	56.2	218	1
LM10-C1	VRM	0.0474	47.40	0.071	1.0181	0.9959	0.986	48.258	47.206	46.736	1.022	1.01	1.033	3.3	2.51	-0.374	303.1	45.1	103.7	43.2	203	10
LM10-E1	VRM	0.0576	57.60	0.033	1.0179	0.9969	0.9852	58.631	57.421	56.748	1.021	1.012	1.033	3.3	2.66	-0.278	313.5	17.9	126.7	72.0	223	2
LM10-E2	VRM	0.0515	51.50	0.043	1.0196	0.9924	0.9879	52.509	51.109	50.877	1.027	1.005	1.032	3.2	2.52	-0.714	311.8	20.9	145.8	68.5	44	5
Mean		**0.0517**	**51.68**										**1.039**	**3.9**	**3.03**	**-0.355**						

Table A2-1. (cont.)

Sample	Granites	Km x 10-3 SI	Km x 10-6 SI	StErr (%)	Pkmax	Pkint	Pkmin	Kmax	Kint	Kmin	L	F	P	P%	Ppara%	T	Kmax Dec	Kmax Inc	Kint Dec	Kint Inc	Kmin Dec	K min Inc
LM11-A1	VRM	0.0523	52.30	0.041	1.0097	1.0058	0.9846	52.807	52.603	51.495	1.004	1.022	1.025	2.5	2.00	0.692	113.7	30.5	314.4	57.8	209	9
LM11-A2	VRM	0.0531	53.10	0.039	1.0136	1.0019	0.9845	53.822	53.201	52.277	1.012	1.018	1.030	3.0	2.33	0.199	306.8	1.8	41.8	70.4	216	20
LM11-B1	VRM	0.0551	55.10	0.049	1.0078	1.0068	0.9854	55.530	55.475	54.296	1.001	1.022	1.023	2.3	1.81	0.908	123.1	49.9	347.7	31.0	243	23
LM11-B2	VRM	0.0471	47.10	0.039	1.014	1.0014	0.9846	47.759	47.166	46.375	1.012	1.017	1.030	3.0	2.29	0.154	130.9	24.9	16.0	42.2	242	38
LM11-C1	VRM	0.0603	60.30	0.061	1.0162	1.0115	0.9723	61.277	60.993	58.630	1.005	1.04	1.045	4.5	3.64	0.791	317.5	23.1	86.0	55.5	217	24
LM11-D1	VRM	0.0521	52.10	0.062	1.0181	1.0052	0.9767	53.043	52.371	50.886	1.013	1.029	1.042	4.2	3.32	0.383	131.1	15.2	16.9	56.5	230	29
LM11-E1	VRM	0.047	47.00	0.205	1.0169	1.0049	0.9783	47.794	47.230	45.980	1.012	1.027	1.039	3.9	3.02	0.388	140	15.2	20.5	61.2	237	24
LM11-E2	VRM	0.0436	43.60	0.08	1.0188	1.0043	0.977	44.420	43.787	42.597	1.014	1.028	1.043	4.3	3.22	0.316	142	0.4	50.8	71.9	232	18
Mean		**0.051**	**51.33**										**1.035**	**3.5**	**2.71**	**0.479**						
LM12-A1	DGM	1.19	1190.00	0.841	1.2625	1.017	0.7205	1502.375	1210.230	857.395	1.241	1.412	1.752	75.2	74.02	0.229	317.8	33.8	205.9	29.1	85	42
LM12-A2	DGM	83.00	83000.00	0.457	1.4037	0.8907	0.7056	116507.100	73928.100	58564.800	1.576	1.262	1.989	98.9	98.91	-0.322	316	32.7	205.8	28.3	84	44
LM12-B1	DGM	36.20	36200.00	0.205	1.0666	1.0158	0.9176	38610.920	36771.960	33217.120	1.05	1.107	1.162	16.2	16.23	0.351	325.2	20.5	217.8	38.6	77	44
LM12-C1	DGM	44.00	44000.00	0.046	1.1166	0.9808	0.9026	49130.400	43155.200	39714.400	1.139	1.087	1.237	23.7	23.70	-0.219	327.1	24.4	222.5	29.1	90	50
LM12-C2	DGM	39.00	39000.00	0.166	1.076	1.0145	0.9095	41964.000	39565.500	35470.500	1.061	1.115	1.183	18.3	18.30	0.300	323.5	24.6	211	39.9	76	40
LM12-D1	DGM	69.90	69900.00	0.071	1.1608	0.9877	0.8515	81139.920	69040.230	59519.850	1.175	1.16	1.363	36.3	36.32	-0.043	328.1	17.1	227	32.1	82	53
LM12-D2	DGM	57.70	57700.00	0.06	1.1582	1.0052	0.8366	66828.140	58000.040	48271.820	1.152	1.202	1.384	38.4	38.43	0.129	326.7	17.4	223	37.2	77	48
LM12-E1	DGM	56.80	56800.00	0.236	1.1763	0.9876	0.8361	66813.840	56095.680	47490.480	1.191	1.181	1.407	40.7	40.68	-0.025	332.6	19	228.6	35.1	86	49
Mean		**48.47**	**48473.75**										**1.435**	**43.5**	**43.32**	**0.050**						
LM13-A1	LO	0.10	99.50	0.03	1.0122	1.0025	0.9853	100.714	99.749	98.037	1.01	1.017	1.027	2.7	2.39	0.285	138.4	66	6.9	16.5	272	17
LM13-A2	LO	10.60	10600.00	0.045	1.0103	1.0018	0.9879	10709.180	10619.080	10471.740	1.009	1.014	1.023	2.3	2.26	0.240	158.2	28.1	32.4	47.6	265	29
LM13-B1	LO	1.14	1140.00	0.009	1.0487	1.0138	0.9376	1195.518	1155.732	1068.864	1.034	1.081	1.118	11.8	11.70	0.396	23.7	29.3	136.7	35	264	41
LM13-B2	LO	92.10	92100.00	0.05	1.0319	1.0086	0.9596	95037.990	92892.060	88379.160	1.023	1.051	1.075	7.5	7.53	0.372	139.6	47.9	354.3	36.6	251	18
LM13-C1	LO	53.60	53600.00	0.086	1.0362	1.004	0.9598	55540.320	53814.400	51445.280	1.032	1.046	1.080	8.0	7.96	0.174	159.1	34.9	10.1	50.9	260	16
LM13-D1	LO	57.10	57100.00	0.013	1.0277	1.0075	0.9648	58681.670	57528.250	55090.080	1.02	1.044	1.065	6.5	6.52	0.373	170.6	2.7	79.2	27	266	63
LM13-E1	LO	49.40	49400.00	0.015	1.0276	0.9997	0.9727	50763.440	49385.180	48051.380	1.028	1.028	1.056	5.6	5.64	-0.002	152.1	22.3	324.5	67.5	61	3
LM13-F1	LO	63.10	63100.00	0.009	1.0484	0.9882	0.9634	66154.040	62355.420	60790.540	1.061	1.026	1.088	8.8	8.82	-0.399	352.8	44.4	155.7	44.3	254	9
LM13-G1	LO	72.30	72300.00	0.151	1.0258	1.0157	0.9585	74165.340	73435.110	69299.550	1.01	1.06	1.070	7.0	7.02	0.708	34.5	68.4	176.9	17.4	271	12
Mean		**44.38**	**44382.17**										**1.067**	**6.7**	**6.65**	**0.239**						
LM14-A1	LO	1.89	1890.00	0.015	1.0258	1.0063	0.9679	1938.762	1901.907	1829.331	1.019	1.04	1.060	6.0	5.94	0.339	145.6	31.5	3.9	52.1	248	19
LM14-A2	LO	1.69	1690.00	0.052	1.0139	1.001	0.9851	1713.491	1691.690	1664.819	1.013	1.016	1.029	2.9	2.90	0.107	165.2	18.7	345.7	71.3	255	0
LM14-B1	LO	1.97	1970.00	0.141	1.0148	1.0114	0.9738	1999.156	1992.458	1918.386	1.003	1.039	1.042	4.2	4.18	0.837	111.8	61.5	342.7	18.9	245	21
LM14-B2	LO	2.13	2130.00	0.022	1.0181	1.0068	0.9751	2168.553	2144.484	2076.963	1.011	1.033	1.044	4.4	4.38	0.484	329.3	27.2	90	44.8	220	33
LM14-C1	LO	2.33	2330.00	0.084	1.0206	1.0111	0.9683	2377.998	2355.863	2256.139	1.009	1.044	1.054	5.4	5.37	0.646	350.2	50.7	141.3	35.6	242	14
LM14-C2	LO	2.88	2880.00	0.083	1.0198	1.0017	0.9784	2937.024	2884.896	2817.792	1.018	1.024	1.042	4.2	4.21	0.137	156	22.3	355.3	66.5	249	7
LM14-D1	LO	2.54	2540.00	0.003	1.0074	1.0042	0.9883	2558.796	2550.668	2510.282	1.003	1.016	1.019	1.9	1.92	0.668	188.5	36.3	320.8	42.5	78	26
LM14-D2	LO	2.00	2000.00	0.113	1.0163	1.0021	0.9817	2032.600	2004.200	1963.400	1.014	1.021	1.035	3.5	3.50	0.186	137.3	33.8	6.7	44.2	247	27
Mean		**2.18**	**2178.75**										**1.041**	**4.1**	**4.05**	**0.426**						
LM15-A1	BA	0.0241	24.10	0.301	1.0154	1.0037	0.9809	24.471	24.189	23.640	1.012	1.023	1.035	3.5	2.21	0.326	151.6	27.7	330.2	62.3	330	62
LM15-B1	BA	0.0255	25.50	0.062	1.0205	1.0029	0.9767	26.023	25.574	24.906	1.018	1.027	1.045	4.5	2.87	0.207	347	15.2	136.5	72.5	137	73
LM15-B2	BA	0.0254	25.40	0.086	1.0177	1.0051	0.9772	25.850	25.530	24.821	1.013	1.028	1.041	4.1	2.65	0.384	163.5	2.6	294.1	86.1	294	86
LM15-C1	BA	0.0246	24.60	0.091	1.0158	1.0043	0.98	24.989	24.706	24.108	1.011	1.025	1.037	3.7	2.31	0.367	7.1	14.2	189.4	75.8	189	76
LM15-C2	BA	0.0216	21.60	0.124	1.0134	1.0064	0.9802	21.889	21.738	21.172	1.007	1.027	1.034	3.4	2.04	0.582	179	26.5	16.3	62.4	16	62
LM15-D1	BA	0.0248	24.80	0.094	1.015	1.0068	0.9782	25.172	24.969	24.259	1.008	1.029	1.038	3.8	2.39	0.557	331.8	1.9	82.1	84.6	82	85
LM15-E1	BA	0.0228	22.80	0.12	1.0202	1.0024	0.9774	23.261	22.855	22.285	1.018	1.026	1.044	4.4	2.69	0.180	174.9	5.9	341.3	83.9	341	84
LM15-E2	BA	0.0251	25.10	0.074	1.0163	1.0044	0.9794	25.509	25.210	24.583	1.012	1.026	1.038	3.8	2.40	0.365	356.2	24.1	183.9	65.7	184	66
Mean		**0.0242**	**24.24**										**1.039**	**3.9**	**2.44**	**0.371**						
LM16-A1	LO	0.0775	77.50	0.02	1.0074	1.0012	0.9914	78.074	77.593	76.834	1.006	1.01	1.016	1.6	1.37	0.228	170.5	1.4	260.8	12.6	74	77
LM16-B1	LO	0.0647	64.70	0.026	1.0057	1.0018	0.9925	65.069	64.816	64.215	1.004	1.009	1.013	1.3	1.09	0.401	354.9	10	113.3	69.7	262	18
LM16-B2	LO	0.0727	72.70	0.04	1.0062	0.9992	0.9946	73.151	72.642	72.307	1.007	1.005	1.012	1.2	0.98	-0.211	333.7	18.2	210.5	59	72	24
LM16-C1	LO	0.0669	66.90	0.031	1.0056	0.9978	0.9966	67.275	66.753	66.673	1.008	1.001	1.009	0.9	0.75	-0.730	355.4	22.8	248.4	34.8	112	46
LM16-D1	LO	0.067	67.00	0.024	1.0058	1.0015	0.9928	67.389	67.101	66.518	1.004	1.009	1.013	1.3	1.08	0.338	17	29.5	215.6	59.1	112	8
LM16-D2	LO	0.0871	87.10	0.027	1.0078	0.9981	0.9941	87.779	86.935	86.586	1.01	1.004	1.014	1.4	1.19	-0.420	8.5	7.9	275.3	21.7	117	67
LM16-E1	LO	0.0542	54.20	0.037	1.0095	0.9978	0.9927	54.715	54.081	53.804	1.012	1.005	1.017	1.7	1.34	-0.392	16.2	14.5	256	62.8	112	23
LM16-E2	LO	0.0463	46.30	0.068	1.0037	1.0016	0.9947	46.471	46.374	46.055	1.002	1.007	1.009	0.9	0.69	0.537	13.9	22.2	113.3	21.8	243	58
Mean		**0.0671**	**67.05**										**1.013**	**1.3**	**1.06**	**-0.031**						

Table A2-1. (cont.)

Sample	Granites	Km x 10-3 SI	Km x 10-6 SI	StErr (%)	Pkmax	Pkint	Pkmin	Kmax	Kint	Kmin	L	F	P	P%	Ppara%	T	Kmax Dec	Kmax Inc	Kint Dec	Kint Inc	Kmin Dec	K min Inc
LM17-A1	LO	0.0871	87.10	0.012	1.0072	1.0013	0.9914	87.727	87.213	86.351	1.006	1.01	1.016	1.6	1.37	0.258	2.6	60.9	161.9	27.5	257	9
LM17-B1	LO	0.0748	74.80	0.024	1.0066	0.9987	0.9948	75.294	74.703	74.411	1.008	1.004	1.012	1.2	1.00	-0.339	359.5	52.9	174.2	37	266	3
LM17-B2	LO	0.0658	65.80	0.046	1.0063	1.0003	0.9934	66.215	65.820	65.366	1.006	1.007	1.013	1.3	1.07	0.062	342	20.9	94.7	45.3	235	37
LM17-C1	LO	0.0712	71.20	0.021	1.0079	0.9997	0.9924	71.762	71.179	70.659	1.008	1.007	1.016	1.6	1.30	-0.056	13.2	38.2	134.8	33.7	251	34
LM17-D1	LO	0.0862	86.20	0.037	1.0048	1.002	0.9932	86.614	86.372	85.614	1.003	1.009	1.012	1.2	1.00	0.527	338.7	48.3	172.8	40.9	77	7
Mean		**0.07702**	**77.02**										**1.014**	**1.4**	**1.15**	**0.090**						
LM18-A1	LO	0.0848	84.80	0.014	1.0065	1.0019	0.9916	85.351	84.961	84.088	1.005	1.01	1.015	1.5	1.29	0.379	169	5.7	279.2	73.7	78	15
LM18-B1	LO	0.0883	88.30	0.024	1.0054	0.9982	0.9964	88.777	88.141	87.982	1.007	1.002	1.009	0.9	0.78	-0.610	9	53.2	131.2	21.8	234	28
LM18-C1	LO	0.0675	67.50	0.043	1.014	0.9971	0.9888	68.445	67.304	66.744	1.017	1.008	1.026	2.6	2.11	-0.337	350.6	22.8	86.3	13.2	204	63
LM18-C2	LO	0.0751	75.10	0.031	1.0116	0.9987	0.9897	75.971	75.002	74.326	1.013	1.009	1.022	2.2	1.86	-0.172	14.4	43.8	106.9	2.6	200	46
LM18-D1	LO	0.0853	85.30	0.029	1.0064	0.9989	0.9947	85.846	85.206	84.848	1.007	1.004	1.012	1.2	1.01	-0.284	195.8	23.3	100.7	11.7	346	64
LM18-E1	LO	0.0751	75.10	0.051	1.0074	0.9988	0.9938	75.656	75.010	74.634	1.009	1.005	1.014	1.4	1.15	-0.265	11.7	7.1	273	50.7	107	38
Mean		**0.07935**	**79.35**										**1.016**	**1.6**	**1.37**	**-0.215**						
LM19-A1	LO	1.55	1550.00	0.083	1.0141	1.0104	0.9755	1571.855	1566.120	1512.025	1.004	1.036	1.040	4.0	3.92	0.815	342	18.7	115.1	63.6	246	18
LM19-A2	LO	1.91	1910.00	0.095	1.0203	1.011	0.9688	1948.773	1931.010	1850.408	1.009	1.044	1.053	5.3	5.28	0.647	30.6	53.8	178.4	31.8	278	16
LM19-B1	LO	1.62	1620.00	0.009	1.0242	1.0137	0.9622	1659.204	1642.194	1558.764	1.01	1.054	1.064	6.4	6.39	0.669	127.6	83.6	346.8	5	256	4
LM19-B2	LO	2.01	2010.00	0.046	1.028	1.0017	0.9703	2066.280	2013.417	1950.303	1.026	1.032	1.059	5.9	5.90	0.102	353.9	9.8	98.3	55.2	258	33
LM19-C1	LO	2.02	2020.00	0.024	1.0378	0.9827	0.9795	2096.356	1985.054	1978.590	1.056	1.003	1.060	6.0	5.91	-0.886	146.9	55.3	287.4	28.1	28	19
LM19-C2	LO	2.39	2390.00	0.058	1.0262	0.9979	0.976	2452.618	2384.981	2332.640	1.028	1.022	1.051	5.1	5.11	-0.116	166.5	52.4	12.7	34.6	274	13
LM19-D1	LO	1.28	1280.00	0.012	1.0416	0.9879	0.9706	1333.248	1264.512	1242.368	1.054	1.018	1.073	7.3	7.23	-0.500	350.7	4.7	86.9	52.5	257	37
LM19-D2	LO	2.17	2170.00	0.007	1.0311	1.0094	0.9595	2237.487	2190.398	2082.115	1.022	1.052	1.075	7.5	7.41	0.407	158	61.6	21.9	21.3	255	18
Mean		**1.86875**	**1868.75**										**1.059**	**5.9**	**5.89**	**0.142**						
LM20-A1	LO	2.3	2300.00	0.017	1.041	0.9989	0.9601	2394.300	2297.470	2208.230	1.042	1.04	1.084	8.4	8.37	-0.021	160.1	20.5	34.9	57.1	260	25
LM20-B1	LO	3.85	3850.00	0.011	1.0219	1.0136	0.9645	3934.315	3902.360	3713.325	1.008	1.051	1.059	5.9	5.93	0.716	110.2	52.8	3.5	12.3	265	34
LM20-C1	LO	2.71	2710.00	0.028	1.0337	1.0028	0.9636	2801.327	2717.588	2611.356	1.031	1.041	1.073	7.3	7.24	0.135	174.1	17.7	62.6	48.9	277	36
LM20-C2	LO	2.75	2750.00	0.027	1.0225	0.9969	0.9806	2811.875	2741.475	2696.650	1.026	1.017	1.043	4.3	4.25	-0.209	126.8	33.4	217.3	0.8	309	57
LM20-D1	LO	2.49	2490.00	0.073	1.0227	0.9998	0.9775	2546.523	2489.502	2433.975	1.023	1.023	1.046	4.6	4.60	-0.001	211.2	42.4	102.9	18.9	355	42
LM20-E1	LO	2.46	2460.00	0.032	1.0326	1.0085	0.9589	2540.196	2480.910	2358.894	1.024	1.052	1.077	7.7	7.64	0.363	168.8	26.7	52	41.9	281	36
Mean		**2.76**	**2760.00**										**1.064**	**6.4**	**6.34**	**0.164**						
LM21-A1	LO	0.206	206.00	0.038	1.0266	0.9962	0.9772	211.480	205.217	201.303	1.031	1.019	1.050	5.0	4.73	-0.220	185.6	66.4	74.4	9	341	22
LM21-A2	LO	0.173	173.00	0.064	1.0204	0.9983	0.9812	176.529	172.706	169.748	1.022	1.017	1.040	4.0	3.69	-0.119	312.1	38.6	91.7	43.7	204	22
LM21-B1	LO	0.200	200.00	0.022	1.0356	0.996	0.9684	207.120	199.200	193.680	1.04	1.029	1.069	6.9	6.47	-0.162	34.8	32.3	189.8	55	297	12
LM21-B2	LO	0.175	175.00	0.015	1.0326	0.9866	0.9808	180.705	172.655	171.640	1.047	1.006	1.053	5.3	4.88	-0.768	55	39.3	280.6	40.5	167	25
LM21-C1	LO	0.119	119.00	0.017	1.0137	0.9979	0.9884	120.630	118.750	117.620	1.016	1.01	1.026	2.6	2.29	-0.243	58.9	32	176.5	36.6	301	37
LM21-C2	LO	0.363	363.00	0.049	1.0293	1.0152	0.9555	373.636	368.518	346.847	1.014	1.062	1.077	7.7	7.42	0.629	127.6	73.4	328.2	15.6	237	6
LM21-D1	LO	0.236	236.00	0.027	1.0274	1.0083	0.9642	242.466	237.959	227.551	1.019	1.046	1.066	6.6	6.17	0.409	102.8	64.6	233.1	17.1	329	18
LM21-E1	LO	0.249	249.00	0.021	1.0121	0.9982	0.9897	252.013	248.552	246.435	1.014	1.009	1.023	2.3	2.14	-0.236	269.8	58.3	7.8	4.9	101	31
LM21-E2	LO	0.379	379.00	0.085	1.0288	0.9979	0.9733	389.915	378.204	368.881	1.031	1.025	1.057	5.7	5.49	-0.098	209	5.2	323.4	77.6	118	11
Mean		**0.233**	**233.33**										**1.051**	**5.1**	**4.81**	**-0.090**						
LM22-A1	LO	0.592	592.00	0.009	1.042	0.988	0.97	616.864	584.896	574.240	1.055	1.019	1.074	7.4	7.25	-0.485	180.3	35.7	352.6	54.1	87.6	3.7
LM22-A2	LO	0.365	365.00	0.01	1.0234	1.0033	0.9733	373.541	366.205	355.255	1.02	1.031	1.052	5.2	4.95	0.210	288.9	44.6	169.3	26.6	59.9	33.7
LM22-B1	LO	0.526	526.00	0.058	1.0167	1.002	0.9813	534.784	527.052	516.164	1.015	1.021	1.036	3.6	3.51	0.180	140.4	48.4	44.2	5.5	309.4	41.1
LM22-B2	LO	0.492	492.00	0.012	1.0197	1.0025	0.9777	501.692	493.230	481.028	1.017	1.025	1.043	4.3	4.17	0.189	246.6	55.7	76.3	33.9	343.2	4.5
LM22-C1	LO	0.647	647.00	0.045	1.0176	0.9976	0.9848	658.387	645.447	637.166	1.02	1.013	1.033	3.3	3.26	-0.210	188	14.1	54.9	69.9	281.6	14.1
LM22-C2	LO	0.918	918.00	0.007	1.0244	1.0034	0.9722	940.399	921.121	892.480	1.021	1.032	1.054	5.4	5.29	0.208	305.3	72.8	163.9	13.6	71.4	10.3
LM22-D1	LO	0.584	584.00	0.016	1.0449	1.0057	0.9494	610.222	587.329	554.450	1.039	1.059	1.101	10.1	9.81	0.203	165.3	26.7	284.4	44.1	55.4	34.1
LM22-D2	LO	0.72	720.00	0.012	1.031	1.0135	0.9555	742.320	729.720	687.960	1.017	1.061	1.079	7.9	7.74	0.551	316.1	53.6	136.4	36.4	46.3	0.1
Mean		**0.6055**	**605.50**										**1.059**	**5.9**	**5.75**	**0.106**						

Table A2-1. (cont.)

Sample	Granites	Km x 10-3 SI	Km x 10-6 SI	StErr (%)	Pkmax	Pkint	Pkmin	Kmax	Kint	Kmin	L	F	P	P%	Ppara%	T	Kmax Dec	Kmax Inc	Kint Dec	Kint Inc	Kmin Dec	K min Inc
LM23-A1	LO	0.152	152.00	0.018	1.0274	0.9986	0.9739	156.165	151.787	148.033	1.029	1.025	1.055	5.5	5.02	-0.062	184.5	49.5	322.8	32.5	67.3	21.4
LM23-B1	LO	0.274	274.00	0.006	1.0177	0.9997	0.9826	278.850	273.918	269.232	1.018	1.017	1.036	3.6	3.40	-0.014	228.3	36.8	8.2	45.6	121.5	21.1
LM23-B2	LO	0.32	320.00	0.038	1.0336	0.9968	0.9696	330.752	318.976	310.272	1.037	1.028	1.066	6.6	6.32	-0.136	341.9	69.4	132.7	18.1	225.8	9.4
LM23-C1	LO	0.221	221.00	0.023	1.025	0.9975	0.9775	226.525	220.448	216.028	1.028	1.02	1.049	4.9	4.56	-0.149	116.6	58.7	17	5.8	283.5	30.7
LM23-C2	LO	0.287	287.00	0.042	1.0335	0.9882	0.9783	296.615	283.613	280.772	1.046	1.01	1.056	5.6	5.37	-0.634	262.8	62	37.8	20.6	134.9	18.1
LM23-D1	LO	0.269	269.00	0.009	1.0199	0.9966	0.9836	274.353	268.085	264.588	1.023	1.013	1.037	3.7	3.51	-0.275	145.6	70.2	305.4	18.6	37.5	6.3
LM23-E1	LO	0.255	255.00	0.049	1.0361	0.9888	0.9751	264.206	252.144	248.651	1.048	1.014	1.063	6.3	5.92	-0.542	165.3	43.6	276.6	20.9	24.7	39.1
Mean		**0.254**	**254.00**										**1.052**	**5.2**	**4.87**	**-0.259**						
LM24-A1	AC	0.179	179.00	0.016	1.0095	1.0021	0.9883	180.701	179.376	176.906	1.007	1.014	1.021	2.1	1.99	0.306	327	42.9	156.1	46.7	61.2	4.6
LM24-B1	AC	0.185	185.00	0.014	1.0107	1.0001	0.9893	186.980	185.019	183.021	1.011	1.011	1.022	2.2	2.01	0.013	17.2	63.2	222.5	24.6	127.8	10.1
LM24-C1	AC	0.224	224.00	0.021	1.0194	1.0031	0.9774	228.346	224.694	218.938	1.016	1.026	1.043	4.3	4.04	0.235	317.8	35.9	123.4	53.2	222.8	6.9
LM24-D1	AC	0.206	206.00	0.02	1.0179	0.9958	0.9863	209.687	205.135	203.178	1.022	1.01	1.032	3.2	3.00	-0.390	165.6	42.7	347.1	47.3	256.3	0.7
LM24-D2	AC	0.359	359.00	0.008	1.0357	1.0033	0.961	371.816	360.185	344.999	1.032	1.044	1.078	7.8	7.47	0.152	143	46.2	342.6	42.1	243.5	9.9
LM24-E1	AC	0.213	213.00	0.014	1.0195	0.9942	0.9863	217.154	211.765	210.082	1.026	1.008	1.034	3.4	3.16	-0.520	174.8	82.6	325.4	6.4	55.8	3.6
LM24-E2	AC	0.307	307.00	0.016	1.017	1.0025	0.9804	312.219	307.768	300.983	1.014	1.023	1.037	3.7	3.57	0.215	4.1	1	97.9	74.8	273.9	15.1
Mean		**0.239**	**239.00**										**1.038**	**3.8**	**3.60**	**0.002**						
LM25-A1	AC	0.161	161.00	0.073	1.0236	0.9996	0.9768	164.800	160.936	157.265	1.024	1.023	1.048	4.8	4.40	-0.014	260.8	76.9	139.8	6.8	48.4	11.1
LM25-A2	AC	0.217	217.00	0.011	1.0232	1.0064	0.9704	222.034	218.389	210.577	1.017	1.037	1.054	5.4	5.10	0.373	174.6	6.8	50.1	78.1	265.8	9.7
LM25-A3	AC	0.159	159.00	0.042	1.0244	0.9995	0.9762	162.880	158.921	155.216	1.025	1.024	1.049	4.9	4.53	-0.022	230.7	64.8	139.9	0.4	49.7	25.2
LM25-B1	AC	0.161	161.00	0.022	1.0388	0.987	0.9743	167.247	158.907	156.862	1.052	1.013	1.066	6.6	6.08	-0.595	210.4	25.2	86.9	49.6	315.7	29.3
LM25-B2	AC	0.136	136.00	0.026	1.0112	1.0003	0.9885	137.523	136.041	134.436	1.011	1.012	1.023	2.3	2.08	0.047	235.7	3.6	144	25.4	333.2	64.3
LM25-C1	AC	0.135	135.00	0.031	1.0086	1.0013	0.9901	136.161	135.176	133.664	1.007	1.011	1.019	1.9	1.69	0.208	185.9	77	329.5	10.5	60.9	7.5
LM25-C2	AC	0.139	139.00	0.039	1.0093	1.0015	0.9892	140.293	139.209	137.499	1.008	1.012	1.020	2.0	1.84	0.226	337	79.1	222.3	4.6	131.5	9.9
LM25-D1	AC	0.181	181.00	0.026	1.0191	1.0072	0.9737	184.457	182.303	176.240	1.012	1.034	1.047	4.7	4.32	0.487	331.9	24.1	208	51.3	75.8	28.3
LM25-D2	AC	0.213	213.00	0.023	1.0191	0.9956	0.9853	217.068	212.063	209.869	1.024	1.01	1.034	3.4	3.22	-0.381	351.3	16.9	237.1	53.4	92	31.3
Mean		**0.167**	**166.89**										**1.040**	**4.0**	**3.70**	**0.037**						
LM26-A1	AC	0.851	851.00	0.065	1.0247	1.0059	0.9694	872.020	856.021	824.959	1.019	1.038	1.057	5.7	5.61	0.335	4.2	41.5	223.7	41.1	114.1	21
LM26-A2	AC	0.905	905.00	0.005	1.042	0.9832	0.9748	943.010	889.796	882.194	1.06	1.009	1.075	7.5	6.79	-0.744	147.4	80.3	4.1	7.8	273.3	5.7
LM26-B1	AC	0.805	805.00	0.091	1.0232	1.0103	0.9665	823.676	813.292	778.033	1.013	1.045	1.062	6.2	5.76	0.555	259.4	72.2	158.9	3.3	67.8	17.4
LM26-C1	AC	0.722	722.00	0.023	1.0229	1.0009	0.9761	738.534	722.650	704.744	1.022	1.025	1.048	4.8	4.70	0.072	342.1	6.5	238.5	64.1	75.1	24.9
LM26-C2	AC	0.878	878.00	0.034	1.0323	1.0042	0.9635	906.359	881.688	845.953	1.028	1.042	1.071	7.1	7.02	0.199	216.5	80.4	332.1	4.2	62.7	8.6
LM26-D1	AC	0.775	775.00	0.007	1.0127	1.0004	0.9869	784.843	775.310	764.848	1.012	1.014	1.026	2.6	2.57	0.056	185.1	29.9	0.4	60	93.9	2
LM26-D2	AC	0.786	786.00	0.007	1.0182	1.0082	0.9737	800.305	792.445	765.328	1.01	1.035	1.046	4.6	4.49	0.559	330.5	66.2	203.7	14.8	108.7	18.2
LM26-D3	AC	0.706	706.00	0.01	1.0158	1.0091	0.9751	717.155	712.425	688.421	1.007	1.035	1.042	4.2	4.09	0.673	251.7	81.4	9.2	4	99.7	7.6
Mean		**0.804**	**803.50**										**1.053**	**5.3**	**5.13**	**0.213**						
LM27-A1	LO	0.080	80.00	0.056	1.0056	1.0019	0.9925	80.448	80.152	79.400	1.004	1.009	1.013	1.3	1.12	0.437	157.4	52	287	26.5	30.6	25.2
LM27-A2	LO	0.060	60.30	0.06	1.0035	1.0015	0.995	60.511	60.390	59.999	1.002	1.007	1.009	0.9	0.69	0.521	164.8	15.2	278.2	55.6	65.9	30
LM27-B1	LO	0.059	59.20	0.059	1.0085	0.9996	0.992	59.703	59.176	58.726	1.009	1.008	1.017	1.7	1.34	-0.078	171.3	32.8	289.7	36.5	52.9	36.5
LM27-C1	LO	0.074	73.50	0.08	1.0068	0.998	0.9952	74.000	73.353	73.147	1.009	1.003	1.012	1.2	0.98	-0.522	168.1	45.2	316.3	40.2	60.7	16.4
LM27-D1	LO	0.073	72.60	0.072	1.0082	0.9997	0.9922	73.195	72.578	72.034	1.009	1.008	1.016	1.6	1.35	-0.061	151.1	54.1	324.6	35.8	56.8	3.1
LM27-D2	LO	0.071	71.20	0.051	1.0037	1.0015	0.9947	71.463	71.307	70.823	1.002	1.007	1.009	0.9	0.76	0.515	324.5	45.6	163.3	42.8	64.4	9.5
Mean		**0.069**	**69.47**										**1.013**	**1.3**	**1.04**	**0.135**						
LM28-A1	LO	2.130	2130.00	0.046	1.0188	1.0043	0.9769	2170.044	2139.159	2080.797	1.014	1.028	1.043	4.3	4.26	0.320	125	38	281.4	49.6	25.6	11.8
LM28-A2	LO	2.180	2180.00	0.036	1.0334	1.0061	0.9604	2252.812	2193.298	2093.672	1.027	1.048	1.076	7.6	7.55	0.269	197.5	64.3	295.2	3.7	26.9	25.4
LM28-B1	LO	1.730	1730.00	0.006	1.0238	1.0072	0.969	1771.174	1742.456	1676.370	1.017	1.039	1.057	5.7	5.61	0.405	288.3	70.3	121	19.2	29.6	4
LM28-C1	LO	2.450	2450.00	0.04	1.0265	1.0158	0.9577	2514.925	2488.710	2346.365	1.01	1.061	1.072	7.2	7.14	0.699	288.1	13.9	136	74.4	19.9	7
LM28-C2	LO	1.800	1800.00	0.013	1.0233	1.0087	0.968	1841.940	1815.660	1742.400	1.014	1.042	1.057	5.7	5.67	0.484	196.9	58	289.4	1.5	20.3	32
LM28-C3	LO	2.050	2050.00	0.018	1.0246	0.9963	0.9792	2100.430	2042.415	2007.360	1.028	1.017	1.046	4.6	4.60	-0.235	98.8	77.1	247.2	11.1	338.5	6.6
LM28-D1	LO	1.840	1840.00	0.068	1.0238	1.0063	0.9698	1883.792	1851.592	1784.432	1.017	1.038	1.056	5.6	5.52	0.364	220.4	67.7	117.4	5.3	25.3	21.6
LM28-D2	LO	2.140	2140.00	0.113	1.0226	1.0054	0.9719	2188.364	2151.556	2079.866	1.017	1.034	1.052	5.2	5.18	0.322	296	25.4	147.9	60.8	32.5	13.5
LM28-E1	LO	1.850	1850.00	0.035	1.024	0.9996	0.9764	1894.400	1849.260	1806.340	1.024	1.024	1.049	4.9	4.84	-0.014	216	68.5	122.7	1.3	32.2	21.4
LM28-E2	LO	2.480	2480.00	0.06	1.0261	1.002	0.9719	2544.728	2484.960	2410.312	1.024	1.031	1.056	5.6	5.54	0.123	287	71.9	119.3	17.7	28.1	3.6
Mean		**2.065**	**2065.00**										**1.056**	**5.6**	**5.59**	**0.274**						

Table A2-1. (cont.)

Sample	Granites	Km x 10-3 SI	Km x 10-6 SI	StErr (%)	Pkmax	Pkint	Pkmin	Kmax	Kint	Kmin	L	F	P	P%	Ppara%	T	Kmax Dec	Kmax Inc	Kint Dec	Kint Inc	Kmin Dec	K min Inc
LM29-A1	LO	1.010	1010.00	0.041	1.0187	0.9959	0.9853	1028.887	1005.859	995.153	1.023	1.011	1.034	3.4	3.34	-0.359	194	59.7	349	27.9	84.9	10.9
LM29-A2	LO	1.030	1030.00	0.076	1.0278	1.007	0.9652	1058.634	1037.210	994.156	1.021	1.043	1.065	6.5	6.40	0.349	137.8	73	7.3	11.2	274.7	12.6
LM29-B1	LO	1.690	1690.00	0.016	1.0341	0.9962	0.9697	1747.629	1683.578	1638.793	1.038	1.027	1.066	6.6	6.58	-0.163	346.9	69.2	164.4	20.8	254.7	0.8
LM29-B2	LO	1.230	1230.00	0.004	1.0345	0.9852	0.9803	1272.435	1211.796	1205.769	1.05	1.005	1.055	5.5	5.47	-0.814	139.8	59.1	324.7	30.8	233.4	2.1
LM29-B3	LO	1.690	1690.00	0.099	1.0291	1.015	0.9558	1739.179	1715.350	1615.302	1.014	1.062	1.077	7.7	7.60	0.627	146.4	50.5	9.6	31	265.6	21.9
LM29-C1	LO	0.928	928.00	0.021	1.0283	1.0029	0.9688	954.262	930.691	899.046	1.025	1.035	1.061	6.1	6.05	0.158	99.7	67.7	192.9	1.3	283.4	22.3
LM29-C2	LO	0.761	761.00	0.003	1.0114	0.9982	0.9905	769.675	759.630	753.771	1.013	1.008	1.021	2.1	2.07	-0.259	40	66.7	277.5	13	182.9	19
LM29-E1	LO	0.837	837.00	0.114	1.0231	1.0075	0.9694	856.335	843.278	811.388	1.015	1.039	1.055	5.5	5.45	0.430	304	52.7	125.1	37.3	34.7	0.5
Mean		**1.147**	**1147.00**										**1.054**	**5.4**	**5.37**	**-0.004**						
LM30-A2	LO	3.17	3170	0.098	1.0219	1.0063	0.9717	3239.423	3189.971	3080.289	1.016	1.036	1.052	5.2	5.14	0.388	159.4	26.8	325.6	62.5	66.6	5.7
LM30-B1	LO	3.01	3010	0.028	1.0214	1.0009	0.9777	3074.414	3012.709	2942.877	1.021	1.024	1.045	4.5	4.45	0.072	344.3	22.6	160.2	67.4	253.7	1.5
LM30-B2	LO	2.6	2600	0.017	1.02	1.0075	0.9725	2652.000	2619.500	2528.500	1.012	1.036	1.049	4.9	4.86	0.485	173.3	16.4	39.9	66.8	268.1	15.9
LM30-C1	LO	2.71	2710	0.023	1.0113	1.0052	0.9835	2740.623	2724.092	2665.285	1.006	1.022	1.028	2.8	2.81	0.567	184.8	21.3	310.4	56.2	84.4	24.9
LM30-C2	LO	3.04	3040	0.041	1.0194	1.0015	0.9791	3098.976	3044.560	2976.464	1.018	1.023	1.041	4.1	4.10	0.122	177.1	59.1	10.3	30.3	276.9	5.8
LM30-D1	LO	1.89	1890	0.059	1.0214	1.0095	0.969	1930.446	1907.955	1831.410	1.012	1.042	1.054	5.4	5.37	0.556	339.4	47.3	158.6	42.7	249	0.4
LM30-D2	LO	1.91	1910	0.057	1.0255	1.0057	0.9688	1958.705	1920.887	1850.408	1.02	1.038	1.058	5.8	5.81	0.314	166.6	30.7	24	53.2	267.8	18.2
LM30-E1	LO	1.63	1630	0.041	1.0298	0.9998	0.9705	1678.574	1629.674	1581.915	1.03	1.03	1.061	6.1	6.06	0.004	148.4	74.3	348.4	14.8	257.1	5.1
LM30-E2	LO	1.8	1800	0.071	1.0222	1.0071	0.9707	1839.960	1812.780	1747.260	1.015	1.038	1.053	5.3	5.26	0.426	171.5	21.5	324.7	66.2	77.6	9.7
LM30-F1	LO	2.46	2460	0.018	1.0147	1.0007	0.9846	2496.162	2461.722	2422.116	1.014	1.016	1.031	3.1	3.04	0.081	358.4	26.9	161.2	62.1	264.8	7.1
LM30-F2	LO	2.02	2020	0.03	1.0223	0.9941	0.9837	2065.046	2008.082	1987.074	1.028	1.011	1.039	3.9	3.90	-0.452	11.4	68.7	192.3	21.3	102.2	0.3
Mean		**2.39**	**2385.45**										**1.046**	**4.6**	**4.62**	**0.233**						
LM31-A1	BA	0.0299	29.9	0.227	1.0072	0.998	0.9948	30.115	29.840	29.745	1.009	1.003	1.013	1.3	0.85	-0.482	351.3	20	99.2	40.1	241.3	43.1
LM31-B1	BA	0.0284	28.4	0.185	1.009	1.0033	0.9877	28.656	28.494	28.051	1.006	1.016	1.022	2.2	1.44	0.472	352.3	50.4	187.6	38.5	91.5	7.6
LM31-B2	BA	0.0378	37.8	0.175	1.0099	0.9988	0.9913	38.174	37.755	37.471	1.011	1.008	1.019	1.9	1.37	-0.188	2.3	10.9	214.1	77.2	93.6	6.6
LM31-C1	BA	0.0292	29.2	0.217	1.0114	1.001	0.9876	29.533	29.229	28.838	1.01	1.014	1.024	2.4	1.62	0.136	170.3	76.5	5.1	13.1	274.3	3.3
LM31-C2	BA	0.0295	29.5	0.218	1.0124	0.996	0.9916	29.866	29.382	29.252	1.016	1.004	1.021	2.1	1.42	-0.576	233.2	75.5	356.5	8.1	88.2	12
LM31-D1	BA	0.032	32	0.135	1.0136	0.9957	0.9908	32.435	31.862	31.706	1.018	1.005	1.023	2.3	1.60	-0.564	1.8	34.9	168	54.3	267.2	6.6
LM31-D2	BA	0.0307	30.7	0.143	1.0222	0.9961	0.9817	31.382	30.580	30.138	1.026	1.015	1.041	4.1	2.82	-0.276	293.2	11.8	197.4	25.6	45.7	61.4
LM31-E1	BA	0.0393	39.3	0.15	1.0082	1.0019	0.9899	39.622	39.375	38.903	1.006	1.012	1.019	1.9	1.36	0.319	4.8	35.9	167.1	52.8	268.5	8.6
LM31-E2	BA	0.0312	31.2	0.178	1.0139	0.9996	0.9865	31.634	31.188	30.779	1.014	1.013	1.028	2.8	1.91	-0.032	342.7	32.4	192.4	53.9	82	14.3
Mean		**0.032**	**32**										**1.023**	**2.3**	**1.60**	**-0.132**						
LM32-A1	LO	2.32	2320	0.087	1.0226	1.0106	0.9668	2372.432	2344.592	2242.976	1.012	1.045	1.058	5.8	5.74	0.581	157.5	12	288.1	71.8	64.6	13.4
LM32-B1	LO	2.3	2300	0.034	1.0341	0.995	0.9709	2378.430	2288.500	2233.070	1.039	1.025	1.065	6.5	6.47	-0.223	168.4	2.8	56.9	82.3	258.8	7.1
LM32-B2	LO	1.64	1640	0.04	1.0194	0.9954	0.9852	1671.816	1632.456	1615.728	1.024	1.01	1.035	3.5	3.44	-0.395	23.9	58.3	149.2	19.7	248.3	23.8
LM32-C1	LO	1.67	1670	0.155	1.0424	1.0132	0.9444	1740.808	1692.044	1577.148	1.029	1.073	1.104	10.4	10.29	0.425	301.7	71.7	143.5	17.1	51.5	6.4
LM32-D1	LO	1.96	1960	0.017	1.0317	0.9866	0.9818	2022.132	1933.736	1924.328	1.046	1.005	1.051	5.1	5.05	-0.803	171	4.9	266.3	47	76.4	42.6
LM32-D2	LO	2.58	2580	0.048	1.0397	0.9944	0.9659	2682.426	2565.552	2492.022	1.045	1.03	1.076	7.6	7.60	-0.208	352.8	5	244	74.7	84.1	14.4
LM32-E1	LO	2.43	2430	0.019	1.0237	0.9973	0.9789	2487.591	2423.439	2378.727	1.026	1.019	1.046	4.6	4.55	-0.167	3.7	11.4	246.6	66.1	98	20.7
LM32-F1	LO	1.75	1750	0.019	1.0326	1.0097	0.9577	1807.050	1766.975	1675.975	1.023	1.054	1.078	7.8	7.76	0.405	109.6	25.9	295.9	64	200.8	2.5
LM32-G1	LO	1.63	1630	0.015	1.0363	1.0042	0.9596	1689.169	1636.846	1564.148	1.032	1.046	1.08	8.0	7.92	0.182	9	15.5	249.3	60.7	106.2	24.2
Mean		**2.03**	**2031.11**										**1.066**	**6.6**	**6.53**	**-0.023**						

Table A2-1. (cont.)

Sample	Granites	Km x 10-3 SI	Km x 10-6 SI	StErr (%)	Pkmax	Pkint	Pkmin	Kmax	Kint	Kmin	L	F	P	P%	Ppara%	T	Kmax Dec	Kmax Inc	Kint Dec	Kint Inc	Kmin Dec	K min Inc
LM33-A1	LO	2.04	2040	0.081	1.0324	0.9881	0.9795	2106.096	2015.724	1998.180	1.045	1.009	1.054	5.4	5.36	-0.667	177.6	28.4	274.4	12.5	25.6	58.5
LM33-B1	LO	2.17	2170	0.161	1.091	0.9679	0.9411	2367.470	2100.343	2042.187	1.127	1.028	1.159	15.9	15.82	-0.62	335.6	20.1	82.2	37.9	223.9	45.3
LM33-C1	LO	2.12	2120	0.05	1.0369	0.9977	0.9655	2198.228	2115.124	2046.860	1.039	1.033	1.074	7.4	7.34	-0.081	341	9.9	80	41.7	240.3	46.6
LM33-D1	LO	1.69	1690	0.054	1.0366	0.9964	0.967	1751.854	1683.916	1634.230	1.04	1.03	1.072	7.2	7.14	-0.14	48.1	45.7	197	39.9	300.9	16.1
LM33.1-A1	LO	0.273	273	0.014	1.0415	1.0002	0.9583	284.330	273.055	261.616	1.041	1.044	1.087	8.7	8.24	0.029	232.7	29	126	27.4	0.8	48.1
LM33.1-B2	LO	1.08	1080	0.02	1.0348	1.001	0.9642	1117.584	1081.080	1041.336	1.034	1.038	1.073	7.3	7.22	0.058	348.2	21.2	206.7	63.7	84.1	14.9
LM33.1-B2	LO	0.583	583	0.017	1.0106	1.0032	0.9862	589.180	584.866	574.955	1.007	1.017	1.025	2.5	2.42	0.396	338.8	45.4	181.9	42.2	81	11.7
LM33.2-A1	LO	1.7	1700	0.003	1.0228	0.999	0.9782	1738.760	1698.300	1662.940	1.024	1.021	1.046	4.6	4.52	-0.058	350.8	44.8	200.2	41.3	96.4	15.2
LM33.2-B1	LO	0.424	424	0.018	1.0327	1.0074	0.9598	437.865	427.138	406.955	1.025	1.05	1.076	7.6	7.34	0.322	159.4	0.9	65.4	77.4	249.6	12.6
LM33.2-B2	LO	0.258	258	0.154	1.0692	0.9857	0.9452	275.854	254.311	243.862	1.085	1.043	1.131	13.1	12.41	-0.319	25.6	10.3	134.5	60.8	290.3	27
LM33.2-C1	LO	0.302	302	0.018	1.0678	1.0071	0.9252	322.476	304.144	279.410	1.06	1.088	1.154	15.4	14.68	0.183	171.6	39.1	12.1	49	270.1	10.3
LM33.2-D1	LO	1.24	1240	0.003	1.0172	1.0005	0.9822	1261.328	1240.620	1217.928	1.017	1.019	1.036	3.6	3.52	0.055	34.5	2.2	124.7	3.6	273.9	85.8
LM33.2-E1	LO	1.59	1590	0.072	1.0328	0.9948	0.9724	1642.152	1581.732	1546.116	1.038	1.023	1.062	6.2	6.16	-0.244	328.8	46.8	119.4	39.3	222.1	15.1
LM33.2-F2	LO	1.45	1450	0.04	1.0486	0.9914	0.96	1520.470	1437.530	1392.000	1.058	1.033	1.092	9.2	9.14	-0.272	351.2	19.4	162.5	70.4	260.2	2.7
LM33.2-G1	LO	1.99	1990	0.111	1.0258	0.9995	0.9748	2041.342	1989.005	1939.852	1.026	1.025	1.052	5.2	5.19	-0.019	302.8	58.4	188.4	14.3	90.8	27.6
Mean		**1.26**	**1260.67**										**1.080**	**8.0**	**7.77**	**-0.092**						
LM34-A1	LO	0.102	102	0.02	1.0074	0.9987	0.9939	102.755	101.867	101.378	1.009	1.005	1.014	1.4	1.19	-0.284	146.9	3.8	55.7	18.4	248.1	71.1
LM34-B1	LO	0.0987	98.7	0.039	1.0053	1.0001	0.9946	99.223	98.710	98.167	1.005	1.005	1.011	1.1	0.94	0.031	172.4	5.8	265.7	29.5	72.3	59.8
LM34-B2	LO	0.108	108	0.018	1.0052	1.0028	0.992	108.562	108.302	107.136	1.002	1.011	1.013	1.3	1.18	0.635	357.8	0.9	267.7	10	92.9	79.9
LM34-C1	LO	0.0984	98.4	0.027	1.0045	0.9992	0.9962	98.843	98.321	98.026	1.005	1.003	1.008	0.8	0.73	-0.274	163.8	3.4	267.7	76.2	73	13.4
LM34-D1	LO	0.0979	97.9	0.012	1.0065	1.0012	0.9923	98.536	98.017	97.146	1.005	1.009	1.014	1.4	1.25	0.262	344.9	13.9	246.7	29.8	96.9	56.5
LM34-D2	LO	0.0901	90.1	0.064	1.0066	0.9983	0.9951	90.695	89.947	89.659	1.008	1.003	1.012	1.2	1.00	-0.43	2.4	7.3	254.8	67.1	95.3	21.6
LM34-E1	LO	0.0962	96.2	0.023	1.005	0.9998	0.9952	96.681	96.181	95.738	1.005	1.005	1.01	1.0	0.86	-0.056	192.2	3.2	288.8	63.6	100.6	26.2
LM34-E2	LO	0.109	109	0.032	1.0055	0.9994	0.9951	109.600	108.935	108.466	1.006	1.004	1.01	1.0	0.93	-0.174	269.2	77.5	104.9	12	14.2	3.3
Mean		**0.10**	**100.04**										**1.012**	**1.2**	**1.01**	**-0.036**						
LM35-A1	LO	0.303	303	0.065	1.0279	1.0086	0.9635	311.454	305.606	291.941	1.019	1.047	1.067	6.7	6.38	0.415	355.2	49.5	183.1	40.2	89.8	3.9
LM35-B1	LO	0.172	172	0.07	1.0285	0.9977	0.9738	176.902	171.604	167.494	1.031	1.025	1.056	5.6	5.18	-0.111	151.6	3.8	19	84.5	241.9	4.1
LM35-C1	LO	0.208	208	0.018	1.0145	1.0044	0.9811	211.016	208.915	204.069	1.01	1.024	1.034	3.4	3.19	0.403	353	67.9	163.4	21.8	254.7	3.4
LM35-D1	LO	0.201	201	0.134	1.0202	1.004	0.9758	205.060	201.804	196.136	1.016	1.029	1.045	4.5	4.25	0.284	170.4	30.5	28.2	53.4	271.7	18.4
LM35-E1	LO	0.143	143	0.033	1.0108	0.9976	0.9917	144.544	142.657	141.813	1.013	1.006	1.019	1.9	1.75	-0.376	24.3	19.2	280.7	34	138.4	49.5
Mean		**0.21**	**205.40**										**1.044**	**4.4**	**4.15**	**0.123**						
LM36-A1	LO	0.288	288	0.009	1.0433	0.9941	0.9626	300.470	286.301	277.229	1.05	1.033	1.084	8.4	7.98	-0.201	9.8	53.5	101.7	1.4	192.7	36.5
LM36-A2	LO	0.231	231	0.021	1.0177	1.0054	0.977	235.089	232.247	225.687	1.012	1.029	1.042	4.2	3.92	0.404	332.4	36.3	180.2	50.3	72.9	13.9
LM36-B1	LO	0.3	300	0.012	1.0241	1.0099	0.9661	307.230	302.970	289.830	1.014	1.045	1.06	6.0	5.73	0.521	187.7	39.2	332.2	44.9	81.8	18.6
LM36-B2	LO	0.219	219	0.012	1.0365	0.9857	0.9777	226.994	215.868	214.116	1.052	1.008	1.06	6.0	5.65	-0.721	329.9	30.2	193.6	51.2	73.5	22
LM36-C1	LO	0.225	225	0.018	1.0048	1.0009	0.9943	226.080	225.203	223.718	1.004	1.007	1.01	1.0	0.99	0.254	334.9	21.3	69.4	11.4	185.8	65.6
LM36-D1	LO	0.222	222	0.04	1.0094	1.0027	0.988	224.087	222.599	219.336	1.007	1.015	1.022	2.2	2.04	0.376	62.3	87.2	329.8	0.1	239.8	2.8
LM36-D2	LO	0.218	218	0.037	1.0187	1.0026	0.9787	222.077	218.567	213.357	1.016	1.024	1.041	4.1	3.84	0.203	253.5	67.3	353.9	4.3	85.7	22.3
LM36-D3	LO	0.234	234	0.021	1.02	0.9974	0.9825	238.680	233.392	229.905	1.023	1.015	1.038	3.8	3.60	-0.198	183.8	0.1	274	61.8	93.7	28.2
LM36-E1	LO	0.239	239	0.028	1.0312	0.9882	0.9806	246.457	236.180	234.363	1.043	1.008	1.052	5.2	4.87	-0.693	328	41.1	123.6	46.2	226.9	12.4
Mean		**0.24**	**241.78**										**1.045**	**4.5**	**4.29**	**-0.006**						
LM37-A1	LO	0.0797	79.7	0.034	1.0084	1.0042	0.9874	80.369	80.035	78.696	1.004	1.017	1.021	2.1	1.81	0.603	351.3	38.9	193.8	48.8	90.6	11.3
LM37-B1	LO	0.11	110	0.041	1.0078	1.0047	0.9876	110.858	110.517	108.636	1.003	1.017	1.02	2.0	1.81	0.693	166.4	31.1	320.8	56.2	69.1	11.9
LM37-C1	LO	0.0868	86.8	0.07	1.0134	0.998	0.9886	87.963	86.626	85.810	1.016	1.009	1.025	2.5	2.16	-0.24	45.1	76.2	212.5	13.5	303.2	2.9
LM37-C2	LO	0.0945	94.5	0.05	1.0095	1.0008	0.9897	95.398	94.576	93.527	1.009	1.011	1.02	2.0	1.74	0.128	349.6	35.3	249.2	14.3	140.8	51.1
LM37-D1	LO	0.103	103	0.045	1.0091	1.0028	0.9881	103.937	103.288	101.774	1.006	1.015	1.021	2.1	1.87	0.403	357.3	46	232	29.2	123.4	29.6
LM37-E1	LO	0.129	129	0.052	1.0262	0.998	0.9758	132.380	128.742	125.878	1.028	1.023	1.052	5.2	4.65	-0.107	1.1	12	256.7	49.7	100.6	37.8
Mean		**0.10**	**100.50**										**1.027**	**2.7**	**2.34**	**0.247**						

Table A2-1. (cont.)

Sample	Granites	Km x 10-3 SI	Km x 10-6 SI	StErr (%)	Pkmax	Pkint	Pkmin	Kmax	Kint	Kmin	L	F	P	P%	Ppara%	T	Kmax Dec	Kmax Inc	Kint Dec	Kint Inc	Kmin Dec	K min Inc
LM38-A1	LO	1.24	1240	0.053	1.0311	0.9924	0.9766	1278.564	1230.576	1210.984	1.039	1.016	1.056	5.6	5.52	-0.409	4.9	36.6	183.7	53.4	274.4	0.6
LM38-A2	LO	1.68	1680	0.345	1.0996	0.9803	0.9201	1847.328	1646.904	1545.768	1.122	1.066	1.195	19.5	19.33	-0.288	12.7	43.1	140	32.9	251.1	29.2
LM38-B1	LO	1.43	1430	0.098	1.0545	0.9869	0.9585	1507.935	1411.267	1370.655	1.068	1.03	1.1	10.0	9.91	-0.388	69.5	30.8	180.4	30.9	305	43.5
LM38-C1	LO	1.54	1540	0.038	1.0447	0.9868	0.9686	1608.838	1519.672	1491.644	1.059	1.019	1.079	7.9	7.78	-0.508	351.3	37.8	142.2	48.4	249.5	14.8
LM38-D1	LO	1.5	1500	0.035	1.0281	0.9921	0.9798	1542.150	1488.150	1469.700	1.036	1.013	1.049	4.9	4.88	-0.483	345.8	33.1	85.7	14.8	196.2	52.9
LM38-E1	LO	1.58	1580	0.028	1.0334	0.9891	0.9774	1632.772	1562.778	1544.292	1.045	1.012	1.057	5.7	5.68	-0.572	331.1	43	68.5	7.9	166.7	45.9
LM38-E2	LO	1.94	1940	0.035	1.0393	0.9911	0.9696	2016.242	1922.734	1881.024	1.049	1.022	1.072	7.2	7.14	-0.367	331.6	40.5	85.7	25.5	198.2	38.8
Mean		**1.56**	**1558.57**										**1.087**	**8.7**	**8.61**	**-0.431**						
LM39-A1	LO	0.074	74	0.075	1.0043	1.002	0.9937	74.318	74.148	73.534	1.002	1.008	1.011	1.1	0.90	0.572	169.2	39.1	26.7	44.3	276.2	19.8
LM39-B1	LO	0.0731	73.1	0.071	1.0049	0.9997	0.9954	73.458	73.078	72.764	1.005	1.004	1.01	1.0	0.80	-0.104	185.5	0.8	275.7	13.3	92.2	76.7
LM39-B2	LO	0.0731	73.1	0.068	1.0091	1	0.9909	73.765	73.100	72.435	1.009	1.009	1.018	1.8	1.54	0.008	1.5	23.9	102	22.3	229.9	56.3
LM39-C1	LO	0.0828	82.8	0.064	1.0056	0.9994	0.995	83.264	82.750	82.386	1.006	1.004	1.011	1.1	0.91	-0.178	336.9	3.9	70	38	242	51.7
LM39-C2	LO	0.0944	94.4	0.062	1.0039	0.9994	0.9967	94.768	94.343	94.088	1.004	1.003	1.007	0.7	0.63	-0.23	337.8	40.9	101	32.3	214.6	32.3
LM39-D1	LO	0.0837	83.7	0.05	1.0083	1	0.9916	84.395	83.700	82.997	1.008	1.008	1.017	1.7	1.44	0.01	2	33.9	129.6	42.2	250	29.1
LM39-E1	LO	0.0937	93.7	0.063	1.0125	0.9951	0.9924	94.871	93.241	92.988	1.017	1.003	1.02	2.0	1.76	-0.724	167.8	74.3	287.1	7.9	19	13.6
LM39-E2	LO	0.076	76	0.042	1.0059	0.9987	0.9954	76.448	75.901	75.650	1.007	1.003	1.011	1.1	0.89	-0.382	349.9	35.1	159.3	54.4	256.4	5
LM39-F1	LO	0.0743	74.3	0.056	1.0059	1.0005	0.9936	74.738	74.337	73.824	1.005	1.007	1.012	1.2	1.04	0.136	45.4	50.6	158.8	18.1	264.4	33.6
LM39-G1	LO	0.0718	71.8	0.091	1.003	1.0001	0.9969	72.015	71.807	71.577	1.003	1.003	1.006	0.6	0.51	0.044	119.7	3.1	214.8	58.9	27.8	30.9
LM39-H1	LO	0.0891	89.1	0.037	1.0057	1.0014	0.9929	89.608	89.225	88.467	1.004	1.009	1.013	1.3	1.11	0.338	332.3	27.9	84.6	35.6	214.1	41.7
Mean		**0.08**	**80.55**										**1.012**	**1.2**	**1.05**	**-0.046**						
LM54-A	LO	0.656	656	0.005	1.04	0.9856	0.9744	682.240	646.554	639.206	1.055	1.012	1.067	6.7	6.59	-0.649	168.1	61.3	18.8	25.2	282.6	12.8
LM54-B1	LO	0.642	642	0.012	1.032	0.9926	0.9754	662.544	637.249	626.207	1.04	1.018	1.058	5.8	5.68	-0.381	139.3	75	237.4	2.1	327.9	14.8
LM54-B2	LO	0.644	644	0.146	1.027	1.0103	0.9627	661.388	650.633	619.979	1.016	1.049	1.067	6.7	6.53	0.495	95.9	46.5	224.3	30.5	332.3	27.7
LM54-C1	LO	0.761	761	0.032	1.0376	1.0021	0.9603	789.614	762.598	730.788	1.035	1.044	1.081	8.1	7.90	0.102	176.9	14.4	66.6	53.5	276.4	32.8
LM54-C2	LO	1.09	1090	0.04	1.048	1.0078	0.9442	1142.320	1098.502	1029.178	1.04	1.067	1.110	11.0	10.85	0.251	186.2	8.7	89	39.6	268.3	49.1
LM54-D1	LO	0.937	937	0.062	1.0325	0.9894	0.9782	967.453	927.068	916.573	1.044	1.011	1.056	5.6	5.47	-0.578	182.3	51.3	72.5	15.2	331.7	34.5
LM54-E	LO	0.536	536	0.041	1.0153	0.9963	0.9884	544.201	534.017	529.782	1.019	1.008	1.027	2.7	2.65	-0.409	264.7	61	118	24.8	21.4	14
Mean		**0.75**	**752.29**										**1.067**	**6.7**	**6.52**	**-0.167**						
LM55-A1	LO	2.54	2540	0.022	1.0361	0.9896	0.9743	2631.694	2513.584	2474.722	1.047	1.016	1.063	6.3	6.31	-0.493	182	45.4	75.8	15.4	332.1	40.6
LM55-A2	LO	2.88	2880	0.002	1.015	1.0056	0.9794	2923.200	2896.128	2820.672	1.009	1.027	1.036	3.6	3.62	0.480	158.7	53.1	12.2	32.1	271.6	16.3
LM55-B1	LO	1.84	1840	0.029	1.021	1.0086	0.9704	1878.640	1855.824	1785.536	1.012	1.039	1.052	5.2	5.17	0.519	199.8	1.9	96.6	81.8	290.1	7.9
LM55-B2	LO	1.78	1780	0.01	1.0364	0.9935	0.9701	1844.792	1768.430	1726.778	1.043	1.024	1.068	6.8	6.78	-0.281	180.1	23.7	50.1	55.7	281	23.3
Mean		**2.26**	**2260.00**										**1.055**	**5.5**	**5.47**	**0.056**						
LM56-A	LO	1.1	1100	0.064	1.0406	1.0036	0.9558	1144.660	1103.960	1051.380	1.037	1.05	1.089	8.9	8.76	0.150	194	36.2	326.2	42.6	83	26.1
LM56-B1	LO	1.3	1300	0.065	1.0251	1.012	0.9629	1332.630	1315.600	1251.770	1.013	1.051	1.068	6.8	6.39	0.588	199	31.1	75.3	42.6	310.8	31.6
LM56-B2	LO	0.696	696	0.011	1.0259	1.0055	0.9686	714.026	699.828	674.146	1.02	1.038	1.060	6.0	5.80	0.301	160.6	86.2	55.2	1	325.1	3.6
LM56-C	LO	0.618	618	0.039	1.0364	0.9989	0.9648	640.495	617.320	596.246	1.038	1.035	1.074	7.4	7.25	-0.030	143.2	30.8	295.9	56.2	45.5	12.7
LM56-D1	LO	1.1	1100	0.008	1.0293	1.0053	0.9654	1132.230	1105.830	1061.940	1.024	1.041	1.066	6.6	6.53	0.262	326.3	6.6	182.8	81.9	56.8	4.8
LM56-D2	LO	0.845	845	0.037	1.032	1.0038	0.9642	872.040	848.211	814.749	1.028	1.041	1.070	7.0	6.91	0.183	202.3	25.2	98.5	27	328.5	51.5
LM56-E1	LO	0.714	714	0.072	1.0272	0.997	0.9758	733.421	711.858	696.721	1.03	1.022	1.053	5.3	5.16	-0.161	220.8	26	334.2	39.3	106.9	39.7
LM56-E2	LO	0.634	634	0.004	1.0626	0.9894	0.948	673.688	627.280	601.032	1.074	1.044	1.121	12.1	11.81	-0.252	193.9	72.5	329.9	12.8	62.6	11.7
Mean		**0.88**	**875.88**										**1.08**	**7.51**	**7.33**	**0.13**						
LM57-A	LO	0.72	720	0.071	1.0662	0.9775	0.9563	767.664	703.800	688.536	1.091	1.022	1.115	11.5	11.26	-0.595	109.8	16.7	233.2	61.4	12.6	22.5
LM57-B	LO	0.538	538	0.005	1.0433	0.9914	0.9653	561.295	533.373	519.331	1.052	1.027	1.081	8.1	7.87	-0.313	324.4	54.2	141.2	35.8	232.3	1.5
LM57-D	LO	1.61	1610	0.058	1.0947	0.9864	0.9189	1762.467	1588.104	1479.429	1.11	1.074	1.191	19.1	18.95	-0.189	351.3	11.1	242.3	59	87.5	28.6
LM57-E	LO	0.802	802	0.067	1.0465	0.9942	0.9593	839.293	797.348	769.359	1.053	1.036	1.091	9.1	8.93	-0.179	150.2	9.7	46.9	53.3	247	35
LM57-F	LO	0.553	553	0.023	1.0331	0.9922	0.9747	571.304	548.687	539.009	1.041	1.018	1.060	6.0	5.84	-0.387	65.6	18.6	169.8	36.1	313.7	47.9
Mean		**0.84**	**844.60**										**1.11**	**10.76**	**10.57**	**-0.33**						

Table A2-1. (cont.)

Sample	Granites	Km x 10-3 SI	Km x 10-6 SI	StErr (%)	Pkmax	Pkint	Pkmin	Kmax	Kint	Kmin	L	F	P	P%	Ppara%	T	Kmax Dec	Kmax Inc	Kint Dec	Kint Inc	Kmin Dec	K min Inc
LM58b-A	BA	0.026	26	0.087	1.0228	1.0084	0.9688	26.593	26.218	25.189	1.014	1.041	1.056	5.6	3.58	0.477	177.9	74.8	3.2	15.1	272.9	1.3
LM58b-B	BA	0.02	20	0.117	1.0404	1.0055	0.9541	20.808	20.110	19.082	1.035	1.054	1.090	9.0	5.22	0.213	7.8	8.8	164.3	80.4	277.2	3.8
LM58b-C	BA	0.0165	16.5	0.097	1.041	1.0115	0.9474	17.177	16.690	15.632	1.029	1.068	1.099	9.9	5.21	0.390	192.3	27.7	28.7	61.3	285.9	6.9
Mean		**0.02**	**20.83**										**1.08**	**8.17**	**4.67**	**0.36**						
LM58a-D	LO-BA	0.0354	35.4	0.082	1.0162	0.997	0.9868	35.973	35.294	34.933	1.019	1.01	1.030	3.0	2.13	-0.300	208.7	26.8	81.1	50.4	313.5	26.8
LM58a-E1	LO	0.0846	84.6	0.021	1.0126	1.0007	0.9867	85.666	84.659	83.475	1.012	1.014	1.026	2.6	2.25	0.093	140.5	8.9	241.8	51.2	43.6	37.4
LM58a-E2	LO	0.0702	70.2	0.05	1.0188	0.9979	0.9833	71.520	70.053	69.028	1.021	1.015	1.036	3.6	3.00	-0.168	173.5	32.1	289.2	34.6	53	39
LM58a-F1	LO	0.194	194	0.012	1.0267	0.9892	0.9841	199.180	191.905	190.915	1.038	1.005	1.043	4.3	4.03	-0.755	10.3	72.2	156	14.8	248.5	9.6
LM58a-F2	LO	0.133	133	0.046	1.023	0.9987	0.9782	136.059	132.827	130.101	1.024	1.021	1.046	4.6	4.13	-0.073	171.5	54.9	357.7	34.9	265.6	2.9
Mean		**0.10**	**103.44**										**1.04**	**3.62**	**3.11**	**-0.24**						
LM59-A	LO	1.85	1850	0.003	1.0368	1.0151	0.9482	1918.080	1877.935	1754.170	1.021	1.071	1.093	9.3	9.27	0.527	154.2	18.6	277.7	58.7	55.5	24.3
LM59-B	LO	1.28	1280	0.009	1.0411	1.0087	0.9502	1332.608	1291.136	1216.256	1.032	1.062	1.096	9.6	9.46	0.309	162.5	13.2	274.3	57.7	65.1	28.9
LM59-C	LO	1.3	1300	0.013	1.0256	1.0089	0.9654	1333.280	1311.570	1255.020	1.017	1.045	1.062	6.2	6.17	0.458	140.8	33.9	287.9	51.3	39.4	16.3
LM59-D	LO	0.96	960	0.024	1.0379	1.0008	0.9613	996.384	960.768	922.848	1.037	1.041	1.080	8.0	7.85	0.051	172.2	13.5	273.1	38.1	66.4	48.7
Mean		**1.35**	**1347.50**										**1.08**	**8.28**	**8.19**	**0.34**						
LM60-A1	LO	0.384	384	0.049	1.0183	1.0086	0.9731	391.027	387.302	373.670	1.01	1.036	1.046	4.6	4.48	0.579	187.9	63.5	315	16.8	51.3	19.9
LM60-A2	LO	0.379	379	0.079	1.0249	1.0019	0.9732	388.437	379.720	368.843	1.023	1.03	1.053	5.3	5.12	0.110	155.6	70.8	328.2	19	59	2.3
LM60-C	LO	0.413	413	0.057	1.0182	0.9925	0.9893	420.517	409.903	408.581	1.026	1.003	1.029	2.9	2.82	-0.782	262.7	54.9	357.9	3.7	90.5	34.9
Mean		**0.39**	**392.00**										**1.04**	**4.27**	**4.14**	**-0.03**						
LM61-A	AC	0.109	109	0.026	1.0144	0.9985	0.9871	110.570	108.837	107.594	1.016	1.012	1.028	2.8	2.45	-0.157	152.4	48.8	23.3	28.9	277.3	26.6
LM61-B	AC	0.16	160	0.016	1.0173	1.006	0.9766	162.768	160.960	156.256	1.011	1.03	1.042	4.2	3.82	0.453	175.5	67.3	328.1	20.4	61.7	9.6
LM61-C1	AC	0.129	129	0.029	1.0199	0.9968	0.9834	131.567	128.587	126.859	1.023	1.014	1.037	3.7	3.34	-0.135	172.3	38.2	289.7	30.3	45.8	37
LM61-C2	AC	0.116	116	0.017	1.0145	0.9987	0.9868	117.682	115.849	114.469	1.016	1.012	1.028	2.8	2.50	-0.135	167.9	44.6	307.6	37.8	55.2	21.3
LM61-D	AC	0.11	110	0.017	1.0071	1.0008	0.992	110.781	110.088	109.120	1.006	1.009	1.015	1.5	1.35	0.171	125.1	25	342.7	59.5	222.9	16.3
Mean		**0.12**	**124.80**										**1.03**	**3.00**	**2.69**	**0.04**						
LM62-A	BA	0.0203	20.3	0.086	1.0526	1.0244	0.923	21.368	20.795	18.737	1.028	1.11	1.140	14.0	8.04	0.586	13.2	5.6	159.9	83.3	282.9	3.7
LM62-B	BA	0.0251	25.1	0.137	1.0418	1.0182	0.94	26.149	25.557	23.594	1.023	1.083	1.108	10.8	6.80	0.554	0.9	9.4	120.5	71.4	268.2	15.9
LM62-C	BA	0.0196	19.6	0.099	1.055	1.0138	0.9312	20.678	19.870	18.252	1.041	1.089	1.133	13.3	7.52	0.361	194.6	2.7	324.1	85.8	104.5	3.2
LM62-D	BA	0.0215	21.5	0.121	1.0324	1.0215	0.9461	22.197	21.962	20.341	1.011	1.08	1.091	9.1	5.40	0.756	16.2	49.1	172.1	38.3	271.8	12.1
Mean		**0.02**	**21.63**										**1.12**	**11.80**	**6.94**	**0.56**						
LM63-A	LO	1.17	1170	0.007	1.0161	1.013	0.9709	1188.837	1185.210	1135.953	1.003	1.043	1.047	4.7	4.60	0.867	315.5	11.6	185.1	72.4	48.2	13
LM63-B	LO	1.1	1100	0.108	1.0272	1.0107	0.9621	1129.920	1111.770	1058.310	1.016	1.051	1.068	6.8	6.68	0.506	243.3	58	342.8	5.8	76.3	31.4
LM63-C1	LO	0.914	914	0.068	1.0258	1.0061	0.968	937.581	919.575	884.752	1.02	1.039	1.060	6.0	5.88	0.332	224.1	82.4	80.4	6.1	349.9	4.5
LM63-C2	LO	0.917	917	0.031	1.0227	1.0041	0.9732	937.816	920.760	892.424	1.019	1.032	1.051	5.1	5.01	0.259	248.8	62.5	62.5	26.2	354	7.7
Mean		**1.03**	**1025.25**										**1.06**	**5.65**	**5.54**	**0.49**						
LM64-A	LO	0.0733	73.3	0.049	1.0033	1.0007	0.996	73.542	73.351	73.007	1.003	1.005	1.007	0.7	0.61	0.284	175	42.6	61	23.8	310.9	38
LM64-B	LO	0.0868	86.8	0.032	1.0053	1.0024	0.9923	87.260	87.008	86.132	1.003	1.01	1.013	1.3	1.13	0.561	136.9	51.9	336.5	36.4	239.3	9.6
LM64-C	LO	0.075	75	0.037	1.0068	0.999	0.9942	75.510	74.925	74.565	1.008	1.005	1.013	1.3	1.07	-0.229	168.3	29.6	35.2	50.3	272.9	23.9
LM64-D	LO	0.0669	66.9	0.041	1.0066	0.9988	0.9946	67.342	66.820	66.539	1.008	1.004	1.012	1.2	1.00	-0.305	185	18.7	290	37.4	74	46.6
LM64-E	LO	0.0795	79.5	0.037	1.0076	0.999	0.9934	80.104	79.421	78.975	1.009	1.006	1.014	1.4	1.21	-0.212	159	28.8	61.2	14	308.3	57.4
Mean		**0.08**	**76.30**										**1.01**	**1.18**	**1.00**	**0.02**						
LM70-A1	VRM	0.0458	45.8	0.03	1.0079	0.9997	0.9924	46.162	45.786	45.452	1.008	1.007	1.016	1.6	1.19	-0.061	181.9	27.4	289.9	30.9	58.8	46.4
LM70-A2	VRM	0.0338	33.8	0.123	1.0156	0.9969	0.9875	34.327	33.695	33.378	1.019	1.009	1.028	2.8	2.00	-0.329	142.5	10.1	232.6	0.7	326.8	79.8
LM70-B1	VRM	0.0464	46.4	0.065	1.0062	1.0016	0.9922	46.688	46.474	46.038	1.005	1.01	1.014	1.4	1.08	0.355	141.7	18.6	246.5	37.2	30.6	46.8
LM70-B2	VRM	0.0419	41.9	0.048	1.01	0.9992	0.9908	42.319	41.866	41.515	1.011	1.008	1.019	1.9	1.45	-0.124	154.1	13.4	253.3	34.1	45.9	52.6
LM70-C1	VRM	0.0431	43.1	0.038	1.0057	0.9981	0.9962	43.346	43.018	42.936	1.008	1.002	1.010	1.0	0.72	-0.612	165.6	5.3	300.4	82.6	75.1	5.3
LM70-C2	VRM	0.0389	38.9	0.065	1.008	1.0019	0.9902	39.211	38.974	38.519	1.006	1.012	1.018	1.8	1.32	0.320	155.8	19.5	267.4	46	50	37.5
LM70-D1	VRM	0.0364	36.4	0.093	1.0128	0.9984	0.9889	36.866	36.342	35.996	1.012	1.019	1.031	3.1	1.74	0.195	147.5	3.8	239.4	25.4	49.5	64.3
LM70-D2	VRM	0.0324	32.4	0.076	1.0144	1.0019	0.9837	32.867	32.462	31.872	1.014	1.01	1.024	2.4	2.17	-0.198	91.2	11	252.9	36.8	195.1	51
Mean		**0.04**	**39.84**										**1.02**	**2.00**	**1.46**	**-0.06**						

Table A2-1. (cont.)

Sample	Granites	Km x 10-3 SI	Km x 10-6 SI	StErr (%)	Pkmax	Pkint	Pkmin	Kmax	Kint	Kmin	L	F	P	P%	Ppara%	T	Kmax Dec	Kmax Inc	Kint Dec	Kint Inc	Kmin Dec	K min Inc
LM72-A1	VRM	0.0311	31.1	0.079	1.0085	0.9991	0.9924	31.364	31.072	30.864	1.009	1.007	1.016	1.6	1.12	-0.172	194.4	27.3	305.6	35	76	42.8
LM72-A2	VRM	0.0354	35.4	0.057	1.0094	0.9968	0.9938	35.733	35.287	35.181	1.013	1.003	1.016	1.6	1.12	-0.604	184.9	26.2	289.8	27.6	58.7	50.3
LM72-B2	VRM	0.0412	41.2	0.082	1.0063	0.9991	0.9946	41.460	41.163	40.978	1.007	1.005	1.012	1.2	0.88	-0.228	213.7	30.1	318.3	23.5	79.8	50.2
LM72-B3	VRM	0.0355	35.5	0.056	1.0058	0.999	0.9952	35.706	35.465	35.330	1.007	1.004	1.011	1.1	0.76	-0.271	212.3	30	326.8	35.6	93.4	39.9
LM72-B4	VRM	0.0393	39.3	0.052	1.0068	0.998	0.9952	39.567	39.221	39.111	1.009	1.003	1.012	1.2	0.86	-0.508	212.6	32.4	321.9	27.5	83.2	45
LM72-D1	VRM	0.042	42	0.043	1.0101	1.0029	0.9869	42.424	42.122	41.450	1.007	1.016	1.024	2.4	1.76	0.383	247	21.4	39.1	66.1	153	10.2
LM72-D2	VRM	0.0199	19.9	0.12	1.0159	0.9961	0.9879	20.216	19.822	19.659	1.02	1.008	1.028	2.8	1.66	-0.408	255.2	20	21.5	58.4	156.1	23.4
Mean		**0.03**	**34.91**										**1.02**	**1.70**	**1.16**	**-0.26**						

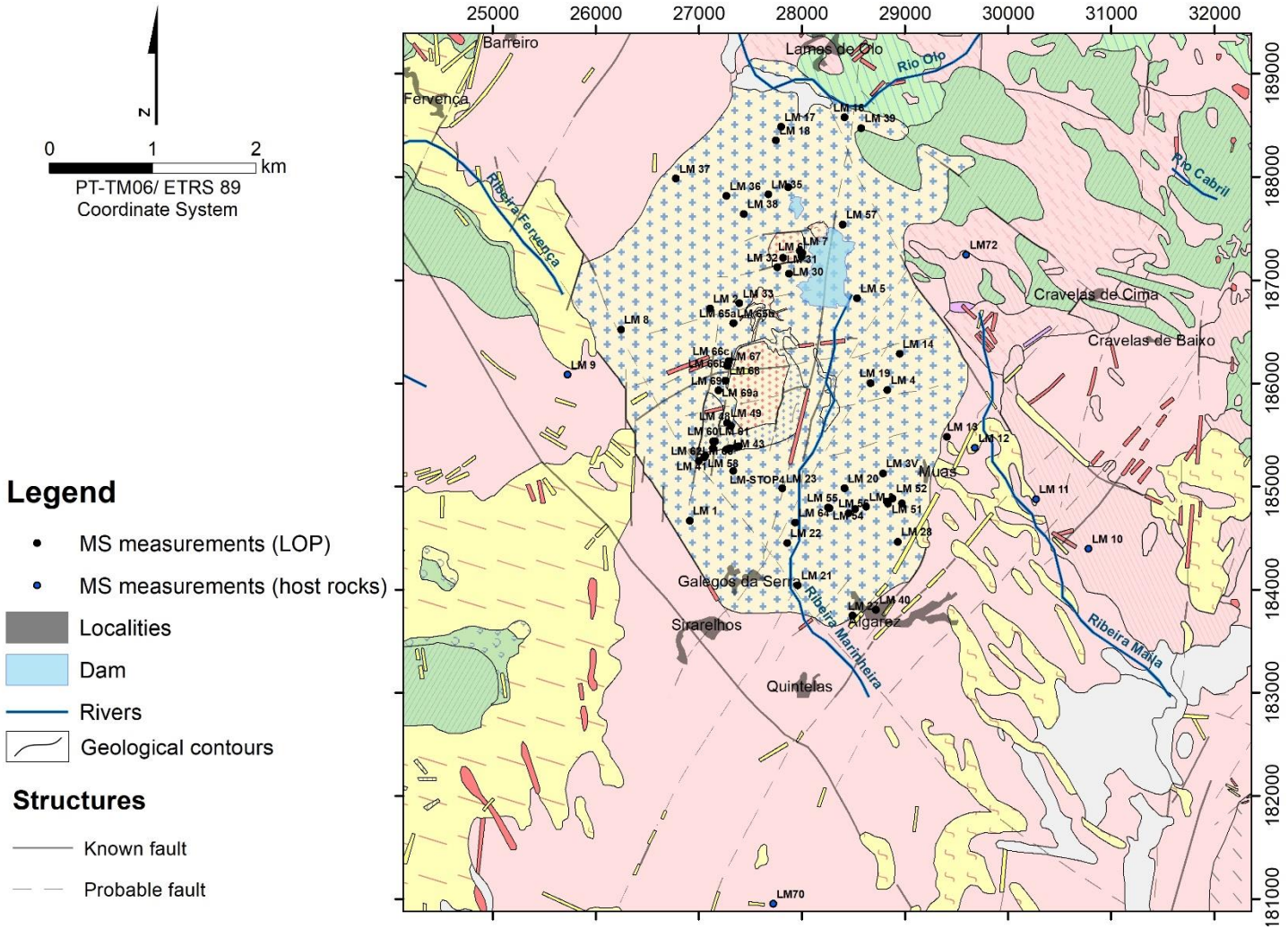


Figure A3-1. Simplified geologic map with location of the measurements of magnetic susceptibility (acquired by both equipment: Terraplus KT-10 magnetic susceptibility meter, and KLY-4S Kappabridge susceptometer Agico model) in LOP and host rocks.

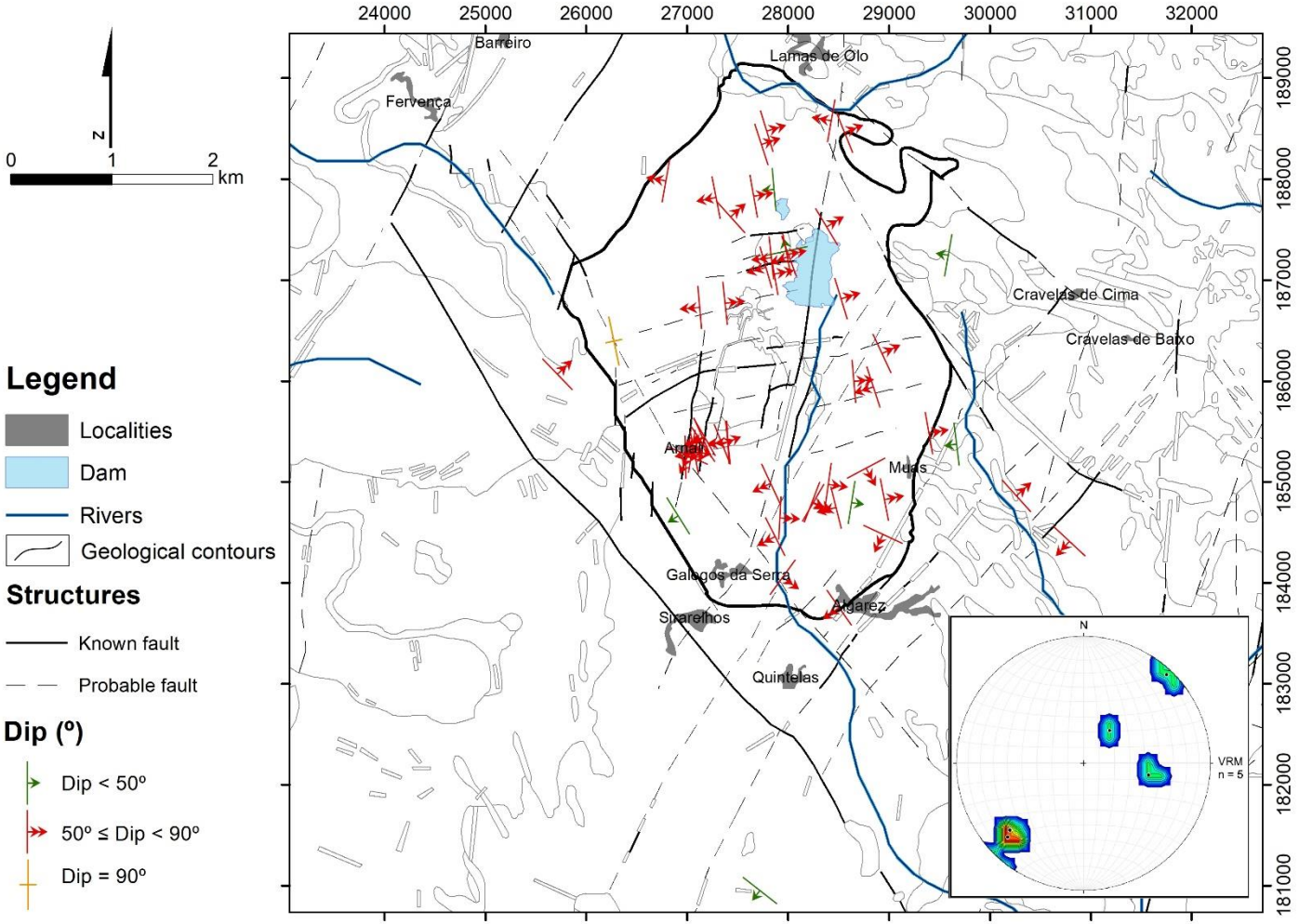


Figure A3-2. Map of the magnetic foliations in LOP and host-rocks, with orientation stereonet for the magnetic foliation poles (K_3) for VRM; Schmidt, lower hemisphere projection, 1–5% area contours.

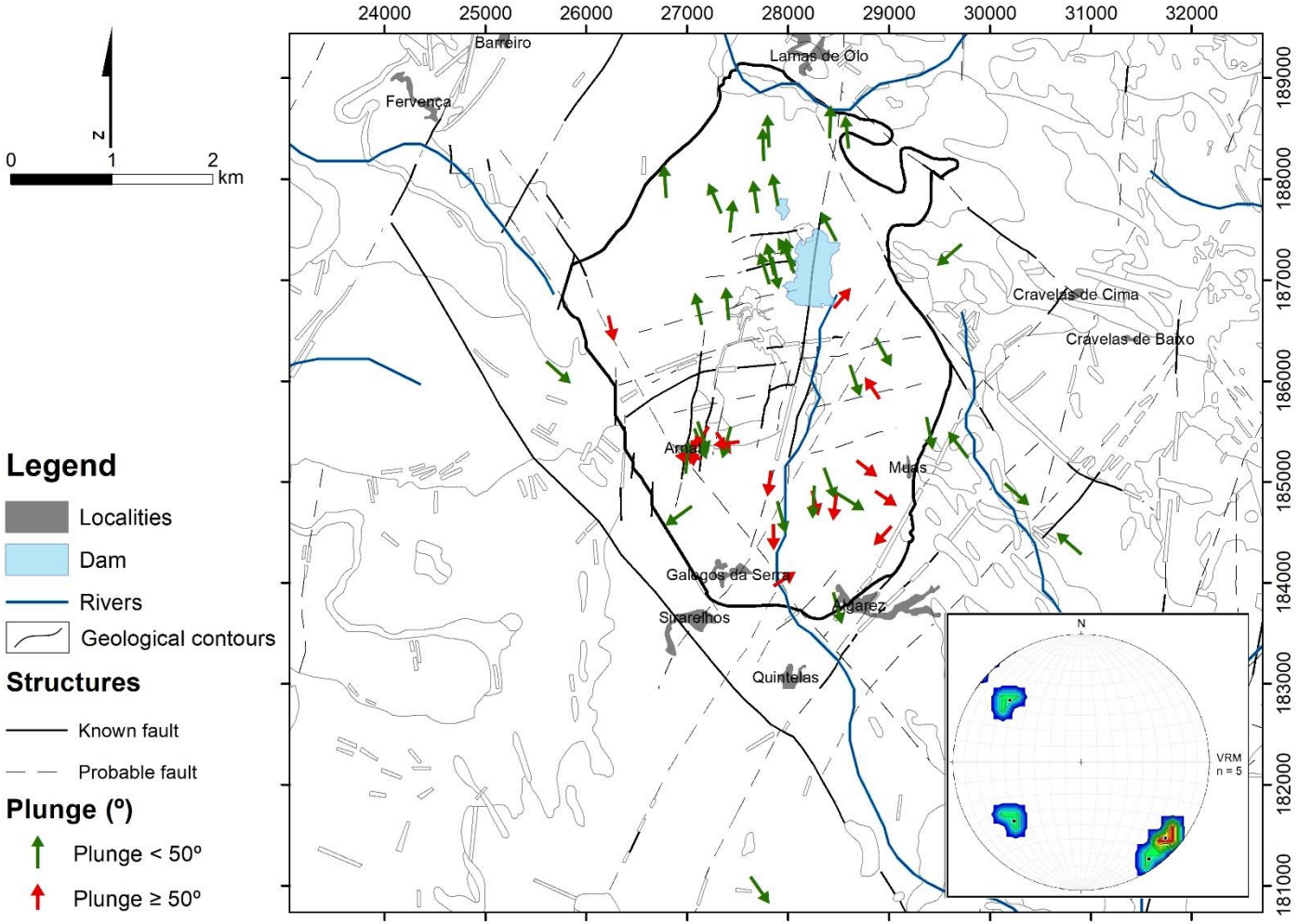


Figure A3-3. Map of the magnetic lineations for LOP and host-rocks, with orientation stereonet for the magnetic lineation (K_1) for VRM; Schmidt, lower hemisphere projection, 1–5% area contours.

Table A4-1. Apparent density, open porosity, and water absorption data from rock specimens from LOP granites and host rocks (data obtains at atmospheric pressure; δ_{water} = 0.9962 g/cm^3).

Lithology	Statistical parameter	Apparent density (kg/m^3)	Apparent density (g/cm^3)	Open porosity (%)	Water absorption (%)	n
Lamas de Olo granite	Mean	2563	2.56	2.8	1.1	24
	Standard deviation	34	0.03	1.1	0.4	
	Maximum	2628	2.63	4.8	1.9	
	Minimum	2490	2.49	1.1	0.4	
Alto dos Cabeços granite	Mean	2585	2.58	2.2	0.8	14
	Standard deviation	18	0.02	0.6	0.2	
	Maximum	2607	2.61	3.1	1.2	
	Minimum	2551	2.55	1.6	0.6	
Barragem granite	Mean	2534	2.53	2.7	1.1	11
	Standard deviation	27	0.03	1.1	0.4	
	Maximum	2560	2.56	4.4	1.7	
	Minimum	2487	2.49	1.5	0.6	
Vila Real granites	Mean	2501	2.50	4.7	1.9	21
	Standard deviation	36	0.04	1.1	0.5	
	Maximum	2563	2.56	6.6	2.7	
	Minimum	2443	2.44	2.9	1.1	
Douro Group Metasedimens	Mean	2740	2.74	1.8	0.7	10
	Standard deviation	84	0.08	1.4	0.6	
	Maximum	2800	2.80	4.5	1.7	
	Minimum	2583	2.58	0.7	0.3	

APPENDIX

Journal of Iberian Geology
https://doi.org/10.1007/s41513-020-00128-x

RESEARCH PAPER

Geostatistical approach to the study of the magnetic susceptibility variation: Lamas de Olo Pluton case study

Cláudia Cruz[1] · **Joaquim Góis**[2] · **Helena Sant'Ovaia**[1] · **Fernando Noronha**[1]

Received: 21 November 2019 / Accepted: 13 May 2020
© Universidad Complutense de Madrid 2020

Abstract
The Lamas de Olo Pluton, in northern Portugal, is a post-tectonic pluton located in the northern part of the Central Iberian Zone of the Iberian Variscan belt. It is a composite massif comprising different granites: Lamas de Olo, Alto dos Cabeços and Barragem. Magnetic susceptibility was measured in 349 oriented cores from 48 sampling sites across the pluton. The measured magnetic susceptibility (K_m) values range between 21 μSI (or 21×10^{-6} SI) and 2769 μSI for all studied granites. The application of the geostatistical methodologies leads to a more detailed mapping of the magnetic susceptibility data and provided a quantification of its spatial dispersion. Kriging interpolation allows the visualization of two different areas in the Lamas de Olo Pluton: (1) areas with higher magnetic susceptibility values, typical of magnetite-bearing granites ($K_m \geq$ 1200 μSI) and (2) areas with lower values, which correspond to ilmenite-type behavior granites (21 μSI $< K_m <$ 1200 μSI), showing the heterogeneity of their granites, with a predominance of ilmenite-type granites. Alto dos Cabeços and Barragem are classified as ilmenite-type granites and Lamas de Olo granite presents both behaviors. The mineralogical and geochemical study of the Lamas de Olo granite with different behaviors does not show significant differences between the two types, allowing us to conclude that the Lamas de Olo granite was originated by the same magma and its mineralogical composition varied during the rise and emplacement of the magma implying the alteration of magnetite into hematite.

Keywords Magnetic susceptibility · Geostatistical methods · Variogram · Kriging · Granites · Lamas de Olo Pluton

Resumen
El plutón de Lamas de Olo, en el norte de Portugal, es un plutón postectónico ubicado en la parte septentrional de la Zona Centro Ibérica del macizo Varisco Ibérico. Es un macizo compuesto que engloba diferentes granitos: Lamas de Olo, Alto dos Cabeços y Barragem. La susceptibilidad magnética se midió en un total de 349 muestras orientadas provenientes de 48 estaciones distribuidas por todo el plutón. Los valores de susceptibilidad magnética (Km) oscilan entre 21 μSI (ó 21 × 10-6 SI) y 2769 μSI en los granitos estudiados. La aplicación de herramientas geoestadísticas permite una cartografía más detallada de la susceptibilidad magnética y proporciona una cuantificación de su dispersión espacial. La interpolación por Kriging permite la visualización de dos áreas diferentes en el plutón de Lamas de Olo: (1) áreas con valores de susceptibilidad magnética más altas, típicos de granitos que contienen magnetita (Km ≥ 1200 μSI) y (2) áreas con valores más bajos, que corresponden a granitos de comportamiento tipo ilmenita (21 μSI < Km < 1200 μSI). Por otra parte los granitos de Alto dos Cabeços y Barragem se clasifican como tipo ilmenita. Esta variabilidad muestra la heterogeneidad de los granitos en los que predominan los de tipo ilmenita. Los estudios mineralógicos y geoquímicos del granito de Lamas de Olo no muestran diferencias significativas entre los dos tipos, lo que nos permite concluir que el granito de Lamas de Olo se originó del mismo magma y su composición mineralógica varió durante el ascenso y emplazamiento del magma conllevando la alteración de la magnetita a hematita.

Palabras clave Susceptibilidad magnética · Métodos geoestadísticos · Variograma · Kriging · Granitos · Plutón de Lamas de Olo

✉ Cláudia Cruz
claudiacruz@fc.up.pt

Extended author information available on the last page of the article

Published online: 05 June 2020

1 Introduction

The magnetic susceptibility study in granites is largely used to distinguish between oxidized- or magnetite-type and reduced- or ilmenite-type granites (Ishihara 1977; Takahashi et al. 1980; Ellwood and Wenner 1981; Ishihara et al. 2000). The main source of the magnetic signal in the magnetite-type granites is the magnetite and/or Ti-poor magnetite and in the ilmenite-type granites is the ferromagnesian silicates and/or ilmenite. The magnitude of the magnetic susceptibility reflects the abundance, nature and chemical composition (Fe and Mg ratio) of constituent minerals (Aydin et al. 2007). Magnetite- and ilmenite-type granite classification is important to understanding the redox conditions in the magma chamber, as well as to infer which kind of mineral occurrence can be associated with the studied granites (Ishihara 1977; Ishihara et al. 1981). However, the occurrence of redox reactions during the ascent and emplacement of granites can change the mineral redox characteristics and oxidize (or reduce) the primary mineral assemblage. To help visualize the distribution of the magnetic signal in granites, a magnetic susceptibility map is usually made, using several interpolation methods, through specific softwares (e.g. ArcGIS, SURFER). The inverse distance weighted (IDW), kriging and the natural neighbor are the most-used interpolation methods.

Several studies have been made in order to classify granites regarding their magnetic behavior, in Japan (e.g. Ishihara et al. 1981), Korea (e.g. Maulana et al. 2013), Spain (e.g. Román-Berdiel et al. 1995; Aranguren et al. 1996; Olivia-Urcia and Pueyo 2012; Villaseca et al. 2017; Porquet et al. 2017) and Portugal (e.g. Sant'Ovaia et al. 2012; Cruz et al. 2016, 2020). Other authors have focused on establishing a relationship between the magnetic susceptibility variation and the mineralogical, geochemical and/or weathering controls on the magnetic susceptibility value (e.g. Aydin et al. 2007; Coleman et al. 2012; Ferré et al. 2012). However, most of these studies have been qualitative rather than quantitative. Applications of geostatistical methodologies have led to a more detailed mapping of the magnetic susceptibility data, quantifying its spatial dispersion.

D.G Krige, a mining engineer, and H.S. Sichel, a statistician, developed geostatistics concepts in the 1950s (e.g. Kridge 1951; Sichel 1952). G. Matheron, a French mathematic and geologist, inspired by D.G. Kridge and H.S. Sichel works, developed the theoretical support of geostatistics (e.g. Matheron 1960).

In the beginning, the geostatistical analyses were mostly applied to geological-mining problems, but they were quickly expanded to embrace other scientific areas like forest resources, hydrogeology, biology, medicine and, in our current area of interest, the mapping of geological variables with spatial dependence. Some of the most recent studies regarding geostatistical analysis applied to the mapping of geological variables, which also constitute main references, are the works published by Journel and Huijbrechts (1978), Goovaerts (1997), Davis (2002), Chilès and Delfiner (2012), Benndorf and Menz (2014), Hanke et al. (2018) and Figueiredo et al. (2019). Concerning the application of the geostatistical approach on the variation of the magnetic susceptibility data, works like Pizarro (2008), Zawadzki et al. (2012, 2015), and Fabijanczyk and Zawadzki (2019) must not be left out.

Geostatistics is the application of the formalism of random functions to the characterization and estimation of a natural phenomenon (Journel and Huijbrechts 1978), applied to a geological context. The natural phenomena have a spatial organization or structure and can be characterized by the distribution of one or more variables called Regionalized Variables (R.V). A R.V. is defined as a variable distributed in space, which is purely descriptive, and from a mathematical point of view, it is simply a function that considers an output value for every point within a spatial field or temporal domain.

This study aims to characterize the granites from Lamas de Olo Pluton (LOP) concerning the presence and alignment of the ferromagnetic minerals, namely magnetite/Ti-poor magnetite, and determine if magnetic susceptibility (K_m) variations across the pluton reflect fundamental mineralogy changes or difference in redox conditions in the magma chamber. Previous studies of K_m were considered (Cruz et al. 2016) and a new quantitative approach is now presented.

A quantitative approach of the magnetic susceptibility values using geostatistical methods was carried out to improve the knowledge about the magnetic behavior of the LOP and validate the previous studies carried out by Cruz et al. (2016). For this, and assuming that the variation of the magnetic susceptibility on rocks may be variable with the direction (Zawadzki et al. 2012, 2015), the kriging interpolation is the only method that considers the influence of spatial structure (the trend) on the regionalized variables (the magnetic susceptibility values). Other interpolation methods, such as IDW or the polynomial fitting location (e.g. Coleman et al. 2012), do not consider the existence of a possible main direction for the distribution of magnetic susceptibility values. The use of interpolating methods that only privilege the distance between the known information (measured points) and the one to be interpolated (interpolated points), ignoring the spatial correlation between the values of the variable, may not correspond to the real situation and the interpolation is less accurate.

Geochemical analyses were also performed in order to compare the pattern of magnetic susceptibility across the pluton with the geochemical characteristics of its granites. The purpose of this comparison was to determine if there

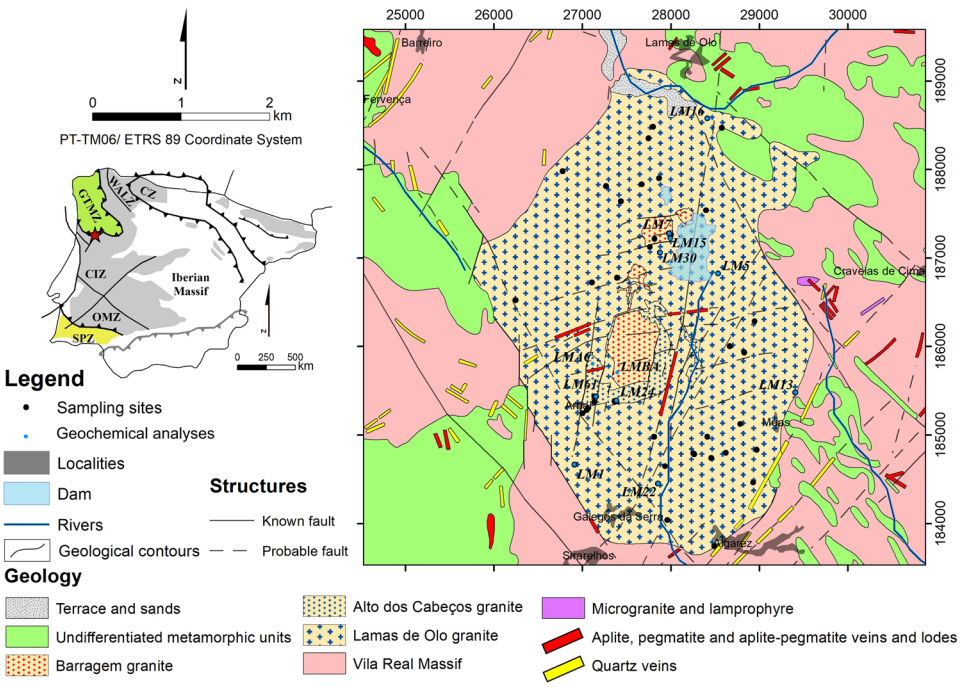


Fig. 1 Simplified geological map of the Lamas de Olo Pluton and sampling sites. (geological map made in ArcGIS 10.7 based on Pereira et al. 1987 and Helal 1992)

are variations in the petrographic, mineralogical and/or geochemical characteristics able to justify the variations in the redox conditions in the granitic magma and consequently variations in the K_m in the LOP. An alternative origin for magnetic susceptibility variations might be various degrees of alteration on primary mineralogy.

2 Geological setting

The Lamas de Olo Pluton (LOP) is located in the Iberian Variscan belt in the northern part of the Central Iberian Zone, near the limit with Galicia-Trás-os-Montes Zone, in northern Portugal (Fig. 1). It is a small post-tectonic pluton of *ca*. 138 km^2, with its rhomboid shape controlled by three fault systems: one at NNW–SSE, conjugated with another at NNE–SSW, which is parallel to the Verin-Régua-Penacova fault regional structure, and another fault system at *ca*. ENE–WSW, corresponding to a Late-Variscan fault network in central–northern Portugal (NW Iberia) (Marques et al. 2002).

The LOP comprises several different granites: (1) Lamas de Olo, the most abundant, corresponding to a medium to coarse-grained porphyritic granite (Biotite > Muscovite), (2) Alto dos Cabeços, a fine- to medium-grained porphyritic granite (Biotite > Muscovite) and (3) Barragem, a leucocratic fine- to medium-grained and slightly porphyritic granite (Biotite = Muscovite) (Pereira 1989; Helal 1992; Fernandes et al. 2013). In the field, the contacts between Lamas de Olo and Alto dos Cabeços granites are generally diffuse, but field observations show that Barragem granite crosscuts Lamas de Olo.

The LOP intrudes the Armorican Quartzite Formation and the schists from Upper Silurian to Middle Ordovician (Lower Paleozoic Formations), the Desejosa Formation (belonging to the metasediments from Upper to Medium Cambrian of the Douro Group) and the two-mica syntectonic granites from the Vila Real Massif (Fig. 1; Pereira 1989). The two-mica granites yielded and weighted average $^{207}Pb/^{235}U$ age of *ca*. 311 ± 1 Ma for the Cabeceiras de Basto granite (Almeida et al. 1998) and of *ca*. 316 ± 7 Ma for the Carrazeda de Ansiões granite (Teixeira 2008) for monazite and zircon. $^{207}Pb/^{235}U$ dating yielded an age of 297.19 ± 0.73 Ma for the Lamas de Olo granite (Fernandes et al. 2013).

3 Materials and methods

The relationship between the magnetization M induced in a material and the external field H is defined as $M = K H$, where K is the magnetic susceptibility (Hrouda 1982; Bouchez 1997). K reflects the mineral composition of the whole rock, comprising the diamagnetic (e.g. quartz, feldspar), paramagnetic (e.g. biotite, muscovite or hornblende) and ferromagnetic s.l. minerals (e.g. magnetite or hematite). K measurements were performed using a Agico KLY-4S Kappabridge susceptometer (Czech Republic) from the *Instituto de Ciências da Terra-Pólo Porto,* in a 300 A/m field. For each site, the ANISOFT 4.2 program package (Chadima and Jelinek 2009) enabled us to calculate the mean susceptibility,

K_m. The K_m values are important in granite characterization to allow the distinction between the two kinds of redox behavior: magnetite- and ilmenite-type. The first group have K_m values above 3.0×10^{-3} SI, indicating a ferromagnetic behavior, due to the presence of iron oxide minerals, such as magnetite, and in the second group, K_m is lower than 3.0×10^{-3} SI, indicating the presence of mostly paramagnetic minerals, like ilmenite and biotite (Ishihara 1977).

Sampling was previously performed in several fieldwork campaigns with a portable drill. At each sampling site, oriented cores (25 mm in diameter and 60–70 mm in length) were collected and subsequently sawed in the laboratory, in order to obtain 22 mm-long cylinders. The studied area comprises the Lamas de Olo Pluton (LOP) and its host rocks, with 52 sampling sites, corresponding to 382 oriented cores. The present study focuses only on the LOP granites, represented by 48 sampling sites (349 oriented cores): 39 sites in the Lamas de Olo granite, 4 in the Alto dos Cabeços granite, and 5 in the Barragem granite (Fig. 1). However, one sample from the Lamas de Olo granite was not considered in the geostatistical analysis. This sample has an unusually much higher K_m value (44,382 µSI) than that recorded in the remaining samples. Nevertheless, in the geostatistical analysis, outlier values are usually removed in order to smooth data. Therefore, in this study, the extreme value was removed, as it differs significantly from the others (it is 16 times greater than the second higher value) and substantially affects the mean and median values. The geostatistical analysis and interpolation map were performed through the SURFER.10 software.

To compare the geochemical signature of samples from the two behaviors, geochemical analyses have been performed. Twelve representative samples for LOP were selected: 6 for Lamas de Olo granite (3 for magnetite-type, and 3 for ilmenite-type), 3 for Alto dos Cabeços granite and 3 for Barragem granites. The analyses were performed at Activation Laboratories (Actlabs, Canada). The whole rock (W.R.) geochemical compositions were analyzed for major-, trace- and rare-earth elements by a lithium metaborate/ tetraborate fusion ICP and ICP-MS. A titration analysis was required too, in order to know the different content of both iron-oxides, the FeO and the Fe_2O_3. The FeO content was determined through titration, using acold acid digestion of ammonium metavanadate, and hydrofluoric acid in an open system. The analysis methods, as well as the detection limits, can be found on the Actlabs website (Actlabs 2020). The geochemical charts were made using the GCDkit software.

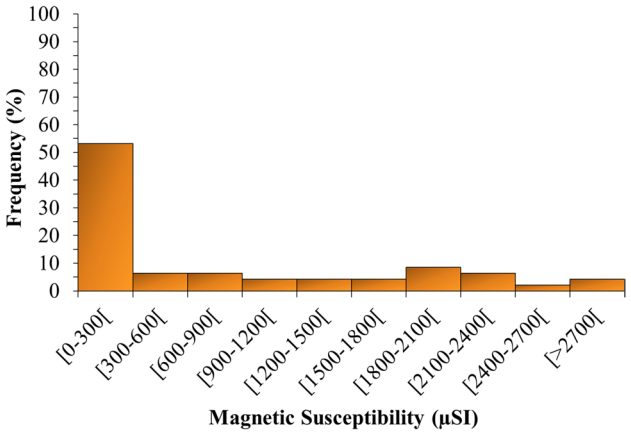


Fig. 2 Histogram of magnetic susceptibility (K_m in µSI) showing the dominantly paramagnetic behavior of the LOP granites

Table 1 Statistics data from magnetic susceptibility values (K_m in µSI))

Statistical parameters	Value
Mean value	809
Median	254
Standard deviation	879
Range	2748
Minimum	21
Maximum	2769
Count	47

4 Results and discussion

4.1 Magnetic susceptibility

4.1.1 Descriptive statistics

The calculation of the basic statistics values (Table 1) and the study of the histogram (Fig. 2) pointed out that:

1. In the same pluton, two types of magnetic behavior were present, and the K_m values show a high heterogeneity (minimum K_m value of 21 µSI and maximum K_m value of 2769 µSI);
2. The K_m mean value *ca.* 809 µSI shows that ilmenite-type granite is predominant over the magnetite-type granite; and the median of 254 µSI indicates that more than half K_m values are lower than the typical magnetite-type;
3. The higher standard deviation value (879 µSI) and the range of 2748 µSI, confirm the heterogeneity and the higher scattering of K_m values.

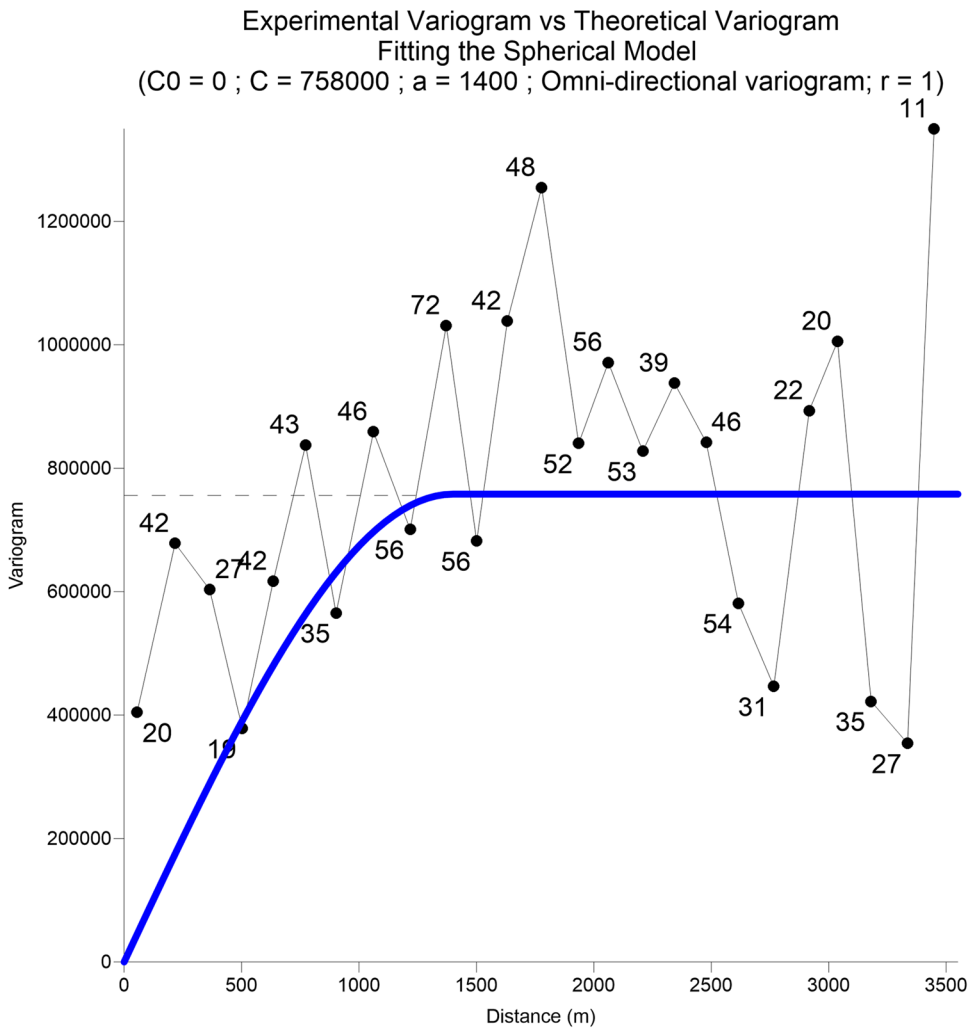


Fig. 3 Experimental variogram and its adjustment to the theoretical variogram of the regionalized variable (magnetic susceptibility)

4.1.2 Variograms and kriging interpolation

The variographic analysis was carried out to find the spatial structure of the magnetic susceptibility (our *R.V*). In order to detect the preferential directions of continuity (anisotropy of the *R.V.*), experimental variograms, with different interval directions of 15° and a tolerance angle of 30°, were investigated. The theoretical models and their parameters were then adjusted accordingly.

Figure 3 represents the experimental variogram adjusted to the theoretical variogram of the magnetic susceptibility *R.V*. The spherical model (Eq. 1) is the theoretical variogram that better adjusts to the magnetic susceptibility data.

$$\gamma(h) = \begin{cases} (C_0 + C_1)\left[1.5\frac{h}{a} - 0.5\frac{h^3}{a^3}\right] & h \le a \\ C_0 + C_1 & h > a \end{cases} \quad (1)$$

where, "γ (h)" represents the function of the spherical model, "C_0" is the nugget effect, the sum of geological microstructure or measurement error, corresponds to the value in the chart origin, "$C = C_1 + C_0$" is the total sill, "h" is the lag vector representing the separation distance between two spatial locations and "a" is the range variation (Journel and Huijbregts 1978).

Other theoretical variograms were tested, such as the exponential or gaussian model, but they did not produce such good results. The spherical semivariogram was the model selected, once is the experimental variogram that clearly shows the existence of a sill and, is the only model that fits the first values of the experimental variogram.

The spherical model adjusts to the majority of the experimental variograms without significant variation of "a" parameter, therefore, in this study, an omnidirectional variogram was adopted.

The study of the experimental variograms, and the subsequently adjusted model, allow us to verify that:

1. In the variographic study, the ranges recorded in all the adjusted experimental variograms were approximately $a = 1400$ m; this means that, although the K_m values

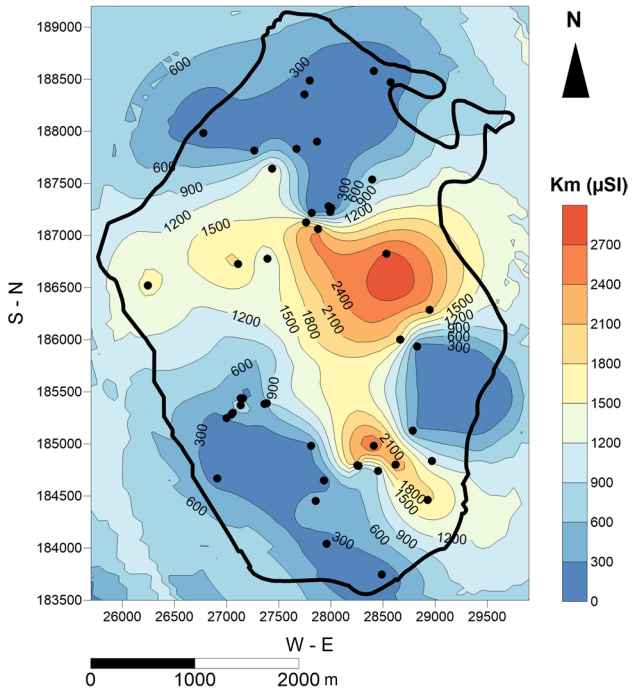


Fig. 4 Map of the magnetic susceptibility (K_m in µSI) values in the Lamas de Olo Pluton (interpolation made by kriging in the SURFER.10 software) with the location of sampling sites and the LOP outline

strongly vary within a few meters (Fig. 4), a spatial correlation between two points that are up to 1400 m apart was verified; beyond this limit, the data are no longer spatially correlated;

2. The absence of the nugget effect, $C_0 = 0$, means that sampling errors do not exist and for one sampling site, only one value is known;
3. Sill value (a priori variance), approximately $C = 758000$, represents the variance of the variable (K_m);
4. The anisotropy ratio is $r = 1$, meaning that the used variogram is "isotropic" since it exhibits the same parameters regardless of the direction.

After the analysis of the relational structure of the georeferenced data and once the model that supported the theoretical variogram was identified, the kriging information interpolation was done. This interpolation represents the spatial behavior of the magnetic susceptibility (Fig. 4). The kriging interpolation of the $K_m$values allows us to recognize two kinds of behavior in the same pluton: magnetite- and ilmenite-type. The areas with higher $K_m$values ($K_m \geq 1200$ µSI), showed the presence of magnetite/Ti-poor magnetite in their composition. It should be noted that, although LOP-magnetite-type granite have K_m values lower than those proposed by Ishihara (1977) to the magnetite-type granites from Japan, detailed magnetic mineralogy studies carried out by Cruz et al. (2020) proved the existence of magnetite and/or Ti-poor magnetite in the LOP granites.

The areas with higher $K_m$values ($K_m \geq 1200$ µSI), are present mainly in the eastern part of the pluton and along a ENE-WSW direction (*ca*. N 80°) system fault (Fig. 1). On the other hand, the ilmenite-type behavior was indicated by the presence of the low $K_m$values (areas with low values; 21 µSI $< K_m <$ 1200 µSI (Fig. 4) which is the predominant granite type in LOP.

The magnetic susceptibility varies between sites spaced a few meters apart, as it is visible in areas with close isolines (Fig. 4). It emphasizes the heterogeneous distribution of the magnetite- and ilmenite-type granites.

The presence of magnetite-type granites is particularly important because their occurrence is spatially related to mineralizations, that were described in the LOP area, namely W–Mo(–Sn). The mineral occurrences appear in quartz veins with *ca*. N80° trending. The mineralized veins have the same direction of the higher magnetic susceptibility zone trending (*ca*. ENE–WSW).

4.2 Geochemical characteristics

The geochemical characteristics of LOP correspond to high-K calc-alkaline, peraluminous granites (Table 2; Fig. 5a, b).

Comparing Lamas de Olo samples from the areas with high susceptibility (magnetite-type) and low susceptibility (ilmenite-type), both facies have similar mineralogy, differing mainly on magnetite quantity and by the presence of hematite resulting from magnetite oxidation (Cruz et al. 2020). The comparison between FeO and Fe_2O_3 contents is inconclusive, showing the same proportion on both facies from Lamas de Olo granite (Table 2). In the Lamas de Olo-magnetite type granite, Ti-poor-magnetite and pure magnetite are observed in larger quantities, whereas in the second one, the presence of martitization (oxidation of magnetite into hematite) is frequent, justifying the lower magnetic susceptibility values and the similar content on the FeO and Fe_2O_3.

The REE spectra are flat for all granites (Lamas de Olo granite – La/Yb* 3.300–4.870 and Gd/Yb* 0.885–1.233; Alto dos Cabeços granite – La/Yb* 4.580–9.410 and Gd/Yb* 1.069–1.245; Barragem granite – La/Yb* 1.060–2.180 and Gd/Yb* 0.545–0.701), with a slightly pronounced Eu anomaly in Lamas de Olo (Eu/Eu* 0.350–0.460) and Alto dos Cabeços (Eu/Eu* 0.440–0.520) granites and more pronounced in Barragem granite (Eu/Eu* 0.140–0.240) (Fig. 5c). The lower B (B = Fe + Mg + Ti) values, pronounced Eu anomaly and flat REE spectra suggest that Barragem corresponds to the most differentiated granite (Table 2; Fig. 5b, c) and has a different source.

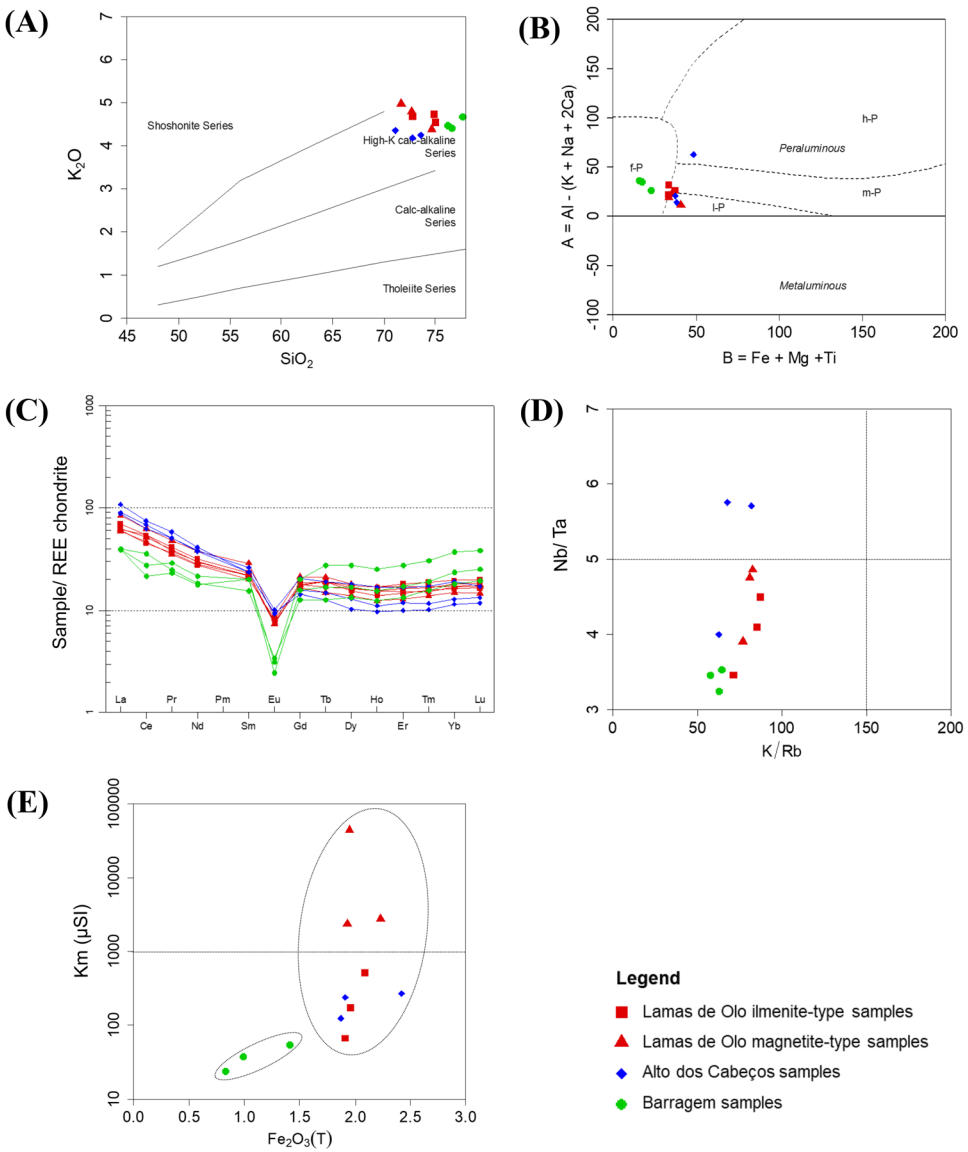


Fig. 5 Geochemical plots of representative samples for Lamas de Olo Pluton: **a** Classification plot K_2O vs SiO_2 (Peccerillo and Taylor 1976); **b** Classification plot A vs B (Villaseca et al. 1998; *h-P* highly peraluminous; *f-P* felsic peraluminous; *m-P* moderately peraluminous; *l-P* low peraluminous); **c** Spider plot of REE normalize to chondrite (Boynton 1984); **d** Evolution of Nb/Ta as a function of K/Rb, where Nb/Ta < 5 is the marker of interaction with hydrothermal fluids (Ballouard et al. 2016); **e** K_m vs Fe_2O_3T, showing the variation of magnetic susceptibility with Fe_2O_3T content (the Lamas de Olo-magnetite type sample with higher K_m value corresponds to the outlier value, which was removed in the geostatistical analysis)

Studies carried out by Ballouard et al. (2016) show that Nb–Ta fractionation is a marker for magmatic differentiation. The Nb/Ta ratio is expected to decrease during differentiation and the Nb/Ta < 5 is a marker to evidence the interaction with latter fluids. Figure 5d, shows mostly samples have Nb/Ta < 5, which proves the existence of hydrothermal fluid percolation, that can change the magnetic mineralogy (e.g. martitization), decreasing the K_m values.

In the Fig. 5e, two groups are individualized: one with lower K_m values, corresponding to the Barragem granite, and another one, constituted by Lamas de Olo + Alto dos Cabeços granites with higher content in Fe_2O_3 T and with a huge K_m values range. Figure 5e also shows that in the Barragem granite a positive correlation exists between the K_m and the Fe_2O_3 T. However, in the group composed by the Lamas de Olo + Alto dos Cabeços granites, no correlation is observed since, for the same Fe_2O_3 T content, the K_m values have a high variation.

5 Conclusions

In this work, a geostatistical analysis was applied to the variation of magnetic susceptibility data obtained from the LOP. Previous studies using the weighted inverse distance interpolation in the ArcGIS software (Cruz et al. 2016) showed the presence of two types of K_m behavior. However, the geostatistical approach proves to be useful in improving the knowledge of the magnetic behavior of the LOP, quantifying and validating the previous results.

Table 2 Major, trace and rare earth elements in the Lamas de Olo Pluton

Samples/granite		LO granite (ilmenite-type)			LO granite (magnetite-type)			AC granite (ilmenite-type)			BA granite (ilmenite-type)		
		LM1	LM16	LM22	LM5	LM13	LM30	LM24	LM61	LMAC	LM7	LM15	LMBA
SiO_2	%	75.04	74.90	72.79	72.71	71.69	74.65	73.60	72.80	71.11	76.64	77.65	76.23
Al_2O_3	%	13.60	13.59	13.76	14.04	14.04	13.30	13.21	13.42	13.86	12.31	12.35	12.37
Fe_2O_3	%	0.60	1.13	0.98	1.01	0.95	1.04	0.69	0.64	0.97	0.21	0.28	0.41
FeO	%	1.20	0.70	1.00	1.10	0.90	0.80	1.10	1.10	1.30	0.70	0.50	0.90
Fe_2O_3 T	%	1.96	1.91	2.09	2.23	1.95	1.93	1.91	1.87	2.42	0.99	0.83	1.41
MnO	%	0.07	0.04	0.06	0.06	0.06	0.06	0.08	0.06	0.04	0.02	0.02	0.05
MgO	%	0.29	0.29	0.34	0.41	0.34	0.29	0.46	0.46	0.59	0.16	0.17	0.16
CaO	%	0.73	0.96	0.98	1.16	1.01	1.02	1.42	1.40	0.96	0.32	0.29	0.55
Na_2O	%	3.48	3.41	3.39	3.74	3.46	3.48	3.23	3.22	2.56	3.15	2.99	3.15
K_2O	%	4.54	4.73	4.68	4.80	4.98	4.39	4.25	4.18	4.36	4.41	4.67	4.47
TiO_2	%	0.17	0.18	0.20	0.21	0.19	0.17	0.23	0.22	0.28	0.09	0.08	0.10
P_2O_5	%	0.05	0.06	0.06	0.07	0.07	0.06	0.07	0.08	0.07	0.03	0.04	0.04
LOI	%	0.73	0.42	0.62	0.42	0.66	0.39	0.66	0.99	2.19	0.99	0.92	0.51
LOI 2	%	0.87	0.50	0.73	0.55	0.76	0.48	0.79	1.11	2.34	1.06	0.97	0.61
Total	%	100.50	100.40	98.86	99.74	98.34	99.66	99.00	98.57	98.31	99.04	99.97	98.94
Total 2	%	100.70	100.50	98.97	99.86	98.44	99.75	99.13	98.69	98.45	99.12	100.00	99.04
Be	ppm	5.0	4.0	4.0	5.0	10.0	4.0	6.0	11.0	5.0	132.0	6.0	6.0
Rb	ppm	265.0	231.0	223.0	246.0	250.0	237.0	261.0	277.0	221.0	291.0	301.0	321.0
Sr	ppm	81.0	93.0	101.0	111.0	114.0	88.0	152.0	142.0	147.0	21.0	23.0	37.0
Y	ppm	33.0	32.0	37.0	35.0	29.0	33.0	23.0	33.0	19.0	32.0	52.0	28.0
Zr	ppm	101.0	100.0	111.0	118.0	107.0	106.0	117.0	113.0	139.0	48.0	45.0	58.0
Nb	ppm	18.0	16.0	18.0	20.0	18.0	18.0	19.0	20.0	16.0	37.0	48.0	27.0
Mo	ppm	4.0	2.0	2.0	3.0	2.0	3.0	2.0	2.0	2.0	3.0	2.0	6.0
Ba	ppm	282.0	369.0	438.0	436.0	483.0	320.0	525.0	481.0	587.0	50.0	61.0	132.0
Ta	ppm	5.2	3.9	4.0	4.2	3.7	4.6	3.3	5.0	2.8	11.4	13.6	7.8
W	ppm	8.0	3.0	3.0	4.0	2.0	4.0	3.0	3.0	3.0	4.0	9.0	9.0
Pb	ppm	32.0	29.0	31.0	30.0	32.0	31.0	30.0	29.0	28.0	35.0	47.0	41.0
Th	ppm	14.3	14.9	16.1	18.3	13.2	14.2	15.6	16.0	17.9	9.4	9.5	9.4
U	ppm	20.9	6.1	9.4	7.9	5.6	10.0	5.4	7.9	9.0	33.1	38.9	12.1
La	ppm	18.6	19.2	21.6	26.0	18.5	19.4	27.9	27.2	33.5	12.0	12.1	12.3
Ce	ppm	36.4	43.8	43.7	50.6	37.4	41.7	55.6	50.2	60.3	22.4	17.4	28.9
Pr	ppm	4.4	4.6	5.1	5.9	4.3	4.7	6.2	6.2	7.1	3.5	2.8	3.0
Nd	ppm	16.8	18.0	19.0	22.8	16.6	17.6	22.6	23.0	24.7	12.9	10.6	11.0
Sm	ppm	4.3	4.2	4.5	5.6	3.9	4.3	4.6	5.1	4.6	3.9	3.9	3.0
Eu	ppm	0.6	0.6	0.6	0.6	0.6	0.5	0.7	0.8	0.7	0.2	0.2	0.3
Gd	ppm	4.6	4.8	4.5	5.5	4.3	4.6	4.1	5.3	3.7	4.1	5.2	3.3
Tb	ppm	0.8	0.9	0.9	1.0	0.7	0.9	0.7	0.9	0.6	0.8	1.3	0.6
Dy	ppm	5.2	5.0	5.6	5.8	4.5	5.3	4.2	5.8	3.3	5.4	8.9	4.3
Ho	ppm	1.1	1.0	1.2	1.2	0.9	1.1	0.8	1.2	0.7	1.1	1.8	0.9
Er	ppm	3.4	3.1	3.8	3.6	2.7	3.2	2.5	3.5	2.1	3.6	5.8	2.8
Tm	ppm	0.5	0.5	0.6	0.6	0.5	0.5	0.4	0.6	0.3	0.6	1.0	0.5
Yb	ppm	3.8	3.4	4.1	3.6	3.1	3.5	2.7	4.0	2.4	4.9	7.7	3.8
Lu	ppm	0.6	0.5	0.6	0.6	0.5	0.6	0.4	0.6	0.4	0.8	1.2	0.6

LO Lamas de Olo, *AC* Alto dos Cabeços granite, *BA* Barragem granite

The most import conclusions are:

1. Although the K_m values strongly vary within a few meters, the geostatistical analysis shows the presence of correlations between two points spaced up to 1400 m apart ($a = 1400$ m);
2. The kriging interpolation validates the existence of two kinds of magnetic behavior in the same pluton, magnetite- and ilmenite-type and its spatial distribution;
3. Although the pluton outcrops in a small area (*ca.* 138 km^2), the K_m values have a huge variation (range = 2748 μSI), showing the heterogeneity of their granites, with the predominance of ilmenite-type granites (K_m mean value *ca.* 809 μSI) but recording the presence of magnetite type-granites;
4. The K_m values are heterogeneous for LOP granites and range between 21 and 2769 μSI;
5. The observation of the kriging map shows that the areas along higher $K_m$values have an alignment that does not correspond to the known and well-defined NNE–SSW regional structures but to the other important family structure ENE–WSW;
6. The geochemical analysis pointed out some differences in the Barragem granite in relation to the other two granites from LOP, showing that the Barragem corresponds to a more differentiated granite, with a different source;
7. The main contrast in the Lamas de Olo-magnetite- or -ilmenite-type granites is due to the different proportions of iron minerals (e.g. magnetite, hematite) and the presence of martitization, mostly in the ilmenite-type granites, which explains the lower magnetic susceptibility values;
8. The Lamas de Olo magnetic behavior cannot be explained by different magma chemistry associated with different magma sources, thus we assume that the two facies from the Lamas de Olo granite was derived from the same magma;
9. The Lamas de Olo granite presents a heterogeneous distribution of iron oxides as Ti-poor magnetite, magnetite, and hematite, which result from complex redox reactions, justifying both types of magnetic behavior;
10. The presence of magnetite in granites pointed out the deep generation of the magma, in oxidizing conditions, which originated the LOP; during the ascent and emplacement, oxidation reactions must have occurred, and they were able to modify magnetite into other oxidized minerals, like hematite; the presence of hematite (mostly as its pseudomorph martite), causes the magnetic signal to decrease and consequently leads to the identification of ilmenite-type behavior;
11. Regarding mineral occurrence, there are W–Mo-(Sn) mineralizations in association with the LOP granites; they show a spatial relationship with magnetite-type granites and both (mineralizations and magnetite-type granites) have the same ENE–WSW (N 80° E) orientation.

Acknowledgements The first author was financially supported by SFRH/BD/109693/2015 (Fundação para Ciência e a Tecnologia-Portugal). The authors acknowledge funding from FCT (Fundação para a Ciência e a Tecnologia) under project UIDB/04683/2020 and from ESMIMET, an INTERREG Spain-Portugal POCTEP project. We thank Helena Brites Martins for the help in interpreting geochemical results. The authors are grateful to the anonymous referee whose comments greatly helped to improve the manuscript.

References

Actlabs. (2020). Geochemistry: Lithogeochemistry and whole rock analysis. Retrieved January 9, 2020 from https://actlabs.com/.

Almeida, A., Leterrier, J., Noronha, F., & Bertrand, J. M. (1998). U–Pb zircon and monazite geochronology of the Hercynian two mica granite composite pluton of Cabeceiras de Basto (Northern Portugal). *Comptes Rendus de l'Académie des Sciences, 326*, 779–785.

Aranguren, A., Tubia, J., Bouchez, J. L., & Vigneresse, J. L. (1996). The Guitiriz granite, Variscan belt of northern Spain: Extension-controlled emplacement of magma during tectonic escape. *Earth and Planetary Science Letters, 139*(1–2), 165–176.

Aydin, A., Ferré, E. C., & Aslan, Z. (2007). The magnetic susceptibility of granitic rocks as a proxy for geochemical composition: Example from the Saruhan granitoids, NE Turkey. *Tectonophysics, 441*, 85–95.

Ballouard, C., Poujol, M., Boulvais, P., Branquet, Y., Tartèse, R., & Vigneresse, J. L. (2016). Nb–Ta fractionation in peraluminous granites: A marker of the magmatic-hydrothermal transition. *Geological Society of America, 4*, 89.

Benndorf, J., & Menz, J. (2014). Improving the assessment of uncertainty and risk in the spatial prediction of environmental impacts: A new approach for fitting geostatistical model parameters based on dual kriging in the presence of a trend. *Stochastic Environmental Research and Risk Assessment, 28*(3), 627–637.

Bouchez, J. L. (1997). Granite is never isotropic: An introduction to AMS studies of granitic rocks. In J. L. Bouchez, D. H. W. Hutton, & W. E. Stephens (Eds.), *Granite: From melt to emplacement fabrics* (pp. 95–112). Dordrecht: Kluwer Academic Publishers.

Boynton, W. V. (1984). Cosmochemistry of the rare earth elements; meteorite studies. In P. Henderson (Ed.), *Rare earth element geochemistry* (pp. 63–114). Amsterdam: Elsevier.

Chilès, J. P., & Delfiner, P. (2012). *Geostatistics. Modelling spatial uncertainty* (2nd ed., p. 695). New York: Wiley.

Chadima, M., & Jelinek, V. (2009). *Anisoft 4.2: Anisotropy data browser for windows*. Brno: Advanced Geoscience Instruments Company (AGICO).

Coleman, D. S., Bartley, J. M., Glazner, A. F., & Pardue, M. J. (2012). Is chemical zonation in plutonic rocks driven by changes in source magma composition or shallow-crustal differentiation? *Geosphere, 8*, 1568–1587.

Cruz, C., & Sant'Ovaia, H. & Noronha, F., (2016). Magnetic susceptibility and $\delta^{18}O$ characterization of Variscan granites related to W–(Mo) and Sn–(W) mineralizations: Lamas de Olo Pluton case study. *Comunicações Geológicas, 103*(1), 143–174.

Cruz, C., & Sant'Ovaia, H. & Noronha, F., (2020). Magnetic mineralogy of Variscan granites from northern Portugal: An approach to their petrogenesis and metallogenic potential. *Geologica Acta, 18*(5), 1–20.

Davis, J. C. (2002). *Statistics and data analysis in geology* (3rd ed.). New York: Wiley.

Ellwood, B. B., & Wenner, D. B. (1981). Correlation of magnetic susceptibility with $^{18}O/^{16}O$ data in late orogenic granites of the southern Appalachian Piedmont. *Earth Planetary Science Letters, 54*, 200–202.

Fabijanczyk, P., & Zawadzki, J. (2019). Using geostatistical Gaussian simulation for designing and interpreting soil surface magnetic susceptibility measurements. *International Journal of Environmental Research and Public Health, 16*, 3497.

Fernandes, S., Gomes, M., Teixeira, R. & Corfu, F. (2013). Geochemistry of biotite granites from the Lamas de Olo Pluton, northern Portugal. *Geophysical Research Abstracts*, EGU General Assembly, Vol. 15, pp. 1. Retrieved April 22, 2016 from https://meetingorganizer.copernicus.org/EGU2013/EGU2013-11566.pdf.

Ferré, E. C., Michelsen, K. J., Ernst, W. G., Boyd, J. D., & Canon-Tapia, E. (2012). Vertical zonation of the Barcroft granodiorite, White Mountains, California: Implications for magmatic processes. *American Mineralogist, 97*, 1049–1059.

Figueiredo, J., Vila, M. C., Góis, J., Biju, B. P., Futuro, A., Martins, D., et al. (2019). Bi-level depth assessment of an abandoned tailings dam aiming its reprocessing for recovery of valuable metals. *Minerals Engineering, 133*, 1–9.

Goovaerts, P. (1997). *Geostatistics for natural resources evaluation*. New York: Oxford University Press.

Hanke, J. R., Fischer, M. P., & Pollya, R. M. (2018). Directional semivariogram analysis to identify and rank controls on the spatial variability of fracture networks. *Journal of Structural Geology, 108*, 34–51.

Helal, B. (1992). *Granitoïdes, granites à métaux rares et hydrothermalisme associe: Géologie, minéralogie et géochimie de plusieurs suites tardi-hercyniennes (Nord du Portugal).* (p. 508). France: Ecole Nacionale Superieure des Mines de Saint-Etienne. **(Thesis submitted for the PhD degree (published thesis))**.

Hrouda, F. (1982). Magnetic anisotropy of rocks and its application in geology and geophysics. *Geophysical Surveys, 5*, 37–82.

Ishihara, S. (1977). The magnetite-series and ilmenite-series granitic rocks. *Mining Geology, 27*, 292–305.

Ishihara, S., Lee, D. S., & Kim, S. Y. (1981). Comparative study of Mesozoic granitoids and related W–Mo mineralization in Southern Korea and Southwestern Japan. *Mining Geology, 31*(4), 311–320.

Ishihara, S., Hashimoto, M., & Machida, M. (2000). Magnetite/ilmenite series classification and magnetic susceptibility of the Mesozoic–Cenozoic batholiths in Peru. *Resource Geology, 50*, 123–129.

Journel, A. G., & Huijbregts, C. J. (1978). *Mining geostatistics*. New York: Academic Press.

Krige, D. G. (1951). A statistical approach to some basic mine valuation problems on the Witwatersrand. *Journal of the Chemical, Metallurgical and Mining Society of South Africa, 188*, 119–139.

Takahashi, M., Aramaki, S., & Ishihara, S. (1980). Magnetite series/ilmenite series vs I-type/S-type granitoids. In I. Ishihara & S. Takenouchi (Eds.), *Granitic magmatism and related mineralization* (pp. 13–28). Tokyo: Nihon Shigen Chishitsu Gakkai-Society of Resource Geologists of Japan.

Teixeira, R. (2008). *Mineralogia, petrologia e geoquímica dos granitos e seus encraves da região de Carrazeda de Ansiães, Thesis submitted for the PhD degree (published thesis)* (p. 463). Portugal: EUniversidade de Trás-os-Montes e alto Douro. **(Thesis submitted for the PhD degree (published thesis))**.

Marques, F. O., Mateus, A., & Tassinari, C. (2002). The Late-Variscan fault network in central–northern Portugal (NW Iberia): A reevaluation. *Tectonophysics, 359*(3–4), 255–270.

Matheron, G. (1960). Traité de géostatistique appliquée. *Mémoires Bureau de Recherches Géologiques et Minières (BRGM), 14*, 333.

Maulana, A., Watanabe, K., Imai, A., & Yonezu, K. (2013). Origin of magnetite- and ilmentite-series granitic rocks in Sulawesi, Indonesia: Magma genesis and regional metallogenic constrains. *Earth and Planetary Sciences, 6*, 50–57.

Olivia-Urcia, B., & Pueyo, E. L. (2012). Gradient of shortening and vertical-axis rotations in the Southern Pyrenees (Spain), insights from a synthesis of paleomagnetic data. *Revista de la Sociedad Geológica de España, 20*(1–2), 105–118.

Peccerillo, A., & Taylor, S. R. (1976). Geochemistry of Eocene calc-alkaline volcanic rocks from the Kastamonu area, Northern Turkey. *Contributions to Mineralogy and Petrology, 58*, 63–81.

Pereira, E. (1989). Carta Geológica de Portugal à escala 1:50 000. *Notícia Explicativa da Folha 10-A (Celorico de Basto)*. Lisboa: Serviços Geológicos de Portugal.

Pereira, E., Silva, N., Moreira, A. & Ribeiro, A. (1987). *Carta Geológica de Portugal à escala 1:50 000*. Folha 10-A (Celorico de Basto). Serviços Geológicos de Portugal.

Pizarro, N. (2008). Magnetic Susceptibility Scaling of Rocks using Geostatistical Analysis: An approach to Geologic and Geophysical model integration. *Thesis submitted for the MSc (Geological Sciences)*, University of British Columbia (Vancouver), September, 195.

Porquet, M., Pueyo, E. L., Róman-Berdiel, T., Olivier, P., Longares, L. A., Cuevas, J., Geokin3DPyr Working Group, et al. (2017). Anisotropy of magnetic susceptibility of the Pyrenean granites. *Journal of Maps, 13*(2), 438–448.

Román-Berdiel, T., Pueyo-Morer, E. L., & Casas-Sainz, A. M. (1995). Granite emplacement during contemporary shortening and normal faulting: Structural and magnetic study of the Veiga Massif (NW Spain). *Journal of Structural Geology, 17*(12), 1689–1706.

Sant'Ovaia, H., Martins, Lopes, J.C., Machado, J. & Noronha, F., (2012). Correlation of magnetic susceptibility with $\delta^{18}O$ data in magnetite- and ilmenite-type granites from Iberian massif. *Mineralogical Magazine, 76*(6), 23–25.

Sichel, H. S. (1952). *New methods in the statistical evaluation of mine sampling data* (pp. 261–288). London: Bulletin Institute of Mining and Metallurgy.

Villaseca, C., Barbero, L., & Herreros, V. (1998). A re-examination of the typology of peraluminous granite types in intracontinental orogenic belts. *Transactions of the Royal Society of Edinburgh: Earth Sciences, 89*, 113–119.

Villaseca, C., Ruiz-Martínez, V. C., & Pérez-Soba, C. (2017). Magnetic susceptibility of Variscan granite-types of the Spanish Central System and the redox state of magma. *Geologica Acta, 15*(4), 379–394.

Zawadzki, J., Magiera, T., Fabijańczyk, P., & Kusza, G. (2012). Geostatistical 3-dimensional integration of measurements of soil magnetic susceptibility. *Environmental Monitoring and Assessment, 184*(5), 3267–3278.

Zawadzki, J., Fabijańczyk, P., Magiera, T., & Rachwał, M. (2015). Geostatistical microscale study of magnetic susceptibility in soil profile and magnetic indicators of potential soil pollution. *Water, Air, and Soil Pollution, 226*(5), 142–148.

Affiliations

Cláudia Cruz[1] · Joaquim Góis[2] · Helena Sant'Ovaia[1] · Fernando Noronha[1]

Joaquim Góis
jgois@fe.up.pt

Helena Sant'Ovaia
hsantov@fc.up.pt

Fernando Noronha
fmnoronh@fc.up.pt

[1] Departamento de Geociências Ambiente e Ordenamento do Território, Faculdade de Ciências, Instituto de Ciências da Terra-Pólo Porto, Universidade do Porto, Rua do Campo Alegre 687, Porto, Portugal

[2] Departamento de Engenharia de Minas, Faculdade de Engenharia, CERENA-Centro de Recursos Naturais e Ambiente-Polo FEUP, Universidade do Porto, R. Dr. Roberto Frias, 4200-465 Porto, Portugal

EGU2020-21596
https://doi.org/10.5194/egusphere-egu2020-21596
EGU General Assembly 2020
© Author(s) 2020. This work is distributed under
the Creative Commons Attribution 4.0 License.

Magnetic fabric of Lamas de Olo Pluton: AMS and AARM fabrics comparison

Cláudia Cruz[1], Helena Sant'Ovaia[1], Maria Irene Bartolomeu Raposo[2], and Fernando Noronha[1]
[1]University of Porto, Faculty of Sciences , Instituto de Ciências da Terra-Polo Porto, Departamento de Geociências, Ambiente e Ordenamento do Território, Porto, Portugal
[2]Instituto de Geociências da Universidade de São Paulo, São Paulo, Brazil

The Lamas de Olo Pluton (LOP) is a small outcrop located in the Northern part of Central Iberian Zone from the Iberian Variscan belt. The LOP is a post-tectonic (ca. 297.19 ± 0.73 Ma) pluton composed of different granites: Lamas de Olo (LO; medium to coarse-grained porphyritic granite, ilmenite, and magnetite-type), Alto dos Cabeços (AC; medium to fine-grained porphyritic, ilmenite-type granite), and Barragem (BA; leucocratic fine- to medium-grained, slightly porphyritic, ilmenite-type granite). The magnetic fabric was characterized by measurements of anisotropy of magnetic susceptibility (AMS), and anisotropy of anhysteretic remanent magnetization (AARM). Both techniques are based on the magnetic properties of rock minerals, but while AMS consider the contribution of all rock minerals (paramagnetic, diamagnetic and ferromagnetic s.l.), in the AARM, the fabric is exclusively given by the ferromagnetic s.l. minerals. A correlation between AMS and AMR tensor was established, in order to compare both fabrics. The magnetic lineation is K_{max} or $AARM_{max}$ and the magnetic foliation is perpendicular to K_{min} or $AARM_{min}$. Considering the global magnetic fabric for all samples from all the granite set, the magnetic foliations (AMS: N166°, 82°NE; AARM: N167°, 83°NE) and the magnetic lineations (AMS: 23°- N166°; AARM: 68°- N163°) are coaxial in both tensors. On the other hand, the analysis of each site sampling shows some differences in the ilmenite-type granites. Magnetic lineations and foliations given by both tensors (AMS and AARM) are coaxial in the magnetite-type granites, meaning that the magnetite and paramagnetic (or diamagnetic) minerals have the same orientation. The coaxial AMS and AARM magnetic foliations are due to magnetite grains imitating the fabrics of paramagnetic phases, through preferred collage, or crystallization of magnetite along grain boundaries, or exsolutions of magnetite along biotite cleavage planes. However, in the ilmenite-type granites, the AMS and AARM foliations are parallel, but the AMS and AARM lineations are not coaxial. Previous magnetic mineralogy studies (e.g. thermomagnetic experiments and isothermal remanent magnetization) pointed out the presence of magnetite/Ti-poor magnetite in all LOP granites, even in the ilmenite-type, but in different proportions. The petrographic observations also showed that, in the ilmenite-type granites, the magnetite is often oxidized to hematite (martite). The presence of martite may justify non-coaxility linear fabrics. Regarding the LOP emplacement, WSW-ENE opening structures provided the space for magma ascending, with an NNW-SSE magmatic flow controlled by regional structures, as shown by the magnetic foliations and lineations ca. N170º trending. The absence of outcrop deformation and the lack of solid-state microstructures precludes the substantial

deformation after full crystallization of LOP.

Citation: Cruz, C., Sant'ovaia, H., Noronha, F., 2020. Magnetic mineralogy of Variscan granites from northern Portugal: an approach to their petrogenesis and metallogenic potential. Geologica Acta, 18.5, 1-20.
DOI: 10.1344/GeologicaActa2020.18.5

geologica acta

Magnetic mineralogy of Variscan granites from northern Portugal: an approach to their petrogenesis and metallogenic potential

C. Cruz[1,2] **H. Sant'Ovaia**[1,2] **F. Noronha**[1,2]

[1]**Departamento de Geociências Ambiente e Ordenamento do Território - Faculdade de Ciências, Universidade do Porto**
Rua do Campo Alegre 687, Porto, Portugal. Cruz E-mail: claudiacruz@fc.up.pt
Sant'Ovaia E-mail: hsantov@fc.up.pt

[2]**Instituto de Ciências da Terra, Polo Porto**
Rua do Campo Alegre 687, Porto, Portugal
Noronha E-mail: fmnoronh@fc.up.pt

ABSTRACT

Northern Portugal is characterized by the occurrence of numerous W hydrothermal deposits spatially associated with granites. The primary goal of this work is to establish a relationship between the magnetic behavior of the granites and the redox conditions during magma genesis, as this can influence the occurrence of mineralizations, namely of W (Mo). To this end, the magnetic mineralogy of the granites of the Lamas de Olo Pluton, a post-tectonic pluton in northern Portugal, with associated W (Mo) occurrences was characterized and compared with the magnetic mineralogy of other post-tectonic Variscan plutons. This pluton is composed of different biotite granites: Lamas de Olo, Alto dos Cabeços and Barragem. To better characterize its magnetic behavior, different analytical techniques that complement previous magnetic susceptibility studies were performed. The magnetic mineralogy of Lamas de Olo Pluton was then compared with other post-tectonic Variscan plutons such as the Vila Pouca de Aguiar, Peneda-Gerês and Lavadores-Madalena plutons. The presence of magnetite in some of these granites is important because it points to melt-oxidized conditions not commonly found in Iberian Variscan granites. Our study shows that granite areas where magnetite and/or magnetite/ilmenite coexist are important targets for W (Mo) mineralizations. The results indicate that a few plutons have granites with a complex redox history which leads to the formation of magnetite and ilmenite.

KEYWORDS | **Magnetic mineralogy. Variscan granites. Post-D_3 biotite granites. Central Iberian Zone. W-Mo mineralizations.**

INTRODUCTION

The northern area of Portugal is characterized by large volumes of granitic intrusions related to Variscan orogeny (321-290Ma). Synorogenic granites represent the plutonic magmatism and, based on their geological, petrographic and geochemical characteristics, are divided into two main groups (*e.g.* Chappell and White, 1974; Dias *et al.*, 2010; Ferreira *et al.*, 1987; Noronha *et al.*, 2006). The first group consists of two-mica peraluminous granites, which are dominantly syntectonic (syn-D_3: 321-312Ma) and considered S-type granites, resulting from the crystallization of wet peraluminous magmas originated at a mesocrustal level. The second group consists of biotite granites considered to have been generated at deep crustal levels and corresponding to dry magmas. The age of their formation is either syn-D_3 (321-312Ma), late-D_3 (312-305Ma), late- to post-D_3 (*ca.* 300Ma), or post-D_3 (299-290Ma) (Dias *et al.*, 2010).

© C. Cruz, H. Sant'Ovaia, F. Noronha, 2020 CC BY-SA

These two types of granites have distinctive whole-rock oxygen isotope ($\delta^{18}O$) values. The highest $\delta^{18}O$ values indicate a crustal origin, and the lowest values suggest a mantle contribution and/or source region dominated by mafic and meta-igneous rocks (Ellwood and Wenner, 1981; Ishihara, 1977). The $\delta^{18}O$ mean values range between 10.65‰ and 12.90‰ for the two-mica granites and 9.75‰ and 12.84‰ for the biotite granites (Antunes *et al.*, 2008; Cruz *et al.*, 2016; Sant'Ovaia *et al.*, 2013a, b; Teixeira *et al.*, 2012).

The magnetic susceptibility (K_m) of granites is an important characteristic and it is mainly controlled by the presence of certain oxide minerals like magnetite and/or ilmenite as well as ferromagnesian silicates such as biotite.

The abundance of magnetite or ilmenite can be explained by different redox conditions in the magma chamber and different magma sources. The presence of magnetite or ilmenite as accessory minerals represents oxidized- or magnetite-type granites and reduced- or ilmenite-type granites, respectively (Ishihara, 1977). Magnetite granites are considered to have been generated at great depth (upper mantle and/or lower crust), whereas the ilmenite-series are considered to have originated at a shallower level (middle to lower continental crust) where small amounts of crustal carbon are present (Ellwood and Wenner, 1981; Ishihara, 1977; Sheppard, 1977). Relative abundances of magnetic minerals in granites can be measured in terms of magnetic susceptibility, with the magnetite-series having $K_m > 3.0 \cdot 10^{-3}$SI and ilmenite-series, in general, with K_m around 10^{-6}SI (or μSI) (*e.g.* Ishihara, 1977; Takagi and Tsukimura, 1997).

In the Iberian Variscan belt, specifically in the Central Iberian Zone (CIZ), in Spain and Portugal, the magnetic behavior of numerous granites has been analyzed. The Spanish granites are mostly ilmenite-type and have been extensively analyzed by several authors, like Aranguren *et al.* (1996); Olivia-Urcia *et al.* (2012); Porquet *et al.* (2017); Román-Berdiel *et al.* (1995). These authors found K_m values between 22μSI and 467μSI. Recent studies carried out by Villaseca *et al.* (2017) proved the existence of both ilmenite- and magnetite-type granites in the Spanish Central System. The magnetic susceptibility of these granites yielded K_m *ca.* 15μSI to 180μSI for S- and I-type granites (ilmenite-type granites) and values between 500μSI and 1,400μSI for the leucogranites I-type granites (magnetite-type granites). Magnetic susceptibility studies in several Portuguese granites (Sant'Ovaia *et al.*, 2014) yielded K_m mean values between 48μSI and 84μSI for two-mica granites corresponding to ilmenite-type granites and between 72μSI and 11,676μSI for biotite granites corresponding to ilmenite-type and/or magnetite-type granites.

Several metallogenic events are identified on the granite bodies: i) Sn-Li pegmatites are essentially associated to syn-D_3 with two-mica granites; ii) W (Sn) and W quartz-vein deposits occur in late- and late- to post- D_3 biotite granites; and iii) W (Mo) deposits are related to post-D_3 biotite sub-alkaline granites (*e.g.* Mateus and Noronha, 2010; Noronha, 2017; Thadeu, 1965).

The magnetic susceptibility (K_m) and $\delta^{18}O$ data allow to establish a relationship between the granite type (ilmenite- or magnetite-type) and the associated mineralizations (Kumar, 2010; Takagi and Tsukimura, 1997). The occurrence of ore deposits associated with ilmenite-type and/or magnetite-type granites has been largely described, for example, in Indonesia (Maulana *et al.*, 2013) and, in southern Korea and southwestern Japan (Ishihara *et al.*, 1981) and, more recently, in Portugal (Cruz *et al.*, 2016; Sant'Ovaia *et al.*, 2014). In Sulawesi, Indonesia, the ilmenite-type granites outcrop in the southern zone of the island while the magnetite-type granites occur in the northern area. Both granites have associated ore mineralization. Cu-Au-Mo mineralizations are associated with magnetite-series granitic rocks, while Sn-W mineralizations related to reduced ilmenite-type granites have not yet been reported (Maulana *et al.*, 2013). Contrastingly, in southern Korea and southwestern Japan (Ishihara *et al.*, 1981), W-Mo occurrences were described in areas with both ilmenite- and magnetite-type granites with no clear separation in the distribution of the two types of granites. In the Portuguese sector of the Central Iberian Zone, the Sn deposits are associated with S- and ilmenite-type granites and the W-(Sn) mineralizations occur in veins that cut the I (peraluminous)- and ilmenite-type granites, both with high $\delta^{18}O$ values, The W (Mo) occurrences are spatially related to I (peraluminous)- and magnetite-type granites (Cruz *et al.*, 2016; Sant'Ovaia *et al.*, 2012).

The study of magnetic mineralogy expands our knowledge of the relation between granites and their related mineralizations, since the redox conditions control the specific mineral occurrences. It is very important to understand the relationship between magnetic mineralogy and ore deposits considering the complexity of magma genesis.

The main goal of this work is to characterize the magnetic behavior of the Lamas de Olo Pluton (LOP) and compare it with the magnetic behavior of other post-tectonic Variscan biotite plutons (Peneda-Gerês Pluton (PGP), Lavadores-Madalena Pluton (LMP) and Vila Pouca de Aguiar Pluton (VPAP). We aim at establishing a relationship between the magnetic behavior of the granites and the occurrence of different kinds of mineralizations.

GENERAL FRAMEWORK

The Iberian Variscan belt

The Iberian Variscan belt was formed as a large curved segment of the European Variscan belt resulting from the Laurussia-Gondwana collision during Devonian to Carboniferous times (Franke, 1989; Kroner and Romer, 2013; Ribeiro *et al.*, 1990). After the collision, during the late Paleozoic, the Pangea amalgamation leads to continuous rock deformation and the C-shaped Cantabrian orocline was formed (*e.g.* Gutiérrez-Alonso *et al.*, 2012; Weil *et al.*, 2013). Other authors suggest a more complex scenario, with the existence of two oroclines, in S-shaped, the Cantabrian, and Central-Iberian (*e.g.* Pastor-Galán *et al.*, 2012; Shaw *et al.*, 2012).

The Iberian belt is subdivided into several geotectonic zones (Fig. 1): the Cantabrian Zone (CZ), the West Asturian Leonese Zone (WALZ), the CIZ, the Ossa Morena Zone (OMZ) and the South Portuguese Zone (SPZ) (Julivert *et al.*, 1974). Farias *et al.* (1987) identified allochthonous and parautochthonous units in the CIZ, which led them to consider another zone, the Galicia Trás-os-Montes Zone (GTMZ).

Three main ductile deformation phases have been documented in northern Portugal, namely D_1, D_2 and D_3 (Noronha *et al.*, 1981). In the CIZ, two main phases of deformation can be recognized in the autochthonous terrane: D_1 (*ca.* 360–337Ma, *e.g.* Castiñeiras *et al.*, 2008; Dallmeyer *et al.*, 1997; Díez Fernández *et al.*, 2016; Martínez Catalán *et al.*, 2014; Pereira *et al.*, 2018), and D_3 (*ca.* 321–300Ma, *e.g.* Ferreira *et al.*, 1987; Pereira *et al.*, 2018). D_1 produced isoclinal folds with a subvertical axial plane with a NW-SE strike and a well-marked axial plane schistosity (S_1), and D_3 is characterized by wide folding of small amplitude on the subvertical axial plane and sub-horizontal NW-SE axis. Simultaneously with the D_3, vertical ductile shear zones were developed in lower structural levels. In the upper

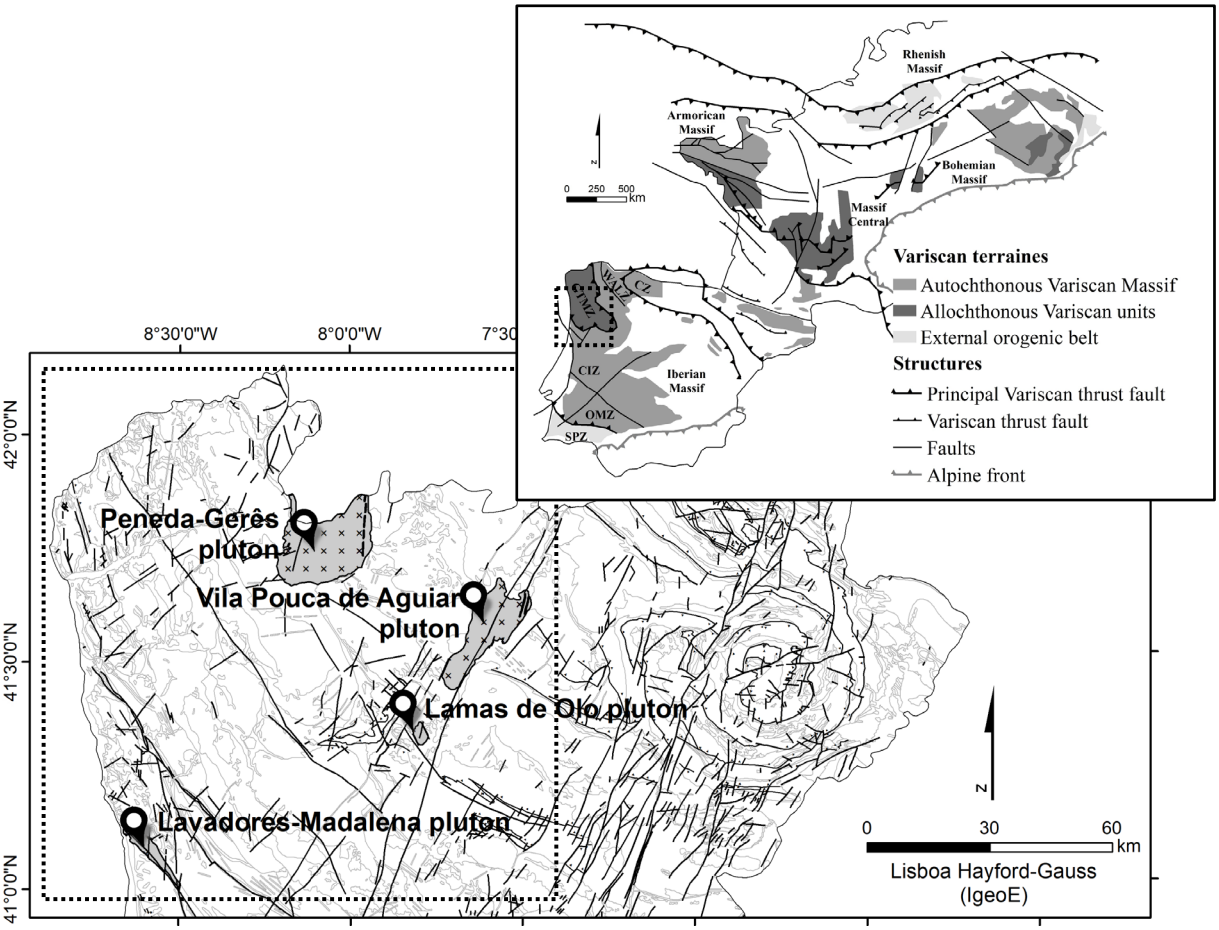


FIGURE 1. Iberian Variscan belt and location of the studied granitic bodies: Lamas de Olo Pluton, Vila Pouca de Aguiar Pluton, Peneda-Gerês Pluton and Lavadores-Madalena Pluton (modified from Ferreira *et al.*, 1987). CZ: Cantabric Zone, WALZ: West Asturian Leonese Zone, GTMZ: Galiza Trás-os-Montes Zone, CIZ: Central Iberian Zone, OMZ: Ossa Morena Zone, SPZ: South Portuguese Zone (based on: Farias *et al.*, 1987; Julivert *et al.*, 1974).

structural levels, a brittle deformation occurred, leading to fracture-conjugate systems in a NNE-SSW and NNW-SSE direction (Marques *et al.*, 2002). D_2 (*ca.* 337-316Ma; *e.g.* Dallmeyer *et al.,* 1997; Díez Fernández *et al.*, 2016; Martínez Catalán *et al.,* 2014; Pereira *et al.*, 2018) is well represented in allochthonous terranes in the GTMZ.

Most of the granite intrusions are coeval with D_3 and the others are late- and post-D_3 (*e.g.* Dias *et al.*, 2010; Ferreira *et al.*, 1987). The development of different tectonic structures, namely shear zones, during D_3 and successive reactivation events controlled the granite emplacement and caused extensive hydrothermal activity throughout the entire crust, involving distinct fluid sources, some transporting significant amounts of ore mineral phases (Mateus and Noronha, 2010; Noronha *et al.*, 2013).

Plutons and associated mineralizations

The LOP is located in the northern part of the CIZ near the limit with the GTMZ (Figs. 1; 2). It is a small post-tectonic pluton with a rhombus shape, controlled by NNW-SSE offsets conjugated with the NNE-SSW fault system, which are parallel to the Verin-Régua-Penacova fault (VRPF). The LOP is composed of distinct outcropping granites (Fig. 2): i) Lamas de Olo (LO), the more representative, a medium- to coarse-grained porphyritic granite (biotite > muscovite); ii) Alto dos Cabeços (AC), a fine- to medium-grained porphyritic granite (biotite > muscovite) and iii) Barragem (BA), a fine- to medium-grained slightly porphyritic leucocratic granite (biotite= muscovite) (Fernandes *et al.*, 2013; Pereira, 1989). $^{207}Pb/^{235}U$ dating in monazite yield an age of 297.19±0.73Ma for the LO granite (Fernandes *et al.*, 2013). Field observations show that the contact between the LO and AC granites is generally diffuse, and that the BA granite crosscuts the LO and AC granites. Previous studies of anisotropy of magnetic susceptibility showed that LOP has two types of behavior granites: magnetite- and ilmenite-type (Cruz *et al.*, 2016). W-Mo (Sn) mineralizations occur, mostly in N 80º E sub-vertical quartz veins (Helal, 1992).

The LOP intrudes Lower Paleozoic formations (Armorican quartzite and schists of Upper Silurian to Middle Ordovician age), the Douro Group metasediments (Upper to Middle Cambrian) and two-mica syntectonic granites in the Vila Real Massif (Fig. 2). The Vila Real Massif is a syn-D_3 two-mica granite composite massif with associated Sn mineralizations in pegmatites, and W-Sn in hydrothermal quartz veins (Pereira, 1989). Monazite and zircon analysis yield a weighted average $^{207}Pb/^{235}U$ age of ca. 311±1Ma (Almeida *et al.*, 1998).

The other granites referred to in this study belong to Vila Pouca de Aguiar, Peneda-Gerês and Lavadores-Madalena plutons (Fig. 1), classified as post-tectonic biotite plutons. Vila Pouca de Aguiar and Peneda-Gerês plutons are located in the GTMZ and Lavadores-Madalena Pluton on the NW border of the CIZ.

The Vila Pouca de Aguiar Pluton is a composite pluton with two main biotite granites: Vila Pouca de Aguiar Granite (VPAG) and Pedras Salgadas Granite (PSG). The two granites have a similar mineralogical composition but different texture, with VPAG displaying a coarse grain porphyritic texture and PSG a more equigranular texture (Martins and Noronha, 2006; Sant'Ovaia *et al.*, 2000). As regards their ages, PSG is younger than VPAG, with 297±14Ma and 298±9.1Ma, respectively (Martins *et al.*, 2009).

The Peneda-Gerês Pluton is also a composite pluton with three main granites: Gerês, Illa-Bouzagrado, and Carris. The Illa-Bouzagrado is a leucogranite (muscovite>biotite) and the other two are biotite granites (Cottard, 1979; Mendes and Dias, 2004). All the granites are contemporaneous and dated to *ca.* 290-296Ma (Dias *et al.*, 1998). Some deposits associated with the granites of this pluton, have been described, namely: Mo (Bouzagrado in Spain) and W (Mo-Sn-Bi) (Carris and Borrageiro in Portugal and Las Sombras in Spain) (Cottard, 1979; Cheilletz and Giuliani, 1982).

The Lavadores-Madalena Pluton, dated to 298±11Ma (Martins *et al.*, 2011), is composed of Lavadores and Madalena granites. The Lavadores granite is a porphyritic, coarse-grained biotite granite (Martins *et al.*, 2011) and the Madalena granite is a porphyritic medium- to coarse-grained biotite granite (Sant'Ovaia *et al.*, 2014). W (Mo) mineralization associated with granites of this pluton has been described (Thadeu, 1965; Teixeira and Perdigão, 1962).

MATERIAL AND METHODS

Representative samples of different Variscan granites were examined. The sampled granites were from the Lamas de Olo Pluton, Vila Pouca de Aguiar Pluton, Peneda-Gerês Pluton and Lavadores-Madalena Pluton (Table 1; Fig. 1). Special attention was given to the LOP (Fig. 2), where 67 sites were sampled for this study.

To attain the primary objective of this work, different analytical methods were used: optical microscopy, magnetic susceptibility measurements, isothermal remanent magnetization acquisition curves, and thermomagnetic experiments. Previous studies (Cruz *et al.*, 2016 for LOP. Martins and Noronha, 2006; Sant'Ovaia, 1993; Sant'Ovaia *et al.*, 2000 for Vila Pouca de Aguiar Pluton. Cottard, 1979; Mendes and Dias, 2004 for Peneda-Gerês Pluton. Martins *et al.*, 2011; Sant'Ovaia *et al.*, 2014 for Lavadores-

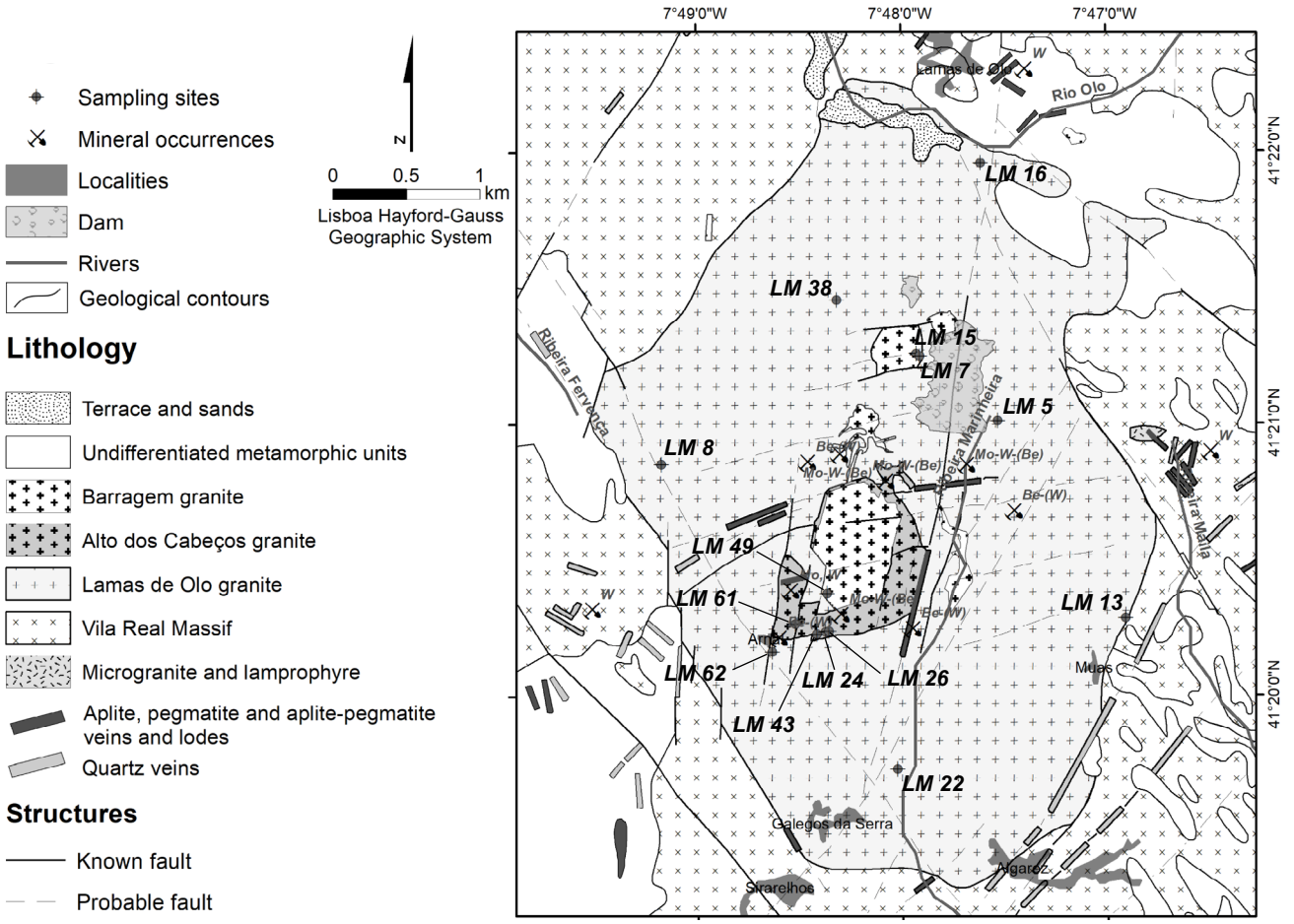


FIGURE 2. Simplified geological map from the Lamas de Olo Pluton (modified from Helal, 1992; Pereira *et al.*, 1987; Pereira, 1989) and location of the samples (LM) used in the isothermal remanent magnetization acquisition curves, frequency-dependent susceptibility measurements and thermomagnetic experiments.

Madalena Pluton) were considered and their data compared with the new data (Table 1).

Microscopy

A Leica petrographic polarizing microscope with a digital camera was used for the reflected and transmitted light petrographic studies. The Raman spectra of different opaque minerals were obtained using a Raman LabRAM HORIBA Jobin Yvon Spex spectrometer interfaced with an Olympus microscope with 50x objective lens, diffraction gratings with 1,800 lines mm^{-1} and equipped with a 632.8nm emission line of a HeNe laser at a power of 20mW. The incident beam perpendicular to the plane of the sample was focused through the microscope lens, which also collected the Raman scattered radiation in back-scattering geometry. A highly sensitive Charge-Coupled Device (CCD) camera was used to collect the Raman spectra. Extended scans were performed on a spectral range from 50 to 1,200cm^{-1}. The time of acquisition and the number of accumulations varied in order to obtain an optimized spectrum for each analyzed mineral. Both equipment belong to the *Departamento de Geociências, Ambiente e Ordenamento do Território* (DGAOT) of the *Faculdade de Ciências da Universidade do Porto* (FCUP) and *Instituto de Ciências da Terra-Polo Porto* (ICT-Porto).

Complementary studies to identify minor mineral amounts and characterize the magnetic mineralogy were carried out using a Scanning Electron Microscope (SEM) and Energy Dispersive Spectroscopy (EDS) X-ray microanalysis at the *Centro de Materiais da Universidade do Porto* (CEMUP). The SEM/EDS studies were performed using a high-resolution JEOL JSM 6301F SEM coupled with an Oxford INCA Energy 350 system. Samples were carbon-coated using a JEOL JEE-4X Vacuum Evaporator.

A total of 13 thin sections from the LOP were used for petrographic studies (Table 1). For complementary studies, some representative samples were selected: 4 for Raman (3 from LO and 1 from BA) and 5 for SEM/EDS (3 from LO and 1 from BA). These samples were selected taking into

account the presence of magnetite, hematite, and ilmenite, which was previously identified under a microscope or by magnetic susceptibility studies. The results from other plutons were compiled from the literature (Table 1).

Magnetic susceptibility and isothermal remanent magnetization

The relationship between the magnetization induced in a material M and the external field H is defined as $M=KH$, where K is the magnetic susceptibility. The K reflects the whole-rock mineral composition, comprising the diamagnetic, paramagnetic and ferromagnetic minerals (Rochette, 1987). K measurements were performed using a KLY-4S Kappabridge susceptometer Agico model (Czech Republic) from the DGAOT-FCUP and ICT-Porto. Measurements were undertaken in a 300A/m field at room temperature. For each site, the ANISOFT 4.2 program package (Chadima and Jelinek, 2009) enabled us to calculate the mean susceptibility K_m. The magnetite is an important ferromagnetic mineral (*s.l.*), easily detected because increases the K_m values to $>10^{-3}$SI (Bouchez, 1997, 2000; Tarling and Hrouda, 1993).

The magnetic susceptibility data were mostly compiled from the literature, and only a few samples from the Peneda-Gerês Pluton were measured in this study (Table 1).

For a detailed magnetic mineralogy study, the acquisition of Isothermal Remanent Magnetization (IRM) curves were performed. The IRM acquisition curves are important to estimate the characteristic coercivity of the ferromagnetic minerals (Butler, 1992). The IRM refers to the remanence acquired by a sample exposed to a direct magnetic field (H), at ambient temperature. These measurements were performed in the *Laboratório de Paleomagnetismo* at the *Instituto Dom Luís*, *Lisboa*. Beforehand, standard samples were demagnetized through an alternating field cleaning at *ca.* 100mT, with an LDA-3A (Agico) demagnetizer. Then, the magnetic field (H) was imparted using an Impulse Magnetizer IM-10-30 (ASC Scientific) and the resulting remanence was measured using a spinner magnetometer JR-6A (Agico). Samples were magnetized in the same direction with increasing magnetic fields from *ca.* 3.51mT up to 1.15T in different steps (*ca.* 40 steps) and the induced magnetization acquired by the specimens was measured after each step of induction. Data were analyzed using a Cumulative Log-Gaussian (CLG) function (Robertson and France, 1994) with the software developed by Kruiver *et al.* (2001). For the IRM studies, 4 granite samples from the LOP were selected according to their magnetic behavior: 1 from the LO-magnetite-type granite, 1 from the LO-ilmenite-type granite, 1 from the BA granite and 1 from the AC granite (Table 1).

Additionally, measurements of frequency-dependent susceptibility were done with a Bartington MS2 System in the *Laboratório de Paleomagnetismo* at the *Instituto Dom Luís, Lisboa*. The low-field magnetic susceptibility was measured at two applied field frequencies (0.46kHz and 46kHz). The percentage of frequency-dependent susceptibility (KfD%) (Dearing *et al.*, 1996) was obtained in 10 samples from the LOP granites (Table 1).

Thermomagnetic experiments

The thermomagnetic experiments allow the identification of ferromagnetic minerals (*s.l.*) based on

TABLE 1. Methodologies applied to studied granites. LOP: Lamas de Olo Pluton; VPAP: Vila Pouca de Aguiar Pluton; PGP: Peneda-Gerês Pluton; LMP: Lavadores-Madalena Pluton; ✓: data obtained in this study; x: no data

Pluton	Granite	Methodologies				
		Optical microscopy studies	Magnetic susceptibility studies	Thermomagnetic curves	Isothermal remanent magnetization	Frequency-dependent susceptibility
LOP	Lamas de Olo	✓ (7 samples)	Cruz *et al.* (2016)	✓ (7 samples)	✓ (2 samples)	✓ (4 samples)
	Alto dos Cabeços	✓ (4 samples)		✓ (4 samples)	✓ (1 sample)	✓ (3 samples)
	Barragem	✓ (2 samples)		✓ (4 samples)	✓ (1 sample)	✓ (3 samples)
VPAP	Pedras Salgadas	Sant'Ovaia (1993) Sant'Ovaia *et al.* (2000) Martins and Noronha (2006)	Sant'Ovaia (1993) Sant'Ovaia *et al.* (2000)	✓ (1 sample)	Sant'Ovaia (1993)	x
	Vila Pouca Aguiar			x		x
PGP	Gerês	Mendes and Dias (2004) Cottard (1979)	✓ (7 samples)	✓ (1 sample)	x	x
	Illa		✓ (3 samples)	x	x	x
	Carris		✓ (3 samples)	x	x	x
LMP	Madalena	Martins *et al.* (2011) Sant'Ovaia *et al.* (2014)	Sant'Ovaia *et al.* (2014)	✓ (1 sample)	Martins *et al.* (2011) Sant'Ovaia *et al.* (2014)	x
	Lavadores			✓ (1 sample)		x

their Curie/Néel temperature. The Curie temperature (T_C) is the temperature above which a ferromagnetic material (*s.s.*) becomes paramagnetic, and the Néel temperature (T_N) is analogous to the T_C but for antiferromagnetic materials.

The Curie/Néel temperature of ferromagnetic minerals (*s.l.*) can be determined in low-field thermomagnetic experiments where the magnetic susceptibility of a sample is monitored while temperature is increased or decreased, and it is defined as the point of major decrease in magnetic susceptibility of the sample during the heating cycle (Butler, 1992). The temperature of this drop in magnetic susceptibility corresponds to the temperature at which a magnetic mineral loses its spontaneous magnetization. In contrast, if magnetic susceptibility, with values much lower than ferromagnetic values, decreases regularly with increasing temperature, the sample has the typical behavior of paramagnetic minerals (Dunlop and Özdemir, 1997).

The Curie/Néel temperature is typical for a particular mineral and is therefore commonly used to identify its composition. For example, the Curie/Néel temperature is 580ºC for magnetite, 680ºC for hematite, 320ºC for pyrrhotite and 120ºC for goethite. However, the rocks can have other iron minerals with titanium in their composition, corresponding to the titanomagnetite and titanohematite series. It should be noted that, in the titanomagnetite series, the Curie point decreases as the Ti content increases; therefore, the T_C can range between 580ºC (T_C of pure magnetite) and -150ºC (T_C of pure ulvospinel) (Dunlop and Özdemir, 1997).

The temperature dependence of low field magnetic susceptibility was monitored with a CS-2 furnace apparatus attached to the KLY-3 susceptometer (Agico) from the *Laboratoire Géosciences Environnement Toulouse, Université de Toulouse III - Paul Sabatier*, using samples obtained from 19 rock specimens (Table 1). Fifteen samples were selected in order to represent all LOP granites and their different magnetic behavior according to previous magnetic susceptibility studies. Regarding the other post-tectonic plutons, 4 samples were selected (Table 1).

The samples were exposed to increasing temperatures up to 700°C in heating/ cooling cycles. The measurements were made in an argon flux in order to minimize oxygen fugacity, which reduces the oxidation of the samples and the consequent formation of new minerals with the increase and/or decrease of temperature. However, a small amount of oxygen is always present in the sample holder, so although the probability is lower, some mineralogical changes may still occur.

RESULTS AND DISCUSSION

Microscopy

The LOP granites are mostly composed of quartz, plagioclase (oligoclase, albite, and oligoclase-andesine), K-feldspars (orthoclase and microcline) and biotite (Table 2; Fig. 3A-C). As accessory minerals, muscovite I and/or II, zircon (Fig. 3A), sphene, allanite (Fig. 3D), fluorite (Fig. 3E), hematite ± magnetite ± ilmenite, chlorite ± rutile, apatite, goethite, epidote, and tourmaline are present. In the BA granite, the muscovite is more abundant than in the LO and AC granites but is mostly of secondary origin resulting from deuteric processes.

The plagioclases occur frequently zoned in all granites (Fig. 3C) and are albite-oligoclase in the BA granite, and oligoclase-andesine in the AC and LO granites. Occasionally, the plagioclases exhibit myrmekitic intergrowths with quartz, common mostly in the LO granite (Fig. 3F), and are altered by sericitization. The K-feldspar, perthitic orthoclase and microcline occur as heterogranular crystals. It is sometimes possible to observe some K-feldspar megacrystals with small plagioclase inclusions. The quartz has sometimes undulatory extinction, subgrain boundaries and fluid inclusion planes (Fig. 3G).

The biotite –brownish to greenish (Fig. 3E) in all granites– sometimes appears partially to completely chloritized. Occasionally, biotite is altered to muscovite, mainly in the leucocratic granite from BA, where biotite is observed in minor amounts (Fig. 3H). Frequently, biotite has pleochroic halos associated with zircon inclusions (Fig. 3A) and curved biotites are rare (Fig. 3H).

For a detailed magnetic mineralogy characterization, complementary studies of opaque minerals were conducted to point out the presence of magnetite, hematite and/or ilmenite. The SEM/EDS analyses showed the presence of different Fe-Ox minerals (Fig. 4) and other minerals in small amounts, like monazite, xenotime (Fig. 4B) and columbo-tantalite. Figure 4E and F are examples of some EDS spectra performed in LOP thin sections, showing the presence of Fe-Ox and Fe-Ox-Ti minerals. Figure 5 shows the micro-Raman spectrum of the principal magnetic minerals present in the LOP, namely magnetite (Fig. 5A), hematite (Fig. 5B) and ilmenite (Fig. 5C).

A summary of the petrographic descriptions of other Variscan granites made in previous studies is presented in Table 2. The Vila Pouca de Aguiar Pluton is located to the NE of the LOP, in the same NNE-SSW alignment, paralell to the Verin-Régua-Penacova Variscan fault. This pluton has two main granite facies with similar mineralogical composition. Both granites are composed

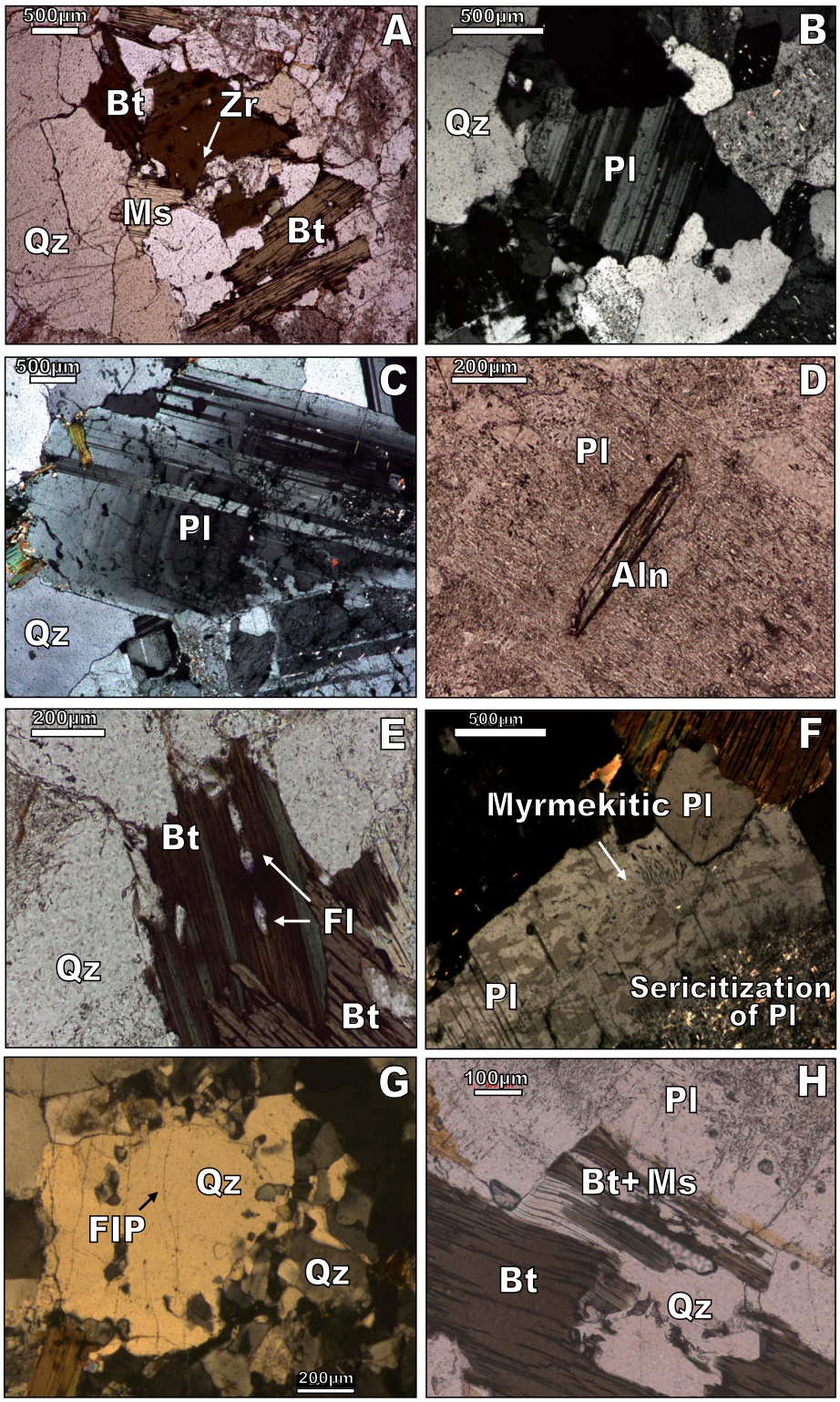


FIGURE 3. Photomicrographs of samples from the Lamas de Olo Pluton: A) Biotite and muscovite in plane-polarised light (Lamas de Olo granite); B, C) Plagioclase in crossed-polars (Barragem and Lamas de Olo granites, respectively); D) Alanite crystal on plagioclase in plane-polarised (Lamas de Olo granite); E) Biotite with brown and green colors cross-cutted by fluorite in plane-polarized (Lamas de Olo granite); F) Myrmekite texture and sericitization of plagioclase, in crossed-polars (Lamas de Olo granite); G) Microstructures in quartz, in crossed-polars (Lamas de Olo granite); H) Curved micas in plane-polarized (Lamas de Olo granite). Bt: biotite, Zr: zircon, Ms: muscovite, Qz: quartz, Pl: plagioclase, Aln: alanite, Fl: fluorite, FIP: fluid inclusion planes.

TABLE 2. Mineralogy and texture description summary for the studied granites. LOP: Lamas de Olo Pluton; VPAP: Vila Pouca de Aguiar Pluton; PGP: Peneda-Gerês Pluton; LMP: Lavadores-Madalena Pluton. According to this study data and previous studies carried out by: Sant'Ovaia *et al.* (2000) and Martins and Noronha (2006) for VPAP; Mendes and Dias (2004) and Cottard (1979) for PGP; Martins *et al.* (2011) and Sant'Ovaia *et al.* (2014) for LMP

Pluton	$^{207}Pb/^{235}U$ dating	Granite	Texture	Mineralogy
LOP	~297Ma (Fernandes *et al.*, 2013)	Lamas de Olo	Medium to coarse-grained porphyritic biotite granite	Quartz, plagioclase, K-feldspar and biotite; zircon, sphene, allanite, fluorite, hematite, magnetite, ilmenite, chlorite, rutile, apatite, goethite, epidote, tourmaline, xenotime, monazite and rare muscovite I and/or II
		Alto dos Cabeços	Fine to medium-grained porphyritic biotite granite	
		Barragem	Leucocratic fine to medium-grained and slightly porphyritic biotite granite	Quartz, plagioclase, K-feldspar and biotite; muscovite I and/or II, zircon, sphene, allanite, fluorite, hematite, ilmenite, chlorite, rutile, apatite, goethite, epidote, tourmaline, xenotime and monazite
VPAP	~297-298Ma (Martins *et al.*, 2009)	Pedras Salgadas	Porphyritic fine to medium-grained biotite monzogranite	Quartz, perthitic K-feldspar, biotite and plagioclase; zircon, apatite, allanite, xenotime, ilmenite, sphene and rare monazite
		Vila Pouca de Aguiar	Porphyritic medium to coarse-grained biotite monzogranite	Quartz, perthitic K-feldspar, biotite and plagioclase; zircon, apatite, allanite, xenotime, ilmenite and sphene
PGP	~290-296Ma (Dias *et al.*, 1998)	Gerês	Porphyritic medium to coarse-grained biotite granite	Perthitic K-feldspar, plagioclase, quartz and biotite; ilmenite, zircon, apatite, allanite, sphene, monazite and scarce hornblende
		Illa	Fine-grained two-mica monzogranite	Perthitic K-feldspar, plagioclase, quartz and biotite; muscovite I and/or II, ilmenite, zircon, apatite and monazite
		Carris	Medium to coarse-grained biotite granite	Perthitic K-feldspar, plagioclase, quartz and biotite; magnetite, ilmenite, zircon, apatite and monazite
LMP	~298Ma (Martins *et al.*, 2011)	Madalena	Porphyritic medium to coarse-grained biotite granite with porphyritic texture	Quartz, K-feldspar, plagioclase and biotite; magnetite, ilmenite, hematite, zircon, apatite, muscovite and chlorite
		Lavadores	Porphyritic coarse-grained biotite granite	Quartz, plagioclase, perthitic K-feldspar and biotite; magnetite, ilmenite, hematite, zircon, sphene, apatite, allanite and amphibole

of quartz, perthitic K-feldspar (orthoclase and microcline) and plagioclase with normal zoning. The Vila Pouca de Aguiar granite contains also oligoclase-andesine and the Pedras Salgadas granite albite-oligoclase. The biotite, the only ferromagnesian phase, is more abundant in the Vila Pouca de Aguiar granite. Accessory minerals include zircon, apatite, allanite, xenotime, ilmenite, sphene and rare monazite (Martins and Noronha, 2006; Sant'Ovaia *et al.*, 2000).

The three granites of the Peneda-Gerês Pluton, the northern pluton, are similar in their mineralogy. They contain perthitic K-feldspar, sometimes as megacrystals, plagioclase (albite–oligoclase, rarely andesine), quartz, biotite, ilmenite, zircon, apatite, and monazite. Some minerals are specific to some granites: allanite, sphene, and hornblende to the Gerês granite; muscovite to the Illa granite, resulting from later muscovitization; and magnetite to the Carris granite (Cottard, 1979; Mendes and Dias, 2004).

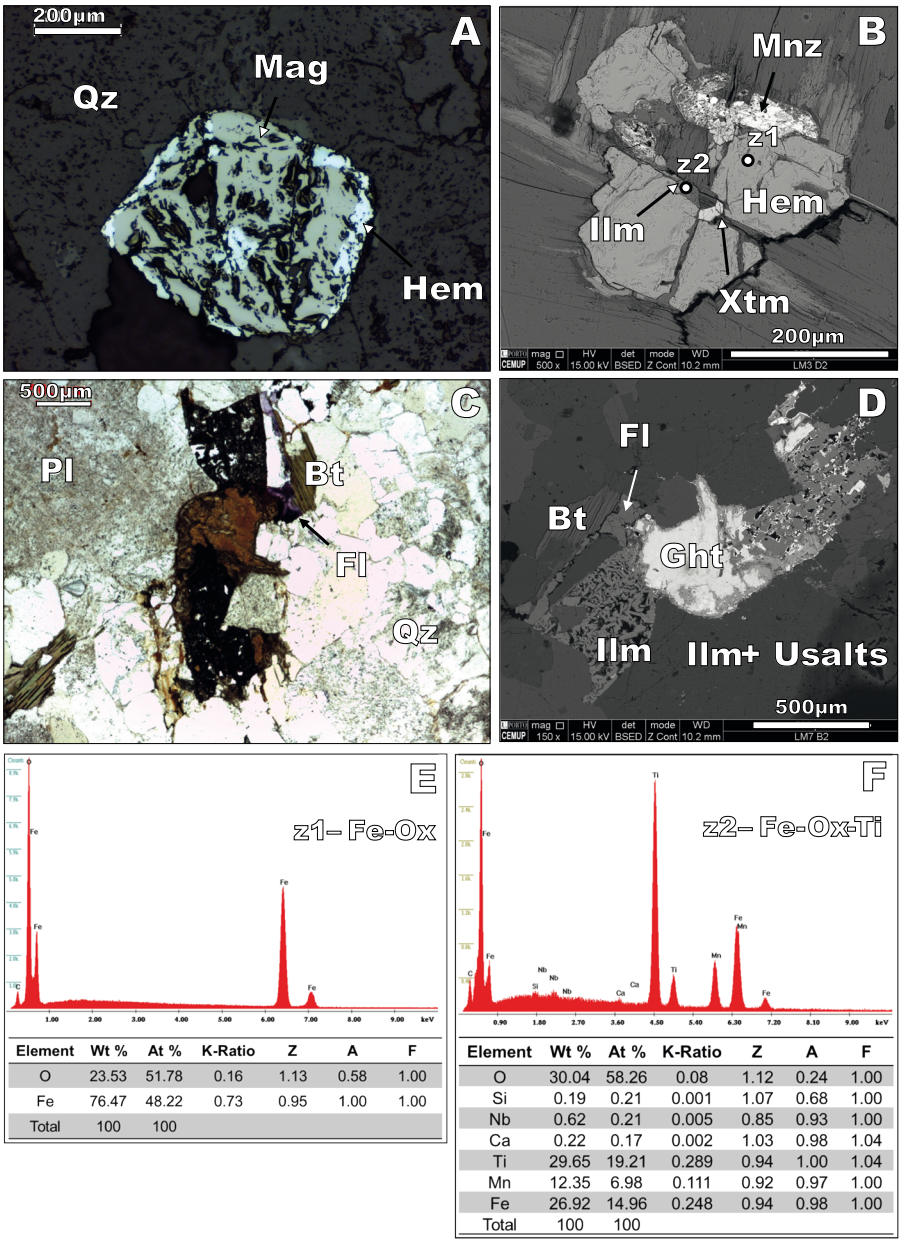
The Lavadores-Madalena Pluton is composed of two similar porphyritic, coarse-grained biotite granites. The Lavadores granite consists of quartz, plagioclase (andesine and oligoclase), perthitic K-feldspar (orthoclase and microcline), biotite, magnetite, ilmenite, hematite, zircon, sphene, apatite, allanite, and amphibole. The Madalena granite is composed of quartz, K-feldspar (orthoclase), plagioclase and biotite. Zircon, apatite, muscovite, chlorite, magnetite, ilmenite and hematite are present as accessory minerals (Martins *et al.*, 2011; Sant'Ovaia *et al.*, 2014).

Magnetic mineralogy

Magnetic susceptibility and isothermal remanent magnetization data

The magnetic susceptibility study in the post-D_3 Variscan granites showed the presence of two types of magnetic behavior : ilmenite- and magnetite-type, with the predominance of the ilmenite-type (K_m< 1,000μSI) (Table 3; Fig. 6). Previous studies in the LOP (Cruz *et al.*, 2016) indicated that: i) the K_m values in the LO granite have a huge variability (ranging from low to high K_m), ii) the AC granite has intermediate K_m values, and iii) the BA granite has the lower K_m values (Table 3). This data show that LO granite is the most heterogeneous granite of the pluton, suggesting that both ferromagnetic and paramagnetic behavior are present. On the other hand, the AC and BA granites have exclusively a paramagnetic behavior. So, the LOP is the most heterogeneous pluton, showing three K_m classes, below 50μSI, between 50μSI and 2,000μSI, and higher than 2,000μSI (Table 3; Fig. 6B). The Vila Pouca de Aguiar Pluton has minor K_m dispersion with values below 300μSI, showing a typical ilmenite-type behavior (Sant'Ovaia *et al.*, 2013a; Table 3; Fig. 6B). In the Peneda-Gerês Pluton, two granite facies are ilmenite-type and one is magnetite- and ilmenite-type. The granites from the Lavadores-Madalena Pluton have both minor K_m dispersion and the highest K_m mean values, always with K_m higher than 1,550μSI (Martins *et al.*, 2011; Sant'Ovaia *et al.*, 2014; Table 3; Fig. 6B).

The IRM data from the LOP are presented in Table 4 and Figure 7. The LM 5 sample shows saturation at



Element	Wt %	At %	K-Ratio	Z	A	F
O	23.53	51.78	0.16	1.13	0.58	1.00
Fe	76.47	48.22	0.73	0.95	1.00	1.00
Total	100	100				

Element	Wt %	At %	K-Ratio	Z	A	F
O	30.04	58.26	0.08	1.12	0.24	1.00
Si	0.19	0.21	0.001	1.07	0.68	1.00
Nb	0.62	0.21	0.005	0.85	0.93	1.00
Ca	0.22	0.17	0.002	1.03	0.98	1.04
Ti	29.65	19.21	0.289	0.94	1.00	1.04
Mn	12.35	6.98	0.111	0.92	0.97	1.00
Fe	26.92	14.96	0.248	0.94	0.98	1.00
Total	100	100				

FIGURE 4. Photomicrographs (A-D) and EDS spectra of Lamas de Olo Pluton (E-F). A) Individual grain with magnetite and hematite, in reflected and plane-polarized light (Lamas de Olo granite); B) SEM image of Fe-Ox and other minerals in minor amounts with location of the EDS spectra z1 and z2 (Lamas de Olo granite); C) A mixture of Fe-Ox minerals in transmitted and plane-polarized light (Barragem granite); D) SEM image of the same textures shown in (C); E) EDS spectrum of a Fe-Ox mineral (z1) with semi-quantitative analyse; F) EDS spectrum of a Fe-Ox-Ti mineral (z2) with semi-quantitative analyse. Mag: magnetite, Hem: hematite, Qz: quartz, Bt: biotite, Mnz: monazite, Ilm: ilmenite, Xtm: xenotime, Pl: plagioclase, Fl: fluorite, Ght: goethite, U salts: uranium salts; Fe-Ox: iron oxide; Fe-Ox-Ti: iron oxide with titanium.

fields *ca.* 338mT, suggesting the dominance of low coercive minerals, while LM 16 does not reach saturation at the maximum imparted field. The $S_{0.3T}$ for these samples is 0.999 and 0.839, respectively, confirming the magnetic heterogeneity of the LO granite, with areas of predominance of low coercive minerals and areas where ferrimagnetic minerals are scarce. The curve for sample LM 26, from the AC granite, indicates higher amounts of ferrimagnetic minerals ($S_{0.3T}$= 0.961), however does not show saturation at the applied field. The acquisition curve at *ca.* 950mT is apparently stable, however, a zoom shows a small increase in intensity with increasing fields, indicating a small amount of a high coercive mineral such as hematite. The LM 7 sample, from to the BA granite, shows some oscillations in the intensity with increasing fields due to a weak magnetic signal. However, the $S_{0.3T}$ from this sample is 0.995, suggesting the presence of low coercive minerals.

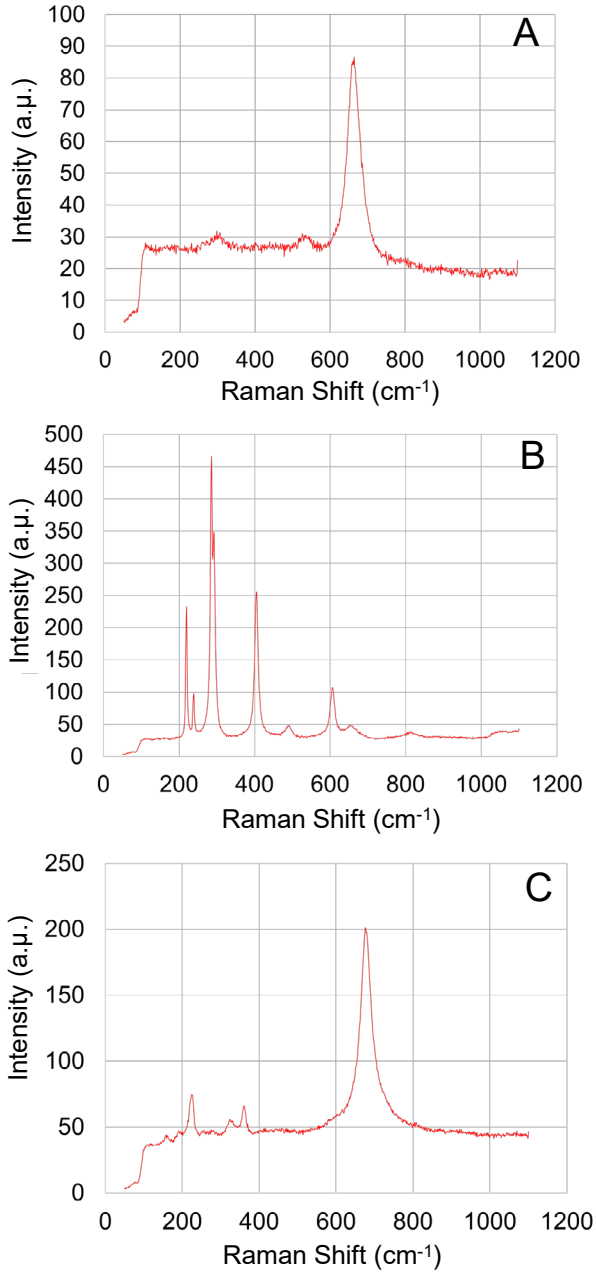


FIGURE 5. Micro-Raman spectra of Fe-Ox minerals from the Lamas de Olo Pluton: A) Magnetite; B) Hematite; C) Ilmenite.

After analising the data using the CLG function (Kruiver *et al.*, 2001; Robertson and France, 1994), best fits of the raw IRM curves are obtained by considering two or three components (Table 4; Fig. 7). All specimens have, at least two components: component 1 with low coercive phase and $B_{1/2}$ (the field at which half of the SIRM is reached) *ca.* 17mT and component 2, showing an intermediated coercive phase and $B_{1/2}$ *ca.* 59mT. Two samples show a third component, with higher coercivity with $B_{1/2}$ *ca.* 466mT.

The Dispersion Parameter (DP) ranges between 0.25 and 0.42 for all components, with mean values of 0.36, 0.31 and 0.34 for component 1, 2 and 3, respectively. According to Dunlop and Özdemir (1997), the coercivity increases with the replacement of Fe^{3+} by Ti in titanomagnetite. Taking this into account, the components 1, 2 and 3 have been interpreted as magnetite, Ti-poor magnetite and hematite, respectively (Abrajevitch and Kodama, 2011; Font *et al.*, 2014; Kruvier *et al.*, 2001; Maxbauer *et al.*, 2016; Robertson and France, 1994). Ti-poor magnetite (component 2) is dominant in all samples (contributes to more than 50% of the total remanence), with exception of LM 7 with 13% of Ti-poor magnetite and 87% of magnetite (component 1; Table 4).

According to some authors (*e.g.* Font *et al.*, 2009; Font *et al.*, 2014; Kruiver *et al.*, 2001), the differences in $B_{1/2}$ and DP values can be interpreted as: varying degrees of oxidation of magnetite for component 1; different Ti-content in the Ti-poor magnetite for component 2; and different magnetic grain sizes for component 3.

IRM studies carried out by Sant'Ovaia (1993) in the Vila Pouca de Aguiar Pluton showed that the Vila Pouca de Aguiar and Pedras Salgadas granites have similar magnetic behavior. The $S_{0.3T}$ ranges between 0.624 and 0.968, with minor values obtained in the Pedras Salgadas granite. Both granites show an absence of saturation, however, the Pedras Salgadas granite presents an acquisition curve with a high slope, showing the depletion of ilmenite (Table 4; Fig. 8). Previous studies in the Lavadores-Madalena Pluton showed saturation fields under 300mT and $S_{0.3T}$ values higher than 0.955 (Table 4; Fig. 8), pointing out high ferromagnetic mineral content (Martins *et al.*, 2011; Sant'Ovaia *et al.*, 2014).

Frequency-dependent susceptibility (KfD%) studies were made in LOP samples. In the BA granite, KfD% was higher than 10% (LM 7 ~ 35%; LM 58 ~29% and LM 62 ~30%), which have been interpreted by some authors (*e.g.* Dearing *et al.*, 1996) as due to the presence of superparamagnetic fine grains, a weak magnetic signal or a high alteration degree. On the other hand, the values acquired for the LO samples (KfD%< 2%) indicated absence of superparamagnetic grains, and for the AC samples (4% <KfD%< 7%) an admixture of superparamagnetic and coarser non-superparamagnetic grains (Dearing *et al.*, 1996). The presence of superparamagnetic minerals in samples from the BA granite could explain the lower values of the magnetic susceptibility (mean K_m ca. 27μSI) and the presence of low coercive minerals.

Thermomagnetic experiments

Figures 9 and 10 show different magnetic susceptibility-temperature curves (*Kt vs* T charts) obtained from samples

TABLE 3. Magnetic mineralogy of studied granites according to this study data and previous studies carried out by: Cruz *et al.* (2016) for LOP; Sant'Ovaia (1993) and Sant'Ovaia *et al.* (2013) for VPAP; Sant'Ovaia *et al.* (2013) for PGP; Martins *et al.* (2011) and Sant'Ovaia *et al.* (2014) for LMP. The maghemite appears between brackets because it is a neoformation mineral due to oxidation of magnetite during thermomagnetic experiments. LOP: Lamas de Olo Pluton; VPAP: Vila Pouca de Aguiar Pluton; PGP: Peneda-Gerês Pluton; LMP: Lavadores-Madalena Pluton, and associated mineralizations; N: number of sampling sites; n: number of samples; n.a.: not attributed

Pluton	Granite	Magnetic behavior	K_m(μSI)				Magnetic mineralogy		Associated mineralizations
			mean	range	N	n	Magnetic susceptibility studies and thermomagnetic experiments	Cumulative log-Gaussian analysis	
LOP	Lamas de Olo	Magnetite- and ilmenite-type	2,078	67-44,382	39	293	Ti-poor magnetite + hematite + pure magnetite + ilmenite (+ maghemite)	Ti-poor magnetite >magnetite > hematite	W-Mo
	Alto dos Cabeços	Ilmenite-type	334	125-804	4	29	Ti-poor magnetite + ilmenite + hematite + magnetite (+ maghemite)	Ti-poor magnetite > magnetite > hematite	
	Barragem	Ilmenite-type	27	21-34	5	28	Hematite + ilmenite + Ti-poor magnetite + magnetite	Magnetite > Ti-poor magnetite	
VPAP	Pedras Salgadas	Ilmenite-type	68	44-121	35	280	Hematite + ilmenite + Ti-poor magnetite	n.a	Without mineralizations
	Vila Pouca de Aguiar	Ilmenite-type	135	60-218	81	648	Hematite + ilmenite + Ti-poor magnetite	n.a	
PGP	Gerês	Magnetite- and ilmenite-type	463	46-1,000	7	7	Hematite + Ti-poor magnetite + ilmenite	n.a	W-Mo Mo W-Sn-Mo-Bi
	Illa	Ilmenite-type	81	55-109	3	3	Hematite + ilmenite + Ti-poor magnetite	n.a	
	Carris	Ilmenite-type	33	29-36	3	3	Hematite + Ti-poor magnetite + ilmenite	n.a	
LMP	Madalena	Magnetite-type	7,037	1,550-9,920	7	80	Ti-poor magnetite + ilmenite + hematite (+ maghemite)	n.a	W-Mo
	Lavadores	Magnetite-type	15,971	10,589-19,303	6	40	Magnetite + ilmenite + hematite (+ maghemite)	n.a	

of the Variscan granites. It should be noted that in the K_t *vs* T charts the susceptibility data, on the y-axes, is referred to as total or bulk susceptibility (K_t), and it is not corrected by volume or mass. These values are, therefore, quite different from the K_m values measured in the magnetic susceptibility experiments, where the K_m values are corrected for the specimen volume or mass.

The K_t *vs* T curves from selected LO granite samples show a significant fall of K_t at *ca.* 580ºC, indicating magnetite T_C (Fig. 9A). Other curves have a K_t drop just before 580ºC corresponding to a Ti-poor magnetite (Fig. 9B, C, D). Some samples have a slighter drop than the others because they have a smaller Ti-poor magnetite content (Fig. 9D). The K_t *vs* T curves from BA samples show the presence of hematite (Fig. 9E, F, G), and some traces of Ti-poor magnetite. The K_t values in the AC granite are, in general, lower than in the LO granite, but some K_t *vs* T curves show a slight drop just before 580ºC, pointing to an ilmenite-type granite, but probably with some traces of Ti-poor magnetite (Fig. 9H, I). This could be related to the circulation of post-magmatic fluids capable of changing the characteristics of the primary magnetic minerals with the formation of new, less magnetic minerals, like hematite, maghemite or goethite (Lagoeiro, 1998; Nédélec *et al.*, 2015). All the LOP curves show the presence of hematite and, in some

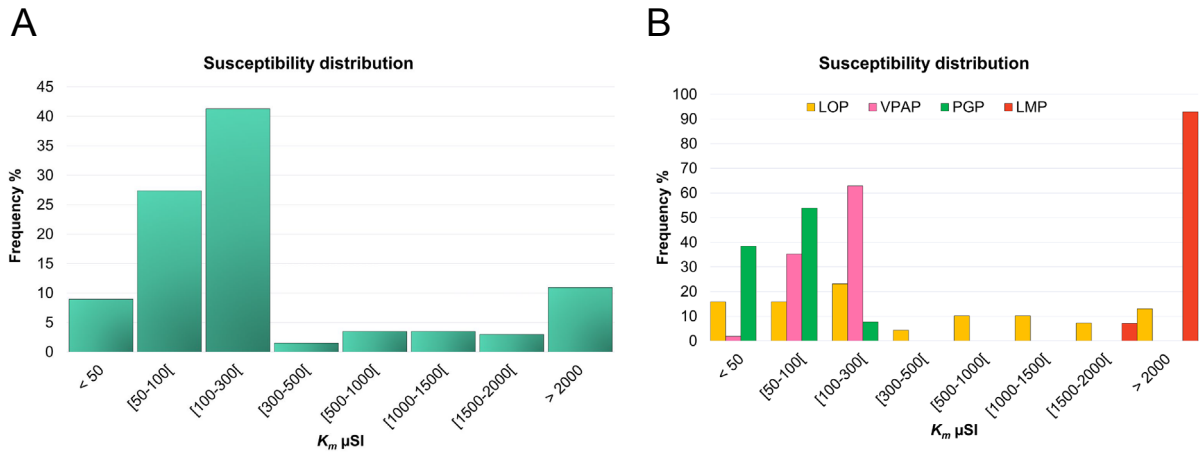


FIGURE 6. Relative frequency magnetic susceptibility histograms: A) for all the studied granites; B) for the plutons; LOP: Lamas de Olo Pluton; VPAP: Vila Pouca de Aguiar Pluton, PGP: Peneda-Gerês Pluton, LMP: Lavadores-Madalena Pluton.

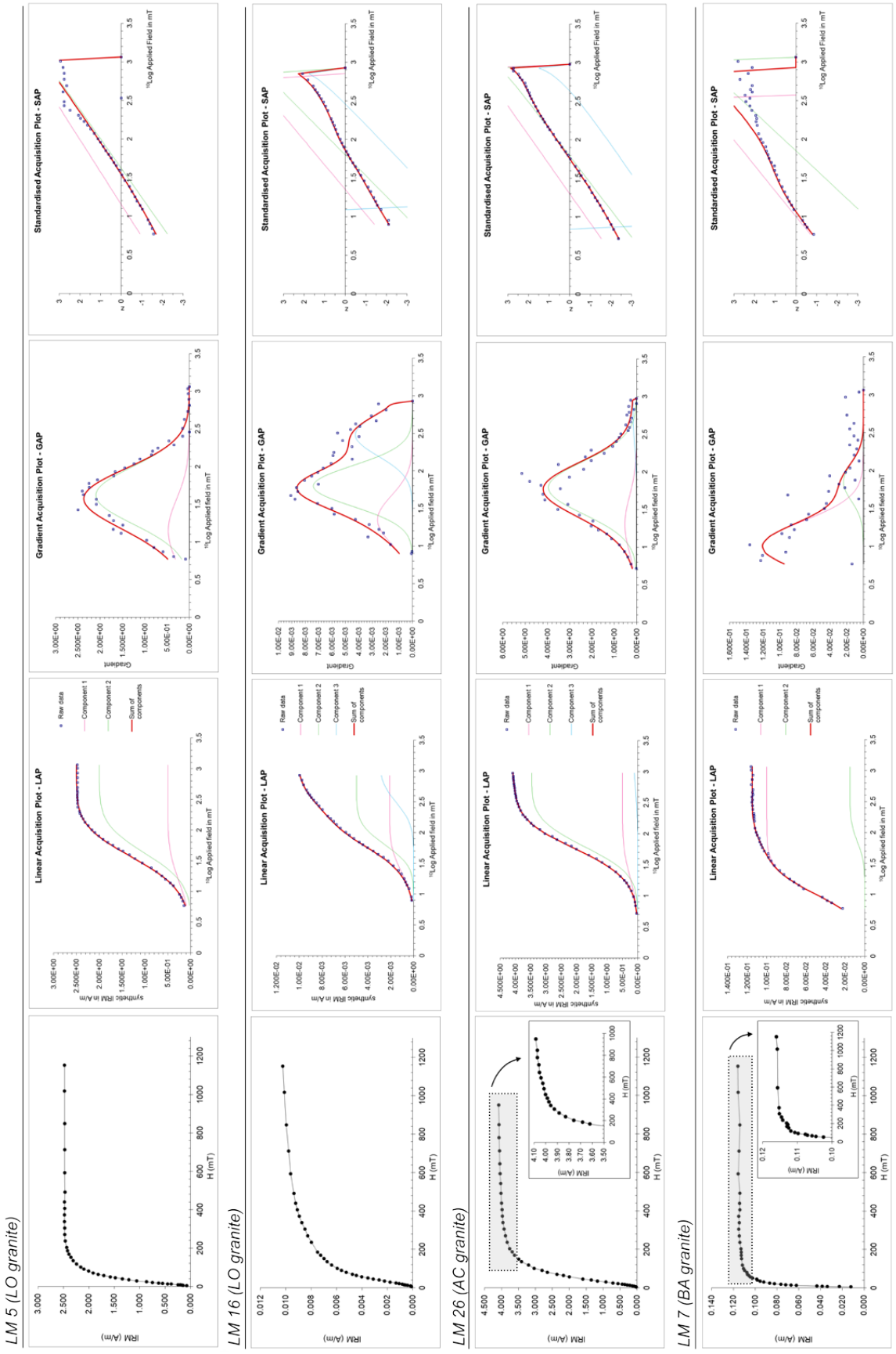


FIGURE 7. IRM acquisition curves for representative samples from the Lamas de Olo Pluton: LM 5 and LM 16 from the Lamas de Olo (LO) granite; LM 26 from the Alto dos Cabeços (AC) granite (with zoom showing the absence of saturation); LM 7 from the Barragem (BA) granite (with zoom showing the absence of saturation). Data were analyzed using a Cumulative Log-Gaussian (CLG) function using the software developed by Kruiver *et al.* (2001).

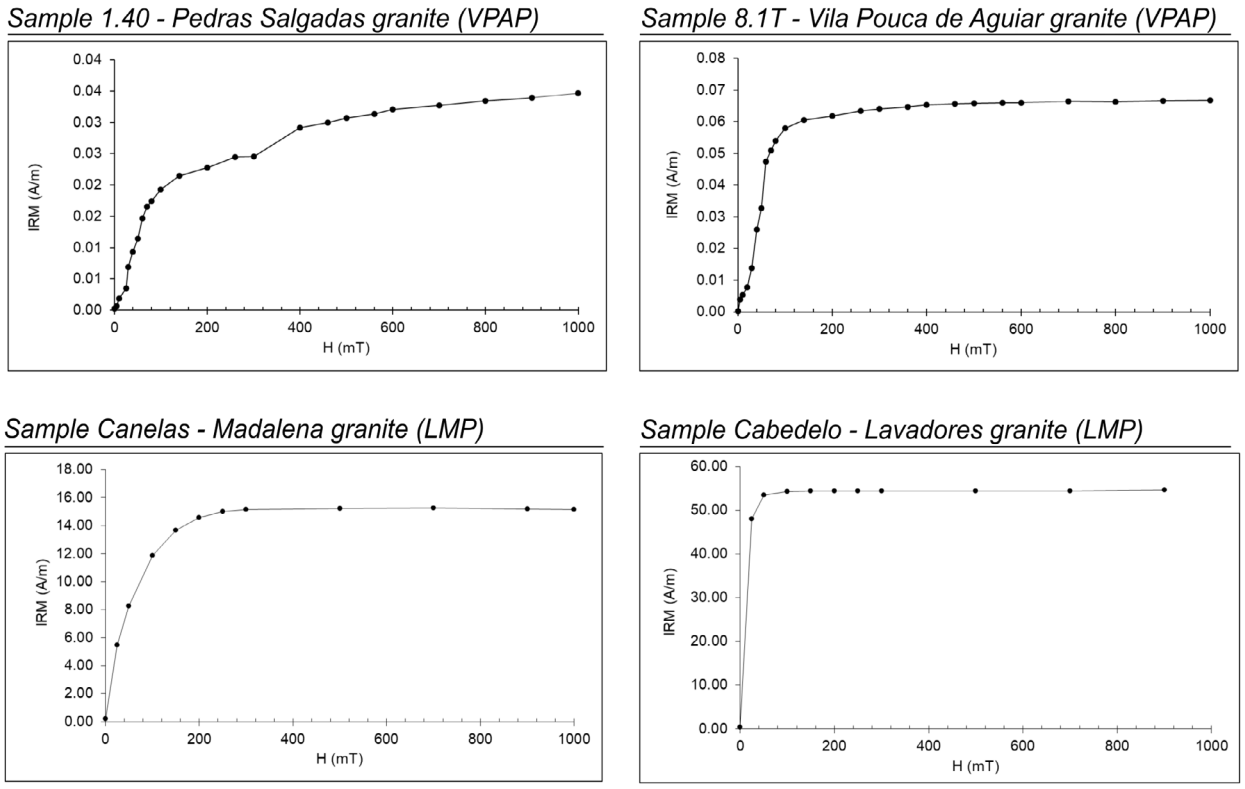


FIGURE 8. Examples of IRM acquisition curves from the Vila Pouca de Aguiar Pluton (VPAP) and the Lavadores-Madalena Pluton (LMP) from earlier studies (Martins *et al.*, 2011; Sant'Ovaia *et al.*, 1993; Sant'Ovaia *et al.*, 2014).

TABLE 4. Isothermal remanent magnetization data from the studied plutons. Vila Pouca de Aguiar Pluton (VPAP) and Lavadores-Madalena Pluton (LMP) data previously published in Sant'Ovaia (1993) and in Martins *et al.* (2011) and Sant'Ovaia *et al.* (2014), respectively. IRM_{1T}: Isothermal remanent magnetization at 1T; $IRM_{0.3T}$: isothermal remanent magnetization at 300mT. The Cumulative log-Gaussian (CLG) analysis were performed only in the LOP samples; CLG treatment allows defining for each magnetic component, %: percent contribution; SIRM: values of saturation of isothermal remanent magnetization; $B_{1/2}$: the field at which half of the SIRM is reached; DP: dispersion parameter; $S_{0.3T}$= $IRM_{0.3T}$/IRM_{1T} (Robertson and France, 1994). The CLG treatment was made using the software developed by Kruiver *et al.* (2001). n.a.: not attributed

Pluton	Granite	Sample	IRM_{1T} (A/m)	$IRM_{0.3T}$ (A/m)	$S_{0.3T}$	CLG analysis											
						Component 1 (20-40 mT)				Component 2 (50-80 mT)				Component 3 (100-250 mT)			
						%	SIRM (A/m)	$B_{1/2}$ (mT)	DP	%	SIRM (A/m)	$B_{1/2}$ (mT)	DP	%	SIRM (A/m)	$B_{1/2}$ (mT)	DP
LOP	Lamas de Olo	LM 5	2.480	2.477	0.999	20	0.50	14.13	0.42	80	2.00	41.69	0.38				
		LM 16	0.010	0.008	0.839	21	0.00	22.39	0.32	50	0.01	63.10	0.27	30	0.00	302.00	0.28
	Alto dos Cabeços	LM 26	4.086	3.925	0.961	12	0.50	19.95	0.38	84	3.47	61.66	0.35	4	0.17	630.96	0.4
	Barragem	LM 7	0.116	0.115	0.995	87	0.10	10.00	0.33	13	0.02	70.79	0.25				
VPAP	Pedras Salgadas	1.40	0.035	0.025	0.706	n.a.											
		4.2T	0.015	0.009	0.624												
	Vila Pouca de Aguiar	13.4T	0.024	0.022	0.883												
		12.20	0.021	0.019	0.881												
		8.1T	0.067	0.064	0.959												
		11.4T	0.061	0.059	0.968												
LMP	Madalena	Cavadão	13.313	13.273	0.997												
		Canelas	15.160	15.158	1.000												
		Carvalhos	53.520	52.786	0.986												
		Saúde	16.618	15.870	0.955												
		Pedroso	32.060	33.566	1.047												
	Lavadores	Cabedelo	54.621	54.435	0.997												

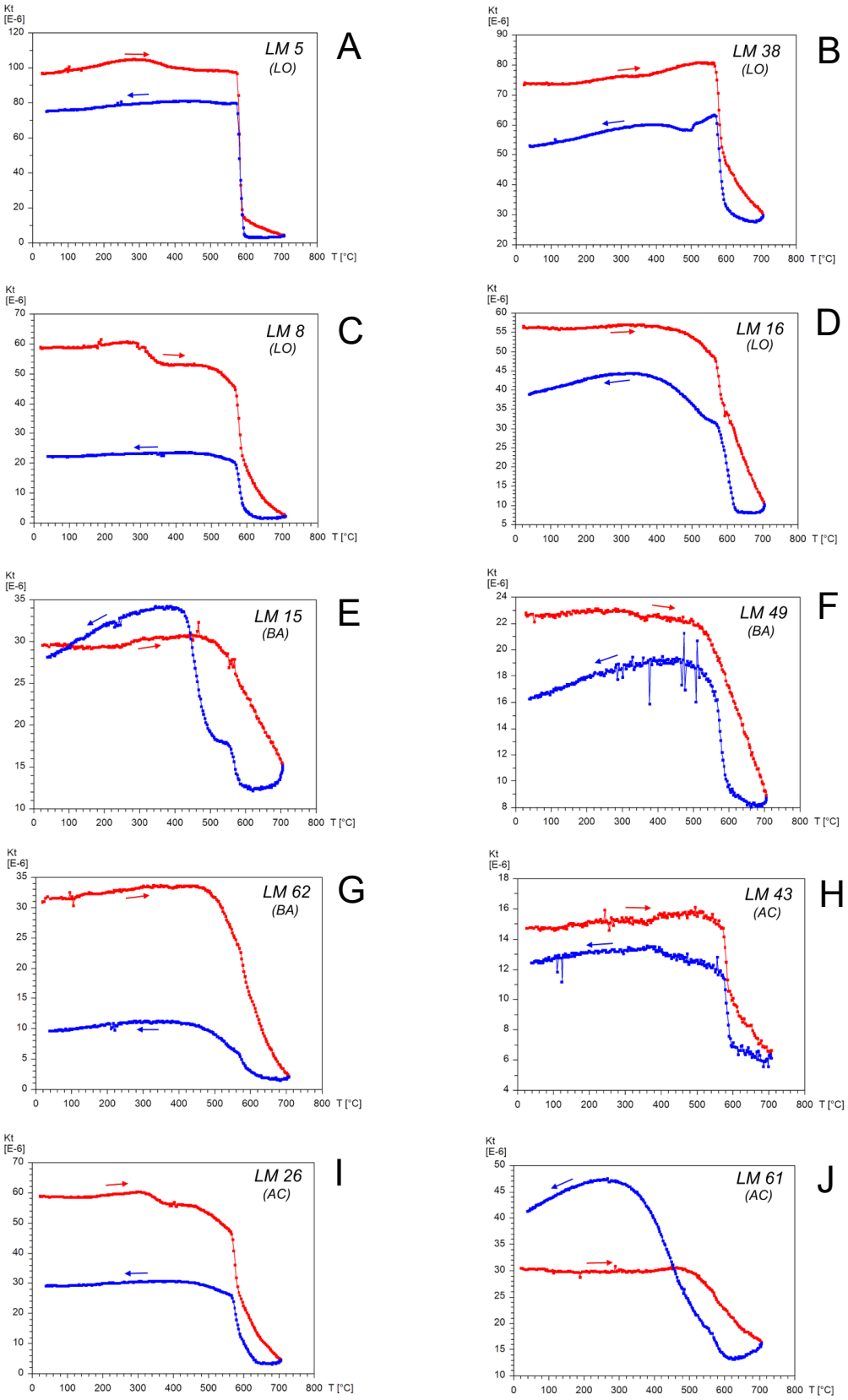


FIGURE 9. Normalized K_t *vs* T during heating (red arrow toward right) and cooling (blue arrow toward left) from representative samples of LOP granites: A-D) from the Lamas de Olo (LO) granite; E-G) from the Barragem (BA) granite; H-J) from the Alto dos Cabeços (AC) granite. Note that the y-axes are not on the same scale in all charts, so it is necessary to consider the K_t values themselves.

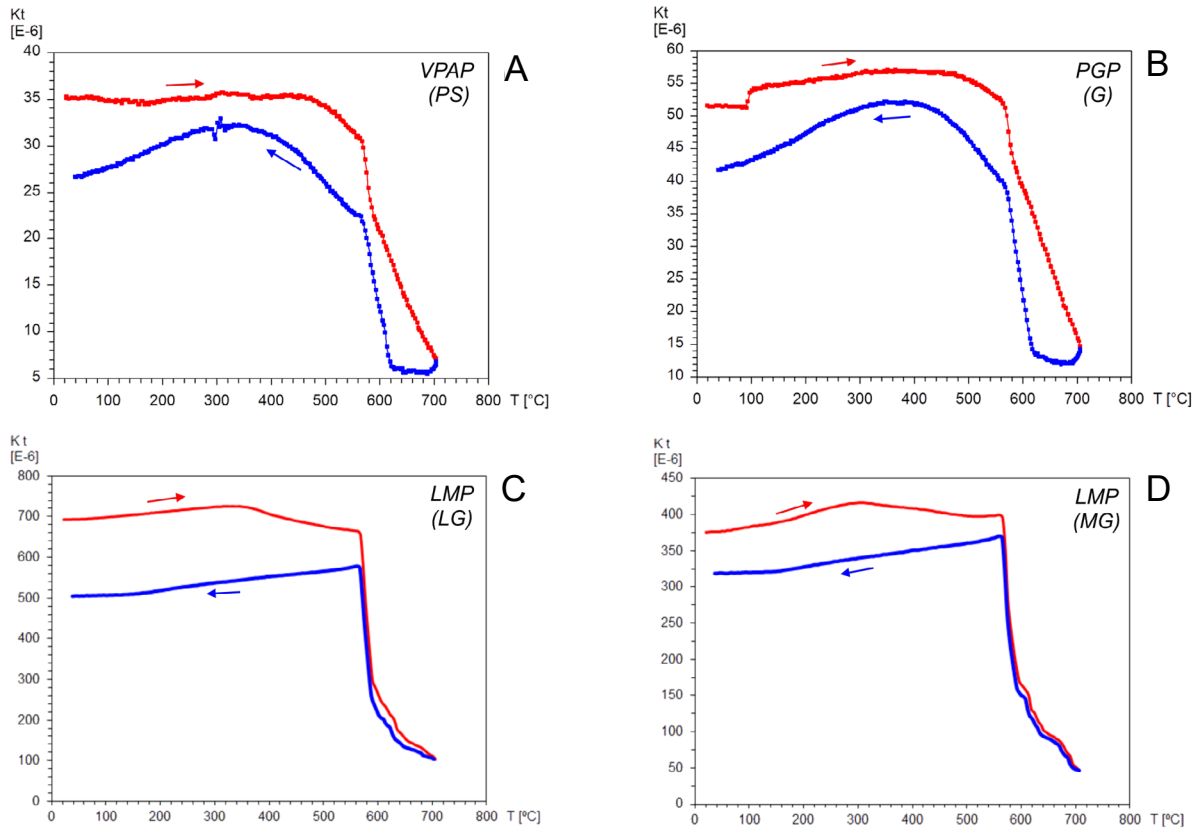


FIGURE 10. Normalized K_t *vs* T during heating (red arrow toward right) and cooling (blue arrow toward left) from Variscan granites other than the LOP granites: A) Pedras Salgadas granite from the Vila Pouca de Aguiar Pluton (VPAP-PS); B) Gerês granite from the Peneda-Gerês Pluton (PGP-G); C) Lavadores granite from the Lavadores-Madalena Pluton (LMP-LG) and D) Madalena granite from the Lavadores-Madelena Pluton (LMP-MG).

cases (Fig. 9E, J), during the cooling cycle, below 580ºC, K_t progressively increases, surpassing the values attained in the heating curve, suggesting the formation of a magnetic mineral, probably Ti-poor magnetite.

In some K_t *vs* T curves from the LO and AC granites, an inflection around 300ºC was observed on the heating curves (Fig. 9A, C, I). This inflection may correspond to pyrrhotite or to maghemite. The pyrrhotite is a ferromagnetic mineral, with T_C at *ca.* 320ºC (Butler, 1992), and is very common in granites (*e.g.* Jover *et al.*, 1989); however, the monoclinic pyrrhotite is chemically stable up to its Curie point (Dekkers, 1989), which cannot explain the disappearance of the inflection in the cooling cycling. The presence of maghemite in the analyzed samples, may be due to the oxidation of magnetite with increased furnace temperatures and the presence of oxygen in the system (Evans and Heller, 2003). Maghemite is normally destroyed before 350ºC, which could explain the inflection around 300ºC in the heating curves and its absence in the cooling cycle. For that reason, maghemite is probably the magnetic mineral responsible for the inflection at 320ºC.

The thermomagnetic behavior of other Variscan granites is quite similar to the LOP. With the exception of the Lavadores-Madalena Pluton, the thermomagnetic curves show a slight drop before 580ºC, indicating a small quantity of magnetic minerals. The K_t drops around 570ºC and 565ºC in the Vila Pouca de Aguiar Pluton (Fig. 10A) and Peneda-Gerês Pluton (Fig. 10B) samples, respectively. These values indicate the presence of Ti-poor magnetite, although Ti content in the sample from Peneda-Gerês Pluton is slightly higher (lower T_c) than the Vila Pouca de Aguiar Pluton. Regarding the Lavadores-Madalena Pluton experiments, the well-marked drop at 580ºC demonstrates the presence of magnetite and the inflection at 300ºC in the heating curve suggests the presence of maghemite in the Lavadores (Fig. 10C) and Madalena (Fig. 10D) granites. All K_t *vs* T curves also revealed the presence of hematite.

FINAL REMARKS AND CONCLUSIONS

The magnetic mineralogy studies in the Portuguese post-tectonic Variscan granites allowed to conclude that these are ilmenite- and magnetite-type-granites. Thermomagnetic curves are quite similar and show the presence of magnetite/Ti-poor magnetite and hematite in all the plutons, though in different proportions. When the magnetite content is compared, a sequence can be established: Lavadores-

Madalena>Lamas de Olo>Peneda-Gerês>Vila Pouca de Aguiar. The presence of magnetite as accessory mineral allowed inferring the generation depth of magmas.

Previous studies in the LOP granites, demonstrated the co-occurrence of ferromagnetic and paramagnetic behavior in the pluton (Cruz *et al.*, 2016). Alteration associated with the circulation of post-magmatic fluids, could explain the presence of other oxides such as Ti-poor magnetite and hematite in the granites.

The complexity of the magnetic mineralogy is not recognized in the magnetic susceptibility measurements, because this parameter only expresses the combined magnetic behavior of all minerals. For that reason, other methodologies (*e.g.* IRM, thermomagnetic curves, and frequency-dependent susceptibility) should be performed to identify magnetic minerals and their complex magnetic behaviors.

In the Vila Pouca de Aguiar Pluton, the magnetic mineralogy is simpler when compared with other plutons. Studies carried out in the Peneda-Gerês and Lavadores-Madalena plutons pointed to a complex mineralogy, with the presence of both magnetite and ilmenite mineralogy in their granites.

With the exception of the Vila Pouca de Aguiar Pluton (where mineralizations have not yet been observed), the Variscan granites have associated mineralizations. The LOP has W (Mo) mineralizations associated with the AC and LO granites (Helal, 1992; Pereira, 1989); the Peneda-Gerês Pluton has W (Sn-Mo-Bi) mineralizations associated with their granites (Cottard, 1979; Cheilletz and Giuliani, 1982; Noronha, 1984), and in the Lavadores-Madalena Pluton, W (Mo) local occurrences have been described associated with the Madalena granite (Teixeira and Perdigão, 1962).

The Lamas de Olo, Peneda-Gerês and Lavadores-Madalena plutons are all post-tectonic and composed of several granites of complex magnetic mineralogy, with magnetite/Ti-poor magnetite and ilmenite. Then we conclude that the presence of ilmenite- and magnetite-type in the same pluton, results from complex redox reactions, that occurs during the ascend and granite emplacement. The presence of magnetite pointing to a deep magma origin and oxidizing conditions in the magma chamber. This is an important metallogenic indicator of the W (Mo) mineralizations associated with post-tectonic biotite granites. Thus, the magnetic mineralogy can be a useful pathfinder for the W (Mo) mineralization exploration in the Iberian Peninsula.

The measurement of magnetic susceptibility is an unexpensive and rapid technique that can be used to characterize the magnetic behavior. The presence of magnetite and/or ilmenite allows to infer the redox condition of the granitic magma and to assess the metallogenic potential. However, the low field magnetic susceptibility measurements have some limitations when complex magnetic mineralogy is present, and for that reason, other magnetic studies should be performed.

ACKNOWLEDGMENTS

The first author was financially supported by SFRH/BD/109693/2015 (Fundação para a Ciência e Tecnologia Portugal). The authors acknowledge funding from COMPETE 2020 through the ICT (Institute of Earth Sciences) project (UID/GEO/04683/2013) with POCI-01-0145 reference-FEDER-007690 and from ESMIMET, an INTERREG Spain-Portugal POCTEP project. The authors also thank Philippe Olivier and Sonia Rousse for the thermomagnetic measurements carried out in Toulouse and their helpful comments and explanations during the advanced training in the Université de Toulouse III - Paul Sabatier. Acknowledgments are given to Alexandra Guedes for the follow-up and explanations given during the micro-Raman analyses. We thank Eric Font for the helpful guidance in paleomagnetism and explanations during the IRM and KfD% analysis carried out in the Instituto Dom Luís facilities. The authors are grateful to Emilio L. Pueyo and another anonymous referee whose comments greatly helped to improve the manuscript.

REFERENCES

Abrajevitch, A., Kodama, K., 2011. Diagenetic sensitivity of paleoenvironmental proxies: A rock magnetic study of Australian continental margin sediments. Geochemistry, geophysics, geosystems, 12, Q05Z24.

Almeida, A., Leterrier, J., Noronha, F., Bertrand, J.M., 1998. U-Pb zircon and monazite geochronology of the Hercynian two mica granite composite pluton of Cabeceiras de Basto (Northern Portugal). Comptes Rendus de l'Académie des Sciences (Paris), 326, 779-785.

Antunes, I.M.H.R., Neiva, A.M.R., Silva, M.M.V.G., Corfu, F., 2008. Geochemistry of S-type granitic rocks from the reversely zoned Castelo Branco pluton (central Portugal). Lithos, 103, 445-465.

Aranguren, A., Tubia, J., Bouchez, J.L., Vigneresse, J.L., 1996. The Guitiriz granite, Variscan belt of northern Spain: extension-controlled emplacement of magma during tectonic escape. Earth and Planetary Science Letters, 139(1-2), 165-176.

Bouchez, J.L., 1997. Granite is never isotropic: an introduction to AMS studies of granitic rocks. In: Bouchez, J.L., Hutton, D.H.W., Stephens, W.E. (eds.). Granite: From Segregation of Melt to Emplacement Fabrics. Dordrecht, Kluwer Academic Publishers, 95-112.

Bouchez, J.L., 2000. Magnetic susceptibility anisotropy and fabrics in granites. Comptes Rendus de l'Académie des Sciences de la Terre et des planets. Earth and Planetary Science, 330(1), 1-14.

Butler, R.F., 1992. Paleomagnetism: magnetic domains to geologic terranes. Blackwell Scientific Publications, 319pp.

Castiñeiras, P., Villaseca, C., Barbero, L., Martín Romera, C., 2008. SHRIMP U-Pb zircon dating of anatexis in high-grade migmatite complexes of Central Spain: implications in the Hercynian evolution of Central Iberia. International Journal of Earth Sciences, 97, 35-50.

Chadima, M., Jelinek, V., 2009. Anisoft 4.2: anisotropy data browser for windows. Advanced Geoscience Instruments Company (AGICO), Incorporated, Brno.

Chappell, B.W., White, A.J.R., 1974. Two contrasting granite types. Pacific Geology, 8, 173-174.

Cheilletz, A., Giuliani, G., 1982. Role de la Deformation du Granite dans la Genese des Episyenites Feldspathiques des Massifs de Lovios-Geres (Galice) et des Zaer (Maroc Central). Mineralium Deposita, 17(3), 387-400.

Cottard, F., 1979. Pétrologie structurale et métallogénie du Complexe Granitique de Lovios Geres. Le modèle de mise en place de la mine de Las Sombras (Sn-W-Mo-Bi) (Sud Galice — Espagne). PhD Thesis. France, Universite de Nancy I, 243pp.

Cruz, C., Sant'Ovaia, H., Noronha, F., 2016. Magnetic susceptibility and $\delta^{18}O$ characterization of Variscan granites related to W-(Mo) and Sn-(W) mineralizations: Lamas de Olo Pluton case study. Comunicações Geológicas, 103(1), 143-174.

Dallmeyer, R.D., Martínez Catalán, J.R., Arenas, R., Gil Ibarguchi, J.I., Gutiérrez Alonso, G., Farias, P., Aller, J., Bastida, F., 1997. Diachronous Variscan tectonothermal activity in the NW Iberian Massif: evidence from $^{40}Ar/^{39}Ar$ dating of regional fabrics. Tectonophysics, 277, 307-337.

Dearing, J.A., Dann, R.J.L., Hay, K., Lees, J.A., Loveland, P.J., Maher, B.A., O'Grady, K., 1996. Frequency-dependent susceptibility measurements of environmental materials. Geophysics Journal International,124, 228-240.

Dekkers, M.J., 1989. Magnetic properties of natural pyrrhotite. II. High- and low-temperature behaviour of Jrs and TRM as function of grain size. Physics of the Earth and Planetary Interiors, 57, 266-283.

Dias, G., Leterrier, J., Mendes, A., Simões, P., Bertrand, J.M., 1998. U-Pb zircon and monazite geochronology of syn- to post-tectonic Hercynian granitoids from the Central Iberian Zone (Northern Portugal). Lithos, 45, 349-369.

Dias, G., Noronha, F., Almeida, A., Simões, P.P., Martins, H.C.B., Ferreira, N., 2010. Geocronologia e petrogénese do plutonismo tardi-Varisco (NW de Portugal): síntese e inferências sobre o processo de acreção e reciclagem crustal na Zona Centro-Ibérica. In: Cotelo Neiva, J.M., Ribeiro, A., Victor, M., Noronha, F., Ramalho, M. (eds.). Geologia Clássica, Volume I - Ciências Geológicas: Ensino, Investigação e sua História. Geologia Clássica, Lisboa, Escolar Editora, 143-160.

Díez Fernández, R., Arenas, R., Pereira, M.F., Sánchez Martínez, S., Albert, R., Martín Parra, L.M., Rubio Pascual, F.J., Matas, J., 2016. Tectonic evolution of Variscan Iberia: gondwana–Laurussia collision revisited. Earth Science Reviewer, 162, 269-292.

Dunlop, D.J., Özdemir, Ö., 1997. Rock magnetism: fundamentals and frontiers. Cambridge, Cambridge University Press, 573pp.

Ellwood, B.B., Wenner, D.B., 1981. Correlation of magnetic susceptibility with 18O/16O data in late orogenic granites of the southern Appalachian Piedmont. Earth Planetary Science Letters, 54, 200-202.

Evans, M.E., Heller, F., 2003. Environmental Magnetism: Principles and Applications of Enviromagnetics. San Diego (California), Academic Press, 304pp.

Farias, P., Gallastegui, G., González Lodeiro, L., Marquínez, J., Martín Parra, L.M., Martínez Catalán, J.R., Pablo Maciá, J.G., Rodríguez Fernández, L.R., 1987. Aportaciones al conocimiento de la litoestratigrafia y estructura de Galicia Central. IX Reunião sobre a geologia do oeste peninsular, Museu e Laboratório Mineralógico e Geológico da Faculdade de Ciências da Universidade do Porto, 1 (Memórias), 411-431.

Fernandes, S., Gomes, M., Teixeira, R., Corfu, F., 2013. Geochemistry of biotite granites from the Lamas de Olo Pluton, northern Portugal. Geophysical Research Abstracts, EGU General Assembly, 15, 1pp.

Ferreira, N., Iglesias, M., Noronha, F., Pereira, E., Ribeiro, A., Ribeiro, M.L., 1987. Granitóides da Zona Centro Ibérica e seu enquadramento geodinâmico. In: Bea, F., Carnicero, A., Gonzalo, J.C., López Plaza, M., Rodriguez Alonso, M.D. (eds.). Geologia de los granitoides y rocas asociadas del Macizo Hespérico. Madrid, Rueda, 37-51.

Font, E., Ernesto, M., Silva, P.F., Correia, P.B., Nascimento, M.A.L., 2009. Palaeomagnetism, rock magnetism and AMS of the Cabo Magmatic Province, NE Brazil, and the opening of South Atlantic. Geophysical Journal International, 179, 905-922.

Font, E., Veiga-Pires, C., Pozo, M., Carvalho, C., Neto, A.C.S., Camps, P., Fabre, S., Mirão, J., 2014. Magnetic fingerprint of southern Portuguese speleothems and implications for paleomagnetism and environmental magnetism. Journal of Geophysical Research Solid Earth, 119, 7993-8020.

Franke, W., 1989. Variscan plate tectonics in Central Europe – current ideas and open questions. Tectonophysics, 169, 221-228.

Gutiérrez-Alonso, G., Johnston, S.T., Weil, A.B., Pastor-Galán, D., Fernández-Suárez, J., 2012. Buckling an orogen: The Cantabrian Orocline. Geological Society of America Today, 22(7), 4-9.

Helal, B., 1992. Granitoïdes, granites à métaux rares et hydrothermalisme associe: géologie, minéralogie et géochimie de plusieurs suites tardi-hercyniennes (Nord du Portugal). Ph.D. Thesis. France, Ecole Nacionale Superieure des Mines de Saint-Etienne, 508pp.

Ishihara, S., 1977. The Magnetite-series and Ilmenite-series Granitic Rocks. Mining Geology, 27, 292-305.

Ishihara, S., Lee, D.S., Kim, S.Y., 1981. Comparative study of Mesozoic granitoids and related W-Mo mineralization in Southern Korea and Southwestern Japan. Mining Geology, 31(4), 311-320.

Jover, O., Rochette, P., Lorand, J.P., Maeder, M., Bouchez, J.L., 1989. Magnetic mineralogy of some granites from the French Massif Central: origin of their low-field susceptibility. Physics of the Earth and Planetary Interiors, 55, 79-92.

Julivert, M., Fontboté, J.M., Ribeiro, A., Conde, L., 1974. Mapa tectónico de la península Ibérica y Baleares a escala 1:1.000.000 y memoria explicativa. Instituto Geologico y Mineiro de España, 113pp.

Kroner, U., Romer, R.L., 2013. Two plates – many subduction zones: The Variscan orogeny reconsidered.Gondwana Research, 24, 298-329.

Kruiver, P., Dekkers, M., Heslop, D., 2001. Quantification of magnetic coercivity components by the analysis of acquisition curves of isothermal remanent magnetisation. Earth and Planetary Science Letters, 189(3-4), 269-276.

Kumar, S., 2010. Magnetite and ilmenite series granitoids of Ladakh batholith, Northwest Indian Himalaya: implications on redox conditions of subduction zone magmatism. Current Science, 99(9), 1260-1264.

Lagoeiro, L.E., 1998. Transformation of magnetite to hematite and its influence on the dissolution of iron oxide minerals. Journal of Metamorphic Geology, 16, 415-423.

Marques, F.O., Mateus, A., Tassinari, C., 2002. The Late-Variscan fault network in central–northern Portugal (NW Iberia): a re-evaluation. Tectonophysics, 359(3-4), 255-270.

Martínez Catalán, J.R., Rubio Pascual, F.J., Díez Montes, A., Díez Fernández, R., Gómez Barreiro, J., Dias da Silva, Í., González Clavijo, E., Ayarza, P., Alcock, J.E., 2014. The late Variscan HT/LP metamorphic event in NW and Central Iberia: relationships to crustal thickening, extension, orocline development and crustal evolution. London, The Geological Society, 405 (Special Publications), 225-247.

Martins, H.C.B., Noronha, F., 2006. Late variscan granite pluton of Vila Pouca de Aguiar (Northern Portugal): an example of low $^{87}Sr/^{86}Sr$ felsic granites. Goldschmidt Conference Abstracts, 395.

Martins, H.C.B., Sant'Ovaia, H., Noronha, F., 2009. Genesis and emplacement of felsic Variscan plutons within a deep crustal lineation, the Penacova-Régua-Verín fault: An integrated geophysics and geochemical study (NW Iberian Peninsula). Lithos, 111, 142-155.

Martins, H.C.B., Sant'Ovaia, H., Abreu, J., Oliveira, M., Noronha, F., 2011. Emplacement of Lavadores granite (NW Portugal): U/Pb and AMS results. Comptes Rendus Geocience, 343, 387-396.

Mateus, A., Noronha, F., 2010. Sistemas mineralizantes epigenéticos na Zona Centro-Ibérica; expressão da estruturação orogénica Meso- a Tardi-Varisca. In: Cotelo Neiva, J.M., Ribeiro, A., Victor, M., Noronha, F., Ramalho, M. (eds.). Geologia Clássica, Volume II - Ciências Geológicas: Ensino, Investigação e sua História. Geologia Aplicada, Lisboa, Escolar Editora, 143-160.

Maulana, A., Watanabe, K., Imai, A., Yonezu, K., 2013. Origin of magnetite- and ilmentite-series granitic rocks in Sulawesi, Indonesia: magma genesis and regional metallogenic constrains. Earth and Planetary Sciences, 6, 50-57.

Maxbauer, D.P., Feinberg, J.M., Fox, D.L., 2016. MAX UnMix: A web application for unmixing magnetic coercivity distributions. Computers & Geosciences, 95, 140-145.

Mendes, A.C., Dias, G., 2004. Mantle-like Sr–Nd isotope composition of Fe–K subalkaline granites: the Peneda–Gerês Variscan massif (NW Iberian Peninsula). Terra Nova, 16, 109-115.

Nédélec, A., Trindade, R., Peschler, A., Archanjo, C., Macouin, M., Poitrasson, F., Bouchez, J.L., 2015. Hydrothermally-induced changes in mineralogy and magnetic properties of oxidized A-type granites. Lithos, 212(215), 145-157.

Noronha, F., Ramos, J.M.F., Rebelo, J., Ribeiro, A., Ribeiro, M.L., 1981. Essai de corrélation des phases de déformation hercyniennes dans le NW de la péninsule Ibérique. Leidse Geologische Mededelingen, 52(1), 87-91.

Noronha, F., 1984. Mineralizações espacial e geneticamente associadas ao maciço granítico da Serra do Gerês. Cuadernos do Laboratorio Xeolóxico de Laxe, 7, 87-99.

Noronha, F., Ferreira, N., Marques De Sá, C., 2006. Rochas granitóides: caracterização petrológica e geoquímica. In: Pereira, E. (coord.). Carta Geológica de Portugal. Notícia explicativa da folha 2, Lisboa, Instituto Geológoco Mineiro (IGM)/Instituto Nacional de Engenharia, Tecnologia e Inovação (INETI), 49-68.

Noronha, F., Ribeiro, M.A., Almeida, A., Dória, A., Guedes, A., Lima, A., Martins, H.C.B., Sant'Ovaia, H., Nogueira, P., Martins, T., Ramos, R., Vieira, R., 2013. Jazigos filonianos hidrotermais e aplitopegmatíticos espacialmente associados a granitos (norte de Portugal). In: Dias, R., Araújo, A., Terrinha, P., Kullberg, J.C. (eds.). Geologia de Portugal. Lisboa, Escolar Editora, Vol. I, 403-438.

Noronha, F., 2017. Fluids and Variscan metallogenesis in granite related systems in Portugal. Procedia Earth and Planetary Science, 17, 1-4.

Olivia-Urcia, B., Pueyo, E.L., 2012. Gradient of shortening and vertical-axis rotations in the Southern Pyrenees (Spain), insights from a synthesis of paleomagnetic data. Revista de la Sociedad Geológica de España, 20(1-2), 105-118.

Pastor-Galán, D., Gutierrez-Alonso, G., Zulauf, G., Zanella, F., 2012. Analogue modeling of lithospheric-scale orocline buckling: Constraints on the evolution of the Iberian-Armorican Arc. Geological Society of America Bulletin, 124, 1293-1309.

Pereira, E., Silva, N., Moreira, A., Ribeiro, A., 1987. Folha 10-A Celorico de Basto da Carta Geológica de Portugal na escala 1/50 000. Serviços Geológicos de Portugal.

Pereira, E., 1989. Carta Geológica de Portugal à escala 1:50 000, Notícia Explicativa da Folha 10-A (Celorico de Basto). Lisboa, Serviços Geológicos de Portugal, 53pp.

Pereira, M.F., Díez Fernández, R., Gama, C., Hofmann, M., Gärtner, A., Linnemann, U., 2018. S-type granite generation and emplacement during a regional switch from extensional to contractional deformation (Central Iberian Zone, Iberian autochthonous domain, Variscan Orogeny). International Journal of Earth Sciences, 107, 251-267.

Porquet, M., Pueyo, E.L., Róman-Berdiel, T., Olivier, P., Longares, L.A., Cuevas, J., Ramajo, J., Geokin3DPyr working group.,

2017. Anisotropy of magnetic susceptibility of the Pyrenean granites. Journal of Maps, 13(2), 438-448.

Ribeiro, A., Pereira, E., Dias, R., 1990. Structure of the Northwest of the Iberian Peninsula. In: Dallmeyer, D., Martinez Garcia, E. (eds.). Pre-Mesozoic Geology of Iberia. Berlin, Springer, 220-236.

Robertson, D., France, D., 1994, Discrimination of remanence-carrying minerals in mixtures, using isothermal remanent magnetization acquisition curves. Physics of Earth and Planetary Interiors, 82(3-4), 223-234.

Rochette, P., 1987. Magnetic susceptibility of the rock matrix related to magnetic fabric studies. Journal of Structural Geology, 9(8), 1015-1020.

Román-Berdiel, T., Pueyo-Morer, E.L., Casas-Sainz, A.M., 1995. Granite emplacement during contemporary shortening and normal faulting: structural and magnetic study of the Veiga Massif (NW Spain). Journal of Structural Geology, 17(12), 1689-1706.

Sant'Ovaia, H., 1993. Características magnéticas dos granitóides biotíticos pós-tectónicos de Vila Pouca de Aguiar. Provas de Aptidão Pedagógica e Capacidade Científica. Universidade do Porto, unpublished, 130pp.

Sant'Ovaia, H., Bouchez, J.L., Noronha, F., Leblanc, D., Vigneresse, J.L., 2000. Composite-laccolith emplacement of the post-tectonic Vila Pouca de Aguiar granite pluton (northern Portugal): a combined AMS and gravity study. Transactions of the Royal Society of Edinburgh Earth Sciences, 91, 123-137.

Sant'Ovaia, H., Martins, H.C.B., Lopes, J.C., Machado, J., Noronha, F., 2012. Correlation of magnetic susceptibility with $\delta^{18}O$ data in magnetite- and ilmenite-type granites from Iberian massif. Mineralogical Magazine, 76(6), 23-25.

Sant'Ovaia, H., Martins, H.C.B., Noronha, F., 2013a. Oxidized and reduced Portuguese Variscan granites associated with W and Sn hydrothermal lode deposits: magnetic susceptibility results. Comunicações Geológicas, 100(1), 33-39.

Sant'Ovaia, H., Martins, H.C.B., Noronha, F., 2013b. Magnetic susceptibility and $\delta^{18}O$ characterization of granites related with W, Sn, Mo and Bi (Au) hydrothermal vein deposits. Mineralogical Magazine, 77(5), 2130-2130.

Sant'Ovaia, H., Ribeiro, M.A., Martins, H.C.B., Ferrão, F., Gomes, C., Noronha, F., 2014. Estruturas e fabric magnético no maciço granítico de Lavadores-Madalena. Comunicações Geológicas, 101(1), 313-317.

Shaw, J., Johnston, S.T., Gutiérrez-Alonso, G., Weil, A.B., 2012. Oroclines of the Variscan orogen of Iberia: Paleocurrent analysis and paleogeographic implications. Earth and Planetary Science Letters, 329-330, 60-70.

Sheppard, S.M.F., 1977. Identification of the origin of ore forming solutions by the use of stable isotopes. London, Volcanic Processes in Ore Genesis. Institution of Mining and Metallurgy and Geological Society, 254pp.

Takagi, T., Tsukimura, M., 1997. Genesis of oxidized- and reduced-type granites. Economic Geology, 92, 81-86.

Tarling, D.H., Hrouda, F., 1993. The magnetic anisotropy of rocks. London, Chapman & Hall, 217pp.

Teixeira, C., Perdigão, J., 1962. Folha 13-A Espinho da Carta Geológica de Portugal na escala 1/50 000. Serviços Geológicos de Portugal.

Teixeira, R.J.S., Neiva, A.M.R., Gomes, M.E.P., Corfu, F., Cuesta, A., Croudace, I.W., 2012. The role of fractional crystallization in the genesis of early syn-D3, tin-mineralized Variscan two-mica granites from the Carrazeda de Ansiães area, northern Portugal. Lithos, 153, 177-191.

Thadeu, D., 1965. Carta Mineira de Portugal, Notícia explicativa. Lisboa, Serviços Geológicos de Portugal, 46pp.

Villaseca, C., Ruiz-Martínez, V.C., Pérez-Soba, C., 2017. Magnetic susceptibility of Variscan granite-types of the Spanish Central System and the redox state of magma. Geologica Acta, 15(4), 379-394.

Weil, A., Gutiérrez-Alonso, G., Johnston, S.T., Pastor-Galán, D., 2013. Kinematic constraints on buckling a lithospheric-scale orocline along the northern margin of Gondwana: a geologic synthesis. Tectonophysics, 582, 25-49.

Manuscript received March 2019;
revision accepted Desember 2019;
published Online March 2020.

Integração de dados de anisotropia da suscetibilidade magnética e de gravimetria para determinação da geometria e modelo de instalação do Plutão de Lamas de Olo

Cruz, Cláudia[1*]; Sant'Ovaia, Helena[1]; Lourenço, Martinho[2]; Almeida, Fernando[3]; Noronha, Fernando[1]
[1] Departamento de Geociências Ambiente e Ordenamento do Território - Faculdade de Ciências, Universidade do Porto; Instituto de Ciências da Terra - Polo Porto
[2] Departamento de Geologia - Universidade de Trás-os-Montes e Alto Douro
[3] Departamento de Geociências - Universidade de Aveiro
*autor correspondente: claudiacruz@fc.up.pt

Resumo

O presente estudo, pretende realizar uma primeira aproximação à geometria e modelo de instalação do Plutão de Lamas de Olo (PLO), utilizando para tal dados de anisotropia da suscetibilidade magnética (ASM) e combinando-os com dados gravimétricos, mais concretamente com os dados relativos ao mapa de anomalia residual.

A integração de dados estruturais e geofísicos permite inferir sobre a geometria dos granitos em profundidade, assim como sobre os seus modelos de instalação. Vários autores têm vindo a utilizar dados de ASM, nomeadamente de lineações e foliações magnéticas, que fornecem informação de caracter estrutural, combinando-os com dados gravimétricos, obtendo, assim, informações sobre a geometria, canais de alimentação e instalação de vários granitos Variscos (*e.g.* Vigneresse, 1995; Améglio et al., 1997; Sant'Ovaia et al., 2000).

O PLO localiza-se na Zona Centro Ibérica, no norte de Portugal, e é um plutão compósito constituído por diversos granitos pós-tectónicos, essencialmente biotíticos (fig. 1): Lamas de Olo (LO), Barragem (BA) e Alto dos Cabeços (AC) (Pereira, 1989; Helal, 1992; Fernandes et al., 2013). Este plutão aflora com forma rômbica numa pequena área, tendo a sua instalação sido controlada por um sistema de falhas NNW-SSE conjugadas com falhas NNE-SSW, sendo estas paralelas ao sistema NNE-SSW representado pela falha Verin-Régua-Penacova. O PLO é intrusivo em litologias diversas, de diferentes idades: quartzitos e xistos do Ordovícico, metassedimentos do Grupo do Douro do Câmbrico inferior e granitos variscos sintectónicos de duas micas do Maciço compósito de Vila Real (Pereira, 1989). Cruz et al. (2016) realizaram estudos de ASM e descrevem para o PLO a coexistência de granitos de diferentes tipos, "ilmenite-type" e "magnetite-type". Os valores de suscetibilidade magnética (K_m) variam entre $21 \cdot 10^{-6}$ SI e $44\,382 \cdot 10^{-6}$ SI, estando os valores mais elevados concentrados numa faixa central de orientação E-W e no sector SE do PLO.

Relativamente ao *fabric* magnético do PLO, verifica-se que (fig. 1):

- lineações magnéticas possuem direções distintas, embora evidenciando uma tendência NNW-SSE, maioritariamente sub-horizontais nos granitos LO e BA e subverticais em AC (fig. 1A);
- foliações magnéticas são maioritariamente subverticais e com orientação geral NNW-SSW no PLO, com uma atitude média N168°; 88° NE (fig. 1B).

De forma a se conseguir determinar a geometria do PLO em profundidade, assim como inferir sobre o modelo de instalação, realizaram-se estudos gravimétricos. O método gravimétrico permite investigar as estruturas geológicas em profundidade, através da medição das variações do campo gravítico terrestre.

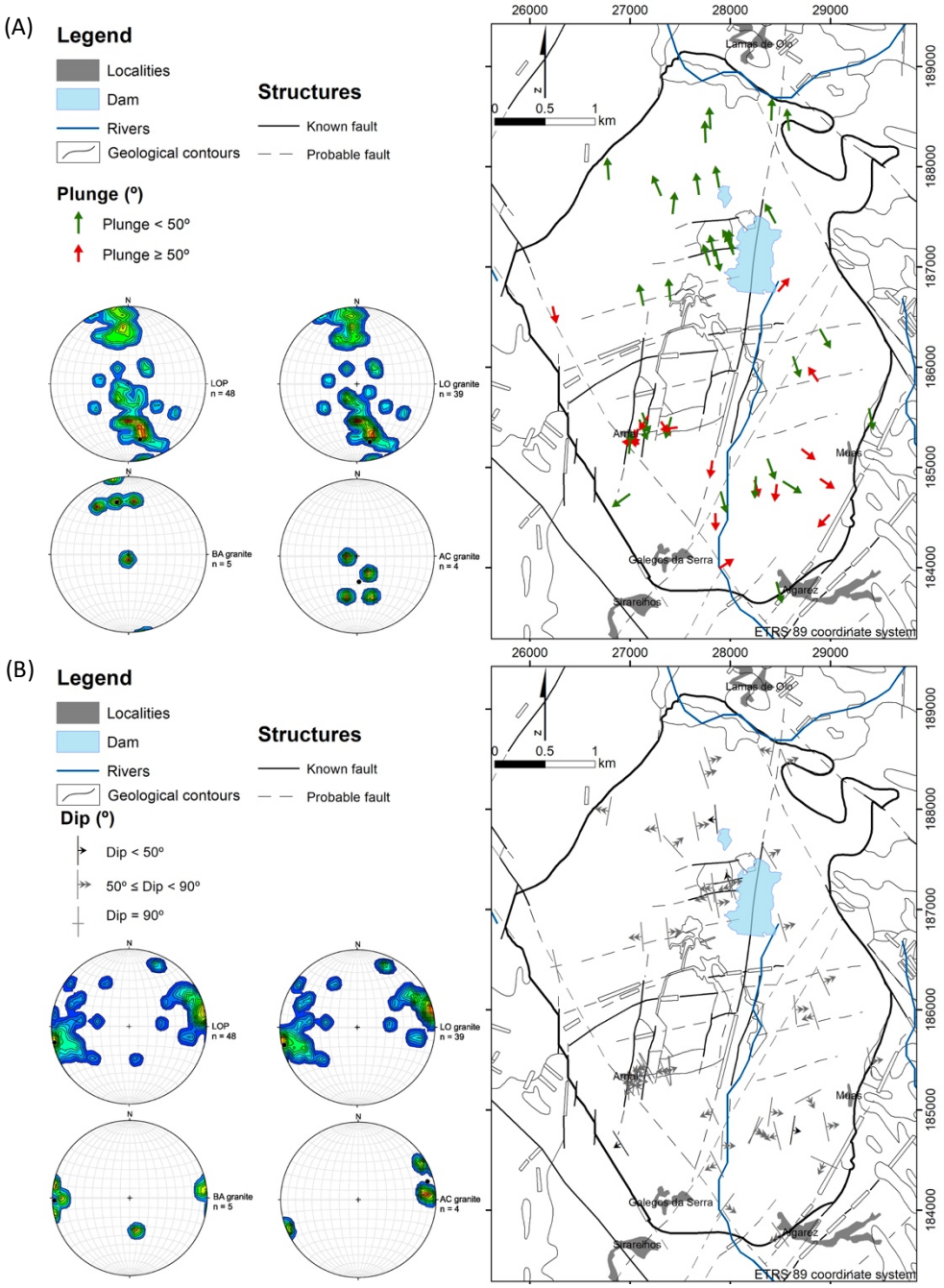


Figura 2.- *Fabric* magnético: (A) Lineações magnéticas com estereogramas das lineações magnéticas (projeção de Schmidt, hemisfério inferior, 1-5% área); (B) Foliações magnéticas com estereogramas dos polos das foliações magnéticas (projeção de Schmidt, hemisfério inferior, 1-5% área).

As variações horizontais e verticais do campo gravítico são provocadas por diferenças de densidade das rochas e permitem identificar perturbações do campo gravítico, designadas por anomalias de gravidade, que estão associadas a uma ampla variedade de situações geológicas. Como tal, as campanhas gravimétricas constituem uma forma eficiente de identificar descontinuidades (falhas e contactos geológicos), estabelecer a geometria e a profundidade de corpos de rochas intrusivas e inferir sobre a sua zona de raiz (Lowrie, 2007). O levantamento dos dados gravimétricos, foi realizado segundo 3 perfis de orientações aproximadas de NNE-SSW, WSW-ENE e NNW-SSE (os dois primeiros paralelos aos sistemas principais de fraturas e o terceiro paralelo ao alinhamento sin-D_3 regional *ca*. N120º), utilizando-se um gravímetro *Lacoste*

& Romberg G1054. No total realizaram-se medições em 271 estações gravimétricas, sensivelmente espaçadas de 100 m no interior do PLO e com maior espaçamento nas litologias encaixantes. Os perfis foram realizados até cerca de 5 km para além dos limites do afloramento do PLO, onde as estações ficaram espaçadas de 200 m, com exceção das últimas 6 que foram realizadas com um espaçamento de 400 m. Para a determinação do mapa da anomalia de *Bouguer*, utilizou-se uma densidade de 2,66. Esta densidade média foi calculada por métodos indiretos, através do método de Nettleton (1939). A separação da anomalia regional de 1ª, 2ª e 3ª ordem, foram realizadas através do *software Oasis Montaj*, obtendo, assim, diferentes mapas da anomalia residual (Anomalia Residual = Anomalia de *Bouguer* - Anomalia Regional) (Lowrie, 2007). Analisando os mapas obtidos conjuntamente com informações geológicas (contactos geológicos, forma do afloramento do PLO, falhas da região) verificou-se que o modelo que melhor se ajusta à superfície da anomalia de *Bouguer*, foi o obtido através de uma superfície polinomial de 3ª ordem (fig. 2). A escolha deste mapa deve-se essencialmente ao facto de:

- a linha zero da anomalia residual ser a que melhor se ajusta aos contornos do PLO, com exceção do bordo W;
- a forma da anomalia junto ao PLO, parece ajustar-se segundo as falhas existentes na região, nomeadamente as *ca.* N150° a N170° e *ca.* N10° a N20°.

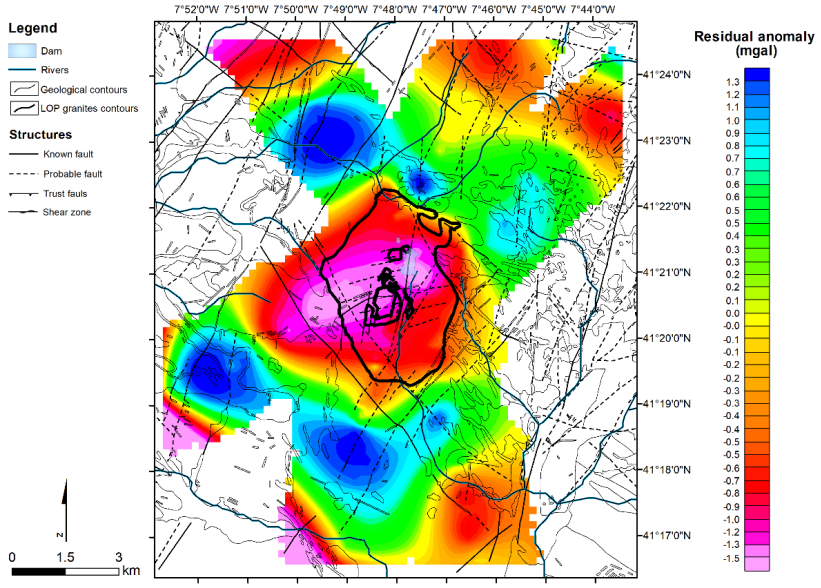


Figura 2.- Mapa da anomalia residual realizado através do *Oasis Montaj*, utilizando o método de interpolação *krigging*.

A compilação de dados estruturais e de dados geofísicos permite inferir sobre a geometria e modelo de instalação do PLO. Assim, pode concluir-se que:

- o estudo gravimétrico, nomeadamente a existência de uma anomalia residual pronunciada alinhada aproximadamente ENE-WSW (~N80°), sugere que a zona de alimentação do PLO se localiza ao longo de uma zona de fratura com esta mesma direção;
- a ascensão magmática terá ocorrido ao longo dessa zona de fratura ENE-WSW ocorrendo o fluxo magmático segundo uma orientação aproximada N-S a NNW-SSE (*ca*. N170°) como mostram as lineações magnéticas dirigidas para norte, a norte do PLO, e para sul, a sul do PLO;

- as lineações magnéticas são maioritariamente sub-horizontais, sugerindo que a zona de alimentação do PLO deverá estar distante em profundidade, e, portanto, que a sua instalação se deu em níveis estruturais altos;
- o alinhamento ENE-WSW visível na carta de anomalia residual é também patente na carta da suscetibilidade magnética (Cruz et al., 2016), que mostra que a fácies granítica com magnetite está orientada segundo essa orientação, sugerindo que esse magma teve origem mais profunda (em condições mais oxidantes), o que corrobora a presença da raiz nesta zona.

Em suma, o *fabric* magnético de direção predominante *ca.* N170° indica um fluxo magmático NNW-SSE condicionado por fraturas com esta orientação. Por outro lado, a anomalia gravimétrica indica que as estruturas ENE-WSW foram fundamentais para a localização da zona de raiz do plutão. A intersecção destas duas famílias de falhas tardi-Variscas (Marques et al., 2002), terá tido um papel importante na localização da raiz do plutão, que, no entanto, se localiza ligeiramente deslocada para WSW relativamente ao afloramento atual.

Agradecimentos: Este trabalho é financiado por uma bolsa de doutoramento: SFRH/BD/109693/2015 (FCT-Portugal). Os autores agradecem também o apoio do ICT através do projeto COMPETE 2020 (UID / GEO / 04683/2013) de referência POCI-01-0145-FEDER-007690 e aos Projetos NewOreS (ERA-MIN / 0002/2014) e ESMIMET (Interreg Spain-Portugal POCTEP project). Agradecemos ainda o apoio fornecido pela colega Ana Machadinho relativo à utilização do programa Oasis Montaj. Os autores agradecem ainda os comentários pertinentes do professor Eric Font.

Referências

Améglio, L., Vigneresse, J.L., Bouchez, J.L. (1997) Granite pluton geometry and emplacement mode inferred from combined fabric and gravity data, In: Bouchez, J.-L., Hutton, D.H.W., Stephens, W.E. (Eds.). Granite: From Segregation of Melt to Emplacement Fabrics, Kluwer Academic Publishers, Dordrecht, pp. 199–214.

Cruz, C., Sant'Ovaia, H., Noronha, F. (2016) Magnetic susceptibility and $\delta^{18}O$ characterization of Variscan granites related to W-(Mo) and Sn-(W) mineralizations: Lamas de Olo Pluton case study, *Comunicações Geológicas*, Vol. 103, 1, 143-174.

Fernandes, S., Gomes, M., Teixeira, R., Corfu, F. (2013) Geochemistry of biotite granites from the Lamas de Olo Pluton, northern Portugal, *Geophysical Research Abstracts*, EGU General Assembly, vol. 15.

Helal, B. (1992) Granitoïdes, granites à métaux rares et hydrothermalisme associe: géologie, minéralogie et géochimie de plusieurs suites tardi-hercyniennes (Nord du Portugal), PhD thesis, Ecole Nacionale Superieure des Mines de Saint-Etienne, France (published thesis).

Lowrie, W. (2007) Fundamentals of geophysics. Cambridge University Press, Cambridge, 381.

Marques, F.O., Mateus, A., Tassinari, C. (2002) The Late-Variscan fault network in central–northern Portugal (NW Iberia): a re-evaluation, *Tectonophysics*, 359 (3–4), 255-270.

Nettleton, L.L. (1939) Determination of Density for Reduction of Gravimeter Observations, *Geophysics*, Vol. 4(3): 176-183

Pereira, E. (1989) Carta Geológica de Portugal à escala 1:50 000, *Notícia Explicativa da Folha 10-A (Celorico de Basto)*, pp. 53. Serv. Geol. Portugal, Lisboa.

Sant'Ovaia, H., Bouchez, J.L., Noronha, F., Leblanc, D., Vigneresse, J.L. (2000) Composite-laccolith emplacement of the post-tectonic Vila Pouca de Aguiar granite pluton (northern Portugal): a combined AMS and gravity study, *Trans. R. Soc. Eding. Earth Sci.*, 91, 123-137.

Vigneresse, J.L. (1995) Control of granite emplacement by regional deformation. *Tectonophysics*, 249, 173-186.

(XCNG-17624)

Instalação do Plutão de Lamas de Olo: relação entre o "fabric" magnético e as estruturas regionais

Cláudia Cruz[1]; Helena Sant'ovaia[1]; Fernando Noronha[1]

1 - Departamento de Geociências Ambiente e Ordenamento do Território, Faculdade de Ciências, Universidade do Porto, Instituto de Ciências da Terra, Pólo-Porto

Palavras-chave: Fabric magnético, Granitos Variscos tardi- a pós-orogénicos, Anisotropia da suscetibilidade magnética, Instalação de granitos

O Plutão de Lamas de Olo (PLO) é um plutão tardi- a pós-orogénico localizado na parte norte da Zona Centro Ibérica da Cadeia Ibérica Varisca no Norte de Portugal. O PLO é um maciço compósito, constituído por diferentes granitos: Lamas de Olo, Barragem e Alto dos Cabeços. O PLO intrui metassedimentos do Grupo do Douro (GD) do "Complexo Xisto-Grauváquico", assim como o Maciço sinorogénico de Vila Real (MVR). Foram realizadas medições de anisotropia de suscetibilidade magnética (ASM) em 382 cilindros orientados, referentes a 52 locais de amostragem distribuídos tanto nos granitos do PLO, como nas rochas encaixantes. As foliações magnéticas do MVR e dos metassedimentos do GD apresentam uma direção de *ca*. N130º e N170º respetivamente e são ambas subverticais. Relativamente às lineações magnéticas, nestas rochas encaixantes, são ligeiramente inclinadas para NW. As foliações magnéticas no PLO são maioritariamente NNW-SSE, com uma atitude média de N168º; 90º e as lineações magnéticas são muito heterógenas. Há lineações magnéticas maioritariamente sub-horizontais, associadas a foliações muito inclinadas, o que sugere que a instalação do PLO foi controlada por uma zona de cisalhamento. No entanto, no setor sul do plutão verifica-se que as lineações magnéticas são maioritariamente verticais (com mergulho > 50º), o que sugere que a zona de enraizamento do plutão se localize nesse local. O *fabric* magnético do PLO, definido pelas lineações e foliações magnéticas, evidencia que a instalação deste plutão foi controlada por estruturas conjugadas tardi-Variscas NNW-SSE e NNE-SSW.

ISSN 1646-3269

(XCNG-17624)

EMPLACEMENT OF LAMAS DE OLO PLUTON: RELATION BETWEEN MAGNETIC FABRIC AND REGIONAL STRUCTURES

Cláudia Cruz[1]; Helena Sant'ovaia[1]; Fernando Noronha[1]

1 - Departamento de Geociências Ambiente e Ordenamento do Território, Faculdade de Ciências, Universidade do Porto, Instituto de Ciências da Terra, Pólo-Porto

Keywords: Magnetic fabric, Late- to post-orogenic Variscan granites, Anisotropy of magnetic susceptibility, Granites emplacement

The Lamas de Olo Pluton (LOP) is a late- to post-orogenic pluton located in the Northern part of Central Iberian Zone from Iberian Variscan belt, in Northern Portugal. The LOP is a composite massif constituted by different granites: Lamas de Olo, Barragem and Alto dos Cabeços. The LOP intrude metasediments from the Douro Group (DG) from the "Complexo Xisto-Grauváquico" and synorogenic granites from Vila Real Massif (VRM). The anisotropy of magnetic susceptibility (ASM) measurements were taken on 382 oriented cores from 52 sampling sites, roughly distributed in the LOP granites and host rocks. The magnetic foliations in the synorogenic granites of VRM and in the DG host rocks are *ca*. N130º and N170º trending respectively and are both subvertical. The magnetic lineations in the host rocks are gently dipping to NW. The magnetic foliations in LOP granites are mainly NNW-SSE with a mean value of N168º; 90º. The magnetic lineations have a heterogeneous behavior over the pluton. The mainly subhorizontal plunges associated to steep magnetic foliations suggest that the emplacement of LOP was controlled by a shear strain. On the other hand, the magnetic lineations in the south sector of LOP are mainly vertical (plunge > 50º), suggesting that the pluton feeder zone is here located. The magnetic fabric in the LOP, defined by magnetic lineations and magnetic foliations shows that pluton emplacement was controlled by NNW-SSE offsets, conjugated with NNE-SSW system faults.

(XCNG-17643)

ABORDAGEM GEOESTATÍSTICA NO ESTUDO DA VARIAÇÃO DA SUSCETIBILIDADE MAGNÉTICA: O CASO DE ESTUDO DO PLUTÃO DE LAMAS DE OLO

Cláudia Cruz[1]; Joaquim Góis[2]; Helena Sant'ovaia[1]; Fernando Noronha[1]

1 - Departamento de Geociências Ambiente e Ordenamento do Território, Faculdade de Ciências, Universidade do Porto, Instituto de Ciências da Terra, Pólo-Porto;

2 - Departamento de Engenharia de Minas, Faculdade de Engenharia da Universidade do Porto, CERENA - Centro de Recursos Naturais e Ambiente - Polo FEUP

Palavras-chave: Suscetibilidade magnética, Métodos geoestatísticos, Variograma, Krigagem, Plutão de Lamas de Olo

O Plutão de Lamas de Olo (PLO) é um plutão granítico tardi- a pós-orogénico localizado na parte norte da Zona Centro Ibérica da Cadeia Ibérica Varisca no norte de Portugal. O PLO é constituído por diferentes granitos: Lamas de Olo, Barragem e Alto dos Cabeços. O principal objetivo deste trabalho consiste na caracterização dos diferentes granitos constituintes do PLO no que diz respeito à presença de minerais ferromagnéticos, nomeadamente de magnetite, para identificação de granitos do tipo "magnetite-type". A aplicação das metodologias de geoestatística, conduzem a uma cartografia mais pormenorizada da suscetibilidade magnética (*Km*), ao quantificar a sua dispersão espacial. Foram realizadas medições de *Km* em 349 cilindros orientados, referentes a 48 locais de amostragem distribuídos pelos diferentes granitos do PLO. Os valores de *Km* considerados neste trabalho variam entre 21 ´ 10^{-6} SI e 2769 ´ 10^{-6} SI no PLO. Estes valores são importantes na caracterização das fácies graníticas, uma vez que permitem distinguir os granitos com magnetite daqueles com ilmenite ("ilmenite-type"), pois estão associados a condições petrogenéticas diferentes que condicionam diferentes tipos de mineralizações. Os granitos "magnetite-type" apresentam valores de *Km* superiores a 3×10^{-3} SI e os "ilmenite-type" possuem *Km* inferiores a 3×10^{-3} SI. Apesar dos valores de *Km* variarem abruptamente em poucos metros de distância, a análise geoestatística permite estabelecer uma correlação entre dois pontos distanciados até cerca de 1400 m. Foi utilizada a interpolação por *krigagem*, uma vez que é considerada como o melhor estimador linear não-enviesado ("BLUE") de variáveis regionalizadas. A interpolação por *krigagem* permitiu definir duas áreas no PLO: (i) uma área com valores elevados de *Km*, típicos de granitos com magnetite (*Km* ³ 1200 ´ 10^{-6} SI) e (ii) áreas com valores baixos de *Km*, que correspondem a granitos com ilmenite (21 ´ 10^{-6} SI ³ *Km* < 1200 ´ 10^{-6} SI). A abordagem geoestatística aplicada neste estudo permitiu quantificar e validar estudos prévios realizados em ArcGIS usando o método do "Inverso da Distância".

ISSN 1646-3269

(XCNG-17643)

GEOSTATISTICAL APPROACH IN THE STUDY OF THE MAGNETIC SUSCEPTIBILITY VARIATION: LAMAS DE OLO PLUTON CASE STUDY

Cláudia Cruz[1]; Joaquim Góis[2]; Helena Sant'ovaia[1]; Fernando Noronha[1]

1 - Departamento de Geociências Ambiente e Ordenamento do Território, Faculdade de Ciências, Universidade do Porto, Instituto de Ciências da Terra, Pólo-Porto;

2 - Departamento de Engenharia de Minas, Faculdade de Engenharia da Universidade do Porto, CERENA - Centro de Recursos Naturais e Ambiente - Polo FEUP

Keywords: Magnetic susceptibility, Geostatistical methods, Variogram, Kriging, Lamas de Olo Pluton

The Lamas de Olo Pluton (LOP) is a late- to post-orogenic pluton located in the Northern part of Central Iberian Zone from Iberian Variscan belt, in Northern Portugal. The LOP is a composite massif constituted by different granites: Lamas de Olo, Barragem and Alto dos Cabeços. The aim of this study is characterizing the granites of LOP concerning the presence of the ferromagnetic minerals, namely magnetite. The presence of the magnetite allows to identify the magnetite-type granites. The applications of the geostatistical methodologies, leads to a more detailed mapping of the magnetic susceptibility (*Km*) data, quantifying, its spatial dispersion. The *Km* measurements were taken on 349 oriented cores from 48 sampling sites, roughly distributed in the LOP. The *Km* values considered in this work range between 21 ´ 10^{-6} SI and 2769 ´ 10^{-6} SI for all LOP granites. The *Km* values are important in granite facies characterization because allow to distinguish two kinds of granites: magnetite- and ilmenite-type granites. The magnetite-type granites have *Km* values above 3 × 10^{-3} SI and in the others, the *Km* values is lower than 3 × 10^{-3} SI. Although the *Km* values quickly increase/ decrease within few meters, the geostatistical analysis shows the presence of correlations between two points spaced until 1400 m. The kriging interpolation was used, once it is considered as the Best Linear Unbiased Estimator (BLUE) of the random field. The kriging interpolation allow to define different areas in LOP: (i) areas with higher *Km* values, typical of granites with magnetite (*Km* ³ 1200 ´ 10^{-6} SI) and (ii) areas with lower values, which corresponded to granites with ilmenite (21 ´ 10^{-6} SI ³ *Km* < 1200 ´ 10^{-6} SI). The geostatistical approach applied in this study comes to quantify and validate the previous interpolation using the interpolation made by Inverse Distance Weighted in the ArcGIS software.

Magnetic mineralogy of Variscan granites: relation to its metallogenic potential on rare metals

CLÁUDIA CRUZ[1], HELENA SANT'OVAIA[1], PHILIPPE OLIVIER[2], FERNANDO NORONHA[1]

[1]Departamento de Geociências Ambiente e Ordenamento do Território - Instituto de Ciências da Terra, Pólo Porto, Faculdade de Ciências, Universidade do Porto, Rua do Campo Alegre 687, Porto, Portugal, claudiacruz@fc.up.pt
[2]Université de Toulouse, UPS, LMTG, Toulouse, France

The Lamas de Olo Pluton (LOP) is a late to post-orogenic massif located in the Northern part of Central-Iberian Zone from Iberian Variscan belt. The LOP is a composite body constituted by different granite facies. The area belongs to the "Northern mineralogenic province", where W-Mo-(Sn) occurrences are present [1]. Previous magnetic susceptibility (MS) measurements pointed out the presence of two types of granites: magnetite- and ilmenite-type granites [2]. In order to identify different ferromagnetic contributions, complementary thermo-magnetic experiments were performed in a low field CS-2 furnace attached to the KLY-3 susceptometer. Two different kind of curves were obtained: (A) showing a significant fall of MS at 580°C, indicating the Curie temperature of magnetite; (B) showing a regularly decreasing of MS with increasing temperature, typical of a paramagnetic behaviour (Fig. 1). These results confirms the existence of granites with magnetite and ilmenite, respectively.

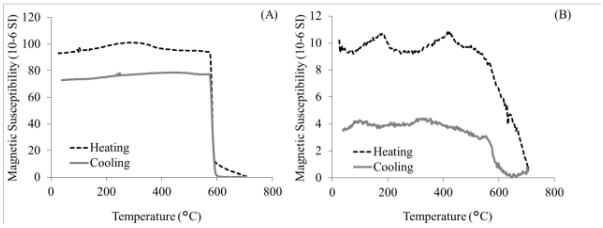


Figure 1: Normalized magnetic susceptibility curves for continuously increasing (and decreasing) temperatures.

The different magnetic behaviours, suggested different redox conditions in the magma genesis which controls the nature of many ore elements [3]. The presence of magnetite in LOP reflects melt oxidized conditions, which can play an important role on the genesis of W (Mo) mineralizations.

The authors acknowledge to DGAOT/FCUP; Project UID/GEO/04683/2013 of FCT-Portugal; COMPETE POCI-01-0145-FEDER-007690; ERA-MIN/0002/2014 project NewOres; SFRH/BD/109693/2015 (FCT-Portugal).

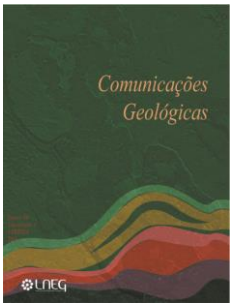
[1] Thadeu (1965) *Carta Mineria de Portugal*; [2] Cruz et al. (2016) *SGEM*, 345-352; [3] Ishihara (1977), Min. Geology, **27**, 292-305.

Versão online: http://www.lneg.pt/iedt/unidades/16/paginas/26/30/209

Comunicações Geológicas

Comunicações Geológicas (2016) 103, 1, 143-147
ISSN: 0873-948X; **e-ISSN:** 1647-581X

Magnetic susceptibility and $\delta^{18}O$ characterization of Variscan granites related to W-(Mo) and Sn-(W) mineralizations: Lamas de Olo Pluton case study



Caracterização da suscetibilidade magnética e $\delta^{18}O$ de granitos Variscos relacionados com mineralizações de W-(Mo) e Sn-(W): Exemplo do Plutão de Lamas de Olo

C. Cruz[1,2*], H. Sant'Ovaia[1,2], F. Noronha[2]

Artigo original
Original article

© 2016 LNEG – Laboratório Nacional de Energia e Geologia IP

Abstract: The "Iberian Sn-W metallogenic province", located in central-northern region of Portugal is characterized by the presence of various W, W-(Sn), W-(Mo) and Sn deposits related with synorogenic Variscan granites, mainly emplaced during the post-collisional stage (321 to 290 Ma). The granites can be classified into magnetite- or ilmenite-type granites according to their magnetic susceptibility. These two types of granites result from different oxygen fugacities during the granitic magma genesis, and have also distinctive whole-rock $\delta^{18}O$ values. Thus, higher values (between 12.3 ‰ and 13.5 ‰) indicate a crustal origin, while the low $\delta^{18}O$ (between 8.9 ‰ and 12.2 ‰) suggests a mantle origin and/or source regions dominated by mafic and meta-igneous rocks. Major W-(Sn) and Sn ore deposits are more related to ilmenite-type granites with high $\delta^{18}O$, while W-(Mo) deposits are related with magnetite-type granite with lower $\delta^{18}O$ values.

Keywords: magnetic susceptibility, post-tectonic Variscan granites, magnetite-type granites, W-(Mo) and Sn-(W) mineralizations.

Resumo: A "Província metalogénica de W-Sn" situada no norte e centro de Portugal é caracterizada pela presença de vários jazigos de W, W-(Sn), W-(Mo) e Sn, espacialmente associados a granitos sinorogénicos Variscos que se instalaram maioritariamente durante a etapa pós-colisional (321 a 290 Ma). Os granitos podem ser classificados em granitos tipo-magnetite ou tipo-ilmenite, consoante a sua suscetibilidade magnética. Estes dois tipos de granitos resultam ainda de diferentes condições de fugacidade de oxigénio durante a génese dos magmas graníticos e possuem ainda valores distintos de $\delta^{18}O$ em rocha-total. Deste modo, valores elevados de $\delta^{18}O$ (entre 12,3 ‰ e 13,5 ‰) indicam origem crustal para os magmas graníticos, enquanto valores baixos de $\delta^{18}O$ (entre 8,9 ‰ e 12,2 ‰) sugerem uma origem mais mantélica e/ou com contribuição de rochas máficas e meta-ígneas. A maioria dos jazigos de W-(Sn) e Sn estão relacionados com granitos tipo-ilmenite com valores de $\delta^{18}O$ altos, enquanto as ocorrências de W-(Mo) tendem a estar relacionadas com granitos tipo-magnetite e com baixos valores de $\delta^{18}O$.

Palavras-chave: suscetibilidade magnética, granitos Variscos pós-tectónicos, granitos tipo-magnetite, mineralizações de W-(Mo) e Sn-(W).

[1] Faculty of Sciences, University of Porto, Department of Geosciences, Environment and Spatial Planning, Rua do Campo Alegre, 4169-007 Porto, Portugal.
[2] Institute of Earth Sciences – Porto Pole, Rua do Campo Alegre, 4169-007 Porto, Portugal.
* Corresponding author / Autor correspondente: claudiacruz@fc.up.pt

1. Geological setting

The Lamas de Olo Pluton (LOP) is a post-tectonic Variscan body and constitutes a small outcrop with rhombus shape. This pluton is located in the northern part of Central-Iberian Zone in Iberian sector from Variscan belt, near the limit with Galiza Trás-os-Montes Zone (Farias *et al*., 1987; Ribeiro *et al*., 1990).

The emplacement of the LOP was controlled by NNW-SSE offsets conjugated with the NNE-SSW Verin-Régua-Penacova fault (VRPF). The LOP has distinct biotite facies: 1) Lamas de Olo (LO), the more representative facies, is a medium to coarse-grained porphyritic granite; 2) Alto dos Cabeços (AC), a medium to fine-grained porphyritic granite and 3) Barragem (BA), a leucocratic fine-grained and slightly porphyritic granite (Pereira, 1989; Fernandes *et al*., 2013). The LOP granites intrude the Douro Group metasediments (Precambrian to Cambrian in age) and two-mica syntectonic granites from Vila Real Massif (Fig. 1) (Pereira, 1989). The studied area belongs to the "Northern mineralogenic province" and W-Mo-(Sn) occurrences are present mostly in N80ºE sub-vertical quartz veins cutting LOP granites (Thadeu, 1965; Pereira, 1989).

2. Materials and methods

2.1. Sampling

At each site of sampling, three, four or five oriented cores (25 mm in diameter and 60 to 70 mm in length) were collected in situ with a portable drill machine. Then, in laboratory each core was sawed in order to obtain around 22 mm long specimens. At least three, or more, specimens per station were obtained for magnetic susceptibility measurements.

This study was based on 292 specimens from 36 sampling sites, roughly distributed in LOP granites: 30 sites in LO facies, 3 in BA and 3 in AC facies (Fig. 1).

2.2. Magnetic susceptibility measurements

The relationship between the magnetization induced in a material M and the external field H is defined as $M=KH$, where K is the magnetic susceptibility. The K values are dimensionless because M (per unit volume) and H have the same units (*e.g.* Hrouda,

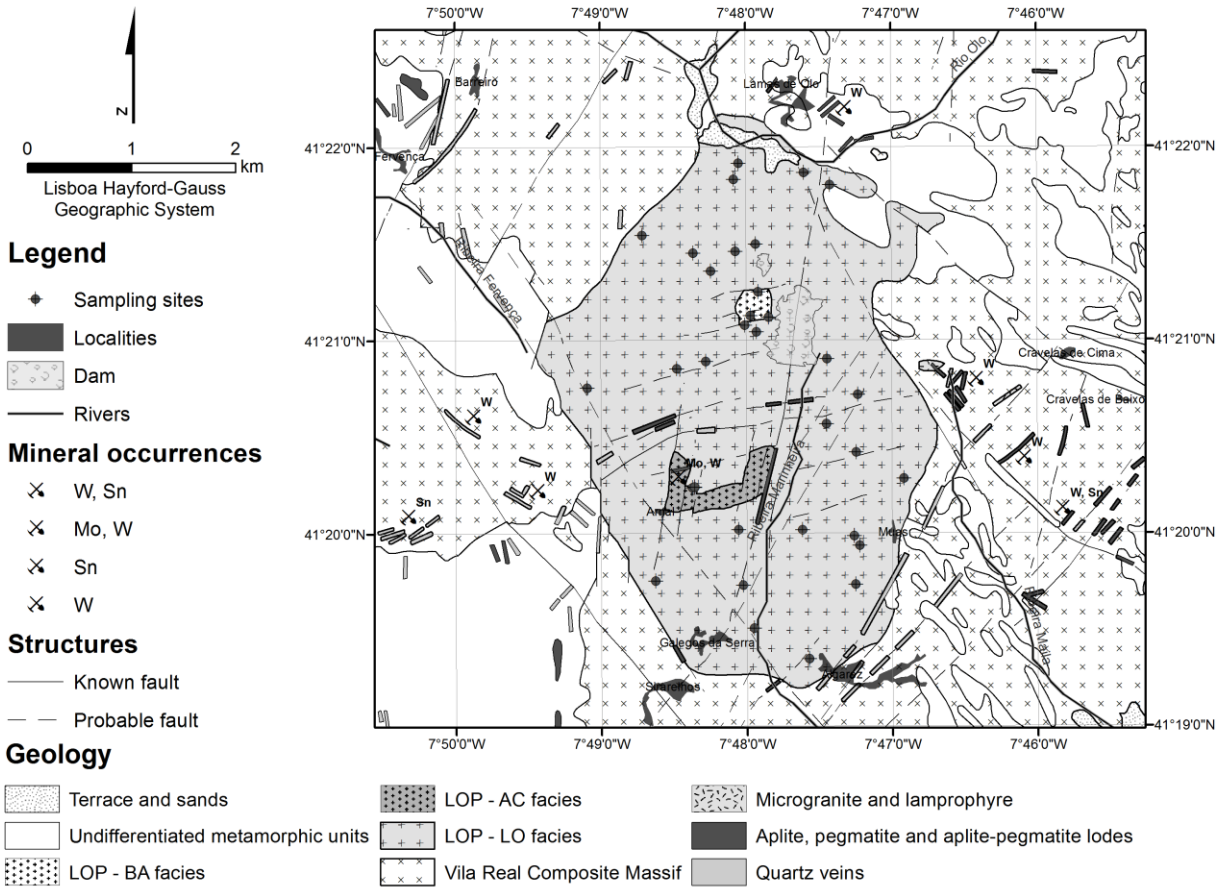


Figure 1. Simplified geological map of the Lamas de Olo Pluton and sampling sites (modified: Pereira *et al*., 1987).

Figura 1. Mapa geológico simplificado do Plutão de Lamas de Olo e localização dos locais de amostragem (modificado: Pereira *et al*., 1987)

1982; Bouchez, 1997). The *K* reflects the mineral composition of the whole-rock (W.R.), comprising the diamagnetic (*e.g.* quartz, feldspar), paramagnetic (*e.g.* biotite, muscovite or hornblende) and ferromagnetic minerals (*e.g.* magnetite or hematite). *K* measurements were performed using a KLY-4S Kappabridge susceptometer Agico model (Czech Republic) from the Institute of Earth Sciences – Porto Pole. Measurements were undertaken in a 300 A/m field. For each site, the ANISOFT 4.2 program package (www.agico.com) enabled us to calculate the mean susceptibility *Km*, which is the mean of the individual arithmetic means $(K_{max} + K_{int} + K_{min})/3$.

The *Km* values can distinguish two kinds of granites: magnetite- and ilmenite-type granites. The first group has *Km* values above 3.0×10^{-3} SI and in the second, *Km* is lower than 3.0×10^{-3} SI (Ishihara, 1977).

The magnetic susceptibility measurements were taken on all 292 samples from the 36 sampling sites (Fig. 1).

2.3. Oxygen fugacities and whole-rock $\delta^{18}O$

The granite rocks reflect redox states of their corresponding magmas, and the presence of magnetite or ilmenite as accessory minerals represents oxidized- and reduced-type respectively. These two types of granites also result from exposure of different oxygen fugacity during the magma genesis. The magnetite-type is generated at great depth where no carbonaceous material exists, whereas the ilmenite-type is originated at a shallow level where small amounts of crustal carbon are present (Ishihara, 1977; Sheppard, 1977; Ellwood and Wenner, 1981).

In nature, the oxygen occurs mainly in the form of the ^{16}O isotope, but it can also occur in very small quantities in the stable ^{18}O isotope form. The abundance of the ^{18}O isotope is expressed as a percentage of the ^{18}O isotope relative to ^{16}O (indicated by *R* in the equation: $R = {}^{18}O / {}^{16}O \times 100$). However, when the differences in the abundance of both isotopes, on the rocks, are very small, the quantity of the isotope is expressed as its ratio in the sample relative to an international accepted standard, normally the VSMOW standard (Vienna Standard Mean Ocean Water). This relative portion in rock samples, represented as ^{18}O, is multiplied by 1000 and is expressed by the equation: $\delta^{18}O = [(R_{sample}/ R_{standard}) - 1] \times 1000$ ‰ (Morrill and Koch, 2002).

The highest $\delta^{18}O$ values indicate a crustal origin, through anatexis of metasedimentary protoliths, and the low values suggest a mantle origin and/or source regions dominated by mafic and meta-igneous rocks (Ishihara, 1977; Ellwood and Wenner, 1981).

Oxygen isotope data measurements were performed on 4 samples from LOP at the Stable Isotopic Laboratory of Salamanca. Oxygen was extracted from rocks by laser fluorination techniques, quantitatively converted to CO_2 by the reaction with a heated carbon rod and analyzed for $^{18}O/^{16}O$ ratio with a dual inlet VG SIRA-II Mass Spectrometer.

3. Results and discussion

3.1. Magnetic susceptibility evidences

The *K* measurements were examined in order to deduce the redox conditions of magma systems as well as the distribution of magnetite- and ilmenite-type granites over the pluton. The high *Km* values (>10^{-3} SI) indicate a ferromagnetic behavior, due to the presence of iron minerals, such as magnetite and the low *Km* values (~10^{-6} SI) indicate the presence of paramagnetic minerals, like ilmenite and biotite (Ishihara, 1977).

Km values are heterogeneous and range between 24 × 10^{-6} and 44382 × 10^{-6} SI for all LOP granites. The *Km* values range between: 65 × 10^{-6} and 44382 × 10^{-6} SI in LO facies, 24 × 10^{-6} and 34 × 10^{-6} SI in BA, and 167 × 10^{-6} and 804 × 10^{-6} SI in AC (Table 1). The mean values by facies are 2447 × 10^{-6} SI in LO, 30 × 10^{-6} SI in BA and 403 × 10^{-6} SI in AC facies.

Table 1. Magnetic susceptibility data for the sampling sites (Km: mean magnetic susceptibility in 10^{-6} SI).

Tabela 1. Valores de suscetibilidade magnética por locais de amostragem (Km: suscetibilidade magnética média em 10^{-6} SI).

Sample	LOP facies	*Km* × 10^{-6} SI
LM 1	LO	174
LM 2	LO	1848
LM 3	LO	2475
LM 3V	LO	316
LM 4	LO	65
LM 5	LO	2873
LM 6	LO	229
LM 8	LO	1677
LM 13	LO	44382
LM 14	LO	2179
LM 16	LO	67
LM 17	LO	77
LM 18	LO	79
LM 19	LO	1869
LM 20	LO	2760
LM 21	LO	233
LM 22	LO	606
LM 23	LO	254
LM 27	LO	69
LM 28	LO	2065
LM 29	LO	1147
LM 30	LO	2385
LM 7	BA	34
LM 15	BA	24
LM 32	LO	2031
LM 33	LO	1261
LM 34	LO	100
LM 35	LO	205
LM 36	LO	242
LM 37	LO	101
LM 38	LO	1559
LM 39	LO	81
LM 31	BA	32
LM 24	AC	239
LM 25	AC	167
LM 26	AC	804

Figure 2 presents the frequency of mean magnetic susceptibility values for all the LOP granites. Concerning the susceptibility, the LO is the more heterogeneous facies, with *Km* varying between, *Km* < 10^{-4} SI to *Km* > 10^{-3} SI.

The BA and AC facies have only *Km* < 10^{-4} SI, but some AC *Km* values were relatively higher for ilmenite-type granites. These values show that the two types of magnetic behavior are present in the same pluton. The interpolation of *Km* data, using the software ArcGIS, shows that magnetite is present in locals where fracturing is well pronounced, namely in the eastern part of the LOP and along an E-W direction (Fig. 3).

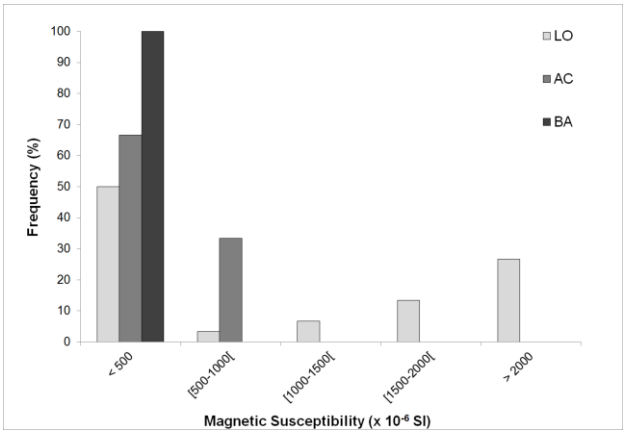


Figure 2. Frequency histogram of mean magnetic susceptibility values for the Lamas de Olo Pluton facies (LO – Lamas de Olo; AC – Alto dos Cabeços; BA – Barragem).

Figura 2. Histograma de frequência da suscetibilidade magnética média das fácies do Plutão de Lamas de Olo (LO – Lamas de Olo; AC – Alto dos Cabeços; BA – Barragem).

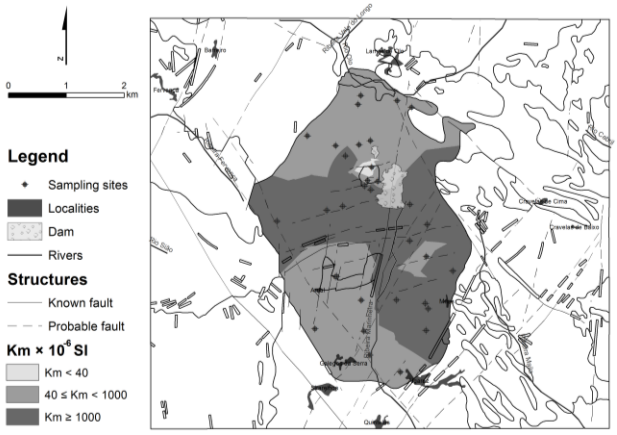


Figure 3. Map of the magnetic susceptibility (*Km*) values in Lamas de Olo Pluton (interpolation made by Inverse Distance Weighted in the ArcGIS software).

Figura 3. Mapa de distribuição dos valores de suscetibilidade magnética (*Km*) do Plutão de Lamas de Olo (interpolação realizada no *software* ArcGIS utilizando o Inverso da Distância).

3.2. Oxygen-isotope data

The W.R. $\delta^{18}O$ data were performed on 4 samples from LOP: 3 from LO facies, being 2 of magnetite-type and 1 of ilmenite-type and 1 sample of BA ilmenite-type granite.

The *Km* versus W.R. $\delta^{18}O$ diagram (Ellwood and Wenner, 1981) permit to compare LOP with other Variscan Portuguese Massifs, in order to establish a relationship between granites and mineralizations.

The studied Variscan granites (Fig. 4) have *Km* values between 28 × 10^{-6} and 92100 × 10^{-6} SI, however the majority of the granites vary from 20 × 10^{-6} to 300 × 10^{-6} SI which corresponding to reduced, ilmenite-type granites. The W.R. $\delta^{18}O$ values from some Variscan granites, obtained from bibliography (Antunes *et al*., 2008; Martins *et al*., 2009; Neiva *et al*., 2009 and Sant'Ovaia *et al*., 2012), shows that studied granites have heterogeneous ^{18}O values ranging from 8.9 ‰ to 13.5 ‰.

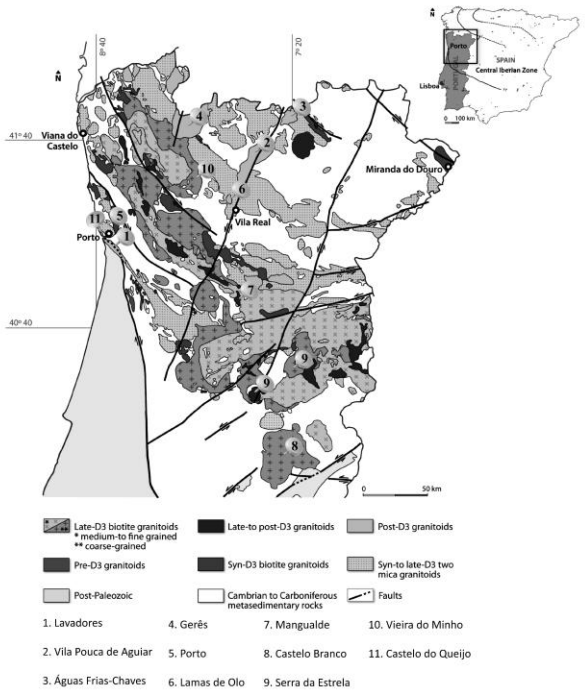


Figure 4. Distribution of the studied variscan granitoids in northern Portugal (modified: Ferreira *et al*., 1987).

Figura 4. Distribuição dos granitóides variscos estudados no norte de Portugal (modificado: Ferreira *et al*., 1987).

The oxidized or magnetite-type granites are scarce and represented by post-tectonic granites with *Km* values ranging from 1×10^{-3} to 92×10^{-3} SI units and low $\delta^{18}O$ values ranging from 8.9 ‰ to 10.4 ‰.

Figure 5 points out that major W-(Sn) ore deposits are related to ilmenite-bearing granites with high $\delta^{18}O$ values, while W-(Mo) deposits are related with magnetite-type granite with lower $\delta^{18}O$ values.

4. Final Remarks

The magnetic susceptibility and $\delta^{18}O$ data allow to establish a difference between ilmenite-type and magnetite-type granites and relate each granite type to a particular metal association (Fig. 5) (Takagi and Tsukimura, 1977; Kumar, 2010). The presence of magnetite reflects melt oxidized conditions, on deeper crustal conditions, which played an important role on the granite genesis related to W-Mo mineralizations (Ishihara, 1977).

Our results confirm the presence in the LOP of ilmenite-type and magnetite-type granites. However, in facies exhibiting post-magmatic alterations the magnetite alteration can change *K* values of the granites because implies the formation of new minerals like hematite (Lagoeiro, 1998). This fact can explain *K* mean values around 403×10^{-6} SI which are lower than the expected to magnetite-type granites in AC facies.

The association between granites with different magnetic behavior in the same pluton is not present in other similar post-tectonic plutons, from northern Portugal, such as Vila Pouca de Aguiar and Águas Frias-Chaves (Fig. 4) (Martins *et al*., 2009). These plutons are very similar to LOP, either in geochemistry or in geochronology characteristics, but they are ilmenite-type granites.

We assume that W-(Mo) mineralizations are present in LOP because magnetite-type granites are present. This relationship between magnetite-type granites and W-(Mo) mineralizations was also found in the post-tectonic (280 Ma) Gerês pluton (Fig. 4) (Noronha *et al*., 2013). The abundant W-(Sn) and Sn mineralizations present in the area can be related with ilmenite-type granites, namely the two-mica granites.

Acknowledgments

The first author is financially supported by SFRH/BD/109693/2015 (FCT Portugal); The authors acknowledge the funding by COMPETE 2020 through the ICT (Institute of Earth Sciences) project (UID / GEO / 04683/2013) with POCI-01-0145 reference - FEDER-007690 and NewOreS Project (ERA-MIN / 0002/2014).

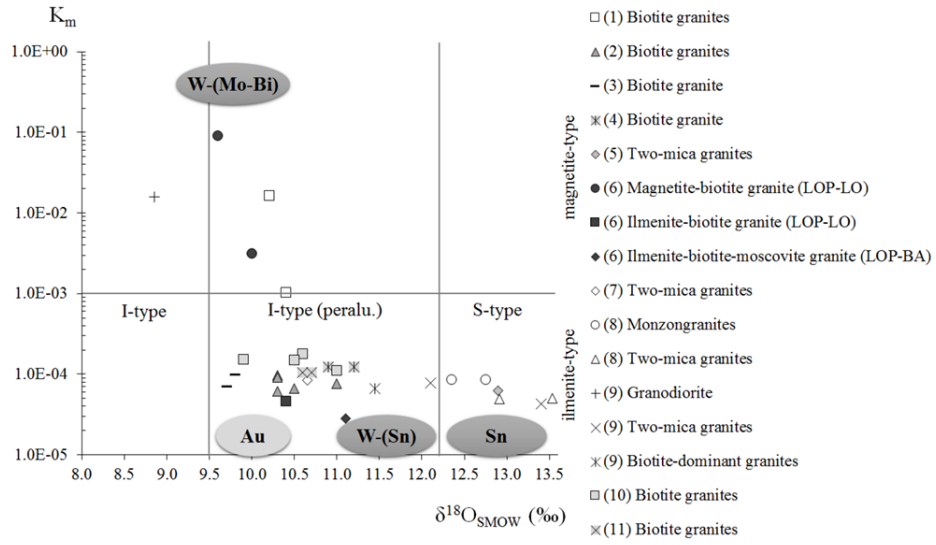


Figure 5. Semi-log plot of *Km* (in SI units) versus $\delta^{18}O$ for the studied granitoids, considering the data in Antunes *et al*. (2008); Martins *et al*. (2009); Neiva *et al*. (2009) and Sant'Ovaia *et al*. (2012).

Figura 5. Gráfico semi-log da Km (unidades em SI) versus $\delta^{18}O$ para os granitóides estudados, considerando os dados reportados em Antunes *et al*. (2008); Martins *et al*. (2009); Neiva *et al*. (2009) and Sant'Ovaia *et al*. (2011).

References

Antunes, I. M. H. R., Neiva, A. M. R., Silva, M. M. V. G., Corfu, F., 2008. Geochemistry of S-type granitic rocks from the reversely zoned Castelo Branco pluton (central Portugal). *Lithos*, **103**: 445-465.

Bouchez, J. L., 1997. Granite is never isotropic: an introduction to AMS studies of granitic rocks. *In: Granite: from melt to emplacement fabrics* (Eds. J. L. Bouchez, D. H. W. Hutton & W. E. Stephens), Kluwer Academic Publishers, Dordrecht, 95-112.

Ellwood, B. B., Wenner, D. B., 1981. Correlation of magnetic susceptibility with 18O/16O data in late orogenic granites of the southern Appalachian Piedmont. *Earth Planet. Sci. Lett*., **54**: 200-202.

Farias, P., Gallastegui, G., González Lodeiro, L., Marquínez, J., Martín Parra, L. M., Martínez Catalán, J. R., Pablo Maciá, J. G., Rodríguez Fernández, L. R., 1987. Aportaciones al conocimiento de la litoestratigrafia y estructura de Galicia Central. Memórias nº1, IX Reunião sobre a geologia do oeste peninsular. *Mus. Lab. miner. geol. Fac. Ciênc. Univ. Porto*, **1**: 411-431.

Fernandes, S., Gomes, M., Teixeira, R., Corfu, F., 2013. Geochemistry of biotite granites from the Lamas de Olo Pluton, northern Portugal. *Geophysical Research Abstracts*, EGU General Assembly, 15.

Ferreira, N., Iglesias, M., Noronha, F., Pereira, E., Ribeiro, A., Ribeiro, M. L., 1987. Granitóides da Zona Centro Ibérica e seu enquadramento geodinâmico. *In: Geologia de los granitoides y rocas asociadas del Macizo Hespérico* (Eds. F. Bea, A. Carnicero, J. C. Gonzalo, M. López Plaza & M. D. Rodríguez Alonso), Ed. Rueda, 37-51.

Hrouda, F., 1982. Magnetic anisotropy of rocks and its application in geology and geophysics. *Geophysical Surveys*, **5**: 37-82.

Ishihara, S., 1977. The Magnetite-series and Ilmenite-series Granitic Rocks. *Mining Geology*, **27**: 292-305.

Kumar, S., 2010. Magnetite and ilmenite series granitoids of Ladakh batholith, Northwest Indian Himalaya: implications on redox conditions of subduction zone magmatism. *Current Science*, **99**: 1260-1264.

Lagoeiro, L. E., 1998. Transformation of magnetite to hematite and its influence on the dissolution of iron oxide minerals. *J. metamorphic Geol*., **16**: 415-423.

Martins, H. C. B., Sant'Ovaia, H., Noronha, F., 2009. Genesis and emplacement of felsic Variscan plutons within a deep crustal lineation, the Penacova-Régua-Verin fault: an integrated geophysics and geochemical study (NW Iberian Peninsula). *Lithos*, **111**(3-4): 142-155.

Morrill, C., Koch, P. L., 2002. Elevation or alteration? Evaluation of isotopic constraints on paleoaltitudes surrounding the Eocene Green River Basin. *Geological Society of America*, **30**(2): 151-154.

Neiva, A. M. R., Williams, I. S., Ramos, J. M. F., Gomes, M. E. P., Silva, M. M. V. G., Antunes, I. M. H. R., 2009. Geochemical and isotopic constraints on the petrogenesis of Early Ordovician granodiorite and Variscan two-mica granites from the Gouveia area, central Portugal. *Lithos*, **111**: 186-202.

Noronha, F., Ribeiro, M. A., Almeida, A., Dória, A., Guedes, A., Lima, A., Martins, H. C., Sant'Ovaia, H., Nogueira, P., Martins, T., Ramos, R., Vieira, R., 2013. Jazigos filonianos hidrotermais e aplitopegmatíticos espacialmente associados a granitos (norte de Portugal). *In: Geologia de Portugal* (Eds. R. Dias, A. Araújo, P. Terrinha & J. C. Kullberg), **I**: 403-438.

Pereira, E., Silva, N., Moreira, A., Ribeiro, A., 1987. Folha 10-A Celorico de Basto da Carta Geológica de Portugal na escala 1/50 000. *Serv. Geol. Portugal*.

Pereira, E., 1989. *Notícia Explicativa da Folha 10-A Celorico de Basto da Carta Geológica de Portugal à escala 1/50 000. Serv. Geol. Portugal*, 53.

Ribeiro, A., Pereira, E., Dias, R., 1990. Structure of the Northwest of the Iberian Peninsula. *In: Pre-Mesozoic Geology of Iberia (Eds. R. D. Dallmeyer & E. Martinez Garcia)*, Springer-Verlag, 220-236.

Sant'Ovaia, H., Martins, H., Lopes, J. C., Machado, J., Noronha, F. (2012). Correlation of magnetic susceptibility with $\delta^{18}O$ data in magnetite- and ilmenite-type granites from Iberian massif. *Mineralogical Magazine*, **76**(6): 2325.

Sheppard, S. M. F., 1977. Identification of the origin of ore formin solutions by the use of stable isotopes. *In: Volcanic Processes in Ore Genesis*, Institution of Mining and Metallurgy and Geological Society, London, 254l.

Takagi, T., Tsukimura, M., 1997. Genesis of oxidized- and reduced-type granites. *Economic Geology*, **92**: 81-86.

Thadeu, D., 1965. *Notícia explicativa da Carta Mineira de Portugal.. Serv. Geol. Portugal*, 46.

MAGNETITE AND ILMENITE GRANITES IN THE LAMAS DE OLO PLUTON (NORTH PORTUGAL): PETROPHYSIC AND METALLOGENIC IMPLICATIONS

MSc. Cláudia Cruz

Assoc. Prof. Dr. Helena Sant'Ovaia

Professor Dr. Fernando Noronha

Institute of Earth Sciences, Department of Geosciences, Environment and Spatial Planning, Faculty of Sciences of University of Porto, **Portugal**

16th International Scientific GeoConference SGEM2016 www.sgem.org

ABSTRACT

In the studied area, situated in Northern Portugal, outcrops, an intrusion of post-tectonic Variscan granites constituting the Lamas de Olo Pluton (LOP) whose emplacement was controlled by NNE-SSW regional Variscan fault, the Verin-Régua-Penacova fault (VRPF). The LOP has distinct biotite granite facies: 1) Lamas de Olo (LO) - a porphyritic, medium to coarse-grained; 2) Barragem (BA) - a leucocratic slightly porphyritic, fine-grained; 3) Alto dos Cabeços (AC) - a porphyritic, medium to fine-grained. The LOP granites intrudes the Douro Group metasediments (Precambrian to Cambrian in age) and syntectonic two-mica granites from Vila Real Massif. The LOP occurs in the "Iberian Sn-W metallogenic province" and in the area exist W (Mo) occurrences.

The LOP granites present as primary accessory minerals biotite, apatite, zircon, sphene, allanite, magnetite and/or hematite, ilmenite, fluorite and tourmaline. As secondary minerals, contains muscovite, chlorite, epidote and rutile.

The magnetic susceptibility (*Km*) measurements were taken on 151 oriented cores (26 sampling sites) roughly distributed in the LOP. The *Km* values range between 11 and 92100 $\times 10^{-6}$ SI in LO facies, pointing out a manly ferromagnetic behavior, due to magnetite, between 22 and 51 x 10^{-6} SI in BA facies and 135 and 905 $\times 10^{-6}$ SI in AC facies, indicating a paramagnetic behavior, due to ilmenite and biotite.

Our results show the presence of ilmenite and magnetite granites in the same pluton. The association between granites with different magnetic behavior in the same pluton is not present in other similar post-tectonic plutons such as Vila Pouca de Aguiar and Águas Frias-Chaves, also emplaced along VRPF, which are ilmenite granites. The presence of magnetite in LOP reflects melt oxidized conditions, which usually played and important role on the genesis of W (Mo) mineralizations. This relationship between magnetite-type granites and W (Mo) mineralizations was also found in the post-tectonic Gerês pluton.

Keywords: post-tectonic variscan granites, magnetite-type granites, ilmenite-type granites, W (Mo) deposits.

GEOLOGICAL SETTING

The Lamas de Olo Pluton (LOP) is a post-tectonic Variscan body and constitutes a small outcrop with rhombus shape. This pluton is located in the northern part of Central-Iberian Zone of the Variscan Iberian sector, near the limit with Galiza Trás-os-Montes Zone [1].

The emplacement of the LOP was controlled by a NW-SE and NNE-SSW fracture system, related to VRPF (NNE-SSW). The LOP has distinct facies: 1) Lamas de Olo (LO), the more representative, is a medium to coarse-grained porphyritic biotite granite; 2) Barragem (BA) a leucocratic fine-grained and slightly porphyritic granite; 3) Alto dos Cabeços (AC) a medium to fine-grained porphyritic biotite granite [2], [3]. The LOP granites intrudes the Douro Group metasediments (Precambrian to Cambrian in age) and two-mica syntectonic granites from Vila Real Massif (Figure 1) [2]. The studied area belongs to the "Northern mineralogenic province" [4] and W (Mo) occurrences are present [2].

MATERIALS AND METHODS

At each site of sampling, four or five oriented cores (25 mm in diameter and 60 to 70 mm in length) were collected *in situ* with a portable drill machine. Then, each core was sawed in two (eventually three) 22 mm long specimens. At least three (or more), specimens per station were obtained for magnetic susceptibility measurements.

Oriented cores were used to obtain oriented thick sections for petrographic and metallographic studies (LM1, LM3, LM3V, LM5 and LM7) and polished sections for metallographic studies (LM13). These studies were carried out using the petrographic/ metallographic microscope at Department of Geosciences, Environment and Spatial Planning, Faculty of Sciences of University of Porto. The magnetic susceptibility (*Km*) study was based on 151 oriented cores from 26 sampling sites roughly distributed in the LOP (Figure 1).

The relationship between the magnetization induced in a material M and the external field H is defined as $M=KH$, where K is the magnetic susceptibility. Because M (per unit volume) and H have the same units, K is dimensionless (*e.g.* [5], [6]). The magnetic susceptibility reflects the mineral composition of the rock which can have a diamagnetic (*e.g.* quartz, feldspar), paramagnetic (*e.g.* biotite, muscovite or hornblende) or a ferromagnetic behaviour (*e.g.* magnetite or hematite).

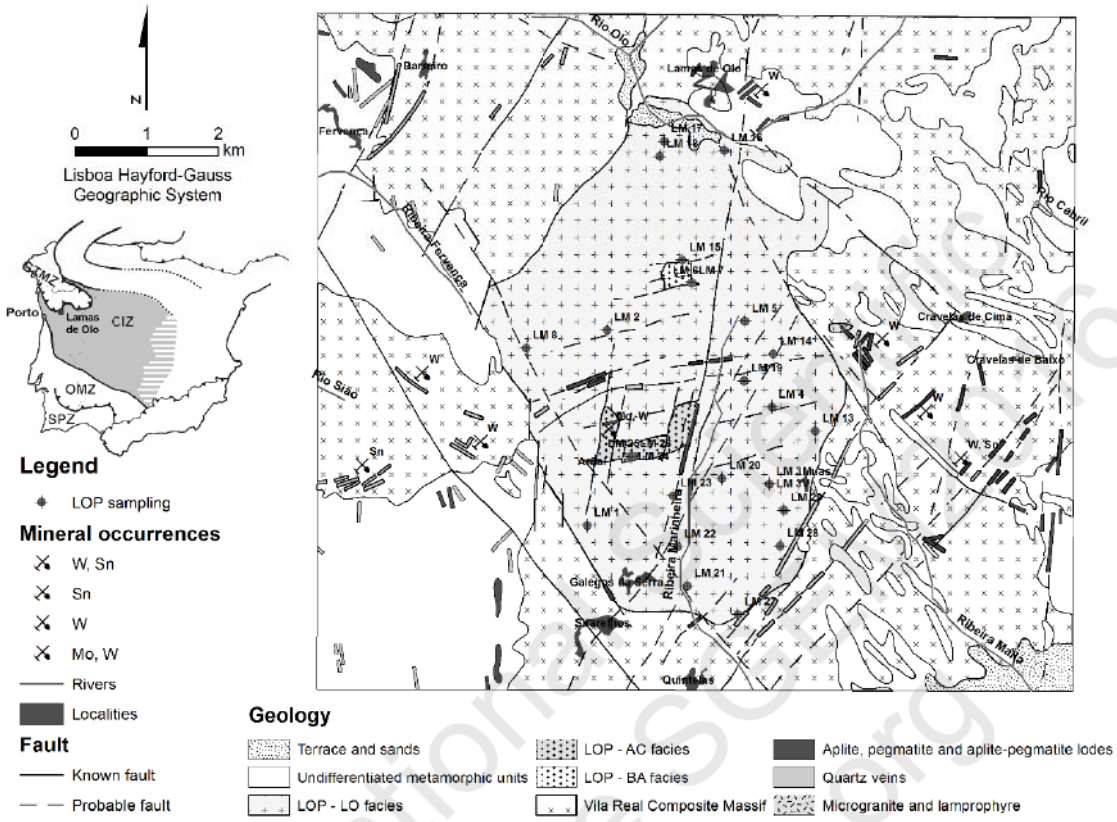


Figure 1. Simplified geological map of the Lamas de Olo Pluton and sampling sites for AMS and petrographic studies.

K measurements were performed using a KLY-4S Kappabridge susceptometer Agico model (Czech Republic) from the Institute of Earth Sciences – Porto. For each site, the ANISOFT 4.2 program package (www.agico.com) enabled us to calculate the mean susceptibility *Km*, which is the mean of the individual arithmetic means (k_{max} + k_{int} + k_{min})/ 3.

PETROGRAPHIC STUDIES

The petrographic studies were made in six samples, five from LO facies (LM1, LM3, LM3V, LM5 and LM13) and one from BA facies (LM7).

The LO facies corresponds to a porphyritic biotite granite medium to coarse-grained and BA facies to a fine-grained and slightly porphyritic biotite granite. In LO facies, can also occur reddish color and fine to medium-grain size zones, related to late hydrothermal alterations also occurring in Gerês pluton [7]. The AC facies is porphyritic and has medium to fine-grain.

The LOP granites present as primary accessory minerals, biotite, apatite, zircon, sphene, allanite, magnetite and/or hematite, ilmenite, fluorite and tourmaline. As secondary minerals, contains muscovite, chlorite, epidote and rutile (Figure 2). In the BA facies the muscovite is more abundant than in LO but is of secondary origin as a result of the biotite alteration.

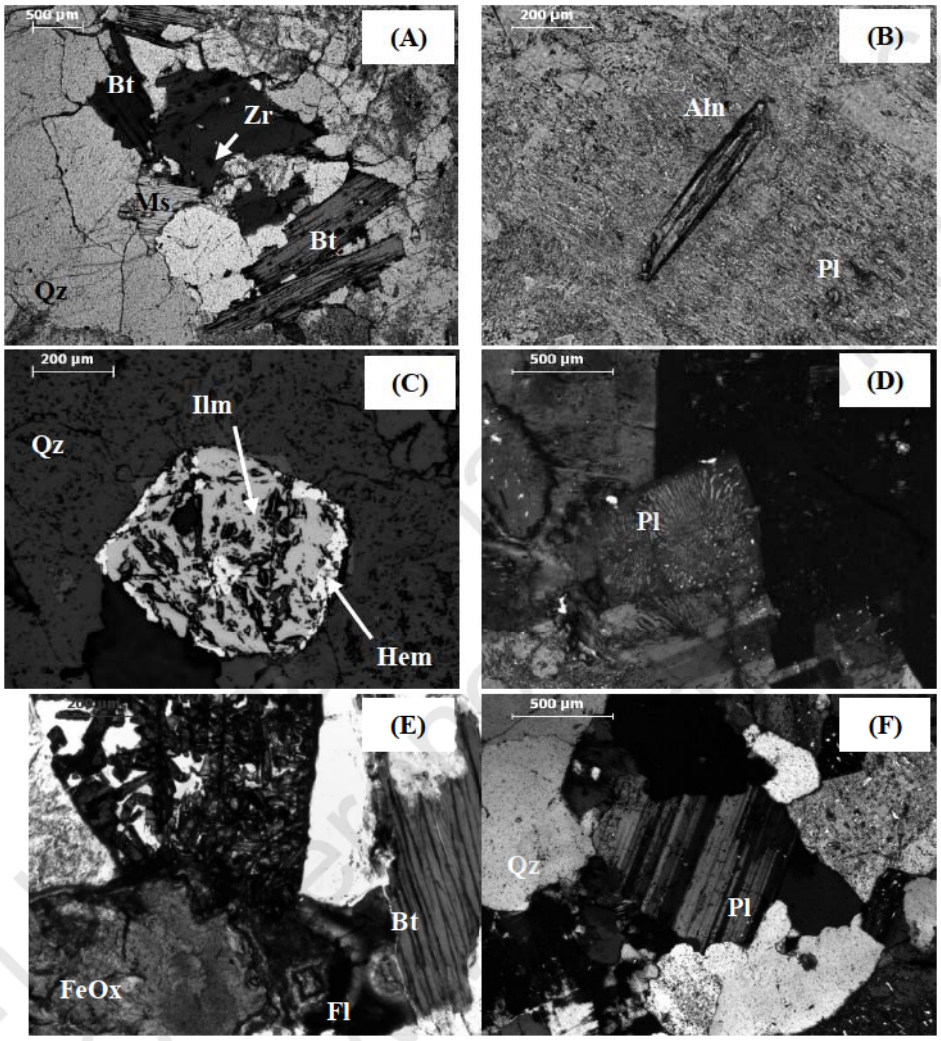


Figure 2 - Photomicrographs of Lamas de Olo Pluton: (A), (B) and (C) LO facies (LM1; under parallel polars); (D) LO facies (LM5; under crossed polars); (E) BA facies (LM7; under parallel polars); (F) BA facies (LM7; under crossed polars).

PETROPHYSICS EVIDENCES

The magnetic susceptibility (*Km*) values in LOP are heterogeneous and range between 11 and 92100 × 10^{-6} SI in LO facies, 22 and 51 × 10^{-6} SI in BA, and 135 and 905 × 10^{-6} SI in AC facies. The mean values is 3116 × 10^{-6} SI in LO, 29 × 10^{-6} SI in BA and 403 × 10^{-6} SI in AC facies (Table 1). The high *Km* values (>10^{-3} SI) indicate a ferromagnetic behavior, due to the presence of iron minerals, such as magnetite. In the other hand the

low *Km* (around 10^{-6} SI) values indicate the presence of paramagnetic minerals, like ilmenite and biotite.

Table 1 - Magnetic susceptibility data for the sampling sites. *Km*: mean magnetic susceptibility in 10^{-6} SI; *N*: number of specimens.

Sampling sites	Lithology	Km × 10^{-6} SI	N
LM 1	LO	174	15
LM 2	LO	1848	11
LM 3	LO	2475	8
LM 3V	LO	316	3
LM 4	LO	65	8
LM 5	LO	2873	6
LM 6	LO	229	8
LM 7	BA	34	10
LM 8	LO	1677	4
LM 13	LO	44382	9
LM 14	LO	2179	8
LM 15	BA	24	8
LM 16	LO	67	8
LM 17	LO	77	5
LM 18	LO	79	5
LM 19	LO	1869	8
LM 20	LO	2760	6
LM 21	LO	233	9
LM 22	LO	606	8
LM 23	LO	254	7
LM 24	AC	239	7
LM 25	AC	167	9
LM 26	AC	804	8
LM 27	LO	69	6
LM 28	LO	2065	10
LM 29	LO	1147	8

The distribution of the *Km* values for the all pluton is present in figure 3, showing that the two types of magnetic behavior are present in the same pluton, mainly in the eastern part of the pluton.

16th International Scientific GeoConference SGEM2016 www.sgem.org

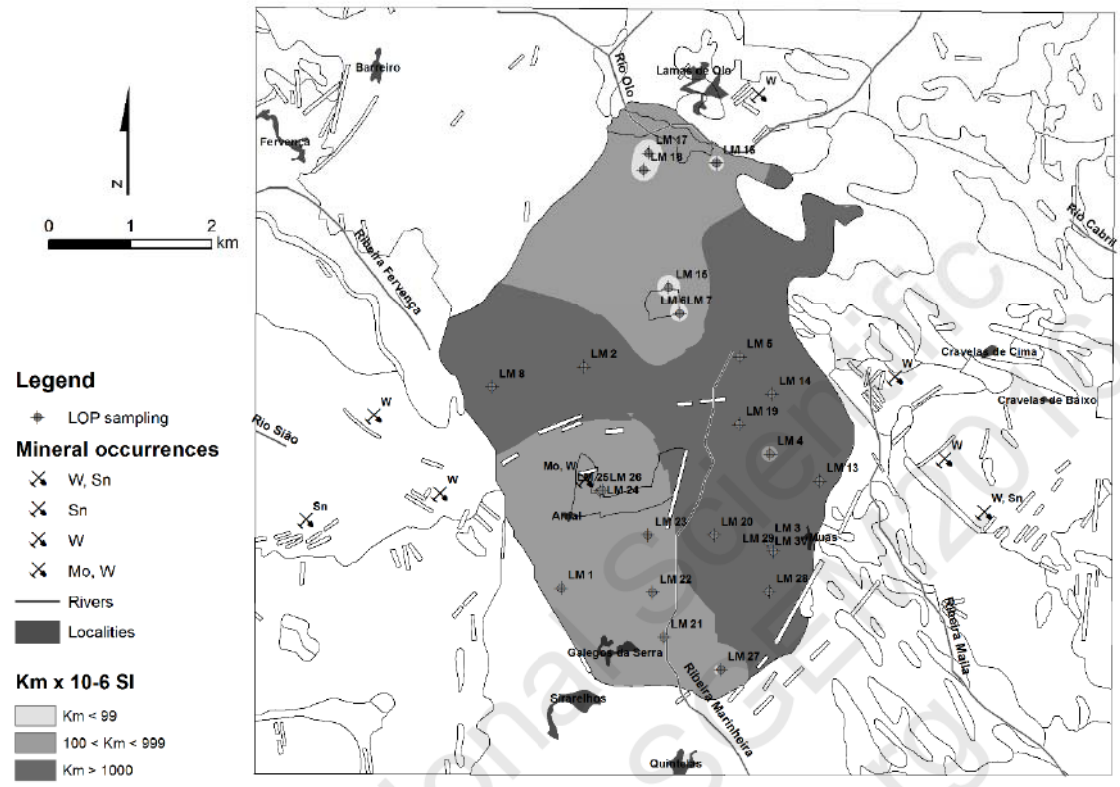


Figure 3. Map of the magnetic susceptibility (*Km*) values in LOP facies (ArcGIS software interpretation).

DISCUSSION AND CONCLUSION

According to Ishihara [7] [8], the oxidation state of magmas controls the nature of many ore elements and indicates the presence of certain oxide accessory mineral phases, the magnetite- and ilmenite- bearing series corresponding to oxidized- and reduced-type, respectively.

Our results show the presence of ilmenite and magnetite granites in the same pluton. The association between granites with different magnetic behavior in the same pluton is not present in other similar post-tectonic plutons such as Vila Pouca de Aguiar (VPA) and Águas Frias-Chaves (AFC; Figure 4), also emplaced along Verin-Régua-Penacova Fault [9]. These plutons are very similar to LOP, either in geochemistry or in geochronology characteristics, but they are ilmenite-type granites and we do not find related mineralizations. On the other hand, LOP exhibits two type of granites (ilmenite- and magnetite-type) and we find W (Mo) occurrences spatially associated. The presence of magnetite in LOP reflects melt oxidized conditions, which can play and important role on the genesis of W (Mo) mineralizations.

This relationship between magnetite-type granites and W (Mo) mineralizations was also found in the post-tectonic (280 Ma) Gerês pluton (Figure 4) [7]. Comparing several similar post-tectonic granite plutons occurring in Northern Portugal (Lamas de Olo, Gerês, Vila Pouca de Aguiar and Águas Frias-Chaves), our study point out the importance between melt oxidized/reduced conditions and the metallogenic potential of the granites.

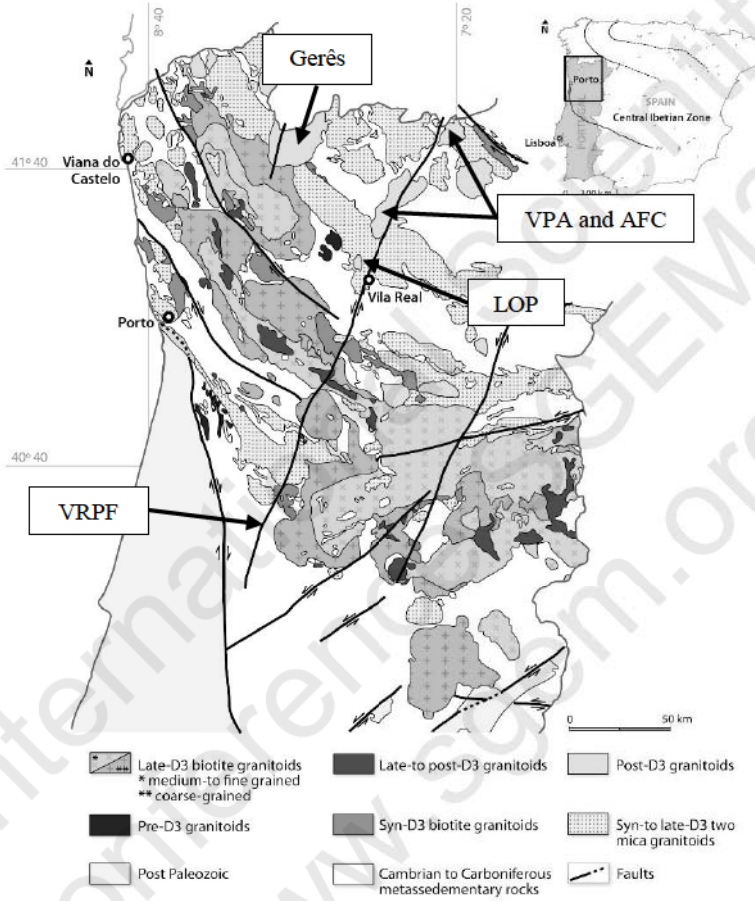


Figure 4. Distribution of Variscan granitoids in Northern Portugal ([11] modified).

16th International Geoscientific GeoConference SGEM2016 www.sgem.org

ACKNOWLEDGEMENTS

The first author is financially supported by SFRH/BD/109693/2015 (FCT Portugal). The authors acknowledge the funding by COMPETE 2020 through the ICT project (UID / GEO / 04683/2013) with POCI-01-0145 reference - FEDER-007690 and by NewOres (ERAMIN Project).

REFERENCES

[1] Ribeiro, A., Pereira, E., Dias, R., Structure of the Northwest of the Iberian Peninsula. In: Pre-Mesozoic Geology of Iberia (Eds. R.D. Dallmeyer & E. Martinez Garcia), pp. 220-236. Springer-Verlag, 1990.

[2] Pereira, E., Carta Geológica de Portugal à escala 1:50 000. Notícia Explicativa da Folha 10-A (Celorico de Basto). Serv. Geol. Portugal, 53 pp, 1989.

[3] Fernandes, S., Gomes, M., Teixeira, R., Corfu, F., Geochemistry of biotite granites from the Lamas de Olo Pluton, northern Portugal. Geophysical Research Abstracts, EGU General Assembly, vol. 15, 2013.

[4] Thadeu, D., "Carta Mineira de Portugal", 1/500000. Noticia explicativa. Serv. Geol. Lisboa, Portugal, 1965.

[5] Hrouda F., Magnetic anisotropy of rocks and its application in geology and geophysics. Geophysical Surveys 5, 37-82, 1982.

[6] Bouchez J.L., Granite is never isotropic: an introduction to AMS studies of granitic rocks. In: Granite: from melt to emplacement fabrics (Eds. J.L. Bouchez, D.H.W. Hutton & W.E. Stephens), pp. 95-112. Kluwer Academic Publishers, Dordrecht, 1997.

[7] Jaques L., Noronha F., Clauer N., Bobos I., Liewig N., Paleofluids circulation associated with the Gerês late-orogenic granitic massif, Northern Portugal. Chemie der Erde. 2016.

[8] Ishihara, S., The Magnetite-series and Ilmenite-series Granitic Rocks. Mining Geology, 27, 292-305, 1977.

[9] Ishihara, S., The granitoid series and mineralization. Economic Geology 75th Anniversary, 458-484. 1981.

[10] Martins, H.C.B., Sant'Ovaia, H., Noronha, F., Genesis and emplacement of felsic Variscan plutons within a deep crustal lineation, the Penacova-Régua-Verín fault: an integrated geophysics and geochemical study (NW Iberian Peninsula). Lithos: 111 (3-4), 142-155. 2009.

[11] Ferreira, N., Iglesias, M., Noronha, F., Pereira, E., Ribeiro, A., Ribeiro, M.L., Granitóides da Zona Centro Ibérica e seu enquadramento geodinâmico. In: F. Bea, A. Carnicero, J.C. Gonzalo, M. López Plaza & M.D. Rodríguez Alonso (eds.). Geologia de los granitoides y rocas asociadas del Macizo Hespérico. Ed. Rueda, Madrid, 37-51, 1987.

16th International Scientific GeoConference SGEM2016 www.sgem.org